Les Rencontres de Physique de la Vallée d'Aoste

Results and Perspectives in Particle Physics

Edited by M. Greco

La Thuile, Aosta Valley *4-10 March, 2007*

INFN
ISTITUTO NAZIONALE DI FISICA NUCLEARE
Laboratori Nazionali di Frascati

Les Rencontres de Physique de la Vallée d'Aoste

Results and Perspectives in Particle Physics

FRASCATI PHYSICS SERIES

Series Editor
Stefano Bianco

Technical Editor
Luigina Invidia

Volume XLIV — Special Issue

Istituto Nazionale di Fisica Nucleare – Laboratori Nazionali di Frascati
Divisione Ricerca – SIS – Ufficio Pubblicazioni
P.O. Box 13, I–00044 Frascati (Roma) Italy
email: sis.publications@lnf.infn.it

FRASCATI PHYSICS SERIES

Les Rencontres de Physique de la Vallée d'Aoste
RESULTS AND PERSPECTIVES IN PARTICLE PHYSICS

Copyright © 2007, by INFN Laboratori Nazionali di Frascati
SIS – Ufficio Pubblicazioni

All rights reserved. No part of this publication may be reproduced, stored in a retrieval system or transmitted, in any form or by any means, electronic, mechanical, photocopying, recording or otherwise, without the prior permission of the copyright owner.

ISBN—978–88–86409–49–4

Printed in Italy by Poligrafica Laziale
P.le della Stazione 1
00044 Frascati

FRASCATI PHYSICS SERIES

Volume XLIV

Les Rencontres de Physique de la Vallée d'Aoste

Results and Perspectives in Particle Physics

Editor
Mario Greco

La Thuile, Aosta Valley, March 4–10, 2007

Conference Organizers

Giorgio Bellettini	*Pisa*
Giorgio Chiarelli	*Pisa*
Mario Greco	*Roma III*

List of Chairpersons

Barbaro-Galtieri Angela	*LBL*
Bellettini Giorgio	*Pisa*
Castaldi Rino	*Pisa*
Chiarelli Giorgio	*Pisa*
Ferroni Fernando	*Roma*
Finley David	*Fermilab*
Flügge Günter	*Aachen*
Greco Mario	*Roma III*
Heusch Clemens	*Santa Cruz*
Khuri Nicola	*New York*
Mannocchi Giampaolo	*Frascati*
Tenchini Roberto	*Pisa*
Vysotsky Mikhail	*Moscow*
Womersley John	*RAL*

FOREWORD

The 2007 Rencontres de Physique de la Vallée d'Aoste were held at the Planibel Hotel of La Thuile, Aosta Valley, on March 4–10, with the twenty–firsth edition of "Results and Perspectives in Particle Physics".

The physics programme included various topics in particle physics, also in connection with present and future experimental facilities, as cosmology, astrophysics and neutrino physics, CP violation and rare decays, electroweak and hadron physics with e^+e^- and hadron colliders, heavy flavours and prospects at future facilities.

The Session on "Physics and Society" included special colloquia on Nanotechnology, Plans to produce "Clean Energy" and Tsunamis.

We are very grateful to Ari Aviram, Ennio Macchi and Emile Okal for their participation..

Giorgio Bellettini, Giorgio Chiarelli and I should like to warmly thank the session chairpersons and the speakers for their contribution to the success of the meeting.

The regional government of the Aosta Valley, in particular through the Minister of Public Education and Culture Laurent Vierin, has been very pleased to offer its financial support and hospitality to the Rencontres of La Thuile. Also on behalf of the participants, representatives of some major Laboratories and Institutes in the world, we would like to thank all the Regional Authorities. Special thanks are also due to Bruno Baschiera, local coordinator of the Rencontres.

We are grateful to the President of INFN Roberto Petronzio, the Directors of INFN Laboratori Nazionali di Frascati, Mario Calvetti and INFN Sezione di Pisa, Rino Castaldi, for the support in the organization of the Rencontres. We would like to thank also Paolo Caponera, Lucia Lilli, Donatella Pierluigi, Claudia Tofani and Paolo Villani for their help in both planning and running the meeting. We are also grateful to

Alessandra Miletto for her valuable contribution to the local organization of the meeting. The excellent assistance provided by Giovanni Nicoletti and Mauro Giannini made it possible to set up the computer link to the international network. Special thanks are due to Luigina Invidia for valuable help in the technical editing of the Proceedings.

Finally we would like to thank the Mayor Gilberto Roullet and the local authorities of La Thuile and the "Azienda di Promozione Turistica del Monte Bianco" for their warm hospitality, and the Planibel Hotel staff for providing us an enjoyable atmosphere.

September 2007 Mario Greco

CONTENTS

SESSION I – COSMOLOGY, ASTROPARTICLE AND NEUTRINO PHYSICS

- *Alexander Dolgov* — Cosmological Charge Asymmetry and Rare Processes in Particle Physics
- *Licia Verde* — Cosmology from the CMB, 15 years after COBE
- *Rodriguez Frias M. Dolores* — Cosmological Charge Asymmetry and Rare Processes in Particle Physics
- *Gennaro Miele* — Footprint of Large Scale Cosmic Structure on the UHECR and Gammas
- *Alvaro De Rujula* — What is being learned on the nature of the Universe
- *Arnon Dar* — SN1987A – 20 Years later
- *Vyacheslav Dokuchaev* — Dark Matter Annihilation in the Clumpy Galactic Halo
- *Jan Conrad* — Searches for Particle Dark Matter with the GLAST Large Area Tetescope
- *Piergiorgio Picozza* — Recent Results from Pamela
- *Seon-Hee Seo* — IceCube: Neutrino Telescope at the South Pole
- *Else De Wolf* — Antares Opens its Eyes
- *Christopher Mauger* — Measuring $\sin^2 2\Theta_{13}$ at the Daya Bay Reactor Neutrino Experiment
- *Dario Autiero* — Recent Results from Opera
- *Niki Saolidou* — Recent Results from Minos
- *Christos A. Eleftheriadis* — Search for Solar Axions in the CAST Experiment at CERN
- *Alexander Studenikin* — Polarization Properties of Spin Light of Electron in Matter

COSMOLOGICAL CHARGE ASYMMETRY AND RARE PROCESSES IN PARTICLE PHYSICS

A.D. Dolgov
Istituto Nazionale di Fisica Nucleare, Sezione di Ferrara, I-44100 Ferrara, Italy
Dipartimento di Fisica, Università degli Studi di Ferrara, I-44100 Ferrara, Italy
Institute of Theoretical and Experimental Physics, 113259, Moscow, Russia

Abstract

Two scenarios of low temperature baryogenesis in theories with TeV scale gravity are discussed. It is argued that strong gravity at TeV energies is very favorable for baryogenesis. In both scenarios the proton decay is either absent or suppressed far below existing bounds. On the other hand, neutron-antineutron oscillations are at the verge of discovery. Some other rare decays with non-conservation of lepton or baryon numbers are predicted.

It is experimentally established that neither baryonic nor individual leptonic numbers are conserved. Neutrino oscillations are known to mix electronic, muonic, and tauonic neutrinos, resulting in nonconservation of all these quantum numbers. On the other hand, astronomy proves that baryon number is not conserved. One can say that since we exist, baryons are not forever. Indeed a suitable for life universe canot be created if baryonic charge were conserved. The chain of arguments goes as follows. First, the asronomical data strongly suggest that inflation is an "experimental" fact. There are many reasons to believe that this is true:

1. We do not know any other way to make the observed universe.
2. It explains the origin of expansion.
3. It solves the problems of homogeneity, isotropy, flatness and predicts $\Omega = 1$.
4. Inflation creates density perturbations with the observed spectrum.

The next important statement is that inflation is impossible with conserved baryons. Inflation could be realized if the total cosmological energy density is (almost) constant. However, if baryons are conserved the energy density might stay constant at most during 4-5 Hubble times, while for successful inflation at least 60 Hubble times are necesary. For more details see e.g. review [1].

If baryon and lepton quantum numbers are not conserved one should expect this nonconservation to manifest itself in particle physics. The well known phenomena searched for are the following: unstable proton, $(n - \bar{n})$-oscillations, some rare decays, as e.g. $\mu \to e\gamma$, and similar decays of heavier quarks with B or L nonconservation. Yet nothing is observed. Though cosmology predicts non-conservation of baryons and consequently a manifestation of this nonconservation in particle physics, the magnitude of such effects is expected to be very small or, at best, unknown because the energy scale of cosmological baryogenesis is normally much higher than that available in terrestrial experiments and, what's more, there is usually no direct relation between physics of baryogenesis and proton decays or neutron-antineutron oscillations.

Here we will discuss some new scenarios of baryogenesis which explain the observed baryon asymmetry of the universe and lead to observable consequences in particle physics. My talk is based on the works made in collaboration with F. Urban [2] and C. Bambi and K, Freese [3, 4].

Let us first consider a rather conservative scenario based on SUSY with broken $\mathcal{R}$-parity . The operators which break $\mathcal{R}$-parity and experimental bounds on their coupling constants are enumerated e.g. in review [5]. Cosmological baryogenesis in this model could proceed through B-nonconserving decays of massive SUSY particles induced by B-nonconserving $\mathcal{R}$-parity vio-

lating operators. If masses of supersymmetric particles are not very large, e.g. $M_{SUSY} \sim$ TeV, deviations from thermal equilibrium in the standard cosmology are negligible:

$$\frac{H}{\Gamma} \sim \frac{M_{SUSY}}{\alpha m_{Pl}} \sim 10^{-14}, \tag{1}$$

where $\alpha \sim 10^{-2}$ is the coupling constant. The baryon asymmetry would be further suppressed at least by factor α because CP-violation manifests itself only in higher orders of perturbation theory.

To obtain a reasonable baryon asymmetry the scale of supersymmetry must be very high:

$$M_{SUSY} \geq 10^{10} \text{ GeV} \tag{2}$$

However, in this case effects in particle physics would be unnoticeable.

A possible solution which allows both for successful baryogenesis and for nonnegligible effects in particle physics is offered by TeV scale gravity.

There are two known mechanisms for TeV gravity:

1. Gravity lives in higher dimensional space, while matter lives in $D = 4$ [6].
2. Time variation of m_{Pl} due to the coupling $\xi R\phi^2$ [7]. It is assumed that initially (in the early universe) $\phi \sim$ TeV, and later, but prior to nucleosynthesis, it rises up to the Planck value 10^{19} GeV.

Both these possibilities are practicaly equally good for cosmological baryogenesis but in the first case care should be taken on the potential problems with light gravitinos [8].

Essential $\mathcal{R}$-parity -violating operators have the form:

$$\mathcal{L}_{int} = \frac{1}{2}\lambda^{ijk}\left(\tilde{u}_i^*\,\bar{d}_j\,d_i^c \;+\; \tilde{d}_k^*\,\bar{u}_i\,d_j^c \;+\; \tilde{d}_j^*\,\bar{u}_j\,d_k^c\right) + h.c., \tag{3}$$

where i, j, k are the flavor indices and u and d are respectively operators of up and down quarks, tidle denotes a superpartner, and λ^{ijk} is a Yukawa type coupling constant. The color indices are suppressed. These operators do not conserve baryonic charge, B, by one unit and conserve leptonic charge, L. Correspondingly proton decay is forbidden but transformations of baryon into antibaryon and, in particular, neutron-antineutron oscillations are allowed. Such transformations inside a nuclei would lead to an energetic annihilation and nuclear decay. Correspondingly experimental bounds on nuclear stability allow to put quite strong constraint on some λ^{ijk}:

$$\lambda_{112} < 10^{-6}, \;\; \lambda_{113} < 10^{-3}, \tag{4}$$

while others could be even well above unity.

Non-zero λ_{112} would lead e.g. to $n\bar{\Xi}$ - transformation. To make $n\bar{n}$ oscillations out of it a $\Delta S = 2$ process is necessary. It is strongly suppressed in MSM but possibly not so much in a supersymmetric extension, in particular in minimal supersymmetric model, MSSM.

The diagramm which induces $\bar{n} - n$ transformation through $\Delta S = 2$ processes has the form:

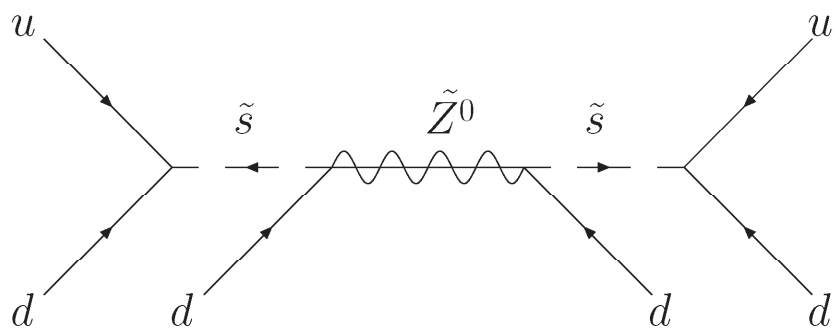

Notice that strangeness non-conserving decays of zino, e.g. $\tilde{Z} \to \bar{u}\tilde{s}$, are allowed, while similar decays of Z-boson, not $Z \to \bar{u}s$, are not. Both successful baryogenesis and $n\bar{n}$ - transformation just above the experimental limit might take place. For more detail see ref. [2].

Much more exotic possibility was put forward in refs. [3, 4] in the frameworks of TeV gravity. The latter is known to suffer from a serious problem related to nonconservation of all global quantum numbers. The idea is basically that some (one or a few) particles, possessing non-zero baryonic, leptonic, or any other global charges, may form a very dense state inside their common gravitational radius. In other words, they would form a small virtual black hole. As is well known, black holes may have "hairs" associated only with conserved quantum numbers related to local (gauge) symmetries, as e.g. electric charge. On the other hand, if a black hole swallows particles with non-zero leptonic, L, or baryonic, B, charges, it immediately "forgets" about these charges and may decay into some state with zero or any other values of B or L. This was first observed by Zeldovich [9], who estimated the life-time of proton due to formation and decay of a virtual black hole:

$$\tau_p \sim m_{Pl}^4/m_p^5 \sim 10^{45} \text{ years} \tag{5}$$

This is by far larger than the existing experimental bound $\tau_p > 10^{33}$ years.

But if $m_{Pl} \sim$ TeV, $\tau_p \sim 10^{-11}$ s. Similar problems exist for $\mu \to e\gamma$ and other rare decays.

These difficulties for low scale gravity was discussed in ref. [10] where it was argued that the fundamental Planck mass should be much larger than TeV, up to 10^{16} GeV. In our recent works [3, 4] we made an attempt to resolve the problem of strong gravitational B and L nonconservation proposing the so called classical black hole conjecture, which "dynamically" forbids an easy formation of black holes (BH). This conjecture is based on the fact that classical charged and rotating black hole can only be formed if it is sufficiently heavy:

$$\left(\frac{M_{BH}}{m_{Pl}}\right)^2 > \frac{Q^2}{2} + \sqrt{\frac{Q^4}{4} + J^2}, \tag{6}$$

where Q and J are respectively electric charge and angular momentum of BH. Formally it follows from this expression that if $M_{BH} < m_{Pl}$, the black hole can be only electrically neutral and non-rotating. The result (6) is valid for classical black holes and may be incorrect for quantum ones. However, physics of quantum black holes is unknown and one is free to make arbitrary and quite wild assumptions.

In addition to this conjecture of neutral and non-rotating BHs we impose some, maybe even more questionable, rules in calculations/estimates of the amplitude of reactions with broken global quantum numbers due to virtual BH. We assume essentially that virtual black holes could be formed only in s-channel with positive mass (energy) of the created black hole. Such an assumption and some of the rules which we use in what follows do not respect many usual conditions existing in quantum field theory, in particular crossing relations between amplitudes. For example, we allow a virtual BH to decay into, say, a proton and a electron, but we do not allow a proton to form a scalar BH plus a positron, with the same amplitude. The picture that we have in mind is a kind of time ordering: a BH could be formed in a collision of a neutral system of particles in the s-channel whereas a BH cannot be in the t-channel of a reaction. We assume that BHs can be formed out of positive energies of real particles only and not from virtual energies of particles in closed loops. For example, BH cannot be formed by vacuum fluctuations, despite the fact that, according to the standard picture, vacuum fluctuations might create a pair or more of virtual particles both with positive and negative energies. The mass of the BH should be of the order of the energy of incoming (or outgoing) particles. In an attempt to describe this in terms of the usual language we come to a version of the old non-covariant perturbation theory with all virtual particles having positive energies. It corresponds to the choice of only one mass-shell pole in

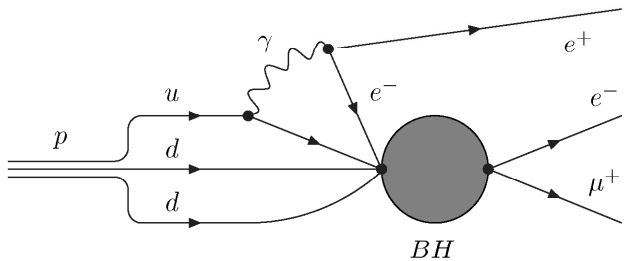

Fig. 1. Gravitationally induced proton decay through non-charged and nonrotating black hole.

the Feynman Green's functions. This rule allows only for BHs with masses which are of the order of the energies of the initial (or final) particles, as we postulated above. It may look very strange, to say the least, but virtual BHs are not well defined objects and we do not know what happens with space-time at the relevant scales. Taken literally these rules would lead to violation of some sacred principles of the standard theory (locality, Lorentz invariance, and more). Let us remind the reader, however, that the existing attempts in the literature to invoke virtual BHs are based on standard quantum field theory in a situation where it is almost surely inapplicable.

So it is not excluded that many properties of the standard field theory are broken, including even Lorentz invariance and locality. We cannot of course present any serious arguments in favor of our construction but it predicts quite impressive phenomena with clear signatures based on a very simple set of rules and if these effects are discovered, the approach, advocated here, may be taken more seriously. Our goal here is to formulate a reasonable(?) set of rules which may possibly describe processes with virtual BHs and are, at least, not self-contradictory. Based on these rules we study phenomenological consequences in particle physics, which are quite rich and may be accessible to experiments after a minor increase of accuracy.

The diagramm that, according to our conjecture, describes gravitationally induced proton decay is presented in fig. 1 Since a 4-body collision is required in order to form a BH devoid of any quantum number, the process is strongly suppressed and experimental constraints can be compatible even with the gravity scale in TeV range.

Similar graphs give rise to $\mu \to e\gamma$ - decay and other rare processess with violation of lepton flavor and baryonic numbers. The results of our calculations, according to ref. [3] are collected in Table 1, where the lower bound on the fundamental gravity scale is presented for different numbers, n, of extra dimensions.

Process	Experiment	M_*, $n = 2\,(7)$
$p \to eee$	$\tau > 10^{33}$ yr	> 2 (8)
$\mu \to \gamma e$	$BR < 10^{-11}$	> 1 (10)
$\mu \to eee$	$BR < 10^{-12}$	> 1 (10)
$K \to \mu e$	$BR < 10^{-12}$	> 3 (4)
$K \to \pi\mu e$	$BR < 10^{-10}$	> 1 (1)
$n \leftrightarrow \bar{n}$	$\tau > 10^{8}$ s	> 1 (3) (MSSM)

Thus we see that TeV scale gravity does not lead to contradiction with experiment if the condition that virtual BH should have positive mass and be electrically neutral and non-rotating, is fulfilled.

TeV scale gravity allows also for succesful, even quite efficinet, baryogenesis at relatively low temperatures [4]. All three Sakharov conditions:
1) baryon non-conservation,
2) deviation from thermal equilibrium,
3) large CP-violation in MSM,
are much easier fulfilled than in the standard case.

Let us start from CP-violation. It is well known that CP-breaking in the minimal standard model (MSM) is extemely weak. The amplitude of CP-violation is known to be proportional to the mass differences of all quark families and their mixing angles, for detials see e.g. [11]:

$$\epsilon_{CP} \approx (m_t^2 - m_c^2)(m_t^2 - m_u^2)(m_c^2 - m_u^2)$$
$$(m_b^2 - m_s^2)(m_b^2 - m_d^2)(m_s^2 - m_d^2)\,(J/T^{12}) \qquad (7)$$

where

$$J = \cos\theta_{12}\cos\theta_{23}\cos^2\theta_{13}\sin\theta_{12}\sin\theta_{23}\sin\theta_{13}\sin\delta_{CP} \approx 3\cdot 10^{-5}.$$

Thus $\epsilon_{CP} \sim 10^{-19}$ at $T \sim 100$ GeV. At lower temperatures the B-nonconserving sphaleron processes are exponentially suppressed and one cannot expect baryon-to-photon ratio larger than 10^{-20}, while the observed value is $\sim 5\cdot 10^{-10}$.

Low scale gravity models lead to nonconservation of baryonic charge at much lower, than 100 GeV, temperatures because nonconservation of B takes place simply in decays of heavy quarks and non-perturbative sphalerons are unnecessary. According to the estimates of ref. [4], non-conservation of baryons remains significant even at $T \leq 10$ GeV and the amplitude of CP-violation (7) becomes 12 orders of magnitude larger.

One may avoid any suppression of CP violation at high temperatures if time variation of quark masses is allowed [12, 4]. In this case both mixing angles and quark mass differences can be large in the early universe.

Deviation from thermal equilibrium would be unsuppressed as it follows from eq. (1) with $m_{Pl} \sim$ TeV.

So to conclude:

1. Low scale gravity allows for much more efficient baryogenesis than the standard model.
2. In conservative SUSY model with broken $\mathcal{R}$-parity successful baryogenesis may proceed with (practically) stable proton and with noticeable neutron-antineutron oscillations.
3. The classical black hole conjecture makes compatible TeV gravity and low probability of B and L nonconserving processes.
4. The probability of such rare processes can be quite close to the existing experimental bounds.

References

1. A. D. Dolgov, Phys. Repts. **222**, 309 (1992).
2. A.D. Dolgov, F. Urban Nucl. Phys. B752 (2006) 297,
3. C. Bambi, A.D. Dolgov, K, Freese, Nucl. Phys. B763 (2007) 91.
4. C. Bambi, A.D. Dolgov, K, Freese, JCAP 0704 (2007) 005.
5. R. Barbier *et al.*, Phys. Rept. 420 (2005) 1.

6. N. Arkani-Hamed, S. Dimopoulos, G. Dvali, Phys. Lett. B 429 (1998) 263; I. Antoniadis, N. Arkani-Hamed, S. Dimopoulos and G. Dvali, Phys. Lett. B 436 (1998) 257;
For a review see:
A. Pérez-Lorenzana, J. Phys. Conf. Ser. 18 (2005) 224;
I. Antoniadis, CERN-PH-TH-2005-249, hep-ph/0512182.

7. T. Biswas, A. Notari, Phys.Rev. D74 (2006) 043508.

8. See e.g. C. Bambi, F.R. Urban, e-Print: arXiv:0705.4227 [hep-ph], arXiv:0705.2176 [hep-ph] and references therin.

9. Ya.B. Zeldovich, Phys. Lett. A 59 (1976) 254; Zh. Eksp. Teor. Fiz. 72 (1977) 18.

10. F.C. Adams, G.L. Kane, M. Mbonye, M.J. Perry, Int. J. Mod. Phys. A 16 (2001) 2399.

11. A.D. Dolgov, Lectures given at International School of Physics "Enrico Fermi": CP Violation: From Quarks to Leptons, Varenna, Italy, 19-29 Jul 2005. e-Print: hep-ph/0511213.

12. M. Berkooz, Y. Nir and T. Volansky, Phys. Rev. Lett. 93 (2004) 051301.

COSMOLOGY FROM THE CMB, 15 YEARS AFTER COBE

Licia Verde
Madrid, Spain

Written contribution not received

COSMOLOGICAL CHARGE ASYMMETRY AND RARE PROCESSES IN PARTICLE PHYSICS

Rodriguez Frias María Dolores
Madrid, Spain

Written contribution not received

FOOTPRINT OF LARGE SCALE COSMIC STRUCTURE ON THE UHECR AND GAMMAS

Gennaro Miele
Napoli, Italy

Written contribution not received

AN INTRODUCTION TO COSMIC RAYS AND GAMMA-RAY BURSTS, AND TO THEIR SIMPLE UNDERSTANDING

Alvaro De Rújula
CERN & Boston University

Abstract

I review the subjects of non-solar cosmic rays (CRs) and long-duration gamma-ray bursts (GRBs). Of the various interpretations of these phenomena, the one best supported by the data is the following. Accreting compact objects, such as black holes, are seen to emit relativistic puffs of plasma: 'cannonballs' (CBs). The inner domain of a rotating star whose core has collapsed resembles such an accreting system. This suggests that core-collapse supernovae (SNe) emit CBs, as SN1987A did. The fate of a CB as it exits a SN and travels in space can be studied as a function of the CB's mass and energy, and of 'ambient' properties: the encountered matter- and light- distributions, the composition of the former, and the location of intelligent observers. The latter may conclude that the interactions of CBs with ambient matter and light generate CRs and GRBs, all of whose properties can be described by this 'CB model' with few parameters and simple physics. GRB data are still being taken in unscrutinized domains of energy and timing. They agree accurately with the model's predictions. CR data are centenary. Their precision will improve, but new striking predictions are unlikely. Yet, a one-free-parameter description of all CR data works very well. This is a bit as if one discovered QED today and only needed to fit α.

1 Introduction

This is a version of an introductory talk to high-energy physicists. Cosmic rays (CRs) were the first item in their field, and will remain the energy record-breakers for the foreseeable future. I shall argue that nothing 'besides the standard model' is required to understand CRs of any energy, subtracting from their interest. 'Long' gamma-ray bursts (GRBs) are flashes of mainly sub-MeV photons, originating in supernova (SN) explosions. The γ-rays are highly collimated. Hence, GRBs are not the publicized 'highest-energy explosions after the big bang', but more modest torches occasionally pointing to the observer. GRBs are of interest because their understanding is intimately related to that of CRs. It might have been more precise to say 'my understanding' of GRBs and CRs, for the work of my coauthors and I is viewed as unorthodox.

What a start! I have already admitted that our stance is not trendy and that the subject is of no post-standard interest. But our claims are based on clear hypothesis, which may be proven wrong, and very basic physics, which is precise enough, very pretty, understandable to undergraduates, and successful.

The information about GRBs and CRs is overwhelming. GRBs are known since the late 60's and CRs since 1912. Surprisingly, no theories have arisen that are both accepted ('standard') and acceptable (transparent, predictive and successful). I cannot refer to a representative subset of the $\sim 70+70$ kilo-papers on CRs and GRBs. For reviews of the standard views on CRs, see e.g. Hillas [1] or Hoerandel [2]. For the accepted 'fireball' model of GRBs see e.g. Meszaros [3] or Piran [4]. Fewer self-citations and many more references, particularly to data, appear in DDD02 [5], DDD03 [6], DD04 [7] and DD06 [8].

2 Most of what you may want to recall about Cosmic Rays

In CR physics 'all-particle' refers to nuclei: all charged CRs but electrons. The CR spectra being fairly featureless, it is customary to weigh them with powers of energy, to over-emphasize their features. The $E^3\,dF/dE$ all-particle spectrum is shown in fig. 1a, not updated for recent data at the high-energy tail. At less than TeV energies the CR flux is larger than $1\,\mathrm{m}^{-2}\,\mathrm{s}^{-1}\,\mathrm{sr}^{-1}$ and it is possible to measure the charge Z and mass number A of individual particles with, e.g., a magnetic spectrometer in a balloon, or in orbit. Some low-energy results for H and He are shown in fig. 1b. They vary with solar activity.

The CR fluxes of the lightest 30 elements at $E=1$ TeV (of a nucleus, not per-nucleon) are shown in fig. 2a, and compared with the relative abundances in the interstellar medium (ISM) of the solar neighbourhood. Elements such as Li, Be and B are relatively enhanced in the CRs, they result from collisional fragmentation of heavier and abundant 'primaries' such as C, N and O. Otherwise, the solar-ISM and CR Z-distributions are akin, but for H and He.

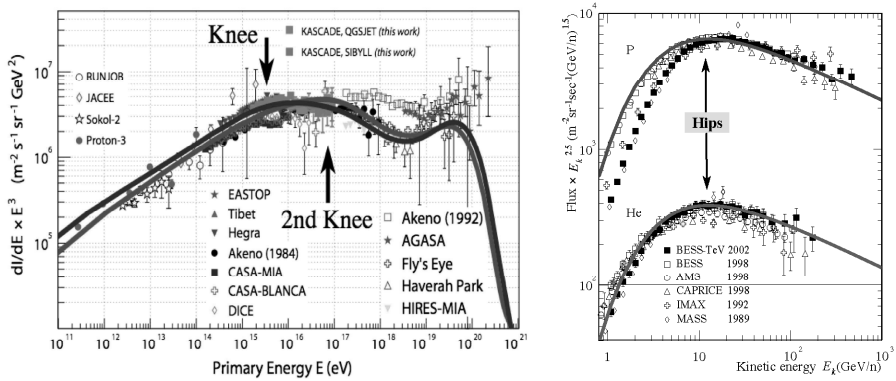

Figure 1: **Left (a)** The weighed all-particle CR spectrum $E^3\,dF/dE$. Some of the high-energy data disagree with others. **Right (b)** The low-energy H an He flux versus the kinetic energy per nucleon, multiplied by $E_{\rm kin}^{2.5}$. In (a) the lines are two extreme CB-model predictions. In (b) both lines are predictions. The data coincide best with the prediction at solar minimum. The normalizations, shown here to coincide with the data, are predicted to within a factor of ~ 3.

In fig. 2b the abundances relative to H of the CR primary elements up to Ni ($Z=28$) are plotted as blue squares. The stars are solar ISM abundances. CR positrons and antiprotons attract attention as putative dark matter products, but it is nearly impossible to prove that their fluxes are not entirely secondary.

The Galaxy has a complex magnetic-field structure with $B_{\rm G}=\mathcal{O}(1\,\mu{\rm G})$ and coherent domains ranging in size up to ~ 1 kpc, $\sim 1/8$ of our distance to the Galactic center. In such a field, a nucleus of $E\simeq p > Z\,(3\times 10^9)$ GeV would hardly be deflected. For $Z=1$, this energy happens to be the 'ankle' energy, at which the flux of fig. 1 bends up. CRs originating within the Galaxy and having $E > E_{\rm ankle}$ would escape practically unhindered. The CR flux does not bend *down* at that energy, thus the generally agreed conclusion that CRs above the ankle are mainly extragalactic. CRs of Galactic origin and $E < E_{\rm ankle}$ are 'confined', implying that their observed and source fluxes obey:

$$F_{\rm o} \propto \tau_{\rm conf}\, F_{\rm s}, \quad \tau_{\rm conf} \propto (Z/p)^{\beta_{\rm conf}}, \quad \beta_{\rm conf} \sim 0.6 \pm 0.1, \tag{1}$$

with $\tau_{\rm conf}$ a 'confinement time', deduced from the study of stable and unstable CRs and their fragments.

At $E = 10^6$-10^8 GeV the all-particle spectrum of fig. 1a bends in one or two 'knees'. The knee flux is too small to measure directly its energy and composition, which are inferred from the properties of the CR shower of hadrons, γ's, e's and μ's, initiated by the CR in the upper atmosphere. The results for H, He and Fe are shown in fig. 3. Note that even the same data leads to in-

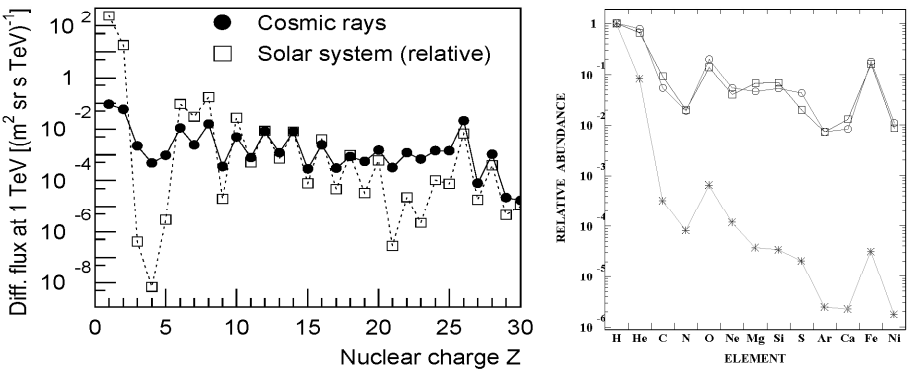

Figure 2: The CR fluxes at 1 TeV and the relative abundances in the ISM. **Left (a)** Fluxes of elements up to Z and abundances in the solar ISM. **Right (b)** Solar ISM abundances (stars), CR fluxes (squares) of the primary CRs, and the corresponding CB-model predictions (circles), all normalized to H.

compatible results, depending on the Monte-Carlo program used to analize the showers. But the spectra of the various elements seem to have 'knees' which scale roughly with A or Z, the data not been good enough to distinguish.

The high-E end of the E^3-weighed CR spectrum is shown in fig. 4a. These data and the more recent ones of HIRES and Auger, clearly show a cutoff, predicted by Greisen, Zatsepin and Kuzmin (GZK) as the result of the inevitable interactions of extragalactic CR protons with the microwave background radiation. The reactions $p+\gamma \to n+\pi^+$; $p+\pi^0$ cut off the flux at $E > E_{\rm GZK} \sim A \times 10^{11}$ GeV, from distances larger than tens of Mpc. Similarly, extragalactic nuclei of $E > 10^9$ GeV are efficiently photo-dissociated in the cosmic infrared radiation, the corresponding CR flux should not contain many.

At very high energies, rough measures of the CR A-distribution are extracted from the 'depth of shower maximum', X, the number of grams/cm^2 of atmosphere travelled by a CR shower before its $e^{\pm}/\gamma$ constituency reaches a maximum. At a fixed energy, X decreases with A, since a nucleus is an easily broken bag of nucleons of energy $\sim E/A$. As in fig. 4b, the data are often presented as $\langle ln[A](E)\rangle$, which approximately satisfies $X(A) \sim X(1) - x\, ln[A]$, with $x \sim 37$ grams/cm^2 the radiation length in air.

If CRs are chiefly Galactic in origin, their accelerators must compensate for the escape of CRs from the Galaxy, to sustain the observed CR flux: it is known from meteorite records that the flux has been steady for the past few Giga-years. The Milky Way's luminosity in CRs must therefore satisfy:

$$L_{\rm CR} = \frac{4\pi}{c} \int \frac{1}{\tau_{\rm conf}}\, E\, \frac{dF_{\rm o}}{dE}\, dE\, dV \sim 1.5 \times 10^{41}\ {\rm erg\ s^{-1}}\,, \qquad (2)$$

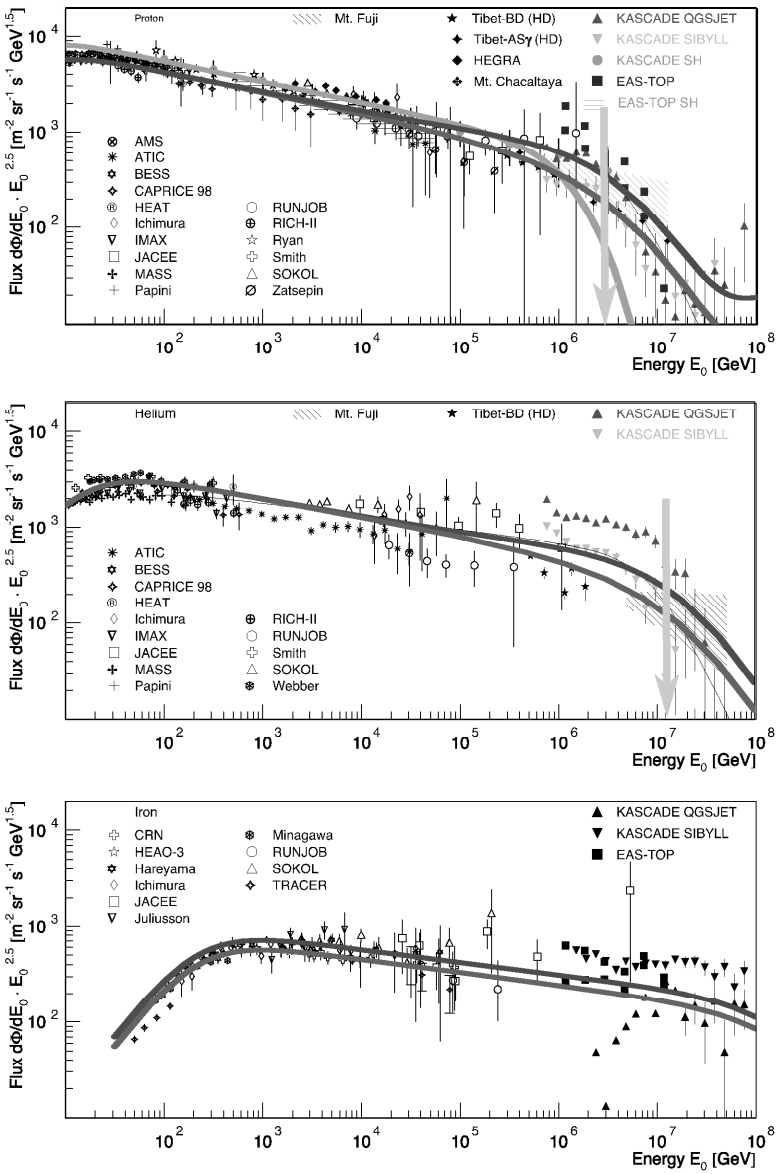

Figure 3: $E^{2.5}\,dF/dE$ CR spectra in the 'knee' region. Top: protons; middle: α particles; bottom: iron nuclei. The data ensemble was kindly provided by K.H. Kampert. The CB-model predictions are explained in the text. Notice the Fe 'hip', occurring at the same γ as the H, He hips of fig. 1b.

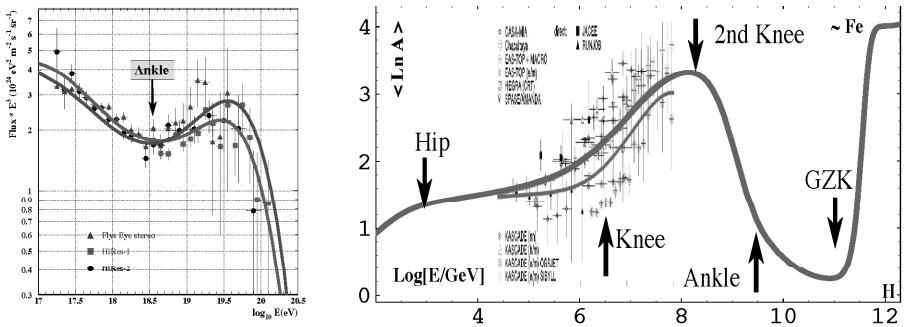

Figure 4: **Left (a)** The E^3-weighed CR flux at the highest observed energies. The data are not the oldest, nor the most recent, but show the currently observed trend. **Right (b)** The CR mean of the Neperian log of A, versus energy. In (a) the lines are two extreme CB-model predictions. The normalizations below and above the ankle, shown here to coincide with the data, are separately predicted to within a factor of $\sim$3. In (b) the lines are as in (a).

where V is a CR-confinement volume. The quoted standard estimate of $L_{\rm CR}$ is very model-dependent [10].

3 More than you ever wanted to know about Gamma-Ray Bursts

Two γ-ray count rates of GRBs, peaking at $dN/dt = \mathcal{O}(10^4)\,{\rm s}^{-1}$, are shown in fig. 5. The typical energy of the γ-ray of GBBs is $\sim$250 keV. The total *'isotropic equivalent'* energy of a source of such photons at a typical redshift, $z = \mathcal{O}(1)$, is $E_\gamma^{\rm iso} \sim 10^{53}$ erg, similar to the available energy in a core-collapse SN explosion, i.e. half of the binding energy of a solar-mass neutron star, maybe a bit more for a black-hole remnant. It is hard to imagine a process with $>1\%$ efficiency for γ-ray production. Since GRBs are observed to be made by SNe, either the parent stars are amazingly special, or the γ-rays are narrowly beamed.

The total-duration distribution of the γ-rays of GRBs has two peaks, with a trough at $\sim$2s dividing (by definition) two distinct types. 'Long' GRBs are more common and better measured than short ones; one is more confident discussing mainly the former, as I shall. The long GRB light curves of fig. 5 are not atypical. The 'pulses' of a given GRB vary in intensity, but have similar widths, a fairly universal exponential rise, and a power decay $\propto t^{-a}$, $a \sim 2$. The number of 'clear pulses' averages to $\sim$5, it may reach $\sim$12. The pulse-to-pulse delays are random, extending from $\mathcal{O}$(1s) to $\mathcal{O}(10^2{\rm s})$. Put all the above in a random-generator and, concerning long GRBs, 'you have seen them all'.

GRBs are not often seen more than once a day, they are baptized with

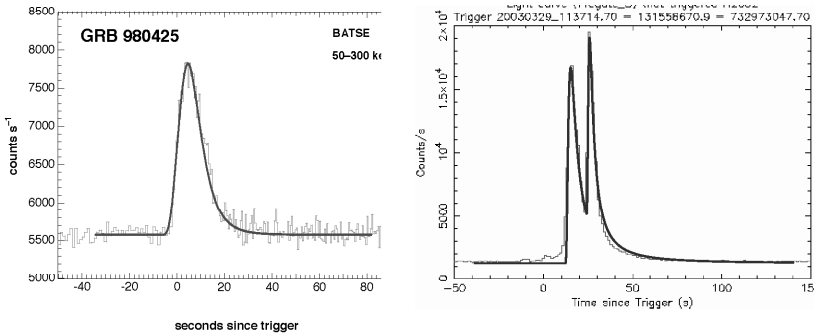

Figure 5: The γ-ray count-rate light curves of GRB 980425 (a: left) and GRB 030329 (b: right). In the CB model, each pulse corresponds to one cannonball. The single pulse in (a) and the two pulses in (b) are fit with Eq. 4.

their observation date. GRBs 980425 and 030329, shown in fig. 5, originated at $z = 0.0085$ (the record smallest) and 0.168, respectively. How are the redshifts known? GRBs have "afterglows" (AGs): they are observable in radio to X-rays for months after their γ-ray signal peters out. The AG of GRB 030329 in the 'R-band' (a red-light interval) and radio is shown in fig. 6a-c. Once the object is seen in optical or radio, its direction can be determined with much greater precision than via γ rays. Very often the source is localized within a galaxy, whose lines can be measured to determine z (in some cases a lower limit on z is deduced from absorption lines in intervening material).

GRB 980425 was *'associated'* with a supernova called SN1998bw: within directional errors and within a timing uncertainty of ~ 1 day, they coincided. The luminosity of a 1998bw-like SN peaks at $\sim 15\,(1+z)$ days. The SN light competes at that time and frequency with the AG of its GRB, and it is not always easily detectable. Iff one has a predictive theory of AGs, one may test whether GRBs are associated with 'standard torch' SNe, akin to SN1998bw, 'transported' to the GRBs' redshifts. The test was already conclusive (to us) in 2001 [5]. One could even foretell *the date* in which a GRB's SN would be discovered. For example, GRB 030329 was so 'very near' at $z = 0.168$, that one could not resist posting such a daring prediction [11] during the first few days of AG observations. The prediction and the subsequent SN signal are shown in fig. 6a,b. The spectrum of this SN was very well measured and seen to coincide snugly with that of SN1998bw, and this is why the SN/GRB association ceased to be doubted: *long GRBs are made by core-collapse SNe.*

Astrophysicists classify SNe in Types, mainly depending on the composition of their ejecta. Within very limited statistics the SNe associated with GRBs are of Type Ib/c. These constitute some 15% of core-collapse SNe, the

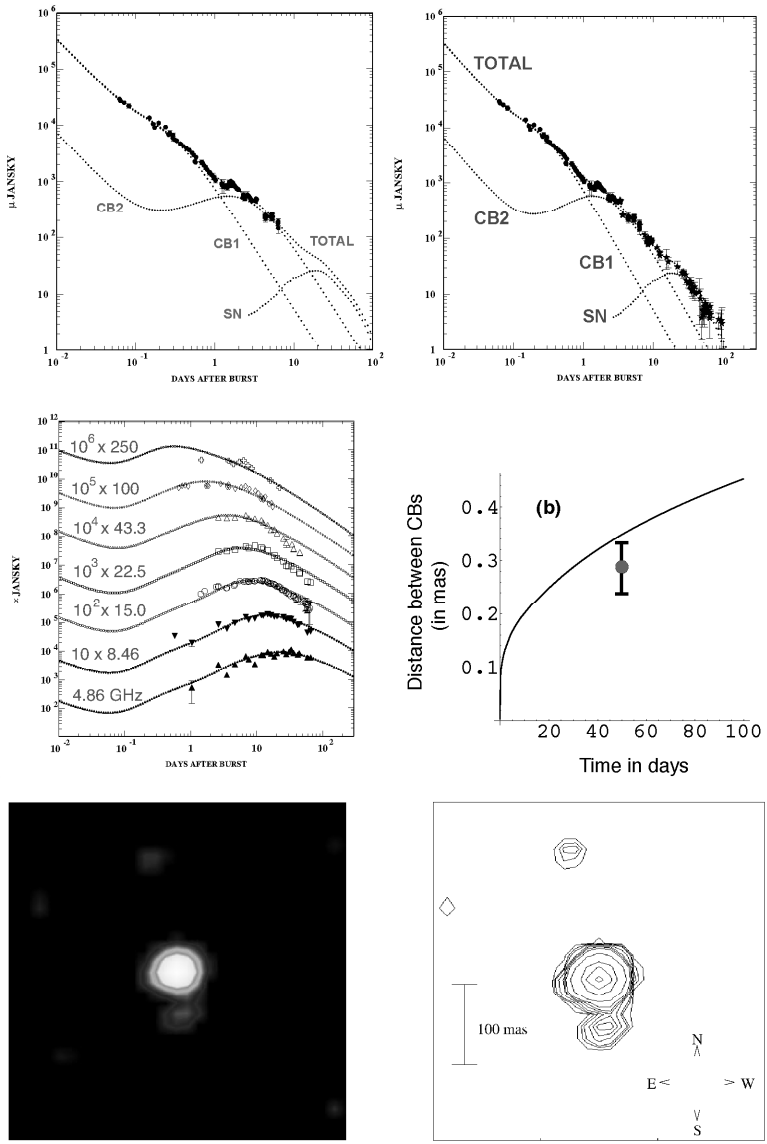

Figure 6: Left to right and top to bottom. a) and b) The R band AG of GRB 030329. A micro-Jansky is 10^{-29} erg cm^{-2} s^{-1}. a) Six days of data are used to predict the next $\sim$100 days, and the SN contribution. b) The SN is seen. c) The radio afterglows of GRB 030329. d) The predicted and observed inter-CB *superluminal* angle in this GRB. (e,f): SN1987A and its two 'mystery spot' CBs [12]. The motion of the Northern one was superluminal.

fascinating ones which beget neutrinos, neutron stars and presumably black holes. Type Ia SNe are probably mere explosions of accreting white dwarfs, but they are very luminous, and of cosmological standard-candle fame.

GRBs have many 'typical' properties. Their spherical-equivalent number of γ-rays is $\sim 10^{59}$. Their spectrum at fixed t is very well approximated by:

$$\left.\frac{dN}{dE}\right|_t \propto \left[\frac{T(t)}{E}\right]^{\alpha} e^{-E/T(t)} + b\,\left[1-e^{-E/T(t)}\right]\,\left[\frac{T(t)}{E}\right]^{\beta} \qquad (3)$$

with $b\sim 1$, $\alpha\sim 1$, $\beta\sim 2.1$. Early in the evolution of a pulse, the 'peak energy' (characterizing the photons carrying most of the GRB's energy) is $E_p\sim T[0]\sim$ 250 keV, evolving later to $T(t)\sim t^{-2}$. A pulse's shape at fixed E is well fit by:

$$\left.\frac{dN}{dt}\right|_E \approx \Theta[t]\, e^{-[\Delta t(E)/t]^2}\left\{1-e^{-[\Delta t(E)/t]^2}\right\};\ \frac{\Delta t(E_1)}{\Delta t(E_2)} \approx \left[\frac{E_2}{E_1}\right]^{\frac{1}{2}}, \qquad (4)$$

with $\Delta t\sim\mathcal{O}(1\mathrm{s})$ at $E\sim E_p$. Eq. (4) reflects an approximate spectro-temporal correlation whereby $E\,dN/(dE\,dt)\approx F[E\,t^2]$, which we call the $E\,t^2$ 'law'.

The values of E_p; of the isotropic-equivalent energy and luminosity, $E_\gamma^{\rm iso}$ and $L_p^{\rm iso}$; of a pulse's rise-time $t_{\rm rise}$; or of its 'lag-time' $t_{\rm lag}$ (a measure of how a pulse peaks at a later time in a lower energy interval) vary from GRB to GRB over orders of magnitude. But they are strongly correlated, as shown in Figs. (7a-d). It is patently obvious that such an organized set of results is carrying a strong and simple message, which we shall decipher.

X-ray flashes (XRFs) are lower-energy kinsfolk of GRBs. They are defined by having $E_p<50$ keV. Their pulses are wider than the ones of GRBs and their overlap is more pronounced, since the total durations of (multi-pulse) XRFs and GRBs are not significantly different. In fig. 7e I show the time at which the single pulse of XRF 060218 peaked (measured from the start of the count-rate rise) as measured in different energy intervals. This is an impressive validation of the $E\,t^2$ law (the red line), also screaming for a simple explanation.

Analytical expressions summarizing the behaviour of GRB and XRF afterglows in time (from seconds to months) and frequency (from radio to X-rays) do exist (DDD02/03), but they are somewhat more complex than Eqs. (3,4). The typical AG behaviour is shown in fig. 7f, as a function of frequency, at 1, 10... 300 days after burst (the value of p is $\sim 2.2\pm 0.2$). This simple figure reflects a rich behaviour in time and frequency. 'Chromatic bends' (called 'breaks' in the literature) are an example. At a fixed time, the spectra steepen from $\sim\nu^{-0.5}$ to $\sim\nu^{-1.1}$ at the dots in the figure. Around a given frequency, such as the optical one marked by a dotted line, the optical spectrum makes this same transition as a function of time (at $t\sim$3d, for the parameters of this example), while the spectral shape at X-ray frequencies stays put.

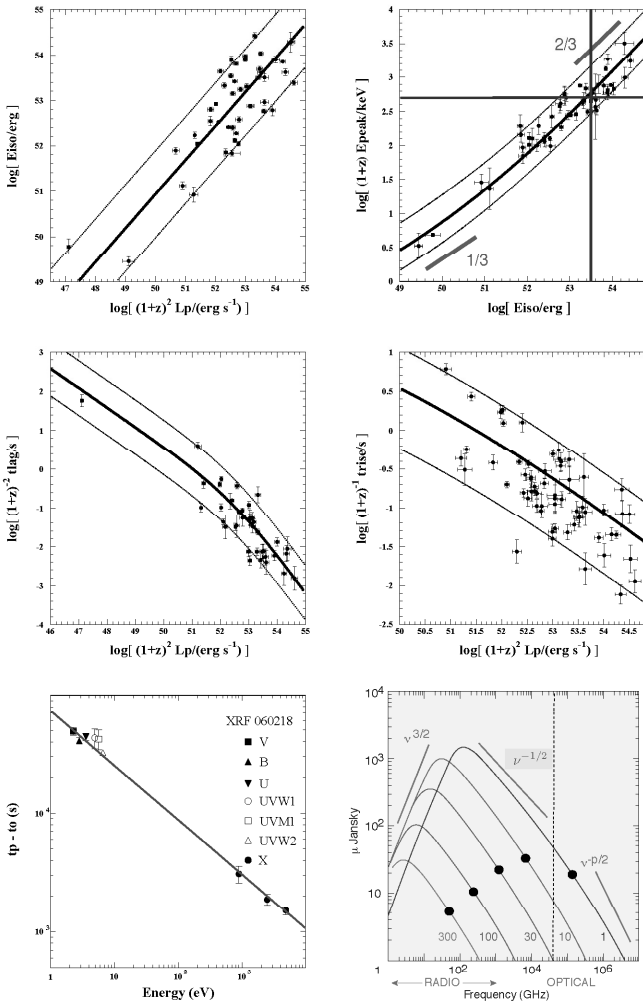

Figure 7: Left to right and top to bottom: a) The $[E_\gamma^{\rm iso}, L_p^{\rm iso}]$ correlation. b) The $[E_p, E_\gamma^{\rm iso}]$ correlation. The limiting slopes are in red, the central predictions in blue. c) The $[t_{\rm lag}, L_p^{\rm iso}]$ correlation. d) The $[t_{\rm min}^{\rm rise}, L_p^{\rm iso}]$ correlation. The data are for Swift-era GRBs of known z. e) The peak times of the one-pulse X-ray flash XRF 060218 at different energy intervals. f) A typical AG spectrum at different number of days after the burst (1, 10,... 300). In the figure $p/2 \sim 1.1$.

3.1 The Swift era

Physicists, unlike ordinary year-counting mortals, live in 'eras'. Many are waiting for the LHC era or the Plank era, GRB astronomers are in their 'Swift era'. Various satellites are currently contributing to a wealth of new data on GRBs and XRFs. Swift is one of them. Within 15 seconds after detection, its 15-150 keV Burst Alert Telescope sends to ground a 1 to 4 arcmin position estimate, for use by robotic optical ground telescopes. In 20 to 75 s, Swift slews to bring the burst location into the field of view of its 0.3-10 keV X-ray Telescope and its 170-650 nm UV/Optical Telescope. With nominal celerity, Swift has filled a gap in GRB data: the very 'prompt' X-ray and optical radiations.

Swift has established a *canonical behaviour* of the X-ray and optical AGs of a large fraction of GRBs. The X-ray fluence decreases very fast from a 'prompt' maximum. It subsequently turns into a 'plateau'. After a time of $\mathcal{O}(1\mathrm{d})$, the fluence bends (has a 'break', in the usual parlance) and steepens to a power decline. In fig. 8a, this is shown for a Swift GRB. This bend is achromatic: the UV and optical light curves vary in proportion to it. Although all this is considered a surprise, it is not. In fig. 8b I show a pre-Swift AG and its interpretation in two models. In fig. 8c one can see that the bend of this GRB was achromatic. Even the good old GRB 980425, the first to be clearly associated with a SN, sketched a canonical X-ray light curve, see fig. 8d.

The γ rays of a GRB occur in a series of *pulses*, 1 and 2 in the examples of fig. 5. Swift has clearly established that somewhat wider X-ray *flares* coincide with the γ pulses, having, within errors, the same start-up time. On occasion, even wider optical *humps* are seen, as in fig. 9a. The X-ray counterpart of the second hump in this figure is clearly seen in fig. 9b. In an XRF the X-ray flares can be very wide, as in the one-flare example of fig. 10a. In such a case, the accompanying optical 'humps' peak very late, at $t = \mathcal{O}(1\mathrm{d})$, as in fig. 10b. All these interconnected γ-pulses, X-ray flares and optical humps are described by Eqs. (3,4). They are obviously manifestations of a common underlying phenomenon, which we shall dig out. Finally, Swift has discovered that not all X-ray light curves are smooth after the onset of their fast decay, as the one in fig. 10a is. Well after γ pulses are no longer seen, relatively weak X-ray flares may still be observable, as is the case in figs. 9c,10d.

4 Breath-taking entities: the astrophysical jets of cannonballs

A look at the web –or at the sky, if you have the means– results in the realization that jets are emitted by many astrophysical systems. One impressive case is the quasar Pictor A, shown in figs. (11a,b). *Somehow*, its active galactic nucleus is discontinuously spitting *something that does not appear to expand sideways before it stops and blows up*, having by then travelled almost 10^6 light years. Many such systems have been observed. They are very relativistic:

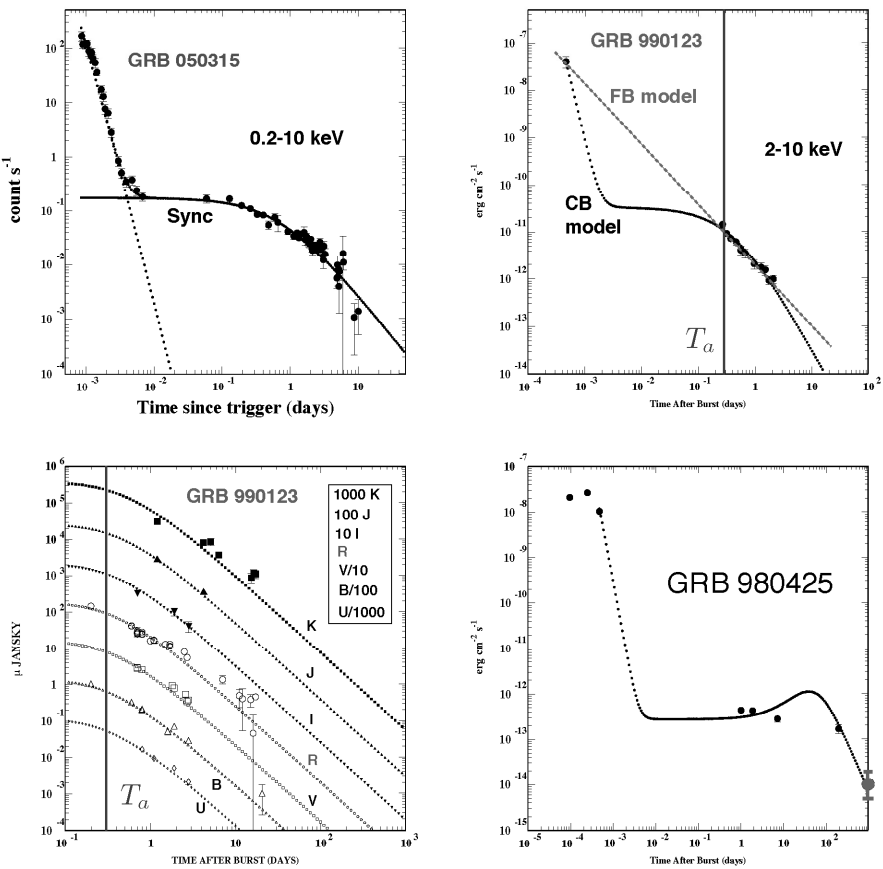

Figure 8: Right to left and top to bottom. a) The canonical 0.2-10 keV X-ray light curve of GRB 050315, fit to the CB model. b) Pre-SWIFT predictions for the 2-10 keV X-ray AG in the CB (DDD02) and fireball [13] models, compared to data for GRB 990123. c) Broad band optical data on GRB 990123, fit in the CB model (DDD03). The 'bend' in (b) and (c) is due to the CBs' deceleration, and is achromatic. d) The X-ray light curve of GRB 980425 showing a very pronounced 'canonical' behaviour and what we called (DDD02) a long 'plateau'. The last (red) point postdates the original figure.

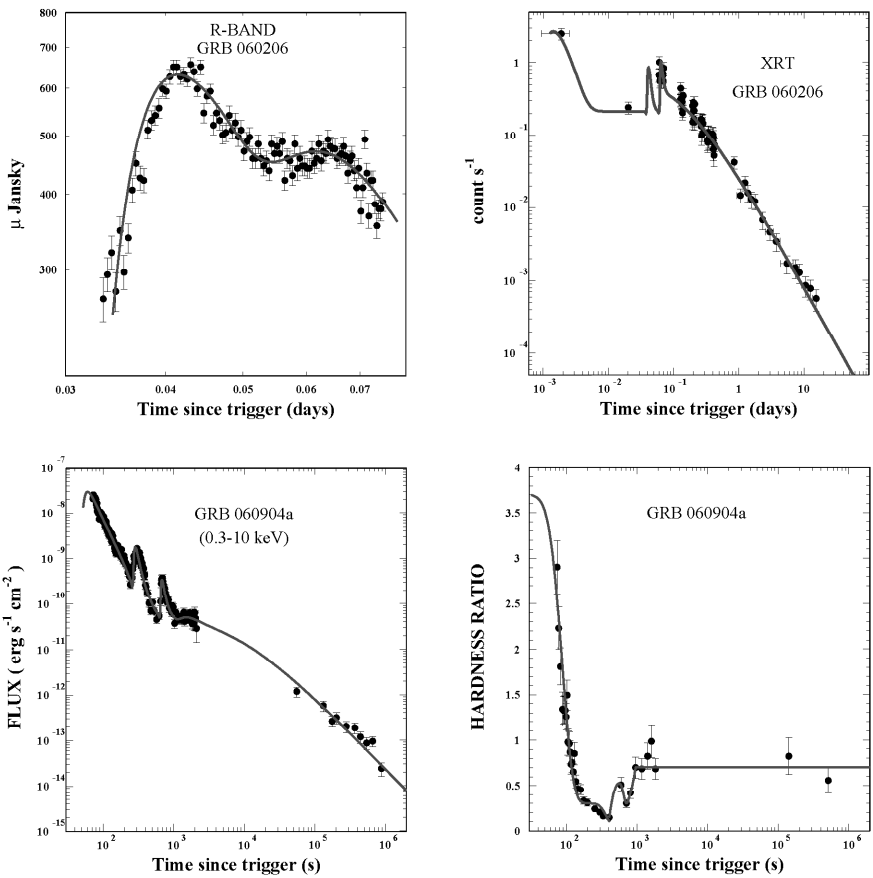

Figure 9: Left to right and top to bottom: a) Early R-band light curves of GRB 060206. b) Its X-ray light curve. c) The X-ray light curve of GRB 060904a with its late flares: the progressively dying pangs of its accreting engine. d) The hardness ratio of GRB 060904a traces the 'prompt' ICS pulses of its light curve, settling to a constant as SR becomes dominant in the 'afterglow'. The above understanding of all these data is specific to the CB model.

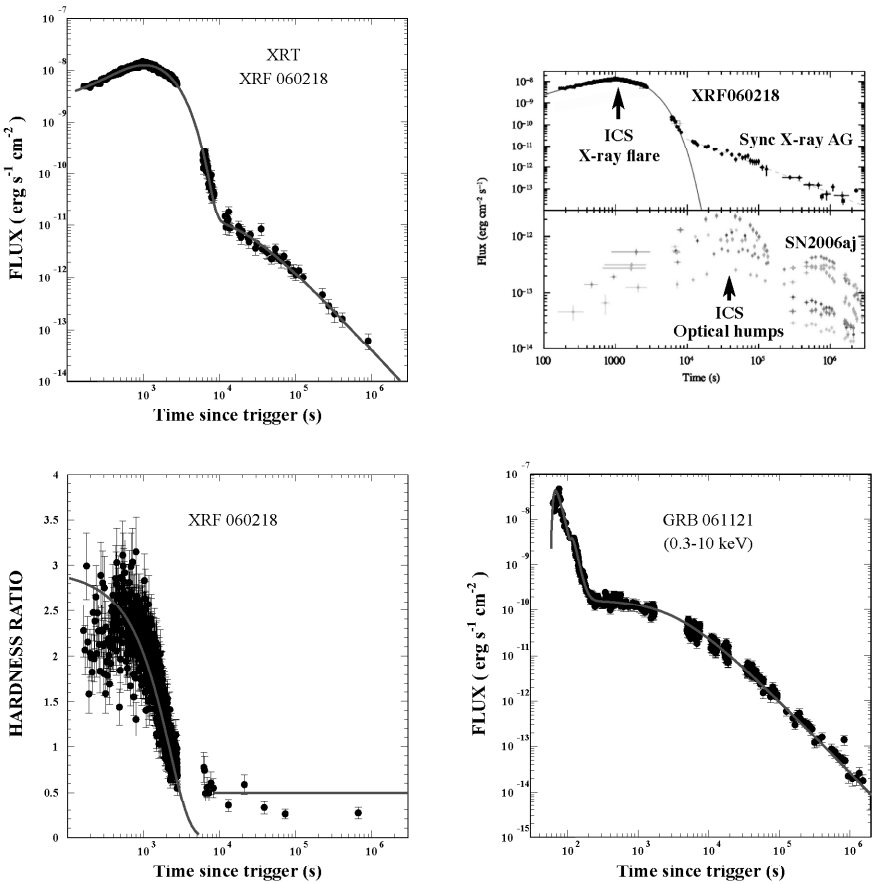

Figure 10: Left to right and top to bottom: a) The X-ray light curve of XRF 060218. b) Data on XRF 060218/SN2006aj. Upper part: the 0.3-10 keV SWIFT-XRT light curve, with fits by Campana et al. [14]. Lower part: UVO light curves. In our model, the X-ray flare and optical humps are made by ICS by a single CB. c) The hardness ratio of XRF 060218. d) The extensive X-ray light curve of GRB 061121. The lines in (a,c,d) are CB-model fits.

the Lorentz factors (LFs) $\gamma \equiv E/(mc^2)$ of their ejecta are typically of $\mathcal{O}(10)$. The mechanism responsible for these mighty ejections —suspected to be due to episodes of violent accretion into a very massive black hole— is not understood.

In our galaxy there are 'micro-quasars', whose central black hole's mass is a few $M_\odot$. The best studied is GRS 1915+105. In a non-periodic manner, about once a month, this object emits two oppositely directed *cannonballs*, travelling at $v \sim 0.92\,c$. When this happens, the continuous X-ray emissions —attributed to an unstable accretion disk— temporarily decrease. Another example is the μ-quasar XTE J1550-564, shown in fig. 11c. The process reminds one of the blobs thrown up as the water closes into the 'hole' made by a stone dropped onto its surface, but it is not understood; for quasars and μ-quasars, the 'cannon's' relativistic, general-relativistic, catastrophic, magneto-hydro-dynamic details remain to be filled in! Atomic lines of many elements have been seen in the CBs of μ-quasar SS 433. Thus, at least in this case, the ejecta are made of ordinary matter, and not of a fancier substance, such as e^+e^- pairs.

5 The Cannonball Model: summary

The 'cannon' of the CB model is analogous to the ones of quasars and microquasars. In an *ordinary core-collapse* SN event, due to the parent star's rotation, an accretion disk is produced around the newly-born compact object, either by stellar material originally close to the surface of the imploding core, or by more distant stellar matter falling back after the shock's passage [15, 16]. A CB made of *ordinary-matter plasma* is emitted, as in microquasars, when part of the accretion disk falls abruptly onto the compact object. *Long-duration* GRBs and *non-solar* CRs are produced by these jetted CBs. To agree with observations, CBs must be launched with LFs, $\gamma_0 \sim 10^3$, and baryon numbers $N_{\rm B} = \mathcal{O}(10^{50})$, corresponding to $\sim 1/2$ of the mass of Mercury, a miserable $\sim 10^{-7}$th of a solar mass. Two jets, each with $n_{\rm CB} = \langle n_{\rm CB} \rangle \sim 5$ CBs, carry

$$E_{\rm jets} = 2\, n_{\rm CB}\, \gamma_0\, N_{\rm B}\, m_p\, c^2 \sim 1.5 \times 10^{51}\ {\rm erg}, \tag{5}$$

comparable to the energy of the SN's non-relativistic shell, that is $\mathcal{O}(1\%)$ of the explosion's energy, $\sim 98\%$ of which is carried away by thermal neutrinos.

We have seen that long GRBs are indeed made by SNe, as advocated in the CB model well before the pair GRB030329/SN2003dh convinced the majority. But do SNe emit cannonballs? Until 2003 [17], there was only one case with data good enough to tell: SN1987A, the core-collapse SN in the LMC, whose neutrino emission was seen. Speckle interferometry data taken 30 and 38 days after the explosion [12] did show two back-to-back relativistic CBs, see fig. 6e,f. The approaching one was *superluminal*: seemingly moving at $v > c$.

A summary of the CB model is given in Fig. 12. The *'inverse' Compton scattering* (ICS) of light by electrons within a CB produces a forward beam of

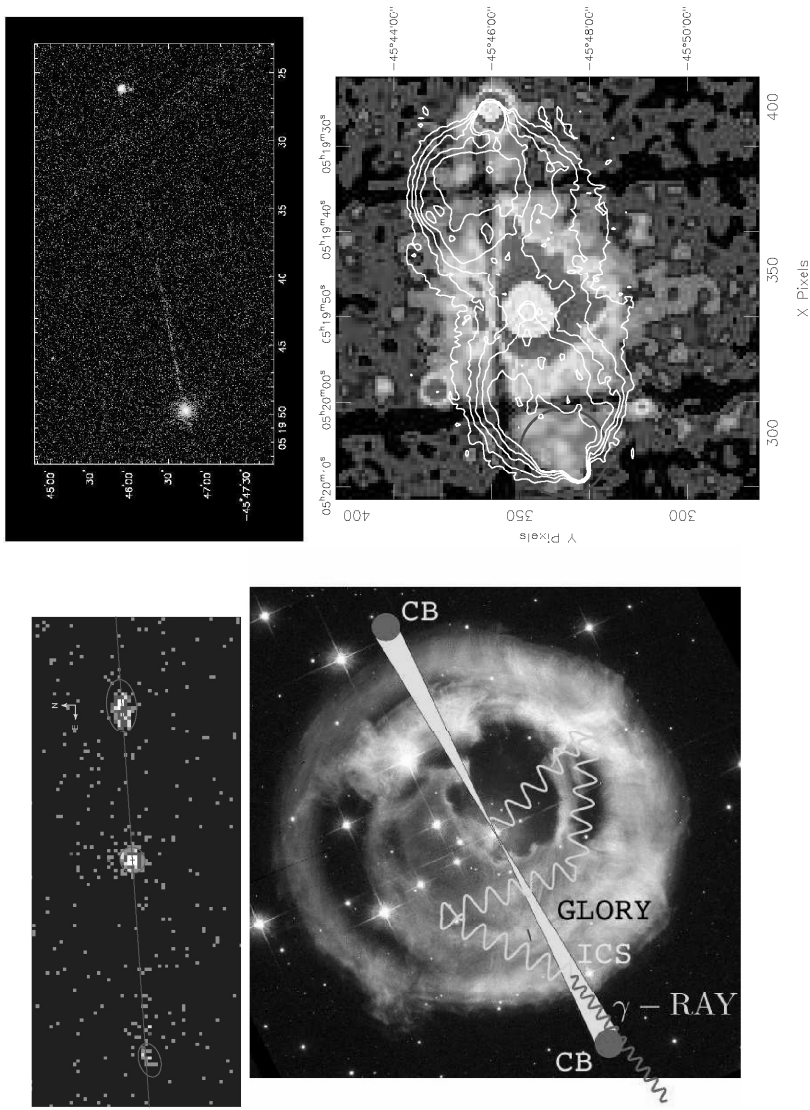

Figure 11: Left to right and top to bottom. a) and b) X-ray images of Pictor A. b) Image centred at the leftmost spot in (a) and superimposed on VLA radio contours. c) Two relativistic CBs emitted in opposite directions by the microquasar XTE J1550-564, seen in X-rays. d) HST picture from 28 October 2002 of the *glory*, or light echo, of a pre-supernova outburst of the red supergiant V838 Monocerotis, doctored with some CB-model art-work.

higher-energy photons: a pulse of a GRB or an XRF. The target light is in a temporary reservoir: the *glory*, illuminated by the early SN light and illustrated by analogy in fig. 11d. A second mechanism, *synchrotron radiation* (SR), takes over later and generally dominates the AG. The γ rays ionize the ISM on the CB's path. The CBs collide with the ISM electrons and nuclei, boosting them to cosmic ray status. The ISM penetrating a CB's plasma creates turbulent magnetic fields within it. The ISM electrons moving in this field emit the mentioned SR. This paradigm accounts for all properties of GRBs and CRs.

The observed properties of a CB's radiation depend crucially on the angle θ of its motion relative to the line of sight to the observer, via the Doppler factor

$$\delta = 1/[\gamma(1-\beta\cos\theta)] \approx 2\gamma/(1+\theta^2\gamma^2) \tag{6}$$

by which a photon's energy is boosted from the CB's rest system to that of a (cosmologically nearby) observer. For an isotropic emission in the CB's system, the observed photon number, energy flux and luminosity are $\propto \delta$, δ^3, δ^4, respectively, just as in a ν beam from π decay. That makes GRBs observable only extremely close to one of their bipolar CB axes, $\theta = \mathcal{O}(1/\gamma) \sim 1$ mrad [typically $\gamma(t=0) = \gamma_0 \sim \delta_0 \sim 10^3$; and AGs are observed till $\gamma(t) \sim \gamma_0/2$].

The relation between CB travel-time in the host galaxy, $dt_\star = dx/(\beta\, c)$, and observer's time, t, is $dt_\star/dt = \gamma\,\delta/(1+z)$. Stop in awe at this gigantic factor: a CB whose AG is observed for 1 day may have travelled for $\mathcal{O}(10^6)$ light days, what a fast-motion video! A CB with $\theta = 1/\gamma = 10^{-3}$ moves in the sky at an apparent transverse velocity of $2000\,c$, yet another large Doppler aberration.

6 GRB afterglows in the CB model

Historically, two GRB phases were distinguished: a prompt one, and the *afterglow*. Swift data have filled the gap, there is no longer a very clear distinction. Nor is there a profound difference between the CB-model's radiation mechanisms, since synchrotron radiation is but Compton scattering on virtual photons and, in a universe whose age is finite, all observed photons were virtual.

In the understanding of GRBs in the CB model, SR-dominated AGs came first. The CB-model AG analysis is strictly a 'model': it contains many simplifications. But the comparison with data determines the distributions of the relevant parameters. Given these, the predictions for CRs and for the ICS-dominated phase of GRBs (such as all properties of the γ-ray pulses) involve only independent observations, basic physics and no 'modeling'. For the reader who might want to move to the more decisive sections, I anticipate the contents of this one. The distribution of γ_0 and $\gamma_0\,\delta_0$ values of pre-Swift GRBs are shown in fig. 13a,b. The radius of a CB evolves as in fig. 13d. A CB does not expand inertially; for most of its trajectory it has a slowly changing radius, as a common *cannonball* does. The baryon number of observed CBs is of $\mathcal{O}(10^{50})$.

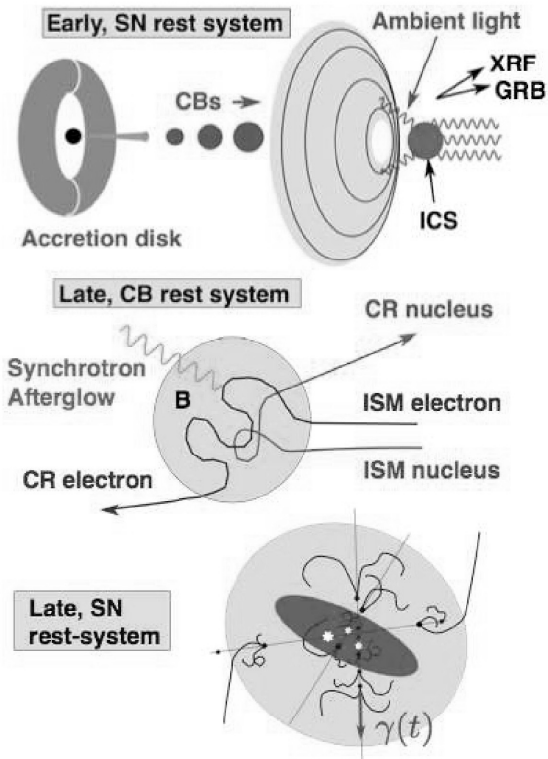

Figure 12: The CB model of GRBs, XRFs and CRs. A core-collapse SN results in a (black) compact object, a fast-rotating torus of non-ejected material and a (yellow) shell of non-relativistic ejecta. Matter (not shown) episodically accreting into the central object produces two narrowly collimated beams of CBs; some of the 'Northern' CBs are depicted. As the CBs move through the *glory* of non-radial light surrounding the star, they forward Compton up-scatter its photons to GRB or XRF energies, depending on how close the line of sight is to the CBs' direction. Each CB produces a GRB 'pulse'. Later, a CB gathers and scatters ISM particles, which are isotropized by its inner magnetic field. In the SN rest system the particles are boosted by the CB's motion: they have become CRs. The synchrotron radiation of the gathered electrons is the late AG of the GRB or XRF. As the CBs' collisions with the ISM slow them down, the CBs generate CRs all along their trajectories, in the galaxy and its halo. CRs are also forward-produced, diffusing thereafter in the local magnetic fields.

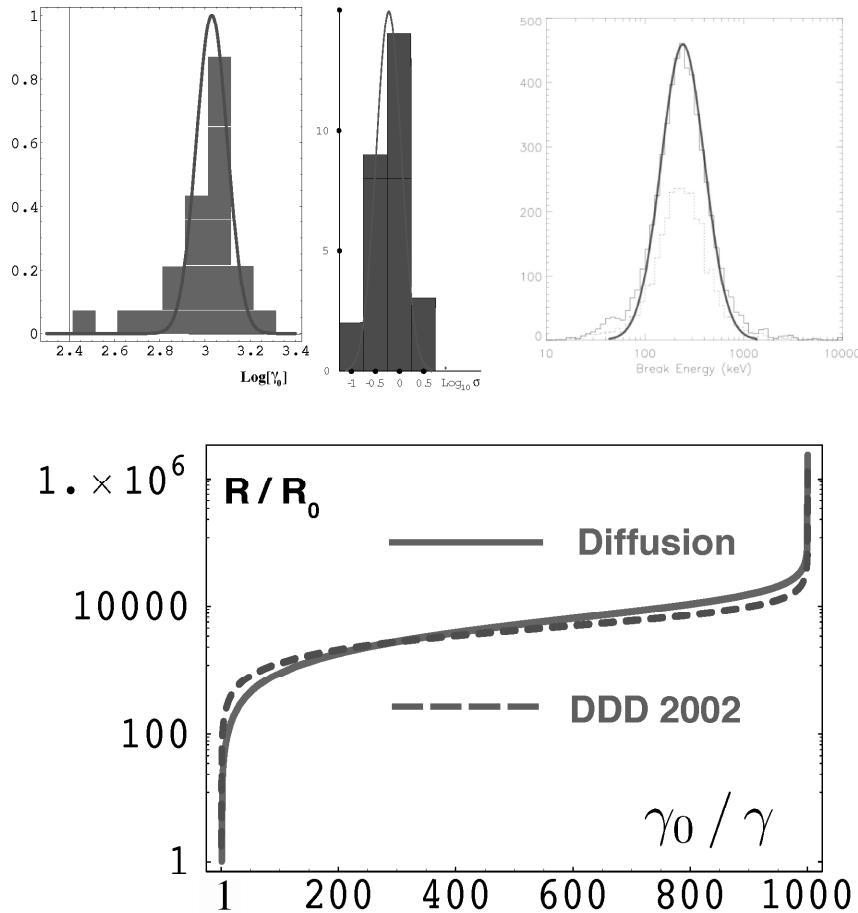

Figure 13: Right to left, top to bottom. a) The distribution of $\mathrm{Log}_{10}(\gamma)$ for a score of pre-Swift GRBs of known z. b) The distribution of $\sigma \equiv \mathrm{Log}_{10}(\gamma\delta/10^6)$ for the same GRBs, also extracted from the analysis of their AGs. c) The distribution of peak or 'break' energies in the spectrum of many pre-Swift GRBs. The line is the CB-model prediction, based on Eq. (12) and the observed σ distribution. d) The behaviour of $R(\gamma/\gamma_0)$ in two extremes (diffusive or instantaneous) for the way the intercepted ISM ions reexit a CB. The coasting behaviour at $R \sim R_c$ and final blow-up at $\gamma \to 1$ are of the form $R \approx R_c\,(\gamma_0/\beta\,\gamma)^{2/3}$.

To determine the fate of a CB, we make the following assumptions. CBs initially expand at $\beta_s\, c = \mathcal{O}(c/\sqrt{3})$, the relativistic speed of sound, swiftly becoming spherical in their rest system and losing memory of their initial size. For the CB's baryon number returned by the analysis, this means that CBs become 'collisionless' fast: their nuclei and electrons do not often collide with the ISM ones they encounter. Hadron and Thompson cross sections being similar, CBs also become transparent, except to long radio waves, losing their radiation pressure. In agreement with first-principle calculations of the relativistic merger of two plasmas [18], a chaotic magnetic field is generated within a CB by the ISM particles it sweeps in. In accordance with observations of similar plasmas (such as the ISM itself and the CRs it contains) the CB's magnetic field is in energy equipartition with the impinging ISM, resulting in:

$$B_{\rm CB}(\gamma) = 3\ {\rm G}\ (\gamma/10^3)\ \left[n/(10^{-2}\ {\rm cm}^{-3})\right]^{1/2}\ , \tag{7}$$

where n is the ISM baryonic number density, normalized to a typical value in the 'superbubbles' in which most SNe and GRBs are born.

In a CB's rest system the motion of its constituents is an inertial memory of the initial radial expansion, whose kinetic energy is larger than the one of the CB's magnetic field. An ISM proton entering a CB will meander it its magnetic field and be isotropically reemitted (in the CB's rest system). The rate of radial momentum loss per unit surface is a surface pressure countering the expansion. We assume that the dominant effect of this pressure is to counteract the expansion. We use Newton's law to compute the ensuing radial deceleration and the CB's radius $R(\gamma)$. The results are shown in fig. 13d. A CB initially expands quasi-inertially. It subsequently settles into a slowly evolving radius till it blows up as its motion becomes non-relativistic (DD06), obeying:

$$R(\gamma) \approx R_c\,(\gamma_0/\beta\gamma)^{2/3},\ \ \text{with}\, R_c = \mathcal{O}(10^{14}{\rm cm}),\ \text{for typical parameters.} \tag{8}$$

This is a complex problem, and ours is a big simplification, once assessed by a cunning referee as "almost baron Munchhausen". Yet, the result describes the surprising 'jet self-focusing' observed, e.g., in Pictor A, see fig. 11a.

The collisions with the ISM continuously decelerate a CB. For a given $R(t)$ and ISM baryon number per unit volume n, energy-momentum conservation dictates the explicit form of the CB's diminishing Lorentz factor $\gamma(t)$. Typically $\gamma(t)$ is roughly constant for a day or so of observer's time, steepening to $\propto t^{\ 1/4}$ thereafter. During the short γ-ray emission time, $\gamma(t) \approx \gamma_0$.

We assume that practically all of the energy of the ISM electrons (of number density $n_e \simeq n$) entering a CB is reemitted fast in the form of SR, so that the corresponding observed frequency-integrated AG power per unit area is $dF/(dt\, d\Omega) = \pi\, R^2\, n_e\, m_e\, c^3\, \gamma^2\, \delta^4/(4\,\pi\, D_L^2)$, with D_L the luminosity distance. The CB deceleration law, dictated by energy-momentum conservation,

is equally simple: $M_0\,\gamma_0\,d\gamma = -\pi\,R^2\,n\,m_p\,\gamma^3\,dx$, for an H-dominated ISM and in the extreme in which the re-emission time of protons is long on the scale of the CB's deceleration time. For constant n, the distance travelled by a CB is:

$$x(\gamma) \approx L\,\left[(\gamma_0/\gamma)^{2/3} - 1\right], \quad L = 3\,N_{\rm B}/(2\pi\,R_c^2\,n\,\gamma_0^3) = 180\,{\rm pc}, \tag{9}$$

where the number is for $N_{\rm B} = 10^{50}$, $n = 10^{-2}\,{\rm cm}^{-3}$, $R_c = 10^{14}\,{\rm cm}$, $\gamma_0 = 10^3$. Given all this, it appears easy to extract from an AG's normalization and shape the values of θ, γ_0 and $N_{\rm B}$, if one trusts the estimate of $R(\gamma)$ and uses a typical n. Limited observational information makes life a bit harder.

The spectrum of fig. 7f is actually the one predicted by the CB model, illustrated for a typical choice of parameters. The chromatic 'bends' shown as dots in this figure, for instance, are 'injection bends': the typical SR energy, in the CB's magnetic field, of the electrons entering it, at time t, with a (relative) LF $\gamma = \gamma(t)$. The small portion of the spectrum above the bend is emitted by a tiny fraction of electrons 'Fermi-accelerated' in the CB's turbulent magnetic fields to a pre-synchrotron-cooling spectrum E_e^{-p}, with $p \sim 2.2$. The prediction fits with no exception the AGs of the first score of well measured GRBs (DDD02/03) of known z. But only on rare occasions can one clearly see in an AG the contributions of the various CBs seen in the γ-ray count rate (a counterexample is the GRB of figs. 5b, 6a,b). Thus, generally, the parameters extracted from AG fits refer to a dominant CB or to an average over CBs.

After an observer's day or so, the optical and X-ray AG are typically SR-dominated, are above the injection bend, and are of the approximate form:

$$F_\nu \propto n_{\rm CB}\,n^{1.05}\,R_c^2\,\gamma^{2.3}\,\delta^{4.1}\,\nu^{-1.1}, \tag{10}$$

where the unwritten proportionality factors, such as D_L^{-2}, are known. From a fit to the shape of $F_\nu(t)$ one obtains $\theta\,\gamma_0$ and the combination L of Eq. (9). At late times $F_\nu \propto \gamma(t)^{6.4} \propto \gamma_0^{6.4}$ with a coefficient determined by the other fit parameters. The value of γ_0 is extracted from the 6.4 root of the inverse of Eq. (10), so that, for a result within a factor of 2, one can tolerate large errors in the chosen n or in the estimate of R_c^2. Trusting these, one can extract $N_{\rm B}$ from L, perhaps with an uncertainty of one order of magnitude[1]. Eq. (10) has been used to fit, after the early fast fall-off, the X-ray and optical data of figs. 8,9,10. The required form of $\gamma(t)$ is Eq. (8), supplemented by the relation between CB's mileage and observer's time, see the end of Sec. 5.

[1]This is what we did in DDD02/03 but not quite what we wrote. I am indebted to J. Steinberger for noticing this error.

7 A GRB's γ rays in the CB model (DD06)

A pulse of a GRB is made by a CB crossing the parent star's *glory*. The glory is a reservoir of non-radially directed light, fed by the parent star's luminosity, as in the artist's view of fig. 11d. For the best studied GRB-associated SN, 1998bw, and for $\mathcal{O}(1\mathrm{d})$ after the explosion, the luminosity was $L_{\rm SN} \sim 5\times10^{52}$ erg/s, in photons of typical energy $E_i \sim 1$ eV. We adopt these values as 'priors' (parameters to be used in calculations, but independent of the CB model). Massive stars destined to 'go supernova' eject solar-mass amounts of matter in successive explosions during their last few thousand pre-SN years. At the 'close' distances of $\mathcal{O}(10^{16}$ cm) relevant here, these stellar coughs generate a thick layer of 'wind-fed' material with an approximate density profile $\rho \propto r^{-2}$ and normalization $\rho\, r^2 \sim 10^{16}$ g cm^{-1}, the last prior we need. The very early UV flash of the SN suffices to ionize the wind-fed matter. The Thompson cross section $\sigma_{\rm T}$ is such that this matter is semitransparent: $\sigma_{\rm T}\, \rho\, r^2/m_p = 4\times10^{15}$ cm. This means that the number of times a SN photon reinteracts on its way out –becoming 'non-radial'– is of $\mathcal{O}(1)$, and that the number density of such photons is $n_\gamma(r) \sim L_{\rm SN}/(4\pi\, r^2\, c\, E_i)$. From emission-time to the time it is still one γ-ray interaction length inside the 'wind', a CB has travelled for

$$t_{\rm tr}^{\rm w} = (0.3\,\mathrm{s})\,\frac{\rho\, r^2}{10^{16}\,\mathrm{g\,cm^{-1}}}\,\frac{1+z}{2}\,\frac{10^6}{\gamma_0\,\delta_0} \tag{11}$$

of observer's time. That is a typical γ-ray pulse rise-time in a GRB, and the reason why, closing the loop, distances of $\mathcal{O}(10^{16}$ cm) were relevant.

In the collapse of a rotating star, material from 'polar' directions should fall more efficiently than from equatorial directions. The CBs would then be emitted into relatively empty space. We assume that the wind-material is also under-dense in the polar directions. This is not the case for the glory's photons, which have been scattered by the wind's matter, and partially isotropised. During the production of γ-rays by ICS, $\gamma \simeq \gamma_0$.

Consider an electron, comoving with a CB at $\gamma = \gamma_0$, and a photon of energy E_i moving at an angle θ_i relative to $\vec{r}$. They Compton-scatter. The outgoing photon is viewed at an angle θ. Its energy is totally determined:

$$E_p = \frac{\gamma\,\delta}{1+z}\,(1+\cos\theta_i)\,E_i = (250\ \mathrm{keV})\,\sigma\,\frac{1+\cos\theta_i}{1/2}\,\frac{E_i}{1\ \mathrm{eV}},\ \sigma \equiv \frac{\gamma\,\delta}{10^6}\,\frac{2}{1+z}\ , \tag{12}$$

where I set $\beta \approx 1$ and, for a *semi* transparent wind, $\langle\cos\theta_i\rangle \sim -1/2$. For pre-Swift GRBs $\langle z\rangle \approx 1$ and, for the typical γ and δ, $E = 250$ keV, the average peak or 'break' energy in Eq. (3). From the fits to the AGs of the subset of known z, we could determine the distribution of σ values, see fig. 13b. Its fitted result is used in Eq. (12) to predict the overall E_p distribution, see fig. 13c.

The rest of the properties of a GRB's pulse can be derived on similarly trivial grounds and with hardly more toil. During the GRB phase a CB is still

expanding inertially at a speed $\beta_s\, c$. It becomes transparent when its radius is $R_{\rm tr} \sim [3\,\sigma_{\rm T}\, N_{\rm B}/(4\pi)]^{1/2}$, at an observer's time very close to that of Eq. (11), for typical parameters. One can simply count the number of ICS interactions of a CB's electrons with the glory, multiply by their energy, Eq. (12), and figure out the isotropic-equivalent energy deduced by an observer at an angle θ:

$$E_\gamma^{\rm iso} \simeq \frac{\delta^3\, L_{\rm SN}\, N_{\rm CB}\, \beta_s}{6\, c}\, \sqrt{\frac{\sigma_{\rm T}\, N_{\rm B}}{4\,\pi}} \sim 3.2\times 10^{53}\,{\rm erg}, \qquad (13)$$

where the number is for our typical parameters, and agrees with observation.

7.1 ¿ Is it Inverse Compton Scattering ...

The γ and δ dependance in Eqs. (12,13) is purely 'kinematical', but specific to ICS: it would be different for self-Compton or synchrotron radiation. To verify that the γ rays of a GRB are made by ICS, as proposed [19] by Shaviv and Dar, we may look at the correlations [20, 21] between GRB observables.

In the CB model, the (γ, δ, z) dependences of the peak isotropic luminosity of a GRB, $L_p^{\rm iso}$; its pulse rise-time, $t_{\rm rise}$; and the lag-time between the peaks of a pulse at different energies, $t_{\rm lag}$; are also simply derived [21] to be:

$$(1+z)^2\, L_p^{\rm iso} \propto \delta^4, \quad t_{\rm rise} \propto (1+z)/(\gamma\,\delta), \quad t_{\rm lag} \propto (1+z)^2/(\delta^2\,\gamma^2). \qquad (14)$$

I have not specified the numerical coefficients in Eqs. (14), which are explicit, as in Eqs. (12,13). Of all the parameters and priors in these expressions, the one explicitly varying by orders of magnitude by simply changing the observer's angle is $\delta(\gamma, \theta)$, making it the prime putative cause of case-by-case variability. For such a cause, Eqs. (13) and the first of (14) imply that $E_\gamma^{\rm iso} \propto [(1+z)^2\, L_p^{\rm iso}]^{3/4}$. This is tested in fig. 7a. A most celebrated correlation is the $[E_p\,, E_\gamma^{\rm iso}]$ one, see Fig. 7b. It evolves from $E_p \propto [E_\gamma^{\rm iso}]^{1/3}$ for small E_p, to $E_p \propto [E_\gamma^{\rm iso}]^{2/3}$ for large E_p. This is because the angle subtended by a moving CB from its place of origin is β_s/γ, comparable to the beaming aperture, $1/\gamma$, of the radiation from a point on its surface. Integration over this surface implies that, for $\theta \ll 1/\gamma$, $\delta \propto \gamma$, while in the opposite case δ varies independently. The straight lines in fig. 7b are the central expectations of Eqs. (12,13), the data are fit to the predicted evolving power law. The predicted $[t_{\rm lag}, L_p^{\rm iso}]$ and $[t_{\rm rise}, L_p^{\rm iso}]$ correlations are tested in figs. 7c,d. The seal of authenticity of inverse Compton scattering —by a quasi-point-like electron beam— is unmistakable in all of this, QED.

7.2 ... on a Glory's light ?

The 'target' photons subject to ICS by the CB's electrons have very specific properties. Their number-density, $n_\gamma(r) \propto L_{\rm SN}/r^2$, translates into the $\sim t^{-2}$

late-time dependence of the number of photons in a pulse since, once a CB is transparent to radiation, ICS by its electrons simply 'reads' the target-photon distribution. As a CB exits the wind-fed domain, the photons it scatters are becoming more radial, so that $1+\cos\theta_i \to r^{-2} \propto t^{-2}$ in Eq. (12). For a semi-transparent wind material, which we have studied in analytical approximations and via Montecarlo, this asymptotic behaviour is reached fast and is approximately correct at all t. This means that the energies of the scattered photons evolve with observer's time as t^{-2}: the '$E\,t^2$ law' of Eq. (4) and fig. 7e.

7.3 The pulse shape and the spectrum

The spectrum of a GRB, Eq. (3), and the time-dependence of its pulses, Eq. (4), describe the data well, and are actually analytical approximations to the results of ICS of an average CB on a typical glory. The spectrum of a semitransparent glory has a 'thermal bremsstrahlung' shape, $dn_\gamma/dE_i \propto (T_i/E_i)^\alpha\,\mathrm{Exp}[-E_i/T_i]$, with $\alpha \sim 1$ and $T_i \sim 1$ eV. The first term in Eq. (3) is this same spectrum, boosted by ICS as in Eq. (12), by electrons comoving with the CB, $E_e = \gamma\, m_e\, c^2$. The second term is due to ICS by 'knock-on' electrons (generated while the CB is not yet collisionless) and electrons 'Fermi-accelerated' by the CB's turbulent magnetic fields. They both have a spectrum $dn_e/dE_e \propto E_e^{-\beta}$, with $\beta \sim 2$ to 2.2. They are a small fraction of the CB's electrons, reflected in the parameter b, which we cannot predict. The temporal shape of a pulse has an exponential rise due to the CB and the windy material becoming transparent at a time $\sim t_{\rm tr}^{\rm w}$, see Eq. (11), the width of pulse (in γ rays) is a few $t_{\rm tr}^{\rm w}$, the subsequent decay is $\propto t^{-2}$. The time-energy correlations obey the '$E\,t^2$ law'. All as observed.

7.4 Polarization

A tell-tale signature of ICS is the high degree of polarization. For a pointlike CB the prediction [19] is $\Pi \approx 2\,\theta^2\,\gamma^2/(1+\theta^4\,\gamma^4)$, peaking at 100% at $\theta = 1/\gamma$, the most probable θ, corresponding to 90° in the CB's system. For an expanding CB, Π is a little smaller. For SR, which dominates the AGs at sufficiently late times, the expectation is $\Pi \approx 0$. The γ-ray polarization has been measured, with considerable toil, in 4 GRBs. It is always compatible, within very large errors, with 100%. The situation is unresolved [22]. I shall not discuss it.

8 Detailed Swift light curves and hardness ratios

Swift has abundantly filled its goal to provide X-ray, UV and optical data starting briefly after the detection of a GRB: compare the Swift result of fig. 8a to the pre-Swift data in fig. 8b. In the CB-model description of the data in figs. 8,9,10, the abruptly falling signal is the tail of one or several γ-ray pulses or

X-ray flares, produced by ICS and jointly described by Eqs. (3,4). The following 'afterglow', its less pronounced decay and subsequent achromatic 'bend' are due to the CBs' synchrotron radiation, described by Eq. (10). Thanks to the quality of SWIFT data one can proceed to test these CB-model predictions in detail.

The two prompt optical 'humps' of GRB 060206 in fig. 9a are the ICS low-energy counterparts of its two late X-ray flares of fig. 9b, simultaneoulsly fit by Eqs. (3,4). Swift provides a rough measure of a GRB's spectrum: the *hardness ratio* of count rates in the [1.5-10] keV and [0.3-1.5] keV intervals. Given the case-by-case parameters of a CB-model fit to the [0.3-10] keV light curve, one can estimate the corresponding hardness ratio [23]. This is done in figs. 9c,d and 10a,c for GRB 060904 and XRF 060218, respectively. This last XFR is observed at a 'large' angle, $\theta \sim 5$ mrad and a correspondingly small δ_0, its single X-ray pulse is, in accordance with Eq. (11), relatively wide. The optical and UV counterparts of the X-ray pulse are clearly visible as the 'humps' in the optical data of fig. 10b. Given the '$E\,t^2$ law' of Section 7.3, the pulse peak times at different frequencies are simply related: $t_{\rm peak} \propto E^{-1/2}$. The prediction, an example of the ubiquitous $1/r^2$ law of 3-D physics, is tested in fig. 7e. The peak fluxes at all frequencies are also related as dictated [9] by Eq. (3). The adequacy of the CB model over many decades in flux and time is exemplified by the X-ray light curve of GRB 061121 in fig. 10d.

The predictions for the peak γ-ray energy of Eq. (12), its distribution as in fig. 13c, the GRB spectrum of Eq. (3), and the correlations of figs. 7a-d are clear proof that ICS is the prompt GRB mechanism. The test of the $E\,t^2$ law in fig. 7e corroborates that the 'target light' becomes increasingly radially directed with distance: *Inverse Compton Scattering on a 'glory's light' by the electrons in CBs is responsible for the γ-ray pulses of a GRB and their sister X-ray flares and optical humps.* The properties of the subsequent *synchrotron-dominated afterglows* are also in accordance with the CB model.

9 The GRB/SN association in the CB model

We have gathered very considerable evidence that the LFs and viewing angles of *observed* GRBs are $\gamma_0 = \mathcal{O}(10^3)$ and $\theta = \mathcal{O}(1)$ mrad. The fraction of GRBs beamed towards us is $\sim \theta^2 = \mathcal{O}(10^{-6})$. The number of such observed GRBs (with a hypothetical $4\,\pi$ coverage) is a few a day. The same coverage would result in the observation of a few million core-collapse SN per day, in the visible Universe. These numbers are compatible with the extreme conclusion that *all* these SNe emit GRBs, but the estimates and errors are sufficient to accommodate a one order of magnitude smaller fraction, which would be compatible with most Type Ib/c emitting (long) GRBs.

10 Short Hard γ-ray Bursts (SHBs)

SHBs share with (long) GRBs the properties not reflected in their name. A good fraction of SHBs have 'canonical' X-ray light curves. The origin of SHBs is not well established, in contrast to that of GRBs and XRFs. Clues to the origin and production mechanism of SHBs are provided by their similarity to long GRBs. The X-ray light curves of some well-sampled SHBs are 'canonical'. The similarities suggest common mechanisms generating the GRB and SHB radiations. This is expected in the CB model, wherein both burst types are produced by highly relativistic, narrowly collimated, bipolar jets of CBs, ejected in stellar processes [19]. The mechanisms for their prompt and AG emissions (ICS and synchrotron) coincide with the ones of GRBs. The 'engine' is different; it is a core-collapse supernova for GRBs and XRFs, in SHBs it may be a merger (of two neutron stars or a neutron star and a black hole), the result of mass accretion episodes on compact objects in close binaries (e.g. microquasars), or phase transitions in increasingly compactified stars (neutron stars, hyper-stars or quark stars), induced by accretion, cooling, or angular-momentum loss.

In the CB model, the 'master formulae' describing prompt and afterglow emissions in long GRBs are directly applicable to SHBs, provided the parameters of the CBs, of the glory, and of the circumburst environment, are replaced by those adequate for SHBs. This results in a good description of the data [24].

11 Cosmic Rays in the CB model

In the CB model, CRs are as simple to understand as GRBs. If relativistic CBs are indeed ejected by a good fraction of core-collapse SNe, it is inevitable to ask what they do as they travel in the ISM. The answer is that they make CRs with the observed properties, simply by interacting with the constituents of the ISM, previously ionized by the γ rays of the accompanying GRB. Early in their voyage, CBs act as *Compton relativistic rackets*, in boosting a glory's photon to γ-ray status. Analogously, all along their trajectories, CBs act as *Lorentz relativistic rackets,* in boosting an ISM nucleus or electron to CR status. Once again, the necessary input is two-fold. On the one hand, there are the properties of CBs: the average number of significant GRB pulses (or CBs) per jet (5), the γ_0 distribution of fig. 13a, and the $N_{\rm B} \sim 10^{50}$ estimate. On the other hand, there are a few 'priors', items of information independent of the CR properties: the rate of core-collapse SNe, the relative abundances, $n_{_A}$ (of the elements of atomic number A) in the ISM, and the properties of Galactic magnetic fields.

We shall see that the CB-model predictions for the normalization of CR spectra are correct to within a factor of $\mathcal{O}(3)$, while the ratios between elements are correct within errors. In figs. 1, 3 and 4a, the predictions have been made to

adjust the data, not reflecting the common overall normalization uncertainty.

11.1 Relativistic rackets: The knees

Our simplest result concerns the 'knees' of the all-particle spectrum in fig. 1a and of the main individual elements in fig. 3. The essence of their understanding is kinematical and trivial. In an *elastic* interaction of a CB at rest with ISM electrons or ions of LF γ, the light recoiling particles (of mass $m \approx A\, m_p$) retain their incoming energy. Viewed in the ISM rest system, they have, for large γ, a flat spectrum extending up to $E \simeq 2\,\gamma^2\, m\, c^2$ [this is recognizable as the forward, massive-particle, $z = 0$, analog of Eq. (12)]. Thus, a moving CB is a gorgeous *Lorentz-boost accelerator:* the particles it elastically scatters reach up to, for $\gamma = \gamma_0 = (1\,\text{to}\,1.5)\times 10^3$, an A-dependent **knee** energy $E_{\rm knee}(A) \sim (2\,\text{to}\,4)\times 10^{15}\, A\,\text{eV}$. If this trivial process is the main accelerator of CRs, there must be a feature in the CR spectra: endpoints at $E_{\rm knee}(A)$. The arrows in fig. 3 show that the H and He data are compatible with this prediction. So does the second knee of fig. 1a, the predicted Fe knee. The CR flux above the H knee, to which we shall return, is $\sim 10^{-15}$ of the total.

11.2 The spectra below the knee

The 'elastic' scattering we just described is dominant below the knees. To compute the resulting spectrum, we assume that the ISM particles a CB intercepts, trapped in its magnetic mesh, reexit it by diffusion, isotropically in the CB's system, and with the same 'confinement' law, Eq. (1), as in the Galaxy (the opposite assumption, that they are immediately elastically scattered, yields a slightly different spectral index). The CB deceleration law is Eq. (9), its radius evolves as in Eq. (8). A modest amount of algebra gives a simple result (DD06), which, for $\gamma > 2$ and to a good approximation, reads[2]:

$$\frac{dF_{\rm elast}}{d\gamma_{\rm CR}} \propto n_{_A} \left(\frac{A}{Z}\right)^{\beta_{\rm conf}} \int_1^{\gamma_0} \frac{d\gamma}{\gamma^{7/3}} \int_{\max[\gamma,\gamma_{\rm CR}/(2\,\gamma)]}^{\min[\gamma_0,2\,\gamma\,\gamma_{\rm CR}]} \frac{d\gamma_{\rm co}}{\gamma_{\rm co}^4}\,, \qquad (15)$$

where $\gamma_{\rm CR}$ is the CR's LF, and $\beta_{\rm conf}$ is the same confinement index as in Eq. (1). The flux $dF_{\rm elast}/d\gamma_{\rm CR}$ depends on the priors $n_{_A}$, $\beta_{\rm conf}$, and γ_0, but not on any parameter specific to the mechanism of CR acceleration. But for the normalization, this flux is A-independent. In the large range in which it is roughly a power law, $dF_{\rm elast}/d\gamma_{\rm CR} \propto [\gamma_{\rm CR}]^{-\beta_{\rm CR}}$, with $\beta_{\rm CR} = 13/6 \approx 2.17$.

The H, He and Fe fluxes of fig. 3 are given by Eq. (15), modified by the Galactic confinement τ-dependence of Eq. (1), with $\beta_{\rm conf} = 0.6$. The fastest-dropping curve in fig. 3a corresponds to a fixed γ_0. The other two curves are for

[2] I am keeping factors of A/Z for kicks. Numerically, they are irrelevant: the theory and data are not so precise, and $(A/Z)^{0.6}$ is 1 for H, 1.6 for Fe.

the γ_0 distribution of fig. 13a, and one twice as wide. The low-energy data of fig. 1b are also described by Eq. (15), whose shape in this region (the 'hip', also visible in fig. 3c for Fe) is insensitive to γ_0 and, thus, parameter-independent.

11.3 The relative abundances

It is customary to discuss the composition of CRs at a fixed energy $E_{_A} = 1$ TeV. This energy is relativistic, below the corresponding knees for all A, and in the domain wherein the fluxes are dominantly elastic and well approximated by a power law of index $\beta_{\rm th} = \beta_{\rm elast} + \beta_{\rm conf} \simeq 2.77$. Expressed in terms of energy ($E_{_A} \propto A\,\gamma$), and modified by confinement as in Eq. (1), Eq. (15) becomes:

$$dF_{\rm obs}/dE_{_A} \propto \bar{n}_{_A}\, A^{\beta_{\rm th}-1}\, E_{_A}^{-\beta_{\rm th}}, \quad X_{\rm CR}(A) = (\bar{n}_{_A}/\bar{n}_p)\, A^{1.77}, \tag{16}$$

with $\bar{n}_{_A}$ an average ISM abundance and $X_{\rm CR}(A)$ the CR abundances relative to H, at fixed E. The results, for input $\bar{n}_{_A}$'s in the 'superbubbles' wherein most SNe occur, are shown in Fig. 2b. In these regions, the abundances are a factor $\sim$3 more 'metallic' than solar (a 'metal' is anything with $Z > 2$). Eq. (16) snugly reproduces the large enhancements of the heavy-CR relative abundances, in comparison with solar or superbubble abundances (e.g. $A^{1.77} = 1242$ for Fe). The essence of this result is deceptively simple: in the kinematics of the collision of a heavy object (a CB) and a light one (the ISM nucleus), their mass ratio ($N_{\rm B}/A \sim \infty$!) is irrelevant.

11.4 Above the knees

We discussed around Eq. (7) the generation of turbulently-moving magnetic fields (MFs) in the merger of two plasmas. Charged particles interacting with these fields tend to gain energy: a relativistic-injection, 'Fermi' acceleration process, for which numerical analyses [18] result in a spectrum $dN/dE \propto E^{-2.2}$, $p \sim 2.2$. For the ISM/CB merger, we (DD04) approximate the spectrum of particles accelerated within a CB, in its rest system, as:

$$dN/d\gamma_{_A} \propto \gamma_{_A}^{-2.2}\, \Theta(\gamma_{_A} - \gamma)\, \Theta[\gamma_{\rm max}(\gamma) - \gamma_{_A}],\ \gamma_{\rm max} \simeq 10^5\, \gamma_0^{2/3}\, (Z/A)\, \gamma^{1/3}, \tag{17}$$

The first Θ function reflects the fact that it is much more likely for the light particles to gain than to lose energy in their elastic collisions with the heavy 'particles' (the CB's turbulent MF domains). The second Θ is the Larmor cutoff implied by the finite radius and MF of a CB, with a numerical value given for the typical adopted parameters. But for the small dependence of $\gamma_{\rm max}$ on the nuclear identity (the factor Z/A), the spectrum of Eq. (17) is universal. Boosted by the CB's motion, an accelerated and re-emitted particle may reach a Larmor-limited $\gamma_{\rm CR}[\max] = 2\,\gamma\,\gamma_{\rm max}$, a bit larger, for $\gamma = \gamma_0 \sim 1.5 \times 10^3$, than

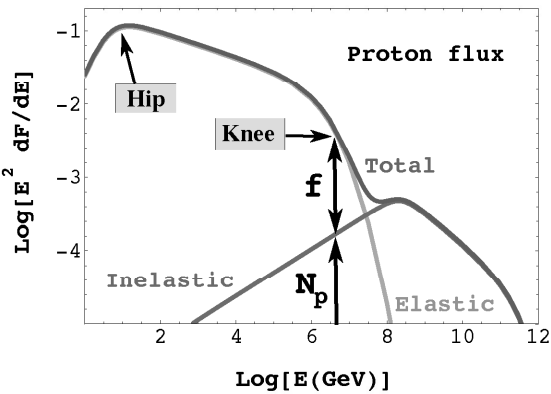

Figure 14: Contributions to the E^2-weighed proton source spectrum.

the corresponding GZK cutoffs. Our model has a *single source*, CBs, for the acceleration of CRs from the lowest to the largest observed energies.

The calculation of the 'elastic' spectrum of Eq. (15) was done for the bulk of the ISM particles entering a CB, assuming that they were not significantly Fermi-accelerated, but kept their incoming energy, i.e. $dN/d\gamma_A \propto \delta(\gamma_A - \gamma)$. The 'inelastic' spectrum, with $dN/d\gamma_A$ as in Eq. (15), yields an equally simple result. The two E^2-weighed spectra are shown (for H) in fig. 14. The inelastic contribution is a tiny fraction of the total, and is negligible below the knee, a point at which we may compare the ratio of fluxes, f, the only parameter freely fit to the CR data. The boost of ISM particles by a CB and their acceleration within it are mass-independent, so that the ratio f is universal.

The E^3-weighed *source* spectra for the main elements are shown in fig. 15a. They are very different from the *observed* spectra of fig. 15b, for many reasons. Below the ankle(s) the slopes differ due to Galactic confinement, see Eq. (1). Above the ankles the flux from Galactic sources is strongly suppressed: we would see their straight-moving CRs only for CB jets pointing to us. The CRs above the ankle are mainly extragalactic in origin, and they also cross the Galaxy just once. Extragalactic CRs of $A > 1$ are efficiently photo-dissociated by the cosmic infrared light. Extragalactic CRs are GZK-cutoff. All this can be modeled with patience and fair confidence. Below the ankle extragalactic CRs may have to fight the CR 'wind' of our Galaxy, analogous to that of the Sun. We have covered our lack of information on this subject by choosing two extreme possibilities (DD06), resulting in the two curves of figs. 1a and 4a,b.

In fig. 4b I have converted the results of fig. 15b into a prediction for $\langle \mathrm{Ln}\, A(E) \rangle$. The flux at the second knee is dominated by Galactic Fe at its knee. Thereafter this flux decreases abruptly to let extragalactic H dominate all the way from the ankle to the nominal position of the proton's GZK cutoff.

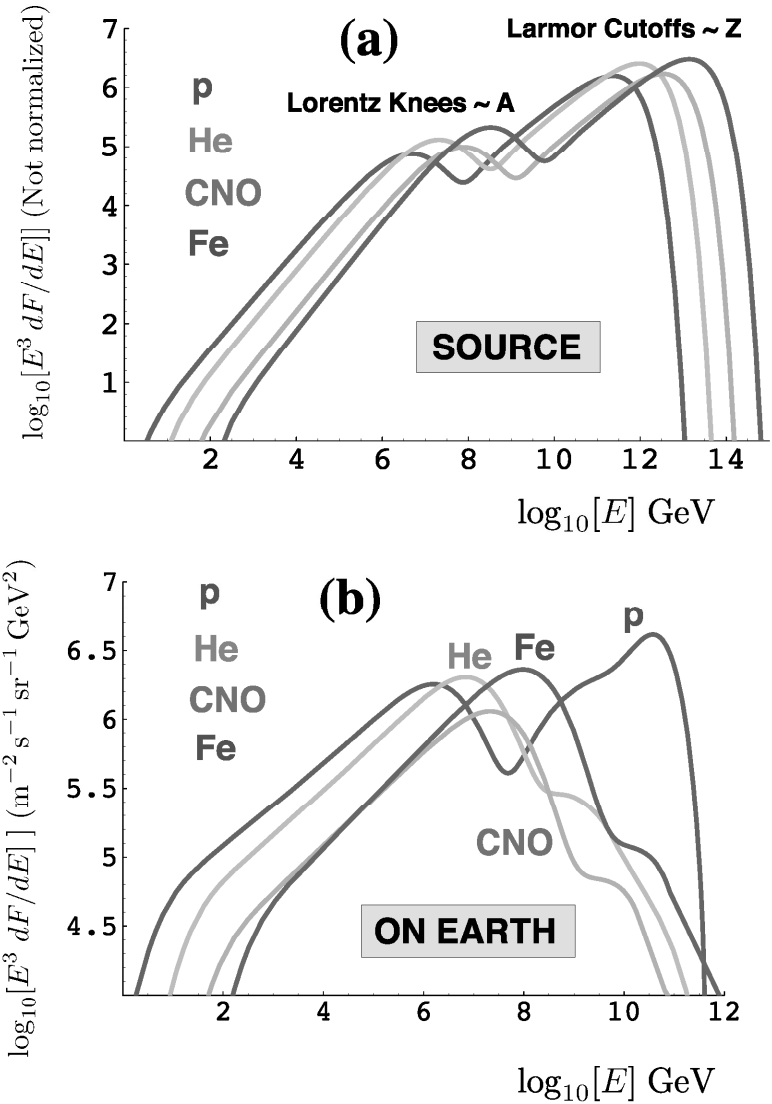

Figure 15: Predicted spectra for the abundant elements and groups. The vertical scales are $E^3\, dF/dE$. (a): The source spectra, with a common arbitrary normalization. (b): The normalized CR spectra at the location of the Earth. Notice that the horizontal and vertical scales are different in (a) and (b).

Above that point the high-energy tail of Galactic Fe may dominate again.

11.5 The CR luminosity, and the overall normalization of the CR flux

The rate of core-collapse SNe in our Galaxy is $R_{\rm SN}\sim 2$ per century. In the CB model, we contend that $\sim 50\%$ of the energy of CRs is transfered to the magnetic fields *they* generate [25]. If all core-collapse SNe emit CBs, the Galactic CR luminosity should be $L_{\rm CR}\sim R_{\rm SN}\,E_{\rm jets}/2\sim 4.7\times 10^{41}$ erg s^{-1}, with $E_{\rm jets}$ as in Eq. (5). This is 3 times larger than the rhs of Eq. (2). The 'discrepancy' is not worrisome. A smaller fraction of SNe may generate high-γ_0 CBs. The rhs of Eq. (2) is for 'standard' CRs, but the confinement volume and time of the CB model are non-standard by factors of ~ 10. All inputs are fairly uncertain.

The calculation of the flux above the ankle is lengthy but straightforward. But for the GZK effect, its shape is that of the source H flux, since protons at that energy should escape other galaxies directly, and enter ours unhindered. Its normalization per SN is fixed. The SN rate per unit volume is measured in the local Universe. The overall flux is the result of the integration over redshift of the flux from past SNe. The integrand must be properly red-shifted and weighed with the star-formation rate as a function of z (SN progenitors have short lives on Hubble-time scales). The integration in z is an integration over look-back time, as opposed to distance, since CRs do not travel straight. The error in the result is hard to estimate, its central value is within a factor of 2 of the observations (DD06). This explains the coincidence that the ankle is the escape energy of protons from the Galaxy *and* the place where the extragalactic flux –not enhanced by confinement and thus less steep– begins to dominate.

11.6 CR diffusion, CR electrons, and the γ background radiation

In the standard paradigm CRs are accelerated by the nonrelativistic ejecta of SNe. SNe occur mainly in the central realms of the Galaxy, so that CRs must diffuse to arrive to our location. A directional asymmetry is predicted, and not observed [26]. For CR electrons the problem is even more severe: their cooling time in the Galaxy's light, and magnetic fields, is so short that they should have lost all their energy on their way here.

Our source distribution is totally non-standard, CBs generate CRs all along their many-kpc-long trajectories, see Eq. (9) and fig. 12c. Depending on the ISM density profile they encounter, CBs may travel for up to tens of kpc before they become nonrelativistic. It takes some 6×10^4 years to travel 20 kpc at $v\sim c$. If a Galactic SN occurs every 50 years, and emits an average of 10 CBs, there are currently several thousand CBs in the Galaxy and its halo. This is a very diffuse CR source, satisfactory in view of the previous paragraph. We have not yet studied the CR source-distribution and diffusion in detail.

Below their knee at $2\gamma_0^2\, m_e\, c^2 \sim 2.3$ TeV, the source spectrum of CB-accelerated electrons has the same index as that of nuclei: $dN/dE_e \propto E^{-\beta_{\rm CR}}$, $\beta_{\rm CR} \approx 2.17$. The predicted spectrum [27], steepened by radiative energy loses, has an index $\beta_e = \beta_{\rm CR} + 1 \approx 3.17$. Its observed slope [28] is 3.2 ± 0.1 above $E_e \sim 10$ GeV, an energy below which other losses should dominate (DD06).

The Gamma Background Radiation (GBR), measured by EGRET from a few MeV to $\sim 10^5$ MeV, was argued to be dominantly of cosmological origin, in directions above the disk of the Galaxy and away from its bulge [29]. A more careful analysis reveals a significant correlation of its intensity with our position relative to the Galactic centre [27]. The CB-model reproduces this correlation, provided a good fraction of the GBR is generated by CR electrons at high galactic latitudes, as they cool radiatively by the very same process that steepens their spectrum. The predicted index of the radiated GBR photons is $\beta_\gamma = (\beta_e - 1)/2 = 2.08$. The observed one [29] is 2.10 ± 0.03.

12 If CBs are so pervasive, why are they not readily observed?

The answer is simple. Cannonballs are tiny astrophysical objects: their typical mass is half of the mass of Mercury. Their energy flux at all frequencies is $\propto \delta^3$, large only when their Lorentz factors are large. But then, the radiation is also extraordinarily collimated, it can only be seen nearly on-axis. Typically, observed SNe are too far to *photograph* their CBs with sufficient resolution.

Only in two SN explosions that took place close enough, the CBs were in practice observable. One case was SN1987A, located in the LMC, whose approaching and receding CBs were photographed, see fig. 6e,f. The other case was SN2003dh, associated with GRB030329, at $z = 0.1685$. In the CB model interpretation, its two approaching CBs were first 'seen', and fit, as the two-peak γ-ray light curve of fig. 5b and the two-shoulder AG of fig. 6a,b. This allowed us to estimate the time-varying angle of their superluminal motion in the sky [17]. Two sources or 'components' were indeed clearly seen in radio observations at a certain date, coincident with an optical AG rebrightening. We claim that the data agree with our expectations[3], including the predicted inter-CB separation [17] of fig. 6d. The observers claimed the contrary, though the evidence for the weaker 'second component' is $> 20\sigma$. They report [30]

[3]The size of a CB is small enough to expect its radio image to scintillate, arguably more than observed [30]. Admittedly, we only realized a posteriori that the ISM electrons a CB scatters, synchrotron-radiating in the ambient magnetic field, would significantly contribute at radio frequencies, somewhat blurring the CBs' radio image [17].

that this component is 'not expected in the standard model'. The unpublished and no-doubt spectacular-discovery picture of the two superluminally moving sources would have been worth a thousand words... in support of the CB model.

13 Discussion and conclusion

We do not have a solid understanding of accretion onto black holes or neutron stars. But such processes are observed to result in the ejection of relativistic and highly collimated jets. We assumed that a similar process takes place as a stellar core collapses, leading to a supernova event. We posited that the SN's relativistic ejecta –two jets of cannonballs– are the sources of GRBs and CRs. The association between SNe and (long) GRBs is now established. We argued that the electrons in a CB, by inverse Compton scattering on the illuminated surroundings of the exploding star, generate the γ rays, X-rays, UV and optical light of the 'prompt' phase of a GRB. The ensuing results are the simplest and most predictive, they are a firm 'theory'. In this paper I have, however, followed the historical development, in which the CB parameters were first extracted from the observations of the afterglow of GRBs. This involves a 'model', a set of arguable but simple hypothesis leading to the prediction of the properties of the AG –dominated by synchrotron radiation by the ISM electrons that a CB intercepts– as a function of frequency and time. In the historical order the 'prompt' results for GRBs are predictions of the theory. Some results for Cosmic Rays –the ISM particles that CBs scatter in their journey– are also 'theory', others can be viewed as further tests of the 'model'.

The results for GRB afterglows may be based on a simplified model, but they work with no exception all the way from radio to X-rays (DDD02,03). In particular, they describe correctly GRB 980425, located at a redshift two orders of magnitude closer than average. Its associated SN is the one we 'transported' to conclude –thanks to the reliability of our AG model– that core-collapse SNe generate long GRBs (DDD02). The X-ray light curve of GRB 980425 and a few others, with extremely scarce data, was described with the 'canonical' properties later observed in detail in many SWIFT-era GRBs. It is not recognized that the two CBs of GRB 030329 were seen, or that their separation in the sky was the predicted 'hyper-luminal' one. In view of the overall success of the CB model, this is a durable hurdle: GRBs so close and luminous are very rare.

The accuracy of the predictions for the prompt phase of GRBs amazes even the CB-model's proponents. The typical values and the correlations between the γ-ray prompt observables leave little doubt that the production mechanism is inverse Compton scattering on 'ambient' light of ~ 1 eV energy. The approximate scaling law $E\,dN_\gamma/dEdt \propto F(E\,t^2)$ –spectacularly confirmed in the case of XRF 060218– demonstrates that the light is that of a 'glory': the early SN light scattered by the 'windy' pre-SN ejecta. A GRB spectrum that works

even better [31] than the phenomenological 'Band' expression is also predicted. The flux and its spectral evolution during the prompt and rapid-decline phases are the expected ones, as we tested in minute detail with SWIFT data.

In the internal-external fireball model of GRBs, highly relativistic thin conical shells of e^+e^- pairs, sprinkled with a finely tuned baryon 'load', collide with each other generating a shock that accelerates their constituents and creates magnetic fields. Each collision of two shells produces a GRB pulse by synchrotron radiation. The ensemble of shells collides with the ISM to produce the AG by the same mechanism. The energy available to produce the GRB pulse –as two shells moving in the *same* direction collide– is more than one order of magnitude smaller than that of the merged shells as they collide with the ISM at rest. The ratio of observed GRB and AG energies is more than one order of magnitude, but in the opposite direction. This 'energy crisis' in the comparison of bolometric prompt and AG fluences [4] is not resolved. Moreover, the GRB spectrum cannot be accommodated on grounds of synchrotron radiation [32], the 'standard' prompt mechanism. The SWIFT-era observations also pose decisive problems to the standard model, whose microphysics [33], reliance on shocks [34] and correlations based on the jet-opening angle [35] have to be abandoned, according to the cited authors.

In spite of the above, the defenders of the fireball model are not discouraged. Their attitude towards the CB model, whose observational support is so remarkable, is not equally supportive. This may be due to cultural differences. Particle physicists believe that complex phenomena may have particularly simple explanations. They thrive on challenging their standard views. Doubting or abandoning a previous consensus in astrophysics is less easy.

The CB-model description of Cosmic Rays is also simplistic: there is only one source of (non-solar) CRs at all energies, and only one parameter to be fit. The model has a certain inevitability: if CBs with the properties deduced from GRB physics are a reality, what do they do as they scatter the particles of the interstellar medium? We have argued that they transmogrify them into CRs with all of their observed properties. The mechanism is entirely analogous to the ICS responsible for a GRB's prompt radiation. Suffice it to substitute the CB's electron, plus the ambient photon, by a moving-CB's inner magnetic field, plus an ambient nucleus or electron.

After a century of CR measurements, the CB-model results lack the glamour of predictions. Yet, the expectations for the knee energies, and for the relative abundances of CRs, are 'kinematical', simple, and verified. They constitute evidence, in my opinion, that the underlying model is basically correct. The prediction for the shape of the spectra: the low energy hips, the large energy stretch very well described by a power-law of (source) index $\beta_s = 13/6$, and the steepening at the knees, are also verified. The index β_s is measured well enough for the adequacy of the prediction to be sensitive to the details of

the underlying model, such as the form of the function $R(\gamma)$ in Eq. (8). I cannot claim that the fact that the prediction is right on the mark is much more than a consistency test, for the physics underlying this aspect of the problem may be terrifyingly complex. The same CR source –cannonballs from supernovae, this time extragalactic– satisfactorily describes the CR data above the ankle. Finally, the properties of CR electrons, and of the high-latitude Gamma 'Background' Radiation, are also correctly reproduced.

Most CR scholars agree with the 'standard' paradigm that the flux well below the knee is produced by the acceleration of the ISM in the frontal shocks of the nonrelativistic ejecta of SNe. In spite of recent observations of large magnetic fields [36] in collisions of SN shells and molecular clouds, nobody has been able to argue convincingly that this process can accelerate particles up to the (modest) energy of the knee, *and* to show that the number and efficiency of the putative sources suffices to generate the observed CR luminosity (to my satisfaction, I add, to make these statements indisputable). From this point on, there is no 'standard' consensus on the origin of CRs, e.g., of the highest-energy ones. In this sense, the CB model is regarded as yet another model, which it is. After all, we are only saying that CRs are accelerated by the jetted relativistic ejecta of SNe, as opposed to the quasi-spherical, non-relativistic ones. Yet, the CB model is also rejected by the CR experts, sometimes even in print [1], though it survives the critique [37]. But, concerning CRs, the model does not trigger the same indignant wrath as in the GRB realm.

I have shown that the problem of GRBs is convincingly –i.e. predictively– solved and that, on the same simple basis, all properties of CRs can be easily derived. Only an overwhelmed minority recognizes these facts, in contradiction with Popper's and Ockham's teachings. I would conclude with a dictum attributed to Lev Landau: *'In astrophysics, theories never die, only people do.'*

Acknowledgement
I thank Shlomo Dado, Arnon Dar and Rainer Plaga for our collaboration.

References

1. A.M. Hillas, arXiv:astro-ph/0607109
2. J.R. Hoerandel, arXiv:astro-ph/0702370v2
3. P. Meszaros, arXiv:astro-ph/0605208
4. T. Piran, Rev. Mod. Phys. **76**, 1143 (2004); Phys. Rep. **333**, 529 (2000).
5. S. Dado, A. Dar & A. De Rújula, Astron. & Astrophys. **388**, 1079 (2002).

6. S. Dado, A. Dar & A. De Rújula, Astron. & Astrophys. **401**, 243 (2003).
7. A. Dar & A. De Rújula, Phys. Reps. **405**, 203, (2004).
8. A. Dar & A. De Rújula, arXiv:astro-ph/0606199
9. S. Dado, A. Dar & A. De Rújula, arXiv:0706.0080
10. A. Dar & A. De Rújula, Astroph. J. **547**, L33, (2001).
11. S. Dado, A. Dar & A. De Rújula, Astroph. J. **594**, L89, (2003).
12. P. Nisenson & C. Papaliolios, Astrophys. J. **518**, L29, (1999).
13. E. Maiorano *et al.* Astron. & Astroph. **438**, 821 (2005).
14. S. Campana, et al. Nature, **442**, 1008 (2006).
15. A. Dar & A. De Rújula, arXiv:astro-ph/0008474
16. A. De Rújula, Phys. Lett. **B193**, 514 (1987).
17. S. Dado, A. Dar & A. De Rújula, arXiv:astro-ph/0402374, 0406325
18. J.K. Frederiksen *et al.*, Astroph. J. **608**, L13 (2004); astro-ph/0303360
19. N. J. Shaviv & A. Dar, Astroph. J. **447**, 863 (1995).
20. A. Dar & A. De Rújula, arXiv:astro-ph/0012227
21. S. Dado, A. Dar & A. De Rújula, Astroph. J. **663**, 400, (2007).
22. S. Dado, A. Dar & A. De Rújula, arXiv:astro-ph/0701294
23. S. Dado, A. Dar & A. De Rújula, arXiv:0709.4307
24. S. Dado, A. Dar & A. De Rújula, to be published.
25. A. Dar & A. De Rújula, Phys. Rev. **D72**, 123002, (2005).
26. R. Plaga, arXiv:astro-ph/0111555
27. A. Dar & A. De Rújula, Mon. Not. Roy, Astron. Soc. **323**, 391, (2001).
28. M. Aguilar *et al.*, Phys. Rep. **366**, 331 (2002).
29. P. Sreekumar *et al.,* Astrophys. J. **494**, 523 (1998).

30. G.B. Taylor *et al.* Astrophys. J. **609**, L1, (2004).

31. C. Wigger *et al.* arXiv:0710.2858

32. G. Ghisellini, A. Celotti, & D. Lazzati, MNRAS **316**, L5 (2000).

33. A. Panaitescu *et al.* MNRAS **369**, 2059 (2006).

34. P. Kumar *et al.* MNRAS **376**, L57, (2007).

35. G. Sato *et al.* Astroph. J. **657**, 359, (2007);
D. N. Burrows & J. Racusin, arXiv:astro-ph/0702633

36. Y. Uchiyama *et al.* Nature **449**, 576, (2007).

37. S. Dado, A. Dar & A. De Rújula, arXiv:astro-ph/0611369

SN1987A 20 YEARS LATER

Arnon Dar
Haifa, Israel

Written contribution not received

DARK MATTER ANNIHILATION IN THE CLUMPY GALACTIC HALO

Veniamin Berezinsky
Laboratori Nazionali del Gran Sasso, INFN, 67010 Assergi (AQ), Italy

Vyacheslav Dokuchaev and Yury Eroshenko
Institute for Nuclear Research of the Russian Academy of Sciences, Moscow

Abstract

We describe the distribution of small-scale Dark Matter (DM) clumps in the Galactic halo in the framework of standard cosmology and hierarchical structure formation. It is shown that DM annihilation in small-scale clumps can be strongly enhanced (boosted) as compared to a diffuse DM distribution. A tidal disruption of clumps by stars in the center of the Galaxy and by interaction with the Galactic disk yields a strong radial dependence of the boost factor. A tidal destruction of clumps in the Galactic disk results in the anisotropic distribution of clumps. The corresponding annihilation of DM particles in the small-scale clumps produces anisotropic gamma-ray signal with respect to the Galactic disk. The resulting enhancement of annihilation signal due to the halo clumpiness strongly depends on the primordial perturbation spectrum and varies in the range $\sim 10 - 100$.

Annihilation in the Galactic halo is a promising indirect manifestation of Dark Matter (DM) particles [1]. An intriguing indication on the possible DM annihilation in the Galactic halo was found in the EGRET gamma ray data, which shows a noticeable excess at energies above 1 GeV in comparison with expectations from the conventional galactic models in all sky directions [2].

The inflation cosmological models predict the near power-law primordial fluctuation spectrum with an power index $n_p \simeq 1.0$ (Harrison-Zeldovich spectrum). Both analytical calculations [3, 4, 5, 6] and numerical simulations [7, 8, 9] with the inflationary-produced adiabatic density fluctuations predict the existence of DM clumps in the Galactic halo. The small-scale clumps are formed earlier than the larger ones and captured by the larger clumps in the process of a hierarchical clustering in the expanding Universe. Eventually all clumps consist in part of the smaller ones and of the separate DM particles. An effective index of the density perturbation power spectrum $n \to -3$ at small-scales (when mass inside the perturbation $M \to 0$). This means that a gravitational clustering of small-scale structures proceeds very fast. As a result the formation of new clumps and their capturing by the larger ones are nearly simultaneous processes.

The resulting enhancement of the annihilation signal due to the presence of clumpy substructures in the Galactic halo strongly depends on the fraction of the most dense small-scale clumps [5, 10]. The most essential characteristics of clumps for calculations of DM annihilation in the Galactic halo are the minimum mass and distribution function of clumps. A mass distribution of small-scale clumps survived in the hierarchical structuring was derived in [5]:

$$\xi_{\rm int} \frac{dM}{M} \simeq 0.01(n+3) \frac{dM}{M}, \qquad (1)$$

where M is a clump mass, n is a power-index of density perturbations at a mass-scale M. The distribution function $\xi_{\rm int}$ is a mass fraction of DM in the form of clumps in the logarithmic mass interval $d \log M$. The minimal mass of DM clumps $M_{\rm min}$ is determined by the leakage of DM particles from the growing density fluctuations (the diffuse leakage and free streaming) and depends on the modelled properties of DM particles [4, 5, 11, 12, 13, 14, 15] and varies e.g. in the range of the Moon and Earth masses, $M_{\rm min} \sim (10^{-8} - 10^{-6}) M_{\odot}$ for some specific neutralino models.

1 Tidal destruction of small-scale DM clumps

The small-scale DM clumps are gravitationally loosely bounded objects. As a result the tidal destruction by stars is a crucial process for a survival of clumps in the Galaxy [10, 16, 17]. An additional source for tidal heating of clumps

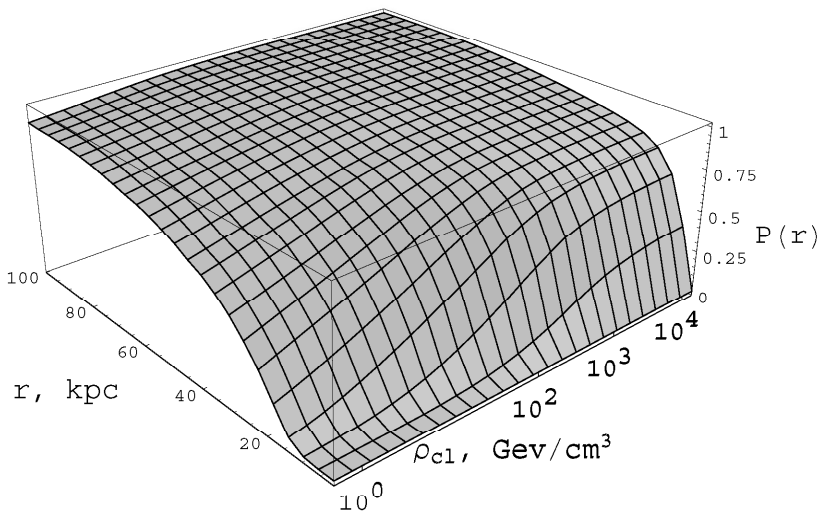

Figure 1: *A survived fraction of small-scale clumps $P(r)$ in the Galaxy halo inside the radial distance* 100 *kpc according to* [18]. *The mean internal density of clump $\rho_{\rm cl}$ is in GeV cm^{-3}.*

is the Galactic disk shocking when clumps intersect the Galactic plane [18]. The Galactic disk shocking turns out to be the most important process of tidal destruction of clumps in the Galaxy. All small-scale DM clumps are totally destroyed by stars inside the Galactic bulge at distances $r \leq 3$ kpc. As a result there must be a void in small-scale clump distribution within the central ~ 3 kpc.

See in the Fig. 1 the modelled local fraction of survived clumps in the Galactic halo $P(r)$ depending on their internal density [18]. For destruction by halo stars there is an additional weak dependence on the clump mass M. At the same time the destruction of clumps by halo stars is much weaker in comparison with the destruction by disk. With a good accuracy we may neglect the M dependence. In the Fig. 2 it is shown the corresponding model calculations of the local fraction (or survival probability) of clumps with mass $M = 2 \times 10^{-8} M_\odot$ in the Galactic halo.

2 Enhancement of annihilation signal by clumps

The relative *enhancement* (*idem* boost-factor or clumpiness-factor) of the annihilation signal due to the presence of DM clumps in the Galactic halo can

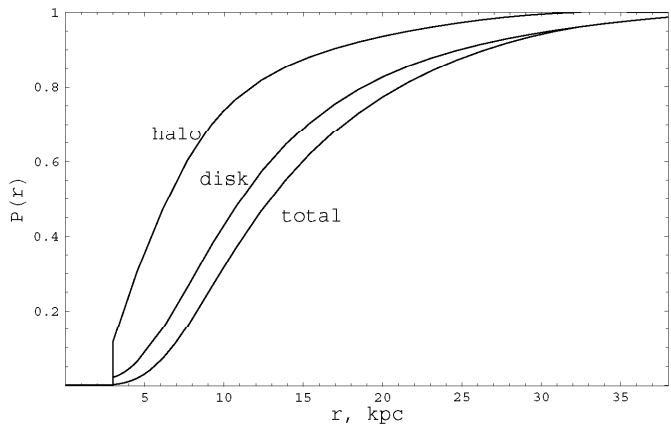

Figure 2: *The fraction of clumps with mass* $M = 2 \times 10^{-8} M_{\odot}$ *and peak-height* $\nu = 2$ *survived a tidal destruction in the Galactic disc* P_d*, in the Galactic halo* $P_{\rm H}$ *and the resulting total fraction* $P(r) = vP_{\rm tot} = P_{\rm H} P_d$ *as a function of distance from the Galactic center. The cutoff at* $r \simeq 3$ *kpc is due to a total destruction of clumps by stars inside the bulge* [18].

than be written as $\eta(r) = (I_{\rm dif} + I_{\rm cl})/I_{\rm dif}$, where $I_{\rm dif}$ and $I_{\rm cl}$ are an annihilation signal from diffuse DM in the halo and clumps respectively. The corresponding integrated along the line of sight (observed) enhancement factor $\eta(\theta)$ see in the Fig. 3 for the model case of a simple isothermal spherical symmetric halo model.

3 Conclusions

The number density distribution of small-scale DM clumps in the Galactic halo was calculated in dependance on a clump mass M, radius R (expressed through the fluctuation peak-height ν) and radial distance r to the Galactic center. These calculations were performed by taking into account the tidal destruction of clumps in the early hierarchical clustering and later in the Galaxy [18]. In the process of hierarchical clustering the small clumps are captured by the bigger ones, and so on. Thus the hierarchical structure is formed, when all clumps consist in part the smaller ones and the free DM particles. Some part of DM clumps are tidally disrupted in the gravitational field of the bigger host clumps. In this scenario we calculated the differential distribution of the survived clumps as a function of two independent parameters: e. g. a clump mass M and fluctuation peak-height ν (or a clump mass M and radius R). The corresponding integral mass function is given by (1), where $\xi_{\rm int}$ gives the mass fraction of clumps survived the tidal destruction in the hierarchical structuring.

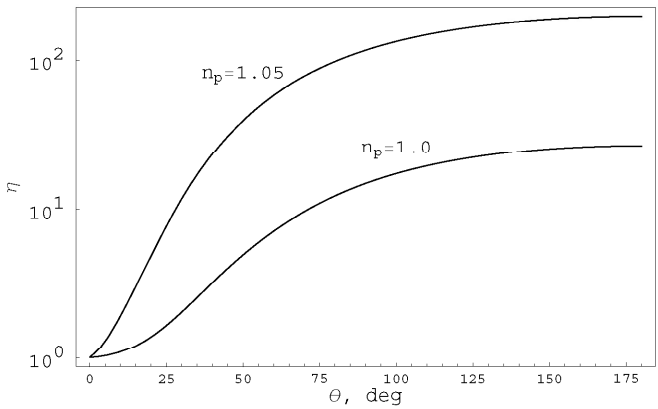

Figure 3: *An integrated along the line of sight (observed) enhancement factor* $\eta(\theta)$ *for clump internal density profile* $\rho_{\rm cl}(r) \propto r^{\beta}$, $\beta = 1.8$, *minimal clump mass* $M_{\rm min} = 2 \cdot 10^{-8}$, $n_p = 1.0$ *and* $n_p = 1.05$ *in the case of isothermal spherical symmetric halo model.*

The predicted differential number density of small clumps is very close to our previous calculations [5], and both are in a good agreement with the recent results of numerical simulations [10].

Our calculations are valid only for small-scale clumps with masses $M \leq 10^3 M_{\odot}$. The physics of larger mass clumps is rather different. For large-scale clumps the dynamical friction, tidal stripping and accretion of new clumps into the halo proceed in a different way. Nevertheless, the calculated mass function is in a good agreement with a mass function of the large clumps (obtained in the numerical simulations) in the intermediate mass-range.

The mutual tidal destruction of small-scale DM clumps is effective only at the early stage of hierarchical clustering. At later stages the DM clumps are additionally destructed by stars and by the collective gravitational field of the Galactic disc. In the Galaxy at radial distance $r \leq 3$ kpc all small-scale clumps are destructed by stars in the central bulge. At radial distances in the range $r = 3 - 40$ kpc the DM clumps are destructed by stars from the halo and by the tidal shocking in the Galactic disk. The latter provides the major contribution to the tidal destruction of clumps outside the bulge.

The tidal destruction of clumps by the Galactic disk and stars affects the annihilating signal mainly in the central region of the Galaxy where destructions are most effective. Therefore, a growing fraction of survived clumps $P(r)$ smooths the anisotropy of the awaited annihilation signal at the Sun position. A local annihilation rate is proportional to the clumps number density and, respectively, to $P(r)$. For example, at the position of the Sun the 17% of clumps survive, and so the local annihilation rate more then 5 times less in comparison with the $P = 1$ case.

This work was supported in part by the Russian Foundation for Basic Research grants 06-02-16029 and 06-02-16342, and the Russian President grants LSS 4407.2006.2 and LSS 5573.2006.2.

References

1. J. Silk and H. Blocmcn, *Astrophys. J. Lett.* **313**, 47 (1987).
2. W. de Boer, C. Sander, V. Zhukov, A.V. Gladyshev and D.I. Kazakov, Astron. Astrophys. **444**, 51 (2005); Phys. Rev. Lett. **95**, 209001 (2005); Phys. Lett. **B636**, 13 (2006).
3. J. Silk and A. Stebbins, Astrophys. J. **411**, 439 (1993).
4. A.V. Gurevich, K.P. Zybin and V.A. Sirota, Sov. Phys. – Usp. **167**, 913 (1997).
5. V. Berezinsky, V. Dokuchaev and Yu. Eroshenko, Phys. Rev. **D 68**, 103003 (2003).
6. P. Brax, C. van de Bruck, A. -C. Davis and A. M.Green, Phys. Lett. **B633**, 441 (2006).
7. B. Moore et al., Astrophys. J. **524**, L19 (1999).
8. S. Ghigna *et al*, Astrophys. J. **544**, 616 (2000).
9. A. Klypin, S. Gottlober, A.V. Kravtsov and A.M. Khokhlov, Astrophys. J. **516**, 530 (2002).
10. J. Diemand, B. Moore and J. Stadel, Nature, **433**, 389 (2005).
11. S. Hofmann, D.J. Schwarz and H. Stocker, Phys. Rev. **D 64**, 083507 (2001).
12. D.J. Schwarz, Annalen Phys. **12**, 220 (2003).
13. A.M. Green, S. Hofmann and D.J. Schwarz, Mon. Not. Roy. Astron. Soc. **353**, L23 (2004).
14. A. Green, S. Hofmann and D. Schwarz, `arXiv:astro-ph/0508553`.
15. A.M. Green, S. Hofmann and D.J. Schwarz, JCAP, **0508**, 003 (2005).
16. H.S. Zhao, J. Taylor, J. Silk and D. Hooper, `arXiv:astro-ph/0502049`.
17. H.S. Zhao, D. Hooper, G.W. Angus, J.E. Taylor and J. Silk, `arXiv:astro-ph/0508215`.
18. V. Berezinsky, V. Dokuchaev and Yu. Eroshenko, Phys. Rev. **D 73**, 063504 (2006).

SEARCHES FOR PARTICLE DARK MATTER WITH THE GLAST LARGE AREA TELESCOPE

Jan Conrad
KTH-Stockholm/High Energy Astrophysics and Cosmology Center (HEAC)
AlbaNova University Centre, 10691 Stockholm
Representing the GLAST-LAT collaboration

Abstract

The Large Area Telescope (LAT), one of two instruments on the Gamma-ray Large Area Space Telescope (GLAST) mission, scheduled for launch by NASA in 2007, is an imaging, wide field-of-view, high-energy gamma-ray telescope, covering the approximate energy range from 20 MeV to more than 300 GeV. Annihilation of Weakly Interacting Massive Particles, predicted in many extensions of the Standard Model of Particle Physics, may give rise to a signal in gamma-ray spectra from many cosmic sources. In this contribution we give an overview of the searches for WIMP Dark Matter performed by the GLAST-LAT collaboration.

1 Introduction

There is compelling experimental evidence for a dark component of the matter density of the Universe from observation of on many different scales such as galaxies, galaxy clusters and cosmic background radiation [1]. The questions of what constitutes this Dark Matter is one of the great mysteries of modern physics. One of the most promising candidates for the Dark Matter is a Weakly Interacting Massive particle (WIMP). WIMPs can be detected indirectly via their annihilation products, in particular neutrinos, anti-protons, positrons and gamma-rays.

The spectrum of gamma-rays due to WIMP annihilation can be constructed in a "generic" fashion, i.e. almost independent of underlying physics model. The light yield per annihilation is given by:

$$\frac{dN_\gamma}{dE} = \frac{dN_{\rm cont}}{dE}(E) + \sum_X b_{\gamma X} n_\gamma \delta\left(E - m_\chi(1 - m_\chi^2/4m_\chi^2)\right) \qquad (1)$$

The first term is the contribution from WIMP annihilations into the full set of tree-level final states, containing fermions, gauge or Higgs bosons, whose fragmentation/decay chain generates photons predominantly via pion decay. For Majorana fermion WIMPs light fermions are suppressed so that the dominant fermionic annihilation products will be $b\bar{b}, t\bar{t}$ and $\bar{\tau}\tau$. The second term is a line originating from annihilation into a two particle final state. As WIMPs are non-relativistic, the photon energy is fixed by the mass of the WIMP, m_χ and the mass of the other particle X (for example a Z boson), $b_{\gamma X}$ is the branching fraction and n_γ is the number of photons per annihilation, i.e. two for the all γ final state, one for the others. For the 2 γ final state the line is centered on energy $E = M_\chi$. This process is forbidden on tree level with a branching fraction of usually 10^{-3} to 10^{-4}. In addition to the light yield and branching functions the flux depends on the velocity averaged cross-section and the WIMP mass.

In this note we will give a short description of the GLAST project and summarize the searches for Dark Matter envisaged to be performed with GLAST. As examples, we will discuss the potential for GLAST to detect Galactic Dark Matter satellites and a possible signal in the extragalactic background flux.

For the sensitivities presented in this paper we assume all annihilations to lead to $b\bar{b}$ and 2γ, the latter with a branching fraction of 10^{-3}. For exclusion of specific models we refer the reader to the contribution by Morselli and Lionetto to the First International GLAST symposium which was held in Stanford, USA, in February 2007 [5].

2 The Large Area Telescope of GLAST

GLAST [2], which is part of the NASA's office of Space and Science strategic plan, is an international space mission that will study cosmic γ-rays in the energy range 20 MeV - 300 GeV. This mission is realized, as a close collaboration between the astrophysics and particle physics communities, including institutions in the USA, Japan, France, Germany, Italy and Sweden. The main instrument on GLAST is the Large Area Telescope (LAT) complemented by a dedicated instrument for the detection of gamma-ray bursts (the Gamma-ray burst monitor, GBM). The baseline LAT is modular, consisting of a 4×4 array of identical towers. Each 40×40 cm^2 tower comprises a tracker, calorimeter and data acquisition module. The tracking detector consists of 18 xy layers of silicon strip detectors. This detector technology has a long and successful history of application in accelerator-based high-energy physics. It is well-matched to the requirements of high detection efficiency (>99%), excellent position resolution (<60 μm), large signal/noise (>20), negligible cross-talk, and ease of trigger and readout. Compared to its predecessor EGRET [3], the LAT (Large Area Telescope) will have a sensitivity exceeding that of EGRET by at least a factor of 50 (at 100 MeV), the energy range will be extended by a factor 10 and the energy (GLAST: 6 % at 10 GeV) and angular resolutions (GLAST $PSF_{68\%} < 0.1^\circ$ at 10 GeV) are improved by a factor of at least two. The improvement in sensitivity is partly due to the choice of silicon tracking detectors instead of the spark-chambers used in EGRET, which reduces the dead-time by more than three orders of magnitude. GLAST is now integrated in the space-craft and undergoes final testing. The launch of GLAST is scheduled for December 2007.

The main science targets are (1) to understand the mechanisms of particle acceleration in active galactic nuclei, pulsars, and supernova remnants (2) to resolve the gamma-ray sky; unidentified sources and diffuse emission (3) determine the high-energy behavior of gamma-ray bursts and transients, and finally (4) to probe dark matter and early Universe.

3 LAT searches for Dark Matter

The GLAST-LAT collaboration pursues complementary searches for Dark Matter each presenting its own challenges and advantages. In table 1 we summarize the most important ones.

The center of our own galaxy is a formidable astrophysical target to search for a Dark Matter signal, the reason being that simulations of Dark Matter halos predict high densities at the center of the galaxy and since the WIMP

annihilation rate is proportional to the density squared, significant fluxes can be expected. On the other hand, establishing a signal requires identification of the high energy gamma-ray sources which are close (or near) the center [4] and also an adequate modeling of the galactic diffuse emission due to cosmic rays colliding with the interstellar medium. The latter is even more crucial for establishing a WIMP annihilation signal from the galactic halo.

Due to the 2γ production channel, a feature in the spectrum from the various astrophysical sources would be the gamma-ray line placed at the WIMP mass. This is a "golden" signal, in the sense that it would be difficult to explain by an astrophysical process different from WIMP annihilation. Also it would be free of astrophysical uncertainties, since the background can be determined from the data itself. However, since the 2γ channel is loop-suppressed, the number of photons will be very low.

In the following sub-sections, we will give a short description of two of the performed searches: (1) the search for cosmological annihilations of WIMPs and (2) the search for galactic satellites.

3.1 Cosmological WIMP annihilation

Pair annihilation WIMP Dark Matter into high energy photons taking place in dark matter halos at all redshifts might contribute to the extragalactic diffuse gamma-ray radiation. The γ- annihilation channel would give rise to a distinct feature in the spectrum, a line which is distorted by the integration over all cosmological redshifts. The number of photons collected by a detector per unit area-time-energy and solid angle on the sky, originating from WIMP annihilations accumulated over all redshifts, can be calculated by [6]:

$$\frac{d\phi_\gamma}{dE_0} = \frac{\sigma v}{8\pi}\frac{c}{H_0}\frac{\bar{\rho}_0^2}{M_\chi^2}\int dz(1+z)^3\frac{\Delta^2(z)}{h(z)}\frac{dN_\gamma(E_0(1+z))}{dE}e^{-\tau(z,\,E_0)}. \qquad (2)$$

where particle physics determines the cross section σ, the WIMP mas M_χ and the gamma-yield per annihilation given in equation 1. The quantity $\Delta^2(z)$ describes the averaged squared over density in halos, as a function of redshift and ρ_0 is the present day mean density. The annihilation rate is proportional to the dark matter density squared, which means "clumpiness" can significantly enhance the possible signal from WIMP annihilation.

The extragalactic gamma-ray signal is strongly affected by absorption in the inter-galactic medium, especially at high energies, dominantly by pair production of GeV-TeV photons on infrared/optical background. The absorption is

Table 1: *Summary of the different searches for Particle Dark Matter undertaken by the GLAST-LAT collaboration. For reference we include the contributions to the 1st International GLAST Symposium describing the respective analyses* [5)]

Search	advantages	challenges	GLAST Symp.
Galactic center	good statistics	Difficult source id, uncertainties in diffuse background	Morselli et al.
Satellites	Low background, good source identification	low statistics	Wang et al.
Galactic halo	Large statistics	Uncertainties in diffuse background	Sander et al.
Extra galactic	Large statistics	Uncertainties in diffuse background, astrophysical uncertainties	Bergström et al.
Spectral lines	No astrophysical uncertainties "golden" signal	low statistics	Edmonds et al.

parameterized by the parameter τ, the optical depth. We include the effect of absorption using parameterizations of the optical depth as function of both redshift and observed energy [7)]. More recent calculation of the optical depth [8)] do not alter our results significantly. The Hubble parameter enters via the present day value, H_0, and the dimensionless quantity $h(z)$, which depends on the energy content of the Universe which changes with redshift. For these values we have used the results from the WMAP three-year data [9)].

To obtain preliminary estimates of the GLAST senstivity to this type of signal, fast detector simulations were performed for a generic model of WIMPs annihilating into 2γ and into $b\bar{b}$ as described in the previous section. A χ^2 analysis was performed, assuming that the background consists of unresolved blazars [6)] to obtain a sensitivity plot in $< \sigma v >$ vs M_χ. The WIMP signal was computed using the Navarro-Frank-White (NFW) profile [10)] for normalization. According to N-body simulations, within larger halos there might exist smaller, bound halos that have survived tidal stripping. Although not as numerous as the primary halos the substructure halos arise in higher density environments

which makes them denser than their parent halo. In addition to a smooth NFW profile, we therefore also consider the case of NFW profile with subhalos. Here, we assumed that they constitute 5% of the mass and have three times the concentration parameter of the parent halo. The distribution of concentration parameters, as a function of halo mass are inferred from N-body simulations [12]. The result (see figure 1, right panel) shows that GLAST should be sensitive to total annihilation cross-sections of the order $10^{-26} - 10^{-25}$ cm^3 s^{-1}, depending on the halo model. One should note that this estimate neglects contributions of instrumental background, uncertainties introduced by the analysis (where point-sources and galactic diffuse emission have to be taken into account) and finally that the extragalactic background spectrum from astrophysical sources is very uncertain, especially at high energies.

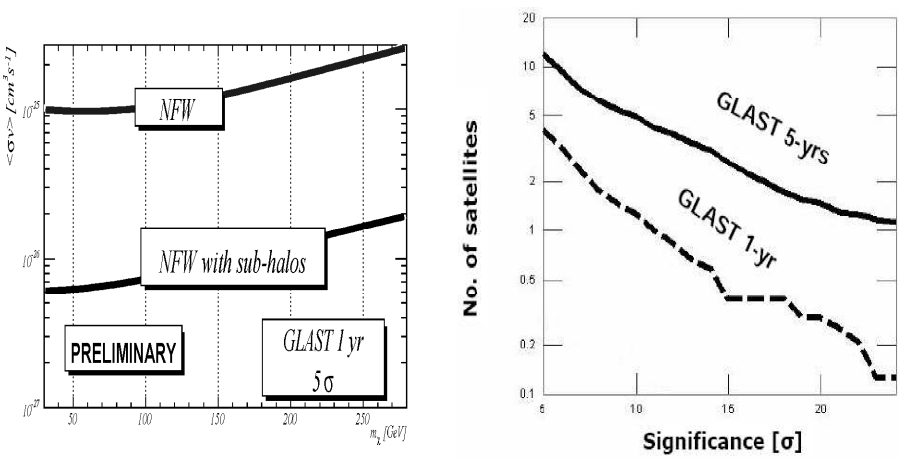

Figure 1: *Left panel:* 5σ exclusion curves for one year of GLAST simulated data. NFW denotes the Navarro Frank White profile, NFW plus sub-halos assumes a substructure in the halos. *Right panel:* The number of satellites that could be detected as a function of required significance. See text for more details

3.2 Searches for Dark Matter satellites

Subhalos which, as seen in the previous section, lead to a signficant enhancement of the WIMP annihilation induced flux in the extragalactic background

would be present also in our own Galaxy. They could be detectable as Dark Matter satellites. We used simulations of Dark Matter satellite formation [13] combined with a fast detector simulation to predict the number of satellites detectable by GLAST. The DM satellite distribution is roughly spherically symmetric about the galactic center, with most of the observable satellites located at high galactic latitude (i.e. relatively low background). For this particular study we used reference [14] to estimate the background as the point source subtracted sky map above 1 GeV [1]. The significance of detection was then calculated by estimating the number of signal events within the satellite tidal radius (or the PSF 68 % containment radius, whichever was bigger) divided by the square root of background events within the same radius. Figure 1, right panel, shows the number of satellites which could be detected by GLAST above a given signficance in 1 and 5 years of GLAST operation. Here a 100 GeV WIMP with a velocity averaged cross-section $< \sigma v >= 2.3 \cdot 10^{-26}$ cm^3 s^{-1} was assumed[2]. Under this assumptions GLAST will be able to detect a few highly significant satellites during 5 years operation. It should be noted that the true significance of detection will also have to take into account the fact that Dark Matter satellites need to be distinguished from other astrophysical sources,the most difficult probably being pulsars (see [15] for further discussion).

4 Conclusions

In this note we summarize the searches for particle Dark Matter to be performed with the GLAST-LAT instrument. Several complementary astrophysical sources will be examined, each presenting its own advantages and challenges. Those mentioned here are the galactic center, galactic halo, extragalactic background and galactic satellites. The golden signal for presence of particle dark matter would be a gamma-ray line at the mass of the WIMP. We showed that the GLAST-LAT has the possibility to detect a contribution of WIMP annihilation at all redshift to the extragalactic gamma-ray background. We also showed that galactic Dark Matter satellites can potentially be detected by the GLAST-LAT. GLAST is now integrated on the space-craft and undergoing final testing. The launch is foreseen for December 2007.

5 Acknowledgments

I would like to thank all members of the Dark Matter and New Physics Working Group of the GLAST-LAT who contributed to this note.

[1] This is probably a conservative assumption, since GLAST will be able to resolve many more point sources.

[2] a line contribution was neglected due to negligible statistics

References

1. G. Bertone, D. Hooper and J. Silk, Phys. Rept. **405** (2005) 279 [arXiv:hep-ph/0404175].
2. P. F. Michelson, *Presented at 6th Compton Symposium On Gamma Ray Astrophysics 2001, 4-6 Apr 2001, Baltimore, Maryland.*
3. http://cossc.gsfc.nasa.gov/docs/cgro/cgro/egret.html
4. H. A. Mayer-Hasselwander *et al.*, Astron. Astrophys. **335** (1998) 161.
5. 1st International GLAST symposium, Stanford, USA, February 2007 http://glast.gsfc.nasa.gov/science/symposium/2007/
6. P. Ullio, L. Bergstrom, J. Edsjo and C. G. Lacey, Phys. Rev. D **66** (2002) 123502 [arXiv:astro-ph/0207125].
7. J. R. Primack, R. S. Somerville, J. S. Bullock and J. E. G. Devriendt, AIP Conf. Proc. **558** (2001) 463 [arXiv:astro-ph/0011475].
8. F. W. Stecker, M. A. Malkan and S. T. Scully, Astrophys. J. **658** (2007) 1392 [arXiv:astro-ph/0612048].
9. D. N. Spergel *et al.* [WMAP Collaboration], arXiv:astro-ph/0603449.
10. J. F. Navarro, C. S. Frenk and S. D. M. White, Astrophys. J. **490** (1997) 493 [arXiv:astro-ph/9611107].
11. B. Moore, T. Quinn, F. Governato, J. Stadel and G. Lake, Mon. Not. Roy. Astron. Soc. **310** (1999) 1147 [arXiv:astro-ph/9903164].
12. J. S. Bullock *et al.*, Mon. Not. Roy. Astron. Soc. **321** (2001) 559 [arXiv:astro-ph/9908159].
13. J. E. Taylor and A. Babul, Mon. Not. Roy. Astron. Soc. **364** (2005) 535 [arXiv:astro-ph/0410049].
14. A. N. Cillis and R. C. Hartman, Astrophys. J. **621** (2005) 291.
15. E. A. Baltz, J. E. Taylor and L. L. Wai, arXiv:astro-ph/0610731.

RECENT RESULTS FROM PAMELA

Piergiorgio Picozza
Università degli Studi di Roma "Tor Vergata"
Via della Ricerca Scientifica 1, 00133 Roma

Written contribution not received

ICECUBE: NEUTRINO TELESCOPE AT THE SOUTH POLE

Seon-Hee Seo
for the IceCube Collaboration
The Pennsylvania State University,
Department of Physics,
University Park, PA 16802, USA

Abstract

IceCube[1] is a cubic kilometer ice-Cherenkov neutrino telescope currently (2007) under construction at the South Pole and operating with its partial (∼28%) detector. IceCube, which incorporates the existing AMANDA detector, is optimized for detecting ∼100 GeV to ∼1 PeV neutrinos and the physics potential of IceCube is relatively versatile, from astronomy to particle physics. The design of IceCube detector has been validated by detecting a few hundreds of up-going atmospheric neutrinos with 2006 data (∼10% detector).

IceCube will collect a square kilometer year of integrated data well before its completion in 2011.

[1] http://icecube.wisc.edu/

1 Introduction

At the Earth we observe high energy particles coming from extra-terrestrial sources. Those particles are cosmic rays (~80% protons) with energies up to $\sim 10^{20}$ eV and photons with energies as high as ~10's of TeV. The existence of those particles can be explained by theoretical models such as hadronic acceleration (bottom-up model) and exotic particle decay (top-down model). Those models predict the existence of high energy neutrinos as well. In the bottom-up model the candidate sources which produce such particles are Gamma Ray Bursts (GRB), Active Galactic Nuclei (AGN) and Supernova Remnants. The top-down models predict Weakly Interacting Massive Particles (WIMP) and topological defects such as monopoles that produce high energy standard particles through their decay.

It would be very interesting to discover what are the sources of these particles and what are the physical mechanisms that produce them. These particles will bring us information about the sources and thus help us to understand the physics at the remote sources.

In studying these sources, different particle types each have pros and cons. Protons with energy less than 10 EeV are bent on their way to the Earth due to (extra-) galactic magnetic fields so that they no longer point back to their sources. Protons with energy greater than 50 EeV are strongly attenuated due to the GZK (Greisen-Zatsepin-Kuzmin) cutoff. Photons are also attenuated due to interactions above 50 TeV.

Neutrinos are neutral so that they keep their directional information regardless of their energy. They also interact weakly so that there is no attenuation, but a big detection volume is needed to compensate for their small cross section. Thus, neutrino telescopes must be large-scale to be effective.

Currently there are several neutrino telescopes under construction using water or ice as their detection medium. The water-based ones are Baikal[2], ANTARES[3], NEMO[4] and NESTOR[5] located in the northern hemisphere. The ice-based one is IceCube (including its sub-detector AMANDA) located at the South Pole. Each medium has advantages and disadvantages. Water has a relatively short absorption length (~70 m at 450 nm wavelength) and also has

[2]http://www-zeuthen.desy.de/baikal/baikalhome.htm
[3]http://antares.in2p3.fr/
[4]http://nemoweb.lns.infn.it/project.htm
[5]http://www.nestor.org.gr/programme/nestor_scientific_programme.htm

a short attenuation length (∼50 m). Noise rates are quite high in sea water due to biological and chemical sources of light production. On the other hand ice has a long absorption length (∼110 m) but has a short scattering length (∼20 m) at 400 nm wavelength. There is no environmental noise in ice. These two types of experiments will complement each other because they look at opposite part of the sky and they use different Cherenkov medium. In the following sections the IceCube detector and its physics will be presented.

2 The IceCube Detector

IceCube is a cubic kilometer scale optical Cherenkov neutrino telescope using ice as its detection medium. The South Pole was selected for the experiment site because the ice there is known to be very clear and deep, which leads to less scattering of Cherenkov light than any other ice on the Earth and removing down-going muons, respectively.

IceCube includes two other detectors as shown in fig.1: IceTop, a surface air shower array and AMANDA[6]. IceCube will consists of at least 4200 Digital Optical Modules (DOM) equally distributed on 70 or more strings 125 m apart and frozen into the deep ice (from 1450 m to 2450 m below the surface). IceTop station is built as an array of stations on top of each IceCube string and it consists of 320 DOMs equally distributed in 80 stations. AMANDA consists of 677 Optical Modules (OM) distributed in 19 strings. AMANDA modules are populated more densely than IceCube, which has 10 $\sim$ 20 m vertical spacing with ∼40 m inter-string distance.

IceCube and IceTop DOMs digitize PMT (Photo Multiplier Tube) signals *in situ*. For the waveform digitization there are two types of chips mounted on each DOM Main Board: Analog Transient Waveform Digitizer (ATWD) and Fast Analog to Digital Converter (FADC). ATWDs are used to capture initial waveforms accurately within 425 ns with 300 MHz sampling rate and the FADC is used to get overall waveform information within 6.4 μs with 40 MHz sampling rate. There are two ATWD chips per DOM and they operate one after the other to reduce the detector dead time to almost zero. In each ATWD there are 3 channels with different gains for large dynamic range. In AMANDA the analog waveforms from PMTs are transmitted to the surface electronics via

[6]AMANDA has been taking data since 1996 and has been integrated to IceCube since 2007.

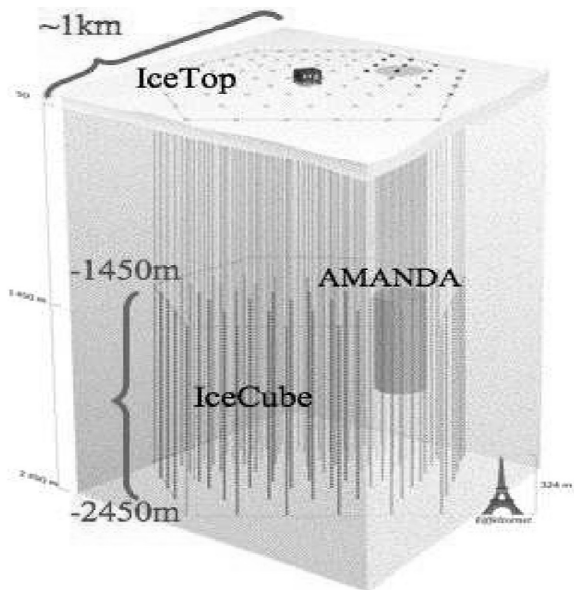

Figure 1: *The IceCube Detector which includes IceTop and AMANDA.*

optical fibers or electrical cables, where the waveforms are digitized by TWRs (Transient Waveform Recorder).

3 IceCube Physics

The IceCube detector combined with AMANDA is optimized for detecting neutrinos with energy from ∼100 GeV to ∼1 PeV. However the combined IceCube can also probe neutrinos with lower (down to ∼30 GeV) and higher (up to ∼1 EeV) energy.

Physics topics of IceCube are broad, from astronomy and astrophysics to particle physics, including: search for neutrino point sources, measurement of diffuse neutrino flux, measuring cosmic ray energy spectrum and its composition, search for exotic particles like WIMPs, monopoles, neuclearites, Q-balls, and stau pairs, search for tau neutrinos, and testing violation of equivalence principle and Lorentz invariance.

In the following subsections I will highlight some of the IceCube physics results and/or techniques.

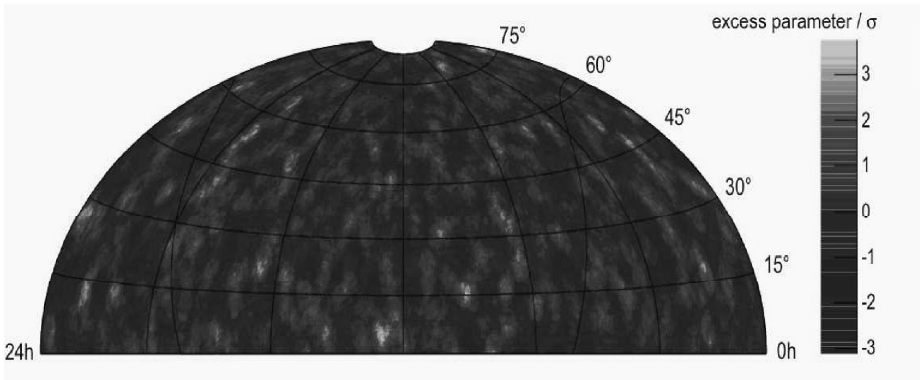

Figure 2: *AMANDA sky map with its 5 years of data.*

3.1 Neutrino Point Sources

Searching for sources which produce high energy neutrinos is one of the main studies in IceCube. Recent AMANDA results [1)] in an all-sky search for point sources using 5 years of data (2000 - 2004, 1001 live days) did not find any significance greater than 3.7σ before correcting for trial factors. For sky maps with randomized right ascensions of the individual neutrinos, a larger significance was found with 70% probability. Thus the sky-map of 5 years' AMANDA events as shown in fig.2 is compatible with random fluctuations and AMANDA could set only upper limits on the neutrino flux from point sources.

The point source sensitivity will be better with IceCube because IceCube has a better pointing resolution ($\sim 1^o$) than AMANDA ($1.5^o \sim 2.5^o$).

3.2 Diffuse Neutrino Search and Atmospheric Neutrinos

AMANDA measured up-going neutrino events with four years of data (2000 - 2003, 807 live days). The number of OMs triggered in the detector (N_channel) was used as an energy estimator. Observations in the high N_channel region can be used to set an upper limit on the diffuse neutrino flux from extra-galactic sources whose energy spectrum is believed to be harder (E^{-2}) than conventional atmospheric neutrinos ($E^{-3.7}$). The upper limit at 90% confidence level is $E^2\Phi_{\nu_\mu}(E) < 7.4 \times 10^{-8} GeV cm^{-2} s^{-1} sr^{-1}$ from 16 TeV to 2.5 PeV energy

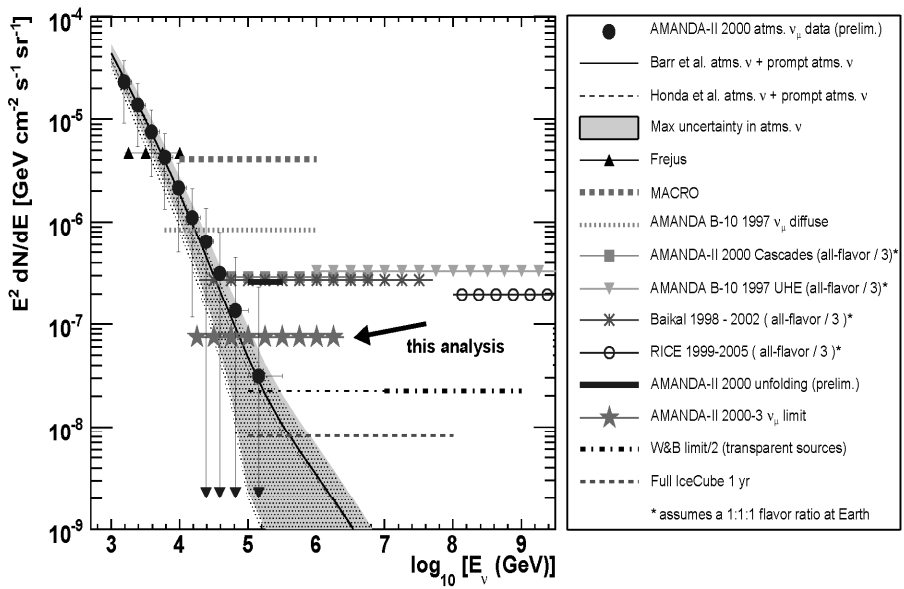

Figure 3: *Various measurements of diffuse neutrino flux limits and AMANDA atmospheric neutrino flux.*

range [2].

Fig.3 shows the upper limit on the diffuse flux of astrophysical muon neutrinos based on AMANDA-II data from 2000 - 2003. The atmospheric neutrino flux measurement made with AMANDA-II data from 2000 is also shown and agrees well with atmospheric neutrino flux predictions [4] [5]. One year of full IceCube (80 string) data is expected to improve the measurement on the diffuse neutrino flux by an order of magnitude.

IceCube has observed 234 candidate up-going atmospheric neutrinos in the 2006 data (137.4 live days with 9 strings) where we expect 211 $\pm$ 76 (syst.) $\pm$ 14 (stat.) events from atmospheric neutrino simulation [3]. This is the first IceCube physics result and demonstrates the success of many aspects of IceCube detector performance.

3.3 WIMP Search

Indirect solar and Earth WIMP searches are one of the main physics topics in IceCube. Minimal Supersymmetric extensions to the Standard Model (MSSM) provides an ideal dark matter candidate in the Neutralino χ. Current limits

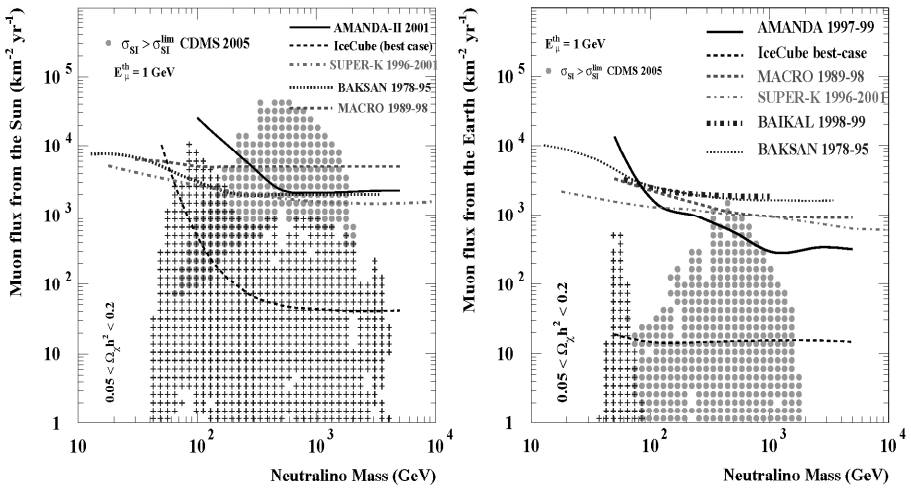

Figure 4: *Solar (left) and Earth (right) WIMP upper limits on the muon flux from neutralino induced muon neutrinos at 90% confidence level (Some calculations in these plots are done in collaboration with J. Edsjö* [8] *).*

on neutralino mass (m_χ) are 46 GeV $< m_\chi <$ 10 TeV.

WIMPs may become gravitationally trapped and accumulate inside massive celestial objects such as the Sun or the Earth. Those accumulated WIMPs can annihilate and produce neutrinos.

AMANDA has looked for muon neutrinos from the Sun and the Earth and set upper limits on the muon flux from neutralino induced muon neutrinos at 90% confidence level as shown in fig.4 [6] [7]. For the solar WIMP limit 2001 data (143.7 live days) were used and for the Earth WIMP limit 1997-1999 data (536.3 live days) were used.

Current AMANDA limits on both solar and Earth WIMPs lie in the region disfavored by the Cryogenic Dark Matter Search (CDMS) [9]. However IceCube sensitivities[7] for these two types of indirect WIMP detection sources will improve due to a combined detector of AMANDA and IceCube, where IceCube can be used as a veto for muon background [10], as well as much larger detection volume and better triggering.

[7]In the fig.4 the IceCube best case study was done without including AMANDA.

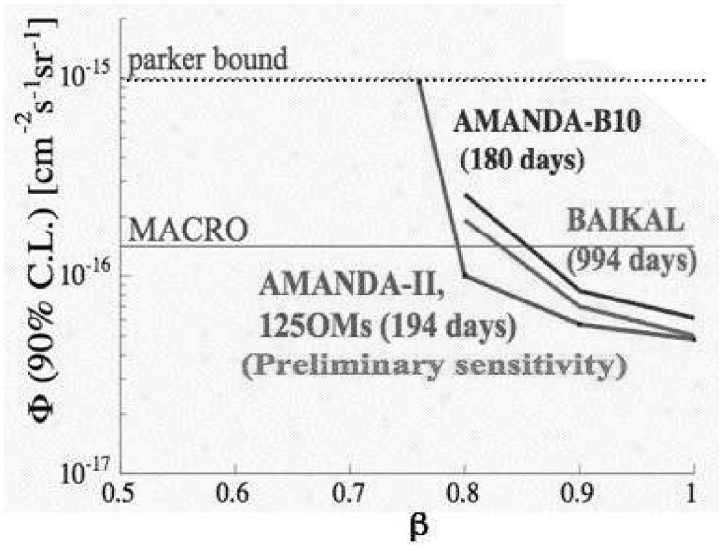

Figure 5: *Relativistic monopole flux upper limits.*

3.4 Monopole Searches

IceCube has the ability to detect relativistic ($\beta >\sim 0.5$) monopoles and non-relativistic GUT scale ($\beta >\sim 10^{-5}$) monopoles. Relativistic monopoles with $\beta >\sim 0.76$ leave very bright tracks ($\sim$8300 times brighter than a bare muon [11]) in the IceCube detector. Relativistic monopoles with $\sim 0.5 < \beta <\sim 0.76$ can be detected via δ electrons generated along the monopole path. Fig.5 shows the preliminary AMANDA sensitivity to relativistic monopoles with 194 live days of data (year 2000). IceCube is expected to push the limit to $\sim 10^{-18}$ to $10^{-19} cm^{-2} s^{-1} sr^{-1}$ due to larger effective area, less saturation of DOMs, and a special trigger for monopoles [12].

The GUT scale monopoles can be detected by Cherenkov radiation from relativistic electrons produced by nucleon decay catalyzed by the monopoles via Rubakov-Callan mechanism [13] [14]. A search for these particles in IceCube is underway.

3.5 Tau Neutrino Physics

When high energy protons interact with photons and/or a nucleus near sources, pions are produced. These pions can decay to muons which decay mostly to electrons with their accompanying neutrinos resulting in ν_e:ν_μ:ν_τ = 1:2:0 ratio, assuming there is no new physics near the sources provided that the environments of the sources are similar to our atmosphere. However neutrinos oscillate as they travel astronomical distance and thus can be detected as ν_e:ν_μ:ν_τ = 1:1:1 at the Earth, given the measurements of $\sin\theta_{23} = 1$ and $\Delta m^2 = \sim 10^{-3}$ eV.

IceCube has the ability to tag all flavors of neutrinos. Measuring the neutrino flavor flux ratio will help us to understand the physics mechanism and environment near sources. Tau neutrinos leave unique signatures in the IceCube detector due to the short lifetime of the tau. These signatures, dubbed 'inverted-lollipop', 'lollipop', 'double bang', 'double pulse', 'low energy μ lollipop' and 'sugar daddy', depend on where the neutrino interaction has occurred, where the tau has decayed and what the tau decays to. Fig.6 illustrates various tau signatures that can be detected in IceCube [15].

The tau neutrino has not been detected in any neutrino telescope as yet. With 22 strings, a tau neutrino search in IceCube is currently feasible.

4 Current Status of IceCube

As of 2007 IceCube has deployed 22 IceCube strings and 26 IceTop stations which makes IceCube the largest neutrino telescope to date. The fiducial volume of the 2007 IceCube configuration is about 8 times larger than that of AMANDA. Data being taken in 2007 will allow us to explore many interesting topics described in previous section.

IceCube plans to deploy 18 additional strings next year over the next 3 years in order to finish the construction by 2011. Until then IceCube will take data with its partial detector continuously except string deployment season (from mid-November to mid-February). The integrated data until the completion will be worth more than a square kilometer year of data.

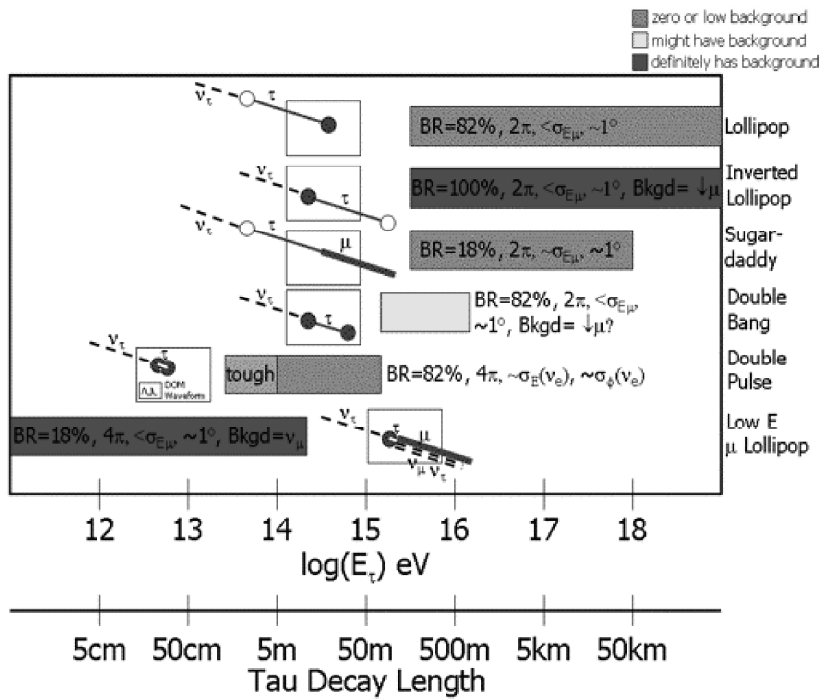

Figure 6: *Unique tau signatures in IceCube.*

5 Summary

IceCube is a cubic kilometer scale neutrino telescope operating at the South Pole. IceCube's range of physics goals is broad and will definitely improve AMANDA measurements with larger detection volume and better angular and energy resolutions.

Five years of AMANDA point neutrino source result did not find any significant sources, but IceCube sensitivity for point sources will be better. One year of IceCube data will improve the diffuse neutrino flux limit by an order of magnitude over that of AMANDA 4 years data. Solar and Earth WIMP sensitivity will be much improved with IceCube in conjunction with AMANDA. Monopole sensitivity will be improved. Tau neutrino searches have started and will play as important a role as other neutrino channels in IceCube.

As of 2007 IceCube is taking data with $\sim$ 28% of the complete detector, and is already the largest neutrino telescope. It has proved many aspects of

its physics performance by detecting 234 candidate atmospheric neutrinos from the data taken with $\sim 10\%$ of the complete detector. Many interesting physics results are expected soon with 2007 data.

References

1. A. Achterberg *et al*, Phys. Rev. **D75**, 102001 (2007).
2. A. Achterberg *et al*, e-print archive arXiv:0705.1315 [astro-ph] (2007).
3. A. Achterberg *et al*, e-print archive arXiv:0705.1781 [astro-ph] (2007).
4. H. Geenen, Energy Reconstruction and Spectral Unfolding of Atmospheric Leptons with the AMANDA Detector, Diploma Thesis, University of Wuppertal, WU-D 2002-10 (2002).
5. K. Münich, Search for a Diffuse Flux of Non-terrestrial Muon Neutrinos with the AMANDA Detector, in: Proc. the 29th International Cosmic Ray Conference, (ed. B. Sripathi Acharya *et al*, Pune, India, 2005), **5**, 17 (Tata Institute of Fundamental Research, Mumbai, 2005).
6. M. Ackermann *et al*, Astroparticle Phys. **24**, 459 (2006).
7. A. Achterberg *et al*, Astroparticle Phys. **26**, 129 (2006).
8. L. Bergström *et al*, Phys. Rev. **D58**, 103519 (1998).
9. D.S. Akerib *et al*, Phys. Rev. Lett. **96**, 011302 (2006).
10. G. Wikström, Methods of Indirect Detection of Dark Matter in IceCube, Licentiate thesis (Stockholm University, May 2007).
11. D. Tompkins, Phys. Rev. **B138**, 248 (1965).
12. D. Hardtke, Exotic Physics with IceCube, in: Proc. the first Workshop on Exotic Physics with Neutrino Telescopes, (ed. C. P. de los Heros, Uppsala, September 2006), ISBN 978-91-506-1913-3, 89 (Uppsala University, Sweden, 2007).
13. V. A. Rubakov, JETP Lett. **33**, 644 (1981).
14. C. G. Callan, Phys. Rev. **D26**, 2058 (1982).
15. T. DeYoung *et al*, Astroparticle Phys. **27** 238 (2007).

ANTARES OPENS ITS EYES

E. de Wolf
*on behalf of the Antares collaboration**
NIKHEF and University of Amsterdam
Kruislaan 409, 1098 SJ Amsterdam, The Netherlands

Abstract

Antares is a neutrino telescope under construction at the bottom of the Mediterranean Sea at a depth of about 2500 m, 40 km off the coast of La Seyne-sur-mer, France. On completion, the telescope will consist of twelve vertical mooring lines each equipped with 75 photomultipliers. The three-dimensional array of photomultipliers will be used to observe the Cherenkov light emitted by neutrino-induced muons. In March 2006 the first full detection line was connected to the shore station via the junction box at the bottom of the sea and is continuously taking data since. A year later, in March 2007, the telescope became operational with five lines and the first upward going neutrino induced muons have been observed.

* For a list of the members of the Antares collaboration see http:antares.in2p3.fr

1 Introduction

One of the most important objectives of neutrino telescopes is to contribute to solving the question about the origin of high energy cosmic rays. Many astrophysical sources [1] like e.g. active galactic nuclei and transient sources like gamma ray bursters are candidates to accelerate hadrons. In their interaction with ambient matter and dense photon fields these hadrons produce pions. Subsequently, neutrinos are created in the decay of charged pions. Since neutrinos travel undisturbed by interstellar magnetic fields and couple only weakly to matter, they are unprecedented as probes of the universe: they point back to their source and can bring information about processes in the core of these sources.
An other objective of neutrino telescopes is the detection of neutrinos produced in the annihilation of neutralinos, gravitationally trapped inside the core of massive objects like the Sun, the Earth or the Galactic centre [2]. The weak coupling of neutrinos to matter require huge detection volumes. For this, using the Cherenkov technique in transparent natural water or ice offers a cheap solution. The detection principle relies on the observation of Cherenkov light produced by neutrino induced muons by a three-dimensional array of photodetectors. The higher the neutrino energy the smaller the angle between the direction of the neutrino and the produced muon. Cosmic rays penetrating the atmosphere cause a cascade of many secondary particles, amongst which high energy muons which constitute an intense source of background in the detector. To suppress this background of atmospheric muons, neutrino telescopes are optimized to detect upward going muons produced by neutrinos beneath or in the vicinity of the detector after traveling through the Earth. An other source of background are atmospheric neutrinos produced in the atmospheric cascades.

2 The Antares telescope

The Antares collaboration is deploying a telescope at a depth of about 2500 m, 40 km off the coast of La-Seyne-sur-Mer, France [3] [4]. The sea water properties have been extensively studied revealing low light scattering, mainly forward and an average optical background induced by bioluminescence and ^{40}K decays of 70 kHz per detection channel [5]. The final detector will consist of an array of 12 mooring lines separated from each other on the sea bed by 60-80 m. The lines are connected to a junction box by a submarine or ROV using wet-mateable connectors. The junction box is connected to the shore station by an electro-optical cable. Each line will be equipped with 75 photomultipliers housed in glass spheres, referred to as optical modules (OM). Fig.1 shows a schematic layout of the Antares telescope. Starting 100 m above the seabed, each line

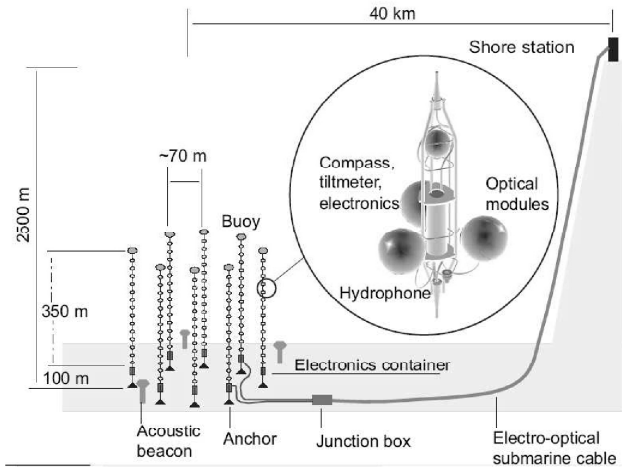

Figure 1: *Schematic layout of the future Antares telescope. The full detector will consist of 12 lines connected to a junction box and will be operated from shore in remote mode through an electro-optical cable.*

contains 25 storeys of a titanium mechanical construction with three OMs and a titanium cylinder for the electronic cards. The separation between storeys is 14.5 m. Some of them contain supplementary calibration equipment like acoustic or optical beacons. The signals of each photomultiplier are readout by two ASICs. For simple pulses charge and arrival time are digitized and stored for transfer to the shore station. For more complex pulses the pulse shape can be digitized with a sampling frequency up to 1 GHz. The time stamps are synchronized by a clock signal which is sent in regular intervals from the shore to all electronic cards. The overall time calibration is better than 0.5 ns. Therefore the time resolution of the signal pulses will be limited by the transition time spread of the photomultipliers ($\sigma \approx 1.3$ ns). All data are sent to the shore station. With a noise light rate of 70 kHz on the one photon level this produces a data flow of 1 Gbit/s to the shore. In the shore station a PC farm performs a data filtering to reduce the data rate by at least a factor of 100.

3 Construction of the telescope

The electro-optical cable connecting the Antares site and the power station and the control room in La Seyne sur mer was deployed in October 2001. The junction box was connected to the remote cable end and deployed in December 2002. Since its deployment it is permanently monitored and has successfully operated. ¿From March to June 2003 two test lines have validated all components for mass production of the full detector. In March 2005 the first permanent line with three storeys with optical modules and equipment to monitor the deep sea environment was installed. One year later, in March 2006, the first complete detector line equipped with 75 optical modules has been deployed and connected to the junction box. Since then a new line is completed about every two month. About every 6 months the new lines are connected to the junction box during a submarine campaign. The most recent connection operations happened in September 2006 and January 2007. Therefore in March 2007 the detector was operating with a total of five detector lines. Completion of the twelve line detector is expected early 2008.

4 Physics performance

Most studies so far concentrated on charged current interactions of ν_μ:

$$\nu_\mu(\bar{\nu}_\mu) + N \rightarrow \mu^-(\mu^+) + X \tag{1}$$

The concept for the reconstruction of the muon is based on the fact that it emits Cherenkov light under a well defined angle and does not suffer from multiple scattering at high energies. In Antares several reconstruction algorithms for muons have been developed which use the direct Cherenkov hits and take into account effects like diffusion, dispersion and electromagnetic showers which accompany high energetic muons. This leads to an angular resolution for the muons of better than 0.2^0 above 1 TeV for the above mentioned 1.3 ns single pulse resolution of the photomultipiers. Taking into account the interaction kinematics the neutrino angular resolution becomes 0.7^0 at 1 TeV and decreases to the detector-dominated 0.2^0 at 100 TeV. The neutrino energy is estimated from the light output of the muon track in the vicinity of the detector, which in the TeV range increases with energy due to radiative processes. However, the fact that radiative processes are stochastic, that the position of the vertex of the neutrino interaction is unknown and the fact that only a short fraction of the muon track is seen in the detector compromise the measurement of the energy. Procedures have been developed which estimate the muon energy within a factor 3 for energies below 100 TeV and within a factor 2 for higher energies. An other important parameter to characterise the performance of the detector is the effective area. Fig. 2 gives the effective areas for a neutrino

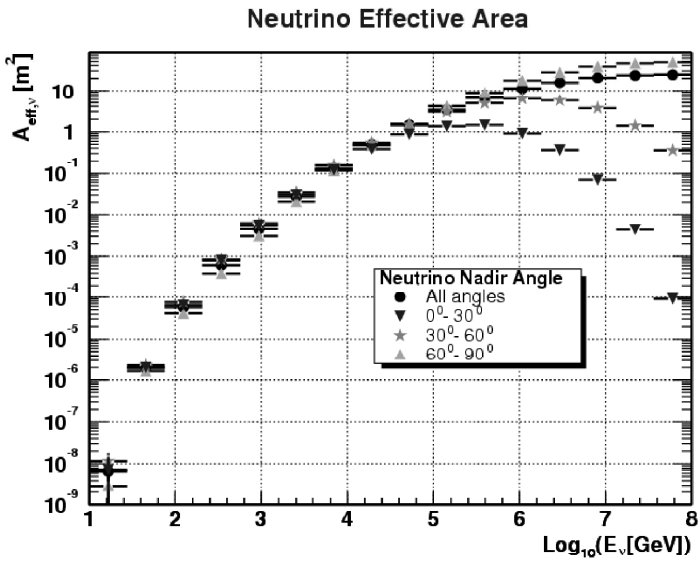

Figure 2: *Energy dependence of the effective area for neutrinos before entering the Earth.*

flux before penetration of the Earth for various nadir angle bins. This has the advantage that such an effective area can be folded directly with neutrino flux predictions from astronomical sources to obtain the number of expected signal events and it can be easily compared to effective areas for muons: the overall scale changes from km^2 to m^2 due to the fact that the neutrino cross section is small. The energy dependence becomes much stronger due to the almost linear rise of the neutrino cross section. The opacity of the Earth limits the effective area to values below 20 m^2. Using the above performance parameters one can estimate that Antares will detect about 3000 upward going muon tracks from atmospheric neutrinos per year. They provide a detectible neutrino signal in the Antares detector, even during its construction phase.

5 First results

From March 2006 until September 2006 data have been taken with a single detector line. During this period the basic concepts of the trigger mechanisms and reconstruction algorithms could be validated. Since February 2007 Antares is operational with five detector line. The five lines make it possible to test for the first time the calibration method on their full scale. Since the detector lines move in the sea current, the position and orientation of all elements must

be monitored with a time interval of a few minutes. For this purpose each line contains several acoustic receivers. They communicate with transmitters at the sea bottom. From each set of acoustic data the distance between the two elements can be established with a precision of a few centimetres. Several such measurements, distributed in space, make it possible to determine their relative positions by triangulation. Fine tuning of the parameters of this system is ongoing to reach the desired precision of about 10 cm. The acoustic system is completed by measurements of the inclination and twist of each storey which determine their orientation in space. To verify the timing calibration of the detector elements and to monitor the water properties optical beacons are distributed in the detector array. They emit short but powerful light flashes which can illuminate neighbouring lines. Large amounts of data have been taken and are being analyzed.
The five line detector make a full three dimensional reconstruction of muon tracks and the distinction of upward and downward going tracks possible. For the latter it is important to reduce the fraction of downward going muons tracks or muon bundles which are misreconstructed as upward going because the flux of downward going muons is several orders of magnitude more important than the upward going atmospheric neutrino flux. Such a method has been developed within a PhD thesis [6] based exclusively on the analysis of simulated data.

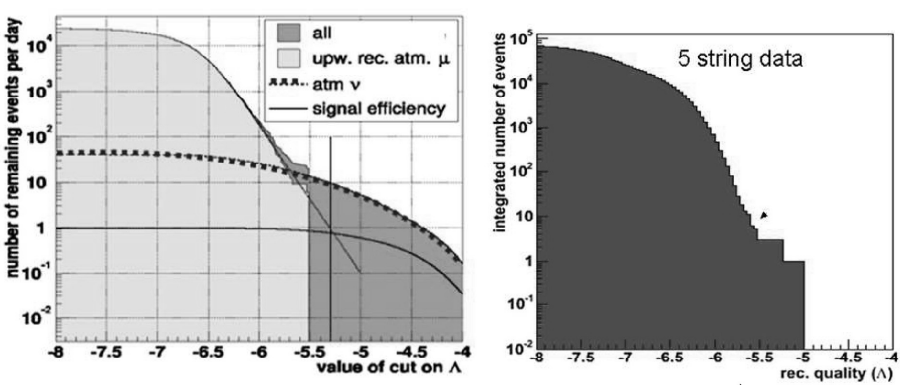

Figure 3: *Reconstructed likelihood, left based on Monte Carlo [6], right from a short data taking period in February 2007. The left plot illustrates the different contributions from misreconstructed atmospheric muons and neutrinos.*

The left plot of Fig.3 shows a trace fit likelihood parameter which can be used to distinguish the two components. A cut of $\Lambda > -5.3$ is suggested to reduce the fraction of misreconstructed atmospheric muons in the sample of upward going tracks to less than 10%. Applying the same method to data without any additional tuning one obtains the right plot in Fig.3. The similarity between the two plots is striking despite of some important differences: the real

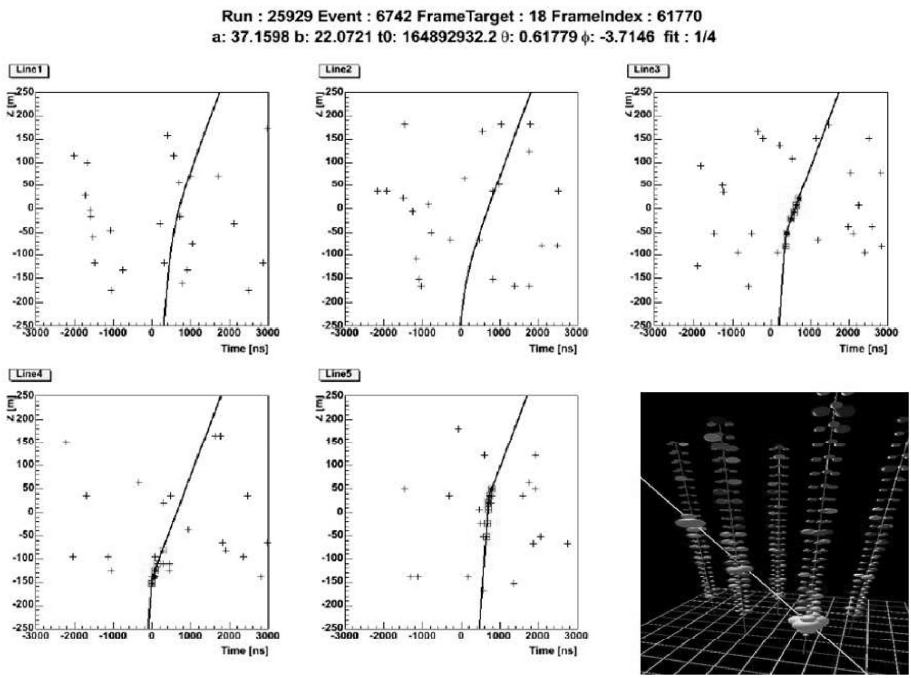

Figure 4: *Atmospheric neutrino induced muon candidate obtained with the five line detector in February 2007. Each plot shows a single line hit distribution as a function of time. The bottom-right drawing is a 3D display of the same event. The muon trajectory is reconstructed upgoing with a zenith angle* 35.4^0 *away from vertical.*

data have been taken with a 5 lines detector whereas the Monte Carlo study was done for the full 12 line detector. For the data sample no positioning calibrations had been applied. Applying the above mentioned cut on Λ to this data sample three candidate events remain. These have been cross checked with an independent reconstruction method and by using an event display.

One of them is illustrated in Fig.4 The reconstructed upward going track passes in the vicinity of three detector lines leaving a large amplitude signal at each of them. The grey color code reveals that these signals are time ordered from bottom to top leaving no doubt on the upward going character of this track.

6 Outlook

The construction and operation of the Antares telescope continues smoothly. The detector is working in nominal mode with five lines and should be completed early 2008. Upward neutrino candidates have been found that validate the conceptual method and the chosen techniques. In the near future the Antares collaboration will be able to present more qualitative results on atmospheric neutrinos and other physics results.

References

1. W. Bednarek, G.F. Burgio, and T. Montaruli, New Astron. Rev., **49**, (2005).
2. E. Falchini, The ANTARES experiment: sensitivity to dark matter candidates, in: Proc. ICRC 2007 (2007).
3. J.A. Aguilar *et al.*, Nucl. Instrum. Meth., **A555:132.141**, (2005).
4. J.A. Aguilar *et al.*, Astropart. Phys., **26:314.324**, (2006).
5. Antares, Astropart. Phys, **23:131-155**, (2005)
6. A. Heijboer, PhD thesis, Track reconstruction and point source searches with Antares, University of Amsterdam, Amsterdam, The Netherlands, (2004).

MEASURING $sin^2 2\Theta_{13}$ AT THE DAYA BAY REACTOR NEUTRINO EXPERIMENT

Christopher Mauger
Pasadena, USA

Written contribution not received

RECENT RESULTS FROM OPERA

Dario Autiero
Lyon, France

Written contribution not received

RECENT RESULTS FROM MINOS

Niki Saolidou
Fermilab, USA

Written contribution not received

SEARCH FOR SOLAR AXIONS IN THE CAST EXPERIMENT AT CERN

Christos Eleftheriadis
Nuclear Physics and Elementary Particles Section
Aristotle University of Thessaloniki
for the CAST Collaboration *

Abstract

Axions are expected to be produced in the sun via the Primakoff process. They may be detected through the inverse process in the laboratory, under the influence of a strong magnetic field, giving rise to X–rays of energies in the range of a few keV. Such an Axion detector is the CERN Axion Solar Telescope (CAST), collecting data since 2003. Results have been published, pushing the axion-photon coupling $g_{a\gamma}$ below the 10^{-10} GeV^{-1} limit at 95% CL, for axion masses less than 0.02 eV. This limit is nearly an order of magnitude lower than previous experimental limits and surpassed for the first time limits set from astrophysical arguments based on the energy-loss concept. The experiment is currently exploring axion masses in the range of 0.02 eV $< m_a <$ 1.1 eV. In the next run, currently under preparation, the axion mass explored will be extended up to the limit of 1.1 eV, testing for the first time the region of theoretical axion models with the axion helioscope method.

* S. Andriamonje[2], S. Aune[2], K. Barth[1], A. Belov[12], B. Beltrán[7], H. Bräuninger[6], J. Carmona[7], S. Cebrián[7], J. I. Collar[8], T. Dafni[4,2], M. Davenport[1], L. Di Lella[1], C. Eleftheriadis[9], J. Englhauser[6], G. Fanourakis[10], E. Ferrer-Ribas[2], H. Fischer[11], J. Franz[11], P. Friedrich[6], T. Geralis[10], I. Giomataris[2], S. Gninenko[12], H. Gómez[7], M. Hasinoff[13], F. H. Heinsius[11], D. H. H. Hoffmann[4,5], I. G. Irastorza[2,7], J. Jacoby[14], K. Jakovčić[16], D. Kang[11], K. Königsmann[11], R. Kotthaus[15], M. Krčmar[16], K. Kousouris[10], M. Kuster[4,6], B. Lakić[16], C. Lasseur[1], A. Liolios[9], A. Ljubičić[16], G. Lutz[15], G. Luzón[7], D. Miller[8], A. Morales[7], J. Morales[7], A. Nordt[4,6], A. Ortiz[7], T. Papaevangelou[1], A. Placci[1], G. Raffelt[15], H. Riege[1], A. Rodríguez[7], J. Ruz[7], I. Savvidis[9], Y. Semertzidis[17], P. Serpico[15], L. Stewart[1], J. Villar[7], J. Vogel[11], L. Walckiers[1], K. Zioutas[17,1]

1. European Organization for Nuclear Research (CERN), Genève, Switzerland
2. DAPNIA, Centre d'Études Nucléaires de Saclay (CEA-Saclay), Gif-sur-Yvette, France

1 Introduction

CP violating terms in quantum chromodynamics give rise to a non vanishing neutron electric dipole moment, EDM. However, experimental efforts have put tight upper limits, $d_n < 2.9 \cdot 10^{-26}$ e $\cdot$ cm [1)], which is orders of magnitude more strict than the prediction of theory. The question of CP conservation in QCD, which is known as the strong CP problem (SCPP), can be answered through the existence of at least one massless quark, a hypothesis which is experimentally excluded, since all quarks have mass [2)]. Up to now, the most convincing solution to the SCPP was given by Peccei and Quinn [3)], [4)] through the introduction of a new global U(1) symmetry, which is spontaneously broken at an energy scale f_a. Through this process, the CP violation in strong interactions is dynamically suppressed. According to the Nambu-Goldstone theorem, the break down of the symmetry generates a Nambu-Goldstone boson, a spinless particle, the axion. Axions are expected to be much alike pions. If they exist, they should interact very weakly, being also very light particles. Depending on their density and mass, they may constitute a candidate for the cold dark matter in the universe. Axion parameters, namely their mass and PQ symmetry breaking scale are related through the following expression

3. Department of Physics, Queen's University, Kingston, Ontario
4. Technische Universität Darmstadt, IKP, Darmstadt, Germany
5. Gesellschaft für Schwerionenforschung, GSI Darmstadt, Germany
6. Max-Planck-Institut für extraterrestrische Physik, Garching, Germany
7. Instituto de Física Nuclear y Altas Energías, Universidad de Zaragoza, Zaragoza, Spain
8. Enrico Fermi Institute and KICP, University of Chicago, Chicago, IL, USA
9. Aristotle University of Thessaloniki, Thessaloniki, Greece
10. National Center for Scientific Research "Demokritos", Athens, Greece
11. Albert-Ludwigs-Universität Freiburg, Freiburg, Germany
12. Institute for Nuclear Research (INR), Russian Academy of Sciences, Moscow, Russia
13. Department of Physics and Astronomy, University of British Columbia, Department of Physics, Vancouver, Canada
14. Johann Wolfgang Goethe-Universität, Institut für Angewandte Physik, Frankfurt am Main, Germany
15. Max-Planck-Institut für Physik (Werner-Heisenberg-Institut), Munich, Germany
16. Rudjer Bošković Institute, Zagreb, Croatia
17. Physics Department, University of Patras, Patras, Greece

$$m_a = 6\ eV\ \frac{10^6\ GeV}{f_a} \tag{1}$$

where f_a is the axion decay constant or breaking scale of the Peccei–Quinn symmetry and m_a is the axion mass.

Axions are also expected to be copiously produced in stellar cores through their coupling to plasma photons, with energies in the range of keV. Since their coupling is small, they escape nearly freely, carrying away amounts of energy from the star. This dissipation mechanism, if present, increases the rate at which the stars consume their fuel, in order to counterbalance the axion energy loss. For supernovae environments the axion energy may reach even 160 MeV. They constitute again an energy dissipation mechanism. In general, in all stellar objects, from white dwarfs to horizontal branch stars, energy dissipation by axions add a new energy loss channel which can affect the evolution timescale of these objects and, therefore, their apparent number density on the sky [5].

Searches for axions are intense nowadays, including not only the idea of the helioscope [6, 7] presently used by CAST [8, 9, 10], but also Bragg scattering [11, 12, 13], cavity searches [14], the PVLAS experiment method [15, 16, 17], the "through the wall" [16, 18, 19]or even "through the sun" method [20]. Astrophysical and cosmological arguments are involved in order to shed light on their characteristic parameters [5, 21]. Solar mysteries may also be explained in terms of axions [22]. Axions with earth origin have been also discussed [23].

CAST is designed to measure axions, produced by the Primakoff effect in the stellar plasma of the central area of our sun. Other potential sources of axions may also become of interest in the future.

2 Axion production in the sun

The dominant mechanism in axion production is the conversion of a plasma photon into an axion, in the field of a charged particle. Other contributions, such as the "electro-Primakoff" effect, are not important, because all charged particles in the sun are not relativistic and, therefore, are not able to provide high B fields. Photons of energy E in a stellar plasma may be transformed into axions through the Primakoff effect at a rate given by

$$\Gamma_{\gamma\to\alpha} = \frac{g_{\alpha\gamma}^2 T\kappa_s^2}{32\pi}\left[\left(1+\frac{\kappa_s^2}{4E^2}\right) ln\left(1+\frac{4E^2}{\kappa_s^2}\right) - 1\right] \tag{2}$$

In this relation, natural units have been used. T is temperature and κ is the screening scale in the Debye-Huckel approximation [24].

$$\kappa_s^2 = \frac{4\pi\alpha}{T}\left(n_e + \sum_{nuclei} Z_j^2 n_j\right) \tag{3}$$

A discussion on the solar axion flux on earth can be found in reference 24, where also the dependence of flux on two different solar models is given.

3 The CAST experiment

The experiment uses a recycled superconducting test magnet from LHC, with a length of 9.26 meters and can reach a magnetic field of 9 T at 13 kA. The magnet has two pipes, as all LHC magnets, with a cross sectional area of 14.5 cm^2 each. It is mounted on a moving structure and it may track the sun for nearly 3 hours a day, half of the time during morning and half in the evening. This limitation comes from the fact that it is not possible to increase the elevation angle of the superconducting magnet more than $\pm 8^o$. Coverage of azimuthal angle is 100^o. On both ends of the magnet, on all four apertures X–ray detectors are mounted. Namely, on the front side, looking for X–rays during sunset, there is a conventional Time Projection Chamber (TPC) detector [25] with an area covering both holes. On the other side, one aperture is covered by a position sensitive gaseous micromegas detector (MM) [26], whereas on the second aperture an X–ray telescope [27] [28] is mounted. Solar axions with an energy spectrum peaking at 4.2 keV, are transformed into photons via time reversed Primakoff effect, under the influence of the transverse magnetic field of 9 T. The conversion probability is given by

$$P_{a\to\gamma} = \left(\frac{g_{a\gamma}B}{q}\right)^2 \sin^2\left(\frac{qL}{2}\right) \tag{4}$$

$q = m_a^2/2E$ being the momentum difference between axion and photon. These photons are expected to be recorded by the three detectors as signal over background, only when the sun and the magnet are aligned. The rest of the time the detectors are measuring pure background. All detectors are able to measure background also simultaneously with the signal, since they are position sensitive and their effective area is bigger than the aperture of the magnet. As a matter of fact, whatever is recorded outside the area of the detector covering the magnet's aperture, is pure background even at the time of the alignment of the magnet to the sun. This is especially true for CCD, since the area of the focal point of the x-ray telescope is very small, less than 10 mm^2. It is an evident advantage to measure background and signal at the same time, leading to reduced systematics. A detailed description of the experiment, as well as of the detectors and the x-ray telescope can be found in references 24, 25, 26, 27, 28, 29, 30.

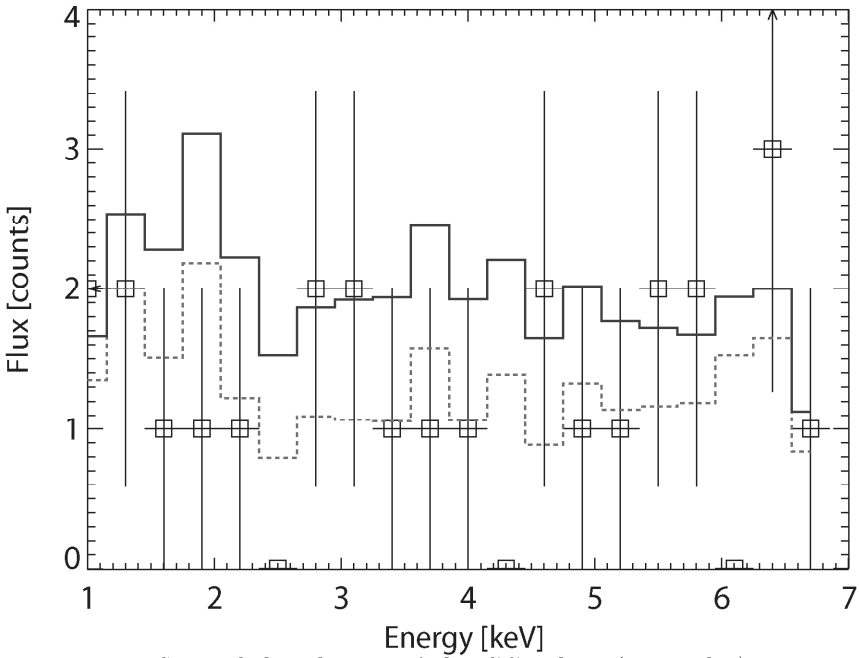

Figure 1: *Spectral distribution of the CCD data (rectangles), expectation for the best fit $g_{a\gamma}$ (dashed line) and expectation for the 95% CL limit on $g_{a\gamma}$ (continuous line), in units of counts per energy bin in the spot area (9.35 mm^2).*

4 Results and discussion

All three CAST detectors were collecting data during 2003 and 2004, the sun tracking data being collected for 300 hours and the background data for an order of magnitude more time. All three detectors were significantly improved from 2003 to 2004. In the system x–ray telescope — CCD detector, the pointing stability of the x–ray telescope was continuously monitored and allowed to reduce the area of the detector where the axion signal was expected, by a factor of 5.8. This was an essential improvement for the signal to noise ratio, since the same expected signal was concentrated in a much smaller area. The integrated background in the spot area, which is now smaller, is consequently reduced by the factor of 5.8 mentioned above. Moreover, with better shielding, the specific background level dropped by another factor of 1.5. Detailed information on the specifics of the x–ray telescope and the CCD detector can be found in references

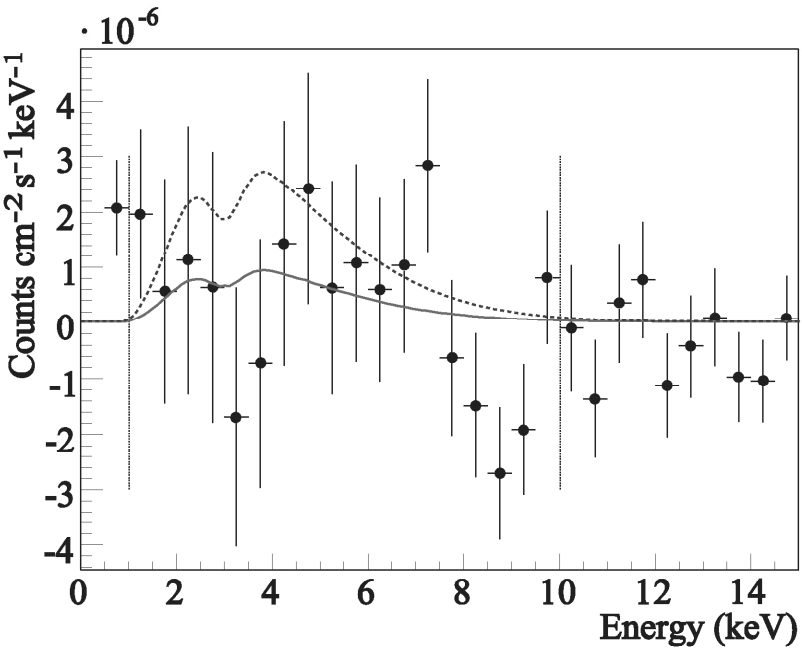

Figure 2: *Experimental subtracted spectrum (bullets), expectation for the best fit $g_{a\gamma}$ (continuous line) and expectation for the 95% CL limit on $g_{a\gamma}$ (dashed line), for the TPC data.*

27,28 and 29. The data set, shown in fig 1 collected during 2004 allowed us to derive a lower upper limit on the axion–photon coupling. The analysis procedure is thoroughly described in reference 24. The result for axion-photon coupling $g_{a\gamma}$ is an upper limit of $8.9{\cdot}10^{-11}$ GeV^{-1}, at the 95% CL.

The TPC detector, looking for sunset axions, was housed in a new shielding, consisting of a 5 mm thick copper box which was inside successive shielding layers of 22 cm of polypropylene, 1 mm of Cadmium and 2.5 cm of Lead. Care has been taken so that all these materials were of low radioactivity. Permanent flushing with nitrogen was creating an overpressure, pushing away any radon contamination in the area of the detector. The background level was succeeded to be reduced by a factor of 4.3. Detailed information on the TPC detector can be found in references 24 and 25. The results are shown in figure 2. The upper limit on $g_{a\gamma}$ from the TPC data for 2004, is $1.29{\cdot}10^{-10}$ GeV^{-1}, at the 95% CL.

The Micromegas detector was placed on the west end of the magnet, looking for sunrise axions. The newly designed version of the detector oper-

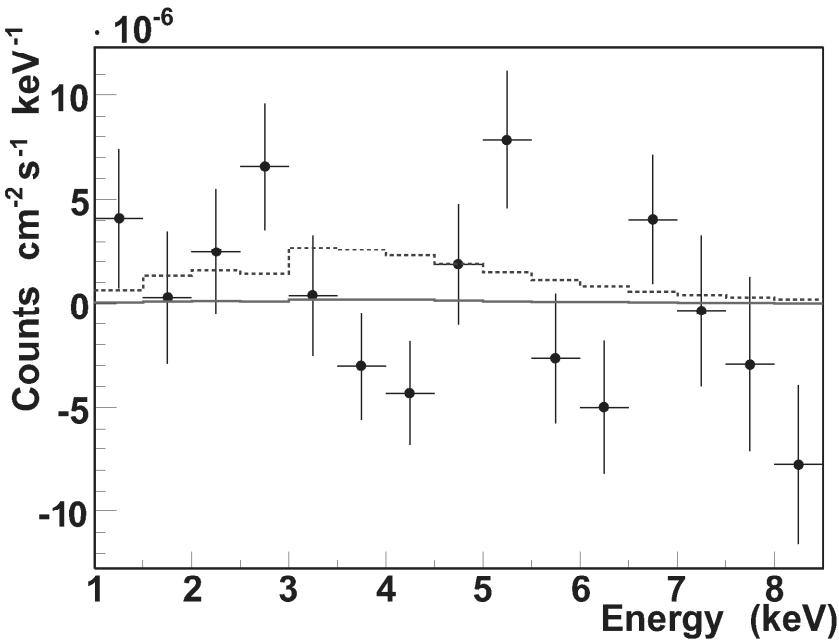

Figure 3: *Experimental subtracted spectrum (bullets), expectation for the best fit $g_{a\gamma}$ (continuous line) and expectation for the 95% CL limit on $g_{a\gamma}$ (dashed line), for the Micromegas data.*

ated smoothly during 2004 data taking and the analysis technique has been also improved, resulting in a background level, suppressed by a factor of 2.5 compared to the 2003 data set [26, 24]. These improvements allowed to set an upper limit to $g_{a\gamma}$ from the MM 2004 data of $1.27{\cdot}10^{-10}$ GeV^{-1}, at the 95% CL. Taking into account all three detectors and the data sets of both years 2003 and 2004, for axion masses below 0.02 eV, we obtained a final upper limit of

$$g_{a\gamma} < 8.8 \cdot 10^{-11} GeV^{-1} \ \ (95\% \ CL)$$

For higher axion masses the axion photon-coherence is lost since their oscillation length is reduced. The exclusion plot in figure 4 shows the CAST result together with results from previous experiments, as well as limits derived from astrophysical and cosmological arguments. For the first time an experimentally set limit is better than the one given from arguments based on the population of Horizontal Branch stars in globular clusters [24].

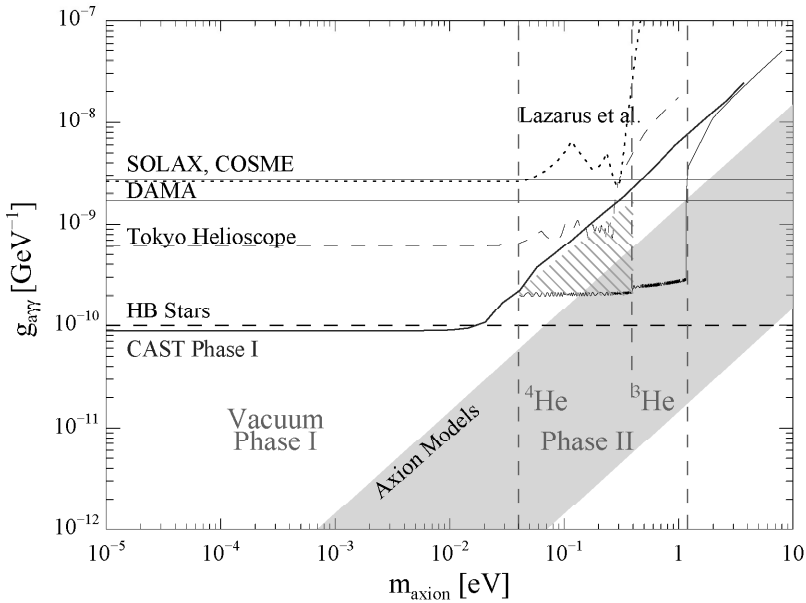

Figure 4: *Exclusion plot for CAST, as well as for previous experiments. Limits from astrophysical and cosmological arguments are also shown. The corridor of axion models below 1 eV is checked for the first time.*

5 Prospects - CAST phase II

For low axion masses, the axion - photon oscillation length exceeds by far the length of the magnet, that is axions and virtual photons are travelling coherently and the axion - photon transformation probability depends on B^2L^2. In this low axion mass region, recoil effects in the Primakoff effect (and its inverse effect) may be neglected and the energies of both particles are considered to be the same. However, at higher axion masses, the axion - photon coherence is lost due to the axion mass which prevents it from travelling in phase with virtual photons in the transverse magnetic field. In order to restore the coherence condition, we fill the magnet channels with gas, so that the photon acquires an effective mass $m_\gamma > 0$. The momentum transfer becomes

$$q = \frac{m_a^2 - m_\gamma^2}{2E} \tag{5}$$

as opposed to

$$q = \frac{m_a^2}{2E} \tag{6}$$

The conversion probability in gas is given by

$$P_{a\to\gamma} = \left[\frac{B\, g_{a\gamma\gamma}}{2}\right]^2 \frac{1}{q^2 + \Gamma^2/4} \left[1 + e^{-\Gamma L} - 2e^{-\Gamma\, L/2} \cos\left(qL\right)\right] \tag{7}$$

where L is magnet length and Γ is the absorption coefficient, which is zero in vacuum. The effective photon mass is given by

$$m_\gamma \approx \sqrt{\frac{4\pi a N_e}{m_e}} = 28.9\sqrt{\frac{Z}{A}\ \rho}\ \ eV \tag{8}$$

and the coherence condition is

$$qL < \pi \Rightarrow \sqrt{m_\gamma^2 - \frac{2\pi E_a}{L}} < m_a < \sqrt{m_\gamma^2 + \frac{2\pi E_a}{L}} \tag{9}$$

The above condition is restored only for a narrow mass range around m_γ, which for helium–4 can be adjusted by changing the gas pressure as follows:

$$m_\gamma\ \ (eV) \approx \sqrt{0.02\ \frac{P(mbar)}{T(K)}} \tag{10}$$

As a matter of fact, every specific pressure allows to test a specific axion mass. It is evident that, the higher the pressure, the higher the photon effective mass, the higher the axion mass under test. The transformation probability is shown in figure 5 for two pressures, namely 6.08 and 6.25 mbar, indicating that the step has to be well below this difference (0.17 mbar) in order to cover fully the axion mass range. In our measurement program we used half this difference as step, namely 0.083 mbar. It is evident that for every step, there is a new discovery potential.

Measurements with helium–4 have been already carried out up to a pressure of 13.43 mbar, with small pressure steps. This is the upper limit in pressure, before condensation effects take place. This search tested the axion mass region up to 0.39 eV. The area explored with helium–4 is designated in figure 4. Analysis is going on for these data and results will be published in a forthcoming paper. CAST is currently upgraded in order to use helium–3 as a buffer gas, allowing to increase the pressure up to about 135 mbar and extending its sensitivity up to 1 eV axions. The above CAST searches will allow to explore experimentally the area of masses and coupling constants predicted by the axion models, as it is shown in figure 4. For higher pressures there is a limitation coming not only from condensation effects, but also from the photon absorption coefficient which increases with pressure.

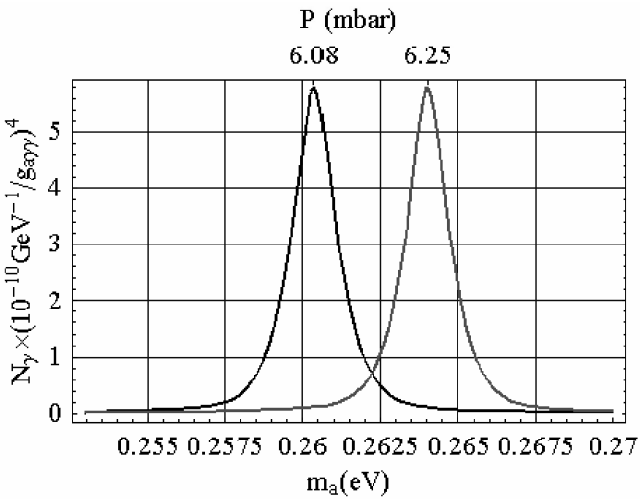

Figure 5: *Probability of axion to photon conversion for two pressures. The step we used was about half this difference in order to scan fully the range of axion masses.*

6 Conclusions

CAST searched for photons arising from axion conversion in a LHC test magnet of 9.26 m length and 9 T magnetic field, for axion masses less than 0.02 eV. Axions are expected to be produced in the sun by the Primakoff process. The experiment obtained the best experimental limit so far (an order of magnitude better than previous experiments). Our result is for the first time better than limits set by astrophysical arguments related to the population of Horizontal Branch stars in globular clusters. This population depends on their helium–burning lifetime. We have searched for higher mass axions, up to 0.39 eV, by filling the magnet bores with helium–4 buffer gas. Under these conditions, photons acquire a small mass depending on pressure and coherence condition between axions and photons is restored. Results from this search will be published in a forthcoming paper. CAST is now under upgrade, in order to fill the magnet bores with helium–3, allowing us to explore axion masses up to 1 eV and testing the range of $g_{a\gamma}$ - m_a values anticipated from QCD axion models and also the possible existence of large extra dimensions [31]. Axions of this range of masses could be candidates for a hot dark matter component of the universe [32].

7 Acknowledgments

I would like to thank K.Zioutas, A.Liolios, I.Savvidis and T.Papaevangelou for fruitful discussions. I would like also to thank E. Ferrer Ribas and M.Kuster for suggestions/comments. We acknowledge support from NSERC (Canada), MSES (Croatia), CEA (France), BMBF (Germany) under the grant numbers 05 CC2EEA/9 and 05 CC1RD1/0, the Virtuelles Institut für Dunkle Materie und Neutrinos – VIDMAN (Germany), GSRT (Greece), RFFR (Russia), CICyT (Spain), NSF (USA) and the helpful discussions within the network on direct dark matter detection of the ILIAS integrating activity (Contract number: RII3-CT-2003-506222). We thank CERN for hosting the experiment and for the contributions of CERN staff.

References

1. C.A.Baker *et al*, arXiv:hep-ex/0602020 **v3** (September 2006).
2. W-M Yao *et al* J. Phys. G: Nucl. Part. Phys. **33** 11232 (2006)
3. R.D. Peccei and H.R.Quinn, Phys. Rev. Lett. **38**, 1440 (1977).
4. R.D. Peccei and H.R.Quinn, Phys. Rev. D **16**, 1791 (1977).
5. G.G.Raffelt, Stars as laboratories for fundamental physics (Chicago, IL: The University of Chicago Press, 1996).
6. P.Sikivie, Experimental tests of the 'invisible'axion, Phys. Rev. Lett **51**, 1415 (1983)
7. D.M.Lazarus *et al*, Search for solar axions, Phys. Rev. Lett. **69**, 2333 (1992)
8. K.Zioutas *et al*, Nucl. Instrum. Meth.A **425**, 480 (1999)
9. C.Elefthcriadis *et al* (for the CAST Collaboration), Axion searches at CERN with the CAST telescope, in Proceedings of the 10th Hellenic Relativity Conference on Recent Developments in Gravity, Kalithea/Chalkidiki, Greece (2002).
10. K.Zioutas *et al* (CAST Collaboration), First results from the CERN Axion Solar Telescope, Phys. Rev. Lett. **94**, 121301 (2005).
11. E.A.Paschos and K.Zioutas, A proposal for solar axion detection via Bragg scattering, Phys. Lett. B **323**, 367 (1994).
12. F.T.Avignone *et al* (SOLAX Collaboration), Experimental search for solar axions via coherent Primakoff conversion in a germanium detector, Phys. Rev. Lett. **81**, 5068 (1998)

13. A.Morales *et al*, Particle dark matter and solar axion searches with a small germanium detector at the Canfranc underground laboratory, Astropart. Phys. **16**, 325 (2002)

14. L.Duffy *et al*, Results of a search for cold flows of dark matter axions, Phys. Rev. Lett. **95**, 091304 (2005).

15. E.Zavattini *et al* (PVLAS Collaboration), Experimental observation of optical rotation generated in vacuum by a magnetic field, Phys. Rev. Lett. **96**, 110406 (2006)

16. R.Cameron *et al*, Search for nearly massless, weakly coupled particles by optical techniques, Phys. Rev. D **47**, 3707 (1993)

17. G.Raffelt and L.Stodolsky, Mixing of the photon with low-mass particles, Phys. Rev. D **37**, 1237 (1988)

18. A.Ringwald, Production and detection of very light bosons in the HERA tunnel, Phys. Rev. Lett B **569**, 51 (2003)

19. P.Sikivie, D.B. Tanner and K.Van Bibber, Resonantly enhanced axion-photon regeneration, Preprint hep-ph/0701198 (2007)

20. M.Fairbairn *et al*, Transparency of the Sun to Gamma Rays due to Axion-like Particles, Phys. Rev. Lett. **98**, 201801 (2007)

21. P.Sikivie, Axion cosmology, Preprint astro-ph/0610440 (2006)

22. K.Zioutas *et al* Quiet sun x-rays as signature for new particles, Astrophys. J. **607**, 575 (2004)

23. A.Liolios, Axions from the earth, Phys. Lett. B **645**, 113 (2007)

24. S.Andriamonje *et al* (CAST Collaboration), An improved limit on the axion–photon coupling from the CAST experiment, Journal of Cosmology and Astroparticle Physics **04**, 010 (2007)

25. D.Autiero *et al* The CAST Time Projection Chamber, 2007, Accepted to New J.Phys. e-Print: physics/0702189

26. P.Abbon *et al* The Micromegas detector of the CAST experiment, 2007, Accepted to New J.Phys. e-Print: physics/0702190

27. M.Kuster *et al* The x–ray telescope of CAST, 2007, Accepted to New J.Phys. e-Print: physics/0702188

28. M.Kuster *et al* pn–CCDs in a Low–Background Environment: Detector Background of the CAST X–ray Telescope, arXiv:physics/0508064 v1 (2005)

29. C.Eleftheriadis and V.Vasileiou, Simulation of the x–ray telescope in the CAST experiment at CERN,
http://cast.mppmu.mpg.de/internal/reports/cstr-01-01.pdf,
http://skiathos.physics.auth.gr/tsg/Publications/cast-14-8-7.pdf

30. S.Cebria'n *et al* "Background study for the pnn-CCD detector of CERN axion solar telescope", submitted to Astrophysical Physics Journal.

31. R.Horvat, M.Krcmar and B.Lakic, CERN Axion Solar Telescope as a probe of large extra dimensions, Phys. Rev. D **69**, 125011 (2004)

32. T.Moroi and H.Murayama, Axionic hot dark matter in the hadronic axion window, Phys. Lett. B **440**, 69 (1998)

POLARIZATION PROPERTIES OF SPIN LIGHT OF ELECTRON IN MATTER

Alexander Grigoriev [a,b], Sergey Shinkevich [a]
Alexander Studenikin [a,b], Alexei Ternov [c], Ilya Trofimov [a]

[a] *Department of Theoretical Physics, Moscow State University, 119992 Moscow, Russia*
[b] *Skobeltsyn Institute of Nuclear Physics, Moscow State University, 119992 Moscow, Russia*
[c] *Department of Theoretical Physics, Moscow Institute for Physics and Technology, 141700 Dolgoprudny, Russia*

Abstract

We further develop the theory of the spin light of electron in matter, a new type of electromagnetic radiation which can be emitted by an electron moving in dense matter, paying special attention to its polarization properties.

1 Introduction

The problem of particles interactions under an external environment influence, provided by the presence of external electromagnetic fields or media, is one of the important issues of particle physics. In addition to possibility for better visualization of fundamental properties of particles and their interactions being imposed by influence of an external conditions, the interest to this problem is also stimulated by important applications to various processes in astrophysics and cosmology, where strong electromagnetic fields and dense matter may play an important role.

Regarding the influence of strong external electromagnetic fields, there is a well known method which enables one to account for an external field influence on a charged particle exactly, rather than within the perturbation-series expansion. In this techniques, known in quantum electrodynamics as the Furry representation [1], consideration of a quantum process is based on the use of exact solutions of the corresponding modified Dirac equation for the particle wave function,

$$\left\{\gamma^{\mu}\left(i\partial_{\mu} - eA^{cl}_{\mu}(x)\right) - m_e\right\}\Psi(x) = 0, \tag{1}$$

which accounts for the external field classical potential $A^{cl}_{\mu}(x)$. The quantized part of the potential $A^{q}_{\mu}(x)$, that corresponds to the electromagnetic radiation field, is treated within the perturbation-series techniques. A detailed discussion of this method can be found in [2].

In a series of our papers [3–9] we have developed a rather powerful method for investigation of different phenomena that can appear when neutrinos and electrons move in background matter. The method discussed is based on the use of the modified Dirac equations for particles wave functions, in which the correspondent effective potentials accounting for the standard model interaction of particles with matter are included. It is similar to the Furry representation [1] in quantum electrodynamics, briefly discussed above. In [3–6] we apply the discussed method for elaboration of the quantum theory of the "spin light of neutrino" ($SL\nu$) in matter. The spin light of neutrino in matter, one of the four new phenomena studied in our recent papers (see for a review [12]), is an electromagnetic radiation that can be emitted by a massive neutrino (due to its non-zero magnetic moment) when the particle moves in the background matter. Within the quasi classical treatment the existence of this radiation was first proposed and studied in [10], while the quantum theory of this phenomenon was developed in [3–6, 11].

It should be mentioned here that different forms of the neutrino quantum wave equations in the presence of matter were used previously for consideration of modifications of a neutrino dispersion relation [13–15]. As it was shown in [13–15], the standard result for the MSW effect [16] can be derived using the

modified Dirac equation for the neutrino wave function with the matter potential proportional to the density being added. It was also shown [17,18] that a neutrino energy minimum is at nonzero momentum. Different interactions of Majorana neutrinos to hypothetical scalar particles (majorons) in the presence of background matter on the basis of the modified Dirac equation were studied in [19]. The problem of a neutrino mass generation in different media [20,21], as well as spontaneous neutrino-pair creation in matter were also studied [22–25].

As it has been discussed [6–9], the approach, developed at first for description of a neutrino motion in the background matter, can be spread for the case of an electron propagating in matter. In this paper we continue the study of an electron motion in matter on the basis of the modified Dirac equation and its exact solutions (see also [26]). We consider interaction of an electron with the nuclear matter [27] within the standard model, a problem which has astrophysical relevance (see, for instance, [24,25]).

As an example of how the developed method works in studies of different possible processes, generated by electrons propagating in matter, we considered below in detail the main properties of electromagnetic radiation that can be emitted by an electron in the background matter. We have termed this radiation the "spin light of electron" (SLe) in matter [6–9]. The term "spin light of electron" was first introduced in [28] for designation of the synchrotron radiation power particular contribution connected with an intrinsic magnetic moment of an electron. In this paper we pay special attention on the polarization properties of the SLe in nuclear matter.

Note that our focus is on the standard model interactions of electrons with the background matter. A similar approach, which implies the use of the exact solutions of the correspondent modified Dirac equations, can be developed in the case when electrons interact with different external fields predicted within various extensions of the standard model (see, for instance, [29,30]).

2 Electron quantum states in nuclear matter

Consider an electron moving in nuclear matter [27]. This model of matter can be used in studies of different processes in astrophysics (see, for instance, [24,25]). The modified Dirac equation for an electron with account for matter motion and polarization can be obtained by the variation procedure applied to the standard Dirac Lagrangian with an additional effective interaction part [6–9])

$$\Delta L^{(e)}_{eff} - \tilde{f}^{\mu}\Big(\bar{e}\gamma_{\mu}\frac{1-4\sin^2\theta_W+\gamma^5}{2}e\Big). \tag{2}$$

This leads to the modified Dirac equation,

$$\left\{i\gamma_{\mu}\partial^{\mu} - \frac{1}{2}\gamma_{\mu}\left(c+\gamma_5\right)\tilde{f}^{\mu} - m_e\right\}\Psi(x) = 0, \tag{3}$$

where m_e is the electron mass, $c = 1 - 4\sin^2\theta_W$, and θ_W is the Weinberg angle. The four-vector $\tilde{f}^\mu$ accounts for the effects of matter motion and polarization and can be written as

$$\tilde{f}^\mu = \frac{G_F}{\sqrt{2}}(j_n^\mu - \lambda_n^\mu), \tag{4}$$

where j_n^μ and λ_n^μ are the neutron current and polarization, respectively (for further details see, for instance, [6]).

It should be mentioned here that the form of the obtained modified Dirac equation (3) for an electron having the standard model interaction with the neutron matter is similar to the modified Dirac equation generated in the framework of standard model extensions with CPT violation and Lorenz breaking [29]. Obviously, the nature of the effective potential $\tilde{f}^\mu$ in our case is completely different.

In several particular cases the modified Dirac equation (3) can be solved exactly. We consider below the case of unpolarized neutrons for which the vector $\tilde{f}^\mu$ is

$$\tilde{f}^\mu = \frac{G_F}{\sqrt{2}}(n_n, n_n\mathbf{v}), \tag{5}$$

where n_n is the number density of the neutron matter and $\mathbf{v}$ is the speed of the reference frame in which the mean momentum of neutrons is zero. Here below we obtain an exact expression for the electron wave function $\Psi(\mathbf{r}, t)$ in a way similar to the one applied previously in [4] for solving the problem of a neutrino motion in the presence of matter background. From Eq.(3) it follows that the operators of electron momentum, $\hat{\mathbf{p}}$, and longitudinal polarization, $\hat{\mathbf{\Sigma}}\mathbf{p}/p$, are the integrals of motion, so that, in particular,

$$\frac{\hat{\mathbf{\Sigma}}\mathbf{p}}{p}\Psi(\mathbf{r}, t) = s\Psi(\mathbf{r}, t), \quad \hat{\mathbf{\Sigma}} = \begin{pmatrix} \hat{\boldsymbol{\sigma}} & 0 \\ 0 & \hat{\boldsymbol{\sigma}} \end{pmatrix}, \tag{6}$$

where $\hat{\boldsymbol{\sigma}}$ are the Pauli matrixes and the values $s = \pm 1$ specify the two electron helicity states. Assuming the plane-wave dependence of the electron wave function in matter,

$$\Psi(\mathbf{r}, t) = e^{-i(E_\varepsilon t - \mathbf{pr})}u_{\varepsilon,\mathbf{p},s}(\mathbf{p}, E_\varepsilon), \tag{7}$$

and applying the condition that the equation (3) has a non-trivial solution, we get the energy spectrum of an electron moving in the background matter:

$$E_\varepsilon = \varepsilon\sqrt{\mathbf{p}^2\Big(1 - s\alpha_n\frac{m_e}{p}\Big)^2 + m_e^2} + c\alpha_n m_e, \tag{8}$$

where the matter density parameter α_n is

$$\alpha_n = \frac{1}{2\sqrt{2}}G_F\frac{n_n}{m_e}. \tag{9}$$

The quantity $\varepsilon = \pm 1$ splits the solutions into the two branches that in the limit of the vanishing matter density, $\alpha_n \to 0$, reproduce the positive and negative-energy solutions, respectively, which is attributed to the particle and anti-particle states. The solution can be written as

$$\Psi_{\varepsilon,\mathbf{p},s}(\mathbf{r},t) = \frac{e^{-i(E^{(e)}_{\varepsilon}t-\mathbf{pr})}}{2L^{\frac{3}{2}}} \begin{pmatrix} \sqrt{1+\frac{m_e}{E^{(e)}_{\varepsilon}-c\alpha_n m_e}}\ \sqrt{1+s\frac{p_3}{p}} \\ s\sqrt{1+\frac{m_e}{E^{(e)}_{\varepsilon}-c\alpha_n m_e}}\ \sqrt{1-s\frac{p_3}{p}}\ e^{i\delta} \\ s\varepsilon\eta\sqrt{1-\frac{m_e}{E^{(e)}_{\varepsilon}-c\alpha_n m_e}}\ \sqrt{1+s\frac{p_3}{p}} \\ \varepsilon\eta\sqrt{1-\frac{m_e}{E^{(e)}_{\varepsilon}-c\alpha_n m_e}}\ \sqrt{1-s\frac{p_3}{p}}\ e^{i\delta} \end{pmatrix} \tag{10}$$

where $\eta = \text{sign}\big(1-s\alpha\frac{m_e}{p}\big)$, L is the normalization length and $\delta = \arctan(p_2/p_1)$, p_i $(i = 1, 2, 3)$ are the electron momentum components. Note that the difference in the obtained electron wave function and energy (given by (10) and (8) respectively) and the corresponding electron neutrino wave function and energy [3] in the neutron background matter is due to the neutron number density n enters the electron and neutrino characteristics with opposite signs and the appearance of an additional factor c in the last term of the electron energy (8).

3 Quantum theory of electron spin light in nuclear matter

As it follows from the expression (8) for the electron energy in matter, for a given momentum p the electron energy of the negative-helicity state exceeds that of the positive-helicity state, thereby enabling the radiation transition $e_{(-)} \to e_{(+)} + \gamma$. This process originates due to the dependence of the electron dispersion law on the density of matter and may proceed even in the case when the photon refractive index in matter equals to $n_\gamma = 1$. We term this radiation the spin light of electron in matter because it originates from the electron magnetic moment while the particle moves in the background matter.

The amplitude of the process is given by S matrix element

$$S_{fi} = -ie\sqrt{4\pi}\int d^4x\bar{\psi}_f(x)(\gamma^\mu e^*_\mu)\frac{e^{ikx}}{\sqrt{2\omega L^3}}\psi_i(x), \tag{11}$$

where $-e$ is the electron charge, ψ_i and ψ_f are the electron wave functions in the initial and final states respectively, $k^\mu = (\omega, \mathbf{k})$ and e^μ are momentum and polarization vectors of the emitted photon. The further calculations are similar to those performed for the spin light of neutrino in matter (see [3–5]). After performing integration over space-time in Eq.(11) we get the law of energy-momentum conservation for the process,

$$E = E' + \omega, \quad \mathbf{p} = \mathbf{p}' + \mathbf{k}, \tag{12}$$

where unprimed and primed quantities refer to the energy and momentum of the initial and final electrons, respectively.

Using the energy-momentum conservation and the exact expressions for the initial and final electron energies, which are given by Eq.(8), we conclude that the only open channel of the process is the transition with change of the electron helicity from $s_i = -1$ to $s_f = 1$. The revealed asymmetry with respect to the electron helicity enables us to predict the existence of the electron spin-polarization effect.

We obtain from (8) and (12) for the SLe photon energy

$$\omega = \frac{2\alpha_n m_e p\ [\tilde{E} - (p + \alpha_n m_e)\cos\theta]}{(\tilde{E} - p\cos\theta)^2 - (\alpha_n m_e)^2}, \tag{13}$$

where

$$\tilde{E} = E - c\alpha_n m_e, \tag{14}$$

and θ is the angle between the directions of the radiation and the initial electron momentum $\mathbf{p}$. In the case of relativistic electron and small values of the matter density parameter α_n, that may be realized for diverse astrophysical and cosmological environments, for the SLe photon energy we get from (13)

$$\omega = \frac{1}{\sqrt{2}} G_F n_n \frac{\beta_e}{1 - \beta_e \cos\theta}, \tag{15}$$

where β_e is the electron speed. From Eq.(15) it follows that for relativistic electrons the energy range of the SLe may even extend up to energies peculiar to the spectrum of gamma-rays (see also [3, 6]).

Using expressions for the amplitude (11) and for the photon energy (13) we obtain the radiation rate Γ and total power I respectively,

$$\Gamma = \frac{e^2}{2} \int_0^\pi \frac{\omega}{1 + \tilde{\beta}'_e\, y} S \sin\theta\, d\theta, \tag{16}$$

$$\mathrm{I} = \frac{e^2}{2} \int_0^\pi \frac{\omega^2}{1 + \tilde{\beta}'_e\, y} S \sin\theta\, d\theta, \tag{17}$$

where

$$S = (1 - y\cos\theta)\left(1 - \tilde{\beta}_e \tilde{\beta}'_e - \frac{{m_e}^2}{\tilde{E}\tilde{E}'}\right). \tag{18}$$

Here we also introduced the following quantities describing the initial and final electron respectively,

$$\tilde{\beta}_e = \frac{p + \alpha_n m_e}{\tilde{E}}, \quad \tilde{\beta}'_e = \frac{p' - \alpha_n m_e}{\tilde{E}'}. \tag{19}$$

The electron energy and momentum in the final state are determined by the relations:

$$E' = E - \omega, \quad p' = K_e\,\omega - p, \tag{20}$$

where

$$K_e = \frac{\tilde{E} - p\cos\theta}{\alpha_n m_e}, \quad y = \frac{\omega - p\cos\theta}{p'}. \tag{21}$$

Performing the integration over the angle θ in (16) and (17) we get closed expressions for the radiation rate

$$\Gamma = \frac{e^2 m^3}{4p^2}\frac{(1+2a)\left[(1+2b)^2\ln(1+2b) - 2b(1+3b)\right]}{(1+2b)^2\sqrt{1+a+b}}, \tag{22}$$

and the total radiation power

$$\mathrm{I} = \frac{e^2 m^4}{6p^2}\frac{(1+a)\left[3(1+2b)^3\ln(1+2b) - 2b(3+15b+22b^2)\right] - 8b^4}{(1+2b)^3}, \tag{23}$$

where $a = \alpha_n^2 + p^2/m_e^2$, $b = 2\alpha_n p/m_e$.

As it follows from the above expressions, the *SLe* rate and total power are rather complicated functions of the electron momentum p and the matter density parameter α_n. It follows from Eqs. (22) and (23) that in the two limiting cases, $m_e \ll \alpha_n p$ and $m_e \gg \alpha_n p$, expressions for the rate and power are analytically tractable and the corresponding much simplified formulas can be obtained. In the case $\alpha_n \gg m_e/p$ we have:

$$\Gamma \approx \begin{cases} \frac{1}{2}e^2\frac{m_e^2}{p}\left[\ln\frac{4\alpha_n p}{m_e} - \frac{3}{2}\right], \\ \frac{1}{2}e^2\alpha_n\frac{m_e^3}{p^2}\left[\ln\frac{4\alpha_n p}{m_e} - \frac{3}{2}\right], \end{cases} \quad \mathrm{I} \approx \begin{cases} \frac{1}{2}e^2 m_e^2\left[\ln\frac{4\alpha_n p}{m_e} - \frac{11}{6}\right], & \text{for } \frac{m_e}{p} \ll \alpha_n \ll \frac{p}{m_e}, \\ \frac{1}{2}e^2\alpha_n^2\frac{m_e^4}{p^2}\left[\ln\frac{4\alpha_n p}{m_e} - \frac{11}{6}\right], & \text{for } \alpha_n^{-1} \ll \frac{p}{m_e} \ll \alpha_n. \end{cases} \tag{24}$$

In the opposite case of $\alpha_n \ll m_e/p$ we get:

$$\Gamma \approx \begin{cases} \frac{32}{3}e^2\alpha_n^3\frac{p^2}{m_e}, \\ \frac{16}{3}e^2\alpha_n^3 p, \\ \frac{32}{3}e^2\alpha_n^4 p, \end{cases} \quad \mathrm{I} \approx \begin{cases} 32e^2\alpha_n^4\frac{p^4}{m_e^2}, & \text{for } \alpha_n \ll \frac{m_e}{p} \ll 1, \\ \frac{32}{3}e^2\alpha_n^4 p^2, & \text{for } \alpha_n \ll 1 \ll \frac{m_e}{p}, \\ 32e^2\alpha_n^6 p^2, & \text{for } 1 \ll \alpha_n \ll \frac{m_e}{p}. \end{cases} \tag{25}$$

The first lines in each case correspond to the radiation of the relativistic electron. The lines two and three in Eq.(25) are for the non-relativistic case. The remaining line two of Eq.(24) describes the relativistic or non-relativistic case depending on the value of the matter density.

With the use of the obtained above values of the SLe rate and total power one can estimate the average emitted photon energy $\langle\omega\rangle = \mathrm{I}/\Gamma$ for different matter density. In the case of $\alpha_n \gg m_e/p$ we get from Eq.(24)

$$\langle\omega\rangle \simeq \begin{cases} p, & \text{for } \frac{m_e}{p} \ll \alpha_n \ll \frac{p}{m_e}, \\ \alpha_n m_e, & \text{for } \alpha_n^{-1} \ll \frac{p}{m_e} \ll \alpha_n, \end{cases} \tag{26}$$

where it is supposed that $\ln \frac{4\alpha_n p}{m_e} \gg 1$. Thus, for the relativistic electrons the emitted photons energy is in the range of gamma-rays what is similar to the case of the spin light of neutrino [4, 11]. Estimations of the initial electron energy obtained from Eq.(8) for the two considered in Eq.(26) limiting cases show that the photon carries away nearly the whole of the initial electron energy. This is reminiscent of the situation has been found in [30] for the standard model extensions.

In the opposite case of $\alpha_n \ll m_e/p$ we get from Eq.(25)

$$\langle\omega\rangle \simeq \begin{cases} 3\alpha_n \frac{p^2}{m_e}, & \text{for } \alpha_n \ll \frac{m_e}{p} \ll 1, \\ 2\alpha_n p, & \text{for } \alpha_n \ll 1 \ll \frac{m_e}{p}, \\ 3\alpha_n^2 p, & \text{for } 1 \ll \alpha_n \ll \frac{m_e}{p}. \end{cases} \tag{27}$$

Estimations of the initial electron energy for the latter three cases give

$$E \simeq \begin{cases} p, & \text{for } \alpha_n \ll \frac{m_e}{p} \ll 1, \\ m_e, & \text{for } \alpha_n \ll 1 \ll \frac{m_e}{p}, \\ \alpha_n m_e, & \text{for } 1 \ll \alpha_n \ll \frac{m_e}{p}, \end{cases} \tag{28}$$

so that small fractions of the initial electron energy are emitted.

4 SLe polarization properties

One of the important features of the SLe is its polarization properties. It should be mentioned here that in our previous studies of the polarization properties of the spin light of neutrino in matter [3–5] we have shown that in the case of dense matter the $SL\nu$ photons are circular-polarized.

We first consider two different linear polarizations of the SLe that are determined by two orthogonal vectors

$$\mathbf{e}_1 = \frac{[\boldsymbol{\varkappa} \times \mathbf{j}]}{\sqrt{1 - (\boldsymbol{\varkappa}\mathbf{j})^2}}, \quad \mathbf{e}_2 = \frac{\boldsymbol{\varkappa}(\boldsymbol{\varkappa}\mathbf{j}) - \mathbf{j}}{\sqrt{1 - (\boldsymbol{\varkappa}\mathbf{j})^2}}, \tag{29}$$

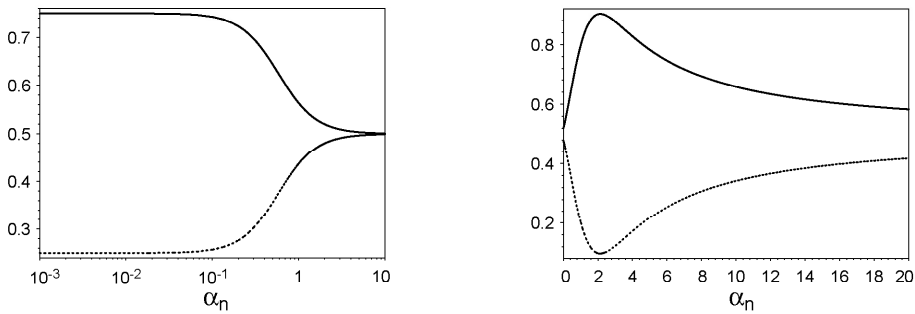

a *b*

Figure 1: Dependence of the SLe linear polarization contributions $\mathrm{I}^{(1)}$ (solid line) and $\mathrm{I}^{(2)}$ (dashed line) on the the matter density parameter α_n: (a) for $p = 1$ keV, (b) – for $p = 1$ MeV.

where $\mathbf{j}$ is the unit vector in the direction of the initial electron momentum $\mathbf{p}$. Decomposing the amplitude of the process considered into contributions from each linear photon polarization, we obtain

$$\mathrm{I}^{(1),(2)} = \frac{e^2}{4}\int_0^{\pi} \frac{\omega^2}{1+\tilde{\beta}'_e y}\left(1 - y\cos\theta \pm \frac{p}{p'}\sin^2\theta\right) \times\left(1 - \tilde{\beta}_e\tilde{\beta}'_e - \frac{m_e^2}{\tilde{E}\tilde{E}'}\right)\sin\theta d\theta. \tag{30}$$

It is interesting to investigate these expressions in different limiting cases. For one particular case determined by the conditions $\alpha_n \ll 1 \ll \frac{m_e}{p}$, which corresponds to the low matter density, we have

$$\mathrm{I}^{(1),(2)} = \left(1 \pm \frac{1}{2}\right)\mathrm{I}, \tag{31}$$

where $\mathrm{I} = \mathrm{I}^{(1)} + \mathrm{I}^{(2)}$. Therefore, the radiation powers corresponding to the two linear polarizations differ by a factor of three. In all other cases the radiation powers corresponding to the linear polarization given by $\mathbf{e}_1$ and $\mathbf{e}_2$ are of the same order, so that the radiation is not polarized:

$$\mathrm{I}^{(1)} \simeq \mathrm{I}^{(2)} \simeq \frac{1}{2}\mathrm{I}. \tag{32}$$

The dependence of the two linear polarization contributions to the SLe power on the matter density parameter α_n is shown in Fig.1 for different initial electron momenta p. For $p = 1\ keV$ (Fig.1,a) and low values of α_n the degree

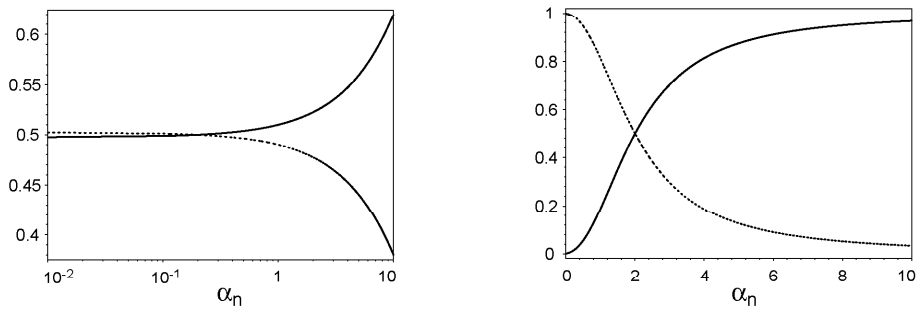

a *b*

Figure 2: Left (solid line) and right (dashed line) circular polarization contributions as functions of the the matter density parameter α_n: (*a*) for $p = 1$ keV, (*b*) – for $p = 1$ MeV.

of linear polarization is equal to $\mathrm{I}^{(1)}/\mathrm{I} = 0.75$. For $p = 1\ MeV$ (Fig.1,b) the degree of linear polarization gets the maximal value ~ 1 when $\alpha_n \frac{m_e}{p} \sim 1$.

Consider the SLe radiation power in the case of the circular polarization of the emitted photons. As usual, we introduce the two orthogonal vectors

$$\mathbf{e}_l = \frac{1}{\sqrt{2}}(\mathbf{e}_1 + il\mathbf{e}_2), \tag{33}$$

that are attributed to the two photon circular polarizations with $l = \pm 1$ for the right and left photon circular polarizations, respectively. For the radiation power of the circular-polarized photons we have

$$\mathrm{I}^{(l)} = \frac{e^2}{4}\int_0^\pi \frac{\omega^2}{1+\tilde{\beta}'_e y}(1+ly)(1-l\cos\theta) \times\left(1-\tilde{\beta}_e\tilde{\beta}'_e - \frac{m_e^2}{\tilde{E}\tilde{E}'}\right)\sin\theta d\theta. \tag{34}$$

If $\alpha_n \gg m_e/p$, then for the two corresponding subcases we get that

$$\begin{aligned} &\mathrm{I}^{(+1)} \simeq 0,\ \mathrm{I}^{(-1)} \simeq \mathrm{I}, \quad \text{for } \tfrac{m_e}{p} \ll \alpha_n \ll \tfrac{p}{m_e}, \\ &\mathrm{I}^{(+1)} \simeq \mathrm{I},\ \mathrm{I}^{(-1)} \simeq 0, \quad \text{for } \alpha_n^{-1} \ll \tfrac{p}{m_e} \ll \alpha_n. \end{aligned} \tag{35}$$

In the opposite case $\alpha_n \ll m_e/p$ we have

$$\begin{aligned} &\mathrm{I}^{(+1)} \simeq 0,\ \mathrm{I}^{(-1)} \simeq \mathrm{I}, \quad \text{for } \alpha_n \ll \tfrac{m_e}{p} \ll 1, \\ &\mathrm{I}^{(+1)} \simeq \mathrm{I}^{(-1)} \simeq \tfrac{1}{2}\mathrm{I}, \quad \text{for } \alpha_n \ll 1 \ll \tfrac{m_e}{p}, \\ &\mathrm{I}^{(+1)} \simeq 0,\ \mathrm{I}^{(-1)} \simeq \mathrm{I}, \quad \text{for } 1 \ll \alpha_n \ll \tfrac{m_e}{p}. \end{aligned} \tag{36}$$

For a wide range of the electron momentum p and the matter density parameter α_n the radiation is circular polarized, however the type of polarization (left or right) depends on the ratio between α_n and p/m_e. The dependence of the two linear polarization contributions to the SLe power on the matter density parameter α_n is shown in Fig.2 for different initial electron momenta p. For a fixed value of the electron momentum p the type of polarization changes from the right to the left with the parameter α_n increase. For $p = 1\ keV$ (Fig.2, a) and small α_n the degree of polarization is very small, however for big α_n the polarization is maximal. For $p = 1\ MeV$ (Fig.2, b) and rather small α_n the radiation is almost right-polarized, for big α_n the type of polarization changes to the left one. The radiation is unpolarized when $\alpha_n \frac{m_e}{p} \sim 1$.

As it can be seen, for rather small values of α_n the SLe is left-polarized, however degree of polarization decreases with α_n increase and at $\alpha_n \sim \frac{p}{m_e}$ the SLe is unpolarized. With the further growth of α_n the right-polarized component dominates and the degree of polarization increases (with increase of α_n).

5 Conclusion

We have developed a method for the study of different processes with participation of electrons subjected to the standard model interactions with dense matter. This method is based on the use of the modified Dirac equation for electron wave function in which an effective matter potential is included. For the nuclear matter composed of neutrons we have found the exact solution of the modified Dirac equation and determined the electron energy spectrum in matter.

The approach developed is similar to the Furry representation which is used in quantum electrodynamics in investigations of particles interactions in the presence of external electromagnetic fields. Note that it is valid in the case when the interaction of neutrinos and electrons with particle of the background is coherent. This condition is satisfied when a macroscopic amount of the background particles are confined within the scale of a neutrino or electron de Broglie wave length. So that for the relativistic neutrinos and electrons ($l = \nu$ or e) the following condition must be satisfied

$$\frac{n}{\gamma_l m_l^3} \gg 1, \tag{37}$$

where n is the number density of matter and $\gamma_l = \frac{E_l}{m_l}$. For instance, let us consider the case of neutrino. If we express n by the non-dimensional number N following to $n = N\ cm^{-3} = N \times 2^3 \times 10^{-15} eV^3$ and take the neutrino mass

of the order of $m_\nu \sim 1\ eV$, then from (37) we have

$$N \gg 10^{14} \times \Big(\frac{E_\nu}{1\ eV}\Big). \tag{38}$$

It follows that even for not extremely dense astrophysical matter with $N \sim 10^{33}$ (this value is about five orders of magnitude lower then one peculiar to densities of neutron stars) the approach developed is valid for the neutrino ultra-high energy band.

To illustrate how the developed method works we have elaborated the theory of electromagnetic radiation of an electron moving in nuclear matter. We have named this radiation the "spin light of electron in matter". It is shown, that for a reasonable values of the matter density the energy range of the SLe photons may even extend up to energies peculiar to the spectrum of gamma-rays. It has been also shown that the SLe photons can carry away a reasonable fraction of the initial electron energy and that electron spin polarization effect can take place. The performed detailed study of the SLe polarization properties (linear and circular polarizations have been considered) has shown that for different values of the matter density the radiation can be significantly polarized and that the type and degree of polarization vary with change of the electron momentum and density of matter.

Finally, we compare the rates of the spin light of electron and spin light of neutrino in matter, Γ_{SLe} and $\Gamma_{SL\nu}$. In a dense matter with $n \sim 10^{37} \div 10^{40}$ cm^{-3}, for the particles momenta $p \sim 1 \div 10^3$ MeV and for the neutrino mass $m_\nu = 1$ eV and magnetic momentum $\mu = 10^{-10}\mu_0$, we have

$$R_\Gamma = \frac{\Gamma_{SLe}}{\Gamma_{SL\nu}} \sim 10^{16} \div 10^{19}, \tag{39}$$

in agreement with our previous naive estimation [6]. The corresponding ratio of total power magnitudes for the SLe and $SL\nu$ is

$$R_{\rm I} = \frac{{\rm I}_{SLe}}{{\rm I}_{SL\nu}} \sim 10^{15} \div 10^{19}. \tag{40}$$

Considering an electron with momentum $p = 1$ MeV moving in matter characterized by the number density $n_n \sim 10^{37}$ cm^{-3} we get for the rate of the process $\Gamma_{SLe} \sim 3.2 \times 10^{-10}$ MeV which corresponds to the characteristic electron life-time $T_{SLe} \sim 2 \times 10^{-2}$ s. Thus, we expect that the SLe in matter can be more effective than the $SL\nu$.

In fact, the considered spin light of electron in matter composed of neutrons is an example of a new mechanism of electromagnetic radiation that can be effectively produced by an electron when it moves in a dense environment. In addition to the considered above case of the SLe being produced due to

interaction with medium composed of neutrons, we should like to mention another situation when the same mechanism of radiation can be realized. In particular, consider the case of a relativistic electron propagating in a jet from a supernova where a rather dense flux of neutrinos is also present. For the modified Dirac equation in this case we obtain again can consider an electron moving in a dense environment composed of electron neutrinos.

Finally, from the studies performed above it follows that for a wide range of matter densities and electron energies the SLe in matter is characterized by high-degree linear and circular polarizations.

The authors are very thankful to Venyamin Berezinsky, Victor Novikov, Yury Popov, Olga Ryazhskaya and Mikhail Vysotsky for useful discussions. One of the authors (A.S.) thanks Giorgio Bellettini, Giorgio Chiarelli and Mario Greco for the kind invitation to participate in this Conference and also thanks all the organizers for their hospitality in La Thuile.

References

1. W.Furry, Phys.Rev. 81 (1951) 115.
2. A.A.Sokolov, I.M.Ternov, "Synchrotron radiation", Pergamon press, Oxford, 1968.
3. A.Studenikin, A.Ternov, Phys.Lett.B 608 (2005) 107, hep-ph/041097, hep-ph/041096, hep-ph/0412408.
4. A.Grigoriev, A.Studenikin, A.Ternov, Phys.Lett.B 622 (2005) 199; Grav.Cosmol. 11 (2005) 132, hep-ph/0502231.
5. A.Grigoriev, A.Studenikin, A.Ternov, Phys.Atom.Nucl. 69 (2006) 1940.
6. A.Studenikin, J.Phys.A: Math. Gen. 39 (2006) 6769, hep-ph/0511311.
7. A.Grigoriev, S.Shinkevich, A.Studenikin, A.Ternov, I.Trofimov, in: A.Studenikin (Ed.), Particle Physics at the Year of 250th Anniversary of Moscow University, World Scientific, Singapore, 2006, p.73, hep-ph/0611103.
8. A.Studenikin, Ann.Fond. Louis de Broglie 31 (2-3) 2006, hep-ph/0611100.
9. A.Studenikin, in: Proceedings of the 22nd International Conference on Neutrino Physics and Astrophysics (Santa Fe, New Mexico, June 13-19, 2006), hep-ph/0611104.
10. A.Lobanov, A.Studenikin, Phys. Lett. B 564 (2003) 27; A.Lobanov, A.Studenikin, Phys. Lett. B 601 (2004) 171; M.Dvornikov, A.Grigoriev, A.Studenikin, Int.J.Mod.Phys. D 14 (2005) 309.

11. A.Lobanov, Phys.Lett. B 619 (2005) 136; Dokl.Phys. 50 (2005) 286.

12. A.Studenikin, Nucl.Phys.(Proc.Suppl.) B 143 (2005) 570.

13. P.Mannheim Phys.Rev.D37 (1988) 1935.

14. D.Nötzold, G.Raffelt, Nucl.Phys.B307 (1988) 924.

15. J.Nieves, Phys.Rev.D40 (1989) 866.

16. L.Wolfenstein, Phys.Rev.D 17 (1978) 2369; S.Mikheyev, A.Smirnov, Sov.J.Nucl.Phys.42 (1985) 913.

17. L.N. Chang and R.K.Zia, Phys.Rev.D38 (1988) 1669.

18. J.Pantaleone, Phys.Lett.B268 (1991) 227; Phys.Rev.D46 (1992) 510; K.Kiers, N.Weiss, Phys.Rev.56 (1997) 5776; K.Kiers, M.Tytgat, Phys.Rev.D57 (1998) 5970.

19. Z.Berezhiani, M.Vysotsky, Phys.Lett.B 199 (1987) 281; Z.Berezhiani, A.Smirnov, Phys.Lett.B 220 (1989) 279.; C.Giunti, C.W.Kim, U.W.Lee, W.P.Lam, Phys.Rev.D 45 (1992) 1557; Z.Berezhiani, A.Rossi, Phys.Lett.B336 (1994) 439.

20. V.Oraevsky, V.Semikoz, Ya.Smorodinsky Phys.Lett.B227 (1989) 255.

21. W.Haxton, W.-M.Zhang, Phys.Rev.D43 (1991) 2484.

22. A.Loeb Phys.Rev.Lett.64 (1990) 115.

23. M.Kachelriess, Phys.Lett.B426 (1998) 89.

24. A.Kusenko, M.Postma, Phys.Lett.B 545 (2002) 238.

25. H.B.J.Koers, Phys.Lett.B 605 (2005) 384.

26. A.Grigoriev, A.Studenikin, A.Ternov, S.Shinkevich, Izv.Vuzov (Physics) No.6 (2007) 66; A.Studenikin, S.Shinkevich, Method of exact solutions in studies of particles interactions in external fields and media, Physics Faculty, Moscow State University, Preprint 1/2007, 19 p.

27. H.Bethe, "Theory of nuclear matter", Palo Alto, California, 1971.

28. I.M.Ternov, Sov.Phys.Usp. 38 (1995) 405; V.A.Bordovitsyn, I.M.Ternov, V.G.Bagrov, Sov.Phys.Usp. 38 (1995) 1037.

29. D.Colladay, V.A.Kostelecky, Phys.Rev.D 55 (1997) 6760; Phys.Rev.D 58 (1998) 11602.

30. V.Ch.Zhukovsky, A.E.Lobanov, E.M.Murchikova, Phys.Rev.D 73 (2006) 065016.

SESSION II – QCD AND HADRONIC INTERACTIONS

- *Oriol Salto* — QCD Studies at the Tevatron
- *Valery A. Khoze* — New Physics with Tagged Forward Protons at the LHC
- *Leif Jönsson* — Determination of the Parton Densities of Protons and α_s at HERA
- *Davide Boscherini* — Diffractive Parton Densities and Factorisation Test
- *Konstantin Goulianos* — Diffraction and Exclusive (Higgs?) Production from CDF to LHC
- *Helena Santos* — Measurements of the Spin Dependent Structure Function $g_1^d(x,Q^2)$ at Compass
- *Boris I. Ermolaev* — Spin–Dependent Structure Function g_1 at Small x: Total Resummation of Leading Logarithms vs Standard Approach

QCD STUDIES AT THE TEVATRON

Oriol Saltó
Institut de Física d'Altes Energies
E-08193 Bellaterra (Barcelona), Spain
(On behalf of the CDF and D0 Collaborations)

Abstract

The Run II of the Tevatron has delivered more than $2\,\mathrm{fb}^{-1}$ of data to the CDF and D0 experiments. This amount of data makes possible very precise QCD measurements. In this contribution, results on inclusive production of jets and photons are discussed, followed by a discussion on Boson+jets production, b-jet production and dedicated measurements on the jet internal structure and jet fragmentation.

1 Introduction

At the Tevatron, $p\bar{p}$ collisions are produced with $\sqrt{s} = 1.96\,\text{TeV}$. Since March 2002, the collider has delivered more than $2.7\,\text{fb}^{-1}$ and the CDF [1] and D0 [2] collaborations have already collected more than $2\,\text{fb}^{-1}$ on tape. Both experiments carry out rich and comprehensive QCD programs that include measurements at large and small momentum transfer. In this contribution, some of the most recent and interesting results are presented.

2 Inclusive Jet Production

The measurement of the inclusive jet cross section constitutes a stringent test of QCD. The increase of the center-of-mass energy from 1.8 to 1.96 TeV in Run II and the increase in integrated luminosity collected by the experiments have allowed to extent the measured cross section by more than $150\,\text{GeV/c}$ in p_T^{jet}. In addition, the measurements have been performed in a wide range of jet rapidity with the aim to further constrain the gluon distribution at high-x.

In Run II, different jet reconstruction algorithms has been used to measure the jet production cross section. In the longitudinally invariant k_T algorithm [3], jets are searched for according to the relative k_T between the particles, a definition conceptually close to the QCD radiation mechanism.

$$k_i = p_{Ti}^2 \qquad k_{ij} = \min\left(p_{Ti}^2, p_{Tj}^2\right) \frac{(y_i - y_j)^2 - (\phi_i - \phi_j)^2}{D^2} \tag{1}$$

The algorithm includes a D parameter that approximately controls the size of the jet in the $y - \phi$ space. By construction, the k_T algorithm is infrared and collinear safe to all orders in perturbative QCD (pQCD) and makes possible a well-defined comparison with parton-level theoretical predictions. The k_T algorithm with $D = 0.7$ has been used to measure the inclusive jet cross section in CDF [4] (see Fig. 1) using $1.0\,\text{fb}^{-1}$ of data for jets with $p_T^{jet} > 54\,\text{GeV/c}$ and $|y^{jet}| < 2.1$. The measurements cover a wide kinematic range and probe distances down to $10^{-19}\,\text{m}$. The measured cross sections are well described by next-to-leading order (NLO) pQCD predictions, as implemented in JETRAD [5] with CTEQ 6.1M [6] parton density functions (PDFs) and renormalization and factorization scales set to $\mu_R = \mu_F = \max p_T^{jet}/2$, that also include non-pQCD effects from Underlying Event (UE) and fragmentation processes. Non-pQCD contributions are about 15-20% at low p_T^{jet} and therefore essential to obtain agreement between the data and the theoretical calculation. In the most-forward region, the uncertainties in the data compared to that on the theoretical predictions indicate that the CDF data will contribute to a better understanding of the gluon PDF.

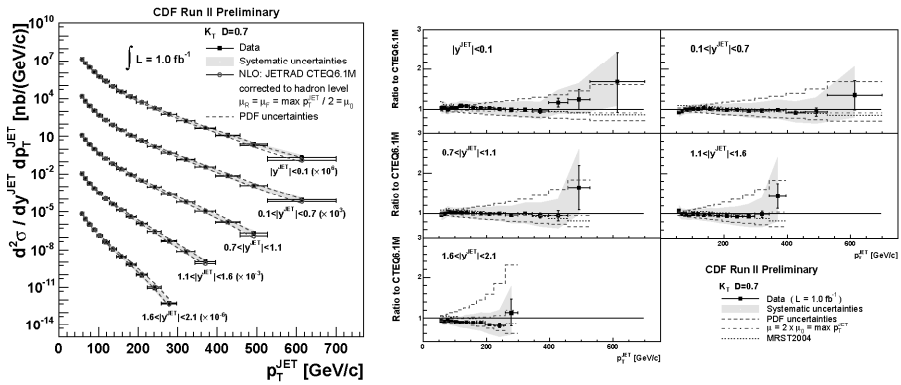

Figure 1: *Inclusive jet production cross section measured by CDF in five rapidity bins up to* $|y^{jet}| < 2.1$. *On the right, the ratio to the NLO pQCD prediction corrected to the particle level is shown.*

Finally, the measurements were carried out with different D parameters (D = 0.5 and D = 1.0). As D increases, the measurements become more sensitive to the UE contributions. The agreement obtained between data and theory shows the good understanding of the non-pQCD contributions to the predicted/measured cross sections.

There are other measurements that use the improved cone-based MidPoint algorithm [7]. MidPoint is a seed-based algorithm that uses additional seeds in the midpoints between protojets to make the clustering procedure infrared safe. Jets are merged or splitted depending on the fraction of energy that they share. Figure 2 shows the inclusive jet cross section measured by D0 using 0.9 fb−1 of data and a cone size R = 0.7 in two rapidity regions, $|y^{jet}| < 0.4$ and $0.4 < |y^{jet}| < 0.8$. The two curves in the left-hand plot present the NLO prediction in the two rapidity regions. In Fig. 2(right) the ratio to the NLO pQCD prediction is presented in the region $|y^{jet}| < 0.4$. The NLO prediction was determined using the FASTNLO program based on NLOJET++ [8]. It uses CTEQ6.1M PDFs and renormalization and factorization scales set to $\mu_R = \mu_F = p_T$. The pQCD prediction has been corrected to take into account the contributions from the non-perturbative effects using PYTHIA [9] Monte Carlo (MC). A good agreement with the measured cross section was found. Similar results have been obtained in CDF using the MidPoint algorithm [10].

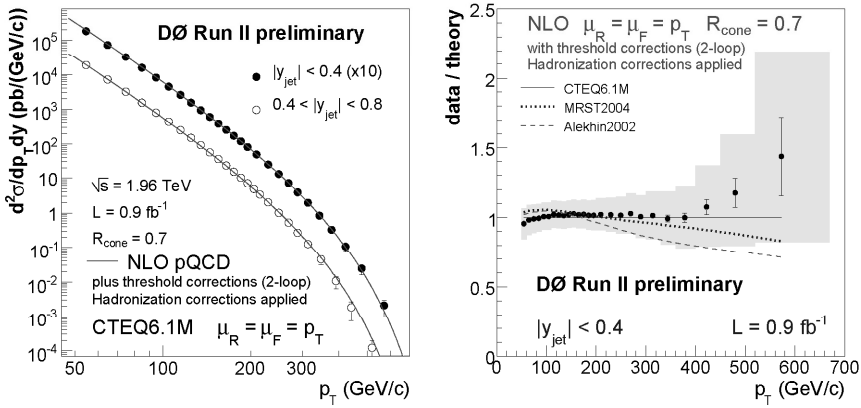

Figure 2: *Inclusive jet production cross section measured by D0 in ranges* $|y^{jet}| < 0.4$ *and* $0.4 < |y^{jet}| < 0.8$. *The measurement is compared to the NLO pQCD prediction with different sets of PDFs and corrected for non-perturbative contributions.*

3 Study of the Jet Internal Structure

As discussed in the previous section, a proper comparison between the measured cross sections and the pQCD predictions require the introduction of non-pQCD effects that are important at low p_T^{jet} and that must be extracted from MC. Detailed studies have been carried out to validate the MC modeling of the soft gluon radiation in the final state.

3.1 Jet Shapes

The internal structure of the jet is dictated by the multi gluon emissions from the primary parton. The measurement of the jet shapes in inclusive jet production constitutes a test of the parton shower modeling in the MC programs and it is sensitive to UE and fragmentation contributions. The integrated jet shape is defined as the fraction of transverse momentum of the jet contained inside a cone of radius r concentric to the cone of the jet (radius R):

$$\Psi(r) = \frac{1}{N_{jet}} \sum_{jets} \frac{p_T(0,r)}{p_T(0,R)} \qquad (2)$$

The integrated jet shapes have been measured for jets reconstructed with the MidPoint algorithm with R = 0.7 using 170 fb−1 of CDF data [11]. The mea-

surement is done for jets with rapidity $0.1 < |y^{jet}| < 0.7$ and transverse momentum $37 < p_T^{jet} < 380\,GeV/c$. Figure 3(left) shows the integrated jet shapes for jets with $37 < p_T^{jet} < 45\,GeV/c$. The data is compared to PYTHIA Tune A [12] and HERWIG [13]. PYTHIA Tune A provides a good description of the measured jet shape. The jet shape predicted by HERWIG tends to be narrower than the data. The effect of the UE on the jet shapes can be understood from the comparison between PYTHIA Tune A and PYTHIA Tune A (no MPI), where for the latter the interactions between proton and antiproton remnants are removed making the jets too narrow. The measurement has been performed in different p_T^{jet} bins. The p_T^{jet} dependence of the jet shapes is presented in Fig. 3(right) where $1 - \Psi(0.3/R)$ is shown as a function of p_T^{jet}. The jets get narrower as p_T^{jet} increases and it is well described by PYTHIA Tune A and HERWIG (at large p_T^{jet}) MC predictions.

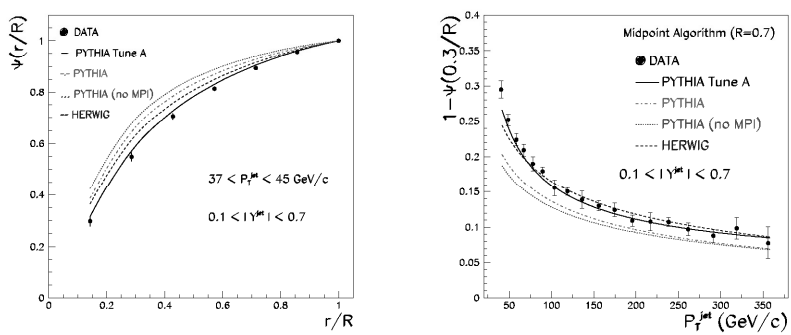

Figure 3: *Left: Integrated jet shapes measured by CDF compared to different MC predictions. Right: Evolution of the jet shapes with the transverse momentum of the jet.*

3.2 k_T Distribution of Particles inside Jets

The transverse momentum, k_T, of the particles inside jets, measured with respect to the jet axis, probes QCD radiation in the perturbative regime as well as the non-perturbative hadronization processes. The k_T distribution has been measured in dijet production at the Tevatron in different regions of dijet mass. The measurements are compared to parton-level theoretical (MLLA [14]) pre-

dictions and parton shower PYTHIA and HERWIG MC predictions (see Fig. 4).

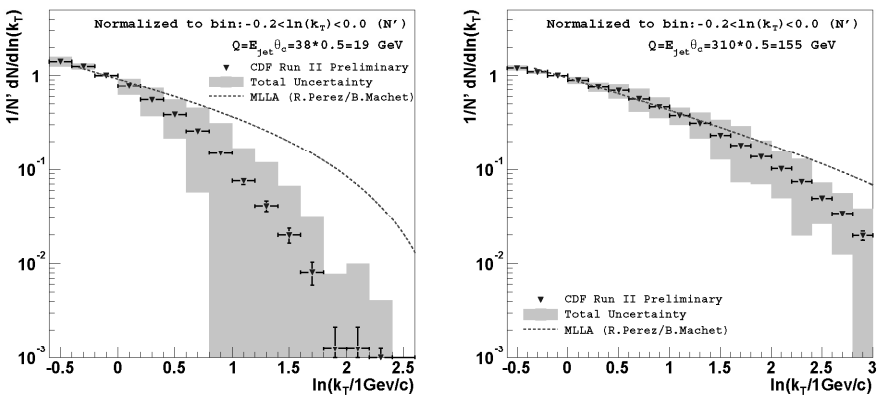

Figure 4: *k_T distribution of the particles inside jets measured at CDF in two different dijet invariant mass bins compared to MLLA predictions. Bottom: k_T distribution of jet particles compared to* PYTHIA *Tune A and* HERWIG *predictions.*

The largest source of uncertainties in the data comes from the possible bias introduced in the measurement due to the requirement on the energy and E_T balance of the jets and on the number of extra jets in the event.

As expected, MLLA predictions provides a reasonable description of the data only at large k_T and large dijet mass values. Parton shower MC predictions describe the data in all the dijet mas range considered (see Fig. 5).

4 Inclusive Photon Cross Section

The measurement of the inclusive prompt photon cross section as a function of photon transverse momentum provides a clean means to test QCD and obtain information on the gluon distribution inside the proton via the contribution of gq Compton scattering diagrams. A good determination of the absolute energy scale in the electromagnetic calorimeters, using the Z mass peak as reference, makes possible a precise measurement of the p_T spectrum of the photon with no additional uncertainties introduces by jet algorithms or underlying event contributions as in the case of inclusive jet production. Figure 6 shows the inclusive photon cross section measured by D0 [15] using $326\,\mathrm{pb}^{-1}$ of data. The cross section is measured for central photons ($|\eta^\gamma| < 0.9$) in the range

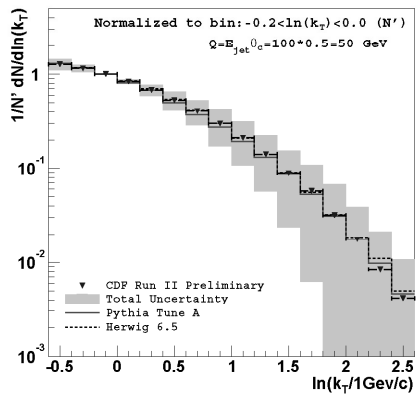

Figure 5: *k_T distribution of jet particles compared to* PYTHIA *Tune A and* HERWIG *predictions.*

$23 < p_T^{\gamma} < 300\,\mathrm{GeV/c}$, but photons up to $p_T^{\gamma} = 442\,\mathrm{GeV/c}$ were observed in data. Photons are required to be isolated to reduce the background from π^0 decays. The purity of the photon sample was estimated using a neural network and it is about 65% for $p_T^{\mathrm{gamma}} > 100\,\mathrm{GeV/c}$. The results are compared to NLO pQCD predictions as computed using JETPHOX [16] with CTEQ6.1M PDFs and $\mu_R = \mu_F = p_T^{\gamma}$. Good agreement is observed between data and the theoretical predictions.

5 Inclusive Jet Production in Association with W and Z Bosons

The measurement of the jet production cross section in association with bosons is also a test of pQCD. The presence of a heavy W or Z boson in the final state provides the necessary hard scale to carry out pQCD calculations. NLO pQCD predictions are available for processes with up to two partons in the final state. The measurement of Boson + jets cross sections are a crucial part of the physics program at the Tevatron since these processes constitute important backgrounds in searches for new physics like SuperSymmetry and the Higgs boson, and some Standard Model processes like $t\bar{t}$ production. By itself, the measurement can be used as a search for compositness and the decay of new heavy objects.

During the last few years a significant effort is being made to build LO MC predictions for Boson + jets final states with large jet multiplicities. These predictions are based on parton-level matrix elements (ME) interfaced with

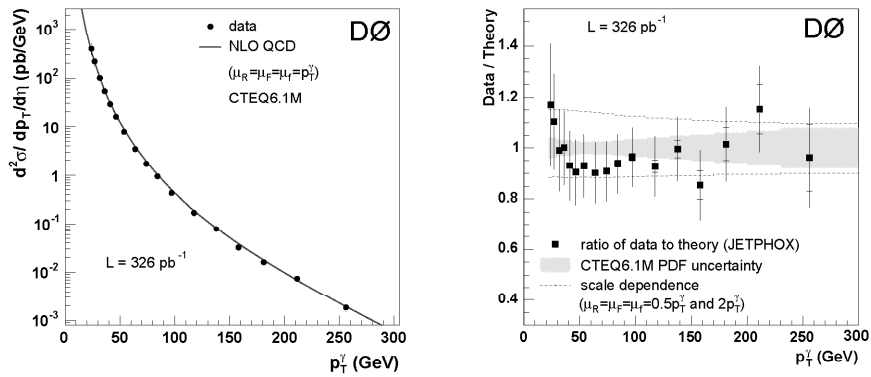

Figure 6: *Inclusive photon cross section measured by D0 compared to NLO pQCD prediction. Right: Ratio Data/Theory including the uncertainties on the measurement and on the prediction.*

parton showers (PS) where special prescriptions are necessary to avoid double counting in the gluon radiation. Boson + jets data samples are thus important to validate the different implementations.

5.1 Inclusive Z + jets cross section

$Z \to ee$ is a clean and almost background free signal, that makes it a very useful tool to validate $Z(\to \nu\nu)$ + jets MC modeling without biasing searches for new physics.

CDF has measured the Z + jets cross section using $1.1\,\mathrm{fb}^{-1}$ of data. The measurement is performed in a well defined kinematic region of the jets and the Z boson decay products. Electrons must have $E_T^e > 25\,\mathrm{GeV}$ and be in range $66 < M_{ee} < 116\,\mathrm{GeV/c^2}$, where one electron has to be in the central region of the calorimeter ($|\eta^e| < 1.0$) and the other can be either in the central or in the forward region ($1.2 < |\eta^e| < 2.8$). Jets are reconstructed using the MidPoint algorithm and are required to have $p_T^{jet} > 30\,\mathrm{GeV/c}$ and $|y^{jet}| < 2.1$. The cross section is corrected to the hadron level and compared to NLO pQCD predictions. The NLO pQCD prediction is determined using MCFM [17] and includes non-pQCD contributions. The latter are obtained using PYTHIA Tune A MC. Observables that are sensitive to the MC modeling, such as jet shapes and energy flows (see below), has been measured and a good agreement was found between data and PYTHIA Tune A predictions, making them a reliable tool to extract the parton-to-hadron corrections.

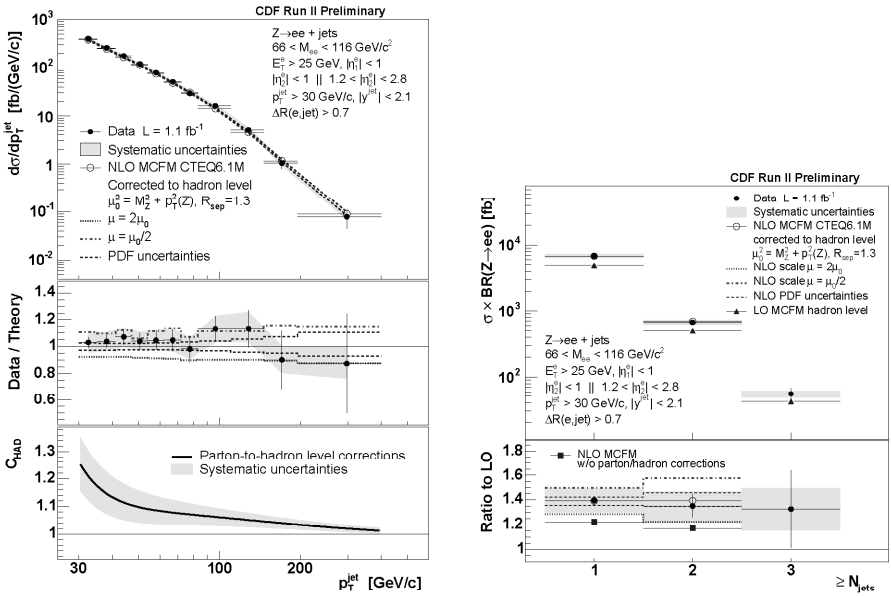

Figure 7: *Left: Inclusive Z + jets cross section as a function of* $\mathrm{p_T^{jet}}$*, compared to NLO pQCD predictions and showing the non-pQCD contributions* ($\mathrm{C_{had}}$)*. Right: Total cross section versus inclusive jet multiplicity compared to LO and NLO pQCD predictions.*

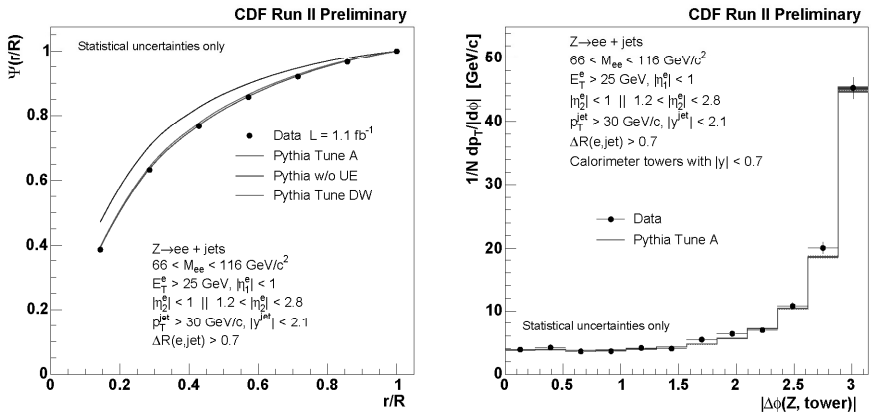

Figure 8: *Left: Integrated jet shapes (as defined in expression 2) in Z + jets events compared to different settings of the UE modeling. Right: Energy flow in the transverse plane in Z + jets events with respect to the Z boson direction ($\phi = 0$)..*

Figure 7(left) shows the inclusive Z + jets cross section as a function of the transverse momentum of the jet. When NLO pQCD predictions are compared with the measurement, a good agreement is found. The corrections for the non-perturbative contributions (C_{had}) are shown in the bottom part of the plot. They account for up to 25% of the cross section at low p_T^{jet}. The total cross section as a function of the inclusive jet multiplicity is shown in Fig. 7(right). The plot also shows the ratio to the nominal LO prediction. A constant NLO/LO k factor is found for $N_{jet} = 1, 2$ and the data suggests a similar factor for $N_{jet} = 3$. When no parton-to-hadron correction is applied to the NLO prediction the result underestimates the measured cross section by about 15%.

As stated previously, the Z + jets production measurement is sensitive to non-perturbative effects: UE and fragmentation. The knowledge and modeling of these contributions is critical in the measurement of jet cross sections and, therefore, in the prediction of Z + jets backgrounds.The CDF experiment has carried out detailed measurements on jets shapes and energy flows in Z + jets final states to validate the MC predictions employed in the calculation of non-pQCD corrections to the NLO calculations. In Fig. 8(left) the measured jet shape is compared to different MC predictions with different UE settings. Both PYTHIA Tune A and PYTHIA Tune DW provide a good description of the data.

As in the case of the inclusive jet production, a MC sample with no interaction between proton and antiproton remnants produces jets significantly narrower than the data.

Alternatively, one can test the UE activity by looking at the energy flow in the transverse plane away from the main jet activity. Figure 8(right) shows the measured energy flows, using calorimeter towers with $|y| < 0.7$, in events with exactly one reconstructed primary vertex and where, event-by-event, $\phi = 0$ is defined along the direction of the momentum of the Z boson. At $|\phi| = \pi$ the measured distribution shows a prominent peak coming from the leading jet, while at $|\phi|$ $\pi/2$ the measured energy flow is dominated by soft UE contributions. Both PYTHIA Tune A and PYTHIA Tune DW (the latter not shown in the plot) provide a good description of the measured energy flow.

5.2 Validation of Boson + jets ME+PS Monte Carlo predictions

Due to the large statistics of W bosons in the Tevatron data, W + jets is an ideal final state to test the procedures followed to match ME and PS in the MC programs.

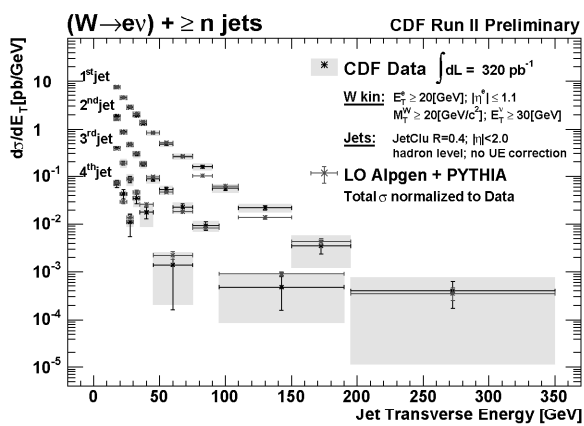

Figure 9: *Inclusive* W+ $\geq$ n jets *cross section measured by CDF. The* E_T^{jet} *spectrum is compared in shape to the predictions of two different ME+PS matching techniques.*

Figure 9 shows the measured inclusive differential cross section as a function of the transverse energy of the nth jet in W+ $\geq$ n jets production, based on $320\,pb^{-1}$ of CDF data. Jets are searched for using a CDF Run I cone based algorithm [18] and are required to have $E_T^{jet} > 15\,GeV$ and $|\eta^{jet}| < 2.0$. The cross section is measured in the region defined by electrons with $E_T^e > 20\,GeV$ and

$|\eta^e| < 2.1$, the missing transverse energy in the event must be $\not\!\!E_T > 30\,\mathrm{GeV}$, and the transverse mass of the reconstructed W boson $m_T^W > 20\,\mathrm{GeV/c^2}$. Figure 9 also shows the comparison between data and the MC prediction, where the latter is normalized to the total measured cross section. The MC produces a reasonable description of the shape of the measured E_T^{jet} spectra.

Z boson production cross section is 10 times smaller than the W boson cross section. However, with more than $1\,\mathrm{fb}^{-1}$ of data, precise differential measurements of the Z + jets production are also possible.D0 has explored the CKKW algorithm [19] to match ME and PS as implemented in SHERPA [20]. The SHERPA prediction was generated using CTEQ6L PDFs. Up to three partons were included in the matrix elements calculation. Jets were defined by the D0 Run II cone algorithm [7] and required to have $p_T > 15\,\mathrm{GeV/c}$. The sample was normalized to the total number of events with a Z boson found in the data. Figure 10(left) shows the measured jet multiplicity and the prediction of SHERPA. The prediction follows the data up to high jet multiplicities. Figure 10(right) presents the prediction from PYTHIA (Drell-Yan+PS) where all the jets are produced via initial state radiation PS. As expected, it only reproduces the lower jet multiplicities.

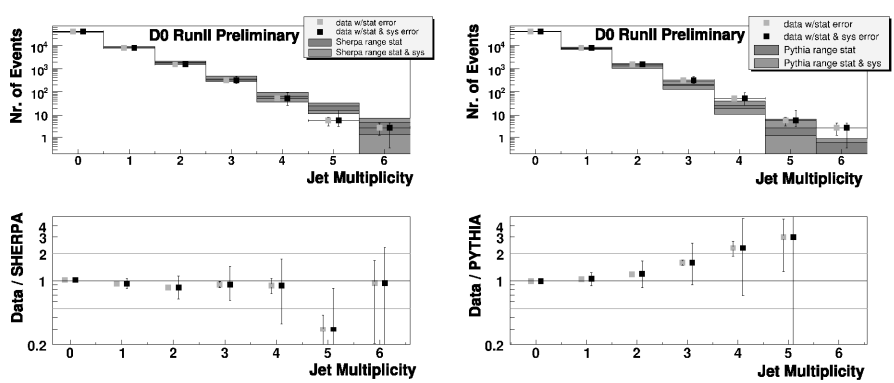

Figure 10: *Left: Measured jet multiplicity in Z + jets events by D0 compared to LO ME+PS* SHERPA *prediction with CKKW matching. Right: Measured jet multiplicity in Z + jets events by D0 compared to the LO+PS* PYTHIA *prediction.*

6 $b\bar{b}$ Dijet Production

The measurement of the $b\bar{b}$ dijet production cross section is a rigorous test of the understanding of the b quark production mechanisms. The $b\bar{b}$ cross section

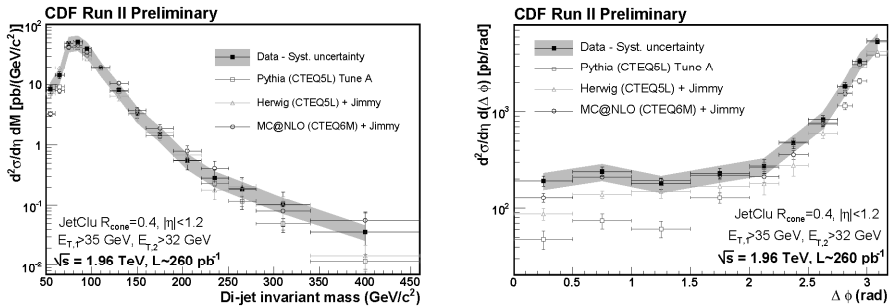

Figure 11: *CDF measurement of the* $\mathrm{b\bar{b}}$ *dijet production cross section as a function of the invariant mass of the dijet system and the* $\Delta\phi$ *between the two jets.*

and the topologies in the final state strongly depend on the different mixture of $b\bar{b}$ processes: flavor creation from $q\bar{q}$ annihilation, gg fusion and $b\bar{b}$ from gluon splitting. Detailed measurements on $b\bar{b}$ production will provide information on the importance of the different subprocess and validate their implementation in the MC programs.

CDF has used $260\,\mathrm{pb}^{-1}$ of data selected by a trigger requiring two displaced tracks to measure the $b\bar{b}$ dijet production cross section. Offline, the jet are reconstructed using a cone algorithm with a cone size R = 0.4. Events with two b jets are required to have $\mathrm{E_T} > 30\,\mathrm{GeV}$ and $|\eta| < 1.2$. The cross section is corrected to the hadron level. The differential cross section is shown in Fig. 11 as a function of the dijet invariant mass and the azimuthal distance ($\Delta\phi$) between the two jets. The measurement is compared to LO MCs (PYTHIA Tune A and HERWIG) and to NLO predictions from MC@NLO [21]. The MC@NLO prediction was generated using CTEQ6.1M PDFs, and a renormalization and factorization scale $\mu_\mathrm{R} = \mu_\mathrm{F} = \sqrt{\mathrm{p_T^2 + m_b^2}}$. It includes contributions from non-pQCD effects obtained using JIMMY [22]. The comparisons show that MC@NLO+JIMMY describes the measurement. This is attributed to the presence of appropriate ME at NLO that provide a better description of the total cross section and final state topologies. In the case of PYTHIA and HERWIG, the predictions underestimate the cross section, specially at low $\Delta\phi$ between the two jets, where it is expected a dominant contribution from gluon splitting into $b\bar{b}$.

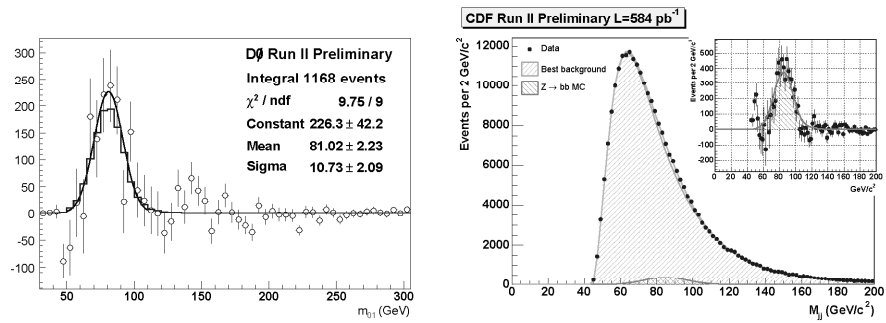

Figure 12: Z $\rightarrow b\bar{b}$ *signal measured by D0 (left) and CDF (right).*

7 Z $\rightarrow b\bar{b}$

The measurement of Z $\rightarrow b\bar{b}$ is an important ingredient of the Tevatron Run II physics program at D0 and CDF. Z $\rightarrow b\bar{b}$ is an essential tool in the calibration of b jets which affects much of the high p_T physics studied at the Tevatron. Uncertainties in the b jet energy scale translate directly into the uncertainty of the *top* quark mass or the dijet mass resolution in Higgs boson searches.

Measuring the Z $\rightarrow b\bar{b}$ is challenging due to the large background from the QCD $b\bar{b}$ production and the b jets mis-identification. D0 has found evidence of the Z $\rightarrow b\bar{b}$ signal in $300\,\mathrm{pb}^{-1}$ of data (see Fig. 12(left)). CDF has also seen the signal in $584\,\mathrm{pb}^{-1}$ of data (see Fig. 12(right)).

8 Summary

A very rich physics program is carried out at the Tevatron by CDF and D0 experiments. The large samples available with more than $1\,\mathrm{fb}^{-1}$ of data lead to a new level of precision of QCD studies. Measurements of the inclusive jet production cross section have been performed with different jet algorithms and show a good agreement with the NLO pQCD predictions. The measurement of the jet cross sections in the forward regions will contribute to a better understanding of the proton PDFs. Photon production cross section measurements will also contribute when more data will be added and uncertainties will decrease. The QCD program also includes measurements like jet shapes and k_T distribution of particles inside jets, that show that MC simulation programs describe the non-perturbative part of the events. Results of the measurements of the boson + jets production has been shown to be in good agreement with the prediction of different LO matrix elements calculations matched to parton

shower programs. In the case of Z + jets, the production cross section has been measured and compared to NLO pQCD predictions. A good agreement was found, also denoting a good understanding of the non-perturbative contributions. Finally, measurements of the $b\bar{b}$ dijet cross section are fairly described by the NLO predictions.

Acknowledgments

I would like to thanks the organizers of the conference for their kind invitation and also to acknowledge the members of the CDF and D0 Collaborations for their works in obtaining the results reported in this contribution.

References

1. D. Acosta *et al* (CDF Collaboration), Phys. Rev. D **71**, 032001 (2001).
2. T. LeCompte and H.T. Diehl, Annu. Rev. Nucl. Part. Sci. **50**, 71 (2000).
3. S.D. Ellis and D.E. Soper, Phys. Rev. D **48**, 3160 (1993).
4. A. Abulencia *et al* (CDF Collaboration), Phys. Rev. D **75**, 092006 (2007).
5. W.T. Giele *et al*, Phys. Rev. Lett. **73**, 2019 (1994).
6. J. Pumplin *et al*, JHEP **0207**, 12 (2002).
   D. Stump*et al*, JHEP **0310**, 046 (2003).
7. G.C. Blazey it et al, hep-ex/0005012.
8. Z. Nagy, Phys. Rev. Lett. **88**, 122003 (2002).
   Z. Nagy, Phys. Rev. D **68**, 094002 (2003).
9. T. Sjöstrand *et al*, Computer Phys. Comm. **135**, 238 (2001).
10. A. Abulencia *et al* (CDF Collaboration), Phys. Rev. D **74**, 071103(R) (2006).
11. D. Acosta *et al* (CDF Collaboration), Phys. Rev. D **71**, 112002 (2005).
12. T. Affolder *et al* (CDF Collaboration), Phys. Rev. D **65**, 092002 (2002).
13. G. Corcella *et al*, JHEP **0101**, 010 (2001).
14. Y. Dokshitzer, V. Khoze, A. Mueller and S. Troyan, *Basics of Perturbative QCD*, Editions Frontières, Gif-sur-Yvette, 1991.
    Y.I. Azimov *et al*, Z. Phys. C **27**, 65 (1985)

15. V.M. Abazov *et al* (D0 Collaboration), Phys. Lett. B **639**, 151 (2006).

16. T. Binoth *et al*, Eur. Phys. J. C **16**, 311 (2000).
S. Catani *et al*, JHEP **05**, 028 (2002);

17. J. Campbell and R.K. Ellis, Phys. Rev. D **65**, 113007 (2002).

18. F. Abe *et al* (CDF Collaboration), Phys. Rev. D **45**, 1448 (1992).

19. S. Catani *et al*, JHEP **0111**, 063 (2001).
F. Krauss, JHEP **0208**, 015 (2002).

20. T. Gleisberg *et al*, JHEP **0402**, 056 (2004).

21. S. Frixione and B.R. Webber, JHEP **06**, 029 (2002).

22. J.M. Butterworth *et al*, Z. Phys. C **72**, 637 (1996).

NEW PHYSICS WITH TAGGED FORWARD PROTONS AT THE LHC

V.A. Khoze, A.D. Martin and M.G. Ryskin
IPPP, Department of Physics, University of Durham, DH1 3LE, UK

Abstract

The addition of forward proton detectors to LHC experiments will significantly enlarge the potential for studying New Physics. A topical example is Higgs production by the central exclusive diffractive process, $pp \to p + H + p$. We discuss the exclusive production of Higgs bosons in both the SM and MSSM. Special attention is paid to the backgrounds to the $H \to b\bar{b}$ signal.

1 Introduction

The use of diffractive processes to study the Standard Model (SM) and New Physics at the LHC has only been fully appreciated within the last few years; see, for example [1, 2, 3, 4], or the recent reviews [5, 6, 7], and references therein. By detecting protons that have lost only about 1-3% of their longitudinal momentum [8, 9], a rich QCD, electroweak, Higgs and BSM programme becomes accessible experimentally, with the potential to study phenomena which are unique to the LHC, and difficult even at a future linear collider. Particularly interesting are the so-called central exclusive production (CEP) processes which provide an extremely favourable environment to search for, and identify the nature of, new particles at the LHC. The first that comes to mind are the Higgs bosons, but there is also a potentially rich, more exotic, physics menu including (light) gluino and squark production, searches for extra dimensions, gluinonia, radions, and indeed any new object which has 0^{++} (or 2^{++}) quantum numbers and couples strongly to gluons, see for instance [2, 10, 11]. By "central exclusive" we mean a process of the type $pp \to p+X+p$, where the $+$ signs denote the absence of hadronic activity (that is, the presence of rapidity gaps) between the outgoing protons and the decay products of the centrally produced system X. The basic mechanism driving the process is shown in Fig. 1.

There are several reasons why CEP is especially attractive for searches for new heavy objects. *First*, if the outgoing protons remain intact and scatter through small angles then, to a very good approximation, the primary active di-gluon system obeys a $J_z = 0$, C-even, P-even, selection rule [12]. Here J_z is the projection of the total angular momentum along the proton beam axis. This selection rule readily permits a clean determination of the quantum numbers

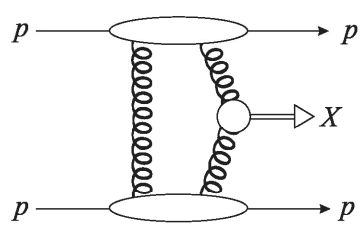

Figure 1: *The basic mechanism for the exclusive process* $pp \to p+X+p$. *The system* X *is produced by the fusion of two active gluons, with a screening gluon exchanged to neutralize the colour.*

of the observed new (for example, Higgs-like) resonance, when the dominant production is a scalar state. *Secondly*, because the process is exclusive, the energy loss of the outgoing protons is directly related to the mass of the central system, allowing a potentially excellent mass resolution, irrespective of the decay mode of the centrally produced system. *Thirdly*, in many topical cases, in particular, for Higgs boson production, a signal-to-background ratio of order 1 (or even better) is achievable [3, 11), 13)- 18)]. In particular, due to $J_z = 0$ selection, leading-order QCD $b\bar{b}$ production is suppressed by a factor $(m_b/E_T)^2$, where E_T is the transverse energy of the b, b jets. Therefore, for a low mass Higgs, $M_H \lesssim 150$ GeV, there is a possibility to observe the main $b\bar{b}$ decay mode [2, 3, 6)], and to directly measure the $H \to b\bar{b}$ Yukawa coupling constant. The signal-to-background ratio may become significantly larger for a Higgs boson in certain regions of the MSSM parameter space [13, 19)].

It is worth mentioning that, by tagging both of the outgoing protons, the LHC is effectively turned into a gluon-gluon collider. This will open up a rich, 'high rate' QCD physics menu (especially concerning diffractive phenomena), which will allow the study of the skewed, unintegrated gluon densities, as well as the details of rapidity gap survival; see, for example, [2, 7, 20)]. Note that CEP provides a source of practically pure gluon jets; that is we effectively have a 'gluon factory' [12)]. This provides an ideal laboratory in which to study the detailed properties of gluon jets, especially in comparison with quark jets. The forward-proton-tagging approach also offers a unique programme of high-energy photon-interaction physics at the LHC; see, for example, [21, 22)].

2 Central Exclusive Higgs production

The 'benchmark' CEP new physics process is Higgs production. Studies of the Higgs sector are at the heart of the recent proposal [9)] to complement the LHC central detectors with proton taggers placed at 420 m either side of the interaction point.

Our current understanding is, that if a SM-like Higgs boson exists in Nature, it will be detected at the LHC. However, various extended models predict a large diversity of Higgs-like bosons with different masses, couplings and CP-parities. The best studied extension of the SM up to now is the Minimal Supersymmetric Standard Model (MSSM) [23)], in which there are three neutral Higgs bosons, the scalars h and H, and the pseudoscalar A.

The forward proton tagging mode is especially advantageous for the study of the MSSM sector [13, 19)]. Note that when using the "standard" non-

diffractive production mechanisms, there is usually an important region of MSSM parameter region, where the LHC can detect only the Higgs boson with SM-like properties. To check that a discovered state is indeed a scalar Higgs boson, and to distinguish between the Higgs boson(s) of the SM or the MSSM and those from of extended Higgs theories will be highly non-trivial task. Without forward proton tagging, it would require interplay with observations at the Next Linear Collider. Moreover, within the MSSM, the weak-boson-fusion channel becomes of no practical use for the production of the heavier scalar H or the pseudoscalar A boson. On the other hand, in the forward proton mode the pseudoscalar A is practically filtered out, and the detection of the H boson should be achievable [13, 19]. In addition, in some MSSM scenarios, CEP provides an excellent opportunity for probing the CP-structure of the Higgs sector, either by measuring directly the azimuthal asymmetry of the outgoing tagged protons [24] or by studying the correlations between the decay products [25].

In Fig. 2 we show, for reference purposes, the total CEP cross section for the SM Higgs boson times branching ratio for the WW and $b\bar{b}$ channels, as a function of the Higgs mass. We see that the expected total cross section for the CEP of a SM Higgs, with mass 120 GeV, is 3 fb, falling to just less than 1 fb for a mass of 200 GeV; see [1].

With a good understanding of the detectors and favourable experimental conditions, the rate for the SM Higgs of mass 120 GeV for the integrated LHC luminosity of $\mathcal{L} = 60$ fb^{-1} would be quite sizeable (around 100 events). However, with the presently envisaged LHC detectors, there are various experimental problems. First of all, trigger signals from protons detected at 420 m cannot reach the central detector in time to be used in the Level 1 trigger. For this, we have to rely on the central detector. Other factors may also strongly reduce the current expectations for the detected signal rate, in particular, the b-tagging efficiency, the jet energy resolution etc. At high luminosities there is also a potentially dangerous problem of backgrounds due to the overlapping events in the same bunch crossing (the so-called "pile-up" events). In summary, with the current hardware, the expectation is that there will be not more than a dozen SM Higgs signal events for an integrated LHC luminosity of $\mathcal{L} = 60$ fb ^{1}. Whether experimental ingenuity will increase this number remains to be seen. Indeed, it is quite possible that "clever" hardware and the use of optimized cuts will increase the rate. For example, the number of $h \to WW^*$ events would double if the trigger thresholds on single leptons could be reduced [14]. Further improvement of the b-tagging efficiency and of the jet energy resolution would be particularly welcome. Note that the forward-proton

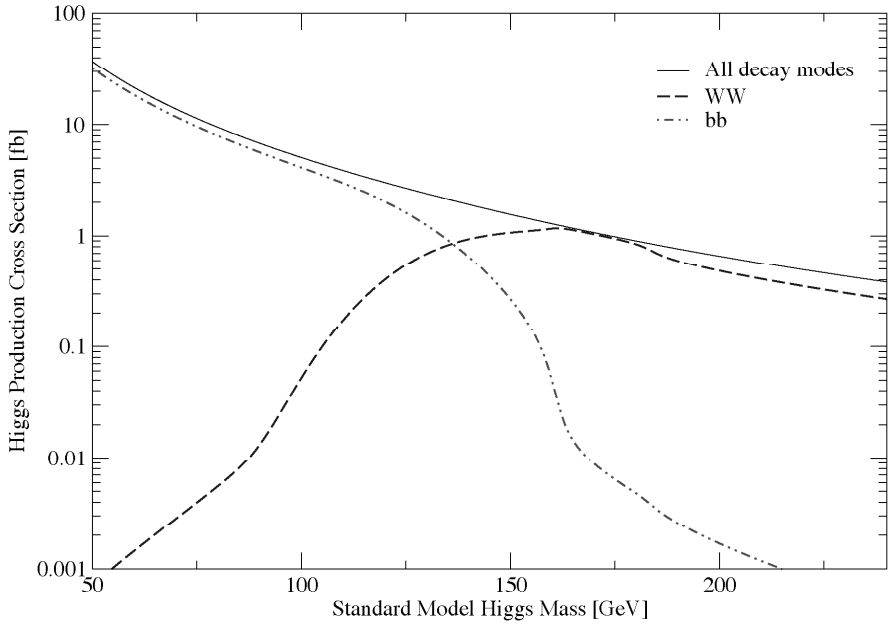

Figure 2: *The cross section times branching ratio for CEP of the SM Higgs* [14].

mode offers the possibility to study the combined event rate using the so-called 'trigger cocktail'.

As we already mentioned, in the MSSM, the CEP cross sections can be an order-of-magnitude or more higher [19]. This is illustrated in Fig. 3, which shows the contours for the ratio R of signal events in the MSSM over those in the SM in the CEP of $H \to b\bar{b}$ in the M_A–$\tan\beta$ plane, see [19].

As discussed above, the exclusive Higgs signal is particularly clean, and the signal-to-background ratio is quite favourable, at least, at an instantaneous luminosity $L \sim 2 \times 10^{33}\,\mathrm{cm}^{-2}\,\mathrm{s}^{-1}$, when the effect of pile-up can be kept under control, see [26, 19]. However, without improving the LHC hardware, the expected event rate in the SM case is quite limited, and so it is important to test various ingredients of the adopted theoretical scheme [1, 12, 2] by studying the related processes at the existing experimental facilities, HERA and the Tevatron. Various such tests have been performed so far, see for

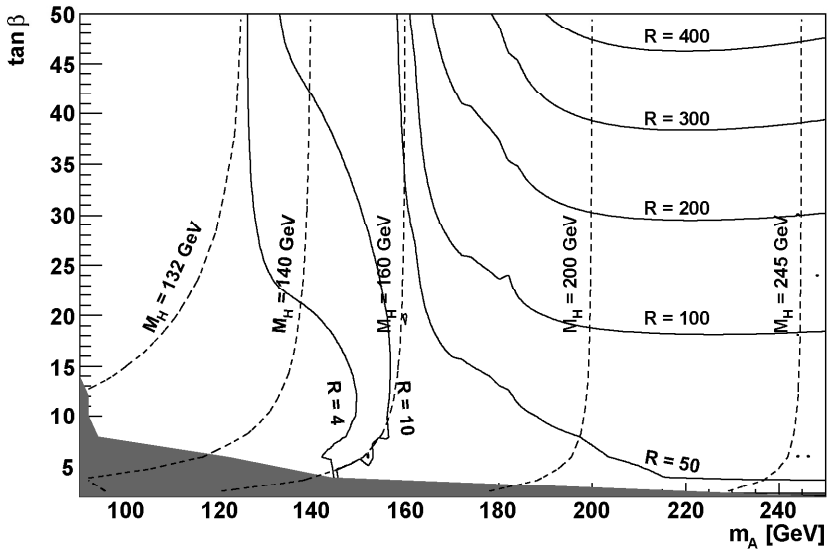

Figure 3: *Contours for the ratio R of the $H \to b\bar{b}$ signal events in the MSSM over those in the SM in CED process in the M_A–$\tan\beta$ plane. The ratio is shown for the $M_h^{\max}$ benchmark scenario (with $\mu = +200$ GeV). The values of the mass of the lighter CP-even Higgs boson, M_h, are indicated by dashed contour lines. The dark shaded region is excluded by the LEP Higgs searches.*

example, [6, 27, 28] and references therein. Quite recently the predictions for the non-perturbative so-called survival factor have been confronted with HERA data on the leading neutron spectra [29].

The straightforward checks come from the study of processes which are mediated by the same mechanism as CEP of the Higgs boson, but with rates which are sufficiently high, so that they may be observed at the Tevatron (as well as at the LHC). The most obvious examples are those in which the Higgs is replaced by either a dijet system, or a χ_c meson, or a $\gamma\gamma$ pair. The reported preliminary CDF data on these CEP processes (see for example, [30, 31, 32]) show a reasonable agreement with the theoretical expectations by Durham group, see also [33].

Especially impressive are the recent CDF data [31, 32] on exclusive pro-

duction of a pair of high E_T jets, $p\bar{p} \to p + jj + \bar{p}$. As discussed in [1, 2] such measurements could provide an effective gg^{PP} 'luminosity monitor' just in the kinematical region appropriate for Higgs production. The corresponding cross section was evaluated to be about 10^4 times larger than that for the production of a SM Higgs boson. Since the dijet CEP cross section is rather large, this process appears to be an ideal 'standard candle'. A comparison of the data with analytical predictions [1, 2] is given in Fig. 4. It shows the $E_T^{\min}$ dependence for the dijet events with $R_{jj} \equiv M_{\rm dijet}/M_{\rm PP} > 0.8$, where $M_{\rm PP}$ is the invariant energy of the incoming Pomeron-Pomeron system. The agreement with the theoretical expectations [1, 2] lends credence to the predictions for the CED Higgs production [31].

3 The backgrounds to the $p + (h, H \to b\bar{b}) + p$ signal

The importance of the $p + (h, H \to b\bar{b}) + p$ process, in particular as a SUSY Higgs search mode, means that the physical backgrounds to this reaction must be thoroughly addressed. Recall that the unique advantage of the $b\bar{b}$ CEP process is the $J_z = 0$ selection rule, which requires the LO $gg^{PP} \to b\bar{b}$ background to vanish in the limit of massless quarks and forward going protons. However, there are still four main sources of background [3, 6, 16]. These are the contributions from the following subprocesses.

(i) The prolific (LO) $gg^{PP} \to gg$ subprocess can mimic $b\bar{b}$ production since we may misidentify the gluons as b and $\bar{b}$ jets.

(ii) An admixture of $|J_z| = 2$ production, arising from non-forward going protons, which contributes to the (QHC[1]) LO $gg^{PP} \to b\bar{b}$ background.

(iii) Because of non-zero mass of the quark there is a contribution to the $J_z = 0$ (QHNC) cross section of order m_b^2/E_T^2. This term currently raises the main concern. The problem is that the result is strongly affected by the (uncomfortably large) higher-order QCD effects see [35, 16]. In particular, the one-loop double logarithmic contribution exceeds the Born term, and the final result becomes strongly dependent on the NNLO effects, as well as on the scale μ of the QCD coupling α_S and on the

[1]It is convenient to consider separately the quark helicity-conserving (QHC) and the quark helicity-non-conserving (QHNC) amplitudes [16]. These amplitudes do not interfere, and their contributions can be treated independently.

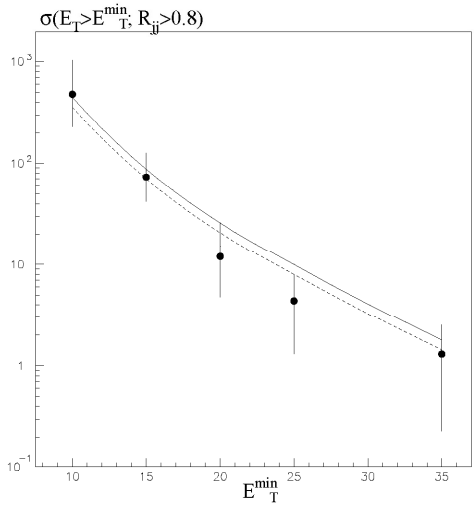

Figure 4: *The cross section for 'exclusive' dijet production at the Tevatron as a function* $E_T^{\min}$ *as measured by CDF* [31]. *These preliminary CDF data correspond to the cross section integrated over the domain* $R_{jj} \equiv M_{\rm dijet}/M_{\rm PP} > 0.8$ *and* $E_T > E_T^{\min}$. *A jet cone of* $R < 0.7$ *is used. The curves are the pure exclusive cross section calculated* [2] *using the CDF event selection. The solid curve is obtained by rescaling the parton (gluon) transverse momentum* p_T *to the measured jet transverse energy* E_T *by* $E_T = 0.8p_T$. *The dashed curve assumes* $E_T = 0.75p_T$. *The rescaling procedure effectively accounts for the hadronization and radiative effects, and for jet energy losses outside the selected jet cone. This prescription for parton jet energy loss is in agreement with the out-of-cone energy measurements in CDF* [34].

running b quark mass. There is no complete calculation of these higher-order effects for the $gg^{PP} \to b\bar{b}$ process, but only estimates based on a seemingly plausible hypotheses regarding the NNLO effects [16]. The validity of these estimates has an accuracy not better than a factor of 2-4. This contribution is the main source of the theoretical uncertainty in the current predictions for the non-pile-up background. The good news is that this contribution decreases with increasing E_T much faster than

the other background terms [13, 24].

(iv) Finally, there is a possibility of NLO $gg^{PP} \to b\bar{b}g$ background contributions, which for large angle, hard gluon radiation do not obey the selection rules, see [3, 16]. Of course, in principle, the extra gluon may be observed experimentally and the contribution of such background events reduced. However, there are important exceptions [3, 16]. First, the extra gluon may go unobserved in the direction of a forward proton. This background is reduced by requiring the approximate equality $M_{\rm missing} = M_{b\bar{b}}$. Calculations [17] show that this background does not exceed 5% of the SM Higgs signal, and so it may be safely neglected. The remaining danger is large-angle hard gluon emission which is collinear with either the b or $\bar{b}$ jet, and, therefore, unobservable. This background source results in a sizeable contribution which should be included, see [19].

There are also other (potentially worrying) background sources, which after a thorough investigation [16, 17], have been omitted in the final expression for the $b\bar{b}g$ background in [19]. This is either because their contributions are numerically small from the very beginning, or because they can be reduced to an acceptable level by straightforward experimental cuts. Among these, there is the NNLO QHC ("cut non-reconstructible") contribution to the exclusive process, which comes from the one-loop box diagrams. This contribution is not mass-suppressed and is potentially important, especially for large M_H. However, for masses below 300 GeV, this contribution is comparatively small.

Next, a potential background source can arise from the collision of two soft Pomerons. This can result in the two main categories of events:

(a) central Higgs boson production accompanied by two (or more) additional gluon jets,

(b) production of a high E_T $b\bar{b}$-pair accompanied by the gluon jets.

In these cases the Higgs boson or the $b\bar{b}$ pair are produced in the collision of two gluons (from the Pomeron wave functions) via the hard subprocesses ($gg \to H$ or $gg \to b\bar{b}$) similar to the usual inelastic event. In both processes the mass, M_{bb}, of the central $b\bar{b}$ system (resulting either from the Higgs decay or from the QCD background) is not equal to the 'Pomeron-Pomeron' mass $M_{PP} = M_{\rm missing}$, measured by the proton detectors. The suppression of such backgrounds is controlled by the requirement that $|M_{\rm missing} - M_{bb}|$ should lie within the ΔM_{bb} mass interval. These backgrounds were carefully evaluated in [17], and it was found that they are quite small. Indeed, if we use the MRW2006

DPDFs [36], and take $\Delta M_{bb} \simeq 24$ GeV, then the $gb\bar{b}g$ and gHg contributions are each less than about 6% of the SM Higgs signal.

Finally, a potential background could result from the emissions of additional gluons. A particular case, caused by the QCD $b\bar{b}$ + gluons process, was already addressed in the item (iv) above. There may also be a contribution coming from the $H+ng$ production process. This contribution is suppressed by the requirement that the t-channel two-gluon exchange across the gap region should be colourless. Thus, there is no single gluon radiation, and the non-zero contribution starts from $n = 2$. Next, we have to impose the mass matching condition discussed in the item (iv) above. Numerically, this background appears to be small (about 15% of the SM Higgs signal [17]) and, again, it can be neglected. It should be noted that the effect of gluon emission off the screening gluon (see Fig. 1) is also numerically small.

In summary, the main background contributions come from exclusive dijet production as listed in the items (i)-(iv) above. Within the accuracy of the existing calculations [12, 3, 16], the overall background to the 0^+ Higgs signal in the $b\bar{b}$ mode can be approximated by the following formula, see [19]

$$\frac{\mathrm{d}\sigma^B}{\mathrm{d}M} \approx 0.5\,\mathrm{fb/GeV}\left[0.92\left(\frac{120}{M}\right)^6 + \frac{1}{2}\left(\frac{120}{M}\right)^8\right], \qquad (1)$$

where the first term in the square brackets corresponds to the processes listed in items (i), (ii) and (iv), while the last term comes from the mass-suppressed term described in item (iii). We emphasize that this approximate expression may be used only for the purposes of making quick estimates of the background, since no detector simulation has been performed. We expect that such a simulation, together with the optimization procedure, will further reduce the effect of background.

4 Detecting the exclusive Higgs $\to WW$ signal

Although the $H \to b\bar{b}$ signal has special advantages, we have discussed problems which arise, in the SM case, to render it challenging from an experimental perspective. In [14, 15], attention was turned to the WW decay mode. Triggering on this channel is not a problem, since the final state is rich in high-p_{T} leptons. Efficiencies of about 20% can be achieved if the standard leptonic and di-leptonic trigger thresholds are applied. The advantages of forward proton tagging are, however, still explicit. Even for the gold-plated double leptonic decay channel, the mass resolution will be very good, and, of course, the observa-

tion of the Higgs with the tagged protons immediately establishes its quantum numbers.

It was demonstrated in [14, 15] that there would be a detectable signal with a small and controllable background for the CED production of a SM-like Higgs boson in the mass interval between 140 GeV and 200 GeV. Unfortunately, with the standard lepton triggers and experimental acceptances and selections [14], currently we can expect only a handful of WW^* events from a 120 GeV SM Higgs for $\mathcal{L} = 60$ fb^{-1}. The rate of detected events could rise after further modifications of hardware. For example, the reduction of the Level 1 leptonic trigger thresholds would allow the statistics to double. As shown in [19], the situation would improve in favourable regions of the MSSM parameter space, but here, unlike the $b\bar{b}$ mode, the expected rise, as compared to SM, is not dramatic, no more than a factor of 4-5. In order to fully exploit all the advantages of the WW channel more dedicated experimental studies are needed.

5 Conclusion

The installation of proton-tagging detectors in the distant forward regions around the ATLAS and/or CMS central detectors would add unique capabilities to the existing LHC experimental programme. The calculation of the rates of CEP processes show that there is a real chance that new heavy particle production could be observed in this mode. For a Higgs boson this would amount to a direct determination of its quantum numbers. For certain MSSM scenarios, the tagged-proton channel may even be the Higgs discovery channel. Moreover, with sufficient luminosity, proton tagging may provide direct evidence of CP-violation within the Higgs sector. There is also a rich QCD, electroweak, and more exotic physics, menu. This includes searches for extra dimensions, light gluino and squark production, gluinonia, radions, and, indeed, any object which has 0^{++} or 2^{++} quantum numbers and which couples strongly to gluons [2].

Here we focused on the unique advantages of CEP Higgs production. The events are clean, but the predicted yield for the SM Higgs for an integrated luminosity of $\mathcal{L} = 60$ fb^{-1} is comparatively low, after experimental cuts and acceptances. Further efforts to optimize the event selection and cut procedure are very desirable. The signal-to-background ratio in the $b\bar{b}$ mode is about 1, depending crucially on the accuracy with which $M_{\rm missing}$ can be measured. In the MSSM there are certain regions of parameter space which can be especially 'proton tagging friendly' [13, 19]. Here the signal-to-background ratios in the

$b\bar{b}$ channel can exceed the SM by up to two orders of magnitude. Moreover, the observation of the decay of Higgs to $b\bar{b}$ would allow a direct determination of the b Yukawa coupling.

From the experimental perspective, the simplest exclusive channel in which to observe a SM Higgs boson with mass between 140 GeV and 200 GeV is the WW decay mode. According to studies in [14], there will be a detectable signal at $\mathcal{L} = 60$ fb^{-1}, and the non-pile-up backgrounds are small and controllable. However, contrary to the $b\bar{b}$ case, no dramatic rise in the rate is expected within the MSSM.

Potentially, the pile-up events could endanger the prospects of CEP studies at high luminosities. Currently the situation is far from being hopeless, but further detailed studies are needed. The pile-up is currently under very intensive scrutiny by both, ATLAS and CMS; for a detailed discussion, see [26], (see also [18, 19]).

6 Acknowledgements

VAK is very grateful to Giorgio Bellettini, Giorgio Chiarelli and Mario Greco for the kind invitation and warm hospitality at La Thuile.

References

1. V.A. Khoze, A.D. Martin and M.G. Ryskin, *Eur. Phys. J.* **C14**, 525 (2000).
2. V.A. Khoze, A.D. Martin and M.G. Ryskin, *Eur. Phys. J.* **C23**, 311 (2002).
3. A. De Roeck, V.A. Khoze, A.D. Martin, R. Orava and M. Ryskin, *Eur. Phys. J.* **C25**, 391(2002).
4. B. Cox, *AIP Conf. Proc.* **753**, 103 (2005) 103.
5. for a recent review see: J. Forshaw, hep-ph/0508274.
6. V.A. Khoze *et al.*, hep-ph/0507040.
7. M.G. Ryskin, A.D. Martin and V.A. Khoze, hep-ph/0506272.
8. M. Albrow and A. Rostovtsev, hep-ph/0009336.
9. FP420 R & D proposal, M.G. Albrow *et al.*, CERN-LHCC-2005-025.
10. A. Kisselev, V. Petrov and R. Ryutin, *Phys. Lett.* **B630**, 100 (2005).

11. P. J. Bussey, T. D. Coughlin, J. R. Forshaw and A. D. Pilkington, JHEP **0611**, 027 (2006).

12. V.A. Khoze, A.D. Martin and M. Ryskin, *Eur. Phys. J.* **C19**, 477 (2001) [Erratum-ibid. **C20**, 559 (2001)].

13. A.B. Kaidalov, V.A. Khoze, A.D. Martin and M.G. Ryskin, *Eur. Phys. J.* **C33**, 261 (2004).

14. B. Cox et al., *Eur. Phys. J.* **C45**, 401 (2006).

15. V.A. Khoze, M. Ryskin and W.J. Stirling, *Eur. Phys. J.* **C44,** 227 (2005).

16. V.A. Khoze, M. Ryskin and W.J. Stirling, *Eur. Phys. J.* **C48**, 797 (2006).

17. V.A. Khoze, A.D. Martin and M. Ryskin, hep-ph/0702213.

18. B. Cox, F. Loebinger and A. Pilkington, to be published.

19. S. Heinemeyer, V.A. Khoze, M.G. Ryskin, W.J. Stirling, M. Tasevsky and G. Weiglein, to be published.

20. for a recent review see: E. Gotsman, E. Levin, U. Maor, E. Naftali and A. Prygarin, hep-ph/0511060.

21. K. Piotrzkowski, Phys. Rcv. **D63**, 071502 (2001).

22. V.A. Khoze, A.D. Martin and M.G. Ryskin, Eur. Phys. J. **C24**, 459 (2002).

23. for reviews see, for example, M. Carena and H. Haber, Prog. Part. Nucl. Phys. **50**, 63 (2003); S. Heinemeyer, *Int. J. Mod. Phys.* **A21**, 2659 (2006).

24. V.A. Khoze, A.D. Martin and M. Ryskin, *Eur. Phys. J.* **C34**, 327 (2004).

25. J. Ellis, J. Lee and A. Pilaftsis, *Phys. Rev.* **D71**, 075007 (2005).

26. CMS and TOTEM diffractive and forward physics working group, CERN/LHCC 2006-039/G-124, CMS Note 2007/002, TOTEM Note 06-5, December 2006.

27. A. B. Kaidalov, V. A. Khoze, A. D. Martin and M. G. Ryskin, Eur. Phys. J. **C21**, 521 (2001); Phys. Lett. B **559**, 235 (2003).

28. A. D. Martin, V. A. Khoze and M. G. Ryskin, hep-ph/0605189.

29. A. B. Kaidalov, V. A. Khoze, A. D. Martin and M. G. Ryskin, *Eur. Phys. J.* **C47**, 385 (2006) ; V. A. Khoze, A. D. Martin and M. G. Ryskin, *Eur. Phys. J.* **C48**, 797 (2006).

30. M. Gallinaro (for the CDF Collaboration), hep-ph/0311192; hep-ph/0505159.

31. K. Goulianos, FERMILAB-CONF-06-429-E, Nov 2006; these proceedings.

32. K. Terashi [CDF and D0 Collaboration], hep-ex/0605084.

33. O. Kepka and C. Royon, arXiv:0704.1956 [hep-ph].

34. K. Terashi, private communication.

35. V. Fadin, V.A. Khoze and A.D. Martin, *Phys. Rev.* **D56**, 484 (1997).

36. A.D. Martin, M.G. Ryskin and G. Watt, Phys. Lett. **B644**, 131 (2007).

DETERMINATION OF THE PARTON DENSITIES OF THE PROTON AND α_S AT HERA

Leif Jönsson
(Representing the H1 and ZEUS collaborations)
Physics Department, University of Lund, Lund, Sweden

Abstract

The inclusive cross section for electron-proton scattering has been measured to a high degree of accuracy at HERA in order to investigate the structure of the proton. Recent measurements by the ZEUS experiment at values of x_{Bj} up to unity, as well as measurements with polarized lepton beams by H1 and ZEUS are discussed. The determination of the strong coupling constant from measurements of jets and from fits where the inclusive cross sections have been combined with additional data, to further constrain the parton density functions, is described.

1 Introduction

The proton structure functions have been extensively studied at the electron-proton collider HERA. The electron-proton scattering cross section can be obtained by convoluting the analytically calculable partonic cross section, σ_{pQCD}, with a parton density function (PDF), f_i, that provides the probability of scattering against a parton carrying a certain fraction x of the proton momentum.

$$\sigma = \left[\sum_{i=g,q,\overline{q}} \int dx f_i(x, \mu_f, \alpha_s(\mu_r)) \sigma_{pQCD}(x, \mu_f, \alpha_s(\mu_r)) \right] (1 + \delta_{had}) \quad (1)$$

The factorization scale μ_f defines at which value of the chosen scale the evolution stops, and μ_r is the renormalization scale, which is the scale variable used in the expansion of the strong coupling constant, α_S. The term δ_{had} takes the hadronization corrections into account.

The parton density function can not be calculated completely but the distribution at a starting scale μ_o has to be extraced experimentally. This is possible through measurements of the proton structure functions, which in leading order QCD are related to the parton density functions. In the quark-parton model (QPM) the inclusive double differential neutral current electron-proton cross section can be expressed in terms of three independent generalised structure functions, $\tilde{F}_2, \tilde{F}_L$ and $x\tilde{F}_3$, according to:

$$\frac{d^2\sigma^{e\pm p}_{NC}}{dxdQ^2} = \frac{2\pi\alpha^2}{xQ^4} \left[(1 + (1-y)^2)\tilde{F}_2(x, Q^2) - \frac{y^2}{2}\tilde{F}_L(x, Q^2) \mp (y - \frac{y^2}{2})x\tilde{F}_3(x, Q^2) \right] \quad (2)$$

with $\tilde{F}_L = \tilde{F}_2 - 2x\tilde{F}_1$ being the longitudinal structure function. The negative square of the boson four-momentum, Q^2, also called the *virtuality*, is a measure of the resolution power of the exchanged boson. α is the fine structure constant, and y is the inelasticity of the process, defined in the proton rest frame as the energy fraction of the incoming electron transferred by the boson. The generalised structure functions $\tilde{F}_2$ and $x\tilde{F}_3$ can be decomposed into terms describing electromagnetic and weak interactions, and the interference between them, in the following way:

$$\tilde{F}_2^{\pm} = F_2 - (v_e \pm P_e a_e) \frac{\kappa Q^2}{(Q^2 + M_Z^2)} F_2^{\gamma Z} + (v_e^2 + a_e^2 \pm P_e 2 v_e a_e) (\frac{\kappa Q^2}{Q^2 + M_Z^2})^2 F_2^Z \quad (3)$$

$$x\tilde{F}_3^{\pm} = -(a_e \pm P_e v_e) \frac{\kappa Q^2}{(Q^2 + M_Z^2)} x F_3^{\gamma Z} + (2 v_e a_e \pm P_e (v_e^2 + a_e^2)) (\frac{\kappa Q^2}{Q^2 + M_Z^2})^2 x F_3^Z \quad (4)$$

where the different signs correspond to electron and positron scattering, respectively. The relative amount of Z and γ exchange is given by $\kappa^{-1} = 4\frac{M_W^2}{M_Z^2}(1 - \frac{M_W^2}{M_Z^2})$, whereas v_e and a_e are the vector and axial-vector couplings of the electron to the Z^o. The lepton beam polarization is denoted P_e and the terms containing P_e express the parity violation.

The structure functions can be given in terms of the cross sections σ_T and σ_L, which correspond to the couplings to transversely and longitudinally polarized photons, respectively, and consequently $\sigma_{tot}^{\gamma p} = \sigma_L + \sigma_T$. At low Q^2, the exchange of Z^o bosons is strongly suppressed compared to the photon exchange, and the cross section is therefore dominated by the contribution from F_2 (electromagnetic), which can be expressed as:

$$F_2(x, Q^2) = \frac{Q^2}{4\pi\alpha^2}(\sigma_L + \sigma_T) = \sum_q e_q^2(xq(x) + x\overline{q}(x)) \tag{5}$$

i.e. the sum of the momentum weighted quark and antiquark densities, $xq(x)$ and $x\overline{q}(x)$, and the electromagnetic couplings to the photon given by the electric charge of the quarks.

The longitudinal structure function, $\tilde{F}_L$, describes the interaction with longitudinally polarized photons, which vanishes in zeroth order α_S processes due to

$$\tilde{F}_L(x, Q^2) = \frac{Q^2}{4\pi\alpha^2}\sigma_L \sim xg \tag{6}$$

with xg being the momentum weighted gluon distribution. From the ratio

$$R = \frac{\tilde{F}_L}{\tilde{F}_2 - \tilde{F}_L} = \frac{\tilde{F}_2 - 2x\tilde{F}_1}{2x\tilde{F}_1} = \frac{\sigma_L}{\sigma_T} \tag{7}$$

we get that $2x\tilde{F}_1 = \sigma_T$.

The structure function $x\tilde{F}_3(x, Q^2)$ is sensitive to the interference between photon and Z^o exchange as well as pure Z^o exchange, and is consequently only important at high Q^2. The sign of the contribution from $x\tilde{F}_3$ to the cross section expression (eq.2) is different for e^-p- and e^+p scattering. Further, $xF_3^{\gamma Z}$ is sensitive to the difference in the quark and antiquark momentum distributions and can in leading order be written as:

$$xF_3^{\gamma Z} = 2x\sum_q (e_q a_q)(q - \overline{q}) = 2x(2u_v + d_v) \tag{8}$$

with u_v and d_v representing the valence quark distributions.

Via the relation to the PDF's the structure functions give us the probability to find a parton in the proton, carrying a fraction x of the proton momentum, if the probe has a resolution power Q^2.

Intuitively one would expect that the probability of scattering against a pointlike parton would be independent of the momentum (resolution) of the probe. Thus, the structure function F_2 should not vary with Q^2, a phenomenon called *scaling*. Experimental data from HERA have, however, clearly demonstrated that scaling is violated. This is related to the resolution power of the exchanged virtual photon in the sense that a high momentum photon is more sensitive to partons carrying a small momentum fraction than a low momentum photon. Since now the structure function depends on Q^2 and the strong coupling, α_S, the scaling violation effect can be used to extract the parton density function and the strength of the strong coupling.

The PDF's are determined through global fits to various experimental data at a smallest starting scale μ_o, at which perturbative calculations are still expected to be valid. Parton evolution equations can then be used to give the PDF at an arbitrary scale. Partonic activites below the starting scale are included into the starting distribution of the PDF.

HERA has measured the proton structure over a large kinematic range, covering almost five orders of magnitude in x_{Bj} and Q^2. One of the most spectacular observations is the strong rise of $F_2(x, Q^2)$ at small x-values. In order to explore this kinematic region special efforts have been made, like:

▷ running HERA with the collisions point shifted in the direction of the proton beam
▷ running HERA with lower electron beam energy
▷ special analysis of events where the incoming electron has suffered from photon radiation

All this leads to an increased detector acceptance for events with lower Q^2.

Due to the relation $Q^2 = x \cdot y \cdot s$, low Q^2 and very small x give access to high y, which is the region where σ_L makes a significant contribution to the cross section and thus F_L may be measured.

2 The high x-region

The high x-region has mainly been covered by previous fixed target experiments. The access to this region at HERA is restricted by acceptance limitations due to the fact that the scattered quark proceeds in the extreme forward direction, close to the beam pipe. Consequently, the jet produced is not well measured above a certain x-value that depends on Q^2. ZEUS [1)] has used a new method to measure the neutral current cross section up to x-values of one, by determining the Q^2 value of the event from the scattered electron and the x-value from the reconstructed jet. If no jet with a transverse energy above 10 GeV was found by the longitudinally invariant k_t cluster algorithm, the event

was assigned to the x-bin not covered by the acceptance. Events with more than one jet were disregarded. The measured double differential cross section, $d^2\sigma/dxdQ^2$, was compared to predictions from Standard Model (SM) NLO calculations in which the CTEQ6M [2)] parametrization of the proton PDF's were used. An overall good agreement between data and the SM predictions was observed although the theory tends to fall below data in the highest x-bin. These measurements will have a significant impact on the determination of the valence quark distributions in the high x-region.

3 Cross section measurements with polarized lepton beams

3.1 Polarization asymmetry

Longitudinally polarized electron beams, delivered by HERA since 2002, have been used to measure the neutral current cross section, which according to the SM should depend on the polariztion of the incoming lepton. The degree of polarization is given by $P_e = (N_R - N_L)/(N_R + N_L)$, where N_R and N_L represents the number of right- and left handed leptons in the beam. The polarization effect is expected to be most significant at large Q^2 where Z^o boson exchange becomes important and may be established by measuring the cross section asymmetry for right- and left handed $e^{\pm}p$ scattering, according to:

$$A^{\pm} = \frac{2}{P_R - P_L} \frac{\sigma^{\pm}(P_R) - \sigma^{\pm}(P_L)}{\sigma^{\pm}(P_R) + \sigma^{\pm}(P_L)} \tag{9}$$

where P_R and P_L stand for right- and lefthanded polarization, respectively. A^+ and A^- will have opposite signs due to the different signs of the $x\tilde{F}_3$-term in the cross section expression (eq.2). The combined data from H1 and ZEUS on the asymmetries ($A^{\pm}$) as a function of Q^2 are shown in Fig.1 and are seen to be in good agreement with the SM predictions from QCD fits performed by H1 and ZEUS, respectively.

3.2 Determination of $x\tilde{F}_3$

A so called reduced cross section can be defined as:

$$\tilde{\sigma}^{\pm}(x, Q^2) = \frac{d^2\sigma^{\pm}_{NC}}{dxdQ^2} \frac{xQ^4}{2\pi\alpha^2} \frac{1}{Y_+} = \tilde{F}_2 \mp \frac{Y_-}{Y_+} x\tilde{F}_3 - \frac{y^2}{Y_+} \tilde{F}_L \tag{10}$$

where the helicity dependence is given by the terms $Y_{\pm} = 1 \pm (1 - y^2)$. The structure function $x\tilde{F}_3$ can be extracted from the difference in magnitude of the reduced cross sections for electron and positron scattering.

$$x\tilde{F}_3 = \frac{Y_+}{2Y_-} (\tilde{\sigma}^{e^-p} - \tilde{\sigma}^{e^+p}) \tag{11}$$

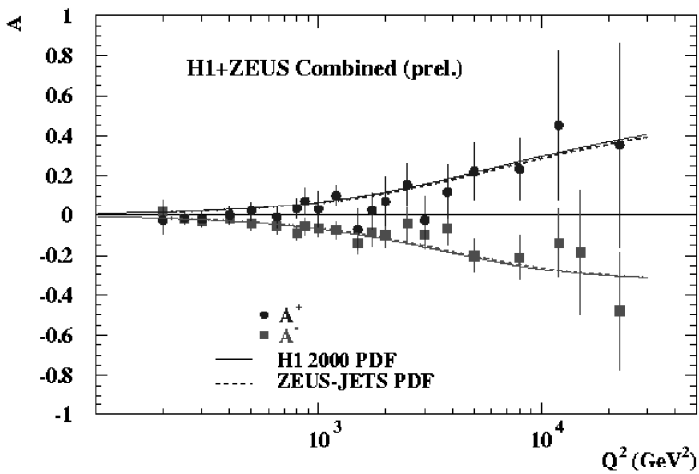

Figure 1: *The Q^2 dependence of the cross section asymmetry $A^{\pm}$ from combined H1 and ZEUS data. The curves represent SM QCD fits by H1 and ZEUS, respectively.*

in which the dominant contribution comes from the γZ interference. Since $x\tilde{F}_3$ depends only slightly on Q^2, the data from different Q^2 regions can be averaged by taking the weak Q^2 dependence into account. The results from H1 and ZEUS at an average Q^2 value of 1500 GeV^2 are shown in Fig.2. Data are reasonably well described, within the fairly large errors, by the NLO fits from both H1 [3] and ZEUS [4]. These results contribute to constrain the valence quark distributions at low x_{Bj}.

4 Determination of the strong coupling constant

The following procedure is used to determine the value of the strong coupling constant, α_S. From a preselected parametrization of the proton parton density function, NLO calculations are performed for different values of $\alpha_S(M_Z)$. The $\alpha_S(M_Z)$-dependence of the experimentally measured variable, denoted A, is parametrized according to:

$$\frac{d\sigma}{dA} = C_1\alpha_S(M_Z) + C_2\alpha_S^2(M_Z) \tag{12}$$

where C_1 and C_2 are parameters in a fit to the calculated $d\sigma/dA$ values at various $\alpha_S(M_Z)$.

The experimentally measured value of $d\sigma/dA$ is then converted to an $\alpha_S(M_Z)$ value via the fitted curve. The error in the measurement is translated into an error of $\alpha_S(M_Z)$ via the slope of the curve. Finally, the Renormalization

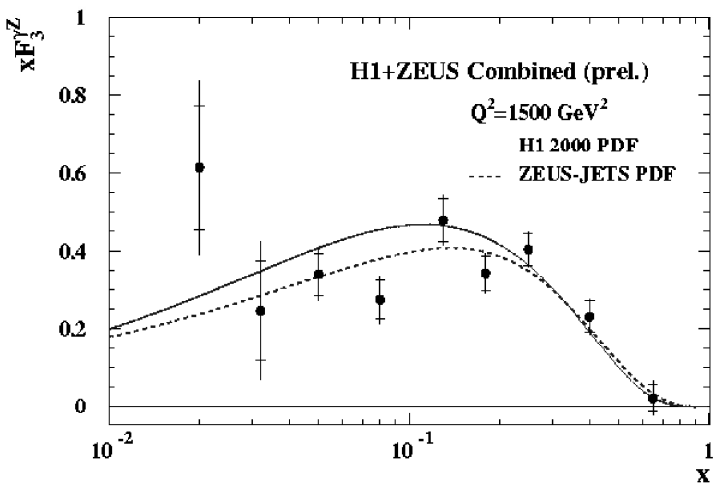

Figure 2: *The structure function xF_3 as a function of x at an average Q^2 value of 1500 GeV^2 from the H1 and ZEUS experiments.*

Group Equation (RGE) is used to extract the α_S values at different scales and thereby the running of the coupling can be established. By using different parametrizations of the PDF's the parton density function dependence may be estimated.

4.1 Measurement of α_S from inclusive jet production at high Q^2

A number of different observables have been measured in order to determine the strong coupling constant. For example the QCD predictions on jet production depend on both the PDF's and α_S. The measured cross sections can be used together with global fits of the proton PDF's to extract α_S. Jets from order α_S processes i.e. QCD-Compton and BGF, provide direct sensitivity to the strong coupling and enable precision tests of QCD. In the Breit frame jets from zeroth order scattering processes produce no transverse energy whereas in leading order processes (BGF or QCD-Compton) transverse jets may be observed.

The longitudinally invariant k_t algorithm [5] is the most frequently used method for reconstructing jets in ep collision events. A cone in the pseudo-rapidity (η) - azimuthal (ϕ) space defines the jet radius as $R = \sqrt{\eta^2 + \phi^2}$. Most analyses so far have been performed with $R = 1$. It turns out that the inclusive jet production cross section provides the experimentally most precise determination of α_S. The ZEUS experiment [6] has studied jet cross sections as a function of the jet radius in order to find an optimal value of R for which the NLO calculations provide the highest precision. Jet radii of $R = 0.5$, 0.7 and 1 have been used to study the Q^2- and E_T-dependence of the jet cross

sections in events containing at least one jet with $E_T > 8$ GeV in the kinematic ranges $Q^2 > 125$ and > 500 GeV^2, respectively. The NLO calculations were performed by DISENT [7] in the $\overline{MS}$ scheme with five flavours, using the ZEUS parametrization of the proton PDF's. The variation of the cross section over several orders of magnitude is well reproduced by the theory. A linear increase of the measured cross section with increasing R is observed and can be understood from the simple fact that more transverse energy is contained in the cone as it opens up, resulting in an increased number of jets exceeding the minimum E_T requirement. The theoretical uncertainties in the cross section integrated over the Q^2 range decreases in both cases slightly when going from $R = 0.5$ to 1, which is mainly attributed to higher order corrections and hadronization.

The H1 experiment has compared cross section measurements of inclusive jets in the Q^2 range 150 - 15000 GeV^2 with NLO calculations provided by the NLOJET++ program [8], in the $\overline{MS}$ scheme with five massless quark flavours, using the CTEQ6.5M parametrization [2] of the proton PDF, and the value of the strong coupling constant has been extracted. The jets were reconstructed by the inclusive k_t algorithm provided they had a transverse momentum greater than 7 GeV. The cross sections as a function of Q^2 and E_T are well described by the NLO predictions within the dominating uncertainties given by the renormalizaion- and factorization scales. Twenty different measurements, subdivided into five Q^2-bins, of the double differential inclusive jet cross section, $d^2\sigma/dQ^2dE_T$, are compatible with the predicted scale dependence of α_S. All the twenty measurements have been used in a combined fit from which the following value of $\alpha_S(M_Z)$ was obtained:

$$\alpha_S(M_Z) = 0.1187 \pm 0.0015(exp.)^{+0.0052}_{-0.0037}(theory)^{+0.0021}_{-0.0014}(PDF) \qquad (13)$$

4.2 Determination of α_S from multi jet production at high Q^2

A measurement of the ratio between three and two jet event cross sections can be used to determine the value of the strong coupling constant, provided the cross sections can be measured with high enough precision. The advantage with this method is that the correlated systematic errors and the renormalization scale uncertainties cancel to a large extent while the disadvantage is the low statistics available. The H1 and ZEUS experiments have performed this analysis in the Breit frame over a wide kinematic range covering $10 < Q^2 < 15000$ GeV^2. Jets with $E_T > 5$ GeV, as reconstructed by the inclusive k_t algorithm, were used for the cross section measurements. In order to avoid problems with the phase space regions sensitive to infrared divergencies, the invariant mass of the jets with the highest transverse energies were required to be $M_{2jet} > 25$ GeV and $M_{3jet} > 25$ GeV, respectively. The reliablility of the NLO calculations are thereby ensured. These calculations are performed by

the NLOJET++ program in the $\overline{MS}$ scheme for five massless quark flavours and with various parametrization of the proton PDF. The Q^2 dependence of the measured cross sections and consequently of the ratio $R_{3/2}$ is in good agreement with the predictions of NLOJET++ in the phase space region where the electroweak effects can be neglected.

From fits to the measured ratios $R_{3/2}$, values of $\alpha_S(M_Z)$ were determined in five different Q^2 bins, but also in the complete Q^2-region giving the results below.
H1:

$$\alpha_S(M_Z) = 0.1175 \pm 0.0017(stat.) \pm 0.0050(syst.)^{+0.0054}_{-0.0068}(theory) \qquad (14)$$

ZEUS:

$$\alpha_S(M_Z) = 0.1179 \pm 0.0013(stat.)^{+0.0028}_{-0.0046}(exp.)^{+0.0064}_{-0.0046}(theory) \qquad (15)$$

4.3 Combined fits of α_S and the gluon density

Measurements of the Q^2 dependence of the structure function (scaling violation) provided by inclusive cross section measurements is the most commonly used method to determine the PDF's via the DGLAP evolution equations. However, fits to the inclusive cross sections alone suffer from strong correlations between the shape of the parton distribution and α_S. These correlations may be reduced by including data which constrain the PDF's in an independent and complementary way.

Recent measurements of the structure function $F_2(x, Q^2)$ at low Q^2, performed by the H1 and ZEUS experiments, provide a considerable improvement compared to previous measurements. The kinematic range covered, $1.5 < Q^2 < 150$ GeV^2 and $3 \cdot 10^{-5} < x < 0.2$, means an extension in x such that an overlap with previous fixed target data is obtained. In spite of this the precision of these data together with previous HERA data at large x and high Q^2 is not sufficient to give enough constraints of both the gluon density and α_S to allow for a simultaneous determination. Instead the low x data from H1, which essentially constrain the gluon distribution, have been combined with large x data provided by the BCDMS μp scattering experiment, in order to reduce the strong correlation between α_S and the gluon distribution, $xg(x, Q^2)$, and thereby enable an accurate simultaneous determination of the two.

The structure function $F_2(x, Q^2)$ has been decomposed into the gluon distribution, $xg(x, Q^2)$, and two independent parton density functions, one of which is defining the valence quark distribution whereas the other constrains the sea-quark distribution and provides a small valence quark correction in order to describe the low x behaviour of F_2. The x dependence of these parton distribution functions have been parametrized at a smallest scale Q_o^2 of 4 GeV^2.

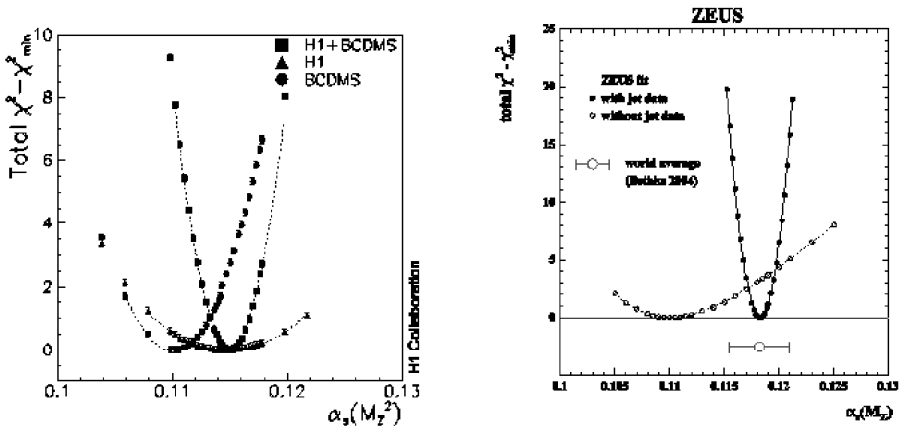

Figure 3: *The χ^2 profiles as a function of $\alpha_S(M_Z)$ for a NLO DGLAP fit using the H1 ep and BCDMS μp data (left) and the ZEUS data with and without the jet data included (right).*

In a NLO QCD fit to the combined H1 and BCDMS data, α_S is left as a free parameter, resulting in a value:

$$\alpha_S(M_Z^2) = 0.1150 \pm 0.0017(exp.)^{+0.0009}_{-0.0005}(model) \tag{16}$$

The fit to the data implies the minimization of a χ^2 function, taking correlations between data points caused by systematic uncertainties into account. The results of the fits are shown in Fig.3(left).

The ZEUS experiment has performed a simultaneous fit to $\alpha_s(M_Z)$ and the proton PDF's in an analysis which includes neutral and charged current inclusive DIS cross sections from e^+p and e^-p scattering together with jet data. Two different jet samples were used in the fit. On one hand the DIS inclusive jet cross sections as a function of the transverse jet energy, E_T, in the Breit frame, for different Q^2 bins were included. On the other hand dijet cross sections in photoproduction as a function of E_T of the most energetic jet, as measured in the laboratory system, for different rapidity regions were also considered. A parametrization of the PDF's at a smallest scale $Q_o^2 = 7$ GeV^2 provides a good fit of the jet cross sections over several orders of magnitude. The quality of the fit demonstrates that NLO QCD is able to simultaneously describe inclusive cross sections as well as jet cross sections.

The strong correlation between the gluon shape and the value of $\alpha_s(M_Z)$, which affects the fits to inclusive cross section data alone, is avoided by including the jet data, since their cross sections depend on the gluon PDF and the value of $\alpha_s(M_Z)$ in a different way compared to the total cross section. An

advantage in using different data sets from the same experiment compared to combining data from different experiments is that the contributions from correlated errors and normalization uncertainties are significantly reduced. The combined fit results in an α_S value of:

$$\alpha_S(M_Z) = 0.1183 \pm 0.0028(exp.) \pm 0.0008(model) \tag{17}$$

The χ^2 profile as a function of α_S, shown in Fig.3(right), illustrates the improved accuracy in the α_S determination from the data sample including the jet data compared to using the inclusive cross sections alone.

Fig.4 gives a compilation of various measurements of $\alpha_S(M_Z)$ at HERA. Within uncertainties all these results agree internally and with the world average.

$$\alpha_S(M_Z) = 0.1189 \pm 0.0010 \tag{18}$$

In Fig.5 the HERA results are complemented with measurements by other experiments to illustrate the running of α_S with the energy scale Q. The Q dependence of α_S is well reproduced by QCD predictions, which makes it relevant to extrapolate all results to a common scale defined by the rest mass of the Z^o boson, M_Z, using the Renormalization Group Equation.

5 Summary

A measurement of the inclusive ep-cross section in the high x_{Bj} region by the ZEUS experiment is well described by recent parametrizations of the parton density function, except for the highest x_{Bj}-bin where the predictions undershoot the data. The first measurements from the H1 and ZEUS experiments with polarized lepton beams at HERA give cross sections which are consistent with the predictions of the Standard Model and the observed asymmetry clearly demonstrates the parity violation at small distances. The structure function $xF_3^{\gamma Z}$, which can be extracted from the polarization cross section asymmetries, is sensitive to the valence quark distributions and turns out to be in good agreement with Standard Model predictions.

The cross section of inclusive jet production as measured by the H1 and ZEUS experiments is well reproduced by NLO QCD calculations and fits to the data have been used to extract $\alpha_S(M_Z)$ and to demonstrate the scale dependence of the coupling constant. The ratio between trijet and dijet cross sections is also well described by NLO calculations over the measured Q^2 range where electroweak effects can be neglected. The strong coupling can be extracted with a precision that profits from cancellations of systematic errors. The inclusive cross section measurements have been combined with other data in order to further constrain the parton density functions and to extract $\alpha_S(M_Z)$ in combined fits. All results on $\alpha_S(M_Z)$ presented, are consistent and in good agreement with the world average value.

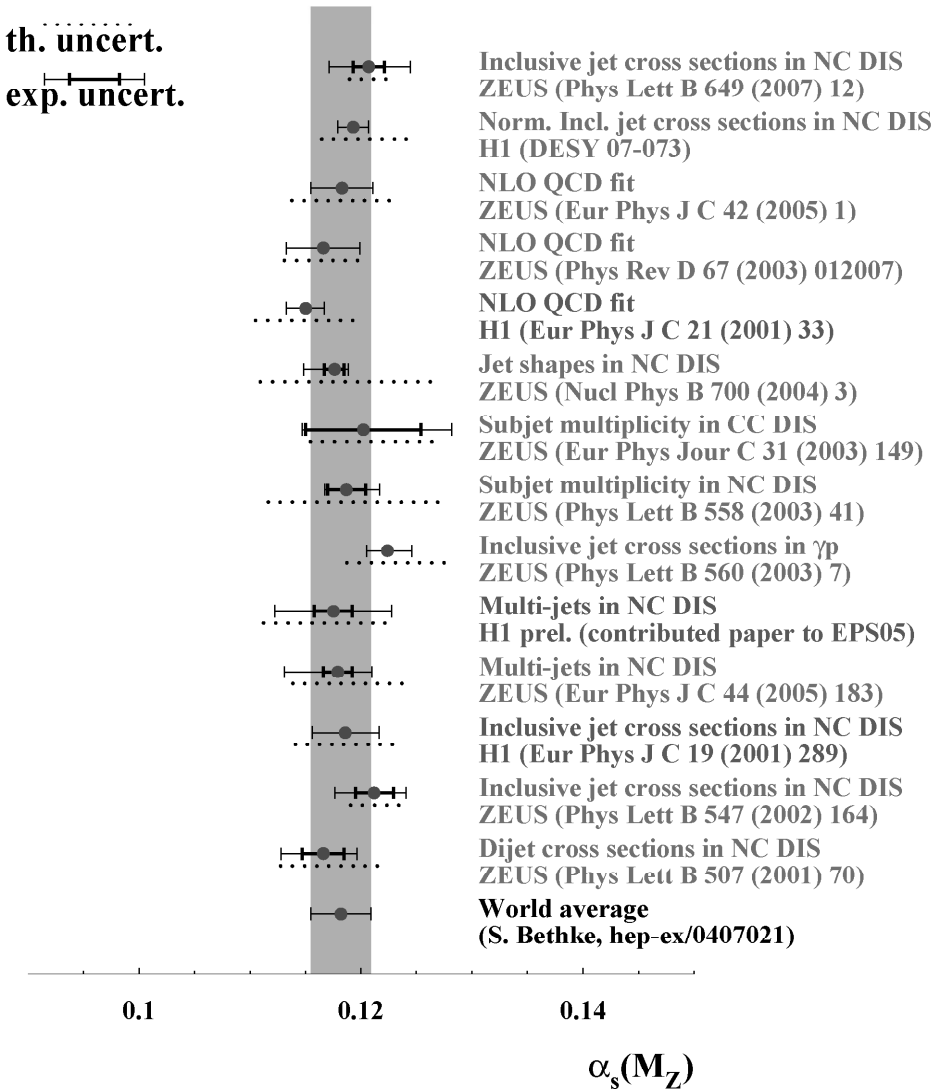

Figure 4: *A compilation of $\alpha_S(M_Z)$ measurements at HERA compared to the world average value.*

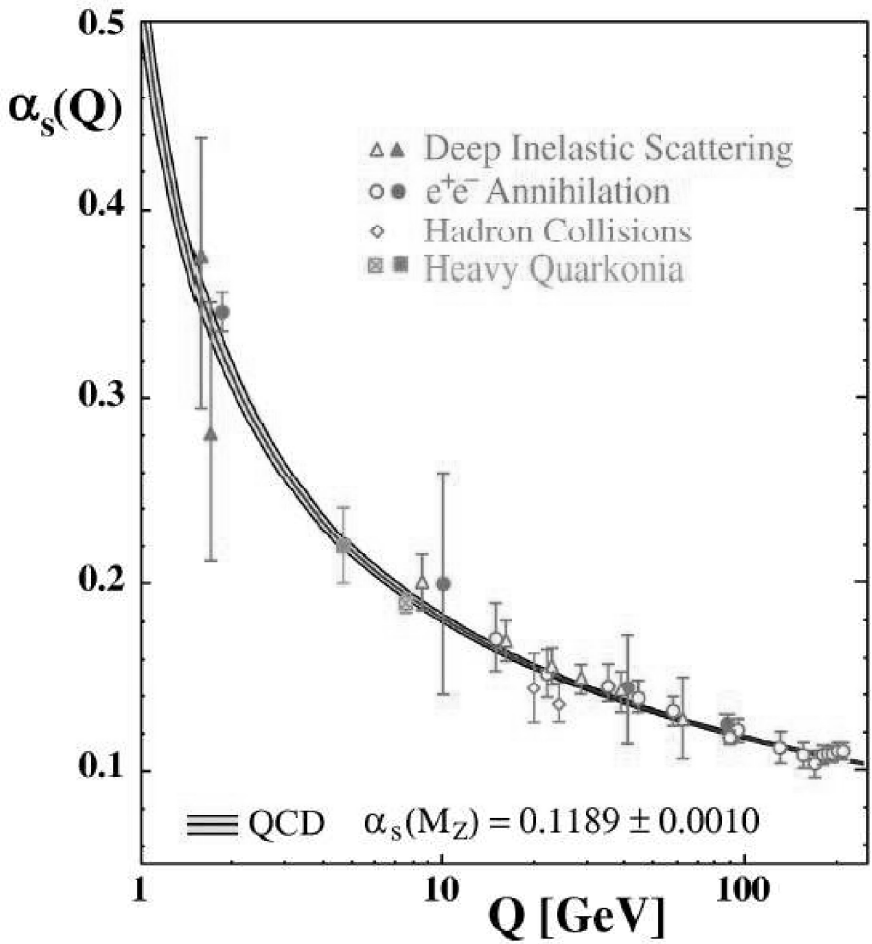

Figure 5: *The scale dependence of $\alpha_S(Q)$ including data from various measurements compared to the QCD prediction.*

6 Acknowledgements

I would like to thank the organizers for an enjoyable and interesting conference. Colleagues from H1 and ZEUS are acknowledged for help with the material of this presentation.

References

1. ZEUS Collaboration, S. Chekanov *et al*, Eur. Phys. J. **C49**, 523 (2007).
2. J. Pumplin *et al*, JHEP **0207**, 012 (2002).
3. H1 Collaboration, C. Adloff *et al*, Eur. Phys. J. **C30**, 1 (2003).
4. ZEUS Collaboration, S. Chekanov *et al*, Phys. Lett. **B637**, 210 (2006).
5. S. Catani *et al*, Nucl. Phys.**B406**, 187 (1993).
6. ZEUS Collaboration, S. Chekanov *et al*, hep-ex/0701039
7. S. Catani and M. Seymour, Nucl. Phys.**B485**, 291 (1997).
8. Z. Nagy and Z. Trocsanyi, Phys. Rev. Lett. **87**, 082001 (2001).
9. ZEUS Collaboration, S. Chekanov *et al*, Eur. Phys. J. **C44**, 183 (2005).

DIFFRACTIVE PARTON DENSITIES AND FACTORISATION TEST

Davide Boscherini
Bologna, Italy

Written contribution not received

DIFFRACTION AND EXCLUSIVE (HIGGS?) PRODUCTION FROM CDF TO LHC *

Konstantin Goulianos
The Rockefeller University, 1230 York Avenue, New York, NY 10023, USA

Abstract

The diffractive program of the CDF Collaboration at the Fermilab Tevatron $p\bar{p}$ Collider is reviewed with emphasis on recent results from Run II at $\sqrt{s}$ =1.96 TeV. Results are presented on the x-Bjorken and Q^2 dependence of the diffractive structure function obtained from dijet production, on the slope parameter of the t-distribution of diffractive events as a function of Q^2 in the range 1 GeV^2 $< Q^2 <$ 10^4 GeV^2, and on cross sections for exclusive dijet, e^+e^-, and $\gamma\gamma$ production. The exclusive dijet and $\gamma\gamma$ production rates are used to check theoretical estimates of exclusive Higgs boson production at the Large Hadron Collider. Other data on soft and hard diffraction from $pp/p\bar{p}$ collisions, and also data from diddractive deep inelastic scattering are presented and interpreted in the RENORM phenomenological model, in which cross sections are obtained from the underlying inclusive parton distribution function of the nucleon and QCD color factors.

* This paper is composed of updated versions of two papers presented at *DIFFRACTION 2006 - International Workshop on Diffraction in High Energy Physics, September 5-10 2006, Adamantas, Milos island, Greece*, published by *Proceedings of Science:* PoS (DIFF2006) 016 and PoS (DIFF2006) 044.

1 Experimental results

1.1 Introduction

The CDF collaboration has been carrying out a systematic and comprehensive program of studies of diffractive interactions since the start of operations of the Fermilab Tevatron $p\bar{p}$ collider in 1989. The ultimate goal of this program is to provide experimental results which will be of help in elucidating the QCD character of hadronic diffraction [1)]. Diffractive interactions are characterized by large rapidity gaps [1] in the final state, presumed to occur via the exchange of a quark/gluon combination carrying the quantum numbers of the vacuum. This exchange is traditionally referred to as *Pomeron* [2)]. The process which is directly analogous to the classical diffraction of light is elastic scattering, but it is inelastic diffraction processes that provide the most stringent tests for QCD inspired models of diffraction. The total cross section is also of interest in testing theoretical models of diffraction, since it is related to the imaginary part of the forward elastic scattering amplitude through the optical theorem. In this paper, we present results obtained at the Tevatron by CDF and comment on their physics significance.

The names/dates of the Tevatron runs and integrated luminosities of data collected by CDF are listed below:

Run Number	Date	$\int$Lum (pb^{-1})
Run I		
IØ	1988-1989	5
Ia	1992-1993	20
Ib	1993-1995	100
Ic	1995-1996	10
Run II		
IIa	2003-2006	1000
IIb	currently in progress	

In Run IØ, CDF measured elastic, single diffractive, and total cross sections at $\sqrt{s}$ =630 and 1800 GeV.

In Runs Ia, Ib and Ic, CDF studied both soft and hard diffractive processes, with the latter incorporating a hard partonic scattering in addition to the characteristic large rapidity gap of diffraction. Fig. 1 shows schematically

[1]Rapidity gaps are regions of rapidity devoid of particles; rapidity, $y = \frac{1}{2}\frac{E+p_L}{E-p_L}$, and pseudorapidity, $\eta = -\ln\tan\frac{\theta}{2}$, are used interchangeably, as in the kinematic region of interest the values of these two variables are approximately equal.

the diagrams and final state event topologies of the processes studied by CDF in Run I.

In Run II, the CDF diffractive program was enhanced by extending the kinematic range of the measurements of hard diffractive processes and by additional studies of exclusive production processes.

All Run I results have been published. These results are briefly summarized. The Run II results are discussed in more detail. Recent results on the x-Bjorken and Q^2 dependence of the diffractive structure function and on the t-dependence of diffractive cross sections are reported and characterized in terms of their physics content. In addition, results on exclusive dijet, e^+e^-, and $\gamma\gamma$ production are presented and their significance in calibrating predictions for exclusive Higgs boson production at the LHC is discussed.

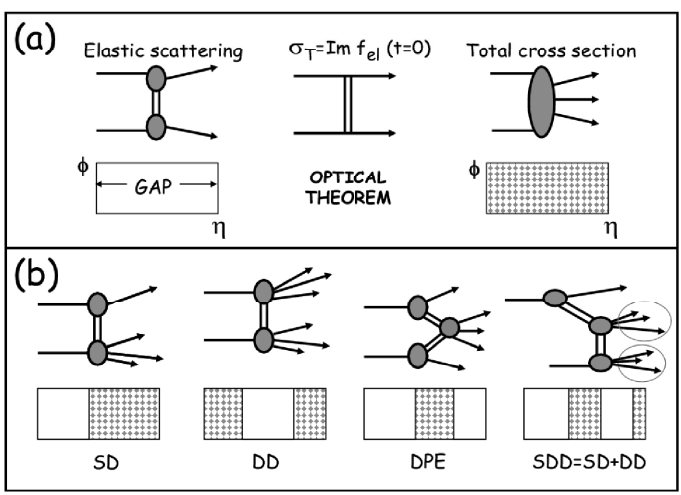

Figure 1: Schematic diagrams and event topologies in azimuthal angle ϕ vs. pseudorapidity η for (a) elastic and total cross sections, and (b) single diffraction (SD), double diffraction (DD), double Pomeron exchange (DPE), and double plus single diffraction cross sections (SDD=SD+DD). The hatched areas represent regions in which there is particle production.

1.2 Run IØ Results

In Run IØ, CDF measured the elastic, soft single diffractive, and total $p\bar{p}$ cross sections at $\sqrt{s}$ =630 and 1800 GeV. The measurement was performed with the CDF I detector, which during run IØ had tracking coverage out to $|\eta| \sim 7$ and Roman Pot Spectrometers on both sides of the Interaction Point (IP). The

normalization was obtained by the luminosity independent method, which is based on simultaneously measuring the total interaction rate, which depends on σ_T, and the elastic scattering differential rate at $t = 0$, which depends on σ_T^2 (optical theorem):

$$\sigma_T \propto \frac{1}{L}(N_{el} + N_{inel}) \quad \& \quad \sigma_T^2 \sim \frac{1}{1+\rho^2}\frac{dN_{el}}{dt}|_{t=0}$$

$$\Rightarrow \quad \sigma_T = \frac{16\pi}{1+\rho^2}\frac{1}{N_{el}+N_{inel}}\frac{dN_{el}}{dt}|_{t=0}$$

Paradoxically, overestimating the total rate, as for example due to background events, yields smaller elastic and total cross sections, while loss of inelastic events results in larger cross sections.

Figure 2 (*left*) shows Regge based fits to total and elastic scattering data using the eikonal approach to ensure unitarity [3]. Good fits are obtained, which are consistent with the CDF cross sections at the Tevatron even if the Tevatron cross sections are not used in the fit [3]. In contrast, the standard Regge fit to total single diffractive cross sections, shown in Fig. 2 (*right*), overestimates the Tevatron cross sections by a factor of ~ 10. This discrepancy represents a breakdown of factorization, which is restored by the renormalization procedure proposed in Ref. [4] and discussed in Sec. 2.

1.3 Run Ia,b,c Results

The diffractive processes studied by CDF in Tevatron Runs Ia,b,c (1992-1996) are schematically shown in Fig. 1b. Both soft and hard processes were studied. A discussion of the results obtained and of their significance in deciphering the QCD nature of the diffractive exchange can be found in Ref. [5]. The most interesting discoveries from this diffractive program were the breakdown of factorization and the restoration of factorization in events with multiple rapidity gaps.

Breakdown of factorization. At $\sqrt{s}$ =1800 GeV, the SD/ND ratios (gap fractions) for dijet, W, b-quark, and J/ψ production, as well the ratio of DD/ND dijet production, are all $\approx 1\%$. This represents a suppression of a factor of $\sim$10 relative to predictions based on diffractive parton densities measured from DDIS at HERA, indicating a breakdown of QCD factorization comparable to that observed in soft diffraction processes relative to Regge theory expectations. However, factorization approximately holds among the four different diffractive processes at fixed $\sqrt{s}$, which indicates that the suppression has to do with the formation of the rapidity gap, as predicted by the generalized gap renormalization model (see [5] and Sec. 2).

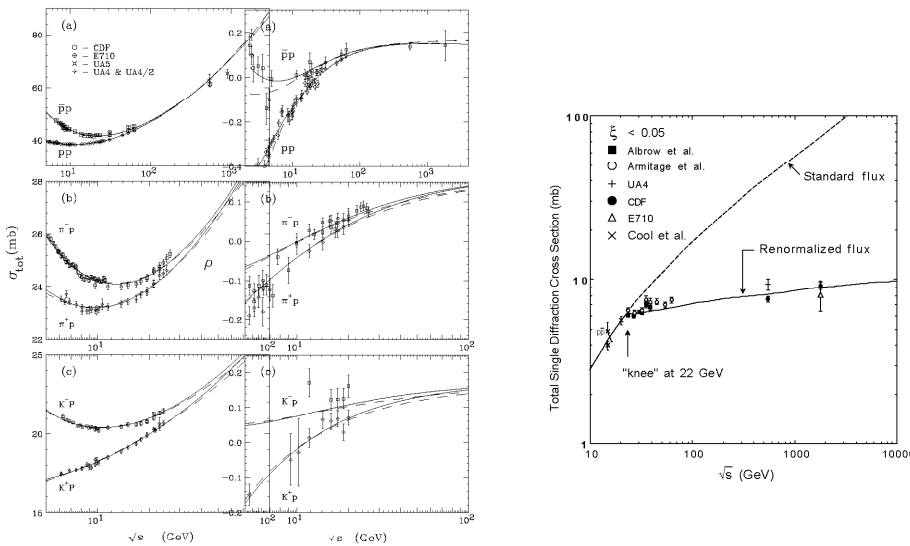

Figure 2: *(left)* Simultaneous fit to $p\bar{p}$, $\pi^{\pm}$, and $K^{\pm}$ total cross section and ρ-value data using eikonalized (solid) and Born level (dashed) amplitudes [3] - the rise of the $p\bar{p}$ cross section with $\sqrt{s}$ is "pulled" by the rise of the $\pi^{\pm}$ cross sections and would pass through the CDF point at $\sqrt{s} = 1800$ GeV even if this point were not used in the fit; *(right)* total $pp/p\bar{p}$ single diffraction dissociation cross section data (sum of $\bar{p}$ and p dissociation) for $\xi < 0.05$ compared with Regge predictions based on standard and renormalized Pomeron flux [4].

Restoration of factorization in multi-gap diffraction. Another interesting aspect of the data is that ratios of two-gap to one-gap cross sections for both soft and hard processes obey factorization. This provides both a clue to understanding diffraction in terms of a composite Pomeron and an experimental tool for diffractive studies using processes with multiple rapidity gaps (see [5]).

1.4 The Run II Diffractive Program

In Run II, CDF has been conducting the following studies of diffraction:

- structure function in dijet production,
- t distributions,
- exclusive dijet, $\gamma\gamma$, and e^+e^- production,
- structure function in W production,
- gap between jets: cross section vs. gap size for fixed $\Delta\eta^{jet}$.

In this paper, we present preliminary results on the first three topics. The diffractive W and 'gap between jets' analyses are in progress and results are expected by Fall of 2007.

1.5 Run II forward detectors

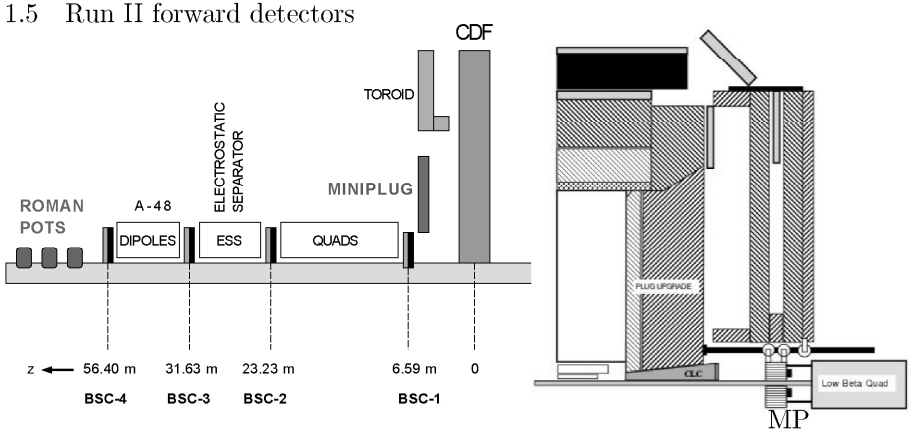

Figure 3: The CDF detector in Run II: *(left)* location of forward detectors along the $\bar{p}$ direction; *(right)* position of the Cerenkov Luminosity Monitor (CLC) and MiniPlug calorimeters (MP) in the central detector.

The Run II diffractive program was made possible by an upgraded CDF detector [6], which includes the following special forward components (Fig. 3):

– Roman Pot Spectrometer (RPS) to detect leading antiprotons,

– MiniPlug (MP) forward calorimeters approximately covering the region $3.5 < |\eta| < 5.5$,

– Beam Shower Counters (BSC) positioned around the beam pipe at four (three) locations along the $\bar{p}$ (p) beam direction to tag rapidity gaps within $5.5 < |\eta| < 7.5$.

The Roman Pot Spectrometer is the same one that was used in Run Ic. It consists of X-Y scintillation fiber detectors placed in three Roman Pot Stations located at an average distance of 57 m downstream in the $\bar{p}$ direction. The detectors have a position resolution of $\pm 100\,\mu m$, which makes possible a $\sim 0.1\%$ measurement of the $\bar{p}$ momentum. In Run Ic, the $\bar{p}$-beam was behind the proton beam, as viewed from the RPS side. Inverting the polarity (with respect to Run I) of the electrostatic beam separators enabled moving the RPS detectors closer to the $\bar{p}$-beam and thereby obtain good acceptance for $|t| < 0.5$ GeV^2 down to $\xi \equiv 1 - x_F(\bar{p}) = 0.03$ (for larger $|t|$, lower ξ values can be reached).

The MiniPlug calorimeters are located within the holes of the muon toroids. They consist of layers of lead plates immersed in liquid scintillator. The scintillation light is picked up by wavelength shifting fibers strung through holes in the lead plates and read out by multi-channel PMT's. The calorimeter "tower" structure is defined by arranging fibers in groups to be read out by individual PMT pixels. There are 84 towers in each MiniPlug, and the signals they provide can be used to measure energy and position for both electromagnetic and hadron initiated showers [7].

The Beam Shower counters are rings of scintillation counters "hugging" the beam pipe. The BSC-1 rings are segmented into four quadrants, while all other BSC rings are segmented into two halves. The BSC-1 are also used to provide rapidity gap triggers and for measuring beam losses.

1.6 Diffractive structure function from dijet production

In Run II, CDF has obtained preliminary results for the x_{Bj}, Q^2, and t dependence of the diffractive structure function from dijet production at $\sqrt{s} = 1960$ GeV. The measured x_{Bj} rates confirm the factorization breakdown observed in Run I (see review in Ref. [8]). The Q^2 and t dependence results are shown in Fig 4.

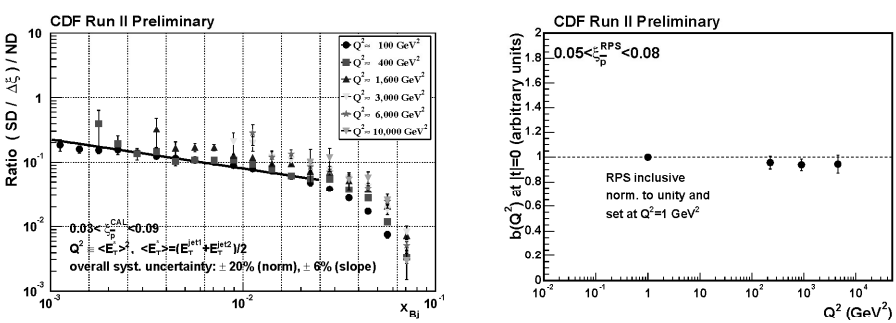

Figure 4: *(left)* Ratio of diffractive to non-diffractive dijet event rates as a function of x_{Bj} (momentum fraction of parton in antiproton) for different values of $E_T^2 = Q^2$; *(right)* the $b(t)|_{t\to 0}$ slope vs. Q^2.

Q^2 dependence. In the range 10^2 GeV^2 $< Q^2 <$ 10^4 GeV^2, where the inclusive E_T distribution falls by a factor of $\sim 10^4$, the ratio of the SD/ND distribution increases, but only by a factor of ~ 2. This result indicates that the Q^2 evolution in diffractive interactions is similar to that in ND interactions.

t-dependence. The slope parameter $b(Q^2,t)|_{t=0}$ of an exponential fit to t distributions near $t=0$ shows no Q^2 dependence in the range 1 GeV^2 $< Q^2 <$ 10^4 GeV^2.

These results support the picture of a composite Pomeron formed from color singlet combinations of the underlying parton densities of the nucleon (see [5] and Sec. 2).

1.7 Exclusive Dijet Production

Exclusive production in $p\bar{p}$ collisions is of interest not only for testing QCD inspired models of diffraction, but also as a tool for discovering new physics. The process that has attracted the most attention is exclusive Higgs boson production. The search for Higgs bosons is among the top priorities in the research plans of the LHC experiments. While the main effort is directed toward searches for inclusively produced Higgs bosons, an intense interest has developed toward exclusive Higgs production, $\bar{p}/p + p \rightarrow \bar{p}/p + H + p$. This Higgs production channel presents the advantage that it can provide clean events in an environment of suppressed QCD background, in which the Higgs mass can accurately be measured using the missing mass technique by detecting and measuring the momentum of the outgoing proton and (anti)proton. However, exclusive production is hampered by expected low production rates [9]. As rate calculations are model dependent and generally involve non-perturbative suppression factor(s), it is considered prudent to calibrate them against processes involving the same suppression factors(s), but have higher production rates that can be measured at the Tevatron. One such processes is exclusive dijet production, which proceeds through the same mechanism as Higgs production, as shown in Fig. 5.

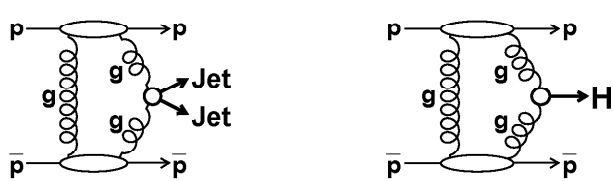

Figure 5: Lowest order diagrams for exclusive dijet (left) and Higgs (right) production in $\bar{p}p$ collisions.

The search for exclusive dijets is based on measuring the dijet mass fraction, R_{jj}, defined as the mass of the two leading jets in an event, M_{jj}, divided by the total mass reconstructed from the energy deposited in all calorimeter towers, M_X. The signal from exclusive diets is expected to appear at high values of R_{jj}, smeared by resolution and radiation effects. Events from inclusive

DPE production, $\bar{p}p \to \bar{p}+gap+jj+X+gap$, are expected to contribute to the entire M_{jj} region. Any such events within the exclusive M_{jj} range contribute to background and must be subtracted when evaluating exclusive production rates.

The method used to extract the exclusive signal from the inclusive R_{jj} distribution is based on fitting the data with MC simulations [10]. Two methods have been used. In the first one, the POMWIG and ExHuME generators are used for simulating inclusive and exclusive events, respectively; in the second, inclusive (exclusive) distributions are simulated using the POMWIG (DPEMC) program. Experimentally, the MC non-exclusive dijet background shape is checked by a study of high E_T b-tagged dijet events, as quark jet production through $gg \to \bar{q}q$ is suppressed in LO and NLO QCD by the $J_z = 0$ selection rule as $m_q/M^{jet} \to 0$.

Figure 6 shows measured R_{jj} distributions plotted vs. dijet mass fraction. On the left, the number of events within the specified kinematic region is compared with fits based on POMWIG⊕ExHuME distribution shapes, and on the right with fits based on POMWIG⊕DPEMC predictions. Both approaches yield good fits to the data. The suppression factor expected for exclusive b-tagged dijet events is checked with CDF data in Fig. 7. Within the quoted errors, this result validates the MC based method for extracting the exclusive signal.

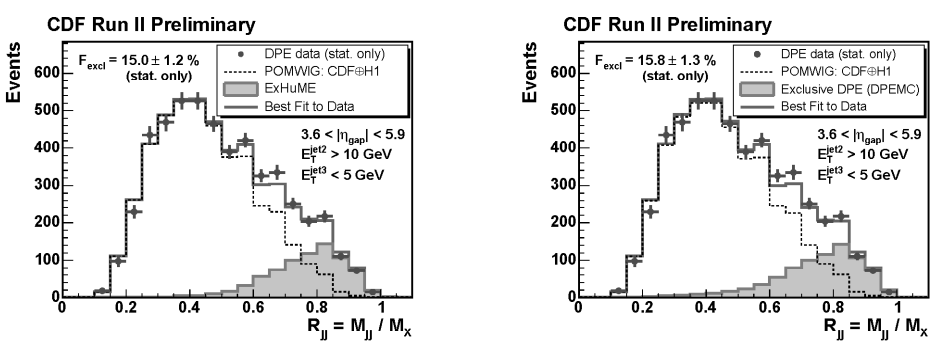

Figure 6: Extraction of exclusive dijet production signal using Monte Carlo techniques to subtract the inclusive dijet background: *(left)* dijet mass fraction in data (points) and best fit (solid line) obtained from MC events generated using the POMWIG (dashed) and ExHuME (filled) MC generators for inclusive and exclusive events, respectively; *(right)* the same data fitted with POMWIG and exclusive DPEMC generators.

In Fig. 8 *(left)*, integrated cross sections above a minimum $E_T^{jet1,2}$ are com-

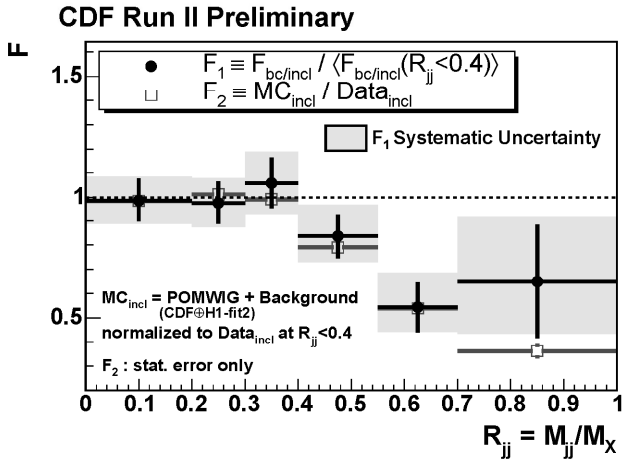

Figure 7: *(circles)* Fraction of heavy flavor (b, c) in all dijet events in data, F_1, as a function of dijet mass fraction showing the expected suppression at high M_{jj}; *(squares)* fraction, F_2, of inclusive MC in data from Fig. 6 (left). The agreement between the measured suppression levels in F_1 and F_2 serves to validate the MC based technique of extracting the exclusive production rate from the data.

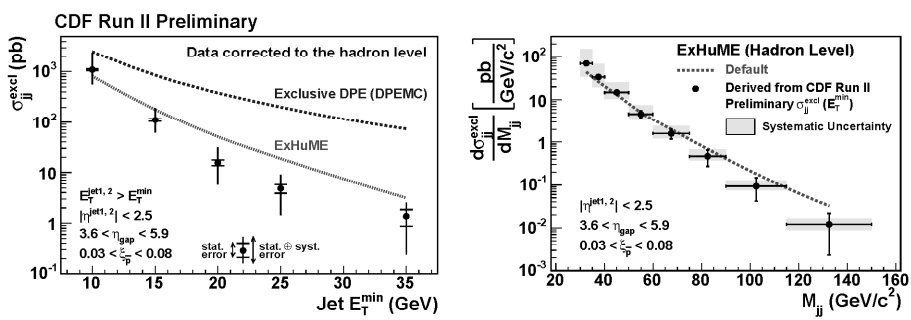

Figure 8: *(left)* Measured exclusive dijet cross sections vs. the minimum E_T of the two leading jets compared with ExHuME and DPEMC predictions; *(right)* ExHuME hadron level differential exclusive dijet cross section vsersus dijet mass normalized to the CDF cross sections at *left*. The systematic errors shown are propagated from those in the data; the ExHuME predictions have comparable systematic uncertainties.

pared with ExHuME and DPEMC predictions. The data favor the ExHuME prediction. ExHuME hadron level differential cross sections $d\sigma^{excl}/dM_{jj}$ normalized to the measured data points of Fig. 8 *(left)* are shown in Fig. 8 *(right)* with errors propagated from the uncertainties in the data. Within the errors, the good agreement with the default ExHuME prediction up to masses in the region of the standard model Higgs mass predicted from global fits to electroweak data lends credence to the calculation of Ref. [9] for exclusive Higgs boson production at the LHC.

1.8 Exclusive $\gamma\gamma$ and e^+e^- production

Exclusive $\gamma\gamma$ production in $p\bar{p}$ collisions proceeds through a lowest order diagram similar to that of Fig. 5 *(right)*, but with the gluons that produce the Higgs replaced by γ's. Therefore, like exclusive dijet production, exclusive $\gamma\gamma$ production can also be used for calibrating models of Higgs production at hadron colliders. Exclusive e^+e^- production is a QED process whose cross section can be reliably calculated and thus can serve validate the procedure used to extract the exclusive $\gamma\gamma$ signal.

A search for exclusive $\gamma\gamma$ production has been performed on a sample of events collected by requiring a high E_T electromagnetic shower in combination with a loose forward rapidity gap requirement. In the data analysis, the rapidity gap requirement was tightened, and the search was narrowed down to events with two high E_T photon showers satisfying certain "exclusivity" requirements. In a data sample of 532 pb^{-1} total integrated luminosity, three exclusive $\gamma\gamma$ candidate events with $E_T^{\gamma} > 5$ GeV were found with no tracks pointing to the electromagnetic clusters. As a check of the robustness of the rapidity gap requirement, CDF measured the cross section for the purely QED process $\bar{p} + p \rightarrow \bar{p} + e^+e^- + p$ [11]. Twelve exclusive e^+e^- candidate events were found in the data with an estimated background of $2.1^{+0.7}_{-0.3}$, yielding $o\,(e^+e^-) = 1.6^{+0.5}_{-0.3}$(stat), which agrees with an expectation of 1.71 ± 0.01 pb. For $\gamma\gamma$ production, three candidate exclusive events were observed, yielding an upper limit on the production cross section of 110 fb at 95% confidence level.

1.9 Summary of experimental results section

The diffractive program of the CDF Collaboration at the Fermilab Tevatron $p\bar{p}$ Collider has been reviewed with emphasis on recent results from Tevatron Run II at $\sqrt{s}$ =1.96 TeV.

Run I results have been briefly presented and their physics significance placed in perspective. Processes studied by CDF in Run I include elastic and total cross sections, soft diffractive cross sections with single and multiple rapidity gaps, and hard single diffractive production of dijet, W, b-quark, and

J/ψ production, as well as central dijet production in events with two forward rapidity gaps (double Pomeron exchange). The results obtained support a picture of universality of diffractive rapidity gap formation across soft and hard diffractive processes, which favors a composite over a particle-like Pomeron made up from color singlet quark and/or gluon combinations with vacuum quantum numbers.

Run II results on the x_{Bj} and Q^2 dependence of the diffractive structure function obtained from dijet production have been presented, as well as on the slope parameter of the t-distribution of diffractive events as a function of Q^2. In the range 10^2 GeV$^2 < Q^2 < 10^4$ GeV^2, where the inclusive E_T distribution falls by a factor of $\sim 10^4$, the ratio of SD/ND distributions varies by only a factor of ~ 2, indicating that the Q^2 evolution in diffractive interactions is similar to that in ND ones; and the slope parameter $b(Q^2)|_{t=0}$ of an exponential fit to t distributions near $t = 0$ in the range 1 GeV$^2 < Q^2 < 10^4$ GeV^2 shows no Q^2 dependence. These results support a picture of a composite diffractive exchange (Pomeron) made up from the underlying parton densities of the nucleon.

Results on cross sections for exclusive dijet, $\gamma\gamma$, and e^+e^- production have also been presented and their significance for calibrating theoretical estimates for exclusive Higgs production at the Large Hadron Collider discussed. The exclusive dijet cross section was measured up to jet E_T^{min} of 35 GeV. When expressed as a function of dijet mass M_{jj}, cross sections up to masses of $M_{jj} \sim 120 - 140$ GeV are obtained, which are in the region of the standard model Higgs mass expected from global fits to electroweak data. A measurement of exclusive $\gamma\gamma$ production, a process which can also be used for calibrating Higgs production models, yielded three exclusive candidate events, setting an upper limit on the production cross section in the neighborhood of that predicted in Ref. [9].

2 Phenomenology

2.1 Introduction

As mentioned in Sec. 1, adronic diffraction is characterized by one or more large rapidity gaps, defined as regions of (pseudo)rapidity devoid of particles. Rapidity gaps may occur in non-diffractive (ND) interactions by fluctuations in particle multiplicity. However, the probability for such occurrences is expected to be exponentially suppressed as a function of gap width, since at a given $\sqrt{s}$ the particle density $\rho_N = dN/d\eta$ is approximately constant vs. η and therefore the probability for no particles being produced at $(\eta, \Delta\eta)$ is by Poisson statistics $P_0(\eta, \Delta\eta) = e^{-\rho_N \Delta\eta}$ [12]. Diffractive rapidity gaps do not exhibit such a suppression. This aspect of diffraction is attributed to the lack of radiation in the diffractive exchange, which proceeds through a colorless quark/gluon construct

with vacuum quantum numbers, historically referred to as the *Pomeron* [2]. In this section, we use the term *Pomeron* generically to denote a diffractive exchange, and describe it in terms of the underlying parton densities of the proton as a function of Q^2. Our phenomenological description is driven by regularities observed in results on soft and hard diffractive processes obtained in pp / $p\bar{p}$ collisions in fixed target and collider experiments, and in ep collisions at HERA (see review in Ref. [5]). A clue to understanding diffraction in QCD

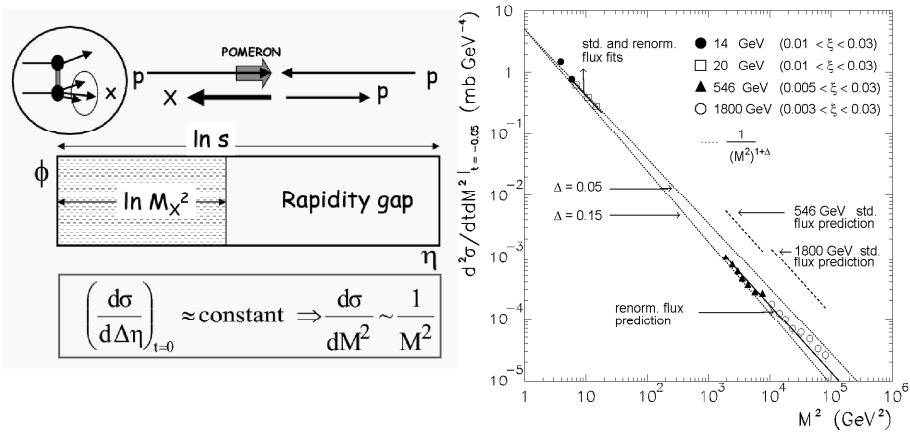

Figure 9: *(left)* Event topology for pp single diffraction dissociation, $pp \to pX$: lack of radiation in "vacuum exchange" leads to a cross section independent of $\Delta\eta$ and thereby to $1/M^2$ behavior; *(right)* Cross sections $d^2\sigma_{sd}/dM^2dt$ for $p + p(\bar{p}) \to p(\bar{p}) + X$ at $t = -0.05$ GeV^2 and $\sqrt{s} = 14$, 20, 546 and 1800 GeV compared with the renormalized Pomeron flux prediction [13] (Δ here is the Pomeron intercept, denoted by ϵ through the rest of this report). At $\sqrt{s}$=14 and 20 GeV, the fits using the standard and renormalized fluxes coincide; at the higher energies, the standard flux prediction overestimates the cross sections by $\sim \mathcal{O}(10)$.

is provided by the $d\sigma/dM^2$ behavior of the soft single diffractive cross section. As shown in Fig. 9 *(left)*, due to absence of radiation in vacuum exchange, a $d\sigma/dM^2 \sim 1/M^2$ behavior is expected with no explicit s-dependence. This is observed in the data plotted in Fig. 9 *(right)*. The deviation from exact $1/M^2$ behavior holds the key to understanding diffractive cross sections in terms of the underlying parton densities of the diffracted nucleon.

2.2 The data

Scaling and factorization properties observed in data provide the input to our model of describing hadronic diffraction in terms of inclusive parton densities and QCD color factors. The foundations of the model are mainly results from the CDF experiment at the Tevatron $p\bar{p}$ collider at Fermilab, and from the H1 and ZEUS experiments at the HERA ep collider at DESY.

Table 1 lists the soft diffractive processes studied by CDF in Run I. Measurement details and results can be found in the references provided.

Table 1: Soft diffractive processes studied by CDF

ND	Non-Diffractive (σ_T) [15]	$\bar{p}+p \to X$ †
EL	Elastic [16]	$\bar{p}+p \to \bar{p}+p$
SD	Single Diffraction [17]	$\bar{p}+p \to \bar{p}+\text{gap}+X$
DD	Double Diffraction [18]	$\bar{p}+p \to X+\text{gap}+Y$
DPE	Double Pomeron Exchange [19]	$\bar{p}+p \to \bar{p}+\text{gap}+X+\text{gap}+p$
SDD	Single plus Double Diffraction [20]	$\bar{p}+p \to \bar{p}+\text{gap}+X+\text{gap}+Y$

† σ_T is included since by the optical theorem it is related to Im $f^{el}(t=0)$

Hard diffractive processes studied by CDF include JJ (dijet), W, b-quark, and J/ψ production. Results from Run I have been published in Phys. Rev. Letters (see review in Ref. [5]), and preliminary Run II results have been presented at various conferences, including the present one (see Sec. 1).

The most interesting aspects of the results in connection with the QCD structure of the diffractive exchange are the breakdown of factorization and the restoration of factorization in events with multiple rapidity gaps. The following two paragraphs are based on excerpts from Sec. 1, and are provided here for the convenience of the reader.

Breakdown of factorization. At $\sqrt{s}$ =1800 GeV, the SD/ND ratios (gap fractions) for dijet, W, b-quark, and J/ψ production, as well the ratio of DD/ND dijet production, are all $\approx$ 1%. This represents a suppression of $\sim \mathcal{O}(10)$ relative to predictions based on diffractive parton densities measured from Diffractive Deep Inelastic Scattering (DDIS) at HERA, indicating a breakdown of QCD factorization comparable to that observed in soft diffraction processes relative to Regge theory expectations (see Sec. 2.1). However, factorization approximately holds among the above four hard diffractive processes

at fixed $\sqrt{s}$, which suggests that the suppression is in the rapidity gap formation probability, as predicted by the generalized gap renormalization model (RENORM), which is the subject of this section.

Restoration of factorization in multi-gap diffraction. Another interesting CDF result is that ratios of two-gap to one-gap cross sections for both soft and hard processes obey factorization. This provides not only a clue to understanding diffraction in terms of a composite Pomeron, but also a potential experimental discovery tool for new physics using processes with multiple rapidity gaps.

2.3 Renormalized diffractive cross sections: soft diffraction

Diffraction has traditionally been treated in Regge theory using factorization. This approach was successful at $\sqrt{s}$ energies below $\sim$ 50 GeV [21], but as the available energies increased to $\sqrt{s}$ =1800 GeV in Run I at the Tevatron, a suppression as large as $\sim \mathcal{O}(10)$ of the SD cross section was observed relative to the Regge theory based predictions [17]. This breakdown of factorization was traced to the energy dependence of $\sigma_{sd}^{tot}(s) \sim s^{2\epsilon}$, which is faster than that of $\sigma^{tot}(s) \sim s^{\epsilon}$, so that at high $\sqrt{s}$ unitarity would have to be violated if factorization held. The s-dependence appears explicitly in the SD differential cross section:

$$\text{Regge theory: } d\sigma_{sd}(s, M^2)/dM^2 \sim \frac{s^{2\epsilon}}{(M^2)^{1+\epsilon}}. \tag{1}$$

As seen in Fig. 9 *(right)*, contrary to the Regge theory based expectation of Eq. (1), the measured SD M^2-distribution does not show any s-dependence over a region of s six orders of magnitude. Thus, it appears that factorization breaks down in such a way as to enforce M^2-scaling. This property is built into the RENORM model, in which the Regge theory Pomeron flux is renormalized to unity [4]. Below, we present a QCD basis for renormalization and its extension to central and multi-gap diffraction [22].

The form of the rise of total cross sections at high energies, $\sim s^{\epsilon}$, which in Regge theory requires a Pomeron trajectory with intercept $\alpha(0) = 1 + \epsilon$, is expected in a parton model approach, where cross sections are proportional to the number of available wee partons [23]. In terms of the rapidity region in which there is particle production [2], $\Delta\eta'$, the total pp cross section is given by

$$\sigma_{pp}^{tot} = \sigma_0 \cdot e^{\epsilon \Delta\eta'}. \tag{2}$$

[2] We take $p_T = 1$ GeV so that $\Delta y' = \Delta\eta'$.

Since from the optical theorem $\sigma_{tot} \sim \mathrm{Im\,f}^{\mathrm{el}}(t=0)$, the full parton model amplitude takes the form

$$\mathrm{Im\,f}^{\mathrm{el}}(t, \Delta\eta) \sim e^{(\epsilon+\alpha' t)\Delta\eta}, \tag{3}$$

where the term $\alpha' t$ is a parameterization of the t-dependence of the amplitude. Based on this amplitude, the diffractive cross sections of table 1 are expected to have the forms

$$\begin{aligned}
\frac{d^2\sigma_{sd}}{dt\, d\Delta\eta} &= N_{gap}^{-1}(s) \qquad F_p(t)\left\{e^{[\epsilon+\alpha'(t)]\Delta\eta}\right\}^2 \qquad \kappa\left[\sigma_0 e^{\epsilon\Delta\eta'}\right] \\
\frac{d^3\sigma_{dd}}{dt\, d\Delta\eta\, d\eta_c} &= N_{gap}^{-1}(s) \qquad \left\{e^{[\epsilon+\alpha'(t)]\Delta\eta}\right\}^2 \qquad \kappa\left[\sigma_0 e^{\epsilon(\Sigma_i \Delta\eta_i')}\right] \\
\frac{d^4\sigma_{sdd}}{dt_1\, dt_2\, d\Delta\eta\, d\eta_c} &= N_{gap}^{-1}(s) \qquad F_p(t)\Pi_i\left\{e^{[\epsilon+\alpha'(t_i)]\Delta\eta_i}\right\}^2 \qquad \kappa^2\left[\sigma_0 e^{\epsilon(\Sigma_i \Delta\eta_i')}\right] \\
\frac{d^4\sigma_{dpe}}{dt_1\, dt_2\, d\Delta\eta\, d\eta_c'} &= N_{gap}^{-1}(s) \qquad \underbrace{\Pi_i\left\{F_p(t_i) e^{[\epsilon+\alpha'(t_i)]\Delta\eta_i}\right\}^2}_{\text{gap probability}} \qquad \kappa^2 \underbrace{\left[\sigma_0 e^{\epsilon(\Delta\eta')}\right]}_{\sigma^{tot}(s')},
\end{aligned} \tag{4}$$

where the (re)normalization factor $N_{gap}(s)$ is the integral of the gap probability over all phase space in $(t_i,\ \Delta\eta_i,\ \eta_c,\ \eta_c')$, and the variables η_c and η_c' represent the center of the floating (not adjacent to a nucleon) rapidity gap in DD or SDD and the floating diffractive cluster in DPE, respectively. In each case, the independent variables are the ones on the left hand side of the equation, but for pedagogical reason we use on the right side the additional variables $\Delta\eta_i'$, which could be be expressed in terms of $\ln s$ and the variables on the left.

The expressions in Eq. (4) are built from the following components:

- *the reduced energy cross section*, $\sigma^{tot}_{pp/p\bar{p}}(s')$, which is the $pp/p\bar{p}$ cross section at the reduced collision energy, which is defined by the equation $\ln(s'/s_0) = \sum_i \Delta y_i'$;
- *the color factors* κ, one for each gap, required to select color neutral exchanges with vacuum quantum numbers to ensure diffractive rapidity gap formation;
- *the gap probability*, which is given by the amplitude squared of the elastic scattering between a diffractively dissociated and a surviving proton, in which case it contains the proton form factor $F_p(t)$, or between two diffractively dissociated protons;
- *the normalization factor* N_{gap}^{-1}, which is the inverse of the integral of the gap probability over all phase space.

A remarkable property of the expressions in Eq. (4) is that they factorize into two terms, one which depends on the sum of the rapidity regions in which there is particle production, and another which depends on the sum of the widths of the rapidity gaps. This is rendered possible by the exponential dependence on $\Delta\eta$ of the elastic amplitude, which allows non-contiguous regions in rapidity to be added in the exponent. A consequence of this type of factorization is that the (re)normalization factor is the same and is $\sim s^{2\epsilon}$ in all cases, ensuring M^2-scaling and universality of the suppression factor across single, central, and multi-gap diffraction.

The parameters ϵ and κ. Experimentally, these parameters have been measured to be [24, 13]

$$\begin{aligned} \epsilon \equiv \quad & \alpha_{I\!P}(0) - 1 \quad = 0.104 \pm 0.002 \pm 0.01 \text{ (syst), and} \\ \kappa \equiv \quad & \frac{g_{I\!P I\!P I\!P}}{\beta_{I\!P p}} \quad = 0.17 \pm 0.02 \text{ (syst)}, \end{aligned} \tag{5}$$

where the systematic uncertainty assigned to ϵ is an estimate based on considering results from fits made to cross section data by various authors. Measurements of parton densities at HERA indicate that partonic structure in the nucleon is expressed down to the hadron mass scale of $Q^2 \approx 1$ GeV^2. This is seen in Fig. 10 (*left*), where the parameter $\lambda(Q^2)$ of $F_2(x, Q^2) \sim x^{-\lambda(Q^2)}$ decreases linearly with $\ln Q^2$ down to $Q^2 \approx 1$ GeV^2, flattening out and becoming consistent with the soft Pomeron intercept only below $Q^2 = 1$ GeV^2. We therefore assume partonic structure in soft diffractive exchanges at the hadron mass scale, and proceed with a "toy estimate" of the parameters ϵ and κ from the nucleon PDF, using the PDF at $Q^2 = 1$ GeV^2 shown in Fig. 10 (*right*) obtained from the CTEQ5L parameterization.

The region of interest to diffraction, $x \leq 0.1$, is dominated by sea gluons and quarks. In this region, a fit of the form $xf(x) \sim x^{-\lambda}$, Fig. 10 (*right*), yields $\lambda_g \approx 0.2$ and $\lambda_q \approx 0.04$ with relative weights $w_g \approx 0.75$ and $w_q \approx 0.25$ [3]. Noting that the number of wee partons grows as $\int_{1/s}^{1} f(x)dx \sim s^{\lambda}$, the Pomeron intercept may be obtained from the parameters λ_g and λ_q appropriately weighted by the gluon and quark color factors

$$c_g = \frac{1}{N_c^2 - 1}, \quad c_q = \frac{1}{N_c}. \tag{6}$$

The weighting procedure places ϵ in the range $\lambda_q < \epsilon < \lambda_g$, or $0.04 < \epsilon < 0.2$, which covers the experimental value of $\epsilon = 0.104$. A precise determination

[3] For valence quarks, $\lambda_q \equiv \lambda_R \approx -0.5$; this is relevant for Reggeon exchange, which is not being considered here, as its contribution is relatively small.

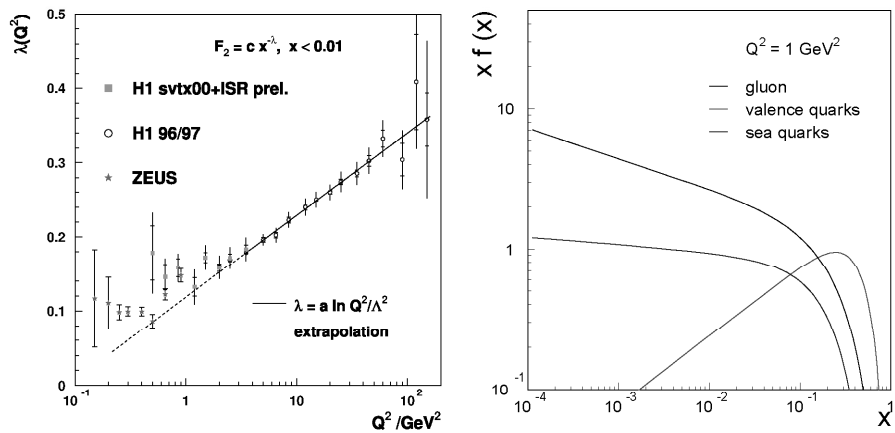

Figure 10: *(left) The parameter $\lambda(Q^2)$ vs. Q^2 of a fit to the structure function $F_2(x,Q^2) \sim x^{-\lambda(Q^2)}$ in DIS at HERA* [25]*; (right) CTEQ5L nucleon parton distribution functions for $Q^2 = 1$ GeV^2.*

is not attempted, as it would require averaging over the Q^2 range of all the particles produced in the collision and proper accounting of the uncertainties in the nucleon PDF in this low Q^2 region.

The parameter κ is obtained from the gluon and quark color factors and weights:

$$\kappa \approx \quad c_g w_g + c_q w_q \quad = 0.182. \tag{7}$$

This RENORM prediction is in remarkably good agreement with $\kappa_{exp} = 0.17 \pm 0.02$.

2.4 Renormalized diffractive cross sections: hard diffraction

Hard diffraction processes are defined as those in which there is a hard partonic scattering in addition to the diffractive rapidity gap signature. Events may have forward, central, or multiple rapidity gaps in topologies similar to those listed in table 1 for soft $\bar{p}p$ collisions at the Tevatron, with the hard scattering products appearing within the region(s) of rapidity where there is particle production.

Hard diffraction data. CDF has measured SD/ND ratios for W, dijet, b-quark and J/ψ production, and also diffractive structure functions extracted from SD and DPE dijet production (see Sec. 1. HERA has reported DPFs extracted from inclusivs DDIS, as well as from exclusive channels [14].

The following interesting characteristics have been observed:

- all SD/ND ratios measured by CDF at $\sqrt{s}$ =1800 GeV are approximately equal, pointing to a flavor independent rapidity gap formation probability;
- the dijet SD/ND ratio measured by CDF varies as $\sim x_{Bj}^{-0.45}$, contrary to results from deep inelastic scattering at HERA, where a constant ratio of DDIS/DIS is observed [25, 14];
- the SD structure function extracted from dijet production at CDF is suppressed by $\sim \mathcal{O}(10)$ relative to expectations from diffractive PDFs measured in DDIS at HERA;
- the Pomeron intercept measured in DDIS at HERA increases with Q^2 and is on average larger than the soft Pomeron intercept, but approximately a factor of ~ 2 smaller than the intercept obtained from inclusive DIS.

Diffractive parton densities. Diffractive parton densities with good statistics have been obtained from DDIS at HERA and diffractive dijet production at the Tevatron:

$$\begin{aligned} \text{HERA:} \quad & \gamma^* + p \to p + jet + X \\ \text{Tevatron:} \quad & \bar{p} + p \to \bar{p} + \text{dijet} + X. \end{aligned} \tag{8}$$

The production process may involve several color "emissions" from the surviving proton, collectively comprising a color singlet with vacuum quantum numbers. Two of the emissions are of special importance: one at $x = x_{Bj}$ from the proton's PDF at scale Q^2, which is responsible for the hard scattering, and another at $x = \xi$ (fractional momentum loss of the diffracted nucleon) from the PDF at scale $Q^2 \approx 1$ GeV^2, which neutralizes the exchanged color and forms the rapidity gap.

At HERA, at small ξ where the proton PDF exhibits power law behavior at both soft and hard scales, the diffractive structure function takes the form [4]

$$F_2^{D(3)}(\xi, x, Q^2) = \frac{A_{\text{norm}}}{\xi^{1+\epsilon_q}} \cdot c_q \cdot F_2(x, Q^2), \tag{9}$$

where A_{norm} is a normalization factor, ϵ_q is the exponent of the soft quark structure function, which from Fig. 10 (*right*) is given by $\epsilon_= \lambda_q(Q^2 = 1) = 0.04$, and $c_q = 1/3$ is the quark color factor.

[4]For simplicity, we do not consider the t dependence in this discussion. This has little affect on our conclusions, as diffractive cross sections are concentrated at small t.

Definition of λ:
$x \cdot f(x) \propto x^{-\lambda}$

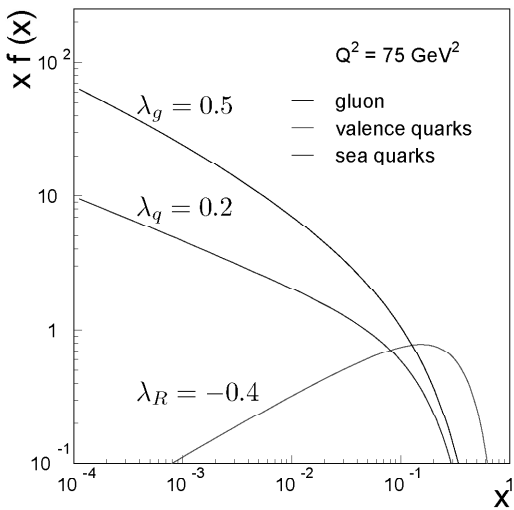

Figure 11: *CTEQ5L nucleon parton distribution functions for $Q^2 = 75\ GeV^2$. The parameters $\lambda_{g,q,R}$ are the slopes of the gluon, sea quark, and valence quark distribution ('R' stands for Reggeon) in the region of $x < 0.1$, where the power law behavior holds.*

At high Q^2, where factorization is expected to hold [4, 26], $A_{\rm norm}$ is the normalization factor of the soft PDF, which is a constant, and F_2 can be expressed as a power law, resulting in

$$F_2^{D(3)}(\xi, x, Q^2) = \frac{A_{\rm norm}}{\xi^{1+\epsilon_q}} \cdot \frac{1}{3} \cdot \frac{C(Q^2)}{(\beta\xi)^{\lambda(Q^2)}} = \frac{A_{\rm norm}}{\xi^{1+\epsilon_q+\lambda(Q^2)}} \cdot \frac{1}{3} \cdot \frac{C(Q^2)}{\beta^{\lambda(Q^2)}}, \quad (10)$$

where $\lambda(Q^2)$ is the power of the fit of inclusive data to the form $F_2(x, Q^2) \sim x^{-\lambda(Q^2)}$ shown in Fig. 10 *(left)*.

The expression in Eq. (10) leads to two important RENORM predictions:

- the Pomeron intercept in DDIS is the average of the soft quark and inclusive interceps,

$$\alpha_{I\!P}^{DIS} = 1 + \lambda(Q^2), \qquad \alpha_{I\!P}^{DDIS} = 1 + \frac{1}{2}\left[\epsilon_q + \lambda(Q^2)\right]; \quad (11)$$

- the ratio of DDIS to DIS structure functions at fixed ξ is independent of x and Q^2,

$$R\left[\frac{F_2^{D3}(\xi, x, Q^2)}{F_2(x, Q^2)}\right]_\xi = \frac{1}{3} \cdot \frac{A_{\rm norm}}{\xi^{1+\epsilon}}. \quad (12)$$

Data from ZEUS and H1 are consistent with these predictions [25].

At low Q^2, the gap probability saturates and renormalization must be applied [4]. In the RENORM model, the resulting suppression factor depends on the size of the rapidity interval available for particle production, which is $\Delta y' = \ln s - \ln Q^2 = \ln(s/Q^2)$. For dijet photoproduction, where $\Delta y' \approx 6$, a suppression factor of ≈ 3 is expected by RENORM [4], similar to that observed in soft SD at the Tevatron. Data from dijet photoproduction at HERA are consistent with this prediction [14]. Moreover, since the suppression in RENORM is due to saturation of the gap probability, the same suppression is expected for both direct and resolved rates at low Q^2 DDIS. This prediction is also consistent with observation [14].

At the Tevatron, where the gap probability saturates and must be renormalized to unity, the RENORM diffractive structure function takes the form

$$F_{JJ}^{D3}(\xi, x, Q^2) = N_{\rm gap}^{-1}(s, \beta) \cdot \frac{1}{\xi^{1+2\epsilon}} \cdot F_{JJ}(\frac{x}{\xi}, Q^2) \tag{13}$$

$$N_{\rm gap}(s, \beta) = \int_{\xi_{mim}}^{\xi=0.1} \frac{d\xi}{\xi^{1+2\epsilon}} \approx \frac{(\beta s)^{2\epsilon}}{2\epsilon}, \tag{14}$$

where, as in DDIS, ϵ is the power from the fit of the soft structure function to the form $x\,f(x) \sim x^{-\epsilon}$, and the limits $\xi_{min} = x_{min}/\beta$ and $x_{min} = 1/s$ are used [4]. Through renormalization, F_{JJ}^{D3} acquires a factor $\sim (1/\beta)^{2\epsilon}$, and the diffractive to inclusive structure function ratio, $R_{JJ}(SD/ND)$, a factor $\sim (1/x)^{2\epsilon}$. Since from color factor considerations F_{JJ} is gluon dominated,

$$F_{JJ}(x) = x\left[g(x) + \frac{4}{9}q(x)\right], \tag{15}$$

where $g(x)$ and $q(x)$ are the gluon and quark densities in the proton, the relevant parameter ϵ is the parameter λ_g of Fig. 10 *(right)*, resulting in $R_{JJ}(SD/ND)$ $1/x^{0.4}$. This RENORM prediction is confirmed by the CDF data, where the x-dependence of the diffractive to inclusive ratio was measured to be $\sim 1/x^{\,0.45\pm0.02}$ [27].

2.5 Summary of phenomenology section

A phenomenological model has been presented (RENORM), in which diffractive cross sections are obtained from parton-level cross sections and the underlying inclusive parton distribution function of the interacting hadrons using QCD color factors and appropriate (re)normalization. Scaling and factorization properties observed in fixed target, Tevatron, and HERA data form both the basis and a testing ground for RENORM.

In soft diffraction, normalized single-gap and double-gap differential cross sections (SD, DD, DPE, SDD) are obtained in RENORM in terms of two free parameters, ϵ and α', which are identified as those of the Regge theory soft Pomeron trajectory, $\alpha(t) = 1+\epsilon+\alpha' t$. Furthermore, the ϵ is obtained from the color-factor weighted exponents of power law fits to soft nucleon PDFs, leaving α' as the only free parameter in the model.

In hard diffraction, RENORM is applied to HERA and Tevatron data. At HERA, interesting features of the data include: $\epsilon(Q^2)_{DDIS} < \epsilon(Q^2)_{DIS}$, $F_2^{D3}(\xi, x, Q^2)/F_2(x, Q^2)|_\xi \sim$ constant, dijet photoproduction suppressed by factor of ~ 3, and direct / resolved low Q^2 DIS both suppressed by approximately the same factor relative to high Q^2 DIS. At the Tevatron, features of the data include: cross sections at fixed collision energy are flavor independent, the ratio of SD/ND rates decreases with increasing x_{Bj}, and the DSF of the proton in DPE events with a leading $\bar{p}$ is suppressed relative to that in SD. Comparing HERA with Tevatron results, factorization breaks down at the Tevetron relative to HERA by a factor of $\sim \mathcal{O}(10)$, but is restored in comparing the double-gap DSF obtained from DPE at CDF with that obtained from DDIS of HERA. All these features are successfully interpreted by RENORM.

3 Conclusion

In light of the success of the parton-model based renormalization (RENORM) approach in describing the data, diffraction may be viewed as an interaction between low-x partons subject to color constraints.

References

1. K. Goulianos, *Diffractive and total cross sections at Tevatron and LHC*, in *Hadron Collider Physics Symposium 2006*, May 22-26, Duke University, Durham, NC, USA.

2. P. D. B. Collins, *An Introduction to Regge Theory and High Energy Physics*, Cambridge University Press (1977); V. Barone and E. Predazzi, *High-Energy Particle Diffraction*, Springer Press (2001); S. Donnachie, G. Dosch, O. Nachtmann, and P. Landshoff, *Pomeron Physics and QCD*, Cambridge University Press (2002).

3. R. J. M. Covolan, J. Montanha, and K. Goulianos, *A New Determination of the Soft Pomeron Intercept*, Phys. Lett. B **389**, 176 (1996).

4. K. Goulianos, *Renormalization of Hadronic Diffraction and the Structure of the Pomeron*, Phys. Lett. B **358**, 379 (1995); Erratum-*ib.* **363**, 268 (1995).

5. K. Goulianos, *Hadronic Diffraction: Where do we Stand?*, in *La Thuile 2004, Results and Perspectives in Particle Physics*, edited by M. Greco, Proc. of Les Rencontres de Physique de la Vallé d'Aoste, La Thuile, Aosta Valley, Italy, February 29 - March 6, 2004, pp. 251-274; e-Print Archive: hep-ph/0407035.

6. R. Blair *et al.* (CDF Collaboration), *The CDF II Detector: Technical Design Report*, FERMILAB-Pub-96/390-E.

7. K. Goulianos and S. Lami, *Performance of a Prototype Position Sensitive Towerless Calorimeter*, *Nucl. Instrum. Meth. A* **430**, 34-47 (1999); K. Goulianos *et al.*, *The CDF MiniPlug calorimeters*, *Nucl. Instrum. Meth. A* **496**, 333-346 (2003).

8. M. Gallinaro (for the CDF collaboration), *Diffractive and exclusive measurements at CDF*, Presented at 14th International Workshop on Deep Inelastic Scattering (DIS 2006), Tsukuba, Japan, 20-24 Apr 2006; e-Print Archive: hep-ex/0606024.

9. V. Khoze, A. Kaidalov, A. Martin, M. Ryskin, and W. Stirling, *Diffractive processes as a tool for searching for new physics*, e-Print Archive:hep-ph/0507040, and references therein.

10. Monte Carlo programs used in the CDF analysis: **POMWIG** (implements diffraction into the HERWIG Monte Carlo Generator) B. Cox and J. Forshaw, *Comput. Phys. Commun.* **144**, 104 (2002); **DPEMC** (extends POMWIG by incorporating inclusive and exclusive DPE) M. Boonekamp and T. Kucs, *Comput. Phys. Commun.* **167**, 217 (2005); **ExHuME** (implements the exclusive dijet production calculation of Ref. [9]), J. Monk and A. Pilkington, e-Print Archive: hep-ph/0502077.

11. A. Abulencia et al. (CDF Collaboration), *Phys. Rev. Lett.* **98**, 112001 (2007).

12. J.D. Bjorken, *Phys. Rev. D* **47**, 101 (1993).

13. K. Goulianos and J. Montanha, *Phys. Rev. D* **59**, 114017 (1999).

14. See talk by Davide Boscherini (Bologna) at this conference.

15. F. Abe et al. (CDF Collaboration), *Phys. Rev. D* **50**, 5518 (1994).

16. F. Abe et al. (CDF Collaboration), *Phys. Rev. D* **50**, 5535 (1994).

17. F. Abe et al. (CDF Collaboration), *Phys. Rev. D* **50**, 5550 (1994).

18. T. Affolder et al. (CDF Collaboration), *Phys. Rev Lett.* **87**, 141802 (2001).

19. D. Acosta *et al.* (CDF Collaboration), *Phys. Rev. Lett.* **93**, 141601 (2004).

20. D. Acosta et al. (CDF Collaboration), *Phys. Rev Lett.* **91**, 011802 (2003).

21. K. Goulianos, *Phys. Reports* **101**, 171 (1983).

22. K. Goulianos, in *Diffraction in QCD*, Corfu Summer Institute on Elementary Particle Physics, Corfu, Greece, 31 Aug - 20 Sep 2001; e-print Archive: hep-ph/0203141.

23. E. Levin, in *An Introduction to Pomerons*, Preprint DESY 98-120.

24. R.J.M. Covolan, J. Montanha, and K. Goulianos, *Phys. Lett. B* **389**, 176, (1996).

25. F.P. Schilling (H1 Collaboration), in *Measurement and NLO DGLAP QCD Interpretation of Diffractive Deep-Inelastic Scattering at HERA*, submitted to 31^{st} International Conference on High Energy Physics, ICHEP02, Amsterdam, The Netherlands, Jul. 24−31, 2001 (abstract 980).

26. J. Collins, *J. Phys. G* **28**, 1069 (2002); arXiv:hep-ph/0107252.

27. T. Affolder *et al.* (CDF Collaboration), *Phys. Rev. Lett.* **84**, 5043 (2000).

MEASUREMENTS OF SPIN DEPENDENT STRUCTURE FUNCTION $g_1^d(x, Q^2)$ AT COMPASS

Helena Santos, on behalf of the COMPASS Collaboration
LIP - Laboratório de Instrumentação e Física Experimental de Partículas
Av. Elias Garcia, 14, 1000-149, Lisboa, Portugal

Abstract

The COMPASS experiment at the CERN SPS measures the spin dependent structure function g_1^d of the deuteron. Results obtained in the kinematic ranges $Q^2 < 1$ (GeV/c)^2 and $0.0005 < x < 0.02$, as well as $1 < Q^2 < 100$ (GeV/c)^2 and $0.004 < x < 0.7$ are presented. The results of a global QCD fit at Next-to-Leading Order to the world g_1 data are discussed.

1 Introduction

The history of the spin structure of the nucleon begun more than 30 years ago with polarised deep inelastic scattering measurements at SLAC [1]. At that time the quark-parton model has predicted that 60% of the nucleon spin was entirely given by the u and d quarks [2]. The validity of this prediction has been supported by the poor x range of the experiment ($x > 0.1$). Then the EMC collaboration extendend the measurements to $x > 0.01$ and came out with the unexpected value of $0.12 \pm 0.09 \pm 0.14$ [3]. Such a result motivated a set of experiments covering different x ranges at CERN [4], SLAC [5, 6, 7, 8], DESY [9] and JLAB [10]. All these experiments confirmed the small contribution of the quarks (about 20–30%), and thus more contributions are necessary. For a nucleon with $+1/2$ helicity one should have the sum rule:

$$S_n = \frac{1}{2} = \frac{1}{2}\Delta\Sigma + \Delta G + L_q + L_G \tag{1}$$

where $\Delta\Sigma$ stands for the contribution from the quarks ($\Delta\Sigma = \Delta u + \Delta d + \Delta s$), ΔG is the contribution of the gluons and $L_{q,G}$ are their angular orbital momenta.

This article reports on the experimental procedure to measure the spin-dependent structure function, g_1, at the COMPASS experiment. A NLO QCD analysis performed in order to obtain $\Delta\Sigma$ and an indirect measurement of ΔG is described.

2 Experimental Procedure

COMPASS makes use of the CERN-SPS facilities, impinging a high intensity 160 GeV muon beam on a ^{6}LiD polarised target. Besides the scattered muon, other particles produced in deep inelastic scattering are detected in a two-stage spectrometer. Data presented in this article have been collected in the years 2002, 2003 and 2004, corresponding to an integrated luminosity of about 2 fb^{-1}.

The target consists in two 60 cm long cells, with 3 cm diameter and separated by 10 cm. They are located inside a superconducting solenoid magnet that provides a field of 2.5 T along the beam direction. The maximum angle of

aperture provided by the solenoid is 70 mrad [1]. The two cells are oppositely polarised by dynamic nuclear polarisation (DNP), so that the deuteron spins are parallel ($\uparrow\uparrow$) or antiparallel ($\uparrow\downarrow$) to the spins of the incoming muons. The polarisations of the two cells are inverted every 8 hours by rotating the magnetic field direction. In this way, acceptances do cancel out in the asymmetry calculation, provided that the acceptance ratios remain unchanged after field rotation. Eventual systematic effects related to the magnetic field do cancel out as well, by reversing the polarisation of each target cell, by DNP, at least once per running period. The two spectrometers (Large Angle Spectrometer (LAS) and Small Angle Spectrometer (SAS)) are located around two dipole magnets, SM1 and SM2. Scintillating fibres and silicon detectors ensure tracking in the beam region, complemented by MicroMeGas and GEM detectors up to 20 cm from the beam. Drift chambers, multi-wire proportional chambers and straw tubes cover both LAS and SAS spectrometers. Electromagnetic and hadronic calorimeters are integrated in both spectrometers. A Ring Imaging Čerenkov Detector separates kaons from pions with momentum up to 43 GeV/c [2]. The COMPASS data acquisition system is triggered by coincidence signals in hodoscopes. Inclusive triggers require the detection of the scattered muon, while semi-inclusive triggers are based on the muon energy loss and on the presence of a hadron signal in the calorimeters. Purely calorimetric triggers are based on the energy deposit in the hadron calorimeter without any condition on the scattered muon. Triggers due to halo muons are eliminated by veto counters installed upstream from the target. The detailed description of the spectrometer can be found in Ref. [11)].

3 The A_1^d Asymmetries

In order to have access to the spin-dependent structure function, g_1^d, the longitudinal photon-deuteron asymmetry, A_1^d, has to be evaluated. In the framework of the quark parton model this quantity can be directly related to the quarks

[1] From the run of 2006 on, COMPASS has a new magnet providing an acceptance a factor 2.5 higher and 3 cells target.

[2] This detector has not been used in the presented analysis.

polarisation via

$$A_1 = \frac{(\sigma^{\uparrow\downarrow}_{\gamma\mu} - \sigma^{\uparrow\uparrow}_{\gamma\mu})}{(\sigma^{\uparrow\downarrow}_{\gamma\mu} + \sigma^{\uparrow\uparrow}_{\gamma\mu})} \simeq \frac{\sum_q e_q^2(\Delta q + \Delta\bar{q})}{\sum_q e_q^2(q + \bar{q})} \tag{2}$$

The starting point for the A_1^d asymmetry extraction is to count the events detected in each target cell, $N_i = a_i\phi_i n_i\sigma_0(1 + P_B P_T f D A_1^d)$, where a_i is the acceptance of the target cell i, ϕ_i is the incoming muon flux, n_i is the number of target nucleons, σ_0 is the muon-deuteron unpolarised cross-section, P_B and P_T are the beam and target polarisations and f and D are the dilution and depolarisation factors, respectively. The ratio $(N_1 N_2')/N_2 N_1')$, where N_i' stands for the number of events after magnetic field rotation, relates to A_1^d through a second order equation, in which the fluxes ϕ_i cancel out by ensuring equal muon fluxes for both target cells. The ratio of acceptances does cancel out as well, if $a_1/a_2 = a_1'/a_2'$. In order to minimize the statistical error of the asymmetry, each event is weighted by the product of the dilution and depolarisation factors and the beam polarisation. As the target polarisation is time dependent it is taken as the average value of the run, instead.

Figure 1 shows A_1^d as a function of x for quasi-real photon interactions for the data collected in the years 2002 and 2003. Events are selected by cuts on the four-momentum transfer squared ($Q^2 < 1\,(\mathrm{GeV}/c)^2$) and the fractional energy of the virtual photon ($0.1 < y < 0.9$). Such a kinematic window allows a wide Bjorken scaling variable interval, $0.0005 < x < 0.02$. Furthermore, strict quality criteria are applied to data ensuring that events originate in the target, preventing fake triggers and demanding equal muon fluxes on the two target cells. 280 million events have been analysed corresponding to an integrated luminosity of about 1 fb^{-1}. The asymmetry is compatible with 0 over the whole x range. The error bars are statistical and the grey band corresponds to the systematic errors, which are due to false asymmetries mainly. Details on this analysis can be found in [12].

Figure 2 shows A_1^d as a function of x for DIS events ($Q^2 > 1\,(\mathrm{GeV}/c)^2$), as measured by COMPASS using 2002, 2003 and 2004 data [13]. One should bear in mind that, although part of the x domain ($0.004 < x < 0.7$) is the same of the low Q^2 events, this plot refers to different physics [12]. After data selection $89{\times}10^6$ events are available for analysis. The results of the SMC [4], E143 [6], E155 [8] and HERMES [14] experiments, are also shown. The asymmetry is 0 for $x < 0.05$ and becomes larger as x increases, reaching 60% at $x \simeq 0.7$.

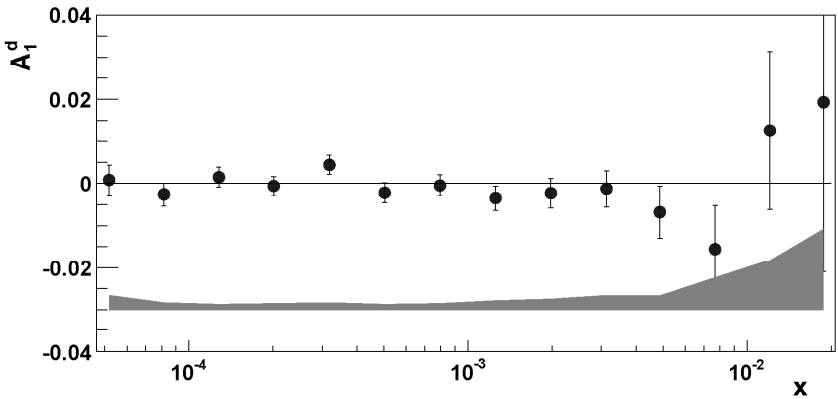

Figure 1: *The asymmetry $A_1^d(x)$ for quasi-real photons($Q^2 < 1\ (GeV/c)^2$) as a function of x. The errors bars are statistical. Grey band shows the systematic errors.*

The agreement is very good between the different data sets. It should be noted that only COMPASS and SMC were able to measure this asymmetry at very low x, the COMPASS results being essential to disentangle the A_1^d behaviour at $x < 0.03$. Error bars are statistical and the grey band corresponds to the systematic errors of the COMPASS measurements, whose sources come from the uncertainty on beam and target polarisations (5%), dilution factor (6%) and depolarisation factor (4-5%). Radiative corrections and neglecting the transverse asymmetry A_2 are found to have a small effect. The upper limit for the systematic error due to false asymmetries is half of the statistical one.

4 The g_1^N Structure Function

The spin-dependent structure function of the nucleon, $g_1(x)$, is obtained from $A_1(x)$ and the spin-independent structure function $F_2(x)$ through

$$g_1(x) = A_1(x)\frac{F_2(x)}{2x(1+R)} \ . \tag{3}$$

Figure 3 shows g_1^d as a function of x for quasi-real photon interactions. g_1^d is found to be consistent with 0 in the investigated x range. The statistical

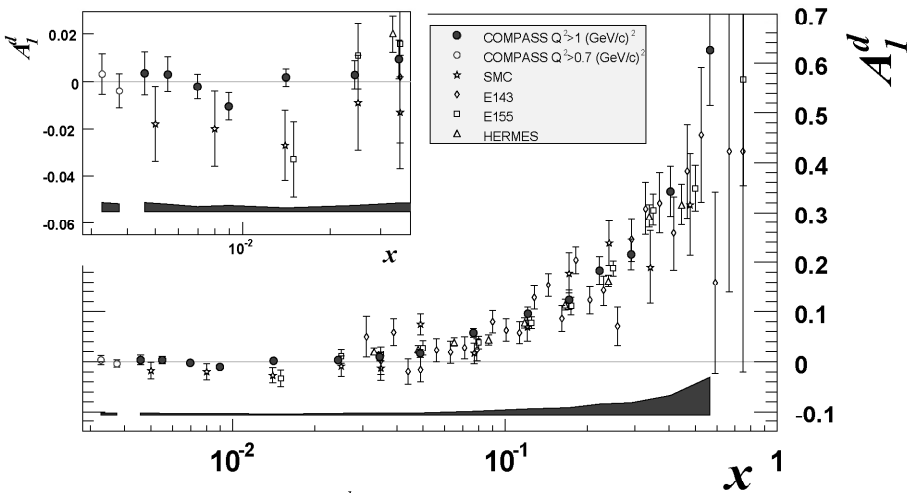

Figure 2: *The asymmetry $A_1^d(x)$ as measured by the world spin experiments. SLAC values of g_1/F_1 have been converted to A_1 and E155 data corresponding to the same x have been averaged over Q^2. The error bars are statistical. The shaded areas show the size of the COMPASS systematic errors; see text for details.*

precision of the COMPASS results [12] is considerably higher than the ones of SMC [15] and HERMES [16].

Figure 4 shows g_1^d, as a function of x for DIS events [13]. The SMC results [4] have evolved to the Q^2 of the corresponding COMPASS points. The two curves are the results of two QCD fits at the Q^2 of each data point. They are performed at NLO in the $\overline{\text{MS}}$ renormalisation and factorisation scheme. These fits require input parameterisations of the quark singlet spin distribution $\Delta\Sigma(x)$, non-singlet distributions $\Delta q_3(x)$ and $\Delta q_8(x)$, and the gluon spin distribution $\Delta G(x)$, which evolve according to the DGLAP equations. They are written as:

$$\Delta F_k \;=\; \eta_k \frac{x^{\alpha_k}\,(1-x)^{\beta_k}\,(1+\gamma_k x)}{\int_0^1 x^{\alpha_k}\,(1-x)^{\beta_k}\,(1+\gamma_k x)dx}\,, \tag{4}$$

where ΔF_k represents each of the polarised parton distribution functions (PDF) and η_k is the integral of ΔF_k. The moments, η_k, of the non-singlet distributions Δq_3 and Δq_8 are fixed by the baryon decay constants (F+D) and (3F−D) respectively [17], assuming $\mathrm{SU}(3)_f$ flavour symmetry. The linear term $\gamma_k x$ is used only for the singlet distribution, in which case the exponent β_G is fixed

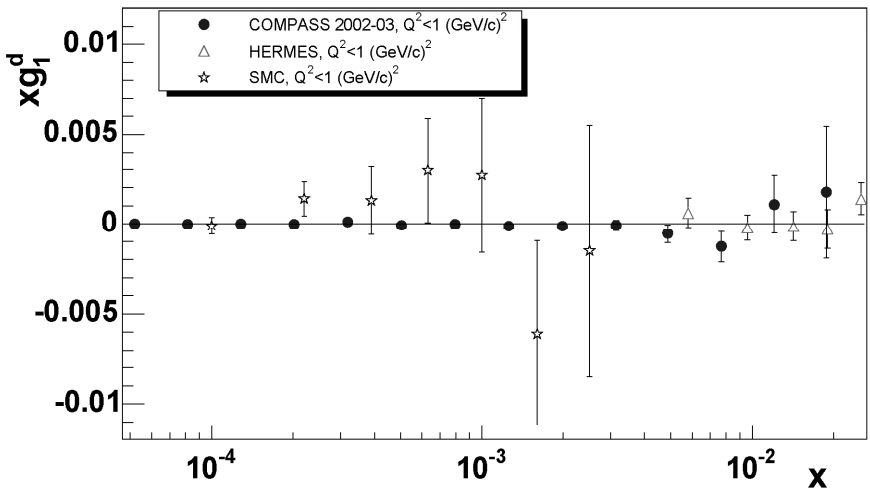

Figure 3: *The COMPASS* [12], *SMC* [27] *and Hermes* [16] *results for spin-dependent structure function of the deuteron,* g_1^d, *in the low* x *and low* Q^2 *region. The errors are statistical.*

because it is poorly constrained by the data; thus, 10 parameters are used in input distributions. Data are well described by two solutions of DGLAP, $\Delta G > 0$ and $\Delta G < 0$. Figure 5 shows the QCD fit to proton, deuteron and neutron targets, with positive ΔG solution (an indistinguishable curve is obtained for the solution with $\Delta G < 0$). All data have been evolved to a common Q_0^2 by means of the $g_1(x, Q^2)$ fitted parameterisation,

$$g_1(x, Q_0^2) = g_1(x, Q^2) + \left[g_1^{fit}(x, Q_0^2) - g_1^{fit}(x, Q^2) \right]. \tag{5}$$

We have used several fits of g_1 from the Durham data base [18]: Blümlein-Böttcher [19], GRSV [20] and LSS05 [21]. The value $Q_0^2 = 3\,(\mathrm{GeV}/c)^2$ has been chosen as reference because it is close to the average Q^2 of the COMPASS DIS data. The deuteron data are taken from Refs [4, 6, 8, 13, 14], the proton data from Refs [4, 6, 14, 22, 23] and the ^{3}He data from Refs [10, 24, 25, 26]. Concerning the COMPASS data in this fit, all x bins, except the last one, have been subdivided into three Q^2 intervals. The number of COMPASS data points used in the fit to deuteron data is 43, out of a total of 230. The resulting values of $g_1(x, Q^2)$ are calculated for the (x_i, Q_i^2) of each data point and compared to the experimental values. The parameters are found by minimizing the sum

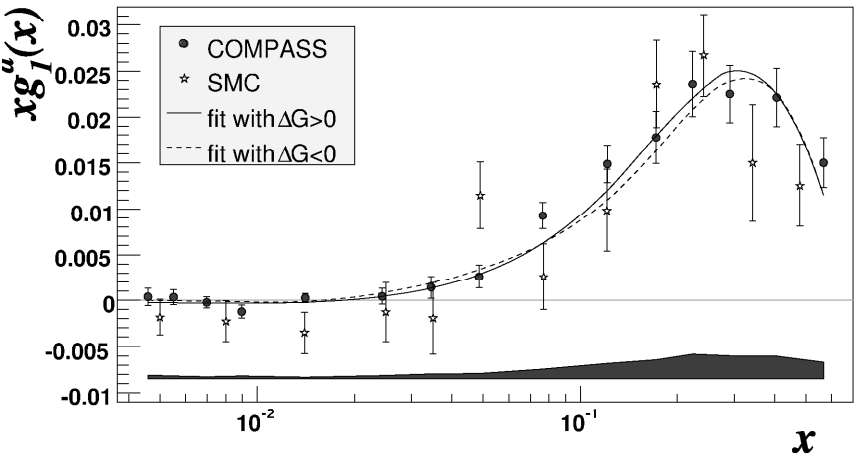

Figure 4: *The spin-dependent structure function of the deuteron, g_1^d, as a function of x ($Q^2 > 1\,(GeV/c)^2$). The COMPASS points are given at the $\langle Q^2 \rangle$ where they were measured. The SMC points have evolved to the Q^2 of the corresponding COMPASS points. Only statistical errors are shown. The shaded band stands for the COMPASS systematic error. The curves show the results of QCD fits with $\Delta G > 0$ and $\Delta G < 0$.*

$$\chi^2 = \sum_{i=1}^{N=230} \frac{\left[g_1^{fit}(x_i, Q_i^2) - g_1^{exp}(x_i, Q_i^2)\right]^2}{\left[\sigma(x_i, Q_i^2)\right]^2}, \tag{6}$$

where $\sigma(x_i, Q_i^2)$ are the statistical errors for all data sets, except for the proton data of E155 where the uncorrelated part of the systematic error on each point is added in quadrature to the statistical one. Two different programs have been used to fit the data – one uses the DGLAP evolution equations for the spin structure functions in x and Q^2 phase space [27], the other uses the DGLAP evolution equations in the space of moments [28]. Both programs give consistent values of the fitted PDF parameters and similar χ^2-probabilities. The polarised parton distributions for the three flavours and ΔG are shown in figure 6 for both $\Delta G < 0$ and $\Delta G > 0$ solutions. Quark distributions are weakly dependent on the sign of ΔG. Although the shapes of the gluon distributions differ over the whole x range, the fitted values of η_G are small and similar in absolute value $|\eta_G| \approx 0.2 - 0.3$. Similarly η_Σ reveals weak dependence on the shape of

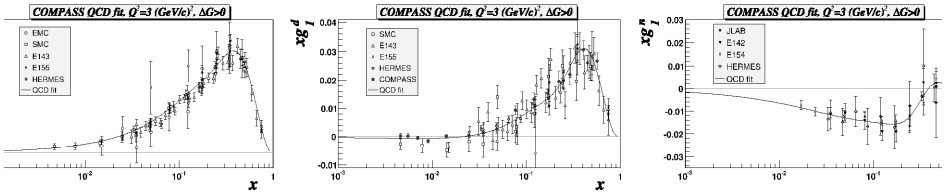

Figure 5: *The world data and QCD fit at* $Q^2 = 3\,GeV^2$*, obtained with the program of Ref.* [27]*. The curve corresponds to the solution with* $\Delta G > 0$.

ΔG, being slightly larger in the fit with $\Delta G < 0$. The results from the two fits have been averaged and give:

$$\eta_\Sigma(Q^2{=}3\,(\mathrm{GeV}/c)^2) \;=\; 0.30 \pm 0.01(stat.) \pm 0.02(evol.). \qquad (7)$$

In the $\overline{MS}$ scheme η_Σ is identical to the matrix element a_0, detailed below. More details on our QCD analysis can be found at Ref. [13].

The direct measurement of $\Delta G/G$, obtained at leading order in QCD, is compared with the indirect approach provided by the NLO QCD fits (figure 7). The unpolarised gluon distribution is taken from the MRST parametrisation [29]. The HERMES value [30] is positive and 2σ away from zero, whereas the preliminar one [31] is compatible with zero. The measured SMC point [32] is too imprecise to discriminate between positive or negative ΔG. Preliminar COMPASS points from measurements on high p_T hadron pairs [33] are consistent with both curves, whereas the value from the open charm channel is compatible with the $\Delta G < 0$ curve.

We have calculated the integral of g_1^N using exclusively the experimental values of COMPASS evolved to $Q_0^2 = 3$ GeV^2 and averaged over the two fits. Taking into account the contributions from the fits in the unmeasured regions of $x \;< 0.003$ and $x \;> 0.7$ we obtain:

$$\Gamma_1^N(Q^2{=}3\,(\mathrm{GeV}/c)^2) \;=\; 0.050 \pm 0.003(stat.) \pm 0.003(evol.) \pm 0.005(syst.). \quad (8)$$

The second error accounts for the difference in Q^2 evolution between the two fits. The systematic error is the dominant one and mainly corresponds to the uncertainty on the beam and target polarisations and on the dilution factor. One should notice that, taking into account only COMPASS data, the unmeasured regions contribute only with 2% to the integral of g_1^N.

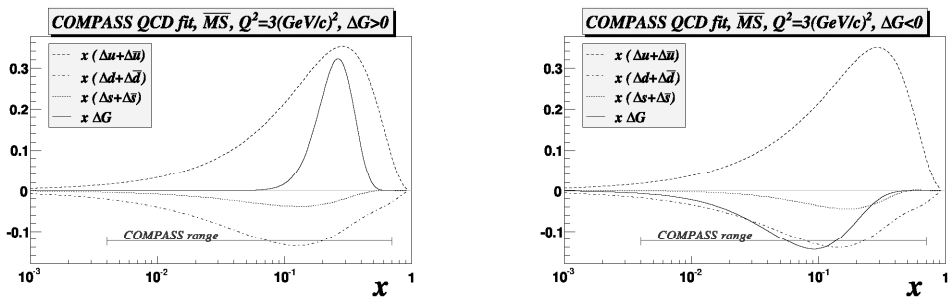

Figure 6: *Distributions* $x(\Delta u + \Delta\bar{u})$, $x(\Delta d + \Delta\bar{d})$, $x(\Delta s + \Delta\bar{s})$ *and* $x\Delta G$ *corresponding to the fits with* $\Delta G > 0$ *(left) and* $\Delta G < 0$ *(right) at* $Q^2 = 3\ GeV^2$.

Γ_1^N is related to the matrix element of the singlet axial current a_0, which measures the quark spin contribution to the nucleon spin. The relation between Γ_1^N and a_0 in the limit $Q^2 \to \infty$ (Ref. [34]) is

$$\Gamma_1^N(Q^2) = \frac{1}{9}\,\hat{C}_1^S(Q^2)\,\hat{a}_0 \;+\; \frac{1}{36}\,C_1^{NS}(Q^2)\,a_8, \tag{9}$$

The coefficients $\hat{C}_1^S$ and C_1^{NS} have been calculated in perturbative QCD up to the third order in $\alpha_s(Q^2)$ [34]. From the COMPASS result of Eq. 8 and taking the value of a_8 measured in hyperon β decay, assuming $SU(3)_f$ flavour symmetry ($a_8 = 0.585 \pm 0.025$ [17]), one obtains:

$$\hat{a}_0 = 0.33 \pm 0.03(stat.) \pm 0.05(syst.), \tag{10}$$

with the value of α_s evolved from the PDG value $\alpha_s(\mathrm{M_z}^2) = 0.1187 \pm 0.005$. Combining this value with a_8, the first moment of the strange quark distribution is:

$$\Delta s(x) + \Delta\bar{s}(x) = \frac{1}{3}(\hat{a}_0 - a_8) = -0.08 \pm 0.01(stat.) \pm 0.02(syst.). \tag{11}$$

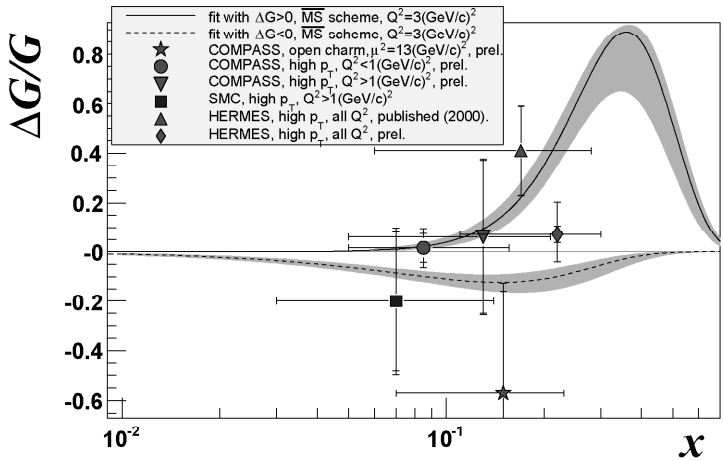

Figure 7: *Distribution of the gluon polarisation $\Delta G(x)/G(x)$ at $Q^2 = 3$ $(GeV/c)^2$ for the fits with $\Delta G > 0$ and $\Delta G < 0$ obtained with the program of Ref. [27]. The error bars associated to the points are statistical. The error bands correspond to the statistical error on $\Delta G(x)$ at a given x. The horizontal bar on each point shows the x-range of measurement.*

5 Conclusions

COMPASS has measured the deuteron spin asymmetry A_1^d and its longitudinal spin-dependent structure function g_1^d with improved precision at $Q^2 < 1$ $(\mathrm{GeV/c})^2$ and $0.0005 < x < 0.02$, as well as $1 < Q^2 < 100$ $(\mathrm{GeV/c})^2$ and $0.004 < x < 0.7$ $Q^2 > 1\,(\mathrm{GeV}/c)^2$. g_1^d is consistent with zero for $x < 0.03$. The measured values have been evolved to a common Q^2 by a NLO QCD fit of the world g_1 data. The fit yields two solutions, one corresponding to $\Delta G(x) > 0$ and other to $\Delta G(x) < 0$, which describe the data equally well. Although the shapes of the distributions are very different, their absolute values of the first moment of $\Delta G(x)$ are similar and not larger than 0.3. Taking into account only COMPASS data the first moment Γ_1^N has been evaluated at $Q^2 = 3$ $(\mathrm{GeV/c})^2$ with a statistical error of about 6%. From this integral the matrix element of the singlet axial current $\hat{a}_0$ in the limit $Q^2 \to \infty$ is extracted. At the order α_s^3, it has been found $\hat{a}_0 = 0.33 \pm 0.03(stat.) \pm 0.05(syst.)$.

Acknowledgments

This work was partially supported by Fundação para a Ciência e a Tecnologia – Portugal.

References

1. M.J. Alguard *et al.* (E80 Coll.), Phys. Rev. Lett. **37**, 1261 (1976).
2. J.R. Ellis and R.L. Jaffe, Phys. Rev. D **9**, 1444 (1974).
3. J. Ashman *et al.* (EMC Coll.), Phys. Lett. B **206**, 364 (1988).
4. B. Adeva *et al.* (SMC Coll.), Phys. Rev. D **58**, 112001 (1998).
5. P.L. Anthony *et al.* (E142 Coll.), Phys. Rev. D **54**, 6620(1996).
6. K. Abe *et al.* (E143 Coll.) Phys. Rev. D **58**, 112003 (1998).
7. K. Abe *et al.* (E154 Coll.), Phys. Lett. B **405**, 180 (1997).
8. P. L. Anthony *et al.,* (E155 Coll.) Phys. Lett. B **463**, 339 (1999).
9. A. Airapetian *et al.* (HERMES Coll.), Phys. Lett. B **442**, 484 (1998).
10. X. Zheng *et al.* (JLAB/Hall A Coll.), Phys. Rev. Lett. **92** 012004 (2004).
11. P. Abbon *et al.* (COMPASS Coll.), CERN-PH-EP/2007-001, hep-ex/0703049. *To be published in Nucl. Inst. and Meths.*
12. V.Yu. Alexakhin *et al.* (COMPASS Coll.), Phys. Lett. B **647**, 330 (2007).
13. V.Yu. Alexakhin *et al.* (COMPASS Coll.), Phys. Lett. B **647**, 8 (2007).
14. A. Airapetian *et al.* (HERMES Coll.), Phys. Rev. D **75**, 012003 (2005)
15. B. Adeva *et al.* (SMC Coll.), Phys. Rev. D **60** 072004 (1999); erratum *ibid.* **62** 079902 (2000).
16. A. Airapetian *et al.* (HERMES Coll.), Phys. Rev. D **75** 012007 (2007).
17. Y. Goto *et al.*, Phys. Rev. D **62**, 037503 (2003).
18. The Durham HEP Databases, http://durpdg.dur.ac.uk/HEPDATA/pdf.htm

19. J. Blümlein and H. Böttcher, Nucl. Phys. B **636**, 225 (2002).

20. M. Glück, E. Reya, M. Stratmann and W. Vogelsang, Phys. Rev. D **63**, 094005 (2001).

21. E. Leader, A. V. Sidorov and D. B. Stamenov, Phys. Rev. D **73** 034023 (2006).

22. P. L. Anthony *et al.* (E155 Coll.), Phys. Lett. B **493**, 19 (2000).

23. J. Ashman *et al.* (EMC Coll.), Nucl. Phys. B **328** (1989).

24. P. L. Anthony *et al.* (E142 Coll.), Phys. Rev. D **54**, 6620 (1996).

25. K. Abe *et al.* (E154 Coll.), Phys. Rev. Lett. **79**, 26 (1997).

26. K. Ackerstaff *et al.* (HERMES Coll.), Phys. Lett. B **404**, 383 (1997).

27. B. Adeva *et al.* (SMC Coll.), Phys. Rev. D **58** 112002 (1998).

28. A. N. Sissakian, O. Yu. Shevchenko and O. N. Ivanov, Phys. Rev. D **70**, 074032 (2004).

29. A. D. Martin, R. G. Roberts, W. J. Stirling and R. S. Thorne, Eur. Phys. J. C **4**, 463 (1998).

30. A. Airapetian *et al.,* (HERMES Coll.), Phys. Rev. Lett. **84**, 2584 (2000).

31. D. Hasch (HERMES Coll.), AIP Conf. Proc. **915**, 307 (2006).

32. B. Adeva *et al.,* (SMC Coll.), Phys. Rev. D **70**, 012002 (2004).

33. E. S. Ageev *et al.,* (COMPASS Coll.), Phys. Lett. B **633**, 25 (2006).

34. S. A. Larin *et al.*, Phys. Lett. B **404**, 153 (1997).

SPIN-DEPENDENT STRUCTURE FUNCTION g_1 AT SMALL x: TOTAL RESUMMATION OF LEADING LOGARITHMS vs STANDARD APPROACH

B. I. Ermolaev
Ioffe Physico-Technical Institute, 194021 St.Petersburg, Russia
M. Greco
Dep.t of Physics and INFN, University Rome III, Rome, Italy
S. I. Troyan
St.Petersburg Institute of Nuclear Physics, 188300 Gatchina, Russia

Abstract

Explicit expressions for the spin-dependent structure function g_1 at small x and arbitrary Q^2 are obtained. They are used for describing g_1 in the kinematic region investigated experimentally by COMPASS collaboration.

1 Introduction

The standard theoretical description of the spin-dependent structure function g_1 is based on the well-known DGLAP evolution equations [1)]

$$d\Delta q/dt = P_{qq}\Delta q + P_{qg}\Delta g\ , \qquad d\Delta g/dt = P_{gq}\Delta q + P_{gg}\Delta g \tag{1}$$

where $t = \ln(Q^2/\mu^2)$, $P_{qq}, P_{qg}, P_{gq}, P_{gg}$ are the splitting functions and Δq, Δg are the parton distributions evolved with respect to Q^2. Convoluting Δq, Δg with the coefficient functions C_q, C_g, one obtains g_1:

$$g_1(x,Q^2) = (< e^2 > /2)\big[C_q(x/y)\otimes\Delta q(y,Q^2) + C_g(x/y)\otimes\Delta g(y,Q^2)\big]. \tag{2}$$

Applying the Mellin transform to Eqs. (1,2) allows to simplify the convolutions and write g_1 in a shorter form:

$$\begin{aligned} g_1(x,Q^2) \quad = \quad & \frac{< e_q^2 >}{2}\int_{-\imath\infty}^{\imath\infty}\frac{d\omega}{2\pi\imath}\Big(\frac{1}{x}\Big)^{\omega}\Big[\Big(C_q^{(+)}e^{\Omega_{(+)}} + C_q^{(-)}e^{\Omega_{(-)}}\Big)\delta q + \\ & \Big(C_g^{(+)}e^{\Omega_{(+)}} + C_g^{(-)}e^{\Omega_{(-)}}\Big)\delta g\Big] \end{aligned} \tag{3}$$

where δq and δg are the initial parton densities and $\Omega_{(\pm)}(\omega,Q^2)$ are well-known combinations of the DGLAP anomalous dimensions $\gamma_{ik}(\omega,t)$, $(i,k = q,g)$. They and the coefficient functions are known in few first orders of PQCD. Eq. (3) describes g_1 at large x and Q^2 because Eqs. (1) were obtained in order to describe Δq and Δg in the region of large x and large Q^2. They account for the Q^2-evolution only and do not account for the x-evolution from $x \sim 1$, where the initial parton densities δq and δg are defined, to values $x \ll 1$ (studied now experimentally). As a result, the DGLAP expressions for g_1 manifest a rather slow growth when x is decreasing. Indeed, the well-known DGLAP small-x asymptotics of g_1, which can easily be found in textbooks, is

$$g_1(x,Q^2) \sim e^{\sqrt{\ln(1/x)}}. \tag{4}$$

2 Using DGLAP at small x

Let us remind that the asymptotics of Eq. (4) is obtained under the assumption that the initial parton densities $\delta q(x)$ and $\delta g(x)$ are decreasing when $x \to 0$, i.e. when they are regular functions of x, being for example polynomials. In reality, fitting experimental data at small x needs a steeper growth and this problem is conventionally solved through including factors $\sim x^a$, with positive a, into expressions for $\delta q(x)$ and $\delta g(x)$. As a result, the standard expressions for δq, δg i.e. Standard Fits for the initial parton densities [2)] acquire the form

$$\delta q, \delta g = Nx^{-a}P(x) \tag{5}$$

where N are normalization constants and $P(x)$ are regular functions of x. They are conventionally defined so that $P(x) \to 1$ when $x \to 0$. Theoretical grounds for invoking the singular factors x^{-a} in the fits are absent in the literature. The practical reason for doing that is meeting experimental data. Besides, there are some popular arguments in favor of using the singular expressions Eq. (5)

(A): The fits Eq. (5) are defined at $x \sim 1$ where the factors x^{-a} are pretty far from being singular. Later, being convoluted with the coefficient functions $C_{q,g}$, they stop to be singular.

(B): Expressions Eq. (5) phenomenologically describe contributions coming from Non-Perturbative QCD (basically unknown) and it is the reason why they are so complicated.

In the next Sect. we prove that the arguments **(A,B)** are inconsistent and show that the only theoretically based way to describe g_1 at small x is complementing the Q^2-evolution of g_1 by the x-evolution so that the total resummation of leading logarithms of x can be done.

3 Total resummation of logarithms of x

Double-logarithmic (DL) contributions $\sim (\alpha_s \ln^2(1/x))^k$ are accounted in the DGLAP expressions for g_1 in few first orders in α_s. As they become quite essential at small x, the total resummation of them would be the most natural and straightforward way to describe g_1 at small x. This was done in Refs. [4, 5] where explicit expressions accounting for the total resummation of DL terms was done. They look similar to the DGLAP expressions Eq. (3), however with new anomalous dimensions and coefficient functions. They account for the total resummaton of DL contributions and for the running α_s effects. We stress that the standard DGLAP parametrization $\alpha_s = \alpha_s(Q^2)$ fails at small x and should be replaced by the new parametrization suggested in Ref. [6]. Extrapolating those expressions into the region $x \to 0$ leads to the Regge asymptotics

$$g_1(x, Q^2) \sim x^{-\Delta} (Q^2/\mu^2)^{\Delta/2}, \tag{6}$$

with Δ being the intercept of g_1. The non-singlet intercept $\Delta_{NS} = 0.43$ and the singlet intercept $\Delta_S = 0.86$. On the other hand, applying the Mellin transform to the DGLAP fits Eq. (5) for initial parton densities and substituting it into Eq. (3) changes the asymptotics Eq. (4) for the Regge asymptotics (see Ref. [3] for detail):

$$g_1(x, Q^2) \sim x^{-a}. \tag{7}$$

Confronting Eqs. (6) and (7) allows to conclude that the singular factors x^{-a}, originally introduced at large x do not stop to be singular at small x. They turn out to be the leading poles in the ω-space, being originally defined at large x, they nevertheless determine the small-x asymptotics of g_1 and of the

parton distributions. This disproves the argument **(A)** of the previous Sect. As the factors x^{-a} mimic the total resummation of the leading logarithms of x, they can be dropped when the resummation is taken into account. When the initial parton densities are defined at sufficiently small x, the regular part $P(x)$ of Eq. (5) can also be simplified. This disproves the argument **(B)** of the previous Sect.

4 Extension to small Q^2

At present, g_1 has been studied experimentally by COMPASS collaboration. The available kinematic region is

$$x \ll 1; \quad 10^{-1}\ GeV^2 \leq Q^2 \leq 3\ GeV^2. \tag{8}$$

As DGLAP works at $Q^2 \gg \mu^2$, it cannot be invoked for explaining experiment in the region Eq. (8). The total resummation of the leading logarithms of x discussed in the previous Sect. was obtained for studying g_1 in the region $x \ll 1$; $Q^2 \gg \mu^2 \approx$ few GeV^2. Therefore, the small-Q^2 region remained unstudied. An extension of our results into this region has recently been obtained in Ref. [7]. According to it, g_1 in the region Eq. (8) can be described with the expressions of Refs. [4, 5] complemented with the shift

$$Q^2 \to Q^2 + \mu^2 \tag{9}$$

where our estimates for μ are (see Refs. [7, 8] for detail): $\mu \approx 1$ GeV for the non-singlet and $\mu \approx 5$ GeV for the singlet g_1. Introducing shifts of Q^2 similarly to Eq. (9) in order to describe small Q^2 has been used by many authors, however they always introduced the shifts from various phenomenological considerations whereas in Ref. [8] we proved the shift with analysis of the involved Feynman graphs.

Results obtained in Refs. [7, 8] can be used for theoretical explaining COMPASS data on g_1. They also allow us to make the following predictions:

Prediction 1: Structure function g_1 at the COMPASS range of Q^2 practically does not depend on x even at very small x.

Prediction 2: In contrast, experimental studying a dependence of g_1 on $2pq$ can bring an interesting information about the initial parton densities (see Ref. [7] for detail).

5 Conclusion

The Standard Approach, being based on DGLAP, successfully describes the structure function g_1 at large x and large Q^2. There are not theoretical grounds

for extrapolating SA into the region of large Q^2 and small x. SA is able to describe g_1 at small x only because of invoking singular fits for the initial parton densities, although SA does not suggest any explanation for the parton densities to be singular. Without the singular factors x^{-a} in the fits, SA would not be able to match experimental data at $x \leq 0.05$. Then, SA cannot be used at small Q^2 either at large or at small x.

In contrast, the total resummation of leading logarithms of x does not involve singular fits for the parton distributions. It allows one considerably simplify the fits. Combining the total resummation with the shift Eq. (9) extends our approach to the small-Q^2 region. Therefore, our approach can be used in the small-x region at large and small Q^2 at the same time. Prediction 1 of the previous Sect. has been confirmed by COMPASS and Prediction 2 is now being analyzed by COMPASS.

6 Acknowledgement

B.I. Ermolaev is grateful to the Organizing Committee of the conference LaThuile 2007 for financial support of his participation in the conference.

References

1. G. Altarelli and G. Parisi. Nucl.Phys.B **126**(1977) 297;
   V.N. Gribov and L.N. Lipatov. Sov.J.Nucl.Phys. **15**(1978) 438 and 675;
   L.N. Lipatov. Sov.J.Nucl.Phys. **20**(1972) 95;
   Yu.L. Dokshitzer. Sov.Phys.JETP **46**(1977) 641.

2. G. Altarelli, R. Ball, S. Forte and G. Ridolfi. Acta Phys.Polon.B **29**(1998) 1201; Nucl.Phys.B**496**(1999) 337;
   E. Leader, A.V. Sidorov and D.B. Stamenov. Phys.Rev.D **73**(2006) 034023;
   J. Blumlein, H. Botcher. Nucl.Phys.B**636**(2002) 225;
   M. Hirai at al. Phys.Rev.D **69**(2004) 054021.

3. B.I. Ermolaev, M. Greco, S.I. Troyan. Phys.Lett.B **622**(2005) 93.

4. B.I. Ermolaev, M. Greco, S.I. Troyan. Nucl.Phys.B **571**(2000) 137; Nucl.Phys.B **594**(2001) 71.

5. B.I. Ermolaev, M. Greco, S.I. Troyan. Phys.Lett.B **579**(2004) 330.

6. B.I. Ermolaev, M. Greco, S.I. Troyan. Phys.Lett.B **522**(2001) 57.

7. B.I. Ermolaev, M. Greco, S.I. Troyan. Eur.Phys.J.C **50**(2007) 823.

8. B.I. Ermolaev, M. Greco, S.I. Troyan. Eur.Phys.J.C **51**(2007) 859.

SESSION III – ELECTROWEAK AND TOP PHYSICS

- *Roberto Petronzio* Recent Results on the Weak Matrix Elements on the Lattice
- *Kristian Harder* Electroweak Measurements at the Tevatron
- *Chris Hays* Precision Measurement of the W mass
- *Michele Weber* Top Quark Production and Decay Properties at the Tevatron
- *Pedro A. Movilla Fernández* Precision Determination of the Top Quark Mass
- *Aurelio Juste* Single Top Quark Production at the Tevatron
- *Michael Dittmar* The first SM Physics results from CMS Some expectations
- *Amine Ahriche* The Electroweak Phase Transition in the Existence of Singlets
- *Fulvio Piccinini* Recent Progress in Theoretical Calculations and Monte Carlo Generators for LHC
- *Pham Q. Hung* Implications of Right-Handed Neutrinos with Electroweak-Scale Masses

RECENT RESULTS ON THE WEAK MATRIX ELEMENTS ON THE LATTICE

Roberto Petronzio
Università degli Studi di Roma "Tor Vergata"
Via della Ricerca Scientifica 1, 00133 Roma

Written contribution not received

ELECTROWEAK MEASUREMENTS AT THE TEVATRON

Kristian Harder
Rutherford Appleton Laboratory
for the CDF and DØ Collaborations

Abstract

The increasing size of the data samples recorded by the CDF and DØ experiments at the Tevatron enables studies of a wide range of processes involving the electroweak bosons W and Z. Single boson production is now looked at in terms of differential cross sections such as rapidity or transverse momentum dependence. Diboson production cross-sections are several orders of magnitude smaller than single boson production cross-sections, but all combinations Wγ, Zγ, WW and WZ have been observed. ZZ production is expected at a rate just below the observation threshold with current data sample sizes, but this channel is expected to be accessible to the Tevatron experiments soon.

1 Introduction

Leptonic final states of W and Z boson decays exhibit a very clear experimental signature and pave the way for precision tests of the Standard Model beyond leading order and possible detection on non Standard Model contributions. These measurements can provide strong constraints to parton density functions.

The hadronic collision data recorded by the Tevatron experiments CDF and DØ as of early 2007 amount to more than $2\,\mathrm{fb}^{-1}$ per experiment, about $1\,\mathrm{fb}^{-1}$ each of which have been made available for electroweak physics analysis so far. While measurements of the total production cross-section of single W or Z bosons were already performed on much smaller size samples, the current data set allows for a much more in-depth analysis of the production process by measuring differential cross-sections. Also, most diboson production processes are now experimentally accessible despite their lower cross-section. In the following, we will summarise the typical W and Z selection procedure applied by the CDF and DØ experiments, and then present recent electroweak results made available by both collaborations.

2 W and Z reconstruction

Both CDF and DØ follow a fairly standard path for boson reconstruction, with only minor variations e.g. in cut thresholds between the different experiments or different analyses from the same collaboration.

Electrons are identified from calorimeter clusters that pass shower shape requirements and have a transverse momentum in excess of typically 20 GeV. Isolation cuts are applied to remove background from fake electrons and electrons in jets. Both DØ and CDF perform their reconstruction separately in the central barrel calorimeters and their forward calorimeters, while not using data from the intermediate region where modelling of the detector response is more difficult.

Muon reconstruction is based on signals identified in the muon detectors or calorimeters. In cases where efficiency is most important, CDF also includes tracks without associated muon or calorimeter signal in their muon selection. A transverse momentum threshold around 20 GeV is applied, and the muon candidates are required to be isolated in the tracking system and/or calorimeter to remove background from muons from heavy quark decay. The pseudorapidity coverage of muons used in the CDF analyses is restricted to $|\eta| \leq 1.1$–1.2, whereas DØ has muons in the range up to $|\eta| \leq 2$ at their disposal.

Tau leptons are not treated separately. Leptonically decaying taus are implicitly included in the electron and muon selections.

Leptonic W boson decays involve a neutrino, which is exploited for the reconstruction by requiring missing transverse energy of typically at least 20 GeV in candidate events. CDF requires the missing momentum vector to be isolated.

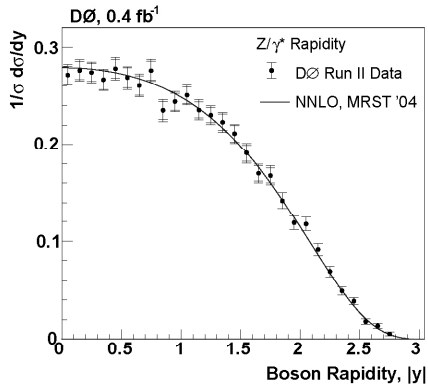

Figure 1: *Z boson rapidity distribution observed by DØ. This recently published 0.4 fb^{-1} result* [1] *is expected to be followed up by a 1 fb^{-1} result soon.*

3 Differential Z cross-sections

Leptonic Z decays can be reconstructed fully and therefore provide the laboratory of choice for studying the intricacies of single electroweak boson production processes, despite the cross-section being an order of magnitude smaller than that of W production. The sample of reconstructed Z bosons collected at the Tevatron is large enough to investigate the dependence of the production cross-section on quantities such as Z rapidity and Z transverse momentum distribution.

The Z rapidity distribution is especially interesting in the forward region, where it provides constraints for parton density functions at low momentum fraction x and large momentum transfer Q^2, as well as at large x. Both DØ [1] and CDF [2] do this measurement in the Z→ee channel due to the larger η coverage of the calorimeter compared to the muon system, $|\eta|$ <3.2 at DØ, $|\eta|$ <2.8 at CDF. The observed distributions are compared to NNLO predictions (MRST '04, CTEQ6.1) and found to be in good agreement, as demonstrated for example in Fig. 1.

DØ also measures the transverse momentum distribution of Z bosons [3]. This distribution is very sensitive to higher order effect because there is no leading order contribution to Z transverse momentum. Prediction of this distribution requires resummation. Although the current revision of the measurement is not yet able to distinguish between different calculations, good agreement is found with the available predictions, and the sensitivity of the analysis to model differences is expected to be improved on a short time scale.

	exp.	sample	evts	prediction (SM, in pb)	measured cross-section (pb)
Wγ (μ)	CDF	1.1 fb^{-1}	855	19.3 ± 1.4	19.11±1.04(stat)±2.40(syst)±1.11(lum)
	DØ	1 fb^{-1}	245	3.21 ± 0.08	3.21±0.49(stat+syst)±0.20(lum)
Wγ (e)	DØ	1 fb^{-1}	389	3.21 ± 0.08	3.12±0.49(stat+syst)±0.19(lum)
Zγ	CDF	1.1 fb^{-1}	390	4.7 ± 0.4	4.9±0.3(stat)±0.3(syst)±0.3(lum)
	DØ	1 fb^{-1}	387	4.2 ± 0.4	4.51±0.37(stat+syst)±0.27(lum)
WW	CDF	0.8 fb^{-1}	95	12.4 ± 0.8	13.6±2.3(stat)±1.6(syst)±1.2(lum)
WZ	CDF	1.1 fb^{-1}	16	3.7 ± 0.3	$5.0^{+1.8}_{-1.4}$(stat)±0.4(syst)
	DØ	1 fb^{-1}	12	3.7 ± 0.3	$4.0^{+1.9}_{-1.5}$(stat+syst)
ZZ	CDF	1.1 fb^{-1}	1	1.4 ± 0.1	<3.8 (95% C.L.)

Table 1: *Overview of diboson production cross-section measurements discussed in this document. Predictions are as quoted in the respective analysis write-up. Analysis of different kinematic regions leads to different cross-section predictions for the same channel. In particular, DØ uses a very stringent FSR veto cut in their Wγ analysis, whereas CDF does not.*

4 Diboson production

Production processes of gauge boson pairs takes place at much lower cross-sections than single W or Z production. While we expect of the order of 100,000 reconstructed Z bosons per experiment per leptonic channel in one femtobarn of data, the expected yield for diboson processes extends down to about one event per femtobarn for ZZ production. Main emphasis of diboson reconstruction at this stage is therefore establishing signals and measuring the absolute absolute cross-section.

Very interesting results can be obtained from a measurement of the Zγ production rate. Since there are no ZZγ or Z$\gamma\gamma$ vertices in the Standard Model, Zγ combinations can only be produced by initial state or final state radiation. Any additional contributions would indicate new physics. CDF [4] and DØ [5] investigate Zγ production in Z$\rightarrow$ee final states with a photon of at least 7 GeV. Photons from initial state and final state radiation can be distinguished by looking at the three-body eeγ mass in addition to the ee mass. Both experiments find agreement of the observed production rate with Standard Model predictions, and in particular no deviation from the expectation is observed at large photon transverse energies or in the ISR/FSR distributions.

Wγ production does have a leading order contribution. Both experiments measure cross-sections in good agreement with the standard model prediction. CDF [4] does this measurement in the W$\rightarrow \mu\nu$ channel, whereas DØ [6] uses both electron and muon final states and employs a very stringent final state radiation veto by requiring the Wγ three-body mass to exceed 110 GeV. DØ increases sensitivity to anomalous couplings by studying the charge signed rapid-

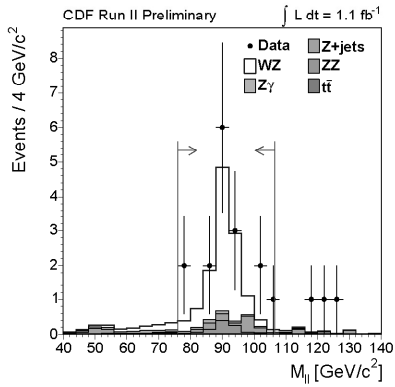

Figure 2: *Dilepton mass distribution of CDF WZ candidate events.*

ity difference $Q_\ell \times [y(\gamma) - y(\ell)]$, which is expected to vanish at zero for the Standard Model. This measurement will clearly unfold its full potential once larger data samples are available.

The production rates of massive boson pairs WW, WZ and ZZ are predicted to spread over an order of magnitude in a similar range as other important processes such as top quark pair production. While the signal of WW production has been clearly established (see 7) for a recent CDF measurement), the WZ state is just barely accessible to observation now. All combinations of electrons and muons in the final state are considered to maximise reconstruction efficiency. CDF [8] finds 16 WZ candidates in their approximately $1\,\mathrm{fb}^{-1}$ data sample (see Fig. 2), with an expected background contribution of $2.65 \pm 0.28 \pm 0.33 \pm 0.09$ events. This six standard deviation excess above the background expectation constitutes the first observation of the WZ channel. DØ [9] did a similar analysis, but due to a combination of various small effects their signal of 12 events including 3.61 ± 0.20 expected background events remains below the formal threshold for an observation. Both experiments do measure cross-sections in good agreement with the Standard Model.

The lowest end of the diboson production cross-section spectrum, ZZ production with an expected Standard Model cross-section of $1.4 \pm 0.1\,\mathrm{pb}$ is hardly accessible to the Tevatron experiments so far. CDF [10] performed a search for this channel, finding one candidate event where approximately two are expected on average. They can therefore quote a cross-section upper limit of 3.8 pb at 95% C.L. It is reasonable to expect that the ZZ channel will be observed at the Tevatron once its full Run II dataset is becoming available.

An overview over recent diboson results is given in Table 1.

5 Discussion

Leptonic final states of W and Z bosons are fairly clear signatures even within the large background associated with hadron colliders. High cross-section processes like single W or Z production therefore provide an ideal laboratory for precision studies of parton density functions. Rare electroweak processes like production of massive boson pairs can already be identified down to cross-sections smaller than top quark pair production. While we can realistically expect to observe signatures like Z pairs (predicted at 1.4 ± 1 pb) at the Tevatron with a 4–8 fb^{-1} data sample per experiment, it seems unlikely that signals much smaller than that can be identified directly, such as a hypothetical Standard Model H→WW contribution at an expected cross-section another order of magnitude below that of ZZ production.

6 Acknowledgements

I thank the personnel involved in operating the Tevatron and the DØ and CDF detectors, as well as the people dedicating their time to providing the software infrastructure for data handling, event reconstruction and physics analysis. I would also like to express my gratitude to the CDF and DØ electroweak physics groups and their conveners for providing me with input for this conference.

References

1. DØ Collaboration, arXiv:hep-ex/0702025, submitted to Phys. Rev. **D**.
2. *http://www-cdf.fnal.gov/physics/ewk/2006/dszdy/public_note_final.ps*
3. *http://www-d0.fnal.gov/Run2Physics/WWW/results/prelim/EW/E18/E18.pdf*
4. *http://fcdfwww.fnal.gov/physics/ewk/2006/wgzg/*
5. DØ Collaboration, arXiv:0705.1550v1, submitted to Phys. Lett. **B**.
6. *http://www-d0.fnal.gov/Run2Physics/WWW/results/prelim/EW/E19/E19.pdf*
7. *http://www-cdf.fnal.gov/physics/ewk/2006/ww/*
8. *http://fcdfwww.fnal.gov/physics/ewk/2006/wz/ZZWZ_1fb/*
9. *http://www-d0.fnal.gov/Run2Physics/WWW/results/prelim/EW/E15/E15.pdf*
10. *http://fcdfwww.fnal.gov/physics/ewk/2006/wz/ZZWZ_1fb/*, see *http://fcdfwww.fnal.gov/physics/ewk/2007/ZZ/ZZ_comb_public_note.ps* for a post-conference update incorporating also ZZ→ $\ell\ell\nu\nu$ candidates.

PRECISE MEASUREMENT OF THE W BOSON MASS

Christopher P. Hays
University of Oxford, Oxford OX1 3RH, United Kingdom

(for the CDF Collaboration)

Abstract

The first measurement of the W boson mass (m_W) in Run II of the Tevatron Collider has been made by the CDF Collaboration, and is the single most precise m_W measurement to date. The measurement of $m_W = 80.413 \pm 0.048$ GeV has a relative precision of 0.06% and results in a new world-average m_W of 80.398 ± 0.025 GeV. The precise knowledge of m_W constrains the properties of new hypothetical particles coupling to electroweak gauge bosons.

1 Introduction

The unification of the electromagnetic and weak forces includes mixing between the fundamental $SU(2)$ and $U(1)$ symmetries. This mixing is parametrized by $\sin^2\theta_W \equiv 1 - m_W^2/m_Z^2$, where m_W and m_Z are the masses of the W and Z gauge bosons that transmit the weak force. Precise measurements of electroweak parameters provide stringent tests of the theory and constrain the existence of new hypothesized particles coupling to the W and Z bosons. The measurement of m_W is an example of such a test.

In the electroweak theory, m_W is predicted to be [1]:

$$m_W^2 = \frac{\pi\alpha_{EM}}{\sqrt{2}G_F \sin^2\theta_W(1-\Delta r)}, \tag{1}$$

where α_{EM} is the electromagnetic coupling at the renormalization scale $Q = m_Z$, G_F is the Fermi weak coupling extracted from the muon lifetime, and Δr includes all radiative corrections.[1] Since the input parameters have been measured to high precision (better than a part in 10,000), the m_W measurement is sensitive to loop corrections from particles with weak couplings. For example, the existence of the unobserved Higgs boson would reduce m_W by a value proportional to the logarithm of the Higgs mass (m_H). For a relative m_W accuracy of 0.03%, m_H is constrained by m_W to within $\approx 50\%$ [2].

Previous m_W measurements at the Large Electron Positron (LEP) and Tevatron colliders have a combined relative m_W precision of 0.036% [1]. The first m_W measurement at Run II of the Tevatron collider has been performed by the CDF Collaboration, and is the single most precise m_W measurement to date. Incorporating the new CDF measurement into the world-average m_W fit results in a relative m_W accuracy of 0.031% [3].

2 CDF II Detector and Model

The Run II CDF detector [3] (CDF II) measures particles resulting from $\sqrt{s} = 1.96$ Tev $p\bar{p}$ collisions. The detector consists of concentric cylindrical layers surrounding the beam line, each with a particular focus: the inner silicon tracker measures charged-particle trajectories close to the interaction, allowing a precise determination of the interaction point; the outer drift chamber (COT) measures charged-particle momenta transverse to the beam line (p_T) with a precision of $\delta p_T/p_T \approx 0.05\% p_T$, after a constraint

[1] The convention $\hbar \equiv c \equiv 1$ is used throughout.

to the interaction region; the 1.4 T solenoid produces a near uniform magnetic field inside the tracking volume; the electromagnetic (EM) calorimeter measures the energy (E) of electron and photon showers to a precision of $\delta E/E \approx \sqrt{0.135^2/E_T + 0.017^2}$; the hadronic calorimeter measures hadronic showers to a precision of $\delta E_T/E_T \approx 80\%/E_T$; and the muon drift chambers identify muons penetrating the detector.

The CDF II detector model used in the m_W measurement consists of a fast parametrized simulation of the components relevant to the measurement. Using a three-dimensional lookup table of the tracking detector's properties, the simulation models ionization energy loss, multiple Coulomb scattering, electron bremsstrahlung, photon conversion, and photon Compton scattering in the tracker. Electron energy loss in the solenoid (before entering the EM calorimeter) and in the hadronic calorimeter (after passing through the EM calorimeter) are parametrized from a GEANT-based detector simulation. Lepton and recoil reconstruction and selection are also modelled in the simulation, whose final products are templates of the distributions used to fit the data.

3 CDF m_W Measurement

To date, the Tevatron collider has produced more than 2.5 fb^{-1} of $\sqrt{s} =$ 1.96 TeV $p\bar{p}$ collision data per experiment. The first m_W measurement [3] is based on ≈ 200 pb^{-1} of CDF data, which contain 51,128 (63,964) resonantly produced W bosons decaying to muons (electrons) after event selection. The selection requires 30 GeV $< p_T^l <$ 55 GeV, 30 GeV $< p_T^\nu <$ 55 GeV, 60 GeV $< m_T(l,\nu) <$ 100 GeV, and recoil $u_T <$ 15 GeV (Fig. 1), where

$$m_T = \sqrt{2p_T^l p_T^\nu [1 - \cos\Delta\phi(l,\nu)]}. \tag{2}$$

A sample of 4,960 (2,919) resonantly produced Z bosons decaying to muons (electrons) provides an important control and is used to fit for the lepton momentum scale and the recoil model parameters.

3.1 Strategy

The m_W measurement relies on a precise calibration of the lepton momenta in the event. Muon momenta are measured with the tracker, which is calibrated using the muonic decays of the J/ψ and Υ quarkonia states, and of the Z boson. Electron momenta are measured with the calorimeter, which is calibrated using the ratio of calorimeter energy to track momentum (E/p) in W boson events, and using $Z \to ee$ events. Neutrino momenta are inferred from the energy

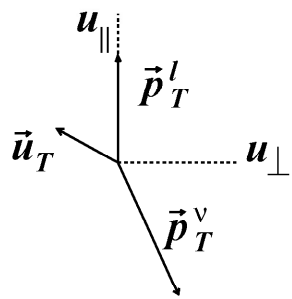

Figure 1: *A W boson event, with the recoil hadron momentum ($\vec{u}_T$) separated into axes parallel ($u_{||}$) and perpendicular ($u_\perp$) to the charged lepton.*

imbalance in the event, and their measurement relies on charged lepton and recoil momenta calibrations.

The recoil momentum in a W or Z boson event is measured as the net momentum in the calorimeter, excluding the contribution(s) from the charged lepton(s). The measurement includes the underlying event and additional $p\bar{p}$ interactions, which reduce the resolution of the recoil measurement. The recoil is modelled using a parametrization of the components, with parameters fit using Z boson data.

The measurement was performed blind, with a single offset applied to the final m_W fits to the measurement distributions (m_T, p_T^l, and p_T^ν). The offset was drawn from a flat distribution between -100 MeV and 100 MeV, and was not removed until the full analysis was complete.

3.2 Track Momentum Calibration

Non-uniformities in the tracker are studied with cosmic ray muons, and alignment corrections are applied when fitting the track parameters. The corrections adjust the positions of each 12-wire cell at each end of the COT, and the shapes of the wires within the tracker. Biases in the measured track curvature are studied by comparing the E/p distributions of electrons and positrons. Differences in E/p as functions of polar (θ) and azimuthal (ϕ) angle are removed by correcting the measured track curvature (Fig. 2). The statistical uncertainties on the corrections result in a 6 MeV uncertainty on the m_W measurement.

Using 606,701 $J/\psi \to \mu\mu$ candidates, the dimuon invariant mass distribution around $m_{\mu\mu} = 3.08$ GeV is fit for $m_{J/\psi}$ as a function of the mean inverse momentum $\left\langle p_T^{-1} \right\rangle$ of the two muons. By comparing the fit result to the

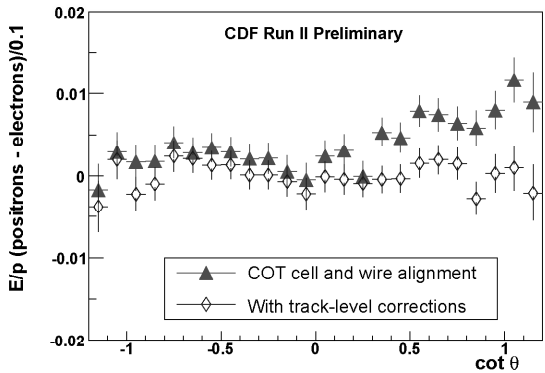

Figure 2: *The difference in E/p between electrons and positrons, as a function of* $\cot\theta$*, before and after curvature corrections are applied to the reconstructed track.*

world-average $m_{J/\psi}$ value [1], a momentum scale correction $\Delta p/p$ is derived (Fig. 3). To obtain zero slope in $\Delta p/p$ as a function of $\langle p_T^{-1} \rangle$, a correction is applied to the simulated energy loss in the silicon tracker, effectively reducing the amount of material by 6% relative to the CDF standard value. The dominant uncertainty of $\sigma_{\Delta p/p} = 0.02\%$ on this calibration arises from the energy loss model.

An additional track momentum calibration results from fits for m_Υ to the dimuon invariant mass distribution around $m_{\mu\mu} = 9.43$ GeV. The measurement is performed both using tracks constrained to the interaction and unconstrained tracks. Comparisons of the two fit results verify that there is no significant bias ($\sigma_{\Delta p/p} = 0.006\%$) from the constraint. The $\Delta p/p$ extracted from the Υ measurement is consistent with that obtained from the J/ψ measurement (Fig. 3), and the two results are combined to give an accuracy of $\sigma_{\Delta p/p} = 0.019\%$.

Given this track momentum calibration, the Z boson mass is measured using its decay to muons. Fitting the dimuon mass distribution for m_Z around $m_{\mu\mu} = 91.19$ GeV, a value of $(91.184 \pm 0.043_{stat})$ GeV is obtained (Fig. 4), consistent with the world average value [1]. This measurement is incorporated into the calibration, but does not significantly reduce its uncertainty. The combined track calibration and alignment uncertainty corresponds to an uncertainty of $\delta m_W = 17$ MeV.

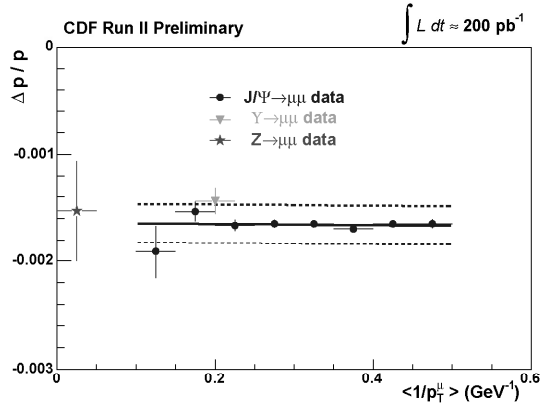

Figure 3: *The track momentum scale correction obtained from fits to the dimuon mass distribution for J/ψ, Υ, and Z boson decays to muons. The dashed line is the systematic uncertainty on the J/ψ measurements, and the error bars indicate statistical uncertainties.*

3.3 Electron Energy Calibration

The calorimeter energy is calibrated using the E/p distribution of electrons from $W \to e\nu$ decays, and the dielectron mass distribution from $Z \to ee$ decays. The E/p calibration relies on an accurate modelling of the electron energy loss in the tracker, which is tested by measuring m_Z with the dielectron invariant mass using the track momentum measurement. The result is consistent with the world average value [1)], within the 143 MeV uncertainty of the measurement. An additional validation of the simulation is the modelling of the data E/p distribution (Fig. 5). Electron shower leakage into the hadronic calorimeter and energy loss in the tracker are the dominant effects in the regions above and below the E/p peak, respectively. The region above the peak is used to fit for an energy loss scale in the tracker simulation, and the result is consistent with a scale of 1. This result is different than for muons because muons have a different dependence on material type, and the mixture of material types in the standard CDF simulation may be inaccurate at the few percent level. The relative statistical uncertainty on the E/p calibration is 0.034%.

The calorimeter energy scale can have an energy dependence due to variations in response as a function of shower depth, or mismodelling of shower leakage into the hadronic calorimeter or energy loss in the tracker. This energy dependence, or "non-linearity," is measured by fitting the E/p peak as a function of E_T in W and Z boson events. A non-linear effect with a statistical significance of 1σ is applied as a correction to the simulation. The uncertainty

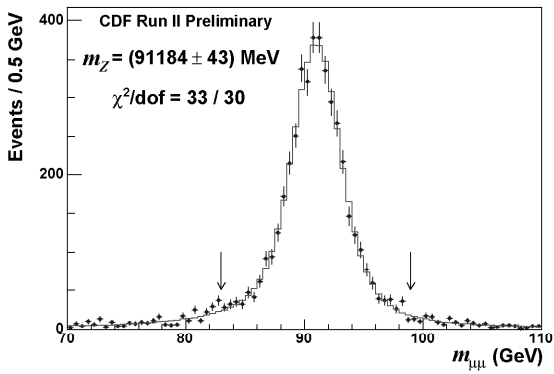

Figure 4: *The fit for m_Z to the dimuon mass distribution. The arrows indicate the fit region and the uncertainty is statistical only.*

on the non-linearity measurement corresponds to a 23 MeV uncertainty on m_W.

As a test of the E/p calibration, and to improve the accuracy of the calorimeter energy calibration, the dielectron mass distribution around $m_{ee} = 91.19$ is fit for m_Z (Fig. 6). The fit result is consistent with the world average value of m_Z, which is used as an additional calibration constraint. The total uncertainty of the calorimeter energy scale corresponds to an uncertainty $\delta m_W = 30$ MeV in the electron channel.

3.4 Recoil Calibration

The recoil momentum scale is modelled as a logarithmic function of recoil momentum. The two fit parameters in the function determine the scale at zero momentum and the rate of scale increase with increasing momentum. The parameters are determined from fits to the balance between recoil and lepton momenta in Z boson events.

The recoil momentum resolution is assumed to arise from stochastic fluctuations in the calorimeter, taking the form $\sigma_{u_T} \propto \sqrt{u_T}$. Additional resolution from the underlying event and additional $p\bar{p}$ interactions is modelled by adding energy in the simulation using a distribution derived from generic interaction data. The additional energy includes a scale parameter to allow for a difference between underlying event energy in generic interactions and in Z boson data. Both the proportionality constant in the recoil resolution function and the scale parameter for the underlying event are determined from a fit to the rms of the momentum balance between the recoil and leptons in Z boson events.

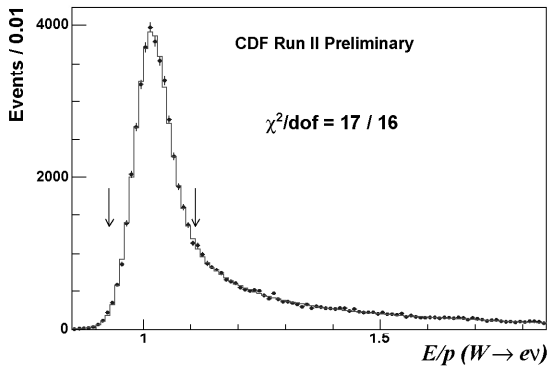

Figure 5: *The fit for the calorimeter energy scale to the peak of the E/p distribution. The arrows indicate the fit region.*

The recoil model is tested with distributions from W boson events. A particularly relevant distribution is the recoil parallel to the charged lepton ($u_{||}$), since to first order m_T can be approximated by $2p_T^l + u_{||}$ (using $p_T^\nu \approx |p_T^l + u_{||}|$). The simulation accurately predicts the mean and rms of this distribution (Fig. 7).

3.5 Production Model and Backgrounds

W and Z boson events are simulated using the RESBOS event generator [4], with the CTEQ6M input parton distribution functions [5]. The generator provides a next-to-leading-log resummation of the QCD corrections, as well as a parametrization of the non-perturbative regime. CDF constrains the parameters using the Z boson p_T distribution, and the resulting uncertainty on the m_T fit for m_W is 3 MeV. The uncertainty on the model of parton distribution functions is determined using the 90% confidence level (CL) eigenvector uncertainties, and the corresponding 1σ uncertainty is $\delta m_W = 11$ MeV for the m_T fit.

Photon radiation from the final-state charged lepton is modelled with energy and angular distributions extracted from a next-to-leading-order event generator (WGRAD) [6]. Higher-order corrections are implemented by scaling up the extracted photon energy by 10%, and a 5% uncertainty is applied. The total uncertainty from photon radiation is $\delta m_W = 8(9)$ MeV for the electron (muon) m_T fit.

Backgrounds to the W boson event sample consist of electroweak boson

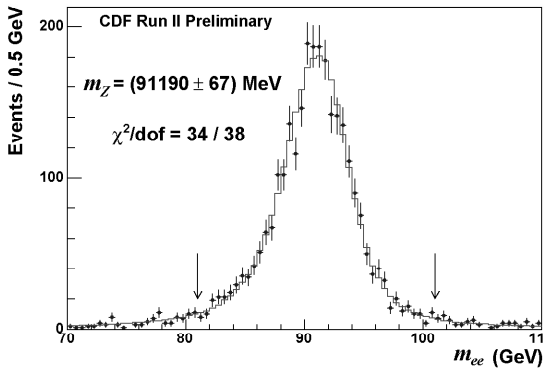

Figure 6: *The fit for m_Z to the dielectron mass distribution. The arrows indicate the fit region and the uncertainty is statistical only.*

Table 1: *Backgrounds to the W boson event sample.*

Background	$W \to \mu\nu$ (%)	$W \to e\nu$ (%)
$Z \to ll$	6.6 ± 0.3	0.24 ± 0.04
$W \to \tau\nu$	0.89 ± 0.02	0.93 ± 0.03
Hadronic jets	0.1 ± 0.1	0.25 ± 0.15
Decays in flight	0.3 ± 0.2	-
Cosmic ray muons	0.05 ± 0.05	-

decays, modelled with the standard CDF simulation, and hadrons and cosmic rays, modelled with the data. The hadronic background can result from jet production, with a high-momentum hadron decaying leptonically, or from a kaon or pion decay in flight, with the decay muon momentum mismeasured. The largest background of 6.6% results from $Z \to \mu\mu$ events, where one of the muons is outside the fiducial volume ($|\eta| < 1$) of the COT. Uncertainties on the background prediction result in uncertainties of $\delta m_W = 11(12)$ MeV for the electron (muon) m_T fit.

3.6 Mass Fits and Results

The W boson mass is fit using the m_T (Fig. 8), p_T^l, and p_T^ν distributions (Table 2). The m_T fit has an 80% weight in the combination of the results, which is $m_W = 80.413 \pm 0.048$ GeV.

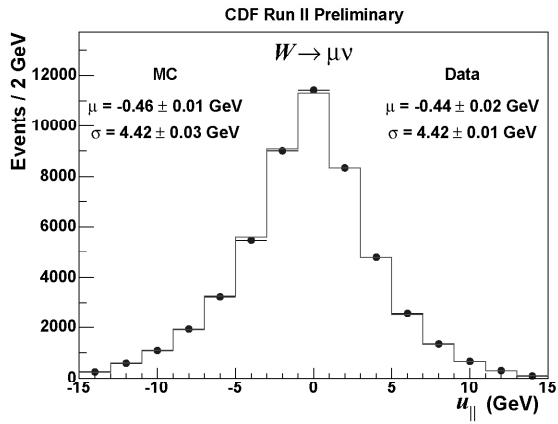

Figure 7: *The data (circles) and simulation (histogram) $u_{||}$ distributions for $W \to \mu\nu$ data. The uncertainties on the data are statistical, and the uncertainties on the simulation result from uncertainties on the recoil model parameters derived from $Z \to ee$ and $Z \to \mu\mu$ data.*

Table 2: *The results of the fits for m_W to the m_T, p_T^l, and p_T^ν distributions in the electron and muon decay channels.*

Distribution	m_W (GeV)	χ^2/dof
$m_T(e,\nu)$	$80.493 \pm 0.048_{stat} \pm 0.039_{sys}$	86/48
$p_T^l(e)$	$80.451 \pm 0.058_{stat} \pm 0.045_{sys}$	63/62
$p_T^\nu(e)$	$80.473 \pm 0.057_{stat} \pm 0.054_{sys}$	63/62
$m_T(\mu,\nu)$	$80.349 \pm 0.054_{stat} \pm 0.027_{sys}$	59/48
$p_T^l(\mu)$	$80.321 \pm 0.066_{stat} \pm 0.040_{sys}$	72/62
$p_T^\nu(\mu)$	$80.396 \pm 0.066_{stat} \pm 0.046_{sys}$	44/62

4 Summary and Outlook

The CDF Collaboration has made the most precise single m_W measurement to date. The new world average of $m_W = 80.398 \pm 0.025$ GeV has a relative uncertainty of 0.031%. Combining the m_W measurement with measurements of other electroweak parameters [1)], the Higgs mass is predicted to be $m_H = 76^{33}_{-24}$ GeV, or $m_H < 144$ GeV at 95% CL [3)]. With a factor of ≈ 10 increase in data already collected, CDF expects its next measurement to have a precision better than 25 MeV.

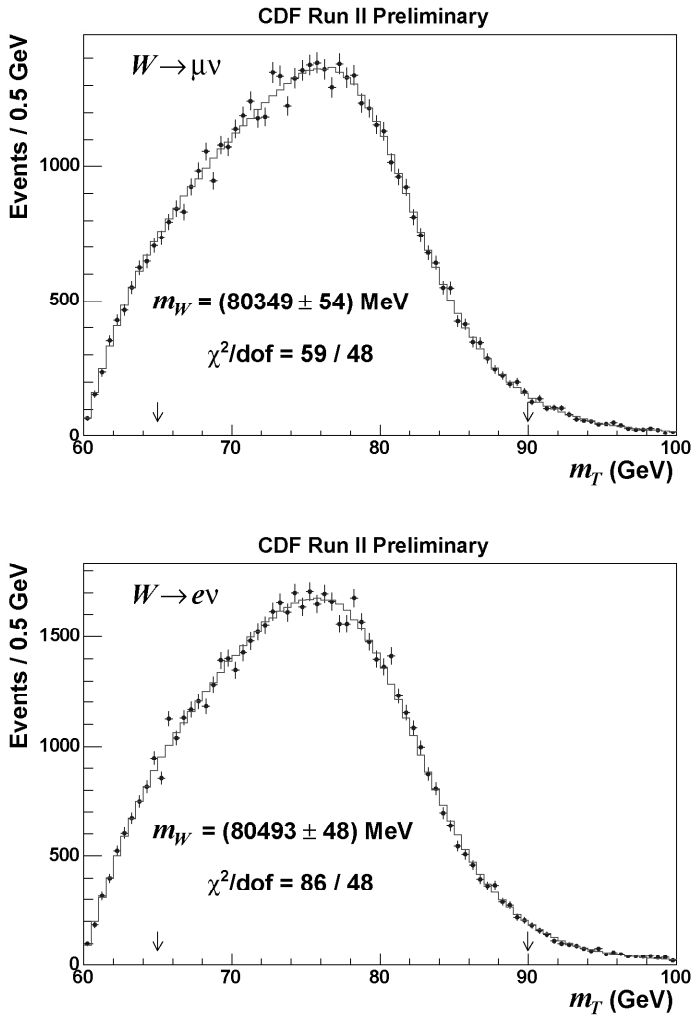

Figure 8: *The fits for m_W to the m_T distribution in $W \to \mu\nu$ (top) and $W \to e\nu$ (bottom) events. The arrows indicate the fit regions and the uncertainties are statistical only.*

References

1. W.-M. Yao *et al.*, J. Phys. G **33**, 1 (2006).
2. M. Awramik *et al.*, Phys. Rev. D **69**, 053006 (2004).
3. CDF Collaboration, to be submitted to Phys. Rev. D.
4. F. Landry, R. Brock, P. M. Nadolsky, and C.-P. Yuan, Phys. Rev. D **67**, 073016 (2003).
5. J. Pumplin *et al.*, Jour. High En. Phys. 0207, 012 (2002).
6. U. Baur, S. Keller and D. Wackeroth, Phys. Rev. D **59**, 013002 (1998).

TOP QUARK PRODUCTION AND DECAY PROPERTIES AT THE TEVATRON

M. Weber
for the CDF and D0 collaborations
Fermilab, P.O. Box 500, Batavia, IL 60510, USA

Abstract

The latest results from the CDF and D0 collaborations on the top-quark pair-production cross section are summarized. Also presented are measurements of the properties of the top quark such as charge, lifetime, and the decay branching ratio $B(t \to Wb)/B(t \to Wq)$. In addition to measurements about the top quark itself, the selected event samples are used to study the helicity of the W boson and to search for additional exotic quarks (t') and resonances in the $t\bar{t}$ invariant mass spectrum.

1 Introduction

The top quark was discovered in 1995 by the CDF and D0 collaborations at the Fermilab Tevatron Collider [1]. The CDF and D0 collaborations are currently taking data in Run 2 of the Tevatron. The increased luminosity and higher collision energy of $\sqrt{s} = 1.96$ TeV allows for precise measurement of top quark production and decay properties. The CDF and D0 detectors are described in Ref. [2] and [3]. The top quark is by far the heaviest particle found to date ($m_t = (170.9 \pm 1.8)$ GeV [4]) [1] and is also the quark with the smallest uncertainty on its mass. Due to its high mass, it plays a central role in the standard model (SM). This article focuses on the latest measurements of the production cross sections, decay, and properties of the top quark. Electroweak production and the top quark mass measurements are discussed in separate articles in these proceedings [5, 6].

2 Top quark pair production via the strong interaction

The top quark can be produced in pairs in $p\bar{p}$ collisions via the strong interaction. Theoretical calculations predict a $t\bar{t}$ production cross section of $6.7^{+0.9}_{-0.7}$ pb at a top quark mass of 175 GeV [7, 8]. This cross section is eleven orders of magnitude lower than the inelastic $p\bar{p}$ cross section and several orders of magnitude lower than b quark and W and Z boson production, which poses a significant challenge to extract a top quark sample with reasonable signal to background ratio.

Once produced, top quarks decay with a lifetime of $\mathcal{O}(10^{-25}$ s), which is shorted than the typical hadronization time of $\mathcal{O}(10^{-24}$ s). In the SM, the top quark decays almost exclusively into a W boson and a b quark, where the W boson decays either hadronically or leptonically. Identification of top quarks require therefore the identification of jets, in particular jets from b quarks, muons, electrons, and neutrinos. The principal algorithm used to identify b quark jets looks for the presence of charged tracks significantly displaced from the primary vertex coming from the decay of B or D mesons, which have finite lifetime (lifetime tagging). Separation of top quark events from background is typically based on the fact, that decay products have hight transverse momenta and good angular separation in the lab frame, which is due to the heavy top quark mass.

The top quark candidate events are classified according to the W boson

[1] This value became available after the conference date.

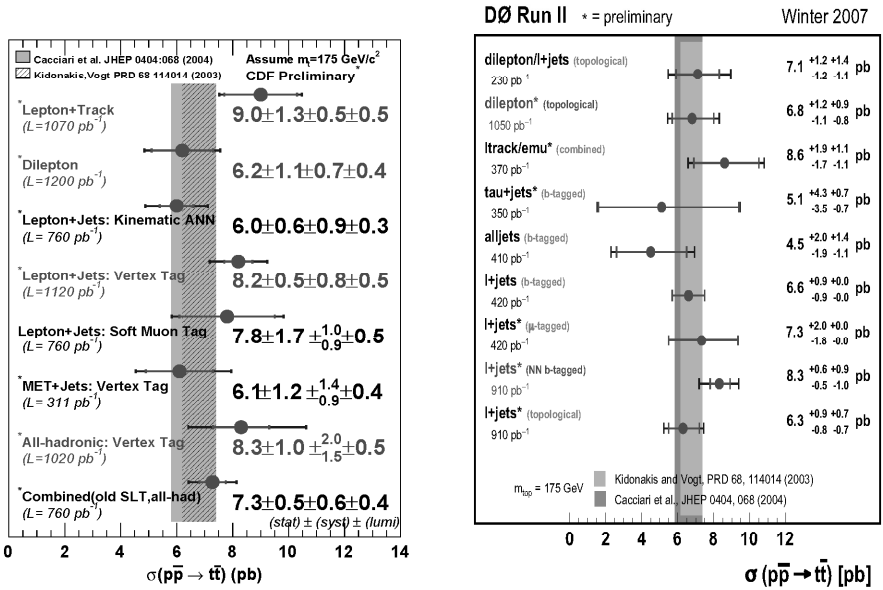

Figure 1: *Compilation of $t\bar{t}$ production cross section measurements by CDF (left) and D0 (right).*

decay mode. Each top quark decays into a W boson, which can decay either hadronically or leptonically. The decay channels are identified as di-lepton (both W bosons decay leptonically), semi-leptonic (mixed), and all-jets (only hadronic decays). The $t\bar{t}$ production cross section has been measured by the CDF and D0 collaborations in all decay channels. Selected measurements are presented here; together with a measurement that distinguishes between gluon fusion and quark anti-quark annihilation production mechanisms. A compilation of top quark production cross section measurements by the CDF and D0 collaborations is shown in Fig. 1.

2.1 Top quark pair production cross section in the semi-leptonic channel

In the semi-leptonic decay channel the identification of the lepton still provides a good signal to background ratio, although not as clean as the di lepton chan nel. The branching ratio is 29% (not including the τ+jets branching ratio) and therefore significantly higher than the di-lepton channel. This makes the semi-leptonic channel the golden channel for top-quark property measurements.

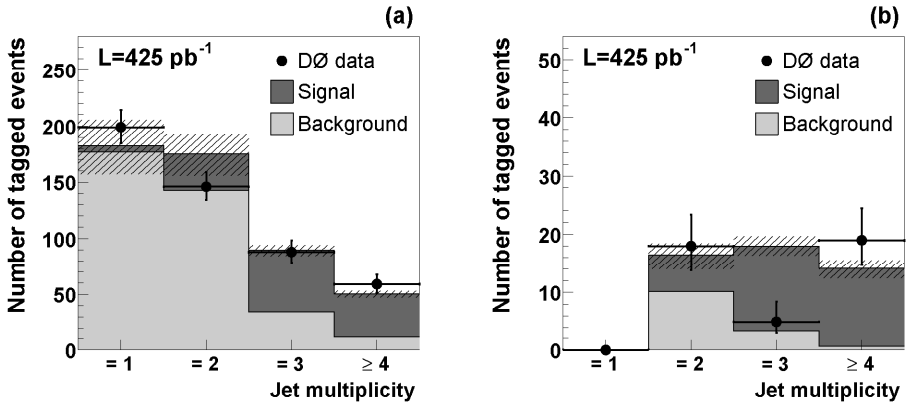

Figure 2: *Observed number of selected events in the lepton+jets sample from D0. The events from data (points) are compared to the total SM prediction (histogram) for (a) single tagged events and (b) double tagged events. The number of $t\bar{t}$ events shown is calculated assuming a cross section of 6.6 pb. The total uncertainty is represented by the hatched band.*

The cross section is measured on a sample of events with an isolated electron (muon) with transverse energy (transverse momentum) $E_T(p_T) > 20$ GeV, missing transverse energy (neutrino) $\not\!\!E_T > 20$ GeV and jets with $E_T > 20$ GeV and $|\eta| < 2.5$. At least one of the jets is also required to be tagged as a b-jet by a lifetime tagger. Efficiency and physics backgrounds (W boson production with jets) are estimated from MC simulation. Instrumental backgrounds (lepton mis-identification in a multi-jet event) are estimated from data. The sample is split by lepton flavor, jet multiplicity, and number of lifetime tagged jets. In figure 2 the selected number of events from 425 pb^{-1} of D0 data are shown as a function of the jet multiplicity in the event. The lower jet multiplicity bins are dominated by background and used to test the SM expectation. The $t\bar{t}$ cross section is then extracted from the excess of events in the bins with $n_{\text{jets}} = 3$ and $n_{\text{jets}} \geq 3$ and is measured to be $\sigma_{t\bar{t}} = (6.6 \pm 0.9(\text{stat.} + \text{syst.}))$ pb for a top quark mass of 175 GeV [9]. This is the most precise measurement of the $t\bar{t}$ production cross section with a relative uncertainty of about 14%, where the main contribution of 11% is statistical; the remaining 8% is due to systematic effects. The measured cross section depends on the assumed mass of the top quark m_t. This dependency was studied and found to be (in pb) $\sigma_{t\bar{t}}(m_t) = 0.000273 m_t^2 + 0.145 m_t + 23.5$.

The best measurement of the $t\bar{t}$ cross section in the semi-leptonic channel from the CDF collaboration yields $\sigma_{t\bar{t}} = (8.2 \pm 0.6(\text{stat.}) \pm 1.0(\text{syst.}))$ pb from 695 pb^{-1} of integrated luminosity. A result based on a smaller dataset was published by the CDF collaboration [10].

2.2 Top quark pair production cross section in the di-lepton channel

The di-lepton channel is characterized by the presence of two isolated high p_T leptons, two high p_T b-jets, and a large missing transverse energy ($\not\!\!E_T$) from the neutrinos. The background contributions due to instrumental effects are multi-jet production, W boson with additional jets (W+jets), and $Z \rightarrow$ll events with mis-measured $\not\!\!E_T$, misidentified jets or misidentified leptons. These backgrounds are estimated from data. Physics background include Z$\rightarrow \tau\tau$ where the τ leptons decay leptonically and WW/WZ (di-boson) production and are estimated from monte carlo (MC) simulation. The di-lepton channel has the advantage of clean lepton identification and therefore high signal to background ratios. However, the branching ratio of 4% (excluding τ lepton decay modes) is low. To increase the efficiency a sample is selected ("lepton+track"), where only one lepton is required to be fully reconstructed, allowing for only a track identified from the decay of the other charge W boson. The signal purity lost by loosening the lepton identification is recovered by the requirement of at least one b-jet to be identified (tagged) by a lifetime tagger. The D0 collaboration excludes events with one W boson decaying into an electron and the other into a muon (electron-muon events) from this analysis and analyzes them separately. The combined cross section from the lepton+track and electron-muon events measured from 370 pb^{-1} of collider data is $\sigma_{t\bar{t}} = (8.6^{+1.9}_{-1.7}(\text{stat.}) \pm 1.1(\text{syst.}) \pm .(\text{lumin.}))$ pb The statistical error is reduced by 15% compared to the D0 result with full lepton identification, keeping the systematic error comparable. The CDF collaboration has recently also performed an inclusive analysis on a lepton+track sample, also including the electron-muon events. ¿From 1.1 fb^{-1} of data a preliminary cross section of $\sigma_{t\bar{t}} = (9.0 \pm 1.3(\text{stat.}) \pm 0.5(\text{syst.}))$ pb is measured, which has a relative uncertainty of only 15%.

2.3 Top quark pair production cross section in the all hadronic channel

The $t\bar{t}$ cross section is also measured in the events where both W boson decay hadronically. This final state is characterized at the tree level by six high p_T jets, two of which are b-jets. The dominant background in this channel is multi-jet production. Although the branching ratio of 46% into this channel

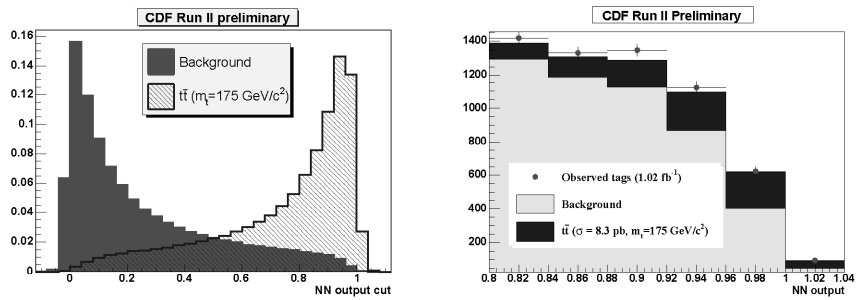

Figure 3: **Left:** *Distribution of the neural network output for test samples of signal and background events.* **Right:** *Distribution of the neural network output on the collider data (points) and the expected background (light histogram). Shown is the the region which is used to extract the cross section (NN> 0.8). The signal histogram is from simulation and normalized to a $t\bar{t}$ cross section of 8.3 pb.*

is relatively large the background processes have much larger cross sections making the signal hard to identify. The CDF collaboration selects 507,000 events with six to eight jets within $\eta < 2$. In this sample it is expected to have 1370 $t\bar{t}$ events, assuming a cross section of 6.6 pb. To improve the signal to background ratio a neural network discriminator (NN) is built from a set of kinematic variables. In figure 3 (left) the NN output is shown for test samples of signal and background.

One can further separate the signal from background by weighting every event with the number of jets that are identified as coming from b quarks (tag). Figure 3 (right) shows the number of tags versus the NN output for collider data from 1.0 fb^{-1} of integrated luminosity. The background expectation comes from data, by applying to the signal sample a probability to tag a jet, measured in a sample of background events (events with $N_{\rm jets} = 4$). ¿From the excess of data events over the background expectation with NN> 0.8, a $t\bar{t}$ cross section of $\sigma_{t\bar{t}} = (8.3 \pm 1.0(\text{stat.})^{+2.0}_{-1.5}(\text{syst.}))$ pb is extracted from 1.0 fb^{-1} of collider data. An earlier measurement based on a smaller dataset is published in [11].

D0 extracts a signal by building invariant masses from two-jet and three-jet combinations in event with at least six jets. The jets for the di-jet invariant mass are required not to be tagged by a lifetime tagger (light jets). For the three-jet invariant mass one of the jets has to be identified as a b-jet. The background estimate is obtained from data by assigning a b-flavor to a jet at

random. After removing the background, an excess of events around the W boson mass is found in the di-jet distribution and around the top quarks mass in the three-jet distribution. ¿From the excess a preliminary cross section of $\sigma_{t\bar{t}} = (12.1 \pm 4.9(\text{stat.}) \pm 4.6(\text{syst.}))$ pb is measured from 360 pb^{-1} of collider data [12].

2.4 Top quark pair production mechanism

Top quarks are produced in pairs via the strong interaction from gluon fusion (gg) and quark-antiquark annihilation ($q\bar{q}$) processes. In proton antiproton collisions at $\sqrt{S} = 1.96$ TeV the contributions from SM calculations are 15% and 85%, respectively [13]. The CDF collaboration performed a measurement of the fraction of the gg over $q\bar{q}$ production rate. This measurement provides a test of the perturbative Quantum Chromo Dynamics(pQCD). Also, it may reveal the existence of exotic top quark production and decay mechanisms [14] that would distort the SM prediction. To discriminate between the gg and $q\bar{q}$ production mechanisms, one takes advantage of the fact that gluons are more likely to radiate a gluon with a low fraction of their momentum than quarks. Thus it is expected to see larger number of low energy particles in gg events than in $q\bar{q}$ events. The observable used for this measurement is the multiplicity of low Pt charged tracks (in the range 0.3 GeV to 2.9 GeV). Figure 4 shows how the number of tracks is sensitive to the number of gluons in the sample. The number of gluons in the top sample is extracted by comparing the distribution of charged tracks in data to calibration samples from almost pure gg or $q\bar{q}$ processes. The di-jet 80-100 GeV sample is used as the "gluon-rich" sample (gg), while the W+0lp is used as "no-gluon" sample ($q\bar{q}$). A residual gg contamination in the W+0lp is removed. The charged tracks density profiles from the gluon-rich and no-gluon distributions are fitted to the of the top events from 1 fb^{-1} of collider data and the fractions extracted. The fit is shown in figure 4, which yields a fraction for the gluon-rich sample of $f_{gg} = 0.07 \pm 0.15$. After correcting for background and different acceptance for the gg and $q\bar{q}$ events one obtains a ratio of $\sigma_{gg\to t\bar{t}}/\sigma_{pp\to t\bar{t}} = 0.01 \pm 0.16(stat) \pm 0.07(syst)$. This result is consistent with the SM expectation.

3 Top quark decay and properties

3.1 Top quark electric charge

The electric charge is a fundamental quantity characterizing a particle. In the SM the top quark is defined as having charge $+2/3e$. In a possible extension

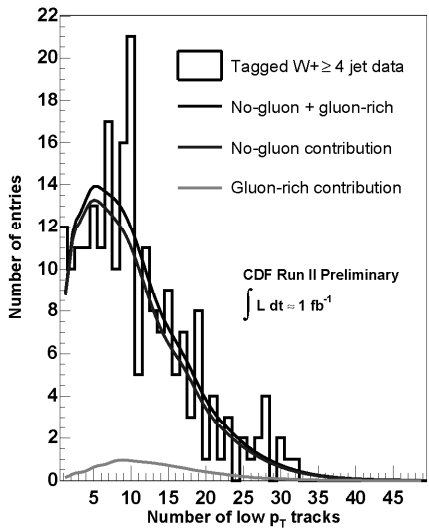

Figure 4: *Distribution of the number of tracks with transverse momentum* P_{t} *between 0.3 GeV and 2.9 GeV for the sample of top quark candidate events from 1* fb^{-1} *of CDF data. The upper line corresponds to the fit result, the two components no-gluon and gluon-rich distributions are also shown as middle and lower line, respectively.*

to the SM an additional quark doublet $(Q_1, Q_4)_R$ with charges (-1/3e,-4/3e) is proposed [15]. The true top quark in such models is too heavy to be observed at the Tevatron and the discovered top quark is indeed Q_4. We can distinguish between the two model by measuring the top quark charge. The measurement is done by the D0 collaboration [16] on a semi-leptonic sample of 32 $t\bar{t}$ candidate events with two jets identified as coming from a b quark. The charge of the top quark is measured from the charge of the lepton and the charge of the associated b-quark. The lepton charge is measured from the curvature of the charged track in the magnetic field of the detector. The b-quark charge is measured from a p_T weighted sum of the charge tracks within jet cone. Although a distinction between the b and $\bar{b}$ is not doable event by event, it is possible on a statistical basis. Figure 5 shows the observed charges in data compared to the expectation from SM and $-4/3e$ scenario.

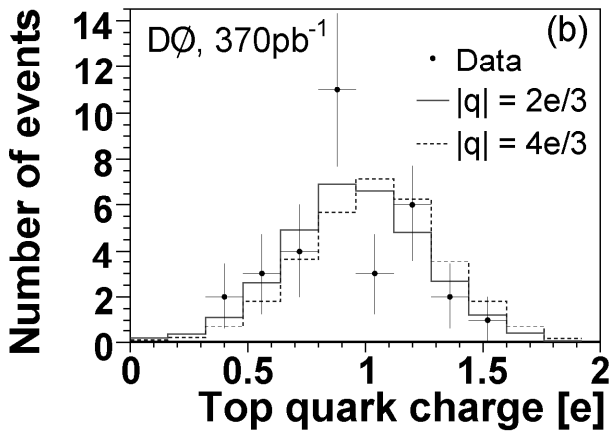

Figure 5: *The measured value of the top quark charge in 32 events selected by D0 compared to the expected distributions in the SM and exotic case.*

To discriminate between the SM and the exotic hypotheses, we form a ratio of the likelihood of the observed set of charges q_i arising from a SM top quark to the likelihood for the set of q_i arising from the exotic scenario, $\Lambda = \prod_i P_{\rm SM}(q_i)/\prod_i P_{\rm EX}(q_i)$. The subscript i runs over all 32 available measurements. The value of the ratio $\Lambda_{\rm obs}$ is determined in collider data and compared with the expected distributions for in the SM and exotic scenarios. Only 7.8% of the ratios Λ obtained from a simulated sample containing exclusively exotic quarks with charge $|q| = 4e = 3$ has a value of equal or larger $\Lambda_{\rm obs}$. This can be used to exclude a scenario with exclusively exotic $|q| = 4/3e$ top quarks at up to a maximal C.L. of 92.2%. A mixture of two heavy quarks, one with $|q| = 2/3e$ and one with $|q| = 4e = 3$ could also be possible. ¿From an unbinned maximum likelihood fit to the observed set of q_i in data, the fraction ρ of exotic quark pairs can be determined. Using a Bayesian prior equal to one in the physically allowed region $0 < \rho < 1$ and zero otherwise, one obtains $0 \leq \rho < 0.80$ at the 90% C.L.

3.2 Top quark lifetime

The top quark lifetime is constrained in the SM to be less than 10^{-25} s. However, there is ample experimental room for long-lived top quark in the experimental data. The top quark lifetime is measured in a sample of $t\bar{t}$ candidates

selected by identifying an electron/muon, at least three jets, and large missing transverse energy. One of the jets is required to be identified as a b jet from a secondary vertex tag. In such events, the impact parameter (d_0) of the lepton to the interaction vertex is typically expected to be very small. The vertex location is constrained by the jets. Large impact parameters would arise from longer-lived top quarks leading to displaced W boson decay vertexes. The distributions of lepton impact parameter d_0, only reflecting the resolution of the measurement is predicted using high momentum electron and muon tracks produced in $Z \to e^+e^-/\mu^+\mu^-$ events. Distribution from non $t\bar{t}$ backgrounds are evaluated from the MC simulation. The observed distribution in data is compared to the predicted distribution. The preliminary result from 318 pb^{-1} of CDF data shows d_0 distributions consistent with expectations and a limit on the top quark lifetime of $c\tau_t < 52.5$ μm at 95% C.L. The analysis is also sensitive to a new long-lived background to $t\bar{t}$ or anomalous top quark production by a long-lived parent particle.

3.3 $B(t \to Wb)/B(t \to Wq)$

CDF and D0 measure the ratio $R = B(t \to Wb)/B(t \to Wq)$ [17]. In the SM this ratio is tightly constrained assuming unitarity of the CKM matrix and exactly three quark generations to the interval 0.9980-0.9984 at 90% CL. Through the measurement of R, the SM and assumptions can be tested. In addition, the cross section measurements using lifetime tagging to identify b-jets also assume R to be unity. A separate determination on R can provide a model independent measurement of the cross section. The measurement is done on a sample similar to the one used for the cross section measurement in the semi-leptonic channel. R is measured from a fit to the relative number of events with zero, one, and two b-tagged jets. Tagging probabilities also affect these relative numbers and is determined from data control samples. The cross section information comes from the sum excess of events over the background expectation. The preliminary result from the simultaneous determination of cross section and R on data from 230 pb^{-1} of integrated luminosity is shown in Fig. 6. R is found to be $1.03^{+0.19}_{-0.17}$(stat.+syst.) and the cross section is $\sigma_{t\bar{t}} = (7.9^{+1.7}_{-1.5}(\text{stat.} + \text{syst.}))$ pb . Using a Bayesian method the lower limit on R is found to be 0.64 at 95% C.L. CDF also measures R and finds a value of $R = 1.12^{+0.21}_{-0.19}(\text{stat.})^{+0.17}_{-0.13}(\text{syst.})$.

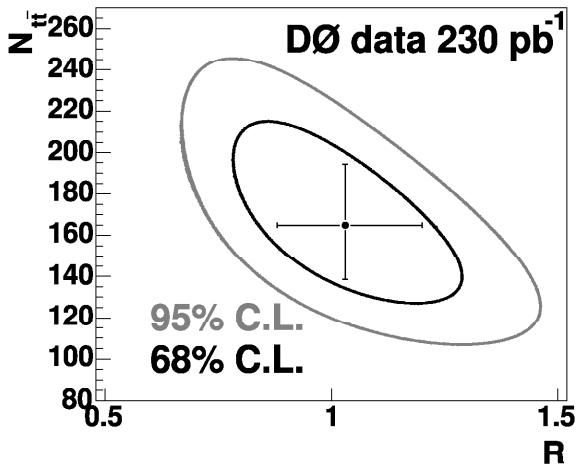

Figure 6: *The 68% and 95% statistical confidence contours in the (R, $N_{t\bar{t}}$) plane. The point indicates the best fit to the data.*

3.4 *W* boson helicity

Given the $V-A$ structure of the electroweak coupling in the SM and the measured top quark mass, the fraction of W bosons from top quark decay with left-handed, longitudinal, and right-handed polarizations are predicted to be $f_0 = 0.70$ and $f_- = 0.30$ with an uncertainty of order 1% and $f_+ = \mathcal{O}(10^{-4})$. A measurement that departs from these values would be a sign of physics beyond the SM. For example, a $V+A$ term in the tWb coupling would increase f_+ but leave f_0 unchanged. Top quark decays with the W boson decaying into an electron or a muon are used to measure the W boson helicity. To measure the helicity of the W boson one looks at the distribution of angles between the charged lepton and the top quark (opposite to the b quark) in the W boson rest frame. By combining events from semi-leptonic and di-lepton decays from 0.37 fb^{-1} of integrated luminosity, the D0 collaboration obtains $f_+ = 0.056 \pm 0.080(\text{stat.}) \pm 0.057(\text{syst.})$ [18]. A value of $f_0 = 0.70$ is assumed for this measurement. The CDF collaboration extracts $f_0 = 0.59 \pm 0.12(\text{stat.}) \pm 0.07(\text{syst.})$ from 1 fb^{-1} and sets a limit of $f_+ < 0.10$ at the 95% C.L.

4 Searches for new physiscs in top quark events

Many models beyond the SM predict new particles that couple preferentially to the top quark. Two searches are presented here, a search for a narrow heavy resonance $Z' \to t\bar{t}$ and the search for an additional quark t' with the same final states as the SM top quark.

4.1 Search for a narrow resonance in $t\bar{t}$ production

A narrow ($\Gamma_{Z'} = 1.2\% M_{Z'}$) heavy resonance decaying into $t\bar{t}$ pairs is predicted in various topcolor models like "topcolor assisted technicolor" [19] and other BSM theories [20]. In some models the resonance couples preferentially to third generation quarks and weakly to leptons. Searches from Run 1 yield limits in the mass of such a resonance of 480 GeV (CDF) and 560 GeV (D0). The search is done by looking at the invariant mass $M_{t\bar{t}}$ distributions of the $t\bar{t}$ pair. A resonance would show as a peak in the exponentially falling $M_{t\bar{t}}$ distribution. CDF performed a search for Z' in a sample of semi-leptonic top quark candidate events. Templates of $M_{t\bar{t}}$ from simulated Z' events with various input masses are compared to the $M_{t\bar{t}}$ spectrum from collider data. No evidence for resonant $t\bar{t}$ production is observed in 955 pb^{-1} of integrated luminosity. A small peak previously reported by CDF in the first 320 pb^{-1} has been diluted. The corresponding preliminary upper cross section limits as a function of $M_{Z'}$ are shown in Fig. 7. A lower limit of the existence of a Z' is set to 720 GeV at the 95% C.L. D0 also performed a search for a resonance in the $t\bar{t}$ invariant mass spectrum. A lower mass limit for a leptophobic narrow Z' resonance of 680 GeV at the 95% C.L. is set from an integrated luminosity of 370 pb^{-1}.

4.2 Search for a heavy fourth generation quark

Several extensions to the SM propose the existence of a heavy fourth generation quark that is not excluded by precision electroweak data or other direct searches [21]. The new quark is referred to here as t', however, it need not to be a standard fourth generation up-type quark. For the presented analysis it is assumed that this new particle is pair produced via the strong interaction, has a mass greater than the SM top quark, and decays promptly into Wq final states. The analysis is performed on a sample of candidate events with a lepton and jets in the final state. The number of expected background events is compared to the number of events selected in data for distributions of the t' mass, M_{reco}, and H_T. The background consists of SM $t\bar{t}$ and W+jets. The

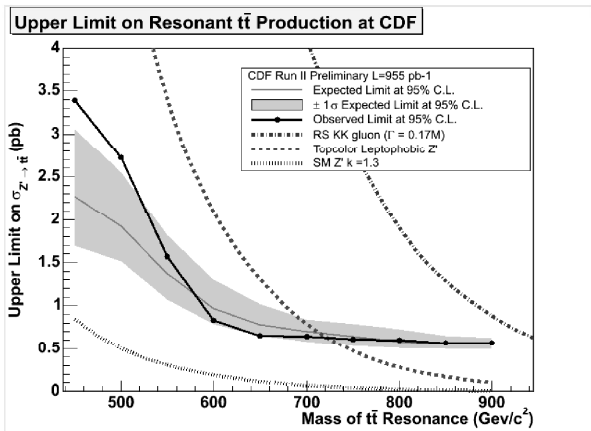

Figure 7: *Upper limit, at 95% C.L., for the production of a heavy narrow resonance decaying into top quark pairs. The dark line is the observed limits, while the band indicates the* ± 1 *and* ± 2 *standard deviation expected limits. Also shown are dotted lines from theoretical predictions for various models of new physics.*

mass of the t' quark is reconstructed from a χ^2-fit to the kinematic properties of the final state objects. The significance of a t' quark signal is extracted from a binned likelihood fit to H_T and $M_{\rm reco}$. No evidence for the production of t' quark is found. The upper limits for the production cross section as a function of t' quark mass are shown in Fig. 8. A lower mass limit for t' can be set at $m_{t'} > 258$ GeV at 95% C.L.

5 Conclusions

Twelve years after the top quark discovery, we are now in the position to make precision measurements. The top quark production cross section via the strong interaction has been measured in all major decay channels and is found to be consistent with the SM expectation. However, the uncertainties on the cross section still allow exotic decay or production mechanisms. Measurements of the properties of the top quark indicate that its charge is consistent with $+2/3e$ and its lifetime $c\tau$ shorter than 52.5 μm at 95% C.L., both consistent with the SM top quark. One also looks at top quark events to make detailed studies of the electroweak Wtb vertex. Branching ratios and W boson helicity are found

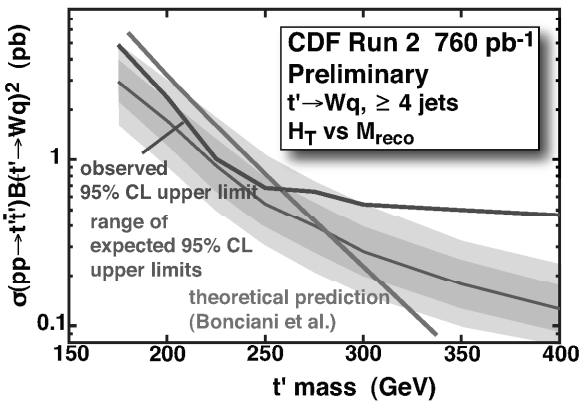

Figure 8: *Upper limit, at 95% CL, for the production of a hypothetical fourth generation t' quark as a function of t' quark mass. Also shown is the a theoretical calculation for the t' production cross section. The band represents ± 1 and ± 2 standard deviation expected limits.*

to be consistent with SM expectation. No evidence for a narrow resonance in top quark decays or additional fourth generation quark is found and limits on the production cross section are set. Understanding top quark production and properties will be crucial for success at the large hadron collider (LHC). What we learn at the Tevatron, both in terms of physics and analysis tools, extends directly to the LHC.

References

1. D0 collaboration, S. Abachi *et al.*, Phys. Rev. Lett. **74**, 2632 (1995); CDF Collaboration, F. Abe *et al.*, Phys. Rev. Lett. **74**, 2626 (1995).

2. P. Azzi *et al.*, Nucl. Instrum. and Method A **360**, 137 (1995).

3. V. Abazov *et al.*, Nucl. Instr. and Methods A **565**, 463 (2006).

4. Tevatron Electroweak Working Group (for the CDF and D0 Collaborations), hep-ex/0703034v1.

5. P. Movilla Fernandez, for the CDF and D0 collaborations, "Precision Determination of the Top Quark Mass", these proceedings.

6. A. Juste, for the CDF and D0 collaborations, "Single Top Quark Production at the Tevatron", these proceedings.
7. M. Cacciari *et al.*, JHEP **404**, 68 (2004).
8. N. Kidonakis and R. Vogt, Phys. Rev. D **68**, 114014 (2003).
9. V.M. Abazov *et al.*(D0 collaboration), Phys. Rev. D **74**, 112004 (2006).
10. A. Abulencia *et al.*(CDF collaboration), Phys. Rev. Lett. 97, 082004 (2006).
11. A. Abulencia *et al.*(CDF collaboration), Phys. Rev. D **74**, 072005 (2006).
12. V.M. Abazov *et al.*(D0 collaboration), hep-ex/0612040.
13. J.H. Kühn, hep-ph/9707321.
14. G.L. Kane and S. Mrenna, Phys. Rev. Lett. **77**, 3502-3505 (1996).
15. D. Chang *et al.*, Phys. Rev. D **59**, 09153 (1999).
16. V.M. Abazov *et al.*(D0 collaboration), Phys. Rev. Lett. **98**, 041801 (2007).
17. V.M. Abazov *et al.*(D0 collaboration), Phys. Lett. B **639**, 616 (2006). S. Abachi *et al.*(CDF collaboration), Phys. Rev. Lett **95**, 102002 (2005).
18. V.M. Abazov *et al.*D0 collaboration), Phys. Rev. D **75**, 031102(R) (2007).
19. C. T. Hill, Phys. Lett. **266B**, 419 (1991).
20. A. Leike, Phys. Rep. **317**, 143 (1999); J. Rosner, CERN-TH/96-169; B. Lillie, L. Randall, L.T. Wang, hep-ph/0701166; T. Rizzo, Phys. Rev. D **61**, 055005 (2000); L. Sehgal, M. Wanninger, Phys. Lett. B **200**, 211 (1988).
21. C. Wagner *et al.*, hep-ph/0109097; T. Han *et al.*, Phys. Lett. **563B**, 191 (2003); H.-J. He, N. Polonsky, and S. Su, hep-ex/0102144; L. Okun *et al.*, hep-ph/0111028.

PRECISION DETERMINATION OF THE TOP QUARK MASS

Pedro A. Movilla Fernández
Lawrence Berkeley National Laboratory,
1 Cyclotron Rd., Berkeley, CA 94720, U.S.A.

For the CDF and DØ Collaborations

Abstract

The CDF and DØ collaborations have updated their measurements of the mass of the top quark using proton-antiproton collisions at $\sqrt{s}$=1.96 TeV produced at the Tevatron. The uncertainties in each of the of top-antitop decay channels have been reduced. The new Tevatron average for the mass of the top quark based on about 1 fb^{-1} of data per experiment is 170.9±1.8 GeV/c^2.

1 Introduction

The discovery of the top quark by the CDF and DØ collaborations 1995 [1] has marked the beginning of a successful physics program at the Tevatron. The mass of the top quark (M_t) is a fundamental parameter of the Standard Model (SM), but more importantly, its surprisingly high value gives the top quark particular relevance in the calculation of other SM parameters. Electroweak corrections to the W propagator introduce a quadratic dependence of the W boson mass (M_W) on M_t. M_W is also expected to depend logarithmically on the mass of the long-hypothesized but still unobserved Higgs boson (M_{H}). Thus, a precision measurement of M_t and M_W provides a mean to impose a constraint to M_{H}. The presence of further loop corrections in which heavy unknown particles are involved might lead to signatures beyond the SM. The Yukawa coupling to the Higgs field of $\mathcal{O}(1)$ indicates that the top quark might play a special role in the mechanism of electroweak symmetry breaking.

The determination of the top quark mass is therefore a very active topic in Tevatron Run-II. The top quark mass has been measured in all $t\bar{t}$ decay topologies with increasing precision. Improvements are based on the performance of the Tevatron, the better understanding of the detectors, and particularly on innovative analysis techniques. Here we report on the state-of-the-art of CDF and DØ measurements based on up to $1\,\mathrm{fb}^{-1}$ of analyzed data per experiment.

2 Experimental Challenges

The upgraded Tevatron complex started in 2001 to produce collisions of protons and antiprotons at $\sqrt{s} = 1.96\,\mathrm{TeV}$ with steadily increasing instantaneous luminosities up to a record of $3{\times}10^{32}\,\mathrm{cm}^{-2}\mathrm{s}^{-1}$. The CDF and DØ experiments [2] have integrated a luminosity of about $2\,\mathrm{fb}^{-1}$ each, the projected goal for the end of Run-II is 4-8 fb^{-1}. Both experiments are multipurpose detectors which cover the interaction points almost hermetically. The inner volumes contain precision tracking systems and silicon vertex detectors embedded in a solenoidal magnetic field. The magnets are surrounded by electromagnetic and hadronic calorimeters. The outermost parts consist of muon systems for the detection of penetrating particles. The experiments are running with a data taking efficiency of better than 80%.

At Tevatron energies, SM top quarks are mainly produced in pairs through quark-antiquark annihilation (85%) and gluon-gluon fusion (15%). The theoretical $t\bar{t}$-prodution cross section is $7.8{\pm}1.0\,\mathrm{pb}$ [3] for a top quark mass of $170\,\mathrm{GeV}/c^2$, which corresponds to approximately one top quark pair produced in 10^{10} inelastic collisions. The top quark does not hadronize and promptly undergoes the transition $t \to Wb$ with a branching ratio of BR$\sim$100%. The event signature is thus defined by the decay modes of the two W bosons. We

distinguish the "di-lepton" channel, $t\bar{t} \rightarrow (l_1^+\nu_1 b)(l_2^-\bar{\nu_2}\bar{b})$ (5% fraction), the "lepton-jets" channel (30% fraction), $t\bar{t} \rightarrow (q_1\bar{q_2}b)(l^-\bar{\nu}\bar{b})$, and the "all-jets" channel, $t\bar{t} \rightarrow (q_1\bar{q_2}b)(q_3\bar{q_4}\bar{b})$ (44% fraction), where the q_i's stand for quarks and l denote an electron e or a muon μ (τ's are usually ignored).[1]

Top quark analyses require full detector capabilities. The measurement of the leptonic W decay modes relies on the clean identification of electrons and muons. The hermeticity of the calorimeter is essential for the partial reconstruction of the momentum of undetectable neutrinos through the measurement of the missing transverse energy. The reconstruction of the primary quarks from $t\bar{t}$ decays involves the accurate measurement of calorimeter energy deposits and their appropriate clustering into jets. Quark flavor information is provided by vertex detectors via the reconstruction of displaced vertices consistent with long-lived b-hadrons, which are present in all decay modes. The "b-tagging" is crucial to reduce background contributions and the number of possible jet-quark assignments.

Top quark measurements critically depend on the accurate knowledge of the jet energy scale (JES), which incorporates corrections of the raw jet energies for physics and instrumental effects as well as for jet definition artefacts. The JES is currently known *a priori* to a level of 2-3% for jets typical in $t\bar{t}$ events [4)] and constitutes the dominant source of systematic uncertainties.

3 Measurement Techniques

The mass extraction techniques employed by CDF and DØ can be subdivided into two categories. The *Template Method* is based on the evaluation of one observable per event correlated with the top quark mass M_t, and a comparison of simulated distributions of this observable ("templates") with varying M_t with the data. Typically, some kind of reconstructed top quark mass m_t is taken, for example the output of the kinematic fit of a $t\bar{t}$ hypothesis to the event. Recent analyses have introduced the JES as a second template variable using distributions of the invariant di-jet mass m_W of the hadronically decaying W boson. The m_t and m_W distributions provide two-dimensional sample likelihoods which allow a simultaneous determination of M_t and the JES *in situ*. The Template Method is computationally simple, but it uses limited event information by evaluating just one or two numbers per event, and it treats well and badly reconstructed events equally. Refined Template Method analyses therefore apply weights to the events using further kinematic information.

The *Matrix Element Method* enhances the mass information by exploring the SM predictions for top quark dynamics. For each event, a probability density curve $\mathcal{P}(M_t)$ is extracted, which expresses the quality of the agreement

[1] A review of top quark property measurements is given by M. Weber in these proceedings.

of the event with a signal or background process as a function of M_t. The per-event probabilities are multiplied, and the maximum position of the resulting curve gives the most likely value for M_t for the whole signal candidate sample. Recent measurements have extended the technique to allow the JES be re-adjusted *in situ* using the invariant mass of the W boson as a reference:

$$\mathcal{P}_{t\bar{t}}(x|M_t, \mathrm{JES}) \propto \sum_{\mathrm{comb}} \int \mathrm{d}\sigma_{t\bar{t}}(y|M_t)\mathrm{d}q_1\mathrm{d}q_2 f(q_1)f(q_2)w(x|y, \mathrm{JES}) \,. \quad (1)$$

$\mathrm{d}\sigma_{t\bar{t}}$ denotes the differential $t\bar{t}$ cross-section (using a tree level matrix element) for a configuration of parton level momenta y, given M_t, and contains all integration details for the six-body phase space. $f(q_i)$ is the proton-parton density function for given momenta q_i of the two incoming quarks. The transfer functions $w(x|y, \mathrm{JES})$ are probabilities of a set of variables x (*e.g.* transverse jet momenta) to be measured given a set of parton level quantities y (*e.g.* quark momenta) and a shift of the JES from its *a priori* known value. A JES hypothesis yielding to a W mass which is inconsistent with the known W mass and width penalizes the event probability. The transfer functions account for hadronization effects and detector resolution. The sum usually goes over all possible jet-quark permutations and neutrino solutions. The background probabilities are calculated analog to Eq. (1) but have no M_t dependence.

Since the method buys its increased statistical power by CPU-intensive numerical integrations, simplifying assumptions must be made in the interest of computational tractability. Lepton momenta and jet angles are often treated as exactly measured quantities, and only the probability density shapes of the dominant background types are calculated. Due to the various approximations, the method must be calibrated using the behavior of fully simulated Monte Carlo (MC) samples with known value for M_t.

Both methods depend on trustworthy physics event generators and detector simulations. The *in-situ* technique has the advantage that the largest part of the JES uncertainty becomes a statistical component of the top quark mass uncertainty, which thus will scale down as more luminosity is collected.

4 Measurements in the Lepton-Jets Channel

The lepton-jets channel is viewed as a good compromise between all decay modes because it has a reasonable branching fraction and a good S/B ratio between ∼0.2-10, dependent on the b-tag requirement. The final state is characterized by well defined kinematics with moderate combinatorial quark-jet ambiguity. There are twelve ways to assign jets to quarks if no b-tag information is used, and six (two) possibilities in case of one (two) b-tags (ignoring the physically equivalent permutations of the quarks from the W boson). The number of kinematic solutions doubles due to the twofold ambiguity of the neutrino longitudinal momentum.

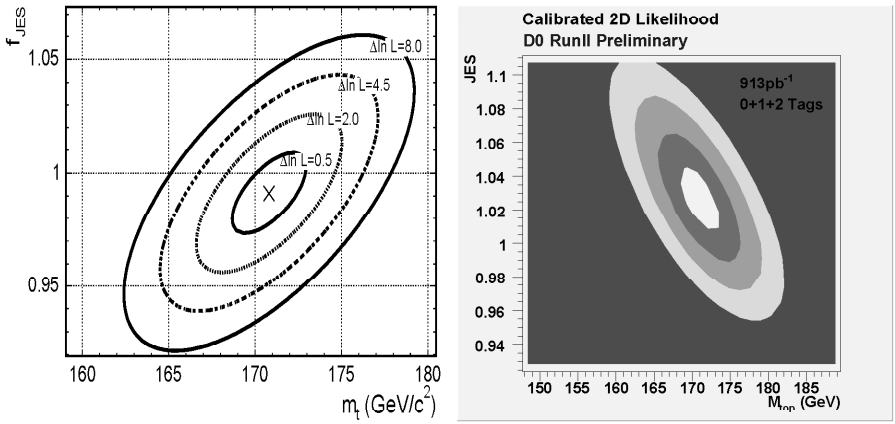

Figure 1: *Likelihood contours obtained using the Matrix Element Method in the lepton-jets channel. Left: CDF result with 955pb^{-1}; Right: DØ result with 913pb^{-1} (shown for e+jets events only).*

The event selection of both experiments usually requires one well contained electron or muon candidate with transverse momentum $p_{\mathrm{T}} > 20\,\mathrm{GeV}/c$, a sizable amount of missing transverse energy $\not\!\!E_{\mathrm{T}} > 20\,\mathrm{GeV}$ to account for the neutrino, and at least four jets with $E_{\mathrm{T}} \geq 15(20)\,\mathrm{GeV}$ at CDF (DØ). Matrix element measurements are restricted to events with exactly four jets, in order to match the predicted final state partons, whereas template based analyses also allow events with sub-leading jets to pass the selection. Various analyses subdivide the data into disjoint samples with different b-tag cuts in order to handle statistical power against sample purity. The background of this channel mainly consists of W+jets final states (*e.g.* $Wb\bar{b}q\bar{q}$, $Wq\bar{q}q\bar{q}$ with fake b-tags, *etc.*) and QCD multi-jets events in which jets are misidentified as leptons.

Both experiments obtain the most precise results using the Matrix Element Method with *in situ* JES calibration. CDF has analyzed [5] a data sample of $955\,\mathrm{pb}^{-1}$ and found 167 b-tagged candidate events (22 ± 8 expected background). The signal ($\mathcal{P}_{t\bar{t}}$) and background probability densities ($\mathcal{P}_{W+\mathrm{jets}}$) are calculated similarly to Eq. (1) using a $t\bar{t}$ leading order matrix element and a MC based parametrization for the W+jets process (which is also found to adequately describe the QCD multi-jets probabilities). A sample likelihood

$$\mathcal{L}(M_t, \mathrm{JES}) \propto \prod_{i}^{\#\mathrm{events}} \left[f_t \mathcal{P}^{(i)}_{t\bar{t}}(M_t, \mathrm{JES}) + (1 - f_t)\mathcal{P}^{(i)}_{W+\mathrm{jets}}(\mathrm{JES}) \right] \qquad (2)$$

is used to extract simultaneously M_t and the JES. The signal fraction f_t is allowed to float. Fig. 1 (left) shows the resulting likelihood contours. The analysis yields $M_t = 170.8 \pm 2.2^{(\mathrm{stat.+JES})} \pm 1.4^{(\mathrm{syst.})}\,\mathrm{GeV}/c^2 = 170.8 \pm 2.6\,\mathrm{GeV}/c^2$, where

the statistical component (stat.+JES) includes an uncertainty of $1.5\,\mathrm{GeV}/c^2$ due to the JES. With a relative uncertainty of 1.5%, this result constitutes the most precise measurement to date.

DØ has reported matrix element analyses [6] based on $913\,\mathrm{pb}^{-1}$ and 507 candidate events with ≥ 0 b-tags (373 ± 39 estimated background). Two measurements are performed, one which uses the b-tagger to assign weights to the jet-quark assignments in the event probabilities, and a second one which focuses on event topology only. The b-tagging analysis calculates individual likelihoods similarly to Eq. (2) for three subsamples with 0, 1 and ≥ 2 b-tags, and joins them using individually optimized values for f_t. Fig. 1 (right) shows the corresponding overall likelihood extracted from an electron-jets subsample. Differently from CDF, a JES prior is used, and also the finite resolution of the electron and muon momentum is considered in the transfer functions. The result obtained is $M_t = 170.5 \pm 2.4^{(\mathrm{stat.+JES})} \pm 1.2^{(\mathrm{syst.})}\,\mathrm{GeV}/c^2 = 170.5 \pm 2.7\,\mathrm{GeV}/c^2$ (1.6% precision), where the uncertainty from the JES is $1.6\,\mathrm{GeV}/c^2$. The result of the pure topological analysis is $M_t = 170.5 \pm 2.5(\mathrm{stat.} + \mathrm{JES}) \pm 1.4^{(\mathrm{syst.})}\,\mathrm{GeV}/c^2 = 170.5 \pm 2.9\,\mathrm{GeV}/c^2$ (1.7% precision). The b-tagging analysis is the most precise DØ measurement and in excellent agreement with the CDF result.

The *in situ* JES calibration technique was pioneered by CDF and originally used in Template Method analyses, of which the most recent one [7] uses a data set of $680\,\mathrm{pb}^{-1}$. Four exclusive samples with different S/B ratio and sensitivity to M_t are selected according to different b-tag requirements and jet E_{T} cuts. For each sample, templates for M_t and the JES are formed using the reconstructed top quark mass (corresponding to the quark-jet assignment with the lowest χ^2) and the invariant W di-jet mass, which are then compared to the data using an unbinned likelihood. A cut to the χ^2 in addition to the standard selection ensures that only well reconstructed events are considered. Using 360 selected candidate events (97 ± 23 background from a constrained fit) the result obtained is $M_t = 173.4 \pm 2.5^{(\mathrm{stat.+JES})} \pm 1.3^{(\mathrm{syst.})}\,\mathrm{GeV}/c^2 = 173.4 \pm 2.8\,\mathrm{GeV}/c^2$ (1.6% precision), which is compatible with the matrix element result. The JES contribution to the statistical uncertainty is $1.8\,\mathrm{GeV}/c^2$. The *in situ* calibration reduced the *a priori* JES uncertainty by about 40%.

CDF has recently demonstrated that the Template Method can be improved by combining the kinematic top quark mass solutions of the three best quark-jet combinations [8]. The analysis addresses the problem that the smallest χ^2 corresponds to the correct association in less than 50% of the time. For each event, the three solutions are combined considering their correlations. A analysis of $1030\,\mathrm{pb}^{-1}$ of data containing 645 candidates (≥ 0 b-tags) yields $M_t = 168.9 \pm 2.2^{(\mathrm{stat.})} \pm 4.2^{(\mathrm{syst.})}\,\mathrm{GeV}/c^2 = 168.9 \pm 4.7\,\mathrm{GeV}/c^2$ (2.8% precision), the best result achieved in this channel without *in situ* JES calibration.

The DØ collaboration has employed the "Ideogram Method" (extended by *in situ* JES calibration) for the first time in the lepton-jets channel us-

ing a $425\,\mathrm{pb}^{-1}$ data sample [9] with 230 candidate events (123 ± 15 expected background). Instead of evaluating matrix elements, the analysis uses the outcome of a kinematic fitter, b-tagging information and a multivariate S/B discriminant to extract per-event probability densities similarly to Eq. (2). The signal probability $\mathcal{P}_{tt}$ considers all possible jet-quark permutations, which are weighted according to fit quality and compatibility with b-tag information. The shape of the M_t distribution of the correct permutation is given by a relativistic top quark Breit Wigner function convoluted with an experimental Gaussian resolution function, whereas the shape corresponding to the wrong permutation as well for the background probability density $\mathcal{P}_{W+\mathrm{jets}}$ is derived using appropriate MC simulations. The result obtained is $M_t = 173.7 \pm 4.4^{(\mathrm{stat.+JES})}\,{}^{+2.1}_{-2.0}{}^{(\mathrm{syst.})}\,\mathrm{GeV}/c^2$ (2.8% precision).

CDF has performed further Template Method analyses in the lepton-jets channel which currently lack statistical precision but are important in the long run because they are aiming at establishing measurements with different inherent systematics. Here we mention the "Decay Length Technique" [10], which uses the transverse distance of a jet's secondary vertex from the primary vertex as a template variable. The method is motivated by the expectation that b-hadrons from top quark decays are boosted and thus correlated with M_t. The analysis solely relies on tracking information and has no JES dependence. Using 375 signal candidates with 456 b-tagged jets found in a $695\,\mathrm{pb}^{-1}$ sample with at least three jets per event yields $M_t = 180.7^{+15.5}_{-13.4}{}^{(\mathrm{stat.})} \pm 8.6^{(\mathrm{syst.})}\,\mathrm{GeV}/c^2$. Despite the low statistical precision, the method has proven its practicability and can make significant contributions at LHC.

5 Measurements in the Di-Lepton Channel

The di-lepton channel provides pure signal samples but suffer from a poor branching ratio of about 5%. Experimentally, the event kinematics is under-constrained due to the presence of two neutrinos and the availability of just one missing E_T observable. Template-based analyses therefore assume values for certain variables (*e.g.* the neutrino η) in order to extract a solution for the top quark mass, and assign weights to the different solutions. Matrix element analyses "naturally" integrate over unconstrained variables.

For the most recent measurements presented here, both CDF and DØ consider only events containing two well identified electrons or muons. Candidate events must have two oppositely charged leptons with typically $E_\mathrm{T} \geq 20(15)\,\mathrm{GeV}$ in case of CDF (DØ) and at least two jets with $E_\mathrm{T} \geq 15(20)\,\mathrm{GeV}$. The required amount of missing transverse energy is typically higher than in the lepton-jets channel, at least $\not\!\!E_\mathrm{T} \geq 25(35)\,\mathrm{GeV}$. Additional cuts are applied based on the angle between the $\not\!\!E_\mathrm{T}$ vector and the transverse direction of the leptons and jets, as well as on further topological variables. For ee and $\mu\mu$ events, the $\not\!\!E_\mathrm{T}$

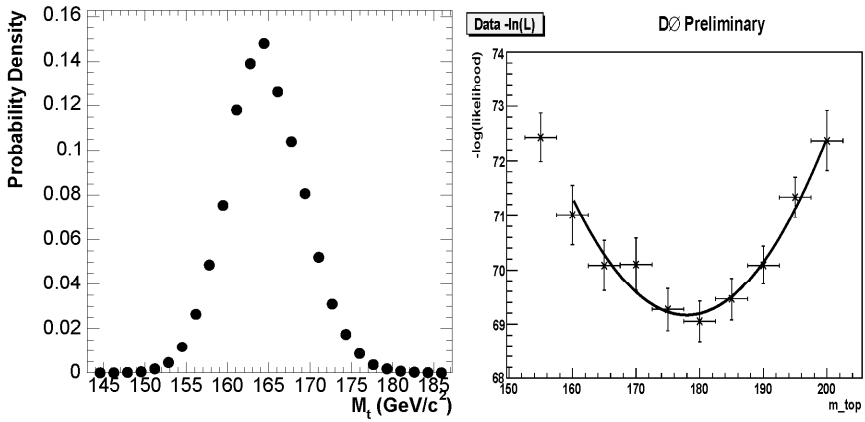

Figure 2: *Di-lepton channel results: Left: Joint likelihood vs. M_t extracted by CDF with the Matrix Element Method (1030 pb^{-1}). Right: Log likelihood curve obtained by DØ using the Matrix Weighting (835 pb^{-1}, $e\mu$ events).*

requirement is modified (or the event is rejected in case of DØ) if the di-lepton invariant mass lies within a given window around the Z boson mass, in order to reduce more effectively background events with $Z \to l^+l^-$ decays. The background is dominated by the Drell-Yan process, di-boson contributions like WW+2 jets, and W+3 jet events where one jet was misidentified as a lepton. The S/B ratios range from ∼2 for ≥ 0 b-tags and ∼20 for ≥ 1 b-tag.

The best measurement in this channel is achieved by CDF using the Matrix Element Method [11]. The event probability density is given by a linear combination of the probabilities for the signal and the three major background processes using M_t-dependent weights from MC predictions. The individual probabilities are calculated similarly to Eq. (1), except for the important difference that no JES *in situ* calibration is possible on the basis of the signal process. Additional transfer functions for the $t\bar{t}$ transverse momentum are introduced using the E_{T} of the sub-leading jets and the unclustered E_{T}, in order to account for recoil effects induced by ISR. The measurement is calibrated to account for limitations due to background modeling and further simplifying assumptions. From a data set of $1030\,\mathrm{pb}^{-1}$ containing 78 candidate events (27 ± 5 expected background), the likelihood curve shown in Fig. 2 (left) is extracted. The result obtained is $M_t = 164.5 \pm 3.9^{(\mathrm{stat.})} \pm 3.5^{(\mathrm{JES})} \pm 1.7^{(\mathrm{syst.})}\,\mathrm{GeV}/c^2 = 164.4 \pm 5.5\,\mathrm{GeV}/c^2$ (3.3% precision). By including background probabilities, the error is reduced by 15% compared to a measurement based on signal probability only. The analysis was cross-checked using a subset of 30 events with at least one b-tag, yielding $M_t = 167.3 \pm 4.6^{(\mathrm{stat.})} \pm 3.3^{(\mathrm{JES})} \pm 1.9^{(\mathrm{syst.})}\,\mathrm{GeV}/c^2 = 167.3 \pm 6.0\,\mathrm{GeV}/c^2$ (3.6% precision).

The CDF and DØ collaborations have also applied the Template Method in the di-lepton channel. DØ has employed two neutrino solution weighting schemes [12]. The "Neutrino Weighting Method" scans over the top quark mass m_t and the pseudorapidity of the two neutrinos (ignoring the measured $\not\!\!E_{\rm T}$), and assigns weights based on the compatibility of the total transverse neutrino energy with the observed $\not\!\!E_{\rm T}$. For a given m_t, the weights resulting from all neutrino η assumptions and two possible jet-quark assignments are summed. Detector resolutions are taken into account by averaging the weights from repeated calculations with input observables randomly smeared within their resolutions. M_t templates are formed using the sum of weights versus m_t distributions. The analysis is performed with separate templates for ee, $e\mu$ and $\mu\mu$ events, which are compared with the data using a maximum likelihood fit. Using a sample of $1050\,{\rm pb}^{-1}$ containing 57 candidate events ($10.3^{+2.9}_{-3.7}$ expected background), the result obtained is $M_t = 172.5 \pm 5.8^{(\rm stat.)} \pm 5.5^{(\rm syst.)}\,{\rm GeV}/c^2 = 172.5 \pm 8.0\,{\rm GeV}/c^2$, which is the best single DØ measurement in this channel (4.6% precision).

Another scheme called "Matrix Weighting Method" assumes a value for m_t and calculates the (at most) four corresponding neutrino solutions given the W mass, the jet and charge lepton momenta and $\not\!\!E_{\rm T}$. A weight is assigned based on the agreement of matrix element predictions for the charged lepton $p_{\rm T}$ with the observed one. Templates are built using the m_t values giving the maximum event weight, and compared with the data using a binned maximum likelihood fit. Fig. 2 (right) shows the log likelihood curve thus obtained. Using 28 signal candidates in the $e\mu$-channel ($4.4^{+2.6}_{-1.4}$ expected background) selected in a sample of $835\,{\rm pb}^{-1}$, DØ extracts $M_t = 177.7 \pm 8.8^{(\rm stat.)}\,^{+3.7}_{-4.5}\,^{(\rm syst.)}\,{\rm GeV}/c^2 = 177.7 \pm 9.7\,{\rm GeV}/c^2$ (5.5% precision).

CDF has also used the Neutrino Weighting Method in early Run-II as well as a weighting scheme which scans the neutrino's azimuth angle. Here we report on a more recent measurement known as "Full Kinematic Method" [13]. The analysis assumes that the distribution of the longitudinal momentum $p_z(t\bar{t})$ of the $t\bar{t}$ system is a zero-centered Gaussian with 195 GeV/c width, as indicated by MC simulations and supported by lepton-jets data. Studies show that the $p_z(t\bar{t})$ distribution has no mass dependence and is equal for $t\bar{t}$ and background. Given $p_z(t\bar{t})$ and using the known b and W masses, one can solve the kinematic equations numerically. The finite resolution is taken into account by smearing the b-quark energies, $\not\!\!E_{\rm T}$ and $p_z(t\bar{t})$ within the expected uncertainties, and repeatedly solving the equations. From the resulting m_t distribution, the most probable value is taken to build templates separately for events with and without b-tag. A maximum likelihood fit to a $1.2\,{\rm fb}^{-1}$ data set with 70 candidates (26 ± 6 background) yields $M_t = 169.1^{+5.2}_{-4.9}\,^{(\rm stat.)} \pm 2.9^{(\rm JES)} \pm 1.0^{(\rm syst.)}\,{\rm GeV}/c^2 = 169.1 \pm 5.9\,{\rm GeV}/c^2$ (3.5% precision). This is the most precise template-based measurement in the di-lepton channel to date.

6 Measurements in the All-Jets Channel

Measurements in the all-jets channel are motivated by the high branching ratio of 44% and the complete reconstruction of the top quarks, relying only on hadronic jets. The final state has well-defined kinematics because no neutrino appears. The channel is challenging due to the huge background contamination and the large combinatorial jet-quark ambiguity. Making no flavor requirement and treating top-antitop permutations and the W di-jet permutations equally gives 90 combinations.

So far, only the CDF collaboration has reported measurements in this channel. The expected multi-jets final state has spherical topology and well-balanced visible energy. The selection therefore requires exactly six well-contained jets with $E_{\mathrm{T}} > 15\,\mathrm{GeV}$ and a missing E_{T} significance $\not\!\!E_{\mathrm{T}}/\sqrt{\sum E_{\mathrm{T}}} < 3\,\mathrm{GeV}^{\frac{1}{2}}$. Events containing high p_{T} electrons or muons are rejected. Further cuts on kinematic and topological variables are applied to purify the sample. The remaining background is dominated by QCD multi-jet events ($bb4q$, $6q$).

The first published Run-II measurement in the all-jets channel is based on the Ideogram Method [14]. The selection used in this analysis yields S/B$\sim$1/25 without b-tagging (compared to $\sim$1/3500 at trigger level) and S/B$\sim$1/5 including b-tag information. Similar to the DØ lepton-jets ideogram analysis described in Sec.4, individual signal probability densities for the right and wrong jet-quark permutations as well as background probability densities are formed, and weights are assigned using the fit χ^2 and a b-tag probability measure. To improve the S/B discrimination in the kinematic fit, the probabilities are expanded in two dimensions using the invariant masses of both the top and the antitop quark. For the signal they are indistinguishable and expected to peak at the "right" value for M_t, but for background events at least one peaks at too low values. The sample likelihood allows for a simultaneous optimization of both M_t and the sample purity, because the QCD background cross sections are not well known. The result obtained using 290 b-tagged signal candidates in a $310\,\mathrm{pb}^{-1}$ sample is $M_t = 177.1 \pm 4.9^{(\mathrm{stat.})} \pm 4.3^{(\mathrm{JES})} \pm 1.9^{(\mathrm{syst.})}\,\mathrm{GeV}/c^2 = 177.1 \pm 6.8\,\mathrm{GeV}/c^2$ (3.8% precision).

The precision in the all-jets channel is greatly improved in a recent template analysis [15] due to the adoption of the JES *in situ* technique and pushing the S/B ratio to $\sim$1. The latter was achieved using a novel neural network approach and by considering samples with one and ≥ 2 b-tags separately. The signal templates are obtained using matrix element calculations and transfer functions, the background probabilities are given by a data driven model using the 0 b-tag sample, which has negligible signal fraction. Priors for the JES and the number of observed and background events are used. Fig. 3 (left) shows the likelihood contours extracted from $943\,\mathrm{pb}^{-1}$ data containing 72 signal candidates ($\sim$44 estimated background). The good S/B ratio achieved in this

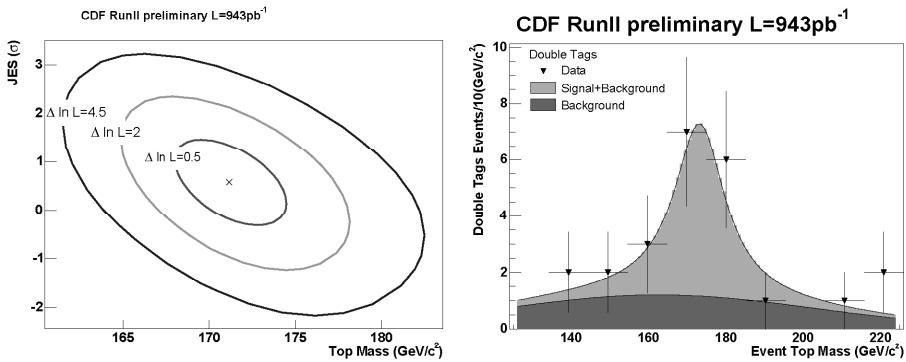

Figure 3: *Left: Likelihood contours extracted by CDF from 943 pb^{-1} data using the Template Method with JES in situ calibration. Right: Top quark mass distribution in data and simulation for doubly tagged events.*

channel is illustrated in Fig. 3 (right), which shows the doubly b-tagged sample together with the fitted signal and background templates. The analysis yields $M_t - 171.1 \pm 2.8^{(\mathrm{stat.})} \pm 2.4^{(\mathrm{JES})} \pm 2.1^{(\mathrm{syst.})}\,\mathrm{GeV}/c^2 - 171.1 \pm 4.3\,\mathrm{GeV}/c^2$ (2.5% precision). The JES uncertainty is much reduced compared to a traditional one-dimensional template analysis [16] based on $1020\,\mathrm{pb}^{-1}$ data containing 772 b-tagged candidate events, which yields $M_t = 174.0 \pm 2.2^{(\mathrm{stat.})} \pm 4.5^{(\mathrm{JES})} \pm 1.7^{(\mathrm{syst.})}\,\mathrm{GeV}/c^2 = 174.0 \pm 5.3\,\mathrm{GeV}/c^2$ (3.0% precision).

7 Systematic Uncertainties

So far, the systematic uncertainties of M_t in all channels are dominated by contributions from the JES. The di-lepton channel has the biggest JES uncertainty because no *in situ* calibration is performed here. Other significant sources are primarily related to the MC simulation. For the best results presented in this report, these are the modeling of gluon ISR and FSR (particularly in the all-jets and lepton-jets channel), the proton-parton density function, the hadronization model, and the modeling of the background (specially in the all-jets channel). The individual contributions are $\sim 1\,\mathrm{GeV}/c^2$ or less, and are expected be the limiting factor in the precision of M_t at the end of Run-II.

8 Tevatron Combination

CDF and DØ have updated the combination of their best results achieved in each channel [17] (see Fig. 4, left), which includes the most precise measurements reported in Sec. 4, 5 and 6. Also the result from the Decay Length Tech-

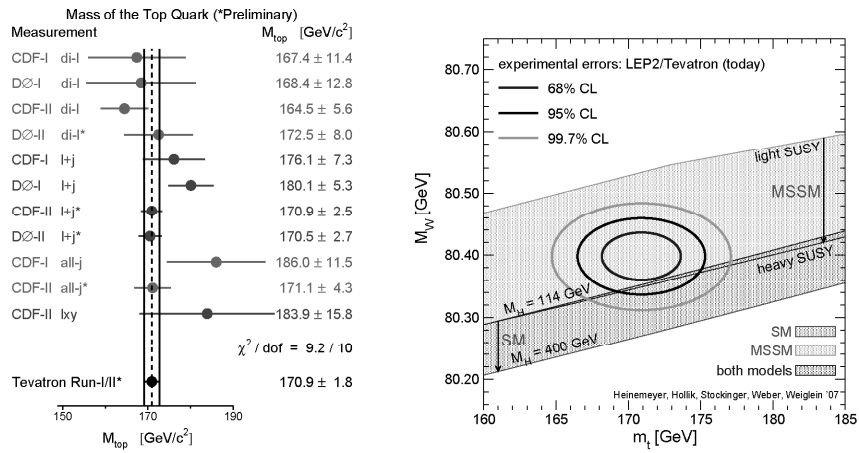

Figure 4: *Left: M_t measurements used to calculate the current world average. Right: M_t versus M_W in the SM and the MSSM compared with the present measurements shown as confidence level contours* [19].

nique is considered since its experimental systematics are largely uncorrelated with those of other methods. Taking all correlations between the systematic uncertainties properly into account, the new world average value obtained is $M_t = 170.9 \pm 1.1^{(\mathrm{stat.})} \pm 1.5^{(\mathrm{syst.})}\,\mathrm{GeV}/c^2 = 170.9 \pm 1.8\,\mathrm{GeV}/c^2$. The χ^2/d.o.f. of 9.2/10 (51% probability) indicates a good agreement among all measurements. New M_t averages are also calculated individually for each channel: $172.2 \pm 4.1\,\mathrm{GeV}/c^2$ (all-jets), $171.2 \pm 1.9\,\mathrm{GeV}/c^2$ (lepton-jets), $163.2 \pm 4.5\,\mathrm{GeV}/c^2$ (dilepton). The results are consistent given their correlations.

9 Conclusions

The CDF and DØ collaborations have established a robust top quark mass measurement program based on a variety of techniques applied to different $t\bar{t}$ final states. The previous Run-I errors have been reduced by a factor of 2-3 in each decay channel. An important achievement is the reduction of the JES uncertainty due to *in situ* calibration, which is a reason why the all-jets channel has become competitive. The new world average value for the top quark mass is $M_t = 170.9 \pm 1.8\,\mathrm{GeV}/c^2$, which corresponds to a precision of 1.1%. The effect of M_t and the recently updated M_W measurement [18] on the mass of the Higgs boson is shown in Fig. 4 (right). The uncertainties translate to a ∼30% constraint for M_H. With full Run-II data, the uncertainty in M_t may be even pushed to $1\,\mathrm{GeV}/c^2$, which is also expected after 5-10 years of LHC operation. The top quark mass might thus be the lasting legacy of the Tevatron.

Acknowledgments

I would like to thank the conference organizers for the kind invitation, and also my colleagues from the CDF and DØ collaborations for their help in preparing the talk. I am also grateful to the Max Planck Society and the Alexander von Humboldt Foundation for their support.

References

1. CDF Coll., F. Abe *et al.*, Phys. Rev. Lett. **74** (1995) 2626; DØ Coll., S. Abachi *et al.*, Phys. Rev. Lett. **74**, 2632 (1995).
2. CDF Coll., R. Blair *et al.*, FERMILAB-PUB-96-390-E (1996); DØ Coll., V.M. Abazov *et al.*, Nucl. Instrumen. Meth. **A565** (2006) 463.
3. N. Kidonakis and R. Vogt, Phys. Rev. D **68** (2003) 114014; M. Cacciari *et al.*, JHEP 0404:068 (2004).
4. CDF Coll., A. Bhatti *et al.*, Nucl. Instrumen. Meth. **A566** (2006) 375; DØ Coll., J. Kvita, AIP Conf. Proc. 867 (2006) 43.
5. CDF Coll., A. Abulencia *et al.*, FERMILAB-PUB-07-070-E (2007), submitted to Phys. Rev. Lett.
6. DØ Coll., public note 5362 (2007), supersedes the $370\,\mathrm{pb}^{-1}$ result presented at the conference: V.M. Abazov *et al.*, Phys. Rev. **D74** (2006) 092005.
7. CDF Coll, A. Abulencia *et al.*, FERMILAB-FN-0794-E (2006).
8. CDF Coll., public note 8669 (2007).
9. DØ Coll., V.M. Abazov *et al.*, Phys. Rev. **D75** (2007) 092001.
10. CDF Coll., A. Abulencia *et al.*, Phys. Rev. **D75** (2007) 071102.
11. CDF Coll., A. Abulencia *et al.*, Phys. Rev. **D75** (2007) 031105; CDF Coll., public note 8401 (2006).
12. DØ Coll., public notes 5200 (2006) and 5347 (2007), supersede the $370\,\mathrm{pb}^{-1}$ results presented at the conference: V.M. Abazov *et al.*, FERMILAB-PUB-06-354-E (2006), submitted to Phys.Rev.Lett.
13. CDF Coll., public note 8803 (2007), supersedes the $1030\,\mathrm{pb}^{-1}$ result presented at the conference.
14. CDF Coll., A. Aaltonen *et al.*, Phys. Rev. Lett. **98** (2007) 142001.

15. CDF Coll., public note 8709 (2007), submitted to Phys.Rev.D.
16. CDF Coll., public note 8745 (2007).
17. CDF and DØ Coll., FERMILAB-TM-2380-E (2007), hep-ex/0703034.
18. C.P. Hays, these proceedings.
19. S. Heinemeyer, W. Hollik, D. Stockinger, A.M. Weber and G. Weiglein, JHEP 0608:052 (2006). Update for Winter 2007 conferences.

SINGLE TOP QUARK PRODUCTION AT THE TEVATRON

Aurelio Juste
Fermilab, USA

Written contribution not received

THE FIRST SM PHYSICS RESULTS FROM CMS SOME EXPECTATIONS

Michael Dittmar
Institute for Particle Physics (IPP), ETH Zürich, CH-8093 Zürich, Switzerland

Abstract

The year 2008 is currently expected to see the first 14 TeV LHC proton proton collisions. CERN's LHC planning for the year 2008, based on various assumptions about the machine and detector performance, leads at best to a data sample corresponding to an integrated luminosity of about 1 fb^{-1}. The potential new SM physics results from CMS, which might be ready in time, for the March 2009 La Thuile conference are presented. Emphasis is put on studies of events, which contain one or two heavy vector bosons, W's and Z's, with subsequent leptonic decays. It is demonstrated that such measurements can already lead to first Higgs limits in the mass range between 200-450 GeV and perhaps to some evidence for a SM Higgs with a mass near 165 GeV.

1 Introduction and Overview

According to the March 2007 planning, a full machine checkout followed by beam commissioning and some running with proton beams at 450 GeV injection energy is foreseen for the end of 2007. This is followed by a busy shutdown and a machine "handover" for beam operations in April 2008.

For the rest of the year 2008, and according to a presentation by R. Bailey [1], one can hope for roughly 40 efficient physics collision days. Three LHC running phases for physics are currently envisaged: The first phase, the pilot run, can perhaps begin in July 2008 with roughly 50% of the active 2008 LHC collsion time, corresponding to a peak luminosity of $5 \times 10^{30}/\mathrm{cm}^{-2}/\mathrm{sec}$. Phase 2 and phase 3 should see a 75 nsec and 25 nsec bunch crossing time respectively, each with roughly 10 effective 14 TeV physics days. The expected peak luminosity for phase 2 is about $2 \times 10^{32}/\mathrm{cm}^{-2}/\mathrm{sec}$. Perhaps during phase 3, as kind of a Santa Claus present for the last running days of 2008, the peak luminosity might reach $10 \times 10^{32}/\mathrm{cm}^{-2}/\mathrm{sec}$.

Thus, the delivered maximal luminosity during these three running periods corresponds to 10 pb^{-1}, 200 pb^{-1} and 1 fb^{-1} respectively [2]. Of course, these numbers should be multiplied by everybody's preferred efficiency performance of the machine and of the detectors. One might optimistically assume that CMS reaches, during phase 3, a data taking efficiency of perhaps 80%. Obviously this number is nothing more than a speculation and should be replaced as soon as possible with hard numbers. After this conference was completed, a design fault was observed in one of the eight so called final triplet magnets. The time needed for this repair is currently unknown, but might shift the entire planning by a few months.

We present now some potential physics results (and in our view the most interesting), which might come from a well prepared and fast data analysis of this 1 fb^{-1} data sample. In this review, we concentrate especially on the unique LHC potential, namely the high p_t and high Q^2 physics, related to events with one and two vector bosons, W's and Z's, and their subsequent leptonic decays. The results presented in the following are based on the simulation results, described in detail in the so called 2006 CMS-Physics TDR [3]. Most of these simulation results are based on a 100% functioning and well understood and calibrated CMS detector. However, as one can not expect that the real detector will achieve quickly the assumed performance, we thus describe what results might at best be achieved with 1 fb^{-1}. The potential statistical and systematic errors as well as potential analysis bottlenecks, as seen by the author, are also discussed.

Thus, imagine that you listen to the "fresh" 1 fb^{-1} SM summary results from CMS, presented at the "first" conference, after the data were taken. With some luck, this conference might be the 2009 La Thuile winter conference.

2 QCD results

Many, still preliminary, QCD measurements have already been performed and presented during the last months of 2008. These measurements cover a wide range of physics topics, multi jet events, the jet E_t spectrum, the multiplicity and the p_t spectrum of charged particles produced from the underlying event and from minimum bias events. We have also seen jet events with large rapidity gaps. All these measurements were performed using the data samples obtained during the first two LHC physics periods and with luminosities of less than 100 pb^{-1} [3]. All results are so far in agreement with the expectations from the different QCD inspired Monte Carlo models. It will take still some time to finalize these measurements and publish hard numbers with more sensitive smaller systematic errors.

Here I would like to report the first measurement of jets with an E_t larger than 1 TeV, using the entire 1 fb^{-1} data sample. About 10 events with a jet E_t above 1.5 TeV, consistent with expectations, have been observed. The jet E_t spectrum is found to be steeply falling as expected from NLO QCD predictions. While it is still too early to give precise values for the limit of the compositeness scale Λ, our data clearly rule out any exotic interpretation of the so called high E_t anomaly, reported by the CDF collaboration during run I [4].

More detailed studies of these TeV jet events are underway and quantitative results on jet-jet masses and jet multiplicities can be expected for the coming summer conferences. Thus in short: "Stay tuned..."

3 From single W and Z production to the first Vector Boson pair production results

At the LHC, the production of W and Z bosons with their decays to electrons and muons, are to some extend the most important manifestation of the SM of electroweak interactions. The SM predictions can now be tested at roughly a factor of 10 higher center of mass energies compared to the energies achieved at LEP200 and the TEVATRON. Because of the theoretically well understood production and their almost background free leptonic decays, W's and Z's are the experimenters most valuable "tool" to test the SM. The abundant resonant production of single W's and Z's allows also to understand and calibrate the "detector" response to isolated high p_t electrons, muons, to jets and thus to missing transverse momentum. These events are also an excellent tool to perform precision QCD tests and to determine the proton-proton and especially the parton-parton luminosity with high accuracy [5]. Furthermore, even though the mass of the W boson is already known with an accuracy of about 40 MeV, the potentially negligible statistical error already with a few fb^{-1} attracts many experimentalists to try to achieve an even better mass measurement.

However, the real interesting measurements are related to the production of diboson pairs at the LHC:

- The production of new heavy particles, like the top quark, with their subsequent decays into WX or ZX.
- The analysis the non-resonant diboson production WW, WZ, and ZZ, especially at high masses, might reveal some deviations from the SM predictions and ...
- perhaps might even lead to the discovery of the so called Higgs boson, the last "missing link" of the SM.

It is well known that all these measurements will become really interesting once high luminosities of 10-100 fb^{-1} can be analyzed. However, the simulation results presented in the following, demonstrate that already the first fb^{-1} of data will allow to obtain perhaps some surprising results within or beyond the SM.

3.1 Resonant W and Z production

The production of W and Z bosons with their subsequent decays to electrons and muons has been studied in detail using the 1 fb^{-1} obtained during the first year of LHC data taking. Even though we have obviously not yet obtained the design detector performance, the results presented in the following are rather independent from such details.

Figures 1a and b show the generated and reconstructed Z mass peak and the generated and "measured" rapidity distribution for the decay to an electron-positron pair using the full GEANT based simulation, event reconstruction and analysis of CMS[1] [6].

Figures 2a and b show the η and the local ϕ distribution of electrons from Z decays in such a way that all 18 even and odd "crystal super-modules" are combined. The inefficiencies from the super-module boundaries are relatively small but can be seen clearly using the "subsample" of roughly 200 pb^{-1}, obtained during the second period of LHC physics. The detailed mapping of the detector acceptance as a function of η and ϕ using the selected Z sample and with electron and muons is still in progress, but we can already say that the stability of the detector is known using these samples, and for all the following results, with an accuracy of better than 2-3%. The precision goal of 1% seems not to be too far away.

[1]Due to a simple technical problem the real data distributions are missing in these and all the following plots. But the reader should believe the author that this problem will soon be solved.

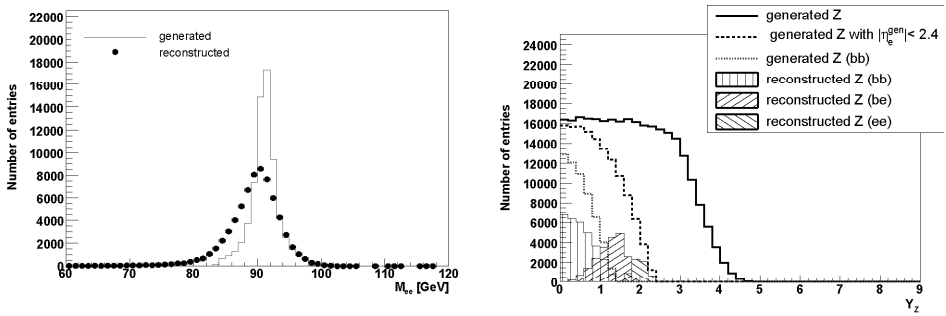

Figure 1: *Generated and reconstructed Z mass peak using electrons and the corresponding Z rapidity distributions.*

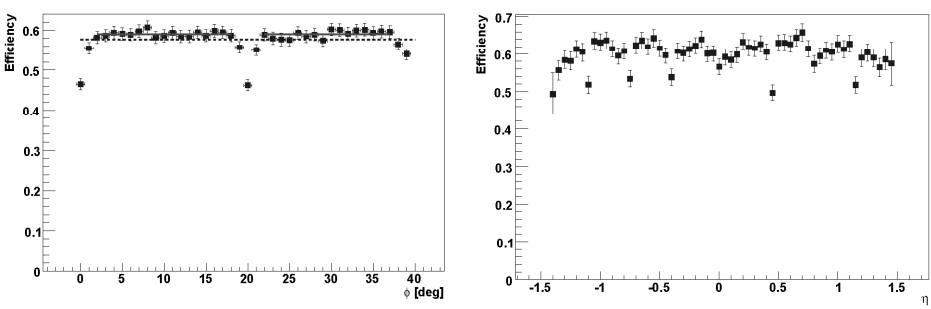

Figure 2: *Efficiency of electrons from reconstructed* $Z \rightarrow e^+e^-$ *decays as a function of* η *and* ϕ_{local}.

The differential and total W an Z cross sections, using the decays to electrons and muons, are so far in excellent agreement with the NNLO SM predictions. Using the decays to muons the following total cross sections accuracies have been obtained so far:

$$\Delta\sigma/\sigma(Z) = \pm 0.13\%(stat) \pm 2.3\%(syst.) \pm 10\%(lumi) \quad (1)$$

and

$$\Delta\sigma/\sigma(W) = \pm 0.04\%(stat) \pm 3.3\%(syst.) \pm 10\%(lumi) \quad (2)$$

These cross section measurements are dominated by the proton-proton luminosity uncertainty of about 10%. This uncertainty is already much larger than the theoretically LHC cross section uncertainty, believed to be about $\pm 5\%$. It seems thus logic to use the W and Z counting result as a $\pm 5\%$ luminosity measurement. Furthermore, cross section ratios for W^+/W^- and W/Z are already measured with an accuracy of 1-2%. These measurement's will soon

be completed and should allow to improve our knowledge of the PDF's and the corresponding parton luminosity [5].

In addition, the data analysis for lower mass Drell-Yan events with large rapidities is in progress and should soon provide interesting new insights into the very very low x physics domain [7]

The large data sample of $W \to \mu\nu$ and $Z \to \mu\mu$ events can be used to perform a so called almost "self-calibrating" W and Z mass measurement. Here one uses the well known Z mass measured at LEP to calibrate the single "leg" transverse mass measurement of the Z and the W at the LHC. It is almost straightforward to obtain a statistical error of 40 MeV, using this method and a data sample of 1 fb^{-1} [8]. However, the detailed understanding of some small differences between the lepton rapidity distributions from W and Z events and the not yet perfect calibration of the entire detector, do not allow so far to quote a correspondingly small systematic error.

3.2 $pp \to t\bar{t} \to WbWb$ physics

The top quark, the heaviest known fermion, is produced abundantly at the LHC. We have so far, using the data set of 1 fb^{-1}, detected about 1800 very clean signal events in the dilepton channel (e.g. both W's decaying to either electrons or muons) [9]. The single lepton channel contains also little background and almost 10 times more events are selected [10]. The cross section has been measured with both channels and is found to be in good agreement within the current systematic uncertainties of about 10%, originating from efficiency and modeling uncertainties. The cross section error, is already dominated by the proton proton luminosity uncertainty, which is currently estimated to be about 10%. This should be compared to the statistical error of roughly 2% in the dilepton channel and about 1.2% in the single lepton channel. Within these errors, both measurements agree with the latest $t\bar{t}$ cross section calculations. We can also conclude that new particles, which would enhance for example the number of events in the dilepton channel, can not have a cross section of more than 20% of the SM tt cross section. More precise studies of the event dynamics and especially the lepton and dilepton p_t spectrum in these top like events will be reported elsewhere. Measurements of the $t\bar{t}$ mass spectrum and of the top p_t spectrum are not yet completed. These measurements will especially benefit from the much larger data samples expected in the near future.

Besides the $t\bar{t}$ cross section results, the measurement of the top mass is of special interest within the SM. However, the most recent measurements from the TEVATRON have constrained the top mass already to an accuracy of about $\pm$ 2 GeV, dominated by systematics. Our single lepton $t\bar{t}$ sample is already much larger and cleaner than the one from the TEVATRON with a corresponding statistical error of $\pm$ 1 GeV. However, the detailed understanding

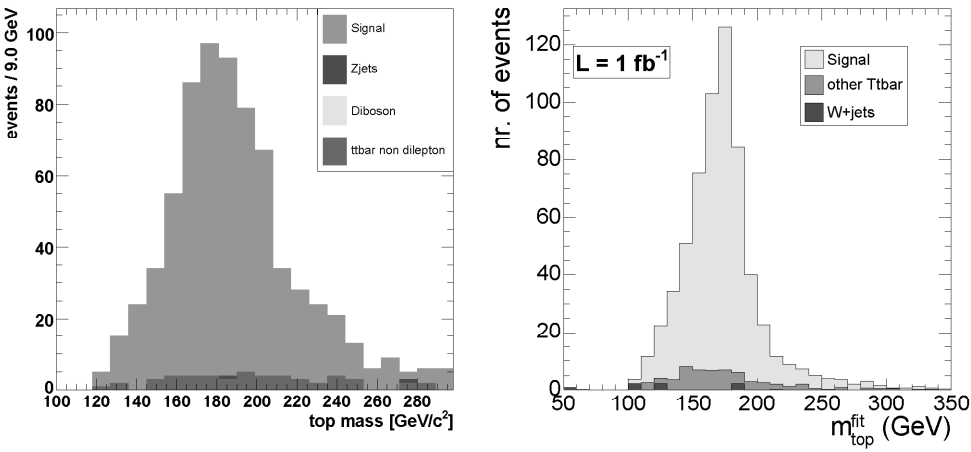

Figure 3: *Reconstructed mass of the top quark using (left) the dilepton sample and (right) the single lepton sample.*

of the systematic effects from selection cuts and from the QCD modeling of the signal is not yet completed. Currently our systematic error for the mass measurement is dominated by the jet energy scale uncertainty, corresponding to roughly ± 4-5 GeV. Our current central value for the top mass is found to be about 6-8 GeV above the current world average mass value. However, the systematic error is still too large to make a useful contribution to the current world average. We are confident that a cross section and competitive top mass measurement, like the one shown in Figures 3a and b and with this first fb^{-1} can be completed within the next few months and in time for the summer conferences.

We expect that the systematic error for the mass measurement can be reduced relatively quickly by a factor of two and that ultimately, using a much larger statistic and the combination of many different methods, a top mass uncertainty of about ± 1 GeV might be achieved.

3.3 $pp \to ZW \to \ell\ell\ell\nu$ and $pp \to ZZ \to \ell\ell\ell\ell$ physics

Here we present the first CMS results on the purely electroweak diboson pair production reactions $pp \to ZW \to \ell\ell\ell\nu$ and $pp \to ZZ \to \ell\ell\ell\ell$. In contrast to the reaction $pp \to WW \to \ell\nu\ell\nu$, both final states can be almost completely reconstructed using the clean lepton final states. Unfortunately the theoretical cross sections within the SM are relatively low, and only some crude measurements, basically existence proofs, of these final states can be made with a luminosity of 1 fb^{-1}. The channel $pp \to ZW$ provides some information about the triple boson vertex (WWZ), which so far has only been tested up to LEP II energies with $\sqrt{s} \approx 200$ GeV.

Using a straight forward selection of events with three well measured and isolated charged leptons (electrons or muons), one lepton pair should be consistent with originating from the decay of a Z boson. In agreement with the expectations, 97± 11 events of the type $WZ \to \ell\ell\ell\nu$ above a background of 17 events are selected [11]. The observed rate, the transverse diboson mass, the p_t spectrum of the leptons and the charge ratio of W^+Z/W^-Z candidate events is consistent with the expected 60%:40% ratio. This analysis is clearly limited by statistics but the analysis shows that the signal can, as expected, be selected with a very small background. We are thus confident that (a) the lepton selection efficiencies and backgrounds are well described by the Monte Carlo and that (b) accurate cross section measurements of this channel with errors of only a few % can be made and (c) that the production of events with WZ masses well above 500 GeV can be easily performed once data samples of a few 10 fb^{-1} become available.

We have also selected events with four charged leptons, which are consistent with coming from the decay of two Z bosons. Events of all possible combinations, $eeee$, $\mu\mu\mu\mu$ and $ee\mu\mu$ have been found and the total number is consistent with the expectations of about 28 events for 1 fb^{-1}. The observed ZZ mass spectrum and the kinematics do not indicate any unexpected behavior. The possible interpretation of these ZZ events and also events of the WW type with respect to the SM Higgs search will be discussed in the next section.

3.4 Limits and first signs for a SM Higgs boson with a mass near 165 GeV

The Higgs boson is considered to be the "missing link" to make the SM the real theory of electroweak interactions. The search for the Higgs boson at the LHC is thus the central question of the LHC experimental program. Before we start to present the first search results from CMS we would like to give a reminder about todays knowledge about the SM Higgs.

Direct searches at LEP2 have resulted in a combined mass limit of 114 GeV. The indirect constraints from the so called SM fit to all electroweak parameters, including the measured mass values of the top quark and of the W mass have resulted in the most often quoted spring 2007 numbers for the 95% c.l. upper mass limit of 144 GeV or 182 GeV (if the direct LEP2 limit is included) [12] However, it should be noted that the χ^2 of this fit is not particularly good, especially if only the most sensitive electroweak observables, the polarization measurements, the forward backward charge asymmetries for leptons and the b-quarks, the top mass and the W mass are used for the fit. Furthermore, as the validity of the SM has been assumed to some extend in the electroweak fit it might have been more sensible to use the Higgs mass constraints coming from the vacuum stability and the perturbation theory as indicated in Figure 4 [13]. The result of the fit would thus be the parameter Λ which indicates

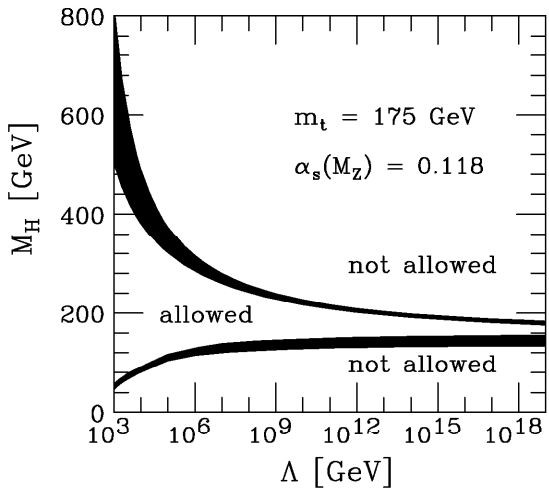

Figure 4: *Expected Higgs mass within the SM and assuming its validity up to very high energies.*

up to what scale the SM can be used as a valuable approximation. In any case, the SM electroweak fit limits are currently perfectly consistent with the assumption that the SM is valid up to essentially the Planck Mass and that with this assumption the most likely value for the SM Higgs will be in the range of 168± 20 GeV. It is important to note that this value is too high for the minimal super-symmetric Standard Model. A discovery in this mass range would thus require either to give up Super-symmetry or to extend the Higgs sector in a rather dramatic way.

Before we discuss in detail the possible evidence for a Higgs signal in the $WW \to \ell\nu\ell\nu$ channel and for a mass between roughly 160-170 GeV, we show the expected Higgs search discovery sensitivity from CMS in Figure 5 [3]. This plot shows that a collected luminosity of about 3 fb^{-1} might be sufficient to observe a Higgs signal in the mass range between 200-450 GeV and that less than 1 fb^{-1} are needed to observe signal with a mass between 160-170 GeV. Thus, one finds that about 4/25 $\times$3 fb^{-1} would be roughly sufficient to obtain the first 95% c.l. exclusion limits. A more accurate estimate would increase this value slightly as Poisson statistics is required for small event numbers. Thus, with some luck, a Higgs with a mass between 160-170 GeV might already be seen using the 1 fb^{-1} data sample.

As already discussed in the previous section , the analysis of the ZZ events has not shown any particular mass clustering of the roughly 30 observed 4 lepton events. As the ZZ mass resolution is already of the order of 5-10 GeV, the events can be split into mass bins corresponding roughly to the expected resolution. We find that a Higgs boson with a mass corresponding to bins with zero entries can already be excluded with todays data. On the other hand, every bin with one event or perhaps even two must for now be considered as

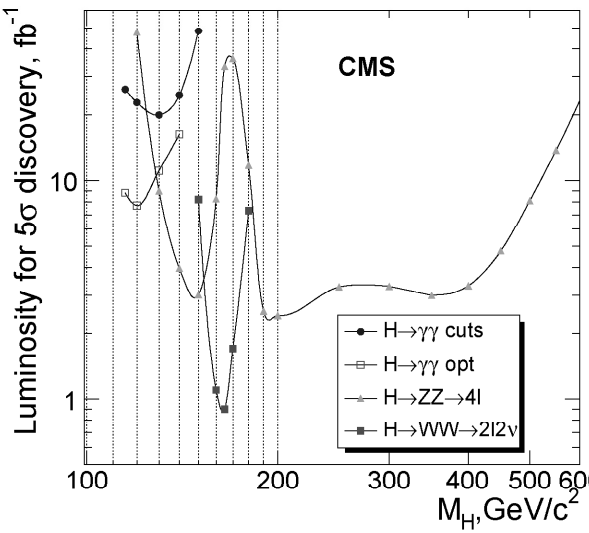

Figure 5: *Required luminosity to discover a SM Higgs boson with a significance of 5 sigma and with the "ideal" CMS detector.*

a potential Higgs signal. We are eagerly awaiting the results from our ATLAS colleagues for high mass ZZ events, which which should help to exclude some mass region where we observe one or two candidate events. In any case, the search in this channel has been opened according to expectations and exciting times are clearly ahead of us.

Finally we present our results for the Higgs search in the decay to $H \to WW \to \ell\nu\ell\nu$ with a mass close to 165 GeV. This channel has been proposed and established as the discovery channel in the mass range between roughly 155 GeV to 180 GeV in 1997 [14]. The signature for this channel is based on the fact that the spin correlations and the V-A interaction result for this mass range in a small opening angle of the two charged leptons. This small opening angle in the plane transverse to the beam direction distinguishes the signal form the non resonant WW background.

The analysis proceeds as follows:

- Events with two oppositely charged and isolated high p_t and rather central leptons, for example the rapidity should be smaller than $|\eta| \leq 1.4$) are selected.
- Events which have some jet activity are removed (top background).
- The opening angle of the two leptons in the plane transverse to the beam should be smaller than 45 degree.
- And finally the p_t spectrum of both leptons is analyzed in detail.

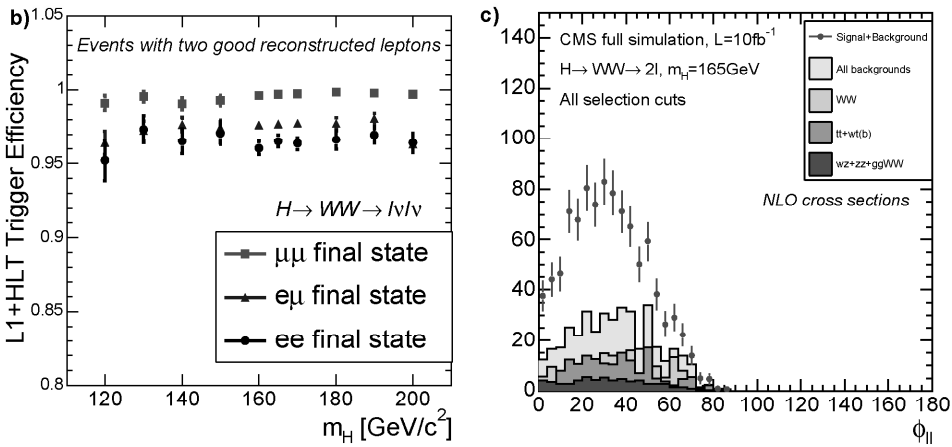

Figure 6: *Simulated trigger efficiency for $H \to WW \to \ell\nu\ell\nu$ candidates and for the applied lepton selection cuts (left Fig.). The right hand Figure shows the angle between the two reconstructed leptons in the plane transverse to the beam direction, ϕ, after all other selection criteria are applied and for signal and backgrounds.*

After these cuts are applied, an excess of 38 events above a background of 28 $\pm$ 6 (stat.) $\pm$ 3 (syst.), corresponding to roughly 5 standard deviations is observed. A detailed study of different signal depleted and background enhanced phase space regions has allowed to determine the background contributions with a systematic accuracy of about 10%. The results of this search are described in detail in Ref. [15].

In summary, we have observed a clear excess of events in the $H \to WW \to \ell\nu\ell\nu$ channel, which is consistent with the expected cross section of a SM Higgs with a mass between 160-168 GeV. While it is too early to claim that the Higgs has been observed, one can safely say that the observed excess "'tastes" and "smells" like the SM Higgs boson. We thus would like to emphasize that many more detailed studies are required before we can be sure that the observed excess can only be described by the SM Higgs boson.

4 Summary

This review describes what kind of SM physics results might be expected a few month after the first data sample of up to 1 fb^{-1} of 14 TeV LHC collision data has been collected by CMS. Emphasis is put on the production of isolated high p_t electrons and muons and the related W and Z boson physics. The presented

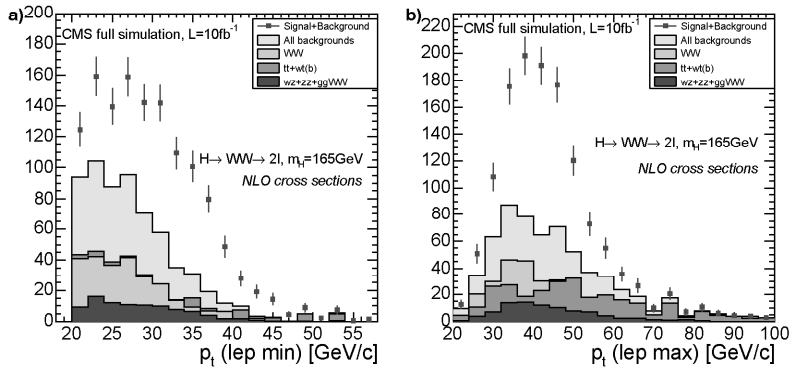

Figure 7: *The Figures show the p_t distribution of the lepton with the lower (a) and higher (b) p_t and for signal and backgrounds after all other cuts are applied.*

results are discussed with respect to statistical and systematic uncertainties, using some "realistic" guesses for the performance of CMS detector(s) during its very first data taking year.

5 Questions and answers

- *Do you believe that the described results can really be achieved only three months after data taking?*
  Well, if we manage to concentrate our physics program on the most important topics, presented here, than indeed these results might be achieved very quickly after the 1 fb^{-1} data taking is completed.

- *Do you believe that an integrated luminosity of 1 fb^{-1} of good data can really be collected during 2008?*
  No, I took the date of the 2009 La Thuile conference as an optimistic milestone. I believe however, that the presented 1 fb^{-1} results can indeed be obtained very quickly after the corresponding data sample have been taken. Furthermore, the quote from V. F. Weisskopf, might apply here as well, if "models" are replaced with "milestones".
  "Models are like printed Austrian train schedules, the trains are always late." A Prussian visitor is asking the conductor: "Why are you putting so much effort in printing train schedules?". The conductor replies: "Because, without them, we wouldn't know how late the trains are".

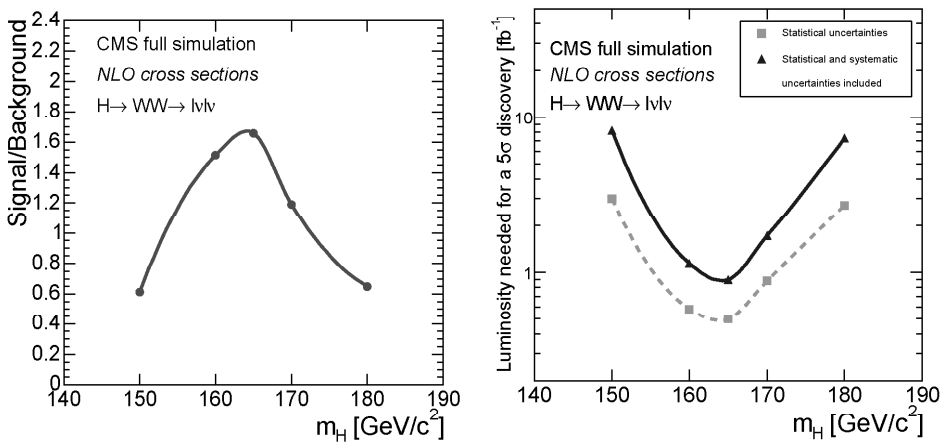

Figure 8: *$H \to WW \to \ell\nu\ell\nu$ signal to background ratio after all cuts and the required luminosity to observe a 5 standard deviation signal as a function of the Higgs mass.*

6 Acknowledgements

I would like to thank the organizers of the 2007 LaThuile conference for the stimulating atmosphere and for the opportunity to present a "vision" view of the first 1 fb^{-1} physics results from CMS.

References

1. See for example: R. Bailey, Jan. 2007 meeting of the LHC commissioning working group and http://lhc-commissioning.web.cern.ch/lhc%2Dcommissioning/ for the latest informations about the LHC expectations and for further references.

2. J. Knobloch, Information on luminosity estimates at: http://lcg.web.cern.ch/lcg/MB/revised_resources/startup%20scenario.pdf.

3. For more details see the CMS-Physics TDR, CERN/LHCC/2006-021.

4. For the original excess see for example http://ppewww.physics.gla.ac.uk/preprints/1997/02/glaswg3/nodc10.html and http://www-cdf.fnal.gov/physics/new/qcd/QCD.html for the most recent results.

5. M. Dittmar, F. Pauss, and D. Zürcher, Phys. Rev. D 56(1997), 7284.

6. How Accurately Can we count the number of $pp \to ZX$ and $pp \to WX$ events using decays to electrons; CMS NOTE-2006/124 and Measurement of $Z \to \mu\mu$ and $W \to \mu\nu$ rates in CMS; CMS NOTE-2006/082

7. Prospects for Diffractive and Forward Physics at the LHC; CMS NOTE-2007/002.

8. Prospects for the Precision Measurement of the W Mass with the CMS Detector at the LHC; CMS NOTE-2006/061.

9. Measurement of top-pair cross section and top-quark mass in the di-lepton and full-hadronic channels with CMS; CMS NOTE-2006/077.

10. Measurement of the cross-section of single leptonic top quark pair events; CMS NOTE-2006/64 and Top quark mass measurement in single leptonic top quark pair events; 2006/66.

11. Study of Diboson Production with the CMS Detector at. the LHC; CMS NOTE-2006/108.

12. For the latest results from the Electroweak Working group see: http://lepewwg.web.cern.ch/LEPEWWG/

13. T. Hambye and K. Riesselmann, Phys. Rev. D 55(1997) 7255.

14. M. Dittmar and H. Dreiner, Phys. Rev. D 55(1997) 167.

15. G. Davatz, M. Dittmar and A. S. Giolo-Nicollerat, J.Phys. G33 (2007) N85 and CMS NOTE-2006/047

THE ELECTROWEAK PHASE TRANSITION IN MODELS WITH GAUGE SINGLETS

Amine Ahriche
Faculty of Physics, University of Bielefeld, D-33501 Bielefeld, Germany.
Department of Physics, University of Jijel, DZ-18000 Jijel, Algeria.

Abstract

Many Standard Model extensions succeeded to have a strong first order phase transition, which is needed for the electroweak baryogenesis scenario. In this talk, we will check whether the criterion used in the literature (especially in Ref. [1, 2, 3]), is true or not? We will use the sphaleron energy at the critical temperature. We find that this criterion, $\Omega(T_c)/T_c \geq 1$, (with $\Omega=(v^2+(x-x_0)^2)^{\frac{1}{2}}$; and x is the singlet vev), is not valid for models containing singlet(s); and the usual condition $v_c/T_c \geq 1$ is the valid one.

1 Introduction

One of the most interesting scenarios for baryogenesis is the electroweak baryogenesis (EWB) [4], where the third Sakharov condition [5]; is realized via a strong first order phase transition at the electroweak scale. The electroweak phase transition (EWPT) proceeds via bubbles nucleation if it is first order. The EWB is realized when the B and CP violating interactions pass through the bubble wall. These interactions are very fast outside the bubbles but suppressed inside. Then a net baryon asymmetry results inside the bubbles which are expanding and filling the universe at the end.

In the Standard Model (SM), B number is violated at the quantum level [6], where the transition between two topologically distinct $SU(2)_L$ ground states, which breaks both lepton and baryon numbers by $\Delta L = \Delta B = 3$, is possible. The rate of these processes can be computed using the so-called Sphalerons, which are static field configurations that interpolate between two distinct ground states. Sphalerons were found in [7] for the $SU(2)_L$ model. A model-independent condition in order that the phase transition should be strong enough was derived in [8]:

$$E_{Sp}\left(T_c\right)/T_c > 45, \tag{1}$$

where E_{sp} and T_c are the sphaleron energy and the critical temperature, respectively. Since it was shown in [9] that $E_{Sp}\left(T\right) \propto \upsilon\left(T\right)$ [1], the condition (1) can be translated for the case of SM to [11]

$$\upsilon_c/T_c > 1, \tag{2}$$

where υ_c is the field value at the critical temperature. However the condition (2) is not fulfilled in the case of SM since it leads to an unacceptable upper bound on the Higgs mass [12, 13]. If the SM is extended by a new scalar (or many scalars which can be singlets or in doublet w.r.t $SU(2)_L$) that acquires a vacuum expectation value x, then the term υ_c in (2) should perhaps be replaced by $\Omega_c = \{\upsilon_c^2 + x_c^2\}^{\frac{1}{2}}$ (or $\{\upsilon_c^2 + (x - x_0)_c^2\}^{\frac{1}{2}}$ if the false vacuum is $(0, x_0)$ instead of $(0,0)$) [1, 2, 3]. Then (2) becomes

$$\Omega_c/T_c > 1, \tag{3}$$

and therefore the cubic terms can exist in the potential at tree-level; that makes the EWPT stronger without the need of the thermally induced one [1, 2, 3].

[1] This was also checked for the Minimal Supersymmetric Standard Model (MSSM) in [10], then (2) is valid also for the MSSM.

In this talk, we want to check whether, for a model with a singlet, if the passage from (1) to (3) is true as in the cases of SM and MSSM? We will do using the model-independent criterion (1) in the simplest extension of the SM with a real singlet. The full analysis is given in [14].

2 The SM with a Singlet 'SM+S'

The Lagrangian in this case is given by

$$\mathcal{L} = -\frac{1}{4}F^a_{\mu\nu}F^{a\mu\nu} + (D_\mu\phi)^\dagger (D^\mu\phi) + \frac{1}{2}(\partial_\mu S)(\partial^\mu S) - V_{eff}(\phi, S), \quad (4)$$

where ϕ is the standard Higgs doublet

$$\phi^T = 1/\sqrt{2}\,(\ \chi_1 + i\chi_2, \quad h + i\chi_3\ ) \quad (5)$$

where h is the scalar standard Higgs, χ's are the three Goldstone bosons, and $F^a_{\mu\nu}$ is the $SU(2)_L$ field strength

$$F^a_{\mu\nu} = \partial_\mu A^a_\nu - \partial_\nu A^a_\mu + g\epsilon^{abc}A^b_\mu A^c_\nu. \quad (6)$$

D_μ is the covariant derivative; when neglecting the $U(1)_Y$ gauge, it is given by

$$D_\mu = \partial_\mu - \frac{i}{2}g\sigma^a A^a_\mu. \quad (7)$$

Finally, $V_{eff}(\phi, S)$ is the effective potential, which is at tree-level given by

$$V_0(\phi, S) = \lambda|\phi|^4 - \mu_h^2|\phi|^2 + \omega|\phi|^2 S^2 + \rho|\phi|^2 S + \frac{\lambda_S}{4}S^4 - \frac{\alpha}{3}S^3 - \frac{\mu_S^2}{2}S^2. \quad (8)$$

Now, we write the explicit formula of the one-loop effective potential. We will consider the contributions of the gauge bosons, the standard Higgs h, the singlet S, the Goldstone bosons $\chi_{1,2,3}$ and the top quark. The field-dependent masses at zero temperature are given by

$$\begin{gathered} m_t^2 = \tfrac{1}{2}y_t^2h^2,\ m_Z^2 = \tfrac{\bar{g}^2+g'^2}{4}h^2,\ m_W^2 = \tfrac{g^2}{4}h^2,\ m_\chi^2 = \lambda h^2 - \mu_h^2 + \omega S^2 + \rho S \\ m_{h,S}^2 \to m_{1,2}^2 - \tfrac{1}{2}[(3\lambda+\omega)h^2 + (3\lambda_S+\omega)S^2 + (\rho-2\alpha)S - \mu_h^2 - \mu_S^2 \\ \mp\left\{\left((3\lambda-\omega)h^2 - (3\lambda_S-\omega)S^2 + (\rho+2\alpha)S - \mu_h^2 + \mu_S^2\right)h^2\right\}^{\frac{1}{2}}] \end{gathered} \quad (9)$$

where y_t is the Yukawa coupling for the top quark, and $\bar{g}^2 = g^2 + g'^2$, however we neglected the $U(1)_Y$ gauge and therefore $g' = 0$ and $m_Z = m_W$; and $m_{1,2}^2$

are the Higgs-singlet eigenmasses. Then the one-loop correction to the effective potential at finite temperature is given by

$$\begin{aligned} V_{eff}^{1-loop}(h,S,T) = V_0(h,S) + \sum_{i=W,Z,t,h,S,\chi} n_i G\left(m_i^2(h,S)\right) \\ + \frac{T^4}{2\pi^2} \sum_{i=W,Z,t,h,S,\chi} n_i J_{B,F}\left(m_i^2(h,S)/T^2\right) \\ - \frac{T}{12\pi} \sum_{i=W,Z,h,S,\chi} n_i \left\{ \left(M_i^2(h,S,T)\right)^{\frac{3}{2}} - \left(m_i^2(h,S)\right)^{\frac{3}{2}} \right\}. \end{aligned} \tag{10}$$

here n_i's are the particle degrees of freedom; which are

$$n_W = 6, n_Z = 3, n_h = 1, n_\chi = 3, n_S = 1, n_t = -12.$$

The first lines in (10) corresponds to the tree-level and the one-loop correction at zero temperature, where $G(x) = \left(x^2/64\pi^2\right)\left\{\log\left(x/Q^2\right) - 3/2\right\}$ and $Q = 246.22$ GeV. The second represents the thermal correction at one-loop level, with

$$J_B(\theta) = \int_0^\infty dx\ x^2 \log\left\{1 - \exp\left[-\sqrt{x^2+\theta}\right]\right\} \tag{11}$$

$$J_F(\theta) = \int_0^\infty dx\ x^2 \log\left\{1 + \exp\left[-\sqrt{x^2+\theta}\right]\right\} \tag{12}$$

The last line represents the so-called daisy term. The capital M's are the bosonic thermal masses, which are given explicitly in [14]. In our theory, we have quite a few parameters: $\lambda,\ \lambda_S,\ \omega,\ \rho,\ \alpha$; in addition to the singlet vev x. The parameters μ_h^2 and μ_S^2 can be eliminated by making (v,x) the absolute minimum of the one-loop effective potential at zero temperature. Then our free parameters are $\lambda,\ \lambda_S,\ \omega,\ \rho,\ \alpha$ and x. We will use the following ranges of parameters:

$$\begin{aligned} 0.001 &\leq \lambda, \lambda_S \leq 0.6 \\ -0.6 &\leq \omega \leq 0.6 \\ 100 &\leq x/GeV \leq 350 \\ -350 &\leq \alpha/GeV \leq 350 \\ -350 &\leq \rho/GeV \leq 350, \end{aligned} \tag{13}$$

with some additional constraints and assumptions which are discussed in details in [14].

3 Sphalerons in the 'SM+S'

In order to find the sphaleron solution for this model, we follow the same steps as in the $SU(2)_L$ model. We will work in the orthogonal gauge where

$$A_0 = 0, \quad x_i \cdot A_i = 0. \tag{14}$$

We will not use the spherically symmetric ansatz for $\{\phi, A_i\}$ in [7], but another equivalent one [15],

$$\begin{aligned} A_i^a(x) &= 2(1-f(r))\frac{\epsilon_{aij}x_j}{gr^2} \\ H(x) &= \frac{h}{\sqrt{2}}\begin{pmatrix} 0 \\ 1 \end{pmatrix}, \quad h = \upsilon L(r) \\ S(x) &= xR(r). \end{aligned} \tag{15}$$

Here υ and x are the Higgs and singlet vevs in the general case (zero or nonzero temperature). Then the field equations are

$$\begin{aligned} \zeta^2\frac{\partial^2}{\partial\zeta^2}f &= 2f(1-f)(1-2f) - \frac{1}{4}\frac{\upsilon^2}{\Omega^2}\zeta^2L^2(1-f) \\ \frac{\partial}{\partial\zeta}\zeta^2\frac{\partial}{\partial\zeta}L &= 2L(1-f)^2 + \frac{\zeta^2}{g^2\upsilon\Omega^2}\left.\frac{\partial V_{eff}(h,S,T)}{\partial h}\right|_{h=\upsilon L, S=xR} \\ \frac{\partial}{\partial\zeta}\zeta^2\frac{\partial}{\partial\zeta}R &= \frac{\zeta^2}{g^2x\Omega^2}\left.\frac{\partial V_{eff}(h,S,T)}{\partial S}\right|_{h=\upsilon L, S=xR} \end{aligned} \tag{16}$$

where $\zeta = g\Omega r$; the parameter Ω can take any non-vanishing value of mass dimension one (for example υ, x or $\sqrt{\upsilon^2+x^2}$); and the energy functional is given by

$$\begin{aligned} E_{Sp}(T) = \frac{4\pi\Omega}{g}\int_0^{+\infty} d\zeta \Bigg\{ & 4\left(\frac{\partial}{\partial\zeta}f\right)^2 + \frac{8}{\zeta^2}f^2(1-f)^2 + \frac{1}{2}\frac{\upsilon^2}{\Omega^2}\zeta^2\left(\frac{\partial}{\partial\zeta}L\right)^2 \\ & + \frac{\upsilon^2}{\Omega^2}L^2(1-f)^2 + \frac{1}{2}\frac{x^2}{\Omega^2}\zeta^2\left(\frac{\partial}{\partial\zeta}R\right)^2 + \frac{\zeta^2}{g^2\Omega^4} \\ & \times\{V_{eff}(\upsilon L, xR, T) - V_{eff}(\upsilon, x, T)\}\Bigg\}, \end{aligned} \tag{17}$$

with the boundary conditions (See Appendix A in [14])

$$\begin{aligned} for\ \zeta\sim 0 \qquad & f\sim\zeta^2 \qquad\qquad for\ \zeta\to\infty \qquad f\to 1 \\ & L\sim\zeta \qquad\qquad\qquad\quad L\to 1 \\ & R\sim a+b\zeta^2; \qquad\qquad\quad R\to 1. \end{aligned} \tag{18}$$

Let us now compare the energy functional (17) to that of MSSM case (Eq. (2.22) in [10]), we find that in the MSSM both Higgs fields, h_1 and h_2, have similar contributions to the sphaleron energy, and the general form of (17) remains invariant under $h_1 \leftrightarrow h_2$. However this is not the case if $h \leftrightarrow S$, because of a missing term like $R^2 (1-f)^2$. The analytic solution of the system (16) is not possible, this should be done numerically. As an example, we solve (16) for four chosen sets of parameters (A, B, C and D); and then we can compute the sphaleron energy (17) at any temperature $T \leq T_c$. All the results for the sets A, B, C and D are summarized in table 1.

	A	B	C	D
λ	0.4000	0.4000	0.5000	0.4150
λ_S	0.4003	0.4200	0.4100	0.5500
ω	0.3818	0.2818	0.3818	0.3000
x/GeV	200	250	350	350
α/GeV	-38.89	38.89	38.89	194.44
ρ/GeV	-272.22	-194.44	-272.22	-300
υ_c/T_c	1.680	0.838	0.495	0.386
Ω_c/T_c	3.138	1.232	1.436	0.703
$E_{Sp}(T_c)/T_c$	64.851	32.980	20.459	13.577

Table 1: *Representative parameter values and the corresponding values of the different quantities needed for the criterion of a strong first order EWPT.*

From table 1, the set (A) satisfies both conditions (3) and (1), (D) does not satisfy either of them, and both (B) and (C) satisfy (3) but not (1).

4 The EWPT in the 'SM+S'

Since $\Omega_c/T_c \geq \upsilon_c/T_c$ is always fulfilled, the EWPT gets stronger for a larger parameter space compared with the minimal SM case [1, 2, 3]. In Ref [1], the authors have studied the EWPT strength using the same tree-level potential as (8) with some differences in the parameter definitions. They easily got a strong first EWPT using (3), even for Higgs masses much larger than the experimental upper bound ($\geq$114 GeV [16]). However the singlet has no relationship to the anomalous processes that violate $B+L$. It is coupled only to Higgs doublet and does not with the fermions. Let us take a random choice of about 3000 parameters in the ranges (13), and make a comparison between the results coming form the two different criteria (1) and (3). We show the plots of the

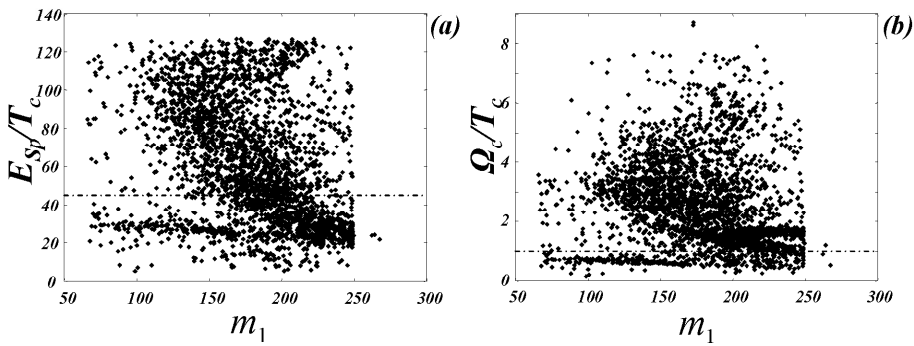

Figure 1: *The points above the dash-dotted lines in (a) and (b), the electroweak phase transition is strongly first order according to (1) and (3), respectively.*

quantities Ω_c/T_c and $E_{Sp}(T_c)/T_c$ as functions of the lightest Higgs mass m_1 in Fig. 1.

Comparing the number of points above and below the dash-dotted line in both cases *(a)* and *(b)* in Fig. 1, we remark that there are a lot of points which satisfy (3) but they do not really give a strong first order EWPT according to (1). The passage from the criterion (1), which is model-independent, to (2), was based on two assumptions [11]:

(I) The sphaleron energy $E_{Sp}(T)$ scales like the vev $v(T)$.

(II) The sphaleron energy at $T = 0$, is taken to be 1.87 in units of $4\pi v/g$.

In general, the value of the sphaleron energy at zero temperature is significantly different from 1.87 in units of $(4\pi\Omega(0)/g)$. In order to probe the assumption *(I)* for our case, i.e:

$$E_{Sp}(T) \propto \Omega(T), \tag{19}$$

we take the sets (A), (B), (C) and (D) used in table 1 in the previous section, and plot the ratios $v(T)/v(0)$, $\Omega(T)/\Omega(0)$ and $E_{Sp}(T)/E_{Sp}(0)$; as functions of temperature, which lies between the critical temperature and another value. The results are shown in Fig. 2.

Let us here comment on Fig. 2. The ratio $E_{Sp}(T)/E_{Sp}(0)$ is close to both $v(T)/v(0)$ rather than $\Omega(T)/\Omega(0)$ for most cases. For the case of (B), at $T \simeq 204.5\,GeV$, there exists a secondary first order phase transition, it happens on the axis $h = 0$, where the false vacuum $(0, x_0)$ is changed suddenly. In the case (D), there is also a secondary first order phase transition at $T \simeq 256\,GeV$; where the true vacuum (v, x) changes discontinuously. We cannot call this an EWPT because the scalar h has already developed its vev.

Therefore we claim that the contribution of the singlet S to the sphaleron

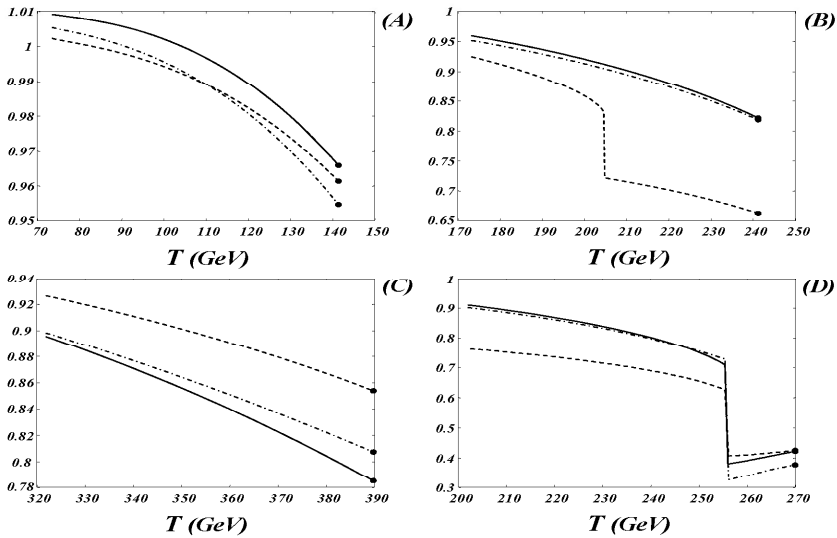

Figure 2: *The solid line denotes the ratio* $\upsilon(T)/\upsilon$*, the dashed one denotes* $\Omega(T)/\Omega$*; and the dot-dashed one denotes* $E_{Sp}(T)/E_{Sp}(0)$*. All the plots end at the critical temperature.*

energy is small, and may be this is the reason why $E_{Sp}(T)$ does not behave like $\Omega(T)$; and also it does not behave exactly like $\upsilon(T)$. We find that the effect of the singlet field S on the sphaleron energy (17), is in general less than 3% except in the case (D) between the two phase transitions. Then in the absence of secondary first order phase transitions, we can neglect the singlet contribution. But in its presence, the singlet contribution can be sizeable but not as large as that of the Higgs doublet or gauge fields. To justify this picture, we take again 3000 random sets of parameters and plot $E_{Sp}(T_c)/T_c$ as a function of both υ_c/T_c and Ω_c/T_c in Fig. 3.

Since in *(b)*, there exist too many points in the region $(E_{Sp}(T_c)/T_c \leq 45 \cap \Omega(T_c)/T_c \geq 1)$, the criterion (3) is not the definition of a strong first order EWPT. From *(a)*, it is clear that $E_{Sp}(T_c)/T_c$ scales almost[2] like υ_c/T_c except for some points, and (2) can describe the strong first order EWPT criterion for most of the points. Then when studying the EWPT in models with a gauge singlet, one should treat the problem as the SM case (as the MSSM in

[2]Except some points due to the existence of secondary first order phase transitions; or due to the significant singlet contribution to the sphaleron energy; especially for smaller Higgs vev values.

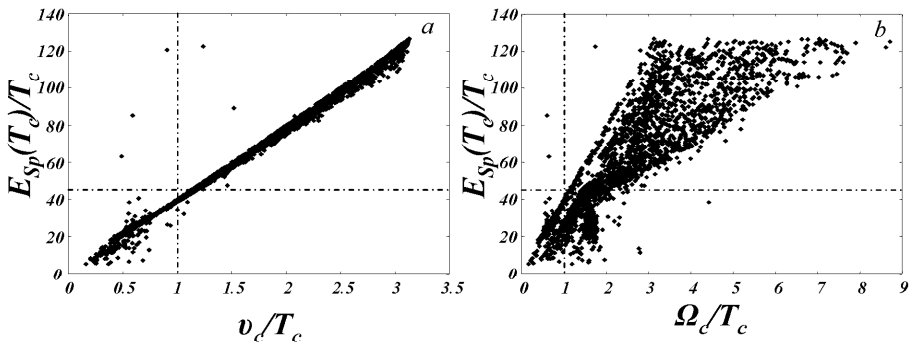

Figure 3: *$E_{Sp}(T_c)/T_c$ vs v_c/T_c in (a) and vs Ω_c/T_c in (b); for 3000 randomly chosen sets of parameters.*

case of a two doublets model) with replacing the singlet by its vev; and look for the Higgs vev in the path $\partial V_{eff}(h,S)/\partial S|_{S=x} = 0$; whether it is larger than the critical temperature i.e, $v_c/T_c \geq 1$. With this modified potential $\mathcal{V}_{eff}(h) = V_{eff}(h,S)|_{S=x}$; the EWPT can be studied easily as done by the authors in [17].

5 Conclusion

In this talk, we studied the EWPT in the SM with a gauge singlet using the known criteria in the literature in addition to the model-independent criterion found in [8]. The authors [1, 2, 3] found that the EWPT gets stronger even for Higgs masses above the bound ($\geq$114 GeV [16]). They modified the simple criterion (2) into (3), where they replaced the Higgs vev by the distance between the two degenerate minima in the $h - S$ plan. Here, we checked whether this criterion is viable for this kind of models or not. We took the SM with a real singlet, then we studied the EWPT using the sphaleron configuration at the critical temperature. We found that the modified criterion (3) does not really describe the strong first order EWPT. We found also that the passage from the model independent criterion (1) to (2) in the SM case, is not true for our case. The reason here is that both of the two assumptions in which (2) is valid for the SM case, are not fulfilled here:

• The sphaleron energy at zero temperature is different from the value 1.87 in units of $(4\pi\Omega/g)$.

• The sphaleron energy at finite temperature does not scale like $\Omega(T)$. We guess that the reason for this is that the singlet does not couple to the gauge

field, then the missing contributions to the sphaleron energy like $R^2\left(1-f\right)^2$ in (17), can spoil the scaling law, $E_{Sp}\left(T\right)\propto\Omega\left(T\right)$. This can be inspired if we compare this situation with the case of the MSSM, where this scaling law does work; and the general form of the sphaleron energy is invariant under $h_1\leftrightarrow h_2$. An important remark here is that the possibility of secondary first order phase transitions can, sometimes, spoil this scaling law also.

We found also that singlet contribution to the sphaleron energy is too small and therefore negligible especially when the Higgs vev is not small comparing to the singlet one. Then the usual condition $v_c/T_c\geq 1$, is still the viable one, which can describe the strong first order EWPT for the majority of the physically allowed parameters as stated in Fig. 3-a. Moreover, this can be satisfied even for Higgs masses in excess of 100 GeV unlike in the SM. Then in such a model where the singlets couple only to the Higgs doublets, it is convenient to study the EWPT within an effective model that contains only doublets, where the singlets are replaced by their vev's. We expect similar conclusion for models like the Next-to-Minimal Supersymmetric Standard Model (NMSSM), where in this model the singlet couples only to the two Higgs doublets. Then the criterion for a strong first order EWPT is $\left\{v_1^2+v_2^2\right\}^{\frac{1}{2}}/T\geq 1$ at the critical temperature, instead of $\left\{v_1^2+v_2^2+\left(x-x_0\right)^2\right\}^{\frac{1}{2}}/T\geq 1$.

6 Acknowledgements

I want to thank the organizers for the invitation and also for the financial help.

References

1. J. Choi and R.R. Volkas, Phys. Lett. **B317**, 385 (1993); S.W. Ham, Y.S. Jeong and S.K. Oh, J. Phys. **G31**, 857 (2005).

2. Y. Kondo, I. Umemura, K. Yamamoto, Phys. Lett. **B263**, 93 (1991); N. Sei, I. Umemura and K. Yamamoto, Phys. Lett. **B299**, 286 (1993).

3. There is also a MSSM extension where the study of the phase transition is based on the same idea as in [1]: S.W. Ham, S.K. Oh, C.M. Kim, E.J. Yoo and D. Son, Phys. Rev. **D70**, 075001 (2004).

4. V.A. Rubakov and M.E. Shaposhnikov, Phys. Usp. **39**, 461 (1996).

5. A.D. Sakharov, JETP Lett. **5**, 392 (1967).

6. G. 't Hooft, Phys. Rev. Lett. **37**, 8 (1976); Phys. Rev. **D14**, 3432 (1976), Erratum-ibid. **D18**, 2199 (1978).

7. R.F. Klinkhamer and N.S. Manton, Phys. Rev. **D30**, 2212 (1984).

8. A.I. Bochkarev, S.V. Kuzmin and M.E. Shaposhnikov, Phys. Rev. **D43**, 369 (1991).

9. S. Braibant, Y. Brihaye and J. Kunz, Int. J. Mod. Phys. **A8**, 5563 (1993).

10. J.M. Moreno, D.H. Oaknin, M. Quiros, Nucl. Phys. **B483**, 267 (1997).

11. M.E. Shaposhnikov, Nucl. Phys. **B287**, 757 (1987); Nucl. Phys. **B299**, 797 (1988).

12. A.I. Bochkarev and M.E. Shaposhnikov, Mod. Phys. Lett **A2**, 417 (1987).

13. Z. Fodor and A. Hebecker, Nucl. Phys. **B432**, 127 (1994).

14. A. Ahriche, Phys. Rev. **D75**, 083522 (2007).

15. T. Akiba, H. Kikuchi and T. Yanagida, Phys. Rev. **D38**, 1937 (1988); **D40**, 588 (1989).

16. Particle Data Group (W-M Yao et al.), J. Phys. G: Nucl. Part. Phys. **33**, 1 (2006).

17. K. Funakubo, S. Tao and F. Toyoda, Prog. Theor. Phys. **114**, 369 (2005); M. Pietroni, Nucl. Phys. **B402**, 27 (1993); A.T. Davies, C.D. Froggatt and R.G. Moorhouse, Phys. Lett. **B372**, 88 (1996); S.J. Huber and M.G. Schmidt, Nucl. Phys. **B606**, 183 (2001); A. Menon, D.E. Morrissey and C.E.M. Wagner, Phys. Rev. **D70**, 035005 (2004).

RECENT PROGRESS IN THEORETICAL CALCULATIONS AND MONTE CARLO GENERATORS FOR LHC

Fulvio Piccinini
INFN Sezione di Pavia, Italy

Abstract

A review on the state of the art of theoretical calculations and their implementation in Monte Carlo event generators for high energy hadronic collisions is presented, with emphasis on the requirements posed by the LHC physics programme.

1 Introduction

The ongoing Tevatron run II data analysis and the approaching of the LHC start up have stimulated an intense activity in improving existing Monte Carlo tools and developing new ones. Two aspects make of the LHC a completely new machine with respect to Tevatron: the increase of a factor of $\mathcal{O}(10^3)$ in luminosity and the increase of a factor of ten in the available center of mass energy. The former makes of the LHC a particle factory with statistics much larger than any other machine built up to now. The latter, the large center of mass energy, should allow the production of new heavy particles, which decay leaving signatures characterized by large jet multiplicities. These signals will be generally hidden by large backgrounds of QCD origin. It is therefore important being able to predict theoretically the features of these events. Moreover, due to the large event statistics, the high precision of several measurements requires a good theoretical control of higher order corrections. For instance in Drell-Yan, the precise W-mass determination with the foreseen accuracy requires the inclusion of $\mathcal{O}(\alpha)$ electroweak and higher-order photonic corrections.

In this contribution I will present some recent development in theoretical calculations, with emphasis on their implementation in Monte Carlo programs, ready to use for experimental data analysis and simulation.

2 Monte Carlo integrators

To this class belong all programs able to calculate cross sections and distributions numerically, the numerical integrations being performed with the Monte Carlo algorithm. Thanks to the flexibility of the Monte Carlo procedure, such programs can give predictions for arbitrary event selections, but only partonic final states are generated. They provide events with flat distribution on the phase space weighted with the matrix element of the process under consideration. For this reason they are also called "generators of weighted events". The typical use of a Monte Carlo integrator is to obtain predictions in fixed order perturbation theory beyond leading order. At present, the techniques are well established to build next-to-leading (NLO) Monte Carlo integrators. The cross section or any other observable distribution is obtained as the sum of the tree-level contribution coherently summed to the one-loop virtual corrections to the process $2 \to n$, plus the real contribution $\sigma(2 \to n+1)$, where the emission of an additional gluon is considered. The knowledge of NLO corrections is important to test the theoretical uncertainty of the calculations by studying their stability against variations of the renormalisation and factorisation scales. Monte Carlo programs able to treat arbitrary event selections can be used to test the

validity of the $K-$factors (defined inclusively as σ_{NLO}/σ_{LO}) at the level of distributions, where different bins can receive different corrections. Even if they are very important tools, Monte Carlo integrators have several limitations: 1) while they work nicely in describing the effects of hard radiation, they fail in the region of soft/collinear singularities, where pure perturbative calculations are unreliable. The accuracy of the calculations can be increased in certain regions of phase space implementing resummed calculations, which are however valid for one observable at a time. Recent work has been devoted to the study of new automatized resummation algorithms [1]; 2) as anticipated in the Introduction, many multiparton final states will be important at LHC. In this case NLO virtual QCD corrections to multi-parton final states are required by a NLO Monte Carlo program. The study of new methods for the calculation of multi-leg virtual amplitudes is the subject of intense research activity. In fact, at present, only $2 \to 2$ and some $2 \to 3$ processes are known with NLO accuracy[1]. For many external legs standard analytical Feynman diagrams calculations become untractable, and new methods are being developed: different groups developed new analytical techniques based on recursion relations [3], while others follow seminumerical methods [4]. The most recent example of application of such tecnhiques is the QCD NLO calculation for the process $gg \to H + 2$ jets [5], which is an important QCD background for Higgs studies in the channel of vector boson fusion; 3) the essential ingredient of any NLO calculation, namely virtual and real corrections, display strong cancellations on the phase space, with the virtual part becoming negative. This prevents a probabilistic interpretation of the elastic event and consequently the generation of unweighted events, which would be distributed in the phase space according to the theory and with unity weight, and would be very useful for detector simulations. These shortcomings allow to introduce the next class of Monte Carlo programs, the Parton Shower Event Generators.

3 Parton Shower Monte Carlo Event Generators

The key ingredient of this class of programs is the parton-shower technique, which allows to generate higher order corrections starting from a simple (tipically $2 \to 1$ or $2 \to 2$) process. The parton-shower technique is a numeric

[1] Actually, several groups are also working on NNLO QCD corrections for simple (but relevant) processes. At present a Monte Carlo integrator (FEWZ [2]) is available for the calculation of exclusive cross section and distributions in Drell-Yan processes at NNLO.

Monte Carlo solution of the DGLAP evolution equations, which allows the calculation of QCD (and also QED) higher order radiative corrections in the region of collinear parton branching and/or soft gluon emission. The subsequent parton emission is a stochastic Markov process in which successive values of the evolution variable Q, the momentum fraction z and the azimuthal angle ϕ are generated (allowing for kinematics reconstruction). With this method, leading logarithms are automatically resummed to all orders of perturbation theory. The process of showering is completely factorized over the kernel amplitude, rendering the Parton Shower event generators general-purpose tools, which provide in a natural way unweighted events. Supplementing the showered events with some model of hadronisation, the Parton Shower event generators allow to describe the complete history of the hadron-hadron interaction, from initial state radiation, hard scattering, showering, hadronization, to final state hadrons and leptons, including the underlying event (beam remnants, collisions between other partons in the hadrons and collisions between other hadrons in the colliding beams). All these stages, apart from the hard subprocess, are process independent. The great advantages of Parton Shower event generators are their universality and the possibility of providing an exclusive description of the events, i.e. the complete information for every particle is recorded. For these reasons they are invaluable tools for detector simulations and they are so widespread among the experimental community. In view of the LHC era, where simulation and data analysis become more and more complex and involve an increasing number of users, transparency and maintenance of the codes start to become an important issue. For this reasons, a number of new codes are being developed within the object oriented framework of the `C++` language.

4 Merging NLO calculations with Parton Shower Event Generators

While Parton Shower event generators describe correctly the radiation in the soft/collinear regions, with automatic resummation of leading logarithmic terms, they fail to describe hard wide-angle radiation because of the approximation in the matrix elements with additional radiation and, as a consequence, the cross sections are correct at Leading Order (LO). During last years, many efforts have been dedicated to the problem of interfacing complete NLO calculations with Parton Shower Event Generators, and a concrete realization of this programme is `MC@NLO` [6], which implements many relevant processes for LHC physics. This programme has several positive features, such as: 1) the normalisations accurate at NLO; 2) the hard tails of the distributions correct as in NLO calculations; 3) soft/collinear emissions treated as in Parton Shower event generator, i.e. automatic resummation of the leading logarithms; 4) soft

matching between soft/collinear and hard regions without double counting; 5) generation of unweighted exclusive events. A potential drawback is the presence of negative weights. Recently a new method of matching parton shower and NLO calculations has been proposed [7], and implemented in POWHEG [8], which allows to avoid negative weights.

5 Multiparton Monte Carlo Event Generators

At present, the previous strategy of merging NLO calculations with Parton Shower Monte Carlo programs is not feasible for arbitrary multiparton processes yet. For such final states, even the calculation of exact LO matrix elements can be a very difficult task, due to the very large number of Feynman diagrams involved. A further difficulty is given by the complex peaking behaviour in the phase space rendering the numerical integration a non trivial task. At present, several matrix element event generators have been constructed, based on helicity amplitudes or completely numerical algorithms for the evaluation of exact LO matrix elements. They can generate partonic weighted and unweighted events. The strategy to describe real final states with hadrons is to pass the unweighted event samples to the Parton Shower Monte Carlo for further showering and hadronization. This kind of modularity (generate events with one program and further use them with another one) has been facilitated by means of the so called Les Houches Accords [9]. During the workshop MC4LHC held at CERN in 2003 [10], there has been an intensive activity aimed at validating the accuracy of the programs through several tuned comparisons.

6 Matching partonic event generators to Parton Shower

The procedure mentioned above of interfacing matrix element unweighted events with Parton Shower is not free of ambiguities. In order to generate partonic events, one needs to implement cuts at the partonic level. They are unphysical, in the sense that the final jet cross-section should be independent of their choice. Moreover, the same configuration of a final state with n jets can be obtained from different partonic configurations with $n+m$ partons, which gives rise to double counting. The general problem of matching multiparton matrix element calculations with parton showers has been extensively studied in the literature and for e^+e^- collisions a solution (CKKW) has been proposed and tested on LEP data [11], which avoids double counting and shifts the dependence on the resolution parameter beyond next-to-leading logarithmic (NLL)

accuracy. The method consists in separating arbitrarily the phase-space regions covered by matrix element and parton shower, and use, for *all* parton multiplicities, vetoed parton showers together with reweighted tree-level matrix elements by means of suitable Sudakov form-factor combinations. The extension of the procedure to hadronic collisions has been proposed in ref. [12], even if a formal proof is still missing. First results of the implementation of the procedure with the programs HERWIG, PYTHIA and SHERPA have been presented in ref. [13]. In the case of hadronic collisions there is a certain degree of arbitrariness, such as the choice of the Sudakov form factors, the choice of the scale of α_s (LO or NLO), the treatment of the highest-multiplicity matrix element, the choice of the clustering scheme, the use of flavour or colour information to define the tree and the related reweighting factors, the treatment of gauge bosons. All these uncertainties entail that a large degree of tuning on the data (possibly process-dependent) will be needed. An independent realization, based on cone algorithms, has been proposed by M.L. Mangano [14]. At present several codes, such as ALPGEN [16], ARIADNE [17], HELAC [18], MADEVENT [19] and SHERPA [20] implement a scheme of matching parton shower and matrix elements. An exhaustive comparison among the above codes has been performed recently in Ref. [21] for the process $W+$ jets. The implementation of the matching procedure in ALPGEN has also been tested through a torough comparison with MC@NLO at LHC energies [22] for $t\bar{t}$ production. This allowed also to point out an inconsistency in MC@NLO in the treatment of the rapidity of the leading jet, thus showing the importance of detailed cross-check among different codes.

In addition to the comparison among different generators, a very important ongoing activity, documented also in the presentations at this conference, is the validation of Monte Carlo programs with Tevatron run II data, thanks to the collaboration between experimentalists and theorists.

7 Electroweak corrections

An important part of the physics program at the LHC is the precision measurement of electroweak parameters, thanks to the huge statistics of charged and neutral current Drell-Yan events. Drell-Yan processes are also very important for detector calibration, collider luminosity determination and new physics searches in the high invariant/transverse mass tail of the leptonic pair.

For all these measurements, precise theoretical predictions, including higher order QCD and electroweak corrections, are needed [23, 24]. Furthermore, the implementation of such contributions in Monte Carlo generators is mandatory, in order to perform realistic studies of the impact of higher-order corrections

on the observables of interest and to compare theory with data. As far as complete $\mathcal{O}(\alpha)$ electroweak corrections to Drell-Yan processes are concerned, they have been computed independently by various authors in [25, 26, 27, 28, 29] for W production and in [30] for Z production. Electroweak tools implementing exact NLO corrections to W production are DK [25], WGRAD2 [26], SANC [28] and HORACE [29], while ZGRAD2 [30] includes the full set of $\mathcal{O}(\alpha)$ electroweak corrections to Z production.

From the calculations above, it turns out that NLO electroweak corrections are dominated, in the resonant region, by final-state QED radiation containing large collinear logarithms of the form $\log(\hat{s}/m_l^2)$, where $\hat{s}$ is the squared partonic center-of-mass energy and m_l is the lepton mass. Since these corrections amount to several per cents around the jacobian peak of the W transverse mass and lepton transverse momentum distributions and cause a significant shift (of the order of 100 MeV) in the extraction of the W mass M_W at the Tevatron, the contribution of higher-order corrections due to multiple photon radiation from the final-state leptons must be taken into account in the theoretical predictions, in view of the expected precision (at the level of 15-20 MeV) in the M_W measurement at the LHC. The contribution due to multiple photon radiation has been computed, by means of a QED PS approach, in [31] for W production and in [32] for Z production, and implemented in the event generator HORACE. Higher-order QED contributions to W production have been calculated independently in [33] using the YFS exponentiation, and are available in the generator WINHAC. The treatment of multi-photon corrections has been recently improved in HERWIG (through the code SOPHTY [34], using the YFS formalism) and in the universal package PHOTOS [35], by means of a QED PS-like approach. Comparisons of such multi-photon calculations are documented in [35, 34, 36], showing good agreement, in spite of the quite different theoretical ingredients. It is worth noting that, for what concerns the precision measurement of M_W, the shift induced by higher-order QED corrections is about 10% of that caused by one-photon emission and of opposite sign, as shown in [31]. Therefore, such an effect is not negligible in view of the aimed accuracy in the M_W measurement at the LHC, especially for the W decays into muons.

A further important phenomenological feature of electroweak corrections is that, in the region important for new physics searches (i.e. where the W transverse mass is much larger than the W mass or the invariant mass of the final state leptons is much larger than the Z mass), the NLO electroweak effects become large (of the order of 20-30%) and negative, due to the

appearance of electroweak Sudakov logarithms $\propto -(\alpha/\pi)\log^2(\hat{s}/M_V^2)$, $V = W, Z$ [25, 26, 29, 30]. Furthermore, in this region, weak boson emission processes (e.g. $pp \to e^+\nu_e V + X$), that contribute at the same order in perturbation theory, can partially cancel the large Sudakov corrections, when the weak boson V decays into unobserved $\nu\bar{\nu}$ or jet pairs, as recently shown in [37].

In spite of this detailed knowledge of higher-order electroweak and QCD corrections, the combination of their effects is still at a very preliminary stage. There is only one attempt known in the literature [38], where the effects of QCD resummation are combined with NLO QED final-state corrections, leaving room for more detailed studies of the interplay between electroweak and QCD corrections to W/Z production at the LHC. Preliminary results in this direction have been presented in Ref. [39].

8 Summary

The last few years have seen intensive efforts in the development of methods to update existing Monte Carlo simulation programs or write new ones, in order to meet the requirements posed by the LHC: very high statistics for all SM processes studied up to now and presence of multi-jet final states. In this contribution a review of the three general classes of simulation codes (Monte Carlo integrators, Parton Shower event generators and Multi-parton event generators) has been presented. After a discussion of the good features and limitations of each approach, the techniques recently studied to merge different classes have been illustrated, namely NLO calculations with Parton Shower event generators on one hand and Multiparton matrix element generators with Parton Shower simulation packages on the other hand. While the field is very active with the approaching of the LHC startup, the programs and methods already available are being validated against the Tevatron run II data. The projected accuracy at LHC, in particular for Drell-Yan processes, will require also the inclusion of electroweak corrections. Actually at present several dedicated Monte Carlo programs already include complete electroweak NLO corrections and/or resummed multi-photon emission.

9 Acknowledgements

We would like to thank G. Bellettini, G. Chiarelli and M. Greco for their invitation and warm hospitality during the conference.

References

1. A. Banfi, G. Salam and G. Zanderighi, JHEP **0503** 073 (2005).
2. K. Melnikov and F. Petriello, Phys. Rev. Lett. **96**, 231803 (2006); Phys. Rev. **D74**, 114017 (2006).
3. See for instance Z. Bern, L.J. Dixon and D.A. Kosower, Annals Phys. **322**, 1587 (2007) and references therein.
4. W.T. Giele and E.W.N. Glover, JHEP **0404**, 029 (2004); R.K. Ellis, W.T. Giele and G. Zanderighi, Phys. Rev. **D73** 014027 (2006); A. Ferroglia, M. Passera, G. Passarino and S. Uccirati, Nucl. Phys. **B650**, 162 (2003); T. Binoth, M. Ciccolini and G. Heinrich, Nucl. Phys. Proc. Suppl. **157**, 48 (2006); G. Ossola, C.G. Papadopoulos and R. Pittau, Nucl. Phys. **B763**, 147 (2007).
5. R.K. Ellis, W.T. Giele and G. Zanderighi, Phys. Rev. **D72**, 054018 (2005); Erratum-ibid. **D74**, 079902 (2006); J.M. Campbell, R.K. Ellis and G. Zanderighi, JHEP **0610**, 028 (2006).
6. S. Frixione, B.R. Webber, JHEP **0206** 029 (2002); `hep-ph/0207182`; `hep-ph/0307146`; `hep-ph/0309186`; `hep-ph/0402116`; S. Frixione, P. Nason, B.R. Webber, JHEP **0308** 007 (2003); S. Frixione et al. `hep-ph/0512250`.
7. P. Nason, JHEP **0411**, 040 (2004).
8. P. Nason and G. Ridolfi, JHEP **0608**, 077 (2006); S. Frixione, P. Nason, G. Ridolfi, arXiv:0707.3081 [hep-ph]; arXiv:0707.3088 [hep-ph]; arXiv:0709.2092 [hep-ph].
9. E. Boos et al., `hep-ph/0109068`; W. Giele et al., `hep-ph/0204316`; J. Alwall et al., Comput. Phys. Commun. **176**, 300 (2007).
10. Workshop on "MC tools for the LHC", CERN, 7 July - 1 August 2003.
11. S. Catani et al., JHEP **0111** (2001) 063; L. Lönnblad, JHEP **0205** 046 (2002); R. Kuhn et al., `hep-ph/0012025`; F. Krauss, R. Kuhn and G. Soff, J. Phys. G **26** L11 (2000).
12. F. Krauss, JHEP **0208** 015 (2002).
13. S. Mrenna and P. Richardson, JHEP **0405** 040 (2004); F. Krauss et al., Phys. Rev. **D70** 114009 (2004), Phys. Rev .**D72** 054017 (2005); A. Schälicke and F. Krauss, JHEP **0507** 018 (2005); T. Gleisberg et al., Phys. Rev. **D72** 034028 (2005).

14. M.L. Mangano, talk given at [15], 15 November 2002.

15. Monte Carlo Tuning Working Group, FNAL, 29-30 April 2003.

16. M.L. Mangano et al., JHEP **0307** 001 (2003).

17. L. Lönnblad, Comput. Phys. Commun. **71**, 15 (1992).

18. A. Kanaki and C.G. Papadopoulos Comput. Phys. Commun. **132**, 306 (2000); C. G. Papadopoulos and M. Worek, Eur. Phys. J. **C50**, 843 (2007).

19. T. Stelzer and W. F. Long Comput. Phys. Commun. **81**, 357 (1994); F. Maltoni and T. Stelzer *JHEP* **02** (2003) 027.

20. T. Gleisberg, S. Höche, F. Krauss, A. Schälicke, S. Schumann and J. Winter JHEP **0402**, 056 (2004); A. Schälicke and F. Krauss JHEP **07**, 018 (2005).

21. J. Alwall et al., arXiv:0706.2569 [hep-ph]; S. Höche et al., hep-ph/0602031.

22. M.L. Mangano,M. Moretti, F. Piccinini and M. Treccani, JHEP **0701**, 013 (2007).

23. P.M. Nadolsky, AIP Conf. Proc. **753** (2005) 158.

24. U. Baur, arXiv:hep-ph/0511064.

25. S. Dittmaier and M. Krämer, Phys. Rev. **D65** (2002) 0703007.

26. U. Baur and D. Wackeroth, Phys. Rev. **D70** (2004) 073015.

27. V. A. Zykunov, Eur. Phys. J. Direct **C3** (2001) 9; Phys. Atom. Nucl. **69** (2006) 1522.

28. A. Arbuzov, D. Bardin, S. Bondarenko, P. Christova, L. Kalinovskaya, G. Nanava and R. Sadykov, Eur. Phys. J. **C46** (2006) 407.

29. C.M. Carloni Calame, G. Montagna, O. Nicrosini and A. Vicini, JHEP **12** (2006) 016.

30. U. Baur, O. Brein, W. Hollik, C. Schappacher and D. Wackeroth, Phys. Rev. **D65** (2002) 033007.

31. C.M. Carloni Calame, G. Montagna, O. Nicrosini and M. Treccani, Phys. Rev. **D69** (2004) 037301.

32. C.M. Carloni Calame G. Montagna, O. Nicrosini and M. Treccani, JHEP **05** (2005) 019.

33. S. Jadach and W. Płaczek, Eur. Phys. J. **C29** (2003) 325.

34. K. Hamilton and P. Richardson, JHEP **0607** (2006) 010.

35. P. Golonka and Z. Was, Eur. Phys. J. **C45** (2006) 97.

36. C.M. Carloni Calame, S. Jadach, G. Montagna, O. Nicrosini and W. Płaczek, Acta Phys. Pol. **B35** (2004) 1643.

37. U. Baur, Phys. Rev. **D75** (2007) 013005.

38. Q.-H. Cao and C.-P. Yuan, Phys. Rev. Lett. **93** (2004) 042001; arXiv:hep-ph/0401171.

39. G. Balossini, C.M. Carloni Calame, G. Montagna, O. Nicrosini, F. Piccinini and A. Vicini, work in preparation. Preliminary results presented at Cracow Epyphany Conference, 4-6 January 2007, Cracow, Poland; DIS 2007, 16-20 April 2007, Munich, Germany; LoopFest VI, 16-18 April 2007, Fermilab, USA; Les Houches 2007, 11-29 June 2007, Les Houches, France; Hera and LHC 2007, 14 March 2007, DESY, Hamburg, Germany; HEP 2007, 19-25 July 2007, Manchester, England; Matter to the Deppest, 5-11 September 2007, Ustron, Poland.

IMPLICATIONS OF RIGHT-HANDED NEUTRINOS WITH ELECTROWEAK-SCALE MASSES

P. Q. Hung
Dept. of Physics, University of Virginia, 382 McCormick Road, P. O. Box 40
Charlottesville, Virginia 22904-4714, USA

Abstract

The possibility of constructing a model in which right-handed neutrinos have electroweak-scale masses as well as being *non-sterile* was espoused in [1]. In this talk, I will review the ideas and results of [1] and discuss its implications for colliders such as the Tevatron, LHC and ILC.

1 Introduction

The origin of neutrino masses and the puzzle over their smallness are two of the outstanding questions in particle physics. Of related importance is the nature of the neutrinos: Are they Dirac or Majorana particles? There is no doubt about the importance that neutrinos have in particle physics and cosmology: The understanding of their masses unquestionably points to features that cannot be explained by staying strictly within the Standard Model (SM) such as, for example, the baryon number asymmetry which might arise through the so-called leptogenesis coming from the decay of a heavy Majorana neutrino. Furthermore, results from neutrino oscillation data indicated a mixing matrix in the lepton sector which is markedly different from that coming out of the quark sector. One cannot help but wonder if, despite this dissimilarity, the two sectors can "learn" from each other.

Neutrino masses are believed to be be tiny compared with other fermion masses, of order $O(< 1\,eV)$. Why this is so is one of the biggest mysteries which we are trying to unlock. The "simplest" way to give a mass to the neutrino is to add a SM singlet right-handed neutrino to the SM and give it a Dirac mass. However, to account for the smallness of the neutrino masses, Yukawa couplings of $O(10^{-11})$ have to be put in *by hand*. This is generally considered to be unnatural unless there are dynamical or symmetrical reasons for it to be so [2]. The by-far most popular scenario is the quintessential see-saw mechanism [3] where, in addition to the Dirac mass (m_D) term which couples left- and right-handed neutrinos, a lepton-number-violating Majorana mass (M_R) term for the right-handed (the simplest version) neutrinos is written down. In the "standard" see-saw mechanism, this Majorana mass term is *huge* compared with the Dirac mass term (which is proportional to the electroweak scale) resulting in a tiny mass $\sim m_D^2/M_R$ for the lighter of the two eigenstates. The right-handed neutrinos being sterile in this scenario and being extremely heavy are practically undetectable, at least directly. Therefore, in its simplest version, one just cannot directly verify the see-saw mechanism since one cannot detect the right-handed neutrinos. Are there other ways?

Since, within the framework of see-saw scenarios, the light neutrino sector is only sensitive to the ratio m_D^2/M_R, it is legitimate to ask how one can change m_D and M_R in such a way as to keep m_D^2/M_R unchanged. The question is the following: Could one lower both of them in such a way as to make M_R slide into a region, in particular around the electroweak scale, where one could have an access to the right-handed neutrino sector? This is one of the motivations for the construction of a model of electroweak-scale right-handed neutrino mass [1]. The organization of the talk will be as follows. First, a brief review of the see-saw mechanism will be presented. Next, we will present arguments on why

the right-handed neutrinos can be as light as or lighter than the electroweak scale. We then discuss the implications of electroweak-scale ν_R's, including the production and decays of ν_R's as well as lepton-number violating processes at colliders. A conclusion will follow the phenomenological discussion.

2 The see-saw mechanism in a nutshell

In the "standard" see-saw scenarios [3], ν_R's are SM *singlets* and are commonly termed *sterile*. This has obviously deep implications on the nature and sizes of the Dirac and Majorana masses.

- Dirac Mass:

  The neutrino Yukawa interaction with a sterile right-handed neutrino which gives rise to the Dirac mass term is usually written as

  $$\mathcal{L}_D = g_L \bar{l}_L \phi \nu_R + H.c.\,, \tag{1}$$

  where $l_L = (\nu_L, e_L)$ and $\phi = (\phi^0, \phi^-)$ are the usual SM $SU(2)_L$ doublets. When $\langle\phi\rangle = (\Lambda_{EW}/\sqrt{2}, 0)$ with $\Lambda_{EW} \approx 246\, GeV$, one obtains the following the neutrino Dirac mass

  $$m_D = g_L\, \Lambda_{EW}/\sqrt{2}\,. \tag{2}$$

  In consequence, the Dirac mass is proportional to the electroweak scale Λ_{EW}, although it crucially depends on an arbitrary Yukawa coupling g_L. It is worth to emphasize again that this is the case because ν_R is a SM singlet. We will see below that when ν_R is *not* a SM singlet, the Dirac mass will no longer be related to Λ_{EW}.

- Majorana mass:

  The source of the right-handed neutrino Majorana mass is quite model-dependent, although it is commonly found within the framework of a Grand Unified Theory (GUT). In what follows, we will write it simply as

  $$\mathcal{L}_M = M_R\, \nu_R^T\, \sigma_2\, \nu_R\,. \tag{3}$$

  The above Majorana mass term violates lepton number by two units.

- Mass eigenvalues:

  The two well-known eigenvalues are $\sim -m_D^2/M_R$ and M_R for $M_R \gg m_D$. The two neutrino mass eigenstates which are now Majorana particles are approximately the left-handed neutrino for the lighter state and the right-handed neutrino for the heavy state. Since m_D is proportional to

the electroweak scale (modulo the unknown Yukawa coupling), a light neutrino with mass of order O($< 1\,eV$) in general requires M_R to be of order O($\sim 10^{13}\,GeV$). In this type of scenarios, one just *cannot directly* detect the right-handed neutrinos.

Since neutrinos (both the light state and the heavy state) are now Majorana particles, it is therefore of utmost importance to test this feature of the model. One should look for processes that violate lepton number conservation. In the light sector, one could look for neutrinoless double beta decay for example which gives an upper bound, not on the mass of the light state, but on the combination $< m_{\beta\,\beta} >= [\sum |U_{ei}|^2 m_i^2]^{1/2} < 0.35\,eV$, where m_i are the light masses [4]. This search is not easy because of various nuclear details. This is where the right-handed neutrino sector comes in if the right-handed neutrinos are light enough. As for the heavy sector, at least in its simplest version, there is no such a possibility for testing the Majorana nature of the right-handed neutrinos. Electroweak-scale SM *singlet* right-handed neutrinos were contemplated as a possibility which could enable one to probe the right-handed sector. There are however a number of delicate issues with these scenarios which might prevent its observability unless some fine tuning is realized [5]. An extensive list of references of works dealing with "light" right-handed neutrinos can be found in [5].

Can the right-handed neutrinos be *non-sterile*? If one can construct such a scenario then one can hope to be able to find them at colliders and test the Majorana nature of neutrinos. In what follows I will describe a model in which right-handed neutrinos are both "light", i.e. having electroweak-scale masses, and "observable", i.e. transforming non-trivially under the SM gauge group.

3 A Model of electrowek-scale right-handed neutrino mass

The objective of [1] was to construct a model in which ν_R's are *not* sterile and have a *low* mass of O(Λ_{EW}). There are two constraints that have to be satisfied in the construction of such a model.

- A non-sterile ν_R will couple to the Z boson. There is however a strong constraint from the Z width: There are only *three* light left-handed neutrinos.
- A Majorana bilinear $\nu_R^T\,\sigma_2\,\nu_R$ will transform *non-trivially* under $SU(2)_L \otimes U(1)_Y$. This imposes a strong constraint on the Higgs field which couples to that bilinear and which develops a non-zero vacuum expectation value, namely one has to preserve the successful relation $M_W = M_Z\,\cos\theta_W$!

As we shall see below, the first constraint sets a *lower bound* on the right-handed neutrino mass while the second will determine the enlargement of the Higgs structure of an extended SM.

The simplest possibility and the one that was used in [1] is to put ν_R into a doublet of $SU(2)_L$. If it belongs to a doublet then its partner would be a *negatively* charged right-handed lepton. Could it be the right-handed SM charged lepton? The answer is negative because neutral current experiments have shown that the SM right-handed charged leptons are $SU(2)_L$ singlets. In consequence, this right-handed charged lepton has to be a new type: the so-called *mirror* lepton. We write this new doublet as follows

$$l_R^M = \begin{pmatrix} \nu_R \\ e_R^M \end{pmatrix}, \tag{4}$$

where now the left-handed charged mirror lepton, namely e_L^M, is a SM singlet. So, the above doublet plus e_L^M will be the mirror copy of the SM doublet $l_L = (\nu_L, e_L)$ and e_R.

In a similar fashion to the "standard" see-saw scenario, one can write down the interactions which will give a Dirac mass term for the neutrino and a Majorana mass term.

- Dirac mass:

  A Dirac mass term for the neutrino is proportional to $\bar{l}_L\, l_R^M$. This combination can couple to a SM *singlet* scalar field ϕ_S as follows

  $$\mathcal{L}_S = g_{Sl}\, \bar{l}_L\, \phi_S\, l_R^M + H.c\,. \tag{5}$$

  When ϕ_S develops a non-vanishing VEV, namely $\langle \phi_S \rangle = v_S$, the neutrino Dirac mass takes the form

  $$m_D = g_{Sl}\, v_S\,. \tag{6}$$

  In this model, the Dirac mass is *not* linked to the electroweak scale. We will see below the range of values that v_S can take.

  Notice that for the charged fermions (leptons and quarks), there are additional couplings to ϕ_S involving the $SU(2)_L$ singlets of the forms $\bar{f}_L^M\, f_R$, where f stands for q or e. For simplicity, one can assume similar Yukawa couplings to the ones given in the above form. This yields the mixing given in [1]. There it was shown that the mixing between SM and mirror charged fermions is *negligible*.

- Majorana mass:

In our model, the lepton-number violating relevant fermion bilinear is $l_R^{M,T}\,\sigma_2 l_R^M$. This transforms as a singlet and as a triplet of $SU(2)_L$. A singlet Higgs field which couples to this bilinear and which develops a VEV would break charge conservation. The only other option is a triplet Higgs $\tilde{\chi} = (3, Y/2 = 1)$ which is written explicitely as

$$\tilde{\chi} = \frac{1}{\sqrt{2}}\,\vec{\tau}.\vec{\chi} = \begin{pmatrix} \frac{1}{\sqrt{2}}\,\chi^+ & \chi^{++} \\ \chi^0 & -\frac{1}{\sqrt{2}}\,\chi^+ \end{pmatrix}. \tag{7}$$

which couples to the bilinear as follows

$$\mathcal{L}_M = g_M\, l_R^{M,T}\,\sigma_2\,\tau_2\,\tilde{\chi}\, l_R^M\,. \tag{8}$$

With $\langle\chi^0\rangle = v_M$, the Majorana mass is now

$$M_R - g_M\, v_M\,. \tag{9}$$

The above VEV breaks $SU(2)_L$. The successful relation $M_W = M_Z\,\cos\theta_W$ ($\rho = 1$ at tree level) which relies primarily on $SU(2)_L$ Higgs fields being doublets would be spoiled unless $v_M \ll \Lambda_{EW}$. This is a severe constraint that needs to be addressed in our model.

An important remark is in order here. In order to prevent the left-handed neutrinos to acquire a Majorana mass of the same order asthe right-handed one as well as to prevent a large Dirac mass (coupling of $\bar{l}_L\, l_R^M$ to $\tilde{\chi}$), a global $U(1)_M$ symmetry is imposed [1] (and explicitely broken by the Higgs sector). A tiny Majorana mass for the left-handed neutrinos arises at one-loop level [1].

An elegant solution to this problem was provided about twenty years ago by [6]: If the Higgs potential which now includes triplet scalars possesses a custodial symmetry such that $M_W = M_Z\,\cos\theta_W$ is preserved at tree-level then the triplet VEV's can be as large as the electroweak scale. $\rho = 1$ is therefore the manifestation of an approximate *custodial* global $SU(2)$ symmetry of the Higgs potential. To maintain that *custodial symmetry*, one can add an additional Higgs triplet $\xi = (3, Y/2 = 0)$ which can be grouped with $\tilde{\chi} = (3, Y/2 = 1)$ to form

$$\chi = \begin{pmatrix} \chi^0 & \xi^+ & \chi^{++} \\ \chi^- & \xi^0 & \chi^+ \\ \chi^{--} & \xi^- & \chi^{0*} \end{pmatrix}, \tag{10}$$

where the full potential now exhibits a global $SU(2)_L \otimes SU(2)_R$ symmetry. The following VEV of χ breaks $SU(2)_L \otimes SU(2)_R$ down to a custodial

$SU(2)$ symmetry

$$\langle \chi \rangle = \begin{pmatrix} v_M & 0 & 0 \\ 0 & v_M & 0 \\ 0 & 0 & v_M \end{pmatrix} . \tag{11}$$

This gives

$$M_W = g\, v/2\,;\, M_Z = M_W/\cos\theta_W\,, \tag{12}$$

with

$$v = \sqrt{v_2^2 + 8\, v_M^2}\,, \tag{13}$$

and

$$\langle \Phi \rangle = v_2/\sqrt{2}\,, \tag{14}$$

where Φ is a doublet. The nice feature of this scenario is the fact that now v_M *can* be of the order of the electroweak scale *without* spoiling $\rho = 1$. As discussed in [1], there are no massless NG bosons in this model since $U(1)_M$ is explicitely broken.

The upshot of all this is the following nice result

$$M_R \sim O(\Lambda_{EW})\,. \tag{15}$$

The right-handed neutrino mass can now be *naturally* of the order of the electroweak scale (but not more)!

How low can M_R be? A right-handed neutrino with a mass lower than half the Z-boson mass would contribute to the Z width with the amount as the left-handed one. This is ruled out experimentally. We therefore conclude that M_R lies in a rather "narrow" range

$$M_Z/2 < M_R < \Lambda_{EW}\,. \tag{16}$$

- Estimate of the singlet Higgs VEV:

  With the light neutrino mass $m_\nu \leq 1\, eV$ and $M_R \sim O(\Lambda_{EW})$, one can get a rough estimate on the singlet VEV by putting $g_{SL} \sim O(1)$ to give

$$m_D \sim v_S \sim 10^5\, eV\,. \tag{17}$$

  A small scale such as v_S is interesting in many respects. First there appears to be some kind of hierarchy problem since v_S is six orders of magnitude smaller than v_M, although it is not as severe as the GUT hierarchy problem. However, one can imagine that v_S might actually be the *present* classical value of the singlet Higgs field $\phi_S(t_0)$ whose effective potential might be of a "slow-rolling" type. This type of scenario was

proposed in a mass-varying neutrino (MaVan) model of the first reference of [7]. The Dirac will keep increasing until ϕ_S reaches the true minimum which could be of the order of the electroweak scale itself!

What (15) and (17) tell us is that, in our scenario, the mass scales participating in the see-saw mechanism are slided "downward" with respect to the "standard" see-saw scenario, but now there is one phenomenological advantage: One can now search for the right-handed neutrinos at colliders. As we have mentioned above, the light neutrinos are only sensitive to the ratios m_D^2/M_R and not directly to the scale m_D. A discovery of an electroweak-scale right-handed neutrino would greatly help us determine what m_D should be. We now turn to the discussion on the detectability of the electroweak-scale right-handed neutrinos.

4 Phenomenology of Electroweak Scale ν_R's

Since we are dealing with *Majorana neutrinos* wirh electroweak scale masses, it is not surprising that we should expect lepton-number violating processes at electroweak scale energies. In particular, we should be able to produce ν_R's and observe their decays at colliders (LHC, etc...). The characteristic signatures will be *like-sign dilepton* events which are a high-energy equivalent of neutrinoless double beta decay.

Since ν_R's are members of $SU(2)_L$ doublets $l_R^M = \begin{pmatrix} \nu_R \\ e_R^M \end{pmatrix}$, they interact with the Z and W bosons. They are *no longer* sterile! Let us now recall that we have the constraint $M_Z/2 < M_R < \Lambda_{EW}$. This means that, in principle, ν_R's can be produced at colliders, being sufficiently light. Unlike the case with low-mass singlet ν_R's whose production at colliders could be suppressed, the right-handed neutrinos in our scenario couple directly to the Z boson and the production of a pair of ν_R's is unsuppressed. One has

$$q + \bar{q} \to Z \to \nu_R + \nu_R \,. \tag{18}$$

Since ν_R's are Majorana particles, they can have transitions such as $\nu_R \to l_R^{M,\mp} + W^{\pm}$. A heavier ν_R can decay into a lighter l_R^M and one can have

$$\nu_R + \nu_R \to l_R^{M,\mp} + l_R^{M,\mp} + W^{\pm} + W^{\pm} \to l_L^{\mp} + l_L^{\mp} + W^{\pm} + W^{\pm} + \phi_S + \phi_S \,, \tag{19}$$

where ϕ_S would be missing energy. This gives rise to interesting *like-sign* dilepton events. Since this involves missing energy, one would have to be careful with background. For example, one of such backgound could be a production of $W^{\pm}\, W^{\pm}\, W^{\mp}\, W^{\mp}$ with 2 like-sign W's decaying into a charged lepton plus

a neutrino ("missing energy"). But...This is of $O(\alpha_W^2)$ in amplitude smaller than the above process. In addition, depending on the lifetime of the mirror leptons, the SM leptons appear at a displaced vertex. Lepton-number violating process with like-sign dileptons can also occur with ν_R's in the intermediate state (from $W^\pm W^\pm \to l_L^\pm + l_L^\pm$) but that involves very small mixing angles of the order $\frac{m_\nu}{M_R}$.

In consequence, within the framework of our model, one has the interesting prospect of producing and detecting electroweak-scale right-handed neutrinos through lepton-number violating processes such as like-sign dileptons as described above. Detailed phenomenological analyses are in progress.

5 Other phenomenological consequences

There are several other interesting consequences of the model which are currently under investigation. One of such consequences involves the phenomenology of the triplet Higgses that exist in this model: $\tilde{\chi}$ and ξ. Since they carry electroweak quantum numbers, they can be produced at colliders such as the LHC or ILC. The various scalars in $\tilde{\chi}$ couple to the mirror fermions through Eq. (8) and can possibly searched for through the decays of the mirror fermions. ξ does not couple directly to fermions (SM and mirror) and the various components would decay either directly to a pair of electroweak gauge bosons either real or virtual.

The mirror fermions carry exactly the same quantum numbers as the SM fermions. They can be produced in exactly the same manner as the SM fermions at colliders. However their decays will be quite interesting. From Eq. (5), one can see that a charged mirror fermion can decay into its SM counterpart plus ϕ_S which would be missing energy. This kind of decay for the charged mirror leptons has already been mentioned above (19).

Last but not least, vacuum stability considerations will link the masses of the scalar sector which now includes the triplet Higgses to those of the fermions (SM and mirror). This is under preparation.

6 Conclusion

- It is possible to have a seesaw mechanism in which the Majorana mass of the right-handed neutrinos can be of the order of the electroweak scale and, in fact, can be situated in a "narrow" range $M_Z/2 < M_R < \Lambda_{EW}$. There is *no* reason why it should be close to some GUT scale.

- The lepton-number violating processes coming from the "heavy" *non-sterile* ν_R's can now be accessible *expermentally* at colliders! In contrast,

in models where ν_R's are SM singlets, it is problematic to both have a light neutrino and a non-negligible coupling between sterile and active neutrinos, resulting in a situation in which it might be extremely hard to detect lepton-number violating processes at the LHC for example [5].

- There is a rich spectrum of particles which can be tested in a not-too-distant future.

Below is a grossly incomplete list of references. My apologies for not being able to list all the references because of length restrictions.

7 Acknowledgements

I would like to thank Mario Greco and the organizers of La Thuile 07 for an exciting conference and the Aspen Center for Physics where part of this manuscript is written. This work is supported in parts by the US Department of Energy under grant No. DE-A505-89ER40518.

References

1. P. Q. Hung, Phys. Lett. B**649**, 275 (2007) [arXiv:hep-ph/0612004].

2. See e.g. P. Q. Hung, Phys. Rev. D**67**, 095011 (2003) [arXiv:hep-ph/0210131].

3. P. Minkowski, Phys. Lett. B **67**, 421 (1977); M. Gell-Mann, P. Ramond and R. Slansky, in *Supergravity*, eds. P. van Niewenhuizen and D. Z. Freedman (North Holland 1979); T. Yanagida, in Proceeding of *Workshop on Unified Theory and Baryon Number in the Universe*, eds. O. Sawada and A. Sugamoto (KEK 1979); S. L. Glashow, *The future of elementary particle physics*, in *Proceedings of the 1979 Cargese Summer Institute on quarks and leptons* (M. Levy, J. -L. Basdevant, D. Speiser, J. Speiser, R. Gatsmans, and M. Jacob, eds.) Plenum Press, New York, 1980, p. 687; R. N. Mohapatra and G. Senjanovíc, Phys. Rev. Lett. **44**, 912 (1980); J. Schechter and J. W. F. Valle, Phys. Rev. D **22**, 2227 (1980). For recent reviews, see V. Barger, D. Marfatia, and K. Whisnant, Int, J,. Mod. Phys. **E12**, 569 (2003) [arXiv:hep-ph/0308123]; R. N. Mohapatra *et al*, arXiv:hep-ph/0510213; G. Altarelli, arXiv:hep-ph/0611117, and references therein.

4. See e.g. Petr Vogel, arXiv:hep-ph/0611243; K. Zuber,Acta Phys. Polon. B**37**, 1905 (2006) [arXiv:nucl-ex/0610007], and references therein.

5. Jörn Kersten and Alexei Yu. Smirnov, arxiV:0705.3221v1, and references therein.

6. H. Georgi and M. Machacek, Nucl. Phys. **B262**, 463 (1985); R. S. Chivukula and H. Georgi, Phys. Lett. B **182**, 181 (1986); P. H. Frampton, M. C. Oh, and T. Yoshikawa, Phys. Rev. **D66**, 033007 (2002) [arXiv:hep-ph/0204273]. For a recent use of a Higgs triplet, see E. Ma and U. Sarkar, Phys. Lett. B **638**, 356 (2006) [arXiv:hep-ph/0602116].

7. P. Q. Hung, arXiv:hep-ph/0010126; P. Gu, X. Wang, and X. Zhang, Phys. Rev. **D68**, 087301 (2003); R. Fardon, A. E. Nelson, and N. Weiner, JCAP **0410**, 005 (2004). Cosmo MSW effects in these models were studied by Pham Quang Hung and Heinrich Päs, Mod. Phys. Lett. A**20**, 1209 (2005) [arXiv:astro-ph/0311131].

SESSION IV – CP VIOLATION AND RARE DECAYS

- *Matteo Rama* — Measurements of the Angles of the Unitarity Triangle at Babar and Belle
- *Christoph Schwand* — Measurements of $|V_{cb}|$ and $|V_{ub}|$
- *Shouhei Nishida* — Rare B Decays Including Penguin Decays (Mini Review)
- *Sasa Fratina* — Hot topics from Belle: Time Dependent CP Violation in $B^0 \rightarrow D^+D^-$
- *Spasimir Balev* — Recent Results from NA48
- *Patrizia De Simone* — Recent Results on KAON Decays from KLOE at DAΦNE
- *Viktor Novikov* — On the Pauli Principle Violations in QFT
- *Marco Ciuchini* — Precision Flavour Physics

MEASUREMENT OF THE ANGLES OF THE UNITARITY TRIANGLE AT BABAR AND BELLE

Matteo Rama
INFN, Laboratori Nazionali di Frascati, Via E. Fermi 40, I-00044 Frascati, Italy

Abstract

Since the start of the operations in 1999 the experiments BaBar and Belle have collected a data sample of more than 1.2 billions $B\bar{B}$ pairs produced at the $\Upsilon(4S)$ energy. This huge sample allows a precise determination of the irreducible phase of the Cabibbo-Kobayashi-Maskawa matrix, responsible for CP violation in the quark sector within the Standard Model of fundamental interactions. We present a review of the main techniques and results of the measurement of the angles β, α and γ of the unitarity triangle.

1 Introduction

The elements of the Cabibbo-Kobayashi-Maskawa (CKM) matrix [1] provide the couplings of the weak charged-current interaction between quarks: the relevant term in the interaction lagrangian of the Standard Model can be written as $\mathcal{L}_I \propto \overline{u_i}\ \gamma^\mu(1-\gamma^5)V_{ij}\ d_j\ W^+_\mu + h.c.$, where $u_i = \{u,c,t\}$ and $d_j = \{d,s,b\}$ are the up- and down- quarks, and V is the CKM matrix. V is unitary and can be parameterized by three mixing angles and one CP-violating phase. A commonly used parameterization was proposed by Wolfenstein [2] in terms of the parameters λ, A, ρ and η (Fig. 1, top). The unitarity condition imposes nine relations between the elements, $\sum_k V^*_{ki}V_{kj} = \delta_{i,j}$, of which $V_{ud}V^*_{ub} + V_{cd}V^*_{cb} + V_{td}V^*_{tb} = 0$ represents a triangle in the complex plane, with sides of the same order of magnitude λ^3 and angles

$$\alpha = arg\left[-\frac{V_{td}V^*_{tb}}{V_{ud}V^*_{ub}}\right], \quad \beta = arg\left[-\frac{V_{cd}V^*_{cb}}{V_{td}V^*_{tb}}\right], \quad \gamma = arg\left[-\frac{V_{ud}V^*_{ub}}{V_{cd}V^*_{cb}}\right]. \qquad (1)$$

This triangle is called *unitarity triangle*. When the sides are divided by $V_{cd}V^*_{cb}$, the apices of the trianlge are $(0,0)$, $(1,0)$ and (ρ,η). (Fig. 1, bottom). The elements of the CKM matrix are fundamental parameters of the Standard Model and their values are not predicted by the theory. It's important not only to measure them precisely, but also to over constrain them and search for inconsistencies between independent measurements, that may show evidence of physics beyond the Standard Model. The measurement of the angles α, β and γ, which alone over constrain (ρ,η), is an important part of this program.

$$V = \begin{pmatrix} 1-\lambda^2/2 & \lambda & A\lambda^3(\rho - i\eta) \\ -\lambda & 1-\lambda^2/2 & A\lambda^2 \\ A\lambda^3(1-\rho-i\eta) & -A\lambda^2 & 1 \end{pmatrix} + \mathcal{O}(\lambda^4)$$

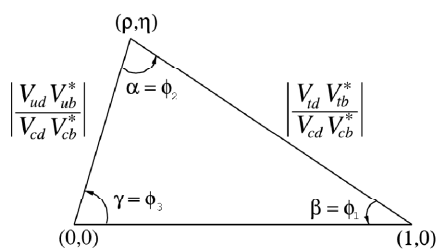

Figure 1: *Top: Wolfenstein parameterization of the CKM matrix. Bottom: the unitarity triangle showing the definition of the angles α, β and γ, also known as ϕ_1, ϕ_2, ϕ_3.*

2 Experimental techniques

The measurements of the angles α and β discussed in the following sections are performed through the study of time-dependent rates and CP asymmetries of neutral B mesons decays. The time-dependent CP asymmetry is defined as

$$\begin{aligned} \mathcal{A}_{CP} &\equiv \frac{N(\bar{B}^0(\Delta t) \to f_{CP}) - N(B^0(\Delta t) \to f_{CP})}{N(\bar{B}^0(\Delta t) \to f_{CP}) + N(B^0(\Delta t) \to f_{CP})} \\ &= S_f \sin(\Delta m_d \Delta t) - C_f \cos(\Delta m_d \Delta t), \end{aligned} \tag{2}$$

where $N(B^0(\Delta t) \to f_{CP})$ is the number of B^0 mesons decayed into the CP eigenstate at a time Δt after the decay of the $\bar{B}^0$ meson, Δm_d is the $B^0 - \bar{B}^0$ oscillation frequency, and the coefficients S_f and C_f are functions of the $B^0\bar{B}^0$ mixing parameters and of the decay amplitudes:

$$S_f = \frac{2\mathrm{Im}\lambda_f}{1+|\lambda_f|^2}, \quad C_f = \frac{1-|\lambda_f|^2}{1+|\lambda_f|^2}, \qquad \text{with } \lambda_f = \frac{q}{p}\frac{\bar{A}_f}{A_f}\,. \tag{3}$$

The Standard Model predicts $q/p \simeq e^{-i2\beta}$ with good precision. If the decay is dominated by a single decay amplitude or by amplitudes with the same weak phase, then $|\lambda_f| = 1$, $C_f = 0$ and $S_f = \mathrm{Im}\lambda_f$. For example, if $f_{CP} = J/\psi K^0_S$ the quantities become $\lambda = -e^{-i2\beta}$, $C_f = 0$ and $S_f = \sin 2\beta$, so that the time-dependent CP-asymmetry has the simple form $A_{CP} = \sin 2\beta \sin(\Delta m_d \Delta t)$. The sign of S_f changes if $f_{CP} = J/\psi K^0_L$.

The results discussed in this paper were obtained by the BaBar and Belle experiments, respectively operating at the PEP-II and KEKB e^+e^- asymmetric-energy B factories at a center-of-mass (CM) energy equal to the $\Upsilon(4S)$ mass. Pairs of $B\bar{B}$ mesons are produced almost at rest in the decay of the $\Upsilon(4S)$ resonance. The separation between their decay vertices is increased in the laboratory frame thanks to the boost given by the asymmetric-energy beams. The decay time difference Δt of the two B mesons is measured from their spatial separation.

Signal candidates are selected using two uncorrelated kinematic variables: the energy-substituted mass $m_{\mathrm{ES}} = \sqrt{E^{*2}_{beam} - p^{*2}_B}$, and the energy difference $\Delta E = E^*_{beam} - E^*_B$, where all quantities are evaluated in the CM frame, E^*_B and p^*_B are the energy and momentum of the reconstructed B meson and E^*_{beam} is the beam energy. The results discussed in the present paper refer to about 380 million $B\bar{B}$ pairs (BaBar) and about 530 million $B\bar{B}$ pairs (Belle) unless otherwise specified.

3 Measurement of β

The measurement of $\sin 2\beta$ with the decays $B^0 \to (c\bar{c})K^{(*)0}$ has been the primary goal of the current B-factories. The amplitude of these processes is

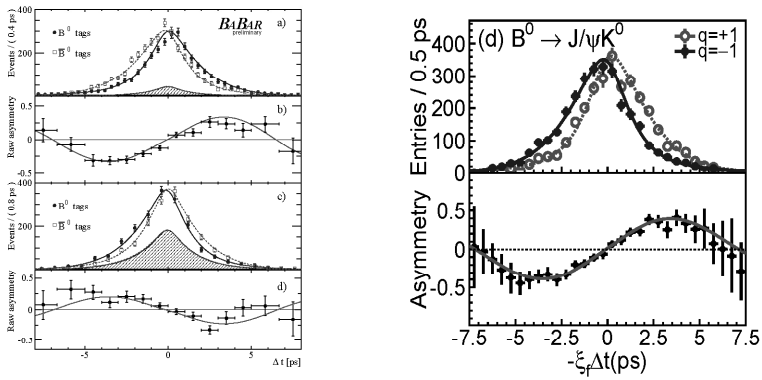

Figure 2: *Left: distribution of the yields and raw CP asymmetry as functions of Δt for CP-odd candidates $J/\psi K^0_S$, $\psi(2S)K^0_S$, $\chi_{c1}K^0_S$, $\eta_c K^0_S$ (top) and for $J/\psi K^0_L$ (bottom), as measured by BaBar. Right: distribution of the yields and raw CP asymmetry as functions of $-\xi_f \Delta t$ for $J/\psi K^0$, as measured by Belle. $\xi_f = +1(-1)$ for CP-even (CP-odd) final states. The sign of ξ_f allows the combination of $J/\psi K^0_S$ and $J/\psi K^0_L$ in the same plot. $q = +1(-1)$ means $B^0(\bar{B}^0)$ tag. Both BaBar and Belle plots are done excluding the low-quality tags. The solid curves show the fit results.*

dominated by a single weak phase to a high level of precision, so that the relation between $\sin 2\beta$ and the CP parameter S is theoretically very clean. BaBar has analyzed the modes $B^0 \to J/\psi K^0_S$, $\psi(2S)K^0_S$, $\chi_{c1}K^0_S$, $\eta_c K^0_S$ (CP-odd), $B^0 \to J/\psi K^0_L$ (CP-even), and $B^0 \to J\psi K^{*0}(\pi^0 K^0_S)$, which requires an angular analysis of the final state to separate the CP-even and CP-odd part. Belle has reconstructed the modes $B^0 \to J/\psi K^0_S$ and $B^0 \to J/\psi K^0_L$. The time-dependent decay rates and CP asymmetries from BaBar and Belle are shown in Fig. 2, separated for B^0 and $\bar{B}^0$ tag. The sinusoidal shape of the asymmetry is clearly visible. The resulting measurement of $\sin 2\beta$ from BaBar is $\sin 2\beta = 0.714 \pm 0.032 \pm 0.018$ [3] while Belle measures $\sin 2\beta = 0.642 \pm 0.031 \pm 0.017$ [4], where the first error is statistical and the second systematic. The main contributions to the systematic errors are the uncertainty in the Δt resolution function, the flavour tagging, and the level and CP asymmetry of the background. The resulting world average is $\sin 2\beta_{WA} = 0.678 \pm 0.026$ [5]. Because of the high experimental accuracy and the very small theoretical error, below the one percent level, this measurement provides one of the tightest constraints to the ρ, η parameters.

The extraction of β from $\sin 2\beta$ has an intrinsic four-fold ambiguity. However, two solutions can be ruled out by measuring $\cos 2\beta$, either through a com-

Table 1: *Measurements of* $\cos 2\beta$ *using* $B^0 \to J/\psi K^{*0}$ *and* $B^0 \to D^0[K^0_S\pi^+\pi^-]h^0$ *decays. The solution with* $\cos 2\beta < 0$ *is strongly disfavored* .

	$\cos 2\beta$ with $B^0 \to J/\psi K^{*0}$	$\cos 2\beta$ with $B^0 \to D^0[K^0_S\pi^+\pi^-]h^0$
BaBar	$3.32^{+0.76}_{-0.96} \pm 0.27$	$0.54 \pm 0.54 \pm 0.08 \pm 0.18$
Belle	$0.56 \pm 0.79 \pm 0.11$	$1.87^{+0.40\ +0.22}_{-0.53\ -0.32}$

bined time-dependent and angular analysis of $B^0 \to J/\psi K^{*0}(\to K^0_S\pi^0)$, where a term proportional to $\cos 2\beta$ appears in the interference between the CP-even and CP-odd amplitudes [6, 7], or by measuring the interference between the $b \to u$ and $b \to c$ amplitudes in the decay $B^0 \to D^0(\to K^0_S\pi^+\pi^-)h^0$ [8], where $h^0 = \pi^0, \eta, \omega$. The measurements from BaBar [9, 10] and Belle [11, 12] are reported in Table 1. BaBar favor the solution of β with $\cos 2\beta > 0$ at 87% CL; Belle determine the sign of $\cos 2\beta$ to be positive at 98.3% CL.

Other classes of processes are sensitive to $\sin 2\beta$ [13]. One is the family of the $b \to c\bar{c}d$ transitions (for example, $B^0 \to D^{(*)+}D^{(*)-}$) which are dominated by a tree level amplitude but where the $b \to d$ penguin contribution is non-negligible. Another important category is the family of $b \to sq\bar{q}$ decays, forbidden at the tree level in the Standard Model and proceeding through penguin diagrams. These categories are potentially sensitive to physics beyond the Standard Model in the loops, and their comparison with the $b \to c\bar{c}s$ transitions to detect hint of new physics is among the main goals of the current and future B-factories.

4 Measurement of α

The angle α of the unitarity triangle can be measured from the time-dependent rates of charmless two-body decays $B^0 \to h^+h^-$ ($h = \pi, \rho$). These processes are described at the tree level by a $b \to u\bar{u}d$ transition. The weak phase difference between $B^0 \to h^+h^-$ and $B^0 \to \bar{B}^0 \to h^+h^-$ is $-2\beta - 2\gamma$, equivalent to 2α when the unitarity condition of the CKM matrix is applied. In a scenario where the tree diagram is the only contribution to the transition amplitude, $S = \sin 2\alpha$ and $C = 0$. However, the penguin contributions are not negligible and the relations are modified to [13]:

$$\begin{array}{lcl} \lambda_{h^+h^-} = \frac{q}{p}\frac{\bar{A}}{A} = e^{i2\alpha} & \longrightarrow & \lambda_{h^+h^-} = e^{i2\alpha}\frac{T - Pe^{-i\alpha}}{T - Pe^{+i\alpha}} \\ S = \sin 2\alpha & \longrightarrow & S = \sqrt{1 - C^2}\sin 2\alpha_{eff} \\ C = 0 & \longrightarrow & C \simeq 2\mathrm{Im}(P/T)\sin\alpha \end{array}$$

Table 2: *CP parameters and branching fractions of* $B \to \pi\pi$.

	BaBar	Belle	HFAG ave.
S	$-0.60 \pm 0.11 \pm 0.03$	$-0.61 \pm 0.10 \pm 0.04$	-0.61 ± 0.08
C	$-0.21 \pm 0.09 \pm 0.02$	$-0.55 \pm 0.08 \pm 0.05$	-0.38 ± 0.07
$\mathcal{B}(\pi^+\pi^-) \times 10^6$	$5.5 \pm 0.4 \pm 0.3$	$5.1 \pm 0.2 \pm 0.2$	5.2 ± 0.2
$\mathcal{B}(\pi^+\pi^0) \times 10^6$	$5.1 \pm 0.5 \pm 0.3$	$6.6 \pm 0.4^{+0.4}_{-0.5}$	5.7 ± 0.4
$\mathcal{B}(\pi^0\pi^0) \times 10^6$	$1.48 \pm 0.26 \pm 0.12$	$1.1 \pm 0.3 \pm 0.1$	1.3 ± 0.2
$A_{CP}(\pi^0\pi^0)$	$0.33 \pm 0.36 \pm 0.08$	$0.44^{+0.73\ +0.04}_{-0.62\ -0.06}$	$0.36^{+0.33}_{-0.31}$

where T and P are the parts of the amplitude depending on $V^*_{ub}V_{ud}$ (including the tree diagram) and $V^*_{tb}V_{td}$, respectively, and α_{eff} is unknown and equals α in the limit of $P/T \to 0$. The problem is how to determine α once α_{eff} is measured from the CP parameters S and C. The difference $\Delta\alpha = \alpha - \alpha_{eff}$ can be measured through an isospin analysis [14] where the penguin contribution is estimated from the isospin-related decays $B^0 \to h^0h^0$, $B^+ \to h^0h^+$ and the CP-conjugated modes. α can also be constrained using $B^0 \to \pi^+\pi^-\pi^0$ decays through a time-dependent Dalitz plot analysis of the final state.

4.1 α with $B^0 \to \pi^+\pi^-$

The result for the CP parameters S and C of $B^0 \to \pi^+\pi^-$ [15, 16] and the branching ratios of the isospin-related modes [17, 18] are reported in Table 2.

4.2 α with $B^0 \to \rho^+\rho^-$

The final state of $B^0 \to \rho^+\rho^-$ has the same quark content as of $B^0 \to \pi^+\pi^-$, and a similar procedure to extract α can be applied. However, since $\rho^+\rho^-$ is a VV state, it requires in principle an angular analysis to disentangle the CP-odd and CP-even components. However, it is found experimentally that the final state is fully longitudinally polarized, making it possible to treat this channel as $B^0 \to \pi^+\pi^-$. Additional complications with respect to $B^0 \to \pi^+\pi^-$ arise from the presence of the π^0 in the final state, which lowers the selection efficiency and increases the background. On the other hand, the branching fraction is about six times larger. The measurement of the S and C parameters [19, 20], together with the branching fractions needed for the isospin analysis [19, 21, 22], are reported in Table 3. BaBar uses a data sample of about 350 million $B\bar{B}$ pairs.

Table 3: *CP parameters and branching fractions of* $B \to \rho\rho$.

	BaBar	Belle	HFAG ave.
S	$-0.19 \pm 0.21^{+0.05}_{-0.07}$	$0.19 \pm 0.30 \pm 0.07$	-0.06 ± 0.18
C	$-0.07 \pm 0.15 \pm 0.06$	$-0.16 \pm 0.21 \pm 0.07$	-0.11 ± 0.13
$\mathcal{B}(\rho^+\rho^-) \times 10^6$	$23.5 \pm 2.2 \pm 4.1$	$22.8 \pm 3.8^{+2.3}_{-2.6}$	$23.1^{+3.2}_{-3.3}$
$\mathcal{B}(\rho^+\rho^0) \times 10^6$	$16.8 \pm 2.2 \pm 2.3$	$31.7 \pm 7.1^{+3.8}_{-6.7}$	18.2 ± 3.0
$A_{CP}(\rho^+\rho^0)$	$-0.12 \pm 0.13 \pm 0.010$	$0.00 \pm 0.22 \pm 0.03$	-0.08 ± 0.13
$\mathcal{B}(\rho^0\rho^0) \times 10^6$	$1.07 \pm 0.33 \pm 0.19$	—	1.07 ± 0.38
$A_{CP}(\rho^0\rho^0)$	—	—	—

4.3 α with $B^0 \to \pi^+\pi^-\pi^0$

There is a third way to constrain α, which uses a time-dependent Dalitz plot analysis of $B^0 \to \pi^+\pi^-\pi^0$. The decay amplitudes of $B^0 \to \pi^+\pi^-\pi^0$ and $\bar{B}^0 \to \pi^+\pi^-\pi^0$ are dominated by the resonances ρ^+, ρ^- and ρ^0, where ρ is the sum of the ground state $\rho(770)$ and the radial excitations $\rho(1450)$ and $\rho(1700)$. The time-dependent and Dalitz plot-dependent decay distributions of $B^0 \to \pi^+\pi^-\pi^0$ and $\bar{B}^0 \to \pi^+\pi^-\pi^0$ are fitted with a likelihood depending on 26 coefficients, that are extracted from the fit. Each coefficient is related in a unique way to physical quantities such as the angle α, the tree-level and penguin-type amplitudes, etc.. These quantities are determined in a least-square fit to the 26 parameters [23, 24]. Figure 3 shows the resulting CL functions for α. The Belle measurement is based on a sample of about 450 million $B\bar{B}$ pairs. Though this decay channel doesn't constrain α at the 2σ level yet, the information is useful when added to the measurements of $B \to \pi\pi$ and $B \to \rho\rho$.

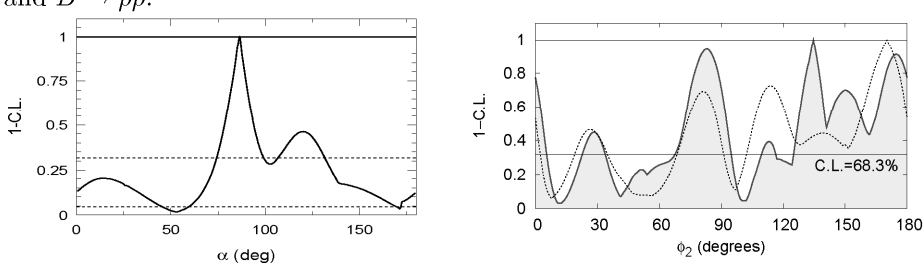

Figure 3: *Confidence level functions for the angle* α *with* $B^0 \to \pi^+\pi^-\pi^0$ *decays from BaBar (left) and Belle (right). The solid curve in the right plot is obtained combining the time Dalitz plot analysis (dashed curve) with an isospin analysis.*

4.4 $B^0 \to a_1\pi$

BaBar has investigated another method to constrain α based on the analysis of the time-dependent rates of $B^0 \to a_1(1260)^{\pm}\pi^{\mp}$, from which an α_{eff} is extracted [25]. It is still unclear, however, what precision on α can be eventually achieved from the measurement of α_{eff}, because the estimate of $\alpha_{eff} - \alpha$ is based on $SU(3)$ flavour symmetry assumptions and depends on the branching fractions of $SU(3)$-related decays which haven't been measured yet.

BaBar has observed the decays $B^0 \to a_1(1260)^{\pm}\pi^{\mp}$, $a_1^- \to \pi^-\pi^+\pi^-$ and has performed the first time-dependent analysis in the quasi two-body approximation [26, 27]. The CP parameters $S \pm \Delta S$ and $C \pm \Delta C$ have been measured: $S = 0.37 \pm 0.21 \pm 0.07$, $\Delta S = -0.14 \pm 0.21 \pm 0.06$, $C = -0.10 \pm 0.15 \pm 0.09$, $\Delta C = 0.26 \pm 0.15 \pm 0.07$. From $S \pm \Delta S$ and $C \pm \Delta C$, $\alpha_{eff} = 78.6^\circ \pm 7.3^\circ$ was measured. BaBar is currently working on the measurement of the $SU(3)$-related decays necessary to bound $\alpha - \alpha_{eff}$.

4.5 Combination of the measurements of α

The constraints of α performed with the decays $B^0 \to \pi^+\pi^-$, $B^0 \to \rho^+\rho^-$ and $B^0 \to \pi^+\pi^-\pi^0$ are combined to provide a joint measurement. Figure 4 shows the result obtained with a Bayesian procedure [34]. The left plot shows the probability density function (PDF) of α, while in the right plot the constraint on $\bar{\rho}, \bar{\eta}$ in the complex plane is drawn, where $\bar{\rho} = \rho(1 - \lambda^2/2 + o(\lambda^2))$ and $\bar{\eta} = \eta(1 - \lambda^2/2 + o(\lambda^2))$. The combination gives $\alpha = (94 \pm 8)^\circ$ at 68% CL.

5 Measurement of γ

The main method to extract γ is based on the interference between the amplitudes of the processes $B^- \to D^{(*)0}K^{(*)-}$ ($b \to c\bar{u}s$, color allowed) and $B^- \to \bar{D}^{(*)0}K^{(*)-}$ ($b \to u\bar{c}s$, color suppressed), which occurs when $D^{(*)0}$ and $\bar{D}^{(*)0}$ decay to a common final state. We focus on $D^0 \to K^0_S\pi^-\pi^+$, which is the channel with the best sensitivity to γ due to its relatively large branching ratio and the rich resonant structure of the three-body final state, which includes Cabibbo-allowed, Cabibbo-suppressed and doubly Cabibbo-suppressed amplitudes. The $B^- \to \tilde{D}^0K^-$ and $B^+ \to \tilde{D}^0K^+$ decay rates[1] can be written as [28, 29]:

$$\Gamma_{\mp}(m^2_-, m^2_+) \propto |\mathcal{A}_{D\mp}|^2 + r_B^2|\mathcal{A}_{D\pm}|^2 + 2\left\{x_{\mp}\mathrm{Re}[\mathcal{A}_{D\mp}\mathcal{A}^*_{D\pm}] + y_{\mp}\mathrm{Im}[\mathcal{A}_{D\mp}\mathcal{A}^*_{D\pm}]\right\}, \tag{4}$$

where m^2_- and m^2_+ are the squared invariant masses of the $K^0_S\pi^-$ and $K^0_S\pi^+$ combinations, respectively, and $\mathcal{A}_{D\mp} \equiv \mathcal{A}_D(m^2_{\mp}, m^2_{\pm})$, with $\mathcal{A}_{D-}$ ($\mathcal{A}_{D+}$) the

[1] The symbol $\tilde{D}^0$ indicates either a D^0 or a $\bar{D}^0$ meson.

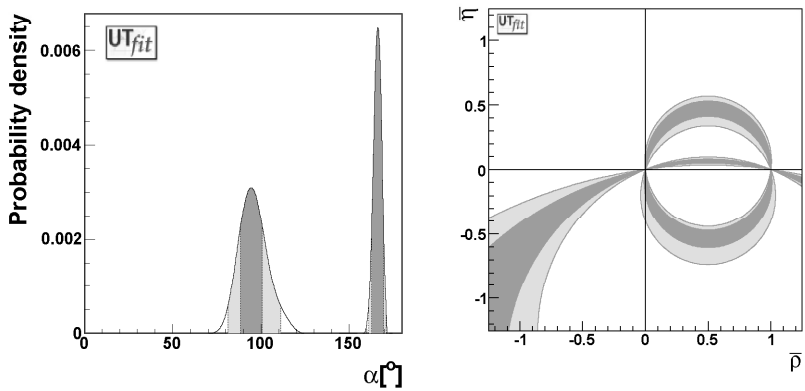

Figure 4: *Left: Probability density function of* α *obtained from the combination of the measurements of* $B \to \pi\pi$, $B \to \rho\rho$ *and* $B^0 \to \pi^+\pi^-\pi^0$ *from BaBar and Belle. Right: constraint on* $\bar{\rho}, \bar{\eta}$ *in the complex plane. Dark and light regions correspond to 68% and 95% probability, respecively* [34].

amplitude of the $D^0 \to K^0_S\pi^-\pi^+$ decay ($\bar{D}^0 \to K^0_S\pi^-\pi^+$). We have introduced the *Cartesian coordinates* $x_\mp \equiv r_B \cos(\delta_B \mp \gamma)$ and $y_\mp \equiv r_B \sin(\delta_B \mp \gamma)$, where $r_B \equiv |A(B^- \to \bar{D}^0 K^-)/A(B^- \to D^0 K^-)|$ and δ_B is the strong phase difference between the two B amplitudes. r_B is expected to be $\mathcal{O}(0.1)$. If $\mathcal{A}_D(m^2_-, m^2_+)$ is known, the Dalitz plot distributions (m^2_-, m^2_+) of $B^- \to \tilde{D}^0 K^-$ and $B^+ \to \tilde{D}^0 K^+$ can be simultaneously fitted to $|\Gamma_-|^2$ and $|\Gamma_+|^2$, and the CP parameters $x_\mp, y_\mp$ are extracted. From $x_\pm, y_\pm$, the quantities γ, r_B and δ_B are measured. Equation (4) also applies, with small modifications, to $B^\pm \to \tilde{D}^{*0} K^\pm$ and $B^\pm \to \tilde{D}^0 K^{*\pm}$ decays. The set of Cartesian coordinates differs for each B mode since δ_B and r_B are different.

$\mathcal{A}_D(m^2_-, m^2_+)$ is determined from a maximum likelihood fit to the Dalitz plot distribution of a high-purity ($\sim 98\%$), flavour-tagged sample of $D^{*+} \to D^0\pi^+$ decays. The decay amplitude is expressed as a sum of two-body decay-matrix elements (subscript r) and a non-resonant (subscript NR) contribution (isobar model),

$$\mathcal{A}_D(m^2_-, m^2_+) = \sum_r a_r e^{i\phi_r} \mathcal{A}_r(m^2_-, m^2_+) + a_{\rm NR} e^{i\phi_{\rm NR}}\,, \qquad (5)$$

where each term is parameterized with an amplitude a_r ($a_{\rm NR}$) and a phase ϕ_r ($\phi_{\rm NR}$), which are determined from the fit. $\mathcal{A}_r$ is the matrix element of a D^0 meson decaying to $K^0_S\pi^-\pi^+$ through an intermediate resonance r, whose parame-

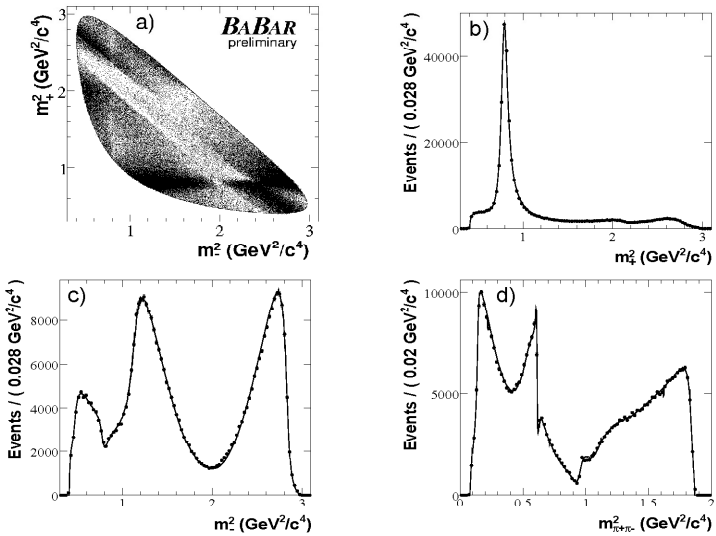

Figure 5: *The $D^0 \to K^0_S\pi^-\pi^+$ Dalitz distribution from $D^{*-} \to \bar{D}^0\pi^-$ events of BaBar, and projections on (b) $m^2_+ = m^2_{K^0_S\pi^+}$, (c) $m^2_- = m^2_{K^0_S\pi^-}$, and (d) $m^2_{\pi^+\pi^-}$. The curves are the reference model fit projections.*

terization is described in ref. [30, 31]. The two-body decay amplitudes include Cabibbo-allowed amplitudes: $K^*(892)^-\pi^+$, $K^*(1410)^-\pi^+$, $K^*_0(1430)^-\pi^+$, $K^*_2(1430)^-\pi^+$ and $K^*(1680)^-\pi^+$; their doubly Cabibbo-suppressed partners (BaBar does not use $K^*(1410)^+\pi^-$, $K^*(1680)^+\pi^-$); and eight $\pi\pi$ amplitudes: $K^0_S\rho$, $K^0_S\omega$, $K^0_S f_0(980)$, $K^0_S f_2(1270)$, $K^0_S f_0(1370)$, $K^0_S\rho(1450)$, $K^0_S\sigma$, $K^0_S\sigma'$. All the resonances considered in the model are well established except for the σ and σ', whose masses and widths are obtained from the fit to the control sample. Fig. 5 shows the flavour-tagged D^0 sample selected by BaBar.

The decays $B^- \to \tilde{D}^0K^-$, $B^- \to \tilde{D}^{*0}[\tilde{D}^0\pi^0]K^-$, $B^- \to \tilde{D}^{*0}[\tilde{D}^0\gamma]K^-$ (BaBar only) and $B^- \to \tilde{D}^0K^{*-}$ are reconstructed with selection criteria described in detail elsewhere [30, 31]. The BaBar analysis of $B^- \to \tilde{D}^{(*)0}K^-$ ($B^- \to \tilde{D}^0K^{*-}$) is based on a sample of approximately 347 (227) million $B\bar{B}$ pairs. The Belle analysis uses 386×10^6 $B\bar{B}$ decays.

A maximum likelihood fit is performed to the selected events to extract simultaneously the CP violation parameters $x_\pm, y_\pm$ and the signal and background yields. The likelihood for each candidate is evaluated using $m_{\rm ES}$, ΔE and a Fisher discriminant that separates $B\bar{B}$ from $e^+e^- \to q\bar{q}$ events using event shape information. Belle analysis cuts on the Fisher discriminant with-

out including it in the fit. The results of $x_\pm, y_\pm$ of the two experiments are reported graphically in Fig. 6 for all the B modes. From the measurement of $x_\pm, y_\pm$ the confidence interval for $\{\gamma,\ r_B(DK),\ \delta_B(DK),\ r_B(D^*K),\ \delta_B(D^*K),\ r_B(DK^*),\ \delta_B(DK^*)\}$ are derived using a frequentist procedure. The resulting 68% confidence intervals of γ are:

$$\gamma = (92 \pm 41 \pm 11 \pm 12)^\circ \text{ (BaBar)} \qquad \gamma = (53^{+15}_{-18} \pm 3 \pm 9)^\circ \text{ (Belle)}\,, \quad (6)$$

where the first error is statistical, the second is systematic and the third includes the uncertainty associated to the Dalitz plot model. The BaBar confidence interval does not include $B \to D^0K^*$. The statistical error of γ of the BaBar measurement is more than twice larger than Belle's, despite the fact that the BaBar measurement of $x_\pm, y_\pm$ is more precise (Fig. 6). This difference does not depend on the fact that $B \to D^0K^*$ was not included in the BaBar combination. Instead, it is explained by noticing that the statistical error of γ is roughly proportional to the $x_\pm, y_\pm$ errors and is inversely proportional to the $(x_\pm, y_\pm)$ distance from zero, i.e., to r_B. Since the Belle measurements of $(x_\pm, y_\pm)$ are consistent with larger values of r_B, the resulting statistical error of γ is smaller. This $1/r_B$ dependence of the error of γ makes its prediction on larger data samples difficult, because it strongly depends on which assumption is made for r_B, whose relative error is still large (about 30% for all the B modes).

The largest single contribution to the systematic uncertainty of γ comes from the choice of the Dalitz model used to describe the $D^0 \to K^0_S\pi^-\pi^+$ decay amplitude. Both BaBar and Belle use sets of alternative models where some resonances are removed or are parameterized in a different way. In particular, for the $\pi\pi$ S-wave BaBar uses the K-matrix approach [32] as an alternative parameterization. Other systematic contributions are associated to the shape of the $m_{\rm ES}$, ΔE and Fisher PDFs, to the distribution of the background events and of the signal efficiency in the Dalitz plane, and to the fraction of background events with real D^0.

6 Conclusions

Though the measurement of β has reached a high level of precision, it is still statistically limited. The B-factories BaBar and Belle will approach the systematic limit in the next two years of data taking, but will not reach it. The world-average measurement $\sin 2\beta_{WA} = 0.678 \pm 0.026$ [5] represents one of the tightest constraints of the ρ, η parameters. The angle α is currently measured with a precision of about 10°. As the data samples collected by BaBar and Belle have increased, new methods have been investigated to reduce its uncertainty. The measurement of the angle γ was considered out of reach at the current B-factories till a few years ago. Instead, thanks especially to the analysis of $B^\pm \to D^{(*)0}K^{(*)\pm}$, $D^0 \to K^0_S\pi^+\pi^-$, the measurement of γ has been

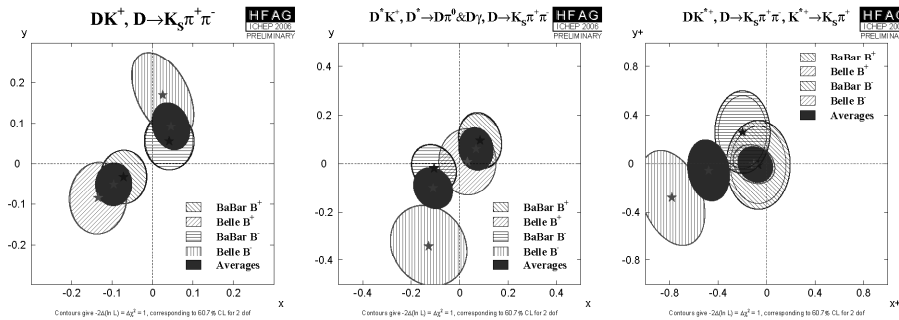

Figure 6: *BaBar and Belle measurements of Cartesian coordinates* $x_\pm, y_\pm$ *for* $B^\pm \to D^0 K^\pm$ *(left),* $B^\pm \to D^{*0} K^\pm$ *(center) and* $B^\pm \to D^0 K^{*\pm}$ *(right). The errors do not include the systematic uncertainty from the Dalitz model.*

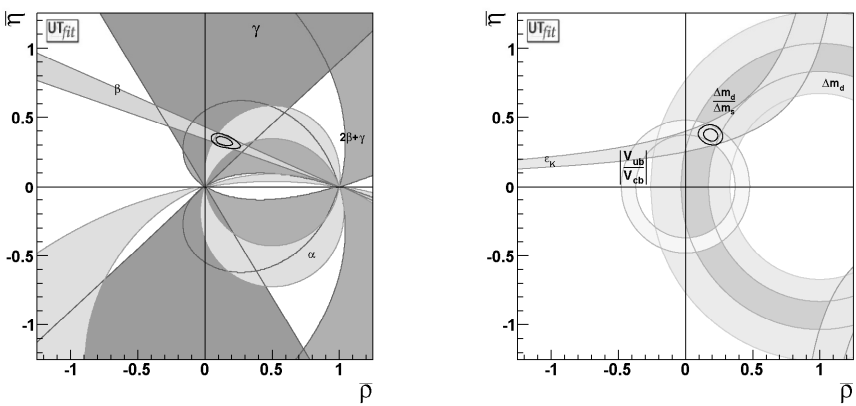

Figure 7: *Constraints in the* $\bar{\rho}-\bar{\eta}$ *plane from the measurements of the angles* α*,* β *and* γ *(left) and from the other measurements (*ϵ_K*,* $|V_{ub}/V_{cb}|$*, etc.) (right). The full lines correspond to 95% probability regions.*

possible, though with a large uncertainty ranging between $\sim 20^\circ$ and $\sim 30^\circ$ depending on the statistical procedure used to combine the available measurements [34, 35]. Figure 7 (left) shows the constraints on $\bar{\rho}, \bar{\eta}$ from α, β and γ: $\bar{\rho} = 0.139 \pm 0.042$, $\bar{\eta} = 0.325 \pm 0.021$. Their uncertainty is comparable to the error resulting from the combination of all the other existing constraints [34], shown in Figure 7 (right).

References

1. N. Cabibbo, Phys. Rev. Lett. **10**, 531 (1963); M. Kobayashi and T. Maskawa, Prog. Theor. Phys. **49**, 652 (1973).
2. L. Wolfenstein, Phys. Rev. Lett. **51**, 1945 (1983).
3. BaBar Collaboration, B. Aubert *et al.*, hep-ex/0703021.
4. Belle Collaboration, K.-F. Chen *et al.*, Phys. Rev. Lett. **98**, 031802 (2007).
5. The Heavy Flavour Averaging Group, `http://www.slac.stanford.ed/xorg/hfag`.
6. I. Dunietz, H. R. Quinn, A. Snyder, W. Toki and H. J. Lipkin, Phys. Rev. D **43**, 2193 (1991).
7. A. S. Dighe, I. Dunietz and R. Fleischer, Eur. Phys. J C**6**, 647 (1999).
8. A. Bondar *et al.*, Phys. Lett. B**624** 1-10 (2005).
9. BaBar Collaboration, B. Aubert *et al.*, Phys. Rev. D **71**, 032005 (2005).
10. BaBar Collaboration, B. Aubert *et al.*, hep-ex/0607105.
11. Belle Collaboration, R. Itoh *et al.*, Phys. Rev. Lett. **95**, 091601 (2005).
12. Belle Collaboration, P. Krokovny *et al.*, Phys. Rev. Lett. **97**, 081801 (2006).
13. Review of *CP violation in meson decays*, W.-M. Yao *et al.*, Journal of Physics G **33**, 1 (2006).
14. M. Gronau *et al.*, Phys. Rev. Lett. **65**, 3381 (1990).
15. BaBar Collaboration, B. Aubert *et al.*, hep-ex/0703016 submitted to Phys. Rev. Lett. .
16. Belle Collaboration, B. Aubert *et al.*, hep-ex/0608035.
17. BaBar Collaboration, B. Aubert *et al.*, hep-ex/0607106.
18. Belle Collaboration, B. Aubert *et al.*, hep-ex/0609015, hep-ex/0610065.
19. BaBar Collaboration, B. Aubert *et al.*, hep-ex/0607098.
20. Belle Collaboration, B. Aubert *et al.*, hep-ex/0702009.
21. BaBar Collaboration, B. Aubert *et al.*, Phys. Rev. Lett. **97**, 261801 (2007); BaBar Collaboration, B. Aubert *et al.*, hep-ex/0612021.

22. Belle Collaboration, J. Zhang *et al.*, Phys. Rev. Lett **91**, 221801 (2003). Belle Collaboration, A. Somov *et al.*, Phys. Rev. Lett. **96**, 171801 (2006).

23. BaBar Collaboration, B. Aubert *et al.*, hep-ex/0703008 submitted to Phys. Rev. Lett. .

24. Belle Collaboration, A. Kusaka *et al.*, hep-ex/0701015 submitted to Phys. Rev. Lett. .

25. R. Aleksan *et al.*, Nucl. Phys. B **361**, 141 (1991). M. Gronau and J. Zupan, Phys. Rev. D **73**, 057502 (2006).

26. B. Aubert *et al.*, Phys. Rev. Lett. **97**, 051802 (2006).

27. B. Aubert *et al.*, Phys. Rev. Lett. **98**, 181803 (2007).

28. D. Atwood, I. Dunietz, A. Soni, Phys. Rev. Lett. **78**, 3257 (1997).

29. A. Giri *et al.*, Phys. Rev. D**68**, 054018 (2003).

30. BaBar Collaboration, B. Aubert *et al.*, hep-ex/0607104.

31. Belle Collaboration, A. Poluektov *et al.*, Phys. Rev. **D73**, 112009 (2006)

32. I. J. R. Aitchison, Nucl. Phys. A **189**, 417 (1972).

33. M. Gronau and J. Zupan, Phys. Rev. D **73**, 057502 (2006).

34. UTfit Collaboration, `http://www.utfit.org`.

35. CKMfitter Collaboration, `http://ckmfitter.in2p3.fr/`

MEASUREMENTS OF $|V_{cb}|$ AND $|V_{ub}|$

Christoph Schwanda
Institute of High Energie Physics, Austrian Academy of Sciences
for the Belle Collaboration

Abstract

A precise determination of $|V_{ub}/V_{cb}|$ is crucial for constraining the Cabibbo-Kobayashi-Maskawa (CKM) mechanism, *i.e.*, the theory of CP violation in the Standard Model, and for searching for new CP violating phases from new, heavy particles. In this article, we review the status of the determination of the CKM magnitudes $|V_{cb}|$ and $|V_{ub}|$ from inclusive and exclusive semileptonic B decays. We highlight recent measurements and give the world average numbers for these quantities.

1 Introduction

The truly historic achievement of the B factory experiments Belle [1] and BaBar [2] was to establish the Cabibbo-Kobayashi-Maskawa (CKM) mechanism [3] – in which the couplings of the quark mass eigenstates are described by a unitary 3×3 matrix – as the theory of CP violation. In particular, the precise determination of the CKM matrix elements $|V_{cb}|$ and $|V_{ub}|$ has been crucial for establishing this result, and further improvements in $|V_{ub}/V_{cb}|$ are required, if the sensitivity to new CP violating phases in B decays should be increased.

The CKM magnitudes $|V_{cb}|$ and $|V_{ub}|$ are determined from semileptonic B decays into charmed and charmless final states, respectively. For both $|V_{cb}|$ and $|V_{ub}|$, there are determinations using all semileptonic final states in a given region of phase space ("inclusive measurements"), and analyses based on specific final states only ("exclusive measurements"). As the theoretical and experimental uncertainties are different for both approaches, consistency between inclusive and exclusive is an important cross-check on our understanding.

The analyses reviewed in this article are based on the data taken by the Belle and BaBar experiments [1, 2]. They are located at asymmetric e^+e^- colliders operating at the center-of-mass energy of the $\Upsilon(4S)$ resonance. As the $\Upsilon(4S)$ mass is just above the $B\bar{B}$ threshold, the B mesons produced in the decay $\Upsilon(4S) \to B\bar{B}$ are almost at rest in the center-of-mass frame. By summer 2007, the integrated luminosity accumulated by both experiments is 715 fb^{-1} and 460 fb^{-1} for Belle and BaBar, respectively.

2 $|V_{cb}|$ from exclusive semileptonic B decays

The extraction of $|V_{cb}|$ from the exclusive decays $B \to D^*\ell\nu$ and $B \to D\ell\nu$ is based on the differential decay rates as a function of $w = vv'$, where v and v' are the (four-)velocities of the initial and final state hadron in the decay [4],

$$\frac{d\Gamma}{dw}(B \to D^*\ell\nu_\ell) = \frac{G_F^2}{48\pi^3}|V_{cb}|^2(m_B - m_{D^*})^2 m_{D^*}^3 (w^2-1)^{1/2}(w+1)^2 \times \left[1 + \frac{4w}{w+1}\frac{m_B^2 + m_{D^*}^2 - 2wm_B m_{D^*}}{(m_B - m_{D^*})^2}\right](\mathcal{F}(w))^2 \quad (1)$$

$$\frac{d\Gamma}{dw}(B \to D\ell\nu_\ell) = \frac{G_F^2}{48\pi^3}|V_{cb}|^2(m_B + m_D)^2 m_D^3 (w^2-1)^{3/2}(\mathcal{G}(w))^2 \,. \quad (2)$$

Here, m_D, m_{D^*} and m_B are the D, D^* and B meson masses, respectively. In the limit of infinite heavy quark masses, Heavy Quark Symmetry (HQS) predicts the normalization of the form factors $\mathcal{F}(w)$ and $\mathcal{G}(w)$ at the zero recoil point $w = 1$, $\mathcal{F}(1) = \mathcal{G}(1) = 1$ [4]. Experiments therefore extrapolate $d\Gamma/dw$

to zero recoil and measure $\mathcal{F}(1)|V_{cb}|$ and $\mathcal{G}(1)|V_{cb}|$. For finite heavy quark masses, Heavy Quark Effective Theory (HQET) can calculate the form factor normalizations at $w = 1$ with an uncertainty of about 4% [4]. More precise determinations are obtained from lattice QCD, *e.g.*, for the $\mathcal{F}$ form factor [5]

$$\mathcal{F}(1) = 0.913^{+0.030}_{-0.035} \; . \tag{3}$$

By summer 2006, BaBar has presented preliminary results for the decay $B^0 \to D^{*-}\ell^+\nu$ based on 79 fb^{-1} of $\Upsilon(4S)$ data. In this analysis, the D^{*+} meson and an oppositely charged lepton are reconstructed and $\mathcal{F}(1)|V_{cb}|$ is measured together with ρ^2, R_1 and R_2 (parameterizing the form factor $\mathcal{F}(w)$) by performing a simultaneous fit to about 52,800 signal events. This measurement dominates the current HFAG average of $\mathcal{F}(1)|V_{cb}| = (36.2 \pm 0.6) \times 10^{-3}$ [7], which yields, Eq. 3,

$$|V_{cb}| = (39.6 \pm 0.7(exp)^{+1.5}_{-1.3}(th)) \times 10^{-3} \; . \tag{4}$$

The uncertainty in $|V_{cb}|$ from $B \to D^*\ell\nu$ is thus dominated by the lattice QCD error (3.5%), the experimental uncertainty being only 1.7%.

For $|V_{cb}|$ from $B \to D\ell\nu$ the situation is different: The form factor $\mathcal{G}(1)$ at zero recoil is rather well known to the level of $1 - 2\%$ [8] but experimental uncertainties are about 10% [7].

3 $|V_{cb}|$ from inclusive B decays

Inclusive determinations of the CKM magnitude $|V_{cb}|$ rely on calculations of the semileptonic B meson decay width in the framework of the Heavy Quark Expansion (HQE) [9, 10]. Predictions of this quantity depend on $|V_{cb}|$ and a number of non-perturbative heavy quark parameters like quark masses and hadronic expectation values. These non-perturbative quantities have to be extracted from other inclusive observables in B decays such as the lepton energy E_ℓ and hadronic mass M_X^2 moments in $B \to X_c\ell\nu$ and the photon energy E_γ moments in $B \to X_s\gamma$ [9, 11, 12].

Belle has recently measured the moments of the electron energy and hadronic mass spectrum in $B \to X_c\ell\nu$ decays [13, 14]. These analyses fully reconstruct the hadronic decay of one B meson and identify the lepton from the decay $B \to X_c\ell\nu$ within the remaining particles in the event. By fully reconstructing the event kinematics, backgrounds in the inclusive spectra are minimized and the resolution in M_X^2 is greatly improved. To minimize the $B \to X_c\ell\nu$ model dependence, the moments are calculated directly from the background subtracted spectra after the finite resolution in E_ℓ respectively M_X^2 has been unfolded, Fig. 1.

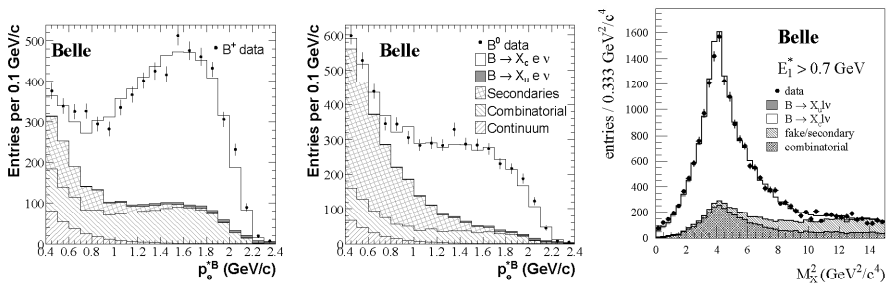

Figure 1: Electron momentum spectrum for charged (left) and neutral (center) B mesons and hadronic mass squared distribution (right) in $B \to X_c \ell \nu$ decays, before background subtraction and detector resolution unfolding.

Table 1: Results of the global fit in the 1S and kinetic mass scheme [15]. The results for m_b are compatible after scheme translation.

1S scheme	kinetic scheme
$\lvert V_{cb}\rvert = (41.49 \pm 0.52(\text{fit}) \pm$ $\pm 0.20(\tau_B)) \times 10^{-3}$	$\lvert V_{cb}\rvert = (41.93 \pm 0.65(\text{fit}) \pm$ $\pm 0.07(\alpha_s) \pm 0.63(\text{th})) \times 10^{-3}$
$m_b^{1S} - 4.729 \pm 0.048$ GeV	$m_b^{\text{kin}} - 4.564 \pm 0.076$ GeV
$\chi^2/\text{ndf.} = 5.7/17$	$\chi^2/\text{ndf.} = 17.8/24$

The analysis of this data in terms of $|V_{cb}|$ and m_b is preliminary [15]: Belle has performed a global analysis using theoretical expressions in the 1S [9] and kinetic mass schemes [11, 12]. As these calculations are completely independent, consistency is an important cross-check of our theoretical understanding. The preliminary results are shown in Table 1.

4 $|V_{ub}|$ from inclusive decays $B \to X_u \ell \nu$

The determination of $|V_{ub}|$ from inclusive charmless semileptonic B decays relies also on the Heavy Quark Expansion. However, as analyses typically need to restrict the $b \to u$ phase space to reduce the $b \to c$ background, the convergence of the HQE is compromised and theoretical approaches usually need to introduce a non-perturbative object, the "shape function". At leading order, the shape function parameters are related to the heavy quark parameters

mentioned in the previous section. The following theoretical calculations of inclusive decays $b \to u$ are available: BLNP [16], DGE [17], BLL [18]

Using the BLNP scheme, the current world average number for $|V_{ub}|$ is [7]

$$|V_{ub}| = (4.52 \pm 0.19(exp) \pm 0.27(th)) \times 10^{-3} \ . \tag{5}$$

The total uncertainty in $|V_{ub}|$ is thus 7.4%. The larges contribution (4.1%) comes from the uncertainty in the shape function parameters, namely the b quark mass.

5 $|V_{ub}|$ from exclusive charmless semileptonic B decays

Also charmless semileptonic decays $B \to \pi\ell\nu$ can be used to determine the magnitude of $|V_{ub}|$. The differential decay width as a function of q^2, $q^2 = (p_\ell + p_\nu)^2$, is given by

$$\frac{d\Gamma}{dq^2}(B \to \pi\ell\nu) - \frac{G_F^2|V_{ub}|^2}{192\pi^3 m_B^3}\lambda(q^2)^{3/2}|f_+(q^2)|^2 \ , \tag{6}$$

where $\lambda(x) = (x + m_B^2 - m_\pi^2)^2 - 4m_B^2 m_\pi^2$. Different theoretical approaches are available for determining the shape and the normalization of the form factor $f_+(q^2)$: relativistic quark models (ISGW2 [19]), light cone sum rules for the region $q^2 < 14$ GeV^2 (Ball-Zwicky [20]) and lattice QCD calculations for the region $q^2 > 16$ GeV^2 (HPQCD [21], FNAL [8]).

By summer 2006, BaBar has presented an analysis of the decay $B^0 \to \pi^-\ell^+\nu$ based on 227×10^6 $B\bar{B}$ pairs collected at the $\Upsilon(4S)$ resonance [22]. Only the π meson and the charged lepton ℓ from the B^0 decay are reconstructed; the neutrino momentum is inferred from the missing momentum in the event. The signal yield is measured in twelve bins of q^2 (Fig. 2); the q^2-integrated branching fraction is found to be $(1.46\pm0.07(stat)\pm0.08(syst))\times10^{-4}$. Recently, another analysis of $B \to \pi\ell\nu$ has been presented by the Belle collaboration [23]: Starting from 535×10^6 $B\bar{B}$ events, not only the signal decay but also the hadronic decay of the other B in the event are reconstructed to minimize backgrounds and the related systematic uncertainties. The $B^0 \to \pi^-\ell^+\nu$ and $B^+ \to \pi^0\ell^+\nu$ branching fractions are measured to be $(1.49 \pm 0.26(stat) \pm 0.06(syst)) \times 10^{-4}$ and $(0.86 \pm 0.17(stat) \pm 0.06(syst)) \times 10^{-4}$),respectively, Fig. 2.

These measurements can be used to extract the value of $|V_{ub}|$: From the HFAG averages in the regions $q^2 < 14$ GeV^2 and $q^2 > 16$ GeV^2 [7] we derive

$$|V_{ub}| = (3.41 \pm 0.12(stat)^{+0.56}_{-0.38}(th)) \times 10^{-3} \quad (\text{Ball} - \text{Zwicky}) \ , \tag{7}$$

$$|V_{ub}| = (3.55 \pm 0.20(stat)^{+0.61}_{-0.40}(th)) \times 10^{-3} \quad (\text{FNAL}) \ . \tag{8}$$

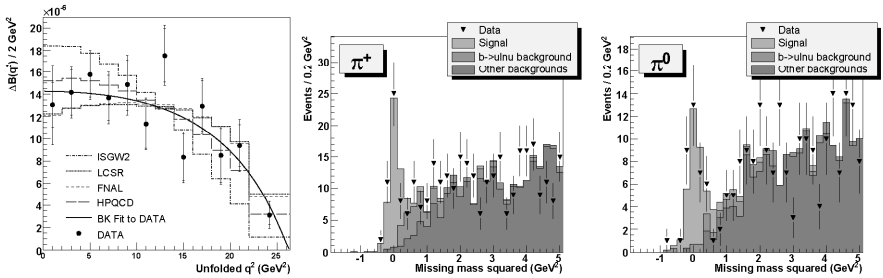

Figure 2: Recent $B \to \pi\ell\nu$ results: The left plot shows the BaBar q^2 spectrum after unfolding the detector resolution [22]. The center and right plots show the Belle $B^0 \to \pi^-\ell^+\nu$ and $B^+ \to \pi^0\ell^+\nu$ signals [23].

6 Summary

We have reviewed the current status of the determination of the CKM magnitudes $|V_{cb}|$ and $|V_{ub}|$ from inclusive and exclusive semileptonic B decays. The consistency between inclusive and exclusive determinations of both $|V_{cb}|$ and $|V_{ub}|$ is good, which gives some confidence in the uncertainties currently assigned. The measured value of $|V_{ub}/V_{cb}|$ is also consistent with expectations from the Cabibbo-Kobayashi-Maskawa theory.

Acknowledgments

We thank the KEKB group for excellent operation of the accelerator, the KEK cryogenics group for efficient solenoid operations, and the KEK computer group and the NII for valuable computing and Super-SINET network support. We acknowledge support from MEXT and JSPS (Japan); ARC and DEST (Australia); NSFC (China); DST (India); MOEHRD, KOSEF and KRF (Korea); KBN (Poland); MES and RFAAE (Russia); ARRS (Slovenia); SNSF (Switzerland); NSC and MOE (Taiwan); and DOE (USA).

References

1. A. Abashian *et al.* [Belle Collaboration], Nucl. Instrum. Meth. A **479**, 117 (2002).
2. B. Aubert *et al.* [BABAR Collaboration], Nucl. Instrum. Meth. A **479**, 1 (2002).
3. N. Cabibbo, Phys. Rev. Lett. **10**, 531 (1963);
   M. Kobayashi and T. Maskawa, Prog. Theor. Phys. **49**, 652 (1973).
4. M. Neubert, Phys. Rept. **245**, 259 (1994).
5. S. Hashimoto, A. S. Kronfeld, P. B. Mackenzie, S. M. Ryan and J. N. Simone, Phys. Rev. D **66**, 014503 (2002).
6. B. Aubert *et al.* [BABAR Collaboration], hep-ex/0607076.
7. http://www.slac.stanford.edu/xorg/hfag/
8. M. Okamoto *et al.*, Nucl. Phys. Proc. Suppl. **140**, 461 (2005).
9. C. W. Bauer, Z. Ligeti, M. Luke, A. V. Manohar and M. Trott, Phys. Rev. D **70**, 094017 (2004).
10. D. Benson, I. I. Bigi, T. Mannel and N. Uraltsev, Nucl. Phys. B **665**, 367 (2003).
11. P. Gambino and N. Uraltsev, Eur. Phys. J. C **34**, 181 (2004).
12. D. Benson, I. I. Bigi and N. Uraltsev, Nucl. Phys. B **710**, 371 (2005).
13. P. Urquijo *et al.*, Phys. Rev. D **75**, 032001 (2007).
14. C. Schwanda *et al.* [BELLE Collaboration], Phys. Rev. D **75**, 032005 (2007).
15. K. Abe *et al.* [BELLE Collaboration], hep-ex/0611047.
16. B. O. Lange, M. Neubert and G. Paz, Phys. Rev. D **72**, 073006 (2005).
17. J. R. Andersen and E. Gardi, JHEP **0601**, 097 (2006).
18. C. W. Bauer, Z. Ligeti and M. E. Luke, Phys. Rev. D **64**, 113004 (2001).
19. D. Scora and N. Isgur, Phys. Rev. D **52**, 2783 (1995).
20. P. Ball and R. Zwicky, Phys. Rev. D **71**, 014015 (2005).

21. E. Dalgic, A. Gray, M. Wingate, C. T. H. Davies, G. P. Lepage and J. Shigemitsu, Phys. Rev. D **73**, 074502 (2006) [Erratum-ibid. D **75**, 119906 (2007)].

22. B. Aubert *et al.* [BABAR Collaboration], Phys. Rev. Lett. **98**, 091801 (2007).

23. K. Abe *et al.* [BELLE Collaboration], arXiv:hep-ex/0610054.

RARE B DECAYS INCLUDING PENGUIN DECAYS (MINI-REVIEW)

Shohei Nishida
High Energy Accelerator Research Organization (KEK)

Abstract

As a review of recent experimental results on rare B decays from Belle and BaBar, this proceeding describes the measurements of $B \to \tau\nu$ and search for $b \to d\gamma$ process. Measurement of time-dependent CP violation at radiative B decays and $b \to s$ penguin decays are also reported.

1 Introduction

The sum of the integrated luminosity of the two B-factory experiments, Belle and BaBar, have exceeded 1ab^{-1}, which corresponds to 1×10^9 $B\bar{B}$. The increasing data accumulated at the two experiments, have been opening the opportunity to study various rare B decays.

There are several possible reasons when a decay mode of B meson is "rare". It may be because the leading diagram of the decay is a higher order diagram such as penguin and box diagrams. Therefore, rare B decays are often very sensitive to physics beyond the Standard Model (SM) because of the contribution of non-SM particles to the loop diagram. Another possible reason is that the dominant diagram of the decay is suppressed by small CKM matrix elements. In such a case, measurement of the decay may provide an information to the CKM matrix. There are also many B decays useful to compare with theoretical calculations.

In this proceeding, we summarize several recent results about rare B decays including $b \to s$ penguin decays, at BaBar and Belle [1].

2 Pure leptonic B decay ($B \to \tau\nu,\ \ell\nu$)

Pure leptonic decay of mesons such as $\pi^+ \to \mu^+\nu_\mu$ is a basic decay of mesons and have been well understood in the SM. Corresponding decay of B mesons is $B^+ \to \tau^+\nu_\tau$ The branching fraction of $B^+ \to \tau^+\nu_\tau$ is calculated to be

$$\mathcal{B}(B^+ \to \tau^+\nu_\tau) = \frac{G_F^2 m_B}{8\pi} m_\tau^2 \left(1 - \frac{m_\tau^2}{m_B^2}\right) f_B^2 |V_{ub}|^2 \tau_B, \tag{1}$$

where G_F is the Fermi coupling constant, m_B and m_τ are the B and τ masses, respectively, and τ_B is the B^+ lifetime. This corresponds to $(1.6 \pm 0.4)^{-4}$, where the uncertainty mainly comes from f_B and $|V_{ub}|$. This decay is sensitive to a charged Higgs boson due to its possible contribution to the diagram (Fig. 1).

However, although the expected branching fraction is not small compared to many other rare B decays studied in the B factories, this mode is experimentally challenging because of the multiple neutrinos in the final state. For example, when τ^+ decays to $e^+\nu_e\bar{\nu_\tau}$ or $\pi^+\bar{\nu_\tau}$, the experimental signature of this decay is just one charged track, which is difficult to apply any powerful kinematical constraints.

Therefore, we make use of the feature of the B factory experiments. Since B mesons are always produced in pair, we reconstruct one B meson (referred as

[1] Charge conjugate modes are implicitly included throughout the text. PDG [1)] is often the reference for many numbers in the text though not explicitly written.

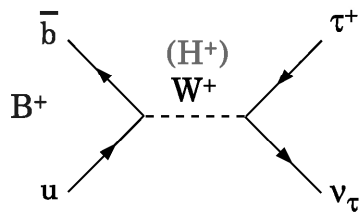

Figure 1: *Diagram for* $B^+ \to \tau^+\nu_\tau$.

Table 1: *Measured branching fractions of* $B^+ \to \tau^+\nu_\tau$ *and* $B^+ \to \ell^+\nu_\ell$ *at Belle and BaBar. Signs of inequality show the upper limit at* 90% *C.L.*

	Belle	BaBar
$B^+ \to \tau^+\nu_\tau$	$(1.79\,^{+0.56\ +0.39}_{-0.46\ -0.46}) \times 10^{-4}$	$(0.88\,^{+0.68}_{-0.67} \pm 0.11) \times 10^{-4}$
		$< 1.80 \times 10^{-4}$
$B^+ \to \mu^+\nu_\mu$	$< 0.98 \times 10^{-6}$	$< 6.2 \times 10^{-6}$
$B^+ \to e^+\nu_e$	$< 1.7 \times 10^{-6}$	$< 7.9 \times 10^{-6}$

"tag" side) in an event and look into the remaining particle (referred as "signal" side). Belle fully reconstructs the tag side B meson using hadronic modes such as $B^- \to \bar{D}^{(*)0}\pi^-$. BaBar use semi-leptonic decays such as $B^- \to D^0\ell^-\nu$ ($\ell = e,\ \mu$). Efficiencies for reconstructing the tag side is around 0.3% and 0.7%, respectively. In general, the former full reconstruction method has lower efficiency but higher purity than the latter semi-leptonic tag method.

Then, they examine whether the signal side is consistent with the decay particles from the following τ^+ decays: $\mu^+\bar{\nu}_\mu\nu_\tau$, $e^+\bar{\nu}_e\nu_\tau$, $\pi^+\nu_\tau$, $\pi^+\pi^0\nu_\tau$ and $\pi^+\pi^+\pi^+\nu_\tau$ (Belle only). Further requirements are applied based on the missing mass in the event and momenta of τ daughters.

An useful variable to extract the $B^+ \to \tau^+\nu_\tau$ signals is the extra energy ($E_{\rm extra}$), which is the sum of neutral clusters not associated with particles from the tag side B meson or τ from the signal side B. $B^+ \to \tau^+\nu_\tau$ signal peaks at $E_{\rm extra} \sim 0$. Figure 2 shows the $E_{\rm extra}$ distribution at Belle and BaBar for a data sample that includes 449×10^6 and 320×10^6 $B\bar{B}$, respectively. Belle finds $17.2\,^{+5.3}_{-4.7}$ signal events with a significance of 3.5σ, which is the first evidence of $B^+ \to \tau^+\nu_\tau$ decay, while BaBar do not find significant peak. Measured branching fractions [2] are summarized in Table 1. The two results are consistent with each other and also with the theoretical expectation. They provides new $\tan\beta$-dependent constraint to charged Higgs mass.

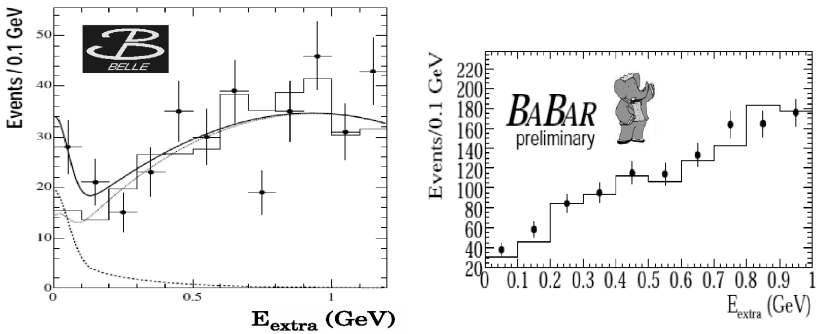

Figure 2: *Extra energy distributions for $B^+ \to \tau^+\nu_\tau$ at Belle (left) and BaBar (right). Histograms show background expectation. The solid curve in the left plot shows the result of the fit with the sum of the signal (dashed) and background (dotted) contributions.*

$B^+ \to \ell^+\nu_\ell$ are also studied with the same motivation. The expected branching fractions for $B^+ \to \mu^+\nu_\mu$ and $B^+ \to e^+\nu_e$ are $(4.7 \pm 0.7) \times 10^{-7}$ and $(1.1 \pm 0.2) \times 10^{-11}$. which are much lower than $B^+ \to \tau^+\nu_\tau$. Belle looks for a high momentum lepton and reconstruct companion B meson using all the remaining particles in the event, using a data sample of 277×10^6 $B\bar{B}$. BaBar, with a sample including 229×10^6 $B\bar{B}$, fully reconstructs the tag side B and looks for a mono-energetic lepton. Both experiments find no significant signal and set the upper limits [3] listed in Table 1. The measured branching fraction of $B^+ \to \mu^+\nu_\mu$ is reaching to the SM predictions and we expect to find the signal in near future with larger luminosity.

3 Search for $b \to d\gamma$

Radiative B decays proceed mainly through the $b \to s\gamma$ and $b \to d\gamma$ processes. These flavor changing neutral current processes are dominated by a electroweak penguin diagram in Fig. 3, and are sensitive to New Physics. Because the $b \to d\gamma$ process is suppressed by a factor of $|V_{td}/V_{ts}|^2$ compared to $b \to d\gamma$, it can also be used for measurement of $|V_{td}/V_{ts}|$. Many studies, including measurements of the branching fractions and charge asymmetries for inclusive and exclusive $b \to s\gamma$, have been done. In this section, search for $b \to d\gamma$ is mentioned. Measurement of time-dependent CP asymmetry in $B \to K^0_S\pi^0\gamma$ is described in the next section.

Belle and BaBar search for the $b \to d\gamma$ process using the final states

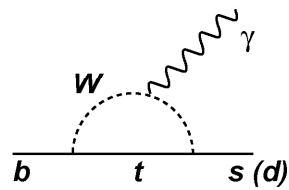

Figure 3: *Diagram for $b \to s\gamma$ and $b \to d\gamma$.*

$\rho^+\gamma$, $\rho^0\gamma$ and $\omega\gamma$ with data samples containing 386×10^6 and 347×10^6 $B\bar{B}$, respectively. These branching fractions have the isospin relation $\mathcal{B}(B \to (\rho,\omega)\gamma) \equiv \mathcal{B}(B^+ \to \rho^+\gamma) = 2\frac{\tau_{B^+}}{\tau_{B^0}}\mathcal{B}(B^0 \to \rho^0\gamma) = 2\frac{\tau_{B^+}}{\tau_{B^0}}\mathcal{B}(B^0 \to \omega\gamma)$, where $\frac{\tau_{B^+}}{\tau_{B^0}} = 1.076 \pm 0.008$. Theoretical predictions of $\mathcal{B}(B \to (\rho,\omega)\gamma)$ are in the range of $(0.9\text{–}2.7) \times 10^{-6}$.

The dominant background comes from the continuum $e^+e^- \times q\bar{q}$ ($q = u$, d, s, c) process and is suppressed using the event shape variables, B meson flight direction and flavor tagging variables. The separation of the signal component from $B \to K^*\gamma$, which has more than 20 times larger branching fraction, is essential. This is realized by excellent performance of K/π separation of the Belle and BaBar detector, with help of several more variables such as ΔE. Contribution from $B \to \rho\pi^0$, $\omega\pi^0$ is suppressed by using the information of the helicity angle. Belle performs two-dimensional fit to $M_{\rm bc}$ ($=M_{\rm ES}$) and ΔE to extract the signal yield, while BaBar also includes the helicity angle and neural-net output in the fit.

Figure 4 shows the $M_{\rm bc}$ distributions after the fit. The obtained branching fractions [4)] are listed Table 2. The branching fraction for combined $B \to (\rho,\omega)\gamma$ is obtained assuming the isospin relation. The observation of the $b \to d\gamma$ process by Belle is now confirmed by BaBar, who also finds evidence of $B^+ \to \rho^+\gamma$. The two results are consistent with each other, and with the theoretical predictions, too.

Using the relation

$$\frac{\mathcal{B}(B \to (\rho,\omega)\gamma)}{\mathcal{B}(B \to K^*\gamma)} = \left|\frac{V_{td}}{V_{ts}}\right|^2 \frac{(1 - m^2_{(\rho,\omega)}/m^2_B)^3}{(1 - m^2_{K^*}/m^2_B)^3}\zeta^2[1 + \Delta R], \qquad (2)$$

where $\zeta(= 0.85\pm0.10)$ is the form factor ratio and $\Delta R(= 0.1\pm0.1)$ is the $SU(3)$-breaking correction, $|V_{td}/V_{ts}|$ is determined to be $0.199\,^{+0.026}_{-0.025}$(exp.)$\,^{+0.018}_{-0.015}$(theo.) and $0.200\,^{+0.021}_{-0.020}$(exp.) $\pm$ 0.015(theo.) by Belle and BaBar, respectively. Although these results give looser constraint than that from B_s-mixing [5)], independent measurement is important to search for the New Physics, because the processes of $b \to d\gamma$ and B_s-mixing are different. In order to obtain constraint

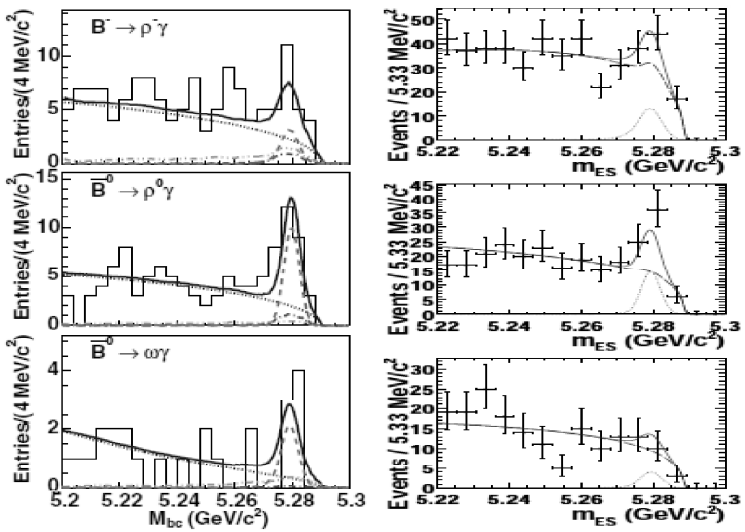

Figure 4: *$M_{\rm bc}$ distributions of $B^+ \to \rho^+\gamma$ (top), $B^0 \to \rho^0\gamma$ (middle) and $B^0 \to \omega\gamma$ (bottom) respectively at Belle (left) and BaBar (right). Curves show the fit results.*

Table 2: *Measured branching fractions ($\times 10^{-6}$) and significance of $B \to \rho\gamma$ and $B^0 \to \omega\gamma$ at Belle and BaBar.*

	Belle		BaBar	
$B^+ \to \rho^+\gamma$	$0.55\,^{+0.42\,+0.09}_{-0.36\,-0.08}$	(1.6σ)	$1.10\,^{+0.37}_{-0.33} \pm 0.09$	(3.8σ)
$B^0 \to \rho^0\gamma$	$1.25\,^{+0.37\,+0.07}_{-0.33\,-0.06}$	(5.2σ)	$0.79\,^{+0.22}_{-0.20} \pm 0.06$	(4.9σ)
$B^0 \to \omega\gamma$	$0.56\,^{+0.34\,+0.05}_{-0.27\,-0.10}$	(2.3σ)	$0.40\,^{+0.24}_{-0.20} \pm 0.05$	(2.2σ)
$B \to (\rho,\omega)\gamma$	$1.32\,^{+0.34\,+0.10}_{-0.31\,-0.09}$	(5.1σ)	$1.25\,^{+0.25}_{-0.24} \pm 0.09$	(6.4σ)

with less theoretical uncertainty, it would be better to use $B^+ \to \rho^+\gamma$ only to avoid the contamination form annihilation diagram in future measurement.

4 tCPV in $b \to s\gamma$

In the SM, photons from from $b \to s\gamma$ are almost left-handedly polarized. This means the time-dependent *CP* violation (tCPV) does not happen in radiative B decays, because tCPV happens only B^0 and $\bar{B}^0$ decay to a common *CP* eigenstate. Therefore, large tCPV in radiative B decay in an indication of the New Physics. In the SM, strong interaction may enhance the *CP*-violation parameter S to be around 10%.

Belle [6] obtains $S = -0.10 \pm 0.31 \pm 0.07$ and $A = -0.20 \pm 0.20 \pm 0.06$ for $B \to K^0_S\pi^0\gamma$ for $M(K\pi) < 1.8$ GeV with a data sample including 535×10^6 $B\bar{B}$. If we select $B \to K^{*0}\gamma$ decay, tCPV is measured to be $S = -0.32\,^{+0.36}_{-0.33} \pm 0.05$ and $A = -0.20 \pm 0.24 \pm 0.05$. BaBar [7] gives $S = -0.21 \pm 0.40 \pm 0.05$ and $C = -0.40 \pm 0.23 \pm 0.03$, where $C = -A$, from a data with 232×10^6 $B\bar{B}$. The statistical errors are still large to derive some conclusions. We need more statistics to reduce them to 10%, which is the present theoretical uncertainty.

5 tCPV in $b \to s$ penguins

In the SM, the *CP* violation parameter S in B decays via $b \to s$ gluonic penguin process is expected to be $S = -\xi \sin 2\phi_1$, where ξ is *CP* eigenvalue in the final state and $\phi_1 = \beta$. $\sin 2\phi_1$ is well-measured using $b \to c\bar{c}s$ process such as $B \to J/\psi K^0_S$. The present world average is $\sin 2\phi_1 = 0.654 \pm 0.026$.

Possible contribution to the $b \to s$ loop diagram by non-SM particles may vary the value of *CP* violation parameter S. Therefore, comparison of $\sin 2\phi_1$ in various $b \to s$ penguin decays (denoted by $\sin 2\phi_1^{\rm eff}$ hereafter) with that in $b \to c\bar{c}s$ process is an important test of the SM. However, we should also note that there is small deviation of S in each mode due to strong interaction.

Of many B decay modes via $b \to s$ penguin, $B^0 \to \eta' K^0$ and $B^0 \to \phi K^0$ are the main targets because of their large branching fraction and small theoretical uncertainty. In a data sample with 535×10^6 $B\bar{B}$ events, Belle find 1872 ± 61 and 421 ± 27 events, respectively for $B^0 \to \eta' K^0$ and $B^0 \to \phi K^0$. BaBar analyzes a data sample with 384×10^6 $B\bar{B}$ events for $B^0 \to \eta' K^0$. Figure 5 shows the Δt distributions and asymmetry for $B \to \eta' K^0$. Belle [8] obtains $\sin 2\phi_1^{\rm eff} = 0.64 \pm 0.10 \pm 0.04$ and BaBar [9] $\sin 2\phi_1^{\rm eff} = 0.58 \pm 0.10 \pm 0.03$, giving an consistent result with $\sin 2\phi_1$. The significances of the mixing-induced *CP* violation are 5.6σ and 5.5σ, respectively. These are the first observation of the *CP* violation in $b \to s$ penguin.

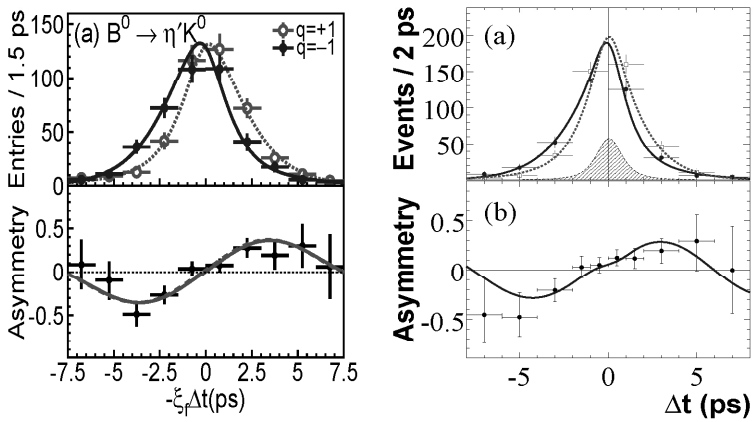

Figure 5: *Background subtracted Δt distributions (top) and asymmetry (bottom) for $B \to \eta' K^0$ at Belle (left) and BaBar. BaBar's plots do not include $B \to \eta' K_L^0$. Curves show the fit results.*

Belle [8] also measures $\sin 2\phi_1^{\rm eff}$ in $B^0 \to \phi K^0$ to be $0.50 \pm 0.21 \pm 0.06$. BaBar [10] measures the Dalitz plot distribution in $K^+K^-K^0$ final states, finding $\phi_1^{\rm eff} = 0.06 \pm 0.16 \pm 0.05$, which corresponds to $\sin 2\phi_1^{\rm eff} = 0.12 \pm 0.31 \pm 0.10$ using 347×10^6 $B\bar{B}$.

CP violation in other $b \to s$ penguin modes are also measured. For example, Belle [8] obtains $\sin 2\phi_1^{\rm eff}(B^0 \to K_S^0 K_S^0 K_S^0) = 0.30 \pm 0.32 \pm 0.08$ with 535×10^6 $B\bar{B}$ data sample. BaBar's recent results [11] show $\sin 2\phi_1^{\rm eff}(B^0 \to K_S^0 K_S^0 K_S^0) = 0.71 \pm 0.24 \pm 0.04$ and $\sin 2\phi_1^{\rm eff}(B^0 \to \pi^0\pi^0 K_S^0) = -0.72 \pm 0.71 \pm 0.08$. If we make a simple average of all measurement of $\sin 2\phi_1^{\rm eff}$ for the $b \to s$ penguin, we obtain $\sin 2\phi_1^{\rm eff} = 0.53 \pm 0.05$ which is 2.6σ away from $\sin 2\phi_1$. This average is too naïve to conclude anything, because correlation of the systematic errors are not considered and because any theoretical uncertainty is not taken into account. In order to explore the New Physics, we need more precise measurement of $\sin 2\phi_1^{\rm eff}$ for each mode, more understanding of the theoretical uncertainty.

6 Summary

In this proceedings, we have listed several recent results on rare B decays from Belle and BaBar. However, these are only a small part of measurements. The existent two B factories provides unique opportunity to study many rare B

decays, especially decays with neutral or missing particles, as shown in the study of $B \to \tau\nu$. With more luminosity accumulated, Belle and BaBar will provide many interesting results on rare B decays rich with various kind of physics.

References

1. W. M. Yao *et al.* (Particle Data Group), J. Phys. G **33** (2006) 1.
2. K. Ikado *et al.* (Belle Collaboration), Phys. Rev. Lett. **97** (2006) 251802; B. Aubert *et al.* (BaBar Collaboration), hep-ex/0608019.
3. N. Satoyama *et al.* (Belle Collaboration), Phys. Lett. B **647** (2007) 67; B. Aubert *et al.* (BaBar Collaboration), hep-ex/0607110.
4. D. Mohapatra *et al.* (Belle Collaboration),, Phys. Rev. Lett. **96** (2006) 221601; B. Aubert *et al.* (BaBar Collaboration), Phys. Rev. Lett. **98** (2007) 151802.
5. A. Abulencia *et al.* (CDF Collaboration), Phys. Rev. Lett. **97** (2006) 242003.
6. Y. Ushiroda *et al.* (Belle Collaboration), Phys. Rev. D **74** (2006) 111104.
7. B. Aubert *et al.* (BaBar Collaboration), Phys. Rev. D **72** (2005) 051103.
8. K. F. Chen *et al.* (Belle Collaboration), Phys. Rev. Lett. **98**, 031802 (2007).
9. B. Aubert *et al.* (BaBar Collaboration), Phys. Rev. Lett. **98** (2007) 031801.
10. B. Aubert *et al.* (BaBar Collaboration), hep-ex/0607112.
11. B. Aubert *et al.* (BaBar Collaboration), hep-ex/0702046; hep-ex/0702010.

HOT TOPICS FROM BELLE: TIME DEPENDENT CP VIOLATION IN $\mathbf{B^0 \to D^+ D^-}$

Saša Fratina (for the Belle collaboration)
Jožef Stefan Institute, Ljubljana

Abstract

We report measurements of the branching fraction and CP violation parameters in $B^0 \to D^+ D^-$ decays. The results are based on a data sample that contains 535×10^6 $B\overline{B}$ pairs collected at the $\Upsilon(4S)$ resonance, with the Belle detector at the KEKB asymmetric-energy e^+e^- (3.5 on 8 GeV) collider. We obtain $[1.97 \pm 0.20\,(\text{stat}) \pm 0.20\,(\text{syst})] \times 10^{-4}$ for the branching fraction of $B^0 \to D^+ D^-$. The measured values of the CP violation parameters are: $\mathcal{S} = -1.13 \pm 0.37 \pm 0.09$, $\mathcal{A} = 0.91 \pm 0.23 \pm 0.06$, where the first error is statistical and the second is systematic. We find evidence of CP violation in $B^0 \to D^+ D^-$ at the $4.1\,\sigma$ confidence level. While the value of $\mathcal{S}$ is consistent with expectations from other measurements, the value of the parameter $\mathcal{A}$ favors large direct CP violation at the $3.2\,\sigma$ confidence level, in contradiction to Standard Model expectations.

1 Introduction

Within the Standard Model (SM), CP violation (CPV) arises from a complex phase in the Cabibbo-Kobayashi-Maskawa (CKM) quark mixing matrix $\mathbf{V}$ [1]. Recently observed $B^0 \to D^+D^-$ decays [2, 3] offer another opportunity to test the unitarity of the CKM mixing matrix and search for possible new physics contributions to these decays. As the final state D^+D^- is accessible for both, B^0 and $\overline{B}^0$ mesons, the CPV in this decay is a result of the interference between the complex phases of two indistinguishable processes, CPV in mixing, $B^0 \to \overline{B}^0 \to D^+D^-$, and decay, $B^0 \to D^+D^-$. Interference between the two terms gives rise to the time-dependent decay rate,

$$\mathcal{P} = \frac{e^{-|\Delta t|/\tau}}{4\tau}\{1 + q[\mathcal{S}\sin(\Delta m \Delta t) + \mathcal{A}\cos(\Delta m \Delta t)]\}\,, \qquad (1)$$

where Δt is the time for which the B meson freely propagates before it decays, τ is the B^0 meson lifetime, Δm is the mass difference of the two B mass eigenstates [4] and q is the flavor of the B meson decaying to the CP eigenstate at $\Delta t = 0$, $q = +1\,(-1)$ for $B_{CP} = \overline{B}^0\,(B^0)$.

The dominant contribution to $B^0 \to D^+D^-$ decays is the tree-level $b \to c\bar{c}d$ transition shown in Fig. 1(a). If this diagram is the only contribution, then the mixing-induced CPV parameter is $\mathcal{S} = -\sin 2\phi_1$, where $\phi_1 = \arg[-V_{cd}V_{cb}^*/V_{td}V_{tb}^*]$ [5], while the direct CPV term $\mathcal{A}$ is zero. The second-order gluonic penguin contribution, shown in Fig. 1(b), is expected to

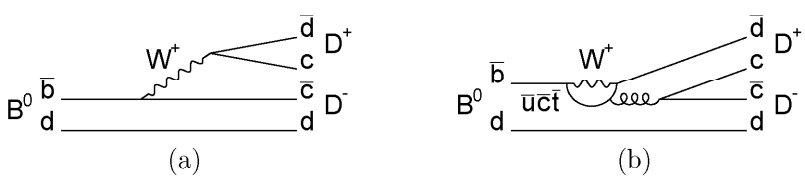

Figure 1: *The tree (a) and the penguin (b) contributions to the* $B^0 \to D^+D^-$ *decay.*

change the value of the parameter $\mathcal{S}$ by less than a few percent and increase the value of $\mathcal{A}$ to about 3% [6, 7]. However, particles from physics beyond the SM may give additional contributions within the loop diagrams mediating flavor-changing $b \to d$ transitions. Such contributions may potentially induce large deviations from the SM expectation for time-dependent CP asymmetries [8].

As sin $2\phi_1$ has already been determined with high precision by measurements in $b \to c\bar{c}s$ charmonium modes [9, 10], the objective here is to focus on deviations from expectations in $b \to c\bar{c}d$ transitions. Similar studies have been carried out for $B^0 \to D^{*\pm}D^{(*)\mp}$ decays, which involve the same quark level weak decay [11, 12, 13, 14]. Here we show a result of a new measurement of CP parameters in $B^0 \to D^+D^-$ decays [15].

The results are based on a data sample that contains $(535 \pm 7) \times 10^6$ $B\overline{B}$ pairs, collected with the Belle detector at the KEKB asymmetric-energy e^+e^- (3.5 on 8 GeV) collider [16]. KEKB operates at the $\Upsilon(4S)$ resonance ($\sqrt{s} = 10.58$ GeV) with a peak luminosity that exceeds 1.7×10^{34} cm^{-2}s^{-1}. At KEKB, the $\Upsilon(4S)$ is produced with a Lorentz boost of $\beta\gamma = 0.425$ nearly along the electron beam line ($-z$ direction). Since the B^0 and $\overline{B}^0$ mesons are approximately at rest in the $\Upsilon(4S)$ center-of-mass (CM) system, Δt can be determined from the displacement in z between the B_{CP} and $B_{\rm tag}$ decay vertices: $\Delta t \simeq (z_{CP} - z_{\rm tag})/\beta\gamma c = \Delta z/\beta\gamma c$.

The Belle detector [17] is a large-solid-angle magnetic spectrometer that consists of a silicon vertex detector, a 50-layer central drift chamber (CDC), an array of aerogel threshold Čerenkov counters (ACC), a barrel-like arrangement of time-of-flight scintillation counters (TOF), and an electromagnetic calorimeter comprised of CsI(Tl) crystals located inside a superconducting solenoid coil that provides a 1.5 T magnetic field. An iron flux-return located outside of the coil is instrumented to detect K_L^0 mesons and to identify muons. Two inner detector configurations were used; a 2.0 cm radius beam pipe and a 3-layer silicon vertex detector was used for the first 152×10^6 $B\overline{B}$ pairs and a 1.5 cm beam pipe, a 4-layer silicon detector and a small-cell inner drift chamber were employed for the remaining 383×10^6 $B\overline{B}$ pairs [18].

2 Event Reconstruction

D mesons are reconstructed using the $D^+ \to K^-\pi^+\pi^+$ and $D^+ \to K_S\pi^+$ decay modes [19]. The shorter notation $K\pi\pi$ is used when both D mesons are reconstructed in the $K\pi\pi$ channel, while $K_S\pi$ is used when at least one of the D mesons is reconstructed in the $K_S\pi$ channel. Charged tracks that are not positively identified as electrons [20] and satisfy a loose requirement on the impact parameter relative to the interaction point (IP) are considered as pion and kaon candidates. For charged particle identification, we form a

likelihood ratio based on the combined information from the CDC, TOF and ACC counters [21]. K_S candidates are reconstructed in the $K_S \to \pi^+\pi^-$ decay mode. The mass of the $D^\pm$ meson candidate is required to be within $10\,\mathrm{MeV}/c^2$ of the nominal $D^\pm$ mass. We select B meson candidates using the energy difference $\Delta E = E_B^* - E_{\mathrm{beam}}^*$ and the beam-energy-constrained mass $M_{\mathrm{bc}} = \sqrt{(E_{\mathrm{beam}}^*/c^2)^2 - (p_B^*/c)^2}$, where E_B^*, E_{beam}^*, and p_B^* are the B meson energy, the beam energy, and the B meson momentum, respectively, in the CM system.

The K_S decay vertex is fitted from two pion tracks. The D^+ meson decay vertex is fitted from three charged tracks or from the K_S and π^+ track. The mass of the $K^-\pi^+\pi^+$ or $K_S\pi^+$ combination is constrained to the D^+ meson mass to obtain better M_{bc} and ΔE resolutions. The B^0 decay vertex is reconstructed from the two D meson tracks and the IP information.

Continuum events are suppressed by forming a likelihood ratio from $\cos\theta_B$, where θ_B is the polar angle between the B meson direction in the CM system and the beam axis, and a variable based on a combination of sixteen modified Fox-Wolfram moments with the scalar sum of transverse momentum [22]. After applying all of the event selection criteria, 16% of the signal events have more than one B^0 candidate. The best candidate is selected based on the value of the invariant mass of the $K\pi\pi$ and $K_S\pi$ combinations.

3 Branching Fraction Measurement

The signal yield is obtained from an extended unbinned 2D maximum likelihood (ML) fit of the M_{bc} and ΔE distributions in the range $M_{\mathrm{bc}} > 5.20\,\mathrm{GeV}/c^2$ and $-0.05\,\mathrm{GeV} < \Delta E < 0.10\,\mathrm{GeV}$. A Gaussian function for the signal and an ARGUS [23] function for the background are used to describe the M_{bc} distribution. For the parameterization of the ΔE distribution we used two Gaussians with the same mean value to describe the signal and a linear function to describe the background. Non-resonant $B^0 \to D^-\overline{K}^0\pi^+$ and $B^0 \to D^-\overline{K}^{*0}(892)\pi^+$ decays are found to be a possible source of background peaking in the M_{bc} and ΔE distributions. The amount of this background is estimated from the D^+ mass sidebands in data and subtracted from the signal. The fit yields 150 ± 15 events in the signal peak, where the error is statistical only. The M_{bc} and ΔE distributions of reconstructed events and the projection of the fit result are shown in Fig. 2. The branching fraction is calculated from the total number of

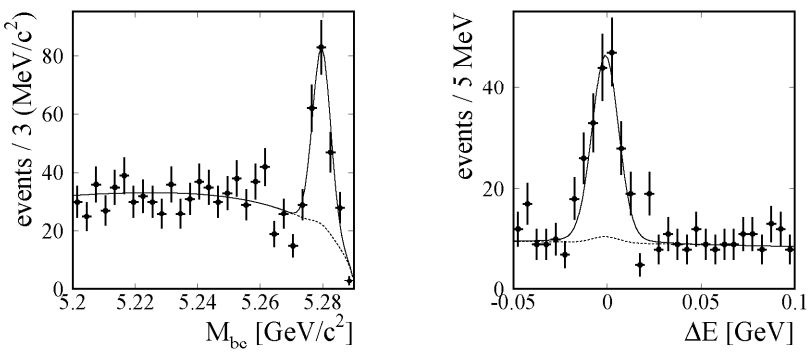

(a) $M_{\rm bc}$, $|\Delta E| < 0.03\,{\rm GeV}$ (b) ΔE, $M_{\rm bc} > 5.27\,{\rm GeV}/c^2$

Figure 2: *Distributions for the reconstructed events in $M_{\rm bc}c^2$ (a) and ΔE (b). The full (dashed) curves show the projections of the result of the 2D unbinned maximum likelihood fit for all (background) events.*

reconstructed events and the average reconstruction efficiency, and is found to be $\mathcal{B}(B^0 \to D^+D^-) = [1.97 \pm 0.20\,({\rm stat}) \pm 0.20\,({\rm syst})] \times 10^{-4}$, which is consistent with previous measurements [2, 3] and has better accuracy. The main sources of the systematic error are the uncertainty in the D meson branching fractions (5%), the error in the pion and kaon track reconstruction efficiency (6%) and the difference in particle identification efficiency for the simulated and real data (6%).

4 Measurement of CP Parameters

The time between the two decays Δt is determined from the two B meson vertices. Once the B meson decaying to the D^+D^- final state is reconstructed, all remaining charged tracks are used to determine the decay vertex of the tag-side B meson. A loose requirement on the quality of the vertex fit is applied for both B mesons. Since the B meson pair is entangled in a spin $S-1$ state, the two B mesons have opposite flavors. At the time of the first B meson decay, the flavor of the B_{CP} meson is opposite to the flavor of the accompanying $B_{\rm tag}$ meson, which is determined from its decay products. Events are divided into six r-bins according to the tagging quality r. The value of r ranges from 0 for events with no flavor information to 1 for unambiguous flavor assignment. Due

to the imperfect flavor tagging, the distribution $\mathcal{P}$ of Eq. 1 is modified to

$$\mathcal{P}_{\rm sig} = \frac{e^{-|\Delta t|/\tau}}{4\tau}\{1 - q\Delta w + q(1-2w)\left[\mathcal{S}\sin(\Delta m\Delta t) + \mathcal{A}\cos(\Delta m\Delta t)\right]\}\,, \quad (2)$$

where w is the wrong tag fraction, and Δw is the difference between the wrong tag fractions if the $B_{\rm tag}$ meson is a $\overline{B}^0$ or B^0. The values of w and Δw for each of the six bins in the tagging quality parameter r are determined separately using flavor specific B meson decays [24].

Time-dependent CP violation parameters are determined by an unbinned ML fit to the Δt distribution of the events in the signal region $5.27\,{\rm GeV}/c^2 < M_{\rm bc} < 5.29\,{\rm GeV}/c^2$ and $|\Delta E| < 0.03\,{\rm GeV}$. The Δt distribution for signal events $\mathcal{P}_{\rm sig}$ described by Eq. 2 is modified by the inclusion of the background contribution and resolution effects. The event-by-event likelihood is given by

$$\mathcal{L}_{\rm ev} = f_{\rm sig}\,\mathcal{P}_{\rm sig} \otimes \mathcal{R} + f_{\rm nr}\,\mathcal{P}_{\rm nr} \otimes \mathcal{R} + f_{\rm bcg}\,\mathcal{P}_{\rm bcg} \otimes \mathcal{R}_{\rm bcg}\,. \quad (3)$$

Subscripts sig, nr and bcg refer to signal, non-resonant and combinatorial background components, respectively. The fractions $f_{\rm i} = f_{\rm i}(M_{\rm bc}, \Delta E, r)$ are determined on an event-by-event basis, $f_{\rm sig}+f_{\rm nr}+f_{\rm bcg} = 1$. The function $\mathcal{R}$ describes the detector resolution of the Δt measurement [25]. Resolution parameters for the B_{CP} meson vertex are determined from a fit to the Δt distribution of kinematically similar $B^0 \to D_s^+ D^-$ decays.

The fraction of the non-resonant decays $f_{\rm nr}$ is assumed to be proportional to the signal fraction, $f_{\rm nr} = a\,f_{\rm sig}$ and their Δt distribution is described by an exponential term $e^{-|\Delta t|/\tau}$. The Δt distribution of the background is described by an exponential and δ-function term and the background resolution function $\mathcal{R}_{\rm bcg}$ is taken to be a Gaussian.

From an unbinned fit to the measured Δt distribution described by Eq. 3, we obtain the CP violation parameters for $B^0 \to D^+ D^-$,

$$\begin{aligned} \mathcal{S} &= -1.13 \pm 0.37 \pm 0.09 \ \text{and} \\ \mathcal{A} &= +0.91 \pm 0.23 \pm 0.06\,, \end{aligned} \quad (4)$$

where the first error is statistical and the second is systematic. The Δt distributions are shown in Fig. 3. The main contributions to the systematic error are fit bias (0.06 for $\mathcal{S}$ and 0.02 for $\mathcal{A}$), uncertainties in the resolution function (0.04 for $\mathcal{S}$ and 0.03 for $\mathcal{A}$) and signal fraction (0.035 for $\mathcal{S}$ and 0.015 for

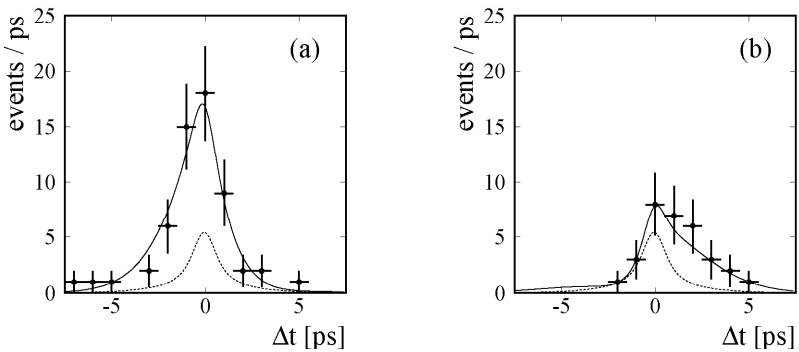

Figure 3: *The Δt distribution for events with good tagging information ($r > 0.5$) when the tag-side B-meson is reconstructed as B^0 (a) or $\overline{B}^0$ (b). The full and dashed curves show the projection of the fit result and background contribution, respectively.*

$\mathcal{A}$). Other uncertainties come from the errors on the parameters τ and Δm (0.023 for $\mathcal{S}$ and 0.007 for $\mathcal{A}$), wrong tag fractions (0.017 for $\mathcal{S}$ and 0.014 for $\mathcal{A}$), description of background Δt distribution (0.01 for $\mathcal{S}$ and $\mathcal{A}$), fraction and possible CP asymmetry of the non-resonant background (0.02 for $\mathcal{S}$ and 0.03 for $\mathcal{A}$), the effect of tag-side interference [26] (0.01 for $\mathcal{S}$ and 0.03 for $\mathcal{A}$) and requirements on the vertex quality and the fitting range (less than 0.01 for $\mathcal{S}$ and 0.01 for $\mathcal{A}$).

To test the consistency of the fitting procedure, the same analysis was applied to the $B^0 \to D_s^+ D^-$ control sample. The result is consistent with no CPV, $\mathcal{S} = -0.064 \pm 0.094$ and $\mathcal{A} = 0.091 \pm 0.060$, where the error is statistical only.

We use the Feldman-Cousins frequentist approach [27] to determine the statistical significance of our measurement. In order to form confidence intervals, we use the $\mathcal{A}$ and $\mathcal{S}$ distributions of the results of fits to the Monte Carlo pseudo-experiments for various input values of $\mathcal{A}$ and $\mathcal{S}$ in a similar way as described in Ref. [28]. The systematic errors and possibility of tails that are wider than Gaussian tails are taken into account. As shown in Fig. 4, the case of no CPV, $\mathcal{S} = \mathcal{A} = 0$, is ruled out at the 4.1σ confidence level (CL). The case of no direct CPV, $\mathcal{A} = 0$, is excluded at more than 3.2σ CL for any value of the parameter $\mathcal{S}$.

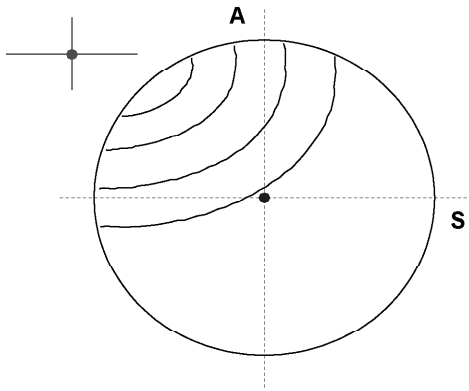

Figure 4: *The* $1-$, $2-$, $3-$ *and* $4-\sigma$ *level CL contours obtained by the Feldman-Cousins significance study.*

5 Summary

In summary, we measure the branching fraction for $B^0 \to D^+D^-$ decays to be $(1.97 \pm 0.20 \pm 0.20) \times 10^{-4}$, superseding our previous measurement [2]. We obtain values for the CP parameters $\mathcal{S} = -1.13 \pm 0.37 \pm 0.09$ and $\mathcal{A} = 0.91 \pm 0.23 \pm 0.06$ and rule out the CP-conserving case, $\mathcal{S} = \mathcal{A} = 0$, at the $4.1\,\sigma$ confidence level. The value of $\mathcal{S}$ is consistent with measurements of $b \to c\bar{c}s$ modes [4]. In addition, we observe evidence for direct CP violation at the $3.2\,\sigma$ confidence level. Some extensions of the SM predict large contributions to the CP violating phases in $b \to c\bar{c}d$ decays that are consistent with our result [8]. Our measurement differs from a previous measurement by the BaBar collaboration [13] by about $2.2\,\sigma$.

6 Acknowledgements

We thank the KEKB group for the excellent operation of the accelerator, the KEK cryogenics group for the efficient operation of the solenoid, and the KEK computer group and the National Institute of Informatics for valuable computing and Super-SINET network support. We acknowledge support from the Ministry of Education, Culture, Sports, Science, and Technology of Japan and the Japan Society for the Promotion of Science; the Australian Research

Council and the Australian Department of Education, Science and Training; the National Science Foundation of China and the Knowledge Innovation Program of the Chinese Academy of Sciences under contract No. 10575109 and IHEP-U-503; the Department of Science and Technology of India; the BK21 program of the Ministry of Education of Korea, the CHEP SRC program and Basic Research program (grant No. R01-2005-000-10089-0) of the Korea Science and Engineering Foundation, and the Pure Basic Research Group program of the Korea Research Foundation; the Polish State Committee for Scientific Research; the Ministry of Education and Science of the Russian Federation and the Russian Federal Agency for Atomic Energy; the Slovenian Research Agency; the Swiss National Science Foundation; the National Science Council and the Ministry of Education of Taiwan; and the U.S. Department of Energy.

References

1. N. Cabibbo, Phys. Rev. Lett. **10**, 531 (1963); M. Kobayashi and T. Maskawa, Prog. Theor. Phys. **49**, 652 (1973).

2. G. Majumder *et al.* (Belle collaboration), Phys. Rev. Lett. **95**, 041803 (2005).

3. B. Aubert *et al.* (BaBar Collaboration), Phys. Rev. D **73**, 112004 (2006).

4. W.-M. Yao *et al.*, J. Phys. G **33**, 1 (2006).

5. Another naming convention, $\beta = \phi_1$, is also used in the literature.

6. M. Gronau, Phys. Rev. Lett. **63**, 14 (1989).

7. Z.-Z. Xing, Phys. Rev. D **61**, 014010 (1999).

8. Y. Grossman, M. Worah, Phys. Lett. B **395**, 241 (1997).

9. K.-F. Chen *et al.* (Belle Collaboration), Phys. Rev. D **72**, 012004 (2005); K. Sumisawa *et al.* (Belle Collaboration), Phys. Rev. Lett. **95**, 061801 (2005).

10. B. Aubert *et al.* (BaBar Collaboration), Phys. Rev. D **71**, 091102(R) (2005); Phys. Rev. Lett. **94**, 191802 (2005); Phys. Rev. Lett. **95**, 011801 (2005).

11. T. Aushev *et al.* (Belle Collaboration), Phys. Rev. Lett. **93**, 201802 (2004).

12. H. Miyake *et al.* (Belle Collaboration), Phys. Lett. B **618**, 34 (2005).

13. B. Aubert *et al.* (BaBar Collaboration), Phys. Rev. Lett. **95**, 131802 (2005).

14. B. Aubert *et al.* (BaBar Collaboration), Phys. Rev. Lett. **95**, 151804 (2005).

15. S. Fratina *et al.* (Belle Collaboration), hep-ex/070231.

16. S. Kurokawa and E. Kikutani, Nucl. Instrum. Methods Phys. Res., Sect. A **499**, 1 (2003), and other papers included in this volume.

17. A. Abashian *et al.* (Belle Collaboration), Nucl. Instrum. Methods Phys. Res., Sect. A **479**, 117 (2002).

18. Z. Natkaniec *et al.*, Nucl. Instrum. Methods Phys. Res., Sect. A **560**, 1 (2006).

19. The inclusion of the charge conjugate mode decay is implied throughout this paper.

20. K. Hanagaki *et al.*, Nucl. Instrum. Methods Phys. Res., Sect. A **485**, 490 (2002).

21. E. Nakano, Nucl. Instrum. Methods Phys. Res., Sect. A **494**, 402 (2002).

22. S.-H. Lee *et al.* (Belle Collaboration), Phys. Rev. Lett. **91**, 261801 (2003).

23. H. Albrecht *et al.* (ARGUS Collaboration), Phys. Lett. B **241**, 278 (1990).

24. H. Kakuno *et al.*, Nucl. Instrum. Methods Phys. Res., Sect. A **533**, 516 (2004).

25. H. Tajima *et al.*, Nucl. Instrum. Methods Phys. Res., Sect. A **533**, 370 (2004).

26. O. Long, M. Baak, R.-N. Cahn and D. Kirkby, Phys. Rev. D **68**, 034010 (2003).

27. G.-J. Feldman and R.-D. Cousins, Phys. Rev. D **57**, 3873 (1998).

28. K. Abe *et al.* (Belle Collaboration), Phys. Rev. D **68**, 012001 (2003).

RECENT RESULTS FROM NA48

Spasimir Balev
Joint Institute for Nuclear Research, 141980 Dubna, Russia

Abstract

Recent results from the experiments NA48, NA48/1 and NA48/2 are presented, including: direct CP-violation and Dalitz plot slopes measurements for $K^{\pm} \to 3\pi$ decays; $\pi\pi$ scattering effects in $K^{\pm} \to \pi^{\pm}\pi^0\pi^0$ and K^{+-}_{e4} decays, as well as $K^{\pm}_{e4}$ form factors and branching fraction; measurements on radiative charged kaons and hyperon decays, semileptonic decays of neutral and charged kaons; $K_L \to \pi^+\pi^-$ branching ratio and $|\eta_{+-}|$ measurement; lepton universality check with $K^{\pm}_{l2}$ decays.

1 Introduction

The series of experiments NA48, having a multipurpose large samples of neutral and charged kaon decays, continues to provide new results in the field of Kaon physics. In this paper briefly are described some of the recent measurements from all three stages of the experimental program: NA48, NA48/1 and NA48/2. The experiment NA48 (1997-2000) was dedicated to the measurement of direct CP-violation in K^0 decays. The next stage, NA48/1 (2002), was orientated mainly to the study of rare K_S decays. The final stage, NA48/2 (2003-2004), was designed to search for direct CP-violation in $K^{\pm}$ decays (see section 3). Besides these central topics, many other analyses were performed.

2 Experimental setup

The NA48 beam line was designed to produce and transport both K_L and K_S beams simultaneously. A description of the beam line, as well as of the NA48 detectors, can be found in [1]. Two of the measurements presented in this paper are performed during a dedicated 1999 NA48 run. The K_L beam was produced by SPS 450 GeV/c proton beam on a beryllium target. The beginning of the decay volume was defined by the last of three collimators, located 126 m downstream of the target.

For the NA48/1 experiment the K_L beam was removed and the proton flux on the K_S target was greatly increased. A 24 mm platinum absorber was placed after the Be target to reduce the photon flux in the neutral beam. A beam of long-lived neutral particles (γ, n, K^0, Λ and Ξ^0) was selected by the sweeping magnet, installed across the 5.2 m long collimator.

The neutral beams were replaced by simultaneous K^+ and K^- beams for the NA48/2 experiment. The momentum (60 ± 3) GeV/c was formed symmetrically for K^+ and K^- in the first achromat (see Fig. 1), in which the two beams were split in the vertical plane. In the second achromat were placed two of the three stations of the Kaon beam spectrometer (KABES). The beams followed the same path in the decay volume, comprised in a 114 m long cylindrical vacuum tank. The beam axes coincided to 1 mm, while their lateral size is about 1 cm.

The NA48 detectors, used in the presented analyses, are:

- a magnetic spectrometer for charged particles reconstruction, with 4 drift chambers; the momentum resolution is $\sigma_p/p = (1.02 \oplus 0.044p)\%$, where p is in GeV/c;
- a charged hodoscope, with good time resolution, which sends fast trigger signals;

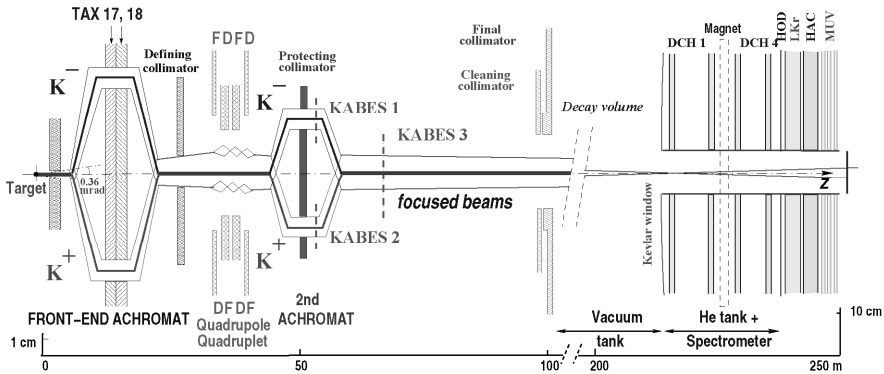

Figure 1: *Schematic side view of the NA48/2 beam line (TAX17,18: motorized beam dump/collimators used to select the momentum of the K^+ and K^- beams; FDFD/DFDF: focusing quadrupoles, KABES1–3: kaon beam spectrometer stations), decay volume and detector (DCH1–4: drift chambers, HOD: hodoscope, LKr: EM calorimeter, HAC: hadron calorimeter, MUV: muon veto). Thick lines indicate beam axes, narrow ones the projection of their envelopes. Note that the vertical scales are different in the two parts of the figure.*

- calorimeter with an active volume of 10 m^3 liquid krypton (LKr) with energy resolution of $\sigma_E/E = 0.032/\sqrt{E} \oplus 0.09/E \oplus 0.0042$ and space resolution of $\sigma_x = \sigma_y = 0.42/\sqrt{E} \oplus 0.06$ cm, where the energy E is in GeV;
- a muon detector.

3 Search for direct CP-violation in $K^\pm \to 3\pi$ decays

One of the most promising observables for direct CP-violation in Kaon physics is the asymmetry between K^+ and K^- decaying to three pions. Usually, the matrix element of $K^\pm \to 3\pi$ decays is parameterized in the following form:

$$|M(u,v)|^2 \sim 1 + gu + hu^2 + kv^2 + ..., \qquad (1)$$

where g, h and k are the slope parameters. The Dalitz-variables are defined as $u = (s_3 - s_0)/m_\pi^2$ and $v = (s_1 - s_2)/m_\pi^2$, where m_π is the charged pion mass, $s_i = (p_K - p_i)^2$, $s_0 = \sum s_i/3$ $(i = 1,2,3)$, p_K and p_i are kaon and i-th pion four-momenta respectively. The index $i = 3$ corresponds to the odd pion, i.e. the pion with a charge different from the other two. The parameter of direct CP-violation is usually defined as

$$A_g = \frac{g^+ - g^-}{g^+ + g^-},$$

where g^+ and g^- are the linear coefficients in (1) for K^+ and K^- respectively. The experimental precision for such asymmetry for both modes, $K^\pm \to \pi^\pm\pi^+\pi^-$ and $K^\pm \to \pi^\pm\pi^0\pi^0$, is at the level of 10^{-3}. The Standard Model (SM) predictions are below few 10^{-5}, however some theoretical calculations involving processes beyond the SM do not exclude enhancements of the asymmetry. The main goal of NA48/2 experiment was a search for direct CP-violation at the level of $2 \cdot 10^{-4}$ in both 3π decay modes.

The method of such a high precision asymmetry measurement is based on direct comparison of the u-ratios for K^+ and K^- decays in which the main possible systematic effects cancel due to the presence of simultaneous K^+ and K^- beams and the frequent alternation of the magnet polarities in the beam optics and in the magnetic spectrometer. In the $K^\pm \to \pi^\pm\pi^+\pi^-$ selection, only the magnetic spectrometer was involved in the reconstruction of the events, while the analysis in $K^\pm \to \pi^\pm\pi^0\pi^0$ mode was based mainly on the information from a charge blinded detector — LKr.

In total ~ 3.1 billion $K^\pm \to \pi^\pm\pi^+\pi^-$ and ~ 91 million $K^\pm \to \pi^\pm\pi^0\pi^0$ decays were collected during 2003 and 2004 runs and the final result on asymmetries A_g^c and A_g^n, respectively, yields:

$$A_g^c = (-1.5 \pm 1.5_{stat} \pm 0.9_{trig} \pm 1.1_{syst}) \cdot 10^{-4},$$

$$A_g^n = (1.8 \pm 1.7_{stat} \pm 0.5_{syst}) \cdot 10^{-4}.$$

Both measurements are limited by the statistics and are one order of magnitude more accurate than the previous experiments. The observed results are compatible with the SM predictions. The method of measurement, selection of the events and the studies of main systematic contributions are described in more details in [2] and [3].

4 Dalitz plot slopes measurement in $K^\pm \to \pi^\pm\pi^+\pi^-$

The last measurements of the Dalitz slopes g, h and k in (1) for $K^\pm \to \pi^\pm\pi^+\pi^-$ decay mode are 30 years old. NA48/2 performed a new high precision measurement in order to verify the validity of the parameterization (1).

Approximately $4.7 \cdot 10^8$ $K^\pm \to \pi^\pm\pi^+\pi^-$ decays were selected for the analysis. The measurement method is based on fitting of the binned reconstructed $(u, |v|)$ data distribution with a sum of four MC components generated according to the four terms in the polynomial expansion. The free parameters in the fitting procedure are the slopes g, h and k, and the overall normalization parameter.

The obtained results, ignoring radiative effects (apart from Coulomb factor) and strong rescaterring effects, are:

$$g = (-21.134 \pm 0.014)\%, \quad h = (1.848 \pm 0.039)\%, \quad k = (-0.463 \pm 0.012)\%.$$

The values are with precision one order of magnitude better, than the previous experiments and are in agreement with the world averages. This is the first measurement of non-zero value of h. The quality of the fit of $(u, |v|)$ distribution ($\chi^2/n.d.f. = 1669/1585$, yielding a satisfactory probability of 7.0%) shows that the polynomial parameterization (1) is still acceptable at an improved level of precision (the rescaterring effects are much weaker than in $K^\pm \to \pi^\pm\pi^0\pi^0$ mode). No significant higher order slope parameters were found. More information on this analysis can be found in [4].

5 $\pi\pi$ scattering effects

The single-flavour quark condensate $\langle 0|\bar{q}q|0\rangle$ is a fundamental parameter of χPT, which determines the relative size of mass and momentum terms in the perturbative expansion. It is a free parameter in the theory and must be determined experimentally. The relation between $\langle 0|\bar{q}q|0\rangle$ and S-wave $\pi\pi$ scattering lengths a_0^0 and a_0^2 in isospin states $I = 0$ and $I = 2$, correspondingly, are known with precision of $\sim 2\%$ [5], so the experimental measurement of a_0^0 and a_0^2 provides an important constraints for χPT Lagrangian parameters. In the framework of NA48/2, the scattering lengths can be measured from $K^\pm \to \pi^\pm\pi^0\pi^0$ and $K^\pm \to \pi^+\pi^- e\nu$ (K^{+-}_{e4}) decays.

5.1 Rescattering effects in $K^\pm \to \pi^\pm\pi^0\pi^0$

During the analysis of $\sim$ 23 million $K^\pm \to \pi^\pm\pi^0\pi^0$ decays, taken in 2003, a sudden "cusp" like structure was found in the spectra of $\pi^0\pi^0$ invariant mass at $M_{00}^2 = 4m_{\pi^\pm}^2$ (see fig. 2, *a*). A fit to the data with the parameterization (1) (see fig. 2, *b*) yielded an unacceptable probability of $\chi^2/n.d.f. = 9225/149$, while the area above the "cusp" was well described ($\chi^2/n.d.f. = 133/110$).

A model at one loop was developed [6] in order to explain the effect. The "cusp" effect is explained as a result of destructive interference below the threshold between the two amplitudes: the direct emission amplitude $M_0 \sim 1 + gu/2 + h'u^2/2 + k'v^2/2$ and the amplitude M_1, which describes the charge exchange $\pi^+\pi^- \to \pi^0\pi^0$ in final state of $K^\pm \to \pi^\pm\pi^+\pi^-$. A more complete formulation of the model, which includes all rescattering processes at one loop and two loop levels with precision $\sim 5\%$ [7], has been used to extract the NA48/2 result:

$$g = 0.645 \pm 0.004_{stat} \pm 0.009_{syst}$$

$$h' = -0.047 \pm 0.012_{stat} \pm 0.011_{syst}$$

$$a_0^2 = -0.041 \pm 0.022_{stat} \pm 0.014_{syst}$$

$$a_0^0 - a_0^2 = 0.268 \pm 0.010_{stat} \pm 0.004_{syst} \pm 0.013_{ext},$$

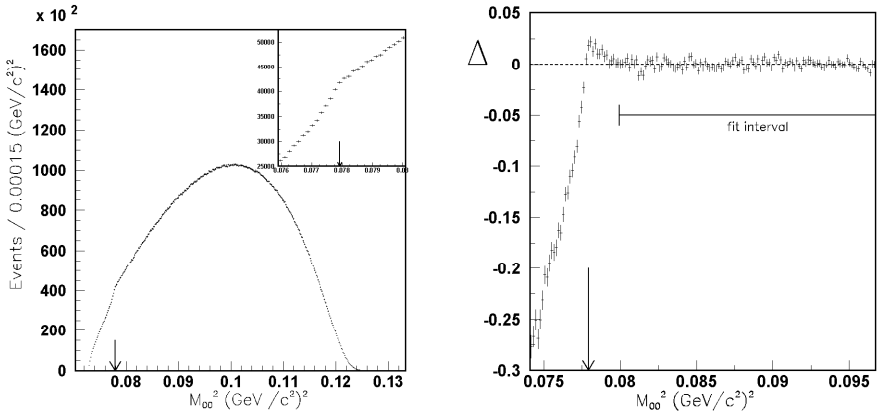

a *b*

Figure 2: *The observed "cusp"-like effect, a, and the fit result by using the parameterization (1), b.*

assuming $k' = 0$. The values for the scattering lengths are in good agreement with the theory [8) 9)]. More details about this analysis can be found in [10)].

Currently, there are two measurements of k in (1), which contradicts to each other [11)]. Taking k' as a free parameter in the fit far from "cusp", a nonzero preliminary value was obtained

$$k' = 0.0097 \pm 0.0003_{stat} \pm 0.0008_{syst}$$

and no change of a_0^0 and a_0^2 was observed.

5.2 K_{e4} decays form-factors

The form factors of K_{e4}^{+-} decay can be parameterized as a function of five kinematic variables: the invariant masses $M_{\pi\pi}$ and $M_{e\nu}$, and the angles θ_π, θ_e and ϕ (see Fig. 3). The hadronic part in the matrix element can be described in terms of two axial (F and G) and one vector (H) form factors [12)]. Their expansion into partial s and p waves (neglecting d waves) and into a Taylor series in $q^2 = M_{\pi\pi}^2/4m_{\pi^\pm}^2 - 1$ allows a measurement of the form factor parameters from the experimental data [13) 14)]:

$$F = F_s e^{i\delta_s} + F_p \cos\theta_\pi e^{i\delta_p}, \quad G = G_p e^{i\delta_g}, \quad H = H_p e^{i\delta_h},$$

where

$$F_s = f_s + f_s' q^2 + f_s'' q^4, \quad F_p = f_p + f_p' q^2 + ...,$$

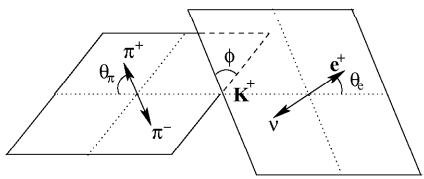

a

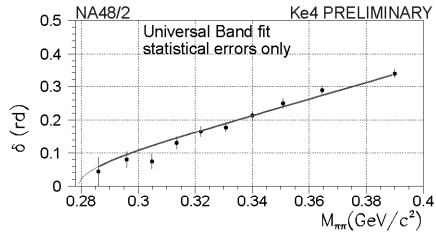

b

Figure 3: *a) Definition of the angle kinematic variables, describing K_{e4} decays; b) $\delta(M_{\pi\pi})$ distribution, fitted to obtain a_0^0.*

$$G_p = g_p + g'_p q^2 + ..., \quad H_p = h_p e + h'_p q^2 + ...$$

Analysing part of 2003 data, $3.7{\cdot}10^5$ K_{e4}^{+-} decays were selected with background of 0.5%, mainly from 3π decays with $\pi \to e\mu$ or pion mis-identification.

The following method was used to extract the form factor parameters: In a first step, in ($M_{\pi\pi}$,$M_{e\nu}$,cosθ_π,cosθ_e,ϕ) space were defined 10x5x5x5x12 iso-populated bins. For each bin in $M_{\pi\pi}$, comparing data and MC, ten independent five-parameter ($F_s, F_p, G_p, H_p, \delta = \delta_s - \delta_p$) fits were performed. In the second step a fit of the distributions in $M_{\pi\pi}$ was performed to extract the form factor parameters. The $\delta(M_{\pi\pi})$ distribution was fitted with a one-parameter function given by the numerical solution of the Roy equations [15)], in order to determine a_0^0, while a_0^2 was constrained to lie on the centre of the universal band. The following preliminary results were obtained:

$$f'_s/f_s = 0.169 \pm 0.009_{stat} \pm 0.034_{syst}$$

$$f''_s/f_s = -0.091 \pm 0.009_{stat} \pm 0.031_{syst}$$

$$f_p/f_s = -0.047 \pm 0.006_{stat} \pm 0.008_{syst}$$

$$g_p/f_s = 0.891 \pm 0.019_{stat} \pm 0.020_{syst}$$

$$g'_p/f_s = 0.111 \pm 0.031_{stat} \pm 0.032_{syst}$$

$$h_p/f_s = -0.411 \pm 0.027_{stat} \pm 0.038_{syst}$$

$$a_0^0 = 0.256 \pm 0.008_{stat} \pm 0.007_{syst} \pm 0.018_{theor},$$

where the systematic uncertainty was determined by comparing two independent analyses and taking into account the effect of the reconstruction method, acceptance, fit method, uncertainty on background estimate, electron identification efficiency, radiative corrections and bias due to the neglected $M_{e\mu}$ dependence. The form factors are measured relative to f_s, which is related to

the decay rate. The obtained value for a_0^0 is compatible with the χPT prediction [16] and with previous experiments [17].

The form factors were measured also for $K^\pm \to \pi^0\pi^0 e\nu$ (K_{e4}^{00}) decays, on $\sim 10^5$ selected events from 2003 run and $\sim 3 \cdot 10^5$ events from 2004 run, using the same formalism. Due to symmetry of $\pi^0\pi^0$ system, the P-wave is not present and only two parameter are left:

$$f_s'/f_s = 0.129 \pm 0.036_{stat} \pm 0.020_{syst}$$

$$f_s''/f_s = -0.040 \pm 0.034_{stat} \pm 0.020_{syst}.$$

The preliminary result is compatible with K_{e4}^{+-}.

In addition, the branching fraction of K_{e4}^{00} was measured by using only 2003 data, normalising to $K^\pm \to \pi^\pm\pi^0\pi^0$:

$$BR(K_{e4}^{00}) = (2.587 \pm 0.026_{stat} \pm 0.019_{syst} \pm 0.029_{ext}) \cdot 10^{-5},$$

where the systematic uncertainty takes into account the effect of acceptance, trigger efficiency and energy measurement of the calorimeter, while the external uncertainty is due to the uncertainty on the $K^\pm \to \pi^\pm\pi^0\pi^0$ branching fraction. The result is ~ 8 times more precise than the previous measurement.

6 New measurements on kaon and hyperon radiative decays

6.1 $K^\pm \to \pi^\pm\pi^0\gamma$ measurements

A measurement of Direct photon Emission (DE) with respect to Inner Bremsstrahlung (IB) and the interference (INT) between these two amplitudes was performed on a subsample of NA48/2 collected during 2003 run. The $K^\pm \to \pi^\pm\pi^0\gamma$ are described in terms of two kinematic variables: the energy of charged pion in kaon center of mass system (T_π^*), and $W^2 = (p_K p_\gamma)(p_\pi p_\gamma)/m_\pi^2 m_K^2$, where p_K, p_π and p_γ are the four-momenta of the kaon, charged pion and the odd gamma. About $124 \cdot 10^3$ events were selected in the ranges $T_\pi^* < 80$ MeV and $0.2 < W < 0.9$. In the previous measurements a lower cut $T^* > 55$ MeV was introduced in order to suppress $K^\pm \to \pi^\pm\pi^0\pi^0$ and $K^\pm \to \pi^\pm\pi^0$ background. In NA48/2 measurement these backgrounds are avoided with an application of a special algorithm, which detects overlapping gamma in the detector and a maximum allowed deviation of reconstructed K mass ± 10 MeV from its nominal value. The upper cut on T_π^* rejects $K^\pm \to \pi^\pm\pi^0$ decays. The background in the selected sample is kept under 10^{-4}. The photon mistagging (i.e., choice of wrong odd photon) is estimated to be less than 0.1%.

The preliminary results:

$$\text{Frac(DE)} = (3.35 \pm 0.35_{\text{stat}} \pm 0.25_{\text{syst}})\%$$

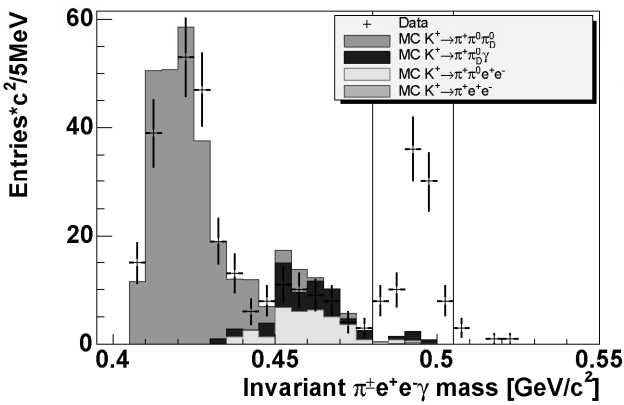

Figure 4: *The invariant mass of $\pi^{\pm}e^{+}e^{-}\gamma$, together with the simulated background.*

$$\mathrm{Frac(INT)} = (-2.67 \pm 0.81_{\mathrm{stat}} \pm 0.73_{\mathrm{syst}})\%$$

are obtained by using extended maximum likelihood method: the experimental W distribution is fitted with proportionally simulated IB, DE and INT distributions. The systematic error is dominated by the trigger efficiency.

This is the first observation of non zero INT component.

6.2 First observation of $K^{\pm} \to \pi^{\pm}\gamma e^{+}e^{-}$

NA48/2 experiment observed for the first time the radiative decay $K^{\pm} \to \pi^{\pm}\gamma e^{+}e^{-}$. 92 candidates were selected, with 1 ± 1 accidental background and 5.1 ± 1.7 misidentification background (Fig. 4). By using $K^{\pm} \to \pi^{\pm}\pi^{0}$ as normalization channel the branching ratio preliminary was estimated to be

$$BR(K^{\pm} \to \pi^{\pm}\gamma e^{+}e^{-}) = (1.27 \pm 0.14_{stat} \pm 0.05_{syst}) \cdot 10^{-8}.$$

6.3 First observation of $\Xi^{0} \to \Lambda^{0}e^{+}e^{-}$

In the 2002 NA48/1 run the weak radiative decay $\Xi^{0} \to \Lambda^{0}e^{+}e^{-}$ was detected for the first time [18]. 412 candidates were selected with 15 background events (Fig. 5). The obtained branching fraction

$$BR(\Xi^{0} \to \Lambda^{0}e^{+}e^{-}) = (7.7 \pm 0.5_{stat} \pm 0.4_{syst}) \cdot 10^{-6}$$

is consistent with inner bremsstrahlung-like $e^{+}e^{-}$ production mechanism.

The decay parameter $\alpha_{\Xi\Lambda ee}$ can be measured from the angular distribution

$$dN/d\cos\theta_{p\Xi} = \frac{N}{2}(1 - \alpha_{\Xi\Lambda ee}\alpha_{-}\cos\theta_{p\Xi}),$$

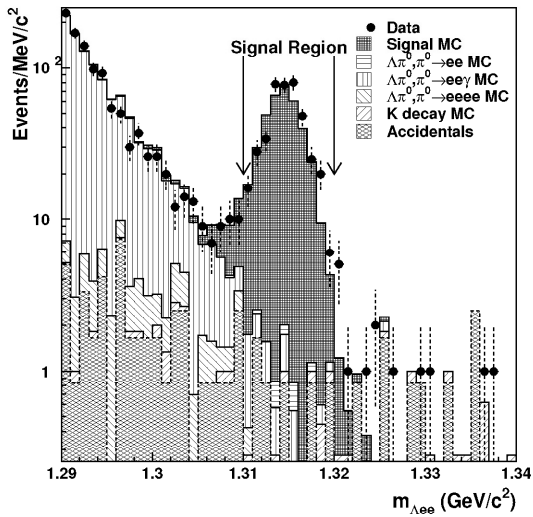

Figure 5: *The invariant mass of* Λe^+e^-*, together with the simulated background.*

where $\theta_{p\Xi}$ is the angle between the proton from $\Lambda \to p\pi$ decay relative to the Ξ^0 line of flight in the Λ rest frame. The obtained value

$$\alpha_{\Xi\Lambda ee} = -0.8 \pm 0.2$$

is consistent with the latest published value of the decay asymmetry parameter for $\Xi \to \Lambda\gamma$.

7 New measurements of K_L decays

In 1999 a dedicated NA48 run employed a minimum bias trigger to collect semileptonic decays of K_L. Two new measurements from this run are presented.

7.1 $K_{L\mu 3}$ form factors

K_{l3} decays provide the cleanest way to extract $|V_{us}|$ element in the CKM matrix. Recent calculations in the framework of χPT show how the vector form factor at zero momentum transfer, $f_+(0)$, can be constrained experimentally from the slope and curvature of the scalar form factor f_0 of the $K_{\mu 3}$ decay. In addition, these form factors are needed to calculate the phase space integrals, which are used in $|V_{us}|$ determination.

Approximately $2.6 \cdot 10^6$ $K_{\mu 3}$ decays were selected from the 1999 minimum bias run. By studying the Dalitz plot density, the following slopes for the vector

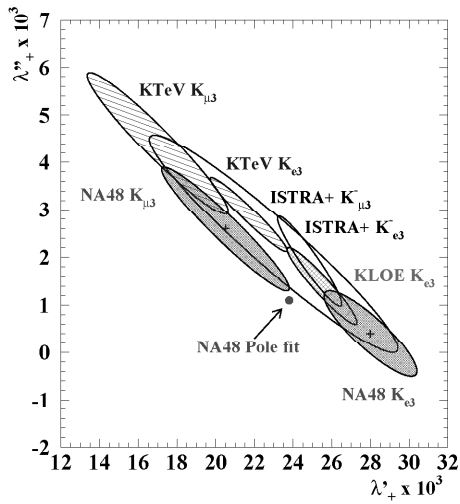

Figure 6: *Comparison between recent results on K_{Ll3} form factors measurements.*

and the scalar form factors were obtained

$$\lambda'_+ = (20.5 \pm 2.2_{stat} \pm 2.4_{syst}) \cdot 10^{-3}$$

$$\lambda''_+ = (2.6 \pm 0.9_{stat} \pm 1.0_{syst}) \cdot 10^{-3}$$

$$\lambda_0 = (9.5 \pm 1.1_{stat} \pm 0.8_{syst}.$$

The results show a presence of quadratic term in the expansion of the vector form factor in agreement with other recent measurements. A comparison between the results of the quadratic fits as reported by the recent experiments is presented in Fig. 6.

The results obtained with linear fit are

$$\lambda_+ = (26.7 \pm 0.6_{stat} \pm 0.8_{syst}) \cdot 10^{-3}$$

$$\lambda_0 = (11.7 \pm 0.7_{stat} \pm 1.0_{syst}) \cdot 10^{-3}.$$

The value for λ_+ is well compatible with the recent KTeV measurement, while λ_0 is shifted towards lower values. Details on NA48 $K_{\mu 3}$ measurement can be found in [19].

7.2 $\Gamma(K_L \to \pi^+\pi^-)/\Gamma(K_{Le3})$ ratio and $|\eta_{+-}|$ measurements

The recent results on $\Gamma(K_L \to \pi^+\pi^-)$ and the CP-violation parameter $|\eta_{+-}|$, performed by the experiments KTeV and KLOE, and the measurement of the ratio $\Gamma(K_L \to \pi^+\pi^-)/\Gamma(K_{Le3})$ by KTeV disagree with 2004 edition of PDG [20] by 10% and 5% respectively (or more than four standard deviations). Additional information could clarify the situation.

During the dedicated 1999 NA48 run $\sim 47 \cdot 10^3$ $K_L \to \pi^+\pi^-$ and $\sim 5 \cdot 10^6$ K_{Le3} decays were collected. The ratio $\Gamma(K_L \to \pi^+\pi^-)/\Gamma(K_{Le3})$ is measured to be

$$\frac{\Gamma(K_L \to \pi^+\pi^-)}{\Gamma(K_{Le3})} = (4.835 \pm 0.022_{stat} \pm 0.016_{syst}) \cdot 10^{-3}.$$

For $BR(K_L \to \pi^+\pi^-)$ and $|\eta_{+-}|$ calculation the CP-conserving direct emission $K_L \to \pi^+\pi^-\gamma$ contribution to the $K_{2\pi}$ signal was estimated and subtracted. The branching fraction of $K_{2\pi}$, including only the inner bremsstrahlung radiative component was measured to be

$$BR(K_L \to \pi^{\prime}\pi \quad + \pi^{\prime}\pi \quad \gamma(IB)) = (1.941 \pm 0.019) \cdot 10 \quad ^{3}.$$

Using this result and the most precise single measurements of τ_{K_S} (by NA48), τ_{K_L} and $BR(K_S \to \pi^+\pi^-)$ (by KLOE), the CP-violation parameter $|\eta_{+-}|$ is calculated:

$$|\eta_{+-}| = \sqrt{\frac{\tau_{K_S} BR(K_L \to \pi^+\pi^-)}{\tau_{K_L} BR(K_S \to \pi^+\pi^-)}} = (2.223 \pm 0.012) \cdot 10^{-3}.$$

All the presented results are in agreement with the recent KTeV and KLOE results. Details on the analysis can be found in [21].

8 Results from K^{+-} semileptonic decays

The branching ratios of semileptonic kaon decays are needed to determine $|V_{us}|$ element in the CKM matrix. In addition $\Gamma(K_{e3})/\Gamma(K_{\mu 3})$ is a function of the slope parameters of the form factors, which can be used for consistency check under the assumption of $\mu - e$ universality.

During 2003 data taking of NA48/2 a special run was dedicated to collect semileptonic decays. Approximately 56000 K^+_{e3}, 31000 K^-_{e3}, 49000 $K^+_{\mu 3}$, 28000 $K^-_{\mu 3}$, 462000 $K^+_{2\pi}$ and 256000 $K^-_{2\pi}$ decays were selected for the measurement. The ratios of decay widths, combined for K^+ and K^-, are:

$$\Gamma(K_{e3})/\Gamma(K_{2\pi}) = 0.2496 \pm 0.0009_{stat} \pm 0.0004_{syst}$$

$$\Gamma(K_{\mu 3})/\Gamma(K_{2\pi}) = 0.1637 \pm 0.0006_{stat} \pm 0.0003_{syst}$$

$$\Gamma(K_{\mu 3})/\Gamma(K_{e3}) = 0.656 \pm 0.003_{stat} \pm 0.001_{syst}$$

Taking the PDG value for the $K_{2\pi}$ branching fraction, 0.2092 ± 0.0012, the branching fractions for the semileptonic decays are found to be:

$$BR(K_{e3}) = (5.221 \pm 0.019_{stat} \pm 0.008_{syst} \pm 0.030_{norm})\%$$

$$BR(K_{\mu 3}) = (3.425 \pm 0.013_{stat} \pm 0.006_{syst} \pm 0.020_{norm})\%$$

The uncertainty is dominated by the existing data for the $BR(K_{2\pi})$. The branching fractions are higher than PDG values for both K_{e3} and $K_{\mu 3}$, confirming the K_{e3} results reported by the BNL-E865 collaboration.

By using the measured values for the vector and the scalar form factors [11], and assuming $e - \mu$ universality, a value 0.6682 ± 0.0017 for the ratio $\Gamma(K_{\mu 3})/\Gamma(K_{e3})$ can be estimated. The NA48/2 result suggests a lower value for λ_0 than the current world average for $K^{\pm}$, as found in recent measurements from K_L decays.

The product $|V_{us}|f_+(0)$ can be calculated by using both K_{e3} and $K_{\mu 3}$ measured branching ratios:

$$\text{From } K_{e3}: \ |V_{us}|f_+(0) = 0.2204 \pm 0.0012$$

$$\text{From } K_{\mu 3}: \ |V_{us}|f_+(0) = 0.2177 \pm 0.0013$$

The errors are dominated by the uncertainties of the external quantities needed for the calculation. Combining the results, assuming lepton universality and taking the value of $f_+(0)$ for neutral kaons, the obtained $|V_{us}|$ element is

$$|V_{us}| = 0.2289 \pm 0.0023,$$

which is consistent with CKM matrix unitarity predictions. For detailed description of the analysis see [22].

9 $\Gamma(K^{\pm}_{e2})/\Gamma(K^{\pm}_{\mu 2})$ measurement

The ratio $R_K = \Gamma(K^{\pm}_{e2})/\Gamma(K^{\pm}_{\mu 2})$ is a test for lepton universality and $V - A$ coupling. The SM prediction is $R_K = (2.472 \pm 0.001) \cdot 10^{-5}$, while the current PDG average is $R_K = (2.45 \pm 0.11) \cdot 10^{-5}$. Recently a new important physical motivation for a precise measurement of this ratio was added [23]: SUSY lepton flavour violating contributions could shift R_K by a relative amount of 2-3%.

The NA48/2 analysis exploits the similarity between both decays to cancel most of the possible systematic effects. In 2003 run 5239 K_{e2} were selected with $\sim 14\%$ background mainly from $K_{\mu 2}$. The obtained preliminary result is

$$R_K = (2.416 \pm 0.043_{stat} \pm 0.024_{syst}) \cdot 10^{-5}.$$

The estimations yield that the combined 2003 and 2004 result will not be sufficient to obtain a total error smaller than 1%. A dedicated 2007 run is in preparation. The conservative estimation for the error, which will be reached in R_K measurement is 0.7%. The experiment P326 could reach a per mill uncertainty, adding a new item to its physics program.

References

1. V. Fanti *et al*, Nucl. Instrum. Meth. A **574**, 433 (2007).
   A. Lai *et al*, Eur. Phys. J. C **22** 231 (2001).
   J.R. Batley *et al*, Phys. Lett. B **544** 97 (2002).
2. J. R. Batley *et al*, Phys. Lett. B **634**, 474 (2006) [arXiv:hep-ex/0602014].
3. J. R. Batley *et al*, Phys. Lett. B **638**, 22 (2006) [Erratum-ibid. B **640**, 297 (2006)] [arXiv:hep-ex/0606007].
4. J. R. Batley *et al*, arXiv:hep-ex/0702045.
5. G. Colangelo, AIP Conf. Proc. **756**, 60 (2005) [arXiv:hep-ph/0501107].
6. N. Cabibbo, Phys. Rev. Lett. **93**, 121801 (2004) [arXiv:hep-ph/0405001].
7. N. Cabibbo and G. Isidori, JHEP **0503**, 021 (2005) [arXiv:hep-ph/0502130].
8. G. Colangelo, J. Gasser and H. Leutwyler, Phys. Lett. B **488**, 261 (2000) [arXiv:hep-ph/0007112].
9. J. R. Pelaez and F. J. Yndurain, Phys. Rev. D **71**, 074016 (2005) [arXiv:hep-ph/0411334].
10. J. R. Batley *et al*, Phys. Lett. B **633**, 173 (2006) [arXiv:hep-ex/0511056].
11. W.-M. Yao *et al*, J. Phys. **G33**, 1 (2006).
12. J. Bijnens *et al*, 2nd DAΦNE Physics Handbook, 315 (1995).
13. A. Pais and S. B. Treiman, Phys. Rev. **168**, 1858 (1968).
14. G. Amoros and J. Bijnens, J. Phys. G **25**, 1607 (1999).
15. B. Ananthanarayan *et al*, Phys. Rept. **353**, 207 (2001).
16. G. Colangelo, J. Gasser and H. Leutwyler, Nucl. Phys. B **603**, 125 (2001) [arXiv:hep-ph/0103088].

17. S. Pislak *et al.*, Phys. Rev. D **67**, 072004 (2003) [arXiv:hep-ex/0301040].

18. J. R. Batley *et al*, arXiv:hep-ex/0703023.

19. M. Veltri, arXiv:hep-ex/0703007.

20. S. Eidelman *et al*, Phys. Lett. B **592** (2004) 1.

21. A. Lai *et al*, Phys. Lett. B **645**, 26 (2007) [arXiv:hep-ex/0611052].

22. J. R. Batley *et al*, arXiv:hep-ex/0702015.

23. A. Masiero, P. Paradisi and R. Petronzio, Phys. Rev. D **74** (2006) 011701 [arXiv:hep-ph/0511289].

RECENT RESULTS ON KAON DECAYS FROM KLOE AT DAΦNE

The KLOE Collaboration
presented by Patrizia de Simone
Laboratori Nazionali di Frascat, INFN

Abstract

New results on $\mathrm{K_S} \to e^+e^-$, $\mathrm{K_S} \to \gamma\gamma$, $\mathrm{K_L} \to \pi e \nu \gamma$, and $K_{L\mu 3}$ form factor from KLOE [1] are presented. The most recent KLOE results on $|V_{us}|$ are reviewed.

[1]KLOE collaboration: F. Ambrosino, A. Antonelli, M. Antonelli, F. Archilli, C. Bacci, P. Beltrame, G. Bencivenni, S. Bertolucci, C. Bini, C. Bloise, S. Bocchetta, V. Bocci, F. Bossi, P. Branchini, R. Caloi, P. Campana, G. Capon, T. Capussela, F. Ceradini, S. Chi, G. Chiefari, P. Ciambrone, E. De Lucia, A. De Santis, P. de Simone, G. De Zorzi, A. Denig, A. Di Domenico, C. Di Donato, S. Di Falco, B. Di Micco, A. Doria, M. Dreucci, G. Felici, A. Ferrari, M. L. Ferrer, G. Finocchiaro, S. Fiore, C. Forti, P. Franzini, C. Gatti, P. Gauzzi, S. Giovannella, E. Gorini, E. Graziani, M. Incagli, W. Kluge, V. Kulikov, F. Lacava, G. Lanfranchi, J. Lee-Franzini, D. Leone, M. Martini, P. Massarotti, W. Mei, S. Meola, S. Miscetti, M. Moulson, S. Müller, F. Murtas, M. Napolitano, F. Nguyen, M. Palutan, E. Pasqualucci, A. Passeri, V. Patera, F. Perfetto, M. Primavera, P. Santangelo, G. Saracino, B. Sciascia, A. Sciubba, F. Scuri, I. Sfiligoi, T. Spadaro, M. Testa, L. Tortora, P. Valente, B. Valeriani, G. Venanzoni, R.Versaci, G. Xu

1 The KLOE experiment at DAΦNE

DAΦNE, the Frascati $\phi - factory$ [1], is an e^+e^- collider working at a center of mass energy of $\sqrt{s} \simeq m_\phi \simeq 1020$ MeV. The ϕ production cross section is $\sim 3\mu$b. The beams collide at the interaction point (IP) with a crossing angle $\theta_x \simeq 25$ mrad, therefore the ϕ's are produced with a small momentum of ~ 12.5 MeV in the horizontal plane, and decay in almost collinear and monochromatic neutral (34%) and charged (49%) kaon pairs.

The KLOE detector consists of a large volume drift chamber surrounded by an electromagnetic calorimeter. A superconducting coil provides a 0.52 T solenoidal magnetic field.

The tracking detector is a cylindrical drift chamber [2] (DC) 4 m diameter and 3.3 m long, with a total of ~ 52000 wires, of which ~ 12000 are sense wires. In order to minimize the multiple scattering and the K_L regeneration, and to maximize the detection efficiency of low energy γ's, the DC works with an helium based gas mixture and its walls are made of light materials (mostly carbon fiber composites). The momentum resolution for tracks produced at large polar angle is $\sigma_p/p \leq 0.4\%$. Charged particle vertices are reconstructed with a spatial resolution of ~ 3 mm [4].

The fine sampling lead-scintillating fiber calorimeter [3] (EMC) consists of a barrel and two end-caps, and has solid angle coverage of 98%. Photon energies and arrival times are measured with resolutions $\sigma_E/E = 5.7\%/\sqrt{E(\mathrm{GeV})}$ and $\sigma_t = 54\mathrm{ps}/\sqrt{E(\mathrm{GeV})} \oplus 50\mathrm{ps}$, respectively. Photon entry points are determined with an accuracy $\sigma_z \sim 1\ \mathrm{cm}/\sqrt{E(\mathrm{GeV})}$ along the fibers and $\sigma_\perp \sim 1$ cm in the transverse direction.

The unique feature of a $\phi - factory$ is the possibility of *tagging*. Specifically the detection of a $\mathrm{K_L}$ ($\mathrm{K_S}$) guarantees the presence of a $\mathrm{K_S}$ ($\mathrm{K_L}$) with known momentum and direction, the same holds for charged kaons pairs. The availability of tagged kaons enables the precision measurement of absolute BR's.

The $\mathrm{K_L}$ beam is identified by the presence of a decay $\mathrm{K_S} \to \pi^+\pi^-$. The $\mathrm{K_L}$ momentum is given by the decay kinematics of $\phi \to \mathrm{K_L K_S}$ using the reconstructed $\mathrm{K_S}$ direction and the small velocity v_ϕ of the ϕ (v_ϕ reconstructed run by run with the Bhabha events). The $\mathrm{K_S}$ beam is identified by a $\mathrm{K_L}$ interacting in the EMC called $\mathrm{K_L}$ -crash. A $\mathrm{K_L}$ -crash has a very clear signature consisting of a high energy (E > 100 MeV) deposit in the calorimeter not associated to tracks and with low velocity $\beta_{K_L} \simeq 0.22$. Furthermore the momentum and the direction of the $\mathrm{K_S}$ is given by the kinematics of the ϕ decay. The selection of the $\mathrm{K^\pm}$ beam is done reconstructing the 2 body decays $\mathrm{K^\pm} \to \pi^\pm\pi^o$ and $\mathrm{K^\pm} \to \mu^\pm\bar{\nu}(\nu)$. These decays are identified from two clear peaks in the momentum of the charged secondary tracks in the kaon rest frame.

KLOE completed the data taking in March 2006 with a total integrated luminosity of ~ 2.5 fb^{-1}, corresponding to $\sim 7.5 \times 10^{+9}$ ϕ-mesons produced.

2 New preliminary KLOE results on neutral kaon decays

2.1 $K_S \to e^+e^-$

The SM prediction of the branching ratio of $K_S \to e^+e^-$ decay is rather low (BR$= 1.6 \times 10^{-15}$) but quite precise [5], leaving room for possible new physics effects.

A data sample corresponding to 1.3 fb^{-1} has been analyzed. The K_S sample is given by the detection of a K_L -crash, the signal events are selected requiring two charged tracks coming from the IP, with an invariant mass M_{inv}, evaluated in the e^+e^- hypothesis, greater than 420 MeV. A χ^2-like variable is built using the measured time of flights of the two particles, E/p, and the transverse distance between the track impact point on the calorimeter and the closest calorimeter cluster. The search for the signal is performed inside a *signal* box in the χ^2-M_{inv} plane, whose definition is optimized with a Monte Carlo (MC) simulation study: $492 \leq M_{inv} \leq 504$ MeV and $\chi^2 \leq 20$. These cuts reject almost all the events due to the background processes $K_S \to \pi^+\pi^- \to \mu\pi$, $K_S \to \pi^+\pi^-$, and $\phi \to \pi^+\pi^-\pi^0$, while retaining 55.8% of the signal. The selection is inclusive for radiated photons with energy in the kaon rest frame $E^*_\gamma < 6$ MeV [2]. We observe $N = 3$ events inside the box, with an expected background of 7.1 ± 3.6 events, corresponding to an upper limit of 4.3 events at 90% c.l.. After normalization to $K_S \to \pi^+\pi^-$ events, we obtain the result:

$$\mathrm{BR}(K_S \to e^+e^-(\gamma)) < 2.1 \times 10^{-8} \ @\ 90\%\ \text{c.l.}$$

improving the previous limit [8] by about an order of magnitude.

2.2 $K_S \to \gamma\gamma$

The measurement of BR$(K_S \to \gamma\gamma)$ is an important test of chiral perturbation theory, as discussed in Ref. [6].

A data sample corresponding to 1.6 fb^{-1} has been analyzed. The K_S sample is given by the detection of a K_L -crash, then the signal events are selected requiring two and only two photons with an energy greater than 7 MeV, back-to-back in the center of mass system of the K_S ($\cos(\theta^\star_{\gamma\gamma}) \leq -0.95$), and coming from the IP ($T_\gamma - R/c \simeq 0$). A kinematic fit constrains the time, the momentum, and the invariant mass $M_{\gamma\gamma}$ of the two γ's. To further reduce the copious

[2] here and after the symbol $\star$ indicates quantities evaluated in the kaon rest frame

background due to $K_S \to 2\pi^0$ with two undetected photons, a γ veto is applied using the two small calorimeters surrounding the focusing quadrupoles near the IP. The background due to $\mathrm{K_L} \to\gamma\gamma$ decays is absent due to the high purity of the selected $\mathrm{K_S}$ sample. The overall efficiency on the signal is $\sim 52\%$. Finally, the signal counts are obtained by fitting the $M_{\gamma\gamma}$ and $\cos(\theta^\star_{\gamma\gamma})$ bi-dimensional distribution with signal and background distributions obtained from MC. The reconstructed energy scale is kept well under control by comparing data samples of $\mathrm{K_L} \to 2\pi^0$ and $\mathrm{K_L} \to\gamma\gamma$ events with MC. The result is

$$\mathrm{BR}(K_S \to \gamma\gamma) = (2.35 \pm 0.14) \times 10^{-6}$$

in agreement with $\mathcal{O}(p^4)$ chiral perturbation theory calculation, and does not confirm the discrepancy from CHPT of $\sim 30\%$ found by the NA48 collaboration [10].

2.3 $\mathrm{K_L} \to\pi e\nu\gamma$

Radiative effects play an important role in kaon semileptonic decays. Both inner bremsstrahlung (IB) and structure dependent (SD) amplitudes contribute to the $\mathrm{K_L} \to\pi e\nu\gamma$ process, as discussed in Ref. [7].

A data sample corresponding to $\sim 330\ \mathrm{pb}^{-1}$ has been analyzed. The inclusive selection of $\mathrm{K_L} \to\pi e\nu(\gamma)$ events requires a $\mathrm{K_L}$ of known momentum and direction, tagged by $\mathrm{K_S} \to\pi^+\pi^-$ decay near the IP. In a fiducial volume extending to $\sim 0.4\lambda_L$, two-tracks decay vertices are selected around the $\mathrm{K_L}$ line of flight. The vast majority of the background due to $\mathrm{K_L} \to\pi\mu\nu$, and $\pi^+\pi^-\pi^0$ is rejected by cutting on the $E_{miss} - P_{miss}$ distribution, where P_{miss} and E_{miss} are the missing momentum and missing energy evaluated in the hypothesis of π's and μ's. The time of flight technique is used to identify electron and pion tracks. The radiative events are selected by further requiring the detection of a γ with a time of flight compatible with the decay vertex; the cluster position is used to close the kinematics $p_\nu^2 = 0 = (p_K - p_\pi - p_e - p_\gamma)^2$, and to evaluate the energy E_γ of the photon. A control sample of $\mathrm{K_L} \to\pi^+\pi^-\pi^0$ decays is used to check the photon efficiency, energy and vertex resolutions. Finally, the signal counts are obtained by fitting the $E^\star_\gamma$ and $\theta^\star_{e-\gamma}$ bi-dimensional distribution with signal and background distributions obtained from MC ($\theta^\star_{e-\gamma}$ is the angle between the $e^\pm$ and the γ).

The result is:

$$R = \frac{\mathrm{BR}(K_L \to \pi e\nu\gamma;\ E^\star_\gamma > 30\ \mathrm{MeV}, \theta^\star_{e-\gamma} > 20^\circ)}{\mathrm{BR}(K_L \to \pi e\nu(\gamma))} = (0.92 \pm 0.02_{\mathrm{stat}} \pm 0.02_{\mathrm{syst}})\%$$

By using the SD spectrum shape evaluated in Ref. [7], we are also able

to measure the SD contribution:

$$\mathrm{BR_{SD}}(K_L \to \pi e\nu\gamma) = (-3.1 \pm 3.0) \times 10^{-5} \; ; \qquad \mathrm{BR_{SD}} \leq 2.5 \times 10^{-5} \; @ \; 90\% \text{ c.l.}$$

in agreement with theoretical predictions based on chiral perturbation theory calculation [7].

The accuracy of the KLOE result on R is not sufficient to shed light on the discrepancy between previous measurements by KTeV and NA48 collaborations [9, 11]. However the analysis of the full KLOE data sample (statistics $\times 5$) will improve the accuracy on both R and $\mathrm{BR_{SD}}$ results.

2.4 $K_{L\mu 3}$ form factor slope λ_0

The knowledge of the K_L scalar form factor $f_0(t)$, where t is the momentum transfer, is relevant for the determination of $|V_{us}|$ and to test e/μ universality. Typically a linear parametrization is used $f_0(t) \propto 1 + \lambda_0(t/m^2_{\pi^+})$, where the slope λ_0 is the parameter to be experimentally determined.

A data sample corresponding to $\sim 330\ \mathrm{pb}^{-1}$ has been analyzed. The $K_{L\mu 3}$ events are selected requiring a $\mathrm{K_L}$ of known momentum and direction, tagged by $\mathrm{K_S} \to \pi^+\pi^-$ decay near the IP. In a fiducial volume extending to $\sim 0.4\lambda_L$, two-tracks decay vertices are selected around the $\mathrm{K_L}$ line of flight. The background due to $\mathrm{K_L} \to \pi e\nu$, $\pi^+\pi^-\pi^0$, and $\pi^+\pi^-$ is rejected by cutting on different combinations of E_{miss} and P_{miss} variables, where E_{miss} is evaluated in different masses hypothesis for the secondary particles. The same variables are used to select the signal. A further reduction of the background at the level of $\sim 1.5\%$ is obtained using neural network and time of flight techniques. Because pure and efficient $\pi - \mu$ separation is difficult to achieve, the analysis aims at measuring λ_0 through a fit of the neutrino energy E_ν distribution, which can be evaluated through a Lorentz transformation of the missing momentum $\vec{P}_{miss}$ in the K_L rest frame. A combined fit of the neutrino energy spectrum with K_{Le3} results for the vector form factor slopes λ'_+, λ''_+ [16] yields the following preliminary result:

$$\lambda_0 = (15.6 \pm 1.8_{\mathrm{stat}} \pm 1.9_{\mathrm{syst}}) \times 10^{-3}$$

with an accuracy similar to other measurements [12]. Using the full KLOE data sample the relative statistical accuracy will be in the range $5 - 10\%$.

3 KLOE summary on $|V_{us}|$

$|V_{us}|$ and $|V_{ud}|$ parameters provide the most precise test of the unitarity of the Cabibbo-Kobayashi-Maskawa (CKM) mixing matrix, as $|V_{ub}|$ contributes

Table 1: *Summary of the KLOE measurements on neutral kaons.*

	K_{Le3}	$K_{L\mu 3}$	K_{Se3}
BR	0.4008(15) [14]	0.2699(15) [14]	$7.046(91)\times10^{-4}$ [13]
τ	50.84(23) ns [15]		89.58(5) ps [12]
λ'_+	0.0256(18) [16]		
λ''_+	0.0014(8) [16]		
λ_o		0.0156(26) prel.	

Table 2: *Summary of the KLOE measurements on charged kaons.*

	$K^{\pm}_{e3}$	$K^{\pm}_{\mu 3}$
BR	0.05047(92) prel.	0.03310(81) prel.
τ	12.367(78) ns prel.	

only at the level of 10^{-5}. Semileptonic kaon decays offer a clean way to extract an accurate value of $|V_{us}|$, the decay rates are given by:

$$\Gamma_i(\mathrm{K} \to \pi l \nu(\gamma)) = \frac{G_F^2 M_K^5}{128\pi^3} C_K^2 S_{EW} |V_{us}|^2 |f_+(0)|^2 I_i(\lambda)(1 + \delta^i_{SU(2)} + \delta^i_{em}) \quad (1)$$

where the index i runs over the 4 modes ($i = \mathrm{K}^+_{e3}$,K^o_{e3},$\mathrm{K}^+_{\mu 3}$,$\mathrm{K}^o_{\mu 3}$). I_i is the phase space integral that is a function of the vector and the scalar form factors. S_{EW}=1.0232(3) is the universal short-distance radiative correction [21]. $\delta^i_{SU(2)}$ and δ^i_{em} are the long-distance electromagnetic and strong isospin-breaking corrections respectively. Finally $f_+(0) \equiv f_+^{\mathrm{K}^\circ\pi^-}(0)$ is the vector form factor at zero momentum transfer which encodes the SU(3) breaking effects in the hadronic matrix element. Differences between the various semileptonic decay modes are due to isospin breaking effects, both of strong and electromagnetic origin. To extract the value of $|V_{us}|$ from eq.1 we need not only accurate experimental values for the Γ_i (evaluated from the γ-inclusive BR's and from the kaon lifetimes) and the parameters describing the t-dependence of the vector and scalar form factors, but also the theoretical estimates of the δ's and $f_+^{\mathrm{K}^\circ\pi^-}(0)$. We can extract $|V_{us}|f_+^{\mathrm{K}^\circ\pi^-}(0)$ from both neutral and charged kaon modes, allowing for a consistency check between experiment and theory.

Table 3: $|V_{\rm us}|f_+(0)$ *values extracted with the KLOE measurements.*

Mode	$\lvert V_{\rm us}\rvert f_+(0)$
K_{Le3}	0.2156(7)
$K_{L\mu 3}$	0.2163(10)
K_{Se3}	0.2154(14)
$K^{\pm}_{e3}$	0.2168(22)
$K^{\pm}_{\mu 3}$	0.2151(30)
Average	0.2158(6)

The KLOE experiment provides the measurements for all the experimental inputs (except the K_S lifetime), the KLOE results are listed in Tables 1 and 2, and the values of $|V_{\rm us}|f_+(0)$ are listed in Table 3. The best accuracy, $\sim 0.3\%$, is obtained for the K_{Le3} mode, the error is dominated by the knowledge of τ_L. The five decay modes average to $|V_{\rm us}|f_+(0) = 0.2158(6)$, and assuming for $f_+(0)$ the standard Leutwyler-Roos evaluation $f_+(0) = 0.961(8)$ [19], the value for $|V_{us}|$ is 0.2246(20).

To test the CKM unitarity:

$$\Delta = |V_{\rm ud}|^2 + |V_{\rm us}|^2 - 1 = (-13 \pm 10) \times 10^{-4}$$

which is consistent with unitarity to $\sim 1.3\sigma$ ($|V_{ud}|$= 0.97377(27) [18], is an average from $0^+ \to 0^+$ nuclear beta decays results).

The values of $|V_{us}|$ obtained from K_{e3} and $K_{\mu 3}$ decays can also be used to test the universality of e and μ couplings to the W boson. The KLOE results are compatible with a ratio of the effective Fermi constants equal to unity:

$$[G(\mu 3)/G(e3)]^2 = 1.0065(98) \qquad \text{for } K_L$$

$$[G(\mu 3)/G(e3)]^2 = 0.984(25) \qquad \text{for } K^{\pm}$$

Recent advances in lattice gauge techniques have allowed the evaluation of the pseudoscalar decay constants f_π and f_K [20]. As a consequence, the $K_{\mu 2}$ partial decay rate provides an alternative method for the determination of $|V_{us}|$ via:

$$\frac{\Gamma(K \to \mu\nu(\gamma))}{\Gamma(\pi \to \mu\nu(\gamma))} \propto \frac{|V_{us}|^2}{|V_{ud}|^2} \frac{f_K^2}{f_\pi^2}$$

The KLOE measurement of the $K_{\mu 2}$ branching ratio BR$(K^+ \to \mu^+\nu) = 0.6366 \pm 0.0009_{\rm stat} \pm 0.0015_{\rm syst}$ [17], with the lattice result of $\frac{f_\pi}{f_K} = 1.208(2)(^{+7}_{-14})$

[20] gives the ratio:

$$|V_{\rm us}/V_{\rm ud}| = 0.2286\,(^{+27}_{-15})$$

This result can be used in a fit togheter with the values of $|V_{us}|$ from the KLOE average and $|V_{ud}|$ from Ref. [18], yielding the result $|V_{us}|$=0.2239(16) and $\Delta = (16 \pm 12) \times 10^{-4}$ with a χ^2 probability of 56%, which is again compatible with unitarity at $\sim 1.3\sigma$ level.

4 Conclusions

New preliminary results on $\rm K_S \to e^+e^-$, $\rm K_S \to \gamma\gamma$, $K_L \to \pi e\nu\gamma$, and $K_{L\mu 3}$ form factor slope λ_o have been presented. The determination of the CKM matrix element $|V_{us}|$ as obtained with the recent KLOE measurements have been presented. The analysis of the full data sample of about 2.5 fb^{-1} is in progress, and new and improved results will be available in the next future.

5 Acknowledgments

I would like to thank the organizers of the conference for the pleasant stay in La Thuile.

References

1. A. Drago, *et al.* **LNF**-03/012 (2003).
2. KLOE Coll., M. Adinolfi, *et al.*, NIM A **488**, 51 (2002).
3. KLOE Coll., M. Adinolfi, *et al.*, NIM A **482**, 363 (2002).
4. KLOE Coll., F.Ambrosino *et al.*, NIM A **534**, 403 (2004).
5. G. Ecker and A. Pich, Nucl. Phys. B **366**, 189 (1991).
6. J. Kambor and B. Holstein, Phys. Rev. D **49**, 2346 (1994).
7. J. Gasser et al., Eur.Phys.J.C **40**, 205 (2005).
8. CPLEAR coll., A. Angelopoulos *et al.*, Phys. Lett. B **413**, 232 (1997).
9. KTeV Coll., T. Alexopoulos *et al.*, Phys. Rev. D **71**, 012001 (2005).
10. NA48 Coll., A. Lai *et al.*, Phys. Lett. B **578**, 276 (2004).
11. NA48 Coll., A. Lai *et al.*, Phys. Lett. B **605**, 247 (2005).
12. PDG, W.-M. Yao *et al.*, J. Phys. G **33**, 1 (2006).

13. KLOE coll., F.Ambrosino, *et al.*, Phys. Lett. B **636**, 173 (2006).
14. KLOE coll., F.Ambrosino, *et al.*, Phys. Lett. B **632**, 43 (2006).
15. KLOE coll., F.Ambrosino, *et al.*, Phys. Lett. B **626**, 15 (2005).
16. KLOE coll., F.Ambrosino, *et al.*, Phys. Lett. B **636**, 166 (2006).
17. KLOE coll., F.Ambrosino, *et al.*, Phys. Lett. B **632**, 76 (2006).
18. W. J. Marciano and A. Sirlin, Phys. Rev. Lett. **96**, 032002 (2006).
19. H. Leutwyler and M. Roos, Z. Phys. C **25**, 91 (1984).
20. MILC coll., hep-lat/0609053
21. A. Sirlin, Nucl. Phys. B **196**, 83 (1982).

ON THE PAULI PRINCIPLE VIOLATION IN QFT

Victor Novikov
TEP, Moscow, Russia

Abstract

We propose a new mechanism for a "small" violation of Pauli Principle in the framework of Quantum Field Theory. Instead of modification of algebra - commutation relations for fields - we introduce spontaneous violation of Pauli Principle which is proportional to the vacuum fermionic condensate.

Getting older some of the theorists turn to the foundations of Quantum Mechanics. This is exactly my case. I am going to discuss the possibility of Pauli Principle breaking - one of the cornerstone of Quantum Field Theory (QFT). My talk is based on yet unpublished paper (un)written in collaboration with my old friend Sasha Dolgov (at early stage Maxim Pospelov participated to our discussions).

1 Introduction

The great merit of Pauli Principle is that it can be formulated in terms understandable to any person from the street. On the other hand the proof of Pauli Principle is based on a rather advanced formalism of QFT comprehensible to the tiny fraction of experts. Feynman wrote in his famous Lectures on Physics:"It appears to be one of the few places in physics where there is a rule which can be stated very simply, but for which no one has found a simple and easy explanation. The explanation is deep down in relativistic quantum mechanics. This probably means that we do not have a complete understanding of the fundamental principle involved." [1].

To understand principle better sometime it is useful to break it. I got involved in this business when I have seen the paper by Dolgov and Smirnov [2], where the authors proposed a fractional statistic for neutrino. (Fractional statistics for charged particles such as electron is excluded by experiment). In this way they wanted to get a Bose condensation of neutrino in vacuum and explain the origin of dark matter. My recollection was that it is absolutely impossible to get Pauli Principle violation in the framework of QFT and that it is well known in literature that it is impossible. I was wrong - it is possible and there is vast literature on this subject.

2 Short History of Discovery and Long History of Breaking

Exclusion Principle was introduced by Pauli in 1925 [3]. The first formal proof in QFT was developed by him fifteen years later [4]. The long list of papers that improved and purified the original proof can be found in any book on axiomatic field theory. The best reference, as I know, is still the book of R.F.Streater and A.S.Wightman [5].

Non-standard types of statistics such as parastatistics had been known for a long time [6]. It was so to say "large" violation of Pauli Principle.

Near a dozen or papers were published on this subject till 1987. In 1987 the first model for small violation of Pauli Principle was constructed in the framework of QM [7]. In this model the bilinear commutation relations for annihilation and creation operators were modified to trilinear relations with small parameter. It was a great success. But it was found immediately that generalization of bilinear relations to trilinear ones is rather difficult procedure in QFT . This modification inevitably leads to some pathology and consistent QFT with fractional statistics does not exist [8]. After this work near a hundred of papers with different modifications of Algebra of Operators were published. In a very recent paper [9] a kind of "No-Go Theorem" was proven. It was found that it is difficult (if possible) to get a small violaion of Pauli Principle in QFT with bilinear algebra. [1]

We suggest not to modify Algebra of Fields and not to destroy Pauli Principle by brute force. Instead of genuine breaking we suggest to imitate Pauli Principle violation exactly like "Spontaneous Symmetry Breaking" imitates symmetry violation.

3 Simulation of Symmetry Breaking

The phenomenon of Spontaneous Symmetry Breaking is getting known to students from a course on general physics when they learn about ferromagnetic material. Suppose that we have a piece of iron. Electromagnetic interaction of electrons in metal is $O(3)$ invariant. Suppose now that we switch-on an external electric current $\mathbf{j}$. Electric current produces magnetic field $\mathbf{B}$. It is clear that interaction of non-zero external current with electrons in metal breaks $O(3)$ invariance If we switch-off the current the $O(3)$ symmetry will be restored. On the other hand due to magnetization of ferromagnet the external magnetic field $\mathbf{B}$ still remains non-zero. As a result we get $O(3)$ invariant system that interacts with $O(3)$ non-invariant external field. This effect has a name "Spontaneous Symmetry Breaking" though symmetry is not broken. We get a sort of imitation of $O(3)$ symmetry violation.

The standard description of Spontaneous Symmetry Breaking in QFT step by step follows that example. First one considers a system with internal symmetry G and Lagrangian $L_{SYM}(\phi)$, where ϕ is a general symbol for fields.

[1] This paper contains rather complete list of references on the Pauli Principle Violation.

We suppose that fields ϕ are transformed in some nontrivial way under symmetry transformation G. At second step one switches-on an external classical source (current) J for field. In this case the total Lagrangian is

$$L = L_{SYM} + J\phi, \tag{1}$$

and external source breaks the symmetry. If the current is nonzero, i.e. $< J >\neq 0$, it produces nonzero classical field in vacuum, i.e.

$$< \phi >_J = \phi_{cl} \tag{2}$$

Fluctuations near this classical fields are described by ϕ_{qu}

$$\phi_{qu} = \phi - \phi_{cl}. \tag{3}$$

They interact with non-invariant object - external classical field.

At last step one switches-off the current, i.e. one puts $J \equiv 0$. In this case the term that breaks the symmetry goes to zero $J\phi = 0$. It happens that for some systems the equation of motion for v.e.v. of the field ϕ is non-zero even for zero current $J = 0$, i.e.

$$< \phi >_0 = \phi_{cl} \neq 0. \tag{4}$$

That is non-zero vacuum condensate.

Symmetric interaction of fluctuations with non-symmetric condensate produces imitation of symmetry breaking. This is Nambu-Goldstone mechanism of spontaneous symmetry breaking.

3.1 Scalar Condensate.

In QFT there exists a unique explicite example of self-interaction that produces a condensation of scalar fields. It is enough to take a special potential for scalars

$$V(\phi) = \lambda[\phi^2 - \phi_{cl}^2]^2. \tag{5}$$

In the Standard model we use similar potential for Higgs fields to produce vacuum condensate. As a result propagating $SU(2)$ and $U(1)$ massless gauge bosons and massless Goldstone bosons scatter on this vacuum condensate. There is also inelastic scattering on the condensate that mixes vector gauge bosons with Goldstone scalar bosons. The net effect is that instead of massless gauge and Goldstone bosons one gets massive gauge bosons

3.2 Vector Condensate.

There exist a vast literature on a Lorentz symmetry breaking. Fortunately in the case of QED any "reasonable" violation of Lorentz symmetry leads to a very simple modification of the Standard Lagrangian L:

$$\delta L = g\epsilon_{\mu\nu\alpha\beta} n_\mu A_\nu F_{\alpha\beta} \tag{6}$$

where A_ν is four-potential for e.m. field, $F_{\alpha\beta}$ is e.m. field-strength tensor, and numerical vector n_μ breaks Lorentz symmetry. There are two schools of thinking: one treats n_μ as an external vector, and the second one treats it as a vacuum condensate of some vector field B_μ, i.e. $n_\mu \equiv < B_\mu >_0$. The explicite mechanism for vector field condensation in vacuum does not exist in 4D QFT. Nowadays it is not a great disaster. One can consider our space-time as a 4D brane in multi-dimensional world. Vector field B_μ can be a zero mode living on this brane.

In any case light propagates through vector condensate and has different refraction indexes for left- and right-polarized photons. That is an explicite violation of Lorentz symmetry and CPT symmetry.

3.3 Fermion condensate.

Let we introduce a source for fermions and change an initial Lagrangian:

$$L \longrightarrow L + \bar{J}\psi + \bar{\psi}J, \tag{7}$$

where $J, \bar{J}$ are "classical" currents for fermions, i.e. some grassmanian numbers. The introduction of a source term for fermions is rather standard trick in QFT. In this way one can construct partition function $Z(J, \bar{J})$ and generate the complete set of fermionic correlators $< \psi_1 ... \bar{\psi}_n >$ as a variational derivatives of $Z(J, \bar{J})$ over currents J,$\bar{J}$ at $J = 0$.

In the case of $J \neq 0$ the nonzero current generates nonzero expectation value of the fermionic field:

$$< \psi >_J = \xi \neq 0, \tag{8}$$

where ξ is also a grassmanian number. Nonzero value of ξ violates Lorentz and rotational symmetry. It is interesting to understand whether it possible to have nonzero value of ξ at zero current $J = 0$. Actual mechanism for spontaneous breaking of symmetry, i.e. for vacuum condensation of ξ, is unknown. In the

standard QFT in four dimension it is impossible. But we can think about our space-time as a four-dimensional brane in multi-dimensional space with fermionic zero mode living on the brane. Another possibility is that our Lord just forgot to switch-off the fermionic current J.

In any case we will assume that ξ is nonzero. Certainly it violates Lorentz symmetry. In addition it should violate the Pauli Principle. Indeed consider a simple QFT model.

$$L = \bar{\psi}(\hat{p} - m)\psi + 1/2\phi(\hat{p}^2 - m^2)\phi + \lambda\phi(\bar{\psi}\psi) + \bar{J}\psi + \bar{\psi}J \tag{9}$$

where $\phi(x)$ and $\psi(x)$ are neutral boson and fermion fields. Equations of motion looks like

$$(\hat{p} - m)\psi + \lambda\phi\psi + J = 0; \quad (\hat{p}^2 - m^2)\phi + \lambda(\bar{\psi}\psi) = 0. \tag{10}$$

For classical nonzero constant current

$$J(x) \equiv J = m\xi \neq 0 \tag{11}$$

we get that

$$< \psi >_J \equiv \xi, \tag{12}$$

$$< \phi >_J \equiv \frac{\lambda}{m^2}\bar{\xi}\xi \tag{13}$$

The propagation of the excitations in the vacuum with these two condensates

$$\psi = \xi + \psi_q; \quad \phi = \frac{\lambda}{m^2}\bar{\xi}\xi + \phi_q, \tag{14}$$

is described by the quadratic form

$$L^{(2)} = \bar{\psi}_q(\hat{p} - \bar{m})\psi_q + \frac{1}{2}\phi_q(\hat{p}^2 - m^2)\phi_q + \lambda\phi_q[\bar{\xi}\psi_q + \bar{\psi}_q\xi], \tag{15}$$

where $\bar{m} = m - \frac{\lambda^2}{m^2}\bar{\xi}\xi$. It is clear that the last term proportional to λ describes inelastic scattering on the fermionic condensate that transforms fermions into bosons and visa verse:

$$Bosons \Longleftrightarrow Fermions \tag{16}$$

Evidently such transformation breaks statistic. The direct way to calculate statistic of the excitations that corresponds to ψ_q and ϕ_q is to diagonalize this quadratic form. Technically this rather tricky problem. The proper way to diagonalize it is to quantize a system in a box. In this way we reduce QFT problem to QM problem of the one given level.

4 QM model.

Consider field operators $\phi(x)$ and $\psi(x)$ as an expansion over plane waves in the box

$$\phi(x) = \sum_p \frac{1}{\sqrt{2\omega(p)}}[a(p)exp(ipx) + a^+(p)exp(-ipx)], \tag{17}$$

and

$$\psi(x) = \sum_p \frac{1}{\sqrt{2\omega(p)}}[b(p)u(p)exp(ipx) + h.c.], \tag{18}$$

where $\omega^2 = \mathbf{p}^2 + m^2$, and $(a(p), a^+(p))$ and $(b(p), b^+(p))$ are annihilation and creation operators for the original scalar and spinor fields. For the mode with given 3-momenta $\mathbf{p}$ we have a system with two degrees of freedom, i.e. simple Quantum Mechanics

$$H = \omega(p)[aa^+ + bb^+] + \lambda[a^+\zeta^+ b + b^+\zeta a], \tag{19}$$

with grasmanian parameter $\zeta = (\bar{u}\xi)/2\omega$ and creation and annihilation operators that satisfy well-known algebra

$$[a, a^+]_- = [b, b^+]_+ = 1; \quad [a, a]_- = [b, b]_+ = [a, b]_- = [a, b^+]_- = 0. \tag{20}$$

One can verify that this algebra is invariant under one-parameter group of invariance $(a, b) \to (A, B)$:

$$a = [1 - \frac{1}{2}(\beta^*\beta)(\zeta^*\zeta)]A + \beta(\zeta^* B) \tag{21}$$

$$b = -\beta^* A\zeta + [1 + \frac{1}{2}(\beta^*\beta)(\zeta^*\zeta)]B, \tag{22}$$

where β is an arbitrary complex number.

Operators A, B satisfy the same algebra

$$[A, A^+]_- = [B, B^+]_+ = 1; \quad [A, A]_- = [B, B]_+ = [A, B]_- = [A, B^+]_- = 0. \tag{23}$$

To diagonalize quadratic Hamiltonian we should take

$$\beta = \beta^* = -\lambda/2\omega(p). \tag{24}$$

In the new canonical coordinates Hamiltonian looks like a sum of bosonic oscillator and fermionic oscillator:

$$H = \omega_1 AA^+ + \omega_2 BB^+ \tag{25}$$

with

$$\omega_1 = \omega + \frac{\lambda^2 m}{16\omega^3}\bar{\xi}\xi, \tag{26}$$

$$\omega_2 = \omega - \frac{\lambda^2 m}{16\omega^3}\bar{\xi}\xi. \tag{27}$$

Mixing between bosonic subsystem (a, a^+) and fermionic subsystem (b, b^+) leads to a repulsion of the levels (with center of mass constrain)

$$\omega_1 + \omega_2 = 2\omega. \tag{28}$$

5 Statistics

In terms of diagonal variables the spectrum of Hamiltonian is known and one can calculate the average number of particle at given state using the standard rules of Statistical Mechanics. For particles that are created by operator A^+ we get a canonical Bose distribution:

$$< N >_{Bose} = < AA^+ > = \frac{1}{exp(\omega_1/T) - 1}. \tag{29}$$

with shifted frequency ω_1. For particles that are created by operator B^+ we get a canonical Fermi distribution

$$< N >_{Fermi} = < BB^+ > = \frac{1}{exp((\omega_2 - \mu)/T) + 1}, \tag{30}$$

where μ is a chemical potential. These are the distributions for the diagonal states.

In terms of the initial particles that are created in collisions the same equations look like a mixed statistic . Indeed if we introduce distributing numbers for initial particles

$$< n >_B = < aa^+ >, \tag{31}$$

and

$$< n >_F = < bb^+ >, \tag{32}$$

we get

$$< n >_F = (1 + \beta^2\zeta^+\zeta)N_{Fermi} - \beta^2\zeta^+\zeta N_{Bose}, \tag{33}$$

and

$$< n >_B = (1 - \beta^2\zeta^+\zeta)N_{Bose} + \beta^2\zeta^+\zeta N_{Fermi}, \tag{34}$$

where $\beta = -\lambda/2\omega$,

As a result for the distribution of initial "neutrinos" we get

$$< n >_\nu = [1 + O(\lambda\bar{\xi}\xi)]\frac{1}{exp((\omega-\mu)/T)+1} - \frac{\lambda^2 m}{32\omega^4}\bar{\xi}\xi\frac{1}{exp(\omega/T)-1}, \quad (35)$$

i.e. a piece of a standard Fermi distribution with slightly modified frequency plus a fraction of Bose distribution. The admixture of Bose statistic is proportional to the condensation of Fermi field $\bar{\xi}\xi$ and can be made arbitrary small.

6 Back to QFT

In terms of field variables

$$\phi(x) - \sum_p \frac{1}{\sqrt{2\omega(p)}}[a(p)exp(ipx) + a^+(p)exp(-ipx)], \quad (36)$$

$$\psi(x) = \sum_p \frac{1}{\sqrt{2\omega(p)}}[b(p)u(p)exp(ipx) + h.c.] \quad (37)$$

the transformation of operators $(a, b) \Rightarrow (A, B)$ looks like non-local transformations:

$$\phi(x) \Rightarrow [1 - \frac{\lambda^2 m}{64}\bar{\xi}\xi\frac{1}{(-\nabla^2+m^2)^2}]\phi(x) - \frac{\lambda}{4}\frac{1}{(-\nabla^2+m^2)}[\xi\bar{\psi} + \psi\bar{\xi}] \quad (38)$$

$$\psi(x) \Rightarrow [1 + \frac{\lambda^2 m}{64}\bar{\xi}\xi\frac{1}{(-\nabla^2+m^2)^2}]\psi(x) + \frac{\lambda m}{4}\frac{1}{(-\nabla^2+m^2)}\phi(x)\xi. \quad (39)$$

By construction it is clear that these non-local transformations do not violate causality.

7 Conclusions

Let me summarize the results.

The Fermion vacuum condensate simulates Pauli Principle breaking. This is a new way to play with Pauli Principle Breaking in QFT. We hope that we have made a step in true direction.

8 Acknowledgments

I would like to thank the organizers of La Thuile conference, particular Mario Greco, for their warm hospitality and for excellent conference.

This research was partly supported by RFBR grant 07-02-00021.

References

1. R.P. Feynman, R.B. Leighton, M. Sands :"The Feynman lectures on physics", Addison-Wesley, Reading,1965.
2. A.D. Dolgov, A.Y. Smirnov, Phys. Lett. **B621**, 1 (2005).
3. W. Pauli, Z. Physik **31**, 765 (1925).
4. W. Pauli, Phys. Rev. **58**, 716 (1940);

   W. Pauli: "Exclusion principle, Lorentz group and reflection of space-time and charge", in "Niels Bohr and the development of physics", Pergamon Press, London, 1955.
5. R.F. Streater & A.S. Wightman: "PCT, spin and statistics, and all that", Mathematical Physics Monograph Series, Benjamin/Cumming Publishing Company, Inc, Advanced Book Program, Reading, Massachusetts (London - Amsterdam - Don Mills, Ontario - Sydney - Tokyo) 1964.
6. H.S. Green, Phys. Rev. **90**, 270 (1953).

   O.W. Greenberg, A.M.L. Messiah, Phys. Rev. **138B**, 1155 (1965).
7. A.Yu. Ignatiev, V.A. Kuzmin, Sov. J. Nucl. Phys. **47**, 6 (1987).
8. L.B. Okun, Pisma ZhETF **46**, 11(1987);

   R.N. Mohapatra, O.W. Greenberg, Phys. Rev. Lett. **62**, 62 (1989).
9. A.Yu. Ignatiev, V.A. Kuzmin, Phys. Lett. **A359**, 26 (2006).

PRECISION FLAVOUR PHYSICS

Marco Ciuchini
INFN Sezione di Roma Tre and Dip. di Fisica, University of Roma Tre,
Via della Vasca Navale 84, I-00146 Roma, Italy

Abstract

The phenomenological interest of doing precision flavour physics is discussed in the light of recent proposals for dedicated experimental facilities.

Flavour physics has already entered the precision era. In the last few years, the B-factory extraordinary performances, complemented by the recent B_s measurements at the Tevatron, allowed to move on from the original goal of testing the CKM paradigm for CP violation to the extraction of the first quantitative information on New Physics (NP) in the flavour sector, particularly affecting $\Delta F = 2$ processes.

Let us summarize the main results [1, 2, 3, 4]:

- the CKM phase is non-vanishing and (very likely) accounts for the bulk of CP violation in the quark sector;
- about 10 independent experimental measurements of flavour-changing processes, both CP-conserving and CP-violating, are compatible with the CKM description within the present accuracy;
- all the CKM parameters are now known with less than 10% accuracy.

There is no evidence of deviation from the Standard Model (SM) at the present level of accuracy, say $\sim 10\%$, but some hint of possible discrepancy, at the level of 2σ or less, are present here and there. Among the most popular ones, we mention:

- the systematic, though not statistically significant, shift towards smaller values of $\sin 2\beta$ extracted from $b \to s$ penguin-dominated decays with respect to the one obtained from the $b \to c\bar{c}s$ tree-dominated decays [5];
- the $\sim 2\sigma$ negative deviation of the measurement of $\sin 2\beta$ using $b \to c\bar{c}s$ decays from the value obtained from the global fit. However this deviation is strongly correlated with the difference in the values of $|V_{ub}|$ measured in inclusive and exclusive semileptonic decays, which are hardly affected by NP contributions. In particular, using only the $|V_{ub}|_{\rm exclusive}$ the deviation disappears [2];
- the measured time-dependent CP asymmetry in the decay $B_d \to K_s\pi^0$ is $\sim 2\sigma$ larger than the theoretical predictions (this mode is particularly useful for NP searches as the hadronic uncertainties can be bounded under very mild assumptions using the abundant $K\pi$ data) [6];
- the $\sim 2\sigma$ negative deviation of the B_s mixing phase, obtained using factorization to reduce the discrete ambiguities of the determination from the $D0$ untagged angular analysis of the decay $B_s \to J/\psi\phi$ [7].

As far as NP is concerned, some model-independent results can already be found using present data: [1]

- $\Delta F = 2$ processes allow for the determination of the CKM parameters $\bar{\rho}$ and $\bar{\eta}$ in the presence of arbitrary NP contributions with an accuracy comparable to the SM case;
- $\Delta F = 2$ NP contributions to B_d and K mixing cannot exceed 10–20% of the SM amplitude unless they are aligned with the SM phase: in such a case, they can be up to ~ 10 times larger. Non-aligned NP contributions to the B_s mixing are less disfavoured. The recent evidence of the D–$\bar{D}$ mixing also suggests alignment to some extent;
- lower bounds on the NP scale from the B sector range from the 2.2×10^3 TeV for non-perturbative, strong-interacting NP models with generic flavour couplings to 0.16 TeV for perturbative, weak-interacting NP models with Minimal Flavour Violation (MFV).

Having proved that information on NP can be effectively obtained from flavour physics exploiting several processes where NP could actually show up, it is natural to think of next-generation experiments aiming at an improved precision, say 1%, in order to increase the sensitivity to NP contributions. [1] However some crucial conditions should be met for this program to be interesting or even pursuable at all:

i) the huge leap in luminosity required for improving the typical precision by an order of magnitude is attainable without degrading the cleanliness of the experimental environment;

ii) experimental systematic errors should not dominate, hence they must be kept at the percent level or less;

iii) theoretical uncertainties must be also kept at the percent level to avoid hindering the extraction of the NP signals;

iv) interesting (*i.e.* large) values of the NP scale have to be potentially accessible with the improved precision, even in the unfavourable scenario of MFV.

Concerning the first condition, new ideas in accelerator physics should allow building a e^+e^- collider able to collect an integrated luminosity of 15 ab^{-1} per year at the $\Upsilon(4S)$ with low background, in an experimental environment similar to the present B factories. Details can be found in Ref. [9, 10]. The experimental validation of these new ideas is under way. Another proposal

[1] It is worth noting that the forerunner of precision flavour physics is LHC*b* which will measure some observables, notably the UT angle γ and the B_s mixing phase, with percent (or better) accuracy [8].

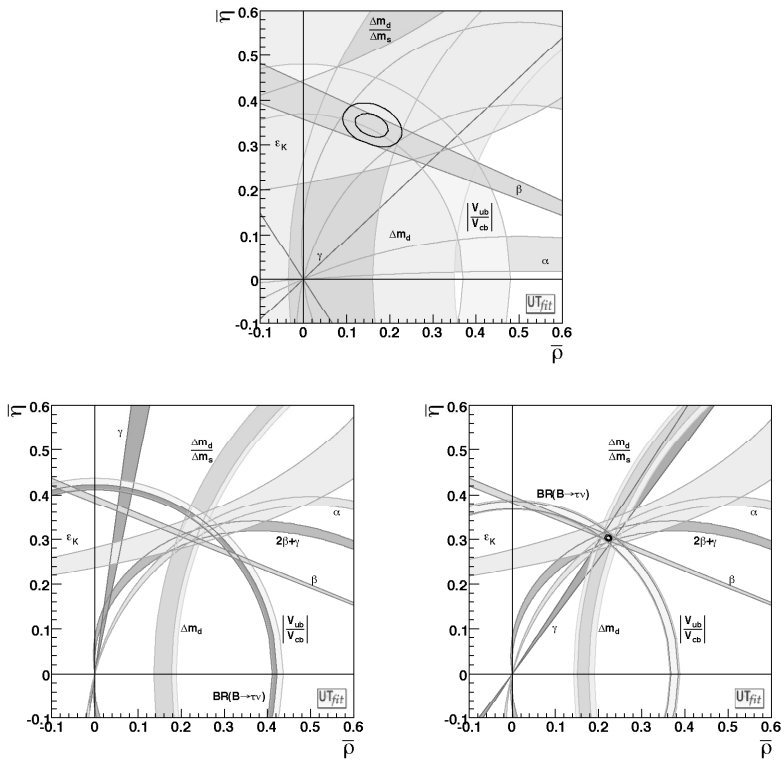

Figure 1: *Regions corresponding to* 95% *probability for* $\bar\rho$ *and* $\bar\eta$ *selected by different constraints, assuming present central values with present errors (top), present central values with errors expected at SuperB (bottom left), or central values tuned to be compatible with errors expected at SuperB (bottom right).*

of super B-factory based on a more conventional approach can be found in Ref. [11].

Extrapolating present experimental analyses done at the B factories, it was shown that many observables in the B_d sector would reach the target 1% accuracy with a data sample of 75 ab^{-1}, as can be seen in Table 1. It is reassuring that almost no measurement is limited by systematic errors larger than the target accuracy.

The condition on the theoretical uncertainties refers mainly to hadronic non-perturbative parameters. It is fulfilled in two ways: first, there exists a

Table 1: *Expected precision of the most important B_d measurements that can be performed at the B factories and at SuperB from* [9]*. Measurements marked (†) will be systematics limited; those marked (∗) will be theoretically limited.*

Observable	B factories (2 ab^{-1})	Super$B$ (75 ab^{-1})
$\sin(2\beta)$ $(J/\psi K^0)$	0.018	0.005 (†)
$\cos(2\beta)$ $(J/\psi K^{*0})$	0.30	0.05
$\sin(2\beta)$ (Dh^0)	0.10	0.02
$\cos(2\beta)$ (Dh^0)	0.20	0.04
$S(J/\psi\pi^0)$	0.10	0.02
$S(D^+D^-)$	0.20	0.03
$S(\phi K^0)$	0.13	0.02 (∗)
$S(\eta' K^0)$	0.05	0.01 (∗)
$S(K^0_S K^0_S K^0_S)$	0.15	0.02 (∗)
$S(K^0_S\pi^0)$	0.15	0.02 (∗)
$S(\omega K^0_S)$	0.17	0.03 (∗)
$S(f_0 K^0_S)$	0.12	0.02 (∗)
γ ($B \to DK$, $D \to CP$ eigenstates)	$\sim 15°$	2.5°
γ ($B \to DK$, $D \to$ suppressed states)	$\sim 12°$	2.0°
γ ($B \to DK$, $D \to$ multibody states)	$\sim 9°$	1.5°
γ ($B \to DK$, combined)	$\sim 6°$	1–2°
α ($B \to \pi\pi$)	$\sim 16°$	3°
α ($B \to \rho\rho$)	$\sim 7°$	1–2° (∗)
α ($B \to \rho\pi$)	$\sim 12°$	2°
α (combined)	$\sim 6°$	1–2° (∗)
$2\beta+\gamma$ ($D^{(*)\pm}\pi^\mp$, $D^\pm K^0_S\pi^\mp$)	20°	5°
$\lvert V_{cb}\rvert$ (exclusive)	4% (∗)	1.0% (∗)
$\lvert V_{cb}\rvert$ (inclusive)	1% (∗)	0.5% (∗)
$\lvert V_{ub}\rvert$ (exclusive)	8% (∗)	3.0% (∗)
$\lvert V_{ub}\rvert$ (inclusive)	8% (∗)	2.0% (∗)
$BR(B \to \tau\nu)$	20%	4% (†)
$BR(B \to \mu\nu)$	visible	5%
$BR(B \to D\tau\nu)$	10%	2%
$BR(B \to \rho\gamma)$	15%	3% (†)
$BR(B \to \omega\gamma)$	30%	5%
$A_{CP}(B \to K^*\gamma)$	0.007 (†)	0.004 († ∗)
$A_{CP}(B \to \rho\gamma)$	~ 0.20	0.05
$A_{CP}(b \to s\gamma)$	0.012 (†)	0.004 (†)
$A_{CP}(b \to (s+d)\gamma)$	0.03	0.006 (†)
$S(K^0_S\pi^0\gamma)$	0.15	0.02 (∗)
$S(\rho^0\gamma)$	possible	0.10
$A_{CP}(B \to K^*\ell\ell)$	7%	1%
$A^{FB}(B \to K^*\ell\ell)s_0$	25%	9%
$A^{FB}(B \to X_s\ell\ell)s_0$	35%	5%
$BR(B \to K\nu\bar{\nu})$	visible	20%
$BR(B \to \pi\nu\bar{\nu})$	–	possible

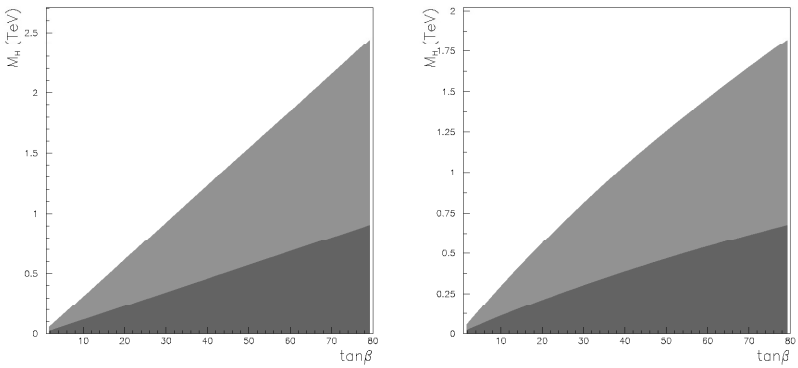

Figure 2: *Exclusion regions at* 95% *CL in the* $M_{H^\pm}$–$\tan\beta$ *plane for the 2HDM-II (left) and the MSSM (right), assuming the Standard Model value of* $BR(B \to \ell\nu)$ *measured with* 2 ab^{-1} *(dark area) and* 75 ab^{-1} *(dark+light area) (see Ref.* [9]*) for details).*

set of observables where the SM contribution and its uncertainty are negligible with respect to measurable NP contributions. Among them, the CP asymmetry $A_{CP}(B \to X_{s+d}\gamma)$, lepton-flavour and lepton-universality violation in τ and B decays, a shift in the dilepton invariant mass where $A_{FB}(B \to X_s\ell^+\ell^-) = 0$, CP violation in τ and Cabibbo-allowed or doubly-Cabibbo-suppressed charm decays are all processes whose SM contribution is either vanishingly small or already very well known. For them, any experimental evidence would be an unmistakable signal of NP and they could be probed at an interesting level with the statistics expected at the new experimental facilities.

Other observables actually require improved information on hadronic parameters in order to disentangle NP effects. To this purpose the only theoretical method that could in principle achieve the required accuracy is Lattice QCD. The limiting factor could be uncontrolled systematic uncertainties. Extrapolations based on the foreseen computing power and taking into account different sources of systematics (chiral extrapolation, heavy mass extrapolation, continuum limit, finite-size effects, etc.) indicate that an accuracy of $\mathcal{O}(1\%)$ is achievable on the hadronic parameters of interest [9]. Additional systematics that may appear in simulations on large lattices are very likely compensate by progresses in theory and algorithms which will certainly occur but are difficult to anticipate. As far as inclusive techniques (mainly the operator product expansion and the heavy-quark expansion) are concerned,

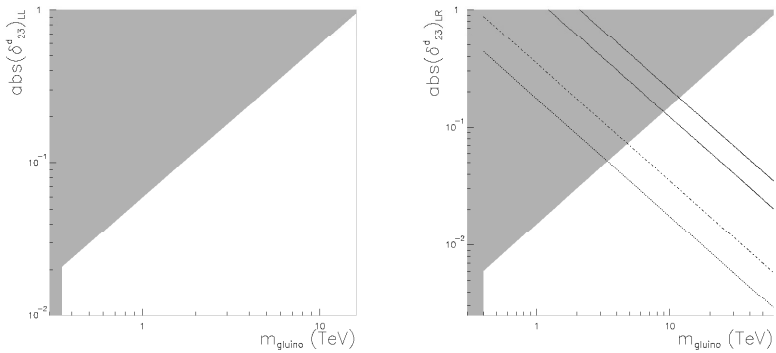

Figure 3: *Sensitivity region of SuperB in the $m_{\tilde{g}}$–$|(\delta^d_{ij})_{AB}|$ plane. The region is obtained by requiring that the reconstructed mass insertion is 3σ away from zero. The cases of $(\delta^d_{23})_{LL}$ (left) and $(\delta^d_{23})_{LR}$ (right) are shown. Details and other cases can be found in Ref.* [9].

theoretical improvements cannot be easily extrapolated. However they would certainly profit from the huge statistics of the new machines which for instance allow to accurately measure hadronic spectra. Finally, in spite of recent theoretical progress, predictions for non-leptonic decays still rely on models to some extent. The main theoretical ideas (factorization, flavour symmetries, etc.) would benefit from the confrontation with the improved measurements, but NP searches with non-leptonic decay in two (or more) bodies likely require methods allowing a data-driven control over the theoretical uncertainties [6].

Let us now discuss the last point, namely whether collecting a data sample of 75 ab^{-1} at the $\Upsilon(4S)$ is interesting and why. The main physics goal can be plainly stated as the search for indirect evidence for NP in the heavy flavour sector (including the τ lepton and the not-so-heavy charm quark) through virtual effects at the percent level. One has the possibility of measuring dozens of NP-sensitive observables with unprecedented precision. The full set of B factory measurements can be repeated pushing the accuracy of several observables, *e.g.* CKM angles, $b \to s$ penguin transitions, $BR(B^+ \to \tau^+\nu_\tau)$, etc. down to $\mathcal{O}(1\%)$. In addition, new NP-sensitive measurements such as the CP asymmetry in $B \to X_s\gamma$ or the forward-backward asymmetry in $B \to X_s\ell^+\ell^-$ become possible. As an example, Fig. 1 extrapolates the determination of the unitarity triangle assuming for the central values of the constraints either the present measurements or values tuned to be compatible also with the reduced

errors.

Furthermore, the flexibility to easily change the center-of-mass energy allows to produce well-defined particle-antiparticle pairs of B^+, B_d, D^0, D^+, D_s mesons and τ leptons, and to exploit quantum-correlations inherent in production via various e^+e^- resonances, particle-antiparticle pairs of B_d, D mesons and τ leptons allows for the study of flavour-violating processes involving the full spectrum of heavy quarks and leptons. For example, signals for violations of lepton flavour or lepton universality symmetries in τ or B decays, CP violation in τ decays, or in Cabibbo-allowed or doubly-Cabibbo-suppressed charm decays, would be unmistakable signs of NP.

To understand the impact of precision flavour physics, we consider two main scenarios:

i) direct searches at LHC find no evidence of NP;

ii) direct searches at LHC find new particles and there are hints of the underlying NP model (*e.g.* supersymmetry).

In the first case, indirect searches with flavour processes become of the utmost importance to probe NP scales in the 10–100 TeV region. Indeed, the 1 TeV NP scale naturally required in order to stabilize the Fermi scale could be higher to some extent without completely invalidating the concept of naturalness. Yet an acceptable shift upward of the natural NP scale would put LHC out of the game and leave the task of discovering NP to indirect searches. Flavour physics would be able to probe the interesting mass range giving naturalness a second chance before discarding it in favour of more exotic explanations of the Fermi scale. Unfortunately, given the presence of the unknown flavour couplings, there is no guarantee that the virtual effects of a new particle with a mass of 100 TeV are observed even with high precision. Still, values of the NP scale in the 10–100 TeV ballpark can be naturally reached in most NP models, including for example the MSSM, and even models with MFV are sensitive to scales larger than 1 TeV in the large $\tan\beta$ regime (see Fig. 2 for an example extrapolating bounds on NP contributions from $B^+ \to \ell^+\nu$ in 2HDM-II and in MSSM with MFV).

In the second case, the importance of precision flavour physics studies becomes twofold: not only the open window on much larger scales could extend the NP mass spectrum found at the LHC, but a detailed study of the flavour- and CP-violating couplings of the recently discovered particles could be carried out even in the unfavorable MFV case. Only with precision flavour physics we would be able to perform a systematic analysis of NP flavour- and CP-violating couplings in processes involving the second and third generations of quarks and leptons. These studies have a unique capability to try to reconstruct the NP Lagrangian from phenomenology. A typical example is supersymmetry (SUSY): most of the terms appearing in the soft SUSY-breaking sector of the Lagrangian

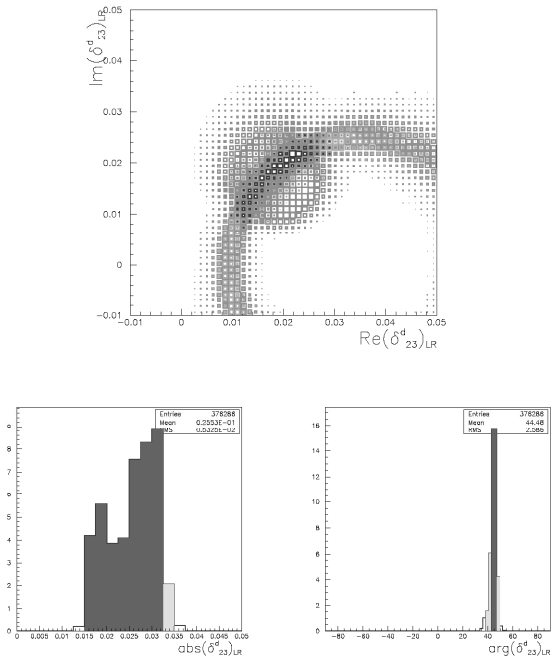

Figure 4: *Density plot of the region in the* $Re(\delta^d_{23})_{LR}$–$Im(\delta^d_{23})_{LR}$ *for* $m_{\tilde{q}} = m_{\tilde{g}} = 1$ *TeV and* $(\delta^d_{23})_{LR} = 0.028e^{i\pi/4}$ *selected using SuperB measurements. Different colours correspond to different constraints, see Ref.* [9] *(top). The distributions of the modulus (bottom left) and phase (bottom right) of the reconstructed* $(\delta^d_{23})_{LR}$ *are also shown.*

could be measured only with flavour-changing processes. For example, Fig. 3 shows the sensitivity of Super$B$ to observe off-diagonal entries of the MSSM squark mass matrices, given in terms of the mass insertions (MI's) $(\delta^d_{ij})_{AB}$. SUSY masses larger than 10 TeV are accessible for MI's ~ 1 while, for masses below the TeV, one can measure MI's as small as few $\times 10^{-2}$. Fig. 4 is an example of how well a $(\delta^d_{23})_{LR} \sim 3 \times 10^{-2}$ could be reconstructed using Super$B$ data given SUSY masses of ~ 1 TeV.

Another unmistakable signal of NP would be the observation of $\tau \to \mu\gamma$. Next-generation experiments will probe values of $BR(\tau \to \mu\gamma) \sim 10^{-9}$, an order of magnitude smaller than previous ones, and the range where most NP

models predict it to be. In Grand-Unified models, the pattern of observations in $\tau \to \mu\gamma$ and $\mu \to e\gamma$ can help identifying the dominant source of lepton-flavour violation [12, 13]. Other topics in τ physics can be studied as well, from the precise determination of the τ properties to the measurement of CP-violating observables.

Finally it should not be forgotten that a huge amount of charmed particles are produced running at the Υ resonances (running at the D–$\bar{D}$ is also possible), ten thousand times the statistics of present charm factories and still much larger than future dedicated facilities. With these statistics at hand, D–$\bar{D}$ oscillation parameters can be precisely measured and NP searches in the D sector become possible, using in particular CP-violating observables.

The above examples and many others [9, 14] show that precision flavour physics offers an unprecedented window of opportunity for NP studies which goes beyond the traditional flavour physics domain and could have a unique impact on our understanding of physics beyond the SM.

Acknowledgements

I warmly thank all the contributors of the Super$B$ CDR and particularly Tim Gershon and Achille Stocchi. I am also indebted with Maurizio Pierini, Luca Silvestrini and all the friends of the UTfit collaboration. Last but not least, I am grateful to the organizers for keeping the *Rencontres* as nice and pleasent as always.

References

1. M. Bona *et al.* [UTfit Collaboration], arXiv:0707.0636 [hep-ph].
2. M. Bona *et al.* [UTfit Collaboration], JHEP **0610** (2006) 081 [arXiv:hep-ph/0606167].
3. M. Bona *et al.* [UTfit Collaboration], Phys. Rev. Lett. **97** (2006) 151803 [arXiv:hep-ph/0605213].
4. M. Bona *et al.* [UTfit Collaboration], JHEP **0603** (2006) 080 [arXiv:hep-ph/0509219].
5. E. Barberio *et al.* [Heavy Flavor Averaging Group (HFAG) Collaboration], arXiv:0704.3575 [hep-ex].
6. L. Silvestrini, arXiv:0705.1624 [hep-ph].
7. A. Lenz and U. Nierste, JHEP **0706** (2007) 072 [arXiv:hep-ph/0612167].

8. O. Schneider, at 1st LHC*b* Collaboration Upgrade Workshop, January 2007, available from
`http://indico.cern.ch/conferenceDisplay.py?confId=8351`

9. M. Bona *et al.*, arXiv:0709.0451 [hep-ex].

10. M. Giorgi, *these proceedings.*

11. S. Hashimoto *et al.*, "Letter of intent for KEK Super B Factory", KEK-REPORT-2004-4.

12. L. Calibbi, A. Faccia, A. Masiero and S. K. Vempati, Phys. Rev. D **74** (2006) 116002 [arXiv:hep-ph/0605139].

13. B. Grinstein, V. Cirigliano, G. Isidori and M. B. Wise, Nucl. Phys. B **763** (2007) 35 [arXiv:hep-ph/0608123].

14. M. Hazumi *et al.* [SuperKEKB Physics Working Group], in preparation.

SESSION V – HEAVY FLAVOUR PHYSICS

- *Jong Yi* Charm and τ Physics at B Factories
- *Harold G. Evans* B_s Physics at CDF and D∅
- *Thomas Kuhr* Studies of B states at the Tevatron
- *Istvan Danko* Recent Charm Results from CLEO-c
- *Giancarlo Piredda* Recent Result from BaBar

CHARM AND τ PHYSICS AT B FACTORIES

Jong Yi
Manchester, UK

Written contribution not received

B_s PHYSICS AT CDF AND DØ

Harold G. Evans
Physics Department, Indiana University, Bloomington, IN, 47405, USA
(for the CDF and D0 Collaborations)

Abstract

Run II at the Tevatron has seen an explosion of results related to the B_s meson, ranging from tests of QCD models, to probes of electro-weak symmetry breaking, to direct searches for new physics effects. I will briefly summarize the CDF and D0 B_s-physics programs, describing the suitability of the detectors for doing this kind of physics, and pointing out how our knowledge of important quantities has improved through Run II measurements.

1 Introduction

Who would have thought it would be so fruitful?[1] In the past two years, CDF and D0 have produced over 35 separate results using B_s mesons. This represents the largest component of the Tevatron B-physics program, and, indeed, puts the B_s meson in the position of being the second-most prolific particle, in terms of physics output, in the Tevatron zoo – right after the top quark. This handy hadron has been used to study such diverse topics as QCD model building, physics beyond the Standard Model, the electro-weak symmetry breaking mechanism, and CP violation, to name just a few. In all of these areas, recent B_s results have sharpened our knowledge of the Standard Model and its weaknesses substantially.

Success comes at a price though – at least for conference audiences. The overwhelming number of results means that we cannot discuss any of their beautiful facets in detail; this article is already long enough. We will therefore concentrate on emphasizing the breadth of physics issues addressed by studies of the B_s meson, and will show how our understanding of these issues has improved since data from Run II at the Tevatron has been analyzed.

Obviously, this represents a snapshot of the Tevatron B_s-physics program, taken with up to 1.3 fb^{-1} of data. The Fermilab Tevatron accelerator continues to deliver proton-antiproton collisions to CDF and D0 at a furious pace. At the time of the conference each experiment had recorded over 2 fb^{-1} of data, with more rolling in every day. The final section of these proceedings will then be devoted to a brief discussion of what we plan to do with the bounty of B_s mesons that will come with this additional data.

2 The B_s at CDF and D0

Before we embark upon a description of results, it's instructive to examine the capabilities of the Tevatron collider experiments in areas important to the study of B_s mesons. Both CDF [1)] and D0 [2)] are well suited to take advantage of the large number of B_s mesons produced in proton-antiproton collisions at the

[1]In fact, many people have recognized the utility of the B_s meson for years now, but it did come as some surprise to the CDF and D0 B-Physics communities that B_s analyses have proven to be such a dominant component of the Tevatron B-Physics program.

Tevatron. The B_s production rate within the CDF and D0 detector acceptance is around 600 Hz, at luminosities of $2{\times}10^{32}$ cm^{-2}s^{-1}. This can be compared to around 1 Hz at the B-factories, when they run at the $\Upsilon(5S)$ resonance; and 5000 Hz at the upcoming LHCb experiment. Thus the Tevatron is the only facility where B_s mesons are produced currently in any large numbers.

This large B_s production rate, however, is dwarfed by the rate of $p\bar{p}$ bunch crossings (1.7 MHz) meaning that triggers are critical to the B-physics program at the Tevatron. Both CDF and D0 use three-level trigger systems and rely heavily (almost exclusively in D0's case) on single or di-lepton signals to collect samples of B_s mesons. D0 makes use of its excellent muon detectors to construct low p_T threshold single- and di-muon triggers without resorting to muon impact parameter cuts, which bias decay length distributions, except at the highest Tevatron luminosities. CDF uses both electrons and muons for B-physics triggers, but applies impact parameter cuts to most single-lepton triggers.

Because the CDF trigger system is capable of accepting events from its first level at a rate of up to 30 kHz (the corresponding D0 level-1 bandwidth limit is around 2 kHz), the CDF collaboration has been able to design triggers that select, at level-1, events with two tracks forming a vertex displaced from the primary $p\bar{p}$ interaction point. Such events are enriched with fully hadronic decays of B mesons, which allows CDF access to the wide range of important studies that can be done using these decay modes.

For many of the analyses discussed in this article the primary means of identifying B_s mesons is through their semileptonic decay: $B_s{\to}D_s^-\ell^+\nu_\ell X$. This decay has a branching fraction of 7.9% [3], and its identification highlights many of the experimental challenges that face CDF and D0. To begin with, there is the issue of lepton identification. D0 has the advantage here because of their muon detectors, which extend to pseudo-rapidities ($\eta = -\ln[\tan(\theta/2)]$) between ± 2, while CDF's muon system covers only $|\eta| < 1$. Additionally, the D0 muon system is shielded by 12–18 interaction lengths of material (a factor of around three more than CDF's) and includes toroidal magnets for local muon momentum measurements. Taken together, these reduce many muon background sources in D0 to a negligible level.

Identification of D_s meson decays, on the other hand, requires excellent tracking capabilities. The experiments use $\phi(K^+K^-)\pi^+$, $\bar{K}^{*0}(K^-\pi^+)K^+$,

$K^0_S(\pi^+\pi^-)K^+$, and $\pi^+\pi^-\pi^+$ decay modes of the D^+_s (and charge conjugates) in a range of analyses. CDF has the edge here, mainly because of the larger volume of their tracking system (extending from radii of 1.5 – 137 cm, as compared to the D0 tracker, which spans 2.8 – 52 cm) and the larger number of space-point measurements it makes (normally more than 100 for CDF, but only ∼20 for D0). This allows CDF to reconstruct multi-particle invariant masses with significantly better accuracy than D0, making combinatorial backgrounds less of a problem.

Finally, both detectors reconstruct displaced vertices with similar resolution, although CDF does a slightly better job because their tracking extends to lower radii[2]. As we will see, resolution is particularly important in B_s-mixing analyses, where time structures on the order of 100 fs must be reconstructed. Both the CDF and D0 tracking systems are capable of this feat in the reconstruction of semileptonic B_s decays, having average resolutions in the 15-20 fs range. However, because of CDF's large fully hadronic B_s decay sample, they are also able to take advantage of the better vertexing resolution (<10 fs) achievable in these types of decay.

Using these upgraded detectors, both experiments have been able to accumulate B_s meson data samples that contain orders of magnitude more events than have previously been observed at LEP or Run I at the Tevatron (1992–1996). Now let's look at what we've done with this harvest.

3 Properties of B_s Mesons

Knowledge of the basic properties of the B_s meson – how it is produced, how massive it is, how long it lives, how it decays – is the foundation upon which we build all subsequent studies using the particle. Accurate measurements of these quantities are thus essential for the tests of the Standard Model, and the searches for its extensions, described later. However, B_s property determinations are also useful in themselves as tests of our ability to use QCD, whether through models or by lattice calculations. Measurements made by CDF and D0 since the start of Run II have substantially increased our knowledge in the full range of this area.

[2]Note that D0 added a *Layer-0* silicon detector at a radius of 1.7 cm in June, 2006. Results using this new detector were not yet available for this conference though.

3.1 Production Fraction

Let's start with production. A major question here concerns whether the fragmentation of quark-antiquark pairs into heavy flavor hadrons is governed by universal functions independent of the type of collisions producing the quarks. CDF has made preliminary measurements of the relative fragmentation fractions of B hadrons in $p\bar{p}$ collisions. Their preliminary measurement of the B_s fraction relative to that of B_u and B_d uses $B_s \to \ell^- D_s^+ X$ decays in 0.36 fb^{-1} of data:

$$\frac{f_s}{f_u + f_d} = 0.160 \pm 0.005 \text{ (stat)} \, ^{+0.011}_{-0.010} \text{ (syst)} \, ^{+0.057}_{-0.034} \text{ (BR)},$$

where the last error reflects the uncertainty on the $D_s^+ \to \phi\pi^+$ branching ratio. When corrected for f_u and f_d, their measurement, $f_s = (12.7 \pm 3.8)\%$ is consistent with, but slightly higher than the LEP average of $(10.4 \pm 0.9)\%$ [4], indicating that no large differences in fragmentation between e^+e^- and $p\bar{p}$ are likely.

3.2 Mass and Lifetime

Mass and lifetime are also important properties of the B_s meson, and Run II results have dramatically improved our knowledge of them. Before the start of Run II, the B_s mass world average of 5369.6 ± 2.4 MeV [5] was dominated by 32 $B_s \to J/\psi\phi$ candidates reconstructed by CDF. Using 0.22 fb^{-1} of data from Run II, corresponding to 185 candidate decays, CDF has improved this measurement by almost a factor of three to $5366.01 \pm 0.73 \pm 0.33$ MeV [6]. On the lifetime side, both CDF and D0 have contributed to a factor of two improvement in the accuracy of the mean B_s lifetime measurement since the start of Run II: from $\tau(B_s) = 1.461 \pm 0.057$ ps in 2003 [5] to $\tau(B_s) = 1.451 \, ^{+0.029}_{-0.028}$ ps in 2006 [4]. Although each experiment has measured the B_s lifetime in several different modes, which contain different mixtures of CP-even and CP-odd states (as discussed later in this article), the most precise measurement, $\tau(B_s) = 1.398 + 0.044 \, ^{+0.029}_{-0.028}$ ps, currently comes from D0's analysis of $B_s \to D_s \mu X$ decays in 0.40 fb^{-1} of data [7].

Using the new average B_s lifetime, we find agreement with predictions of the lifetime ratio $\tau(B_s)/\tau(B_d)$, calculated using heavy quark effective theory, at the 2.3-sigma level:

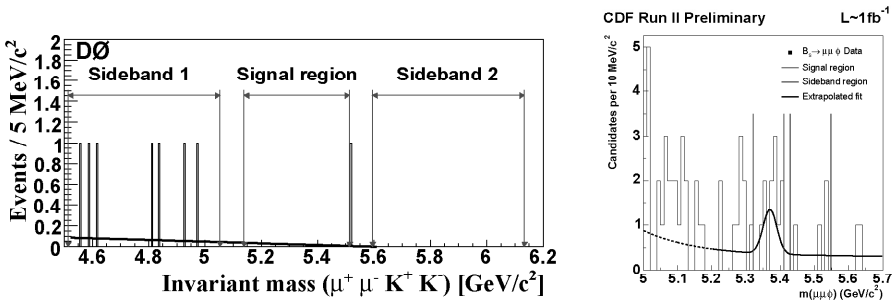

Figure 1: *The $\mu^+\mu^-\phi$ invariant mass distribution observed by D0 (left) and CDF (right).*

$$\begin{array}{ll} \text{Experiment} & 0.950 \pm 0.019\ ^{4)} \\ \text{NLO Theory} & 1.00 \pm 0.01\ ^{8)}. \end{array}$$

Note especially that the accuracy of the experimental measurements is now approaching that of the theoretical predictions for this ratio.

3.3 Hadronic Branching Ratios

Making use of their 2-track trigger, CDF has been able to accumulate an unprecedented sample of fully hadronic B_s decays. This allows them to make measurements, often for the first time ever, of various rare mode branching ratios as shown in tab. 1. These measurements provide valuable tests of QCD models, particularly of the applicability of SU(3) quark symmetries. With more statistics, some of them will also allow sensitive tests of CP violation: the angle γ/ϕ_3 of the CKM triangle from studies of $B_s \to h^+h'^-$, and probes of CP-even vs. CP-odd contributions using the $\psi(2S)\phi$ and $\phi\phi$ modes.

Measurements of orbitally excited B_s mesons have also been made by CDF and D0. However, these are discussed in another contribution to these proceedings [18].

4 Flavor Changing Neutral Current Decays

Decays of B hadrons governed by flavor changing neutral currents provide sensitive probes for new physics because these decays are highly suppressed in

Table 1: *Hadronic B_s branching ratio measurements compared to theoretical expectations.*

Mode	**Lumi**	**Signal**	**Measurement [Prediction]**
$\frac{\mathcal{B}(B_s \to D_s^- \pi^+)}{\mathcal{B}(B^0 \to D^- \pi^+)}$	0.355 fb^{-1}	494 ± 28	1.13 ± 0.08 ± 0.23 [9] [1.05 ± 0.24] [10]
$\frac{\mathcal{B}(B_s \to D_s^- \pi^+ \pi^+ \pi^-)}{\mathcal{B}(B^0 \to D^- \pi^+ \pi^+ \pi^-)}$	0.355 fb^{-1}	309 ± 26	1.05 ± 0.10 ± 0.22 [9]
$\mathcal{B}(B_s \to K^+ K^-)$ ($\times 10^6$)	1.0 fb^{-1}	1307 ± 64	24.4 ± 1.4 ± 4.6 (prelim) [19.7 ± 0.06] [11] [35 ± 7] [12]
$\mathcal{B}(B_s \to K^- \pi^+)$ ($\times 10^6$)	1.0 fb^{-1}	230 ± 38	5.00 ± 0.75 ± 1.00 (prelim) [4.9] [13]
$\mathcal{B}(B_s \to \pi^+ \pi^-)$ ($\times 10^6$)	1.0 fb^{-1}	26 ± 21	<1.36 at 90% CL (prelim)
$\frac{\mathcal{B}(B_s \to \psi(2S)\phi)}{\mathcal{B}(B_s \to J/\psi\phi)}$	0.36 fb^{-1}	32.5 ± 6.5	0.52 ± 0.13 ± 0.07 [14] [0.54 ± 0.06] [15]
$\mathcal{B}(B_s \to \phi\phi)$ ($\times 10^6$)	0.18 fb^{-1}	7.3 ± 2.9	$14\ ^{+6}_{-5} \pm 6$ [16] [10 – 37] [17]

the Standard Model, proceeding through loop diagrams. In many models of physics beyond the Standard Model, however, these types of decays can be enhanced in some regions of model parameter space. For example, $\mathcal{B}(B_s \to \mu^+\mu^-)$ is proportional to $\tan^6 \beta$ [3] in the minimal supersymmetric standard model [19].

CDF and D0 have searched for flavor changing neutral currents in decays of B_s mesons to $\mu^+\mu^-$ and in the decay $B_s \to \mu^+\mu^-\phi$. Results are shown in tab. 2. The new limits on $\mathcal{B}(B_s \to \mu^+\mu^-)$ represent more than an order of magnitude improvement over those available before Run II data was analyzed [5] and are now only a factor of 30 from the Standard Model prediction. In the decay $B_s \to \mu^+\mu^-\phi$, studied for the first time with Run II data, CDF sees a 2.3-sigma excess of events, as shown in fig. 1 – so observation of this mode could be just around the corner!

[3] β is the ratio of the vacuum expectation value of the two Higgs doublets.

Table 2: *Experimental limits and standard model predictions for flavor changing neutral current B meson decays.*

Mode	Exp.	Lumi	Evts	Bgrd	95% CL Limit
$B_s \to \mu^+\mu^-$	D0	0.30 fb^{-1}	4	4.3 ± 1.2	$<4.0\times10^{-7}$ (prelim)[a]
	CDF	0.78 fb^{-1}	1	1.27 ± 0.37	$<1.0\times10^{-7}$ (prelim)
	Pred.				$(3.42\pm0.54)\times10^{-9}$ 20)
$B_s \to \mu^+\mu^-\phi$	D0	0.45 fb^{-1}	0	1.6 ± 0.4	$<4.1\times10^{-6}$ 21)
	CDF	0.92 fb^{-1}	11	3.5 ± 1.5	$<2.4\times10^{-6}$ (prelim)
	Pred.				$(1.6\perp0.5)\times10^{-6}$ 22)

[a]Shortly after the end of this conference D0 announced a new, preliminary $B_s \to \mu^+\mu^-$ limit of 9.3×10^{-8} at the 95% CL, using 2 fb^{-1} of data.

5 Mixing and CP Violation

The phenomenon of mixing between neutral mesons and anti-mesons provides a very sensitive probe of the mechanism of electro-weak symmetry breaking. This sensitivity is due to the fact that flavor structure in the Standard Model, in particular the difference between quark weak and mass eigenstates, arises through Yukawa couplings of fermions to the Higgs boson [23]. Thus, time evolution in the neutral B systems is governed by the Schrödinger equation:

$$i\frac{d}{dt}\begin{pmatrix} |B(t)\rangle \\ |\bar{B}(t)\rangle \end{pmatrix} = \begin{pmatrix} M - \frac{i\Gamma}{2} & M_{12} - \frac{i\Gamma_{12}}{2} \\ M_{12}^* - \frac{i\Gamma_{12}^*}{2} & M - \frac{i\Gamma}{2} \end{pmatrix}\begin{pmatrix} |B(t)\rangle \\ |\bar{B}(t)\rangle \end{pmatrix} \quad (1)$$

and the eigenstates of the mass matrix, B_L, B_H, are different than the weak eigenstates, $B, \bar{B}$, which oscillate between each other. These oscillations can be described by three parameters: $|M_{12}|$, $|\Gamma_{12}|$, and the CP-violating phase, $\phi = \arg(-M_{12}/\Gamma_{12})$, which are related to physical observables:

$$\begin{array}{lcll} \Delta m & = & M_H - M_L & \sim 2|M_{12}| \\ \Delta\Gamma & = & \Gamma_L - \Gamma_H & = \Delta\Gamma_{CP}\cos\phi \\ \Delta\Gamma_{CP} & = & \Gamma_{CP-even} - \Gamma_{CP-odd} & \sim 2|\Gamma_{12}| \end{array} \quad (2)$$

In the B_s system, a measurement of the mass difference, Δm_s, which also gives the frequency of oscillations between particle and anti-particle states, allows the determination of the CKM matrix element V_{ts}. Although important

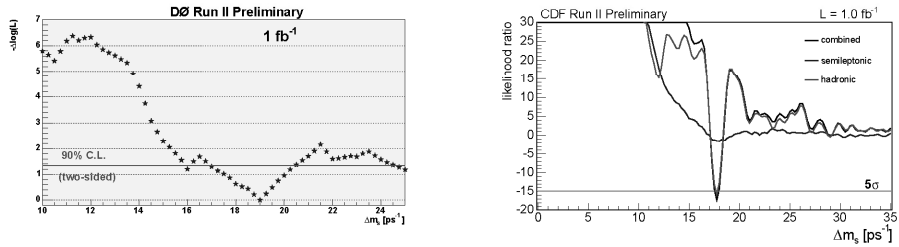

Figure 2: *Likelihood scans of the D0 (left) and CDF (right) combined oscillation samples vs.* Δm_s.

as parameters of the Standard Model, Δm_s and V_{ts} are most useful in constraining new physics when used in conjunction the B_d oscillation frequency via:

$$\frac{\Delta m_d}{\Delta m_s} = \frac{M(B_d)}{M(B_s)} \xi \left| \frac{V_{td}}{V_{ts}} \right|^2 \qquad \xi = \frac{f_{B_d}^2 B_{B_d}}{f_{B_s}^2 B_{B_s}} \tag{3}$$

The ratio of Δm_d to Δm_s gives a more precise determination of V_{td}, related to one of the sides of the unitarity triangle [23], because the theoretical uncertainty on ξ is much less than that on the individual lattice calculations of the B meson decay constants (f) and bag parameters (B) [24].

The other B_s mixing observables are also important in searches for new physics. The ratio $\Delta\Gamma_s/\Delta m_s$ is a function of QCD parameters only, and thus provides a measurement in this system that is independent of new physics. The CP-violating phase, ϕ_s, however, is expected to be tiny in the Standard Model, $\sim 0.25^o$ [25]. Theories of physics beyond the Standard Model, however, often include other sources of CP-violation than the single Standard Model phase, and can thus yield large predictions for ϕ_s.

5.1 B_s Oscillations

Spring 2006 was a watershed period in the study for B_s oscillations. After nearly two decades of searching for a B_s oscillations signal by many experimental groups, D0 was able to set the first two-sided bound on the parameter Δm_s by a single experiment [26]. CDF followed quickly thereafter with three-sigma evidence for B_s oscillations [27].

The current status of B_s mixing measurements is shown in fig. 2 where a preliminary combination of D0 results is presented as well as the final CDF observation [28], which is now significantly more than a 5-sigma effect. Numerically, the results are:

$$\begin{array}{ll} \text{D0 } (1 \text{ fb}^{-1}) & 17 < \Delta m_s < 21 \text{ ps}^{-1} \quad (90\% \text{ CL}) \\ \text{CDF } (1 \text{ fb}^{-1}) & 17.77 \pm 0.10 \pm 0.07 \text{ ps}^{-1}. \end{array}$$

Some details of the analyses are presented in tab. 3, including the B_s decay modes used; sample sizes; the quality of the flavor taggers used to distinguish events where a B_s oscillated to a $\bar{B}_s$ before decaying and vice-versa[4]; and the sensitivity of the analysis, defined as the expected limit in the absence of any signal. For reference, information about the previously most sensitive single channel – ALEPH's fully hadronic signal [5] – is also included.

CDF uses their measurement of Δm_s to derive a value for the ratio of CKM matrix elements:

$$\left|\frac{V_{td}}{V_{ts}}\right| = 0.2060 \ \pm \ 0.0007(\text{exp}) \ ^{+0.0081}_{-0.0060}(\text{theory}).$$

The accuracy on this quantity is now completely dominated by the uncertainty of the ratio of B_s and B_d decay constants and bag parameters, ξ, from lattice calculations [24].

BaBar and Belle have also recently measured $|V_{td}/V_{ts}|$ using B_d decays to $\rho\gamma$ and $K^*\gamma$ [35]. The average of their results, $0.200 \pm 0.016(\text{exp})^{+0.016}_{-0.015}(\text{theory})$, is consistent with the CDF measurement but of significantly lower sensitivity. Interestingly, however, the B-factory measurement is still dominated by experimental uncertainties, while the theoretical error on its value is only slightly larger than that on CDF's measurement. The addition of enough data to bring the experimental uncertainty on the B-factory measurements below that from theory will make this measurement competitive with, and complimentary to, the matrix element ratio measurements from the Tevatron.

Table 3: *Details of the D0 and CDF B_s oscillation analyses. Also shown are comparable numbers for the previously most sensitive analysis from ALEPH.*

Mode	**Sample**	**Average εD^2**		**Sensitivity**
		OST	**SST**	
ALEPH fully hadronic	28.5	27%		13.6 ps^{-1}
D0 Semileptonic ℓD_s; $D_s \to \phi\pi^-, K^{*0}K^-, K^0_S K^-$	43,000	2.48%		16.5 ps^{-1}
CDF Semileptonic ℓD_s; $D_s \to \phi\pi^-, K^{*0}K^-, 3\pi^\pm$	61,500	1.8%	4.8%	19.3 ps^{-1}
CDF Hadronic $D_s\pi^+$, $D_s 3\pi^\pm$; $D_s \to \phi\pi^-, K^{*0}K^-, 3\pi^\pm$	8,700	1.8%	3.7%	30.7 ps^{-1}

5.2 B_s Width Difference and CP-violating Phase

Not content with measuring only the mass difference part of B_s mixing, intrepid analysts also made major progress on the other parameters, $\Delta\Gamma_s$ and ϕ_s, in the last year. These quantities can be accessed by combining information from several sources:

1. $B_s \to J/\psi\phi$: the time evolution, mass and angular distributions in $B_s \to J/\psi$ decays;
2. τ_{fs}: lifetimes of flavor-specific B_s decays, for example semi-leptonic decays, which contain an equal mixture of CP-even and CP-odd components;
3. $A^{\mu\mu}_{SL}$: charge asymmetries in like-sign dimuon production;
4. A^s_{SL}: charge asymmetries in $B_s \to \mu^\pm D_s^\mp$ decays;
5. τ_{even}, $\mathcal{B}_{even}$: lifetimes and branching ratios of CP-specific B_s decays, such as $B_s \to K^+K^-$ and $B_s \to D_s^{(*)} D_s^{(*)}$.

[4]This quality is defined as εD^2, the efficiency of the tagger times the dilution squared (where the dilution, $D = 1 - 2P_{mis-tag}$, with $P_{mis-tag}$ being the probability to incorrectly tag the event). It is measured using information about the *other* B hadron in the event (OST) or using particles associated with the B_s meson (SST)

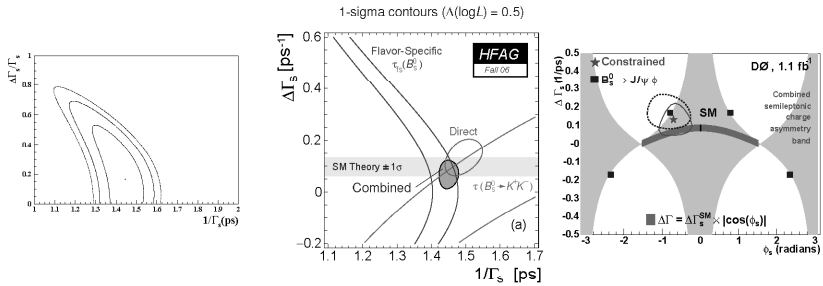

Figure 3: *Plots of the world average values of* $\Delta\Gamma_s$ *vs.* $1/\Gamma_s$ *from winter 2003* [5] *(left) and the end of 2006* [4] *(middle). Also show is the combination* [34] *of D0 measurements of* $\Delta\Gamma_s$ *vs* ϕ_s *(right) .*

In the past, analyses centered on the extraction of $\Delta\Gamma_s$ using the first two methods described above. The state-of-the-art in early 2003 can be seen in the left-most plot of fig. 3, which shows that no statistically significant extraction of the value of $\Delta\Gamma_s$ could be made before Run II results were available.

This has changed dramatically in the past year, with a flurry of new results from D0 and CDF, which are summarized in tab. 4. Combining these results (with the exception of the D0 and CDF $B_s \to D_s^{(*)} D_s^{(*)}$ measurements where the assumption of CP-even state dominance is unproven) yields averages summarized in the center plot of fig. 3 [4]. Progress is clearly substantial, with a new world-average value of

$$\Delta\Gamma_s = 0.071^{+0.053}_{-0.057}\ \text{ps}^{-1} \qquad (-0.04 < \Delta\Gamma_s < +0.17)\ \text{ps}^{-1}\ \ (95\%\ \text{CL}).$$

This measurement, favors a positive, non-zero value for $\Delta\Gamma_s$, and is in agreement with the Standard Model expectation of $0.088 \pm 0.017\ \text{ps}^{-1}$ [25].

Their large B_s data samples and multiple handles on mixing also allow D0 to perform a combination of their results [34], shown in the right-hand plot of fig. 3, that is sensitive to ϕ_s. This combination results in a value of $\Delta\Gamma_s = 0.13 \pm 0.09\ \text{ps}^{-1}$, which is consistent with the world average; and finds:

$$\phi_s = -0.70^{+0.47}_{-0.39}$$

which is nearly 2-sigma away from $(4.2 \pm 1.4) \times 10^{-3}$ [25], the Standard Model prediction.

Table 4: *A summary of recent analyses sensitive to* $\Delta\Gamma_s$ *and* ϕ_s.

Tech.	**Exp.** **Lumi** **Signal**	**Observables** **Measurement**	**Sens. to** $\Delta\Gamma_s$, ϕ_s
$B_s \to J/\psi\phi$	CDF [29] 0.355 fb^{-1} 203±15	$M(J/\psi\phi)$, proper time, 3 decay angles $\Delta\Gamma_s = 0.47^{+0.19}_{-0.24}\pm0.01$ ps^{-1}	fit for: $\Delta\Gamma_s$, τ_{fs} helicity amplitudes
$B_s \to J/\psi\phi$	D0 [30] 1.1 fb^{-1} 1039±45	$M(J/\psi\phi)$, proper time, 3 decay angles $\Delta\Gamma_s - 0.17\pm0.09$ ps^{-1} $\phi_s = -0.79\pm0.56$	fit for: $\Delta\Gamma_s$, ϕ_s, τ_{fs} helicity amplitudes, strong phases
τ_{fs}	W.A. [4]	$\tau_{fs} = 1.440\pm0.036$ ps	τ_{fs} $= \frac{1}{\Gamma_s}\left[\frac{1+(\Delta\Gamma_s/2\Gamma_s)^2}{1-(\Delta\Gamma_s/2\Gamma_s)^2}\right]$
$A^{\mu\mu}_{SL}$	D0 [31] 1.0 fb^{-1}	$\frac{N(bb\to\mu^+\mu^+) - N(bb\to\mu^-\mu^-)}{N(b\bar{b}\to\mu^+\mu^+) - N(b\bar{b}\to\mu^-\mu^-)}$ $A^{\mu\mu}_{SL}$= (-0.92±0.44±0.32)%	$A^{\mu\mu}_{SL} = A^d_{SL} + \frac{f_s Z_s}{f_d Z_d} A^s_{SL}$ $Z_q = \frac{1}{1-(\Delta\Gamma_q/2\Gamma_q)^2}$ $-\frac{1}{1+(\Delta m_q/\Gamma_q)^2}$
A^s_{SL}	D0 [32] 1.3 fb^{-1} 27,300±300	$\frac{N(\mu^+ D_s^-) - N(\mu^- D_s^+)}{N(\mu^+ D_s^-) + N(\mu^- D_s^+)}$ A^s_{SL}= (1.23±0.97±0.17)%	A^s_{SL} $= \frac{1}{2}\frac{x_s^2+y_s^2}{1+x_s^2}\frac{\Delta\Gamma_s}{\Delta m_s}\tan\phi_s$
τ_{even}	CDF prelim 360 fb^{-1} 718±55	$\tau(B_s \to K^+K^-)$ 1.53±0.18±0.02 ps	τ_{even} $\sim \frac{1}{\Gamma_s}\left[\frac{1}{1+(\Delta\Gamma_{CP}/2\Gamma_s)}\right]$
$\mathcal{B}_{even}$	CDF prelim 360 fb^{-1} 718±55	$\mathcal{B}(B_s \to D_s^+ D_s^-)$ = (1.3±0.6)%	$2\mathcal{B}_{even}$ $\sim \frac{\Delta\Gamma_{CP}}{\Gamma_s}\left[\frac{1}{1+(\Delta\Gamma_{CP}/2\Gamma_s)}\right.$
$\mathcal{B}_{even}$	D0 [33] 1.3 fb^{-1} 718±55	$\mathcal{B}(B_s \to D_s^{(*)} D_s^{(*)})$ $= (3.9^{+1.9\ +1.6}_{-1.7\ -1.5})\%$	

5.3 Direct CP- violation

As a final note to this section on CP measurements using the B_s, CDF has taken the first steps toward measuring direct CP-violation in the B_s system using their preliminary $B_s \to K^-\pi^+$ measurement, discussed previously. In addition to measuring the branching ratio for this mode, they also determine its CP asymmetry:

$$A_{CP} \equiv \frac{|A(B_s^0 \to K^-\pi^+)|^2 - |A(\bar{B}_s^0 \to K^+\pi^-)|^2}{|A(B_s^0 \to K^-\pi^+)|^2 + |A(\bar{B}_s^0 \to K^+\pi^-)|^2} = 0.39 \pm 0.15 \pm 0.08,$$

which differs from zero by 2.5-sigma and is in good agreement with the Standard Model expectation of $\sim$0.37 [36].

6 Future Prospects and Conclusions

Looking back on the last few years, we can take pride in the good use to which the B_s meson has been put at the Tevatron in Run II. We have observed many decay modes of this particle for the first time and are zeroing in on an observation of the flavor changing neutral current in $B_s \to \mu^+\mu^-\phi$ decays, while being only a factor of 30 away from the Standard Model prediction for $B_s \to \mu^+\mu^-$. We have also made remarkable progress in our understanding of B_s mixing, with a first observation of its oscillation frequency after more than a decade of searching; and new sensitivity to the CP-violating phase in this system. However, we certainly do not plan to rest on our laurels.

The Tevatron is operating extremely well, delivering luminosity at a pace where we can expect a total Run II data sample of up to 8 fb^{-1} per experiment. In addition, both experiments are upgrading their capabilities, with D0's new Layer-0 silicon detector of particular importance to the B-physics program. Although the larger instantaneous luminosities seen by CDF and D0 will force the imposition of more restrictive triggers, significantly larger B_s data samples should be available in the next 1–2 years. As many of the measurements presented here remain statistics limited (a notable expectation is the extraction of V_{td} from Δm_d and Δm_s) this added data should allow a vibrant continuing program of measurements of rare decay modes and CP-violation in the B_s system.

You have, most certainly, not heard the last of the B_s meson at the Tevatron!

Acknowledgments

I would like to thank the D0 and CDF B-physics working group convenors, Brendan Casey, Cheng-Ju Lin, Manfred Paulini, and Andrzej Zieminski, for their help in preparing this presentation. My warmest gratitude also goes to the conference organizers for preparing such a fascinating program (not to mention the excellent food, drink, and skiing)!

References

1. D. Acosta, *et al.* (CDF), Phys. Rev. **D 71**, 032001 (2005); R. Blair, *et al.* (CDF), Fermilab-Pub-96/390-E (1996); C.S. Hill, *et al.*, Nucl. Instrum. and Methods **A 530**, 1 (2004); W. Ashmanskas, *et al.*, Nucl. Instrum. and Methods **A 518**, 532 (2004); S. Cabrera, *et al.*, Nucl. Instrum. and Methods **A 494**, 416 (2002).
2. V.M. Abazov, *et al.* (D0), Nucl. Instrum. and Methods **A 565**, 463 (2006).
3. W.-M. Yao, *et al.* (The Particle Data Group), Journal of Phys. **G 33**, 1 (2006).
4. The Heavy Flavor Averaging Group (end of 2006 results), `http://www.slac.stanford.edu/xorg/hfag/`.
5. The Heavy Flavor Averaging Group (PDG 2003 results), `http://www.slac.stanford.edu/xorg/hfag/`; K. Hagiwara, *et al.* (The Particle Data Group), Phys. Rev. **D 66**, 1 (2002).
6. D. Acosta, *et al.* (CDF), Phys. Rev. Lett. **96**, 202001 (2006).
7. V.M. Abazov, *et al.* (D0), Phys. Rev. Lett. **97**, 241801 (2006).
8. C. Tarantino, Eur. Phys. J. **C 33**, S895 (2004); Nucl. Phys. Proc. Suppl. **156**, 33 (2006).
9. D. Acosta, *et al.* (CDF), Phys. Rev. Lett. **98**, 061802 (2007).
10. P. Colangelo and R. Ferrandes, Phys. Lett. **B 627**, 77 (2005).
11. from $\mathcal{B}(B_s \to K^+K^-) \sim \mathcal{B}(B^0 \to K^+\pi^-)$
S. Descotes-Genon, J. Matias, and J. Virto, Phys. Rev. Lett. **97**, 061801 (2006); S. Baek, D. London, J. Matias, and J. Virto, `arXiv:hep-ph/0610019`.

12. from QCD sum rules, implying large U-spin violation
A.J. Buras, *et al.*, Nucl. Phys. **B 697**, 133 (2004); A. Khodjamirian, T. Mannel, and M. Melcher, Phys. Rev. **D 68**, 114007 (2003).
13. A.R. Williamson and J. Zupan, Phys. Rev. **D 74**, 014003 (2006).
14. D. Acosta, *et al.* (CDF), Phys. Rev. Lett. **98**, 061802 (2007).
15. from $\mathcal{B}(B^0 \to \psi(2S)K^{*0})$ / $\mathcal{B}(B^0 \to J/\psi K^{*0})$.
16. D. Acosta, *et al.* (CDF), Phys. Rev. Lett. **95**, 031801 (2005).
17. Y.-H. Chen, *et al.*, Phys. Rev. **D 59**, 074003 (1999); X.Q. Li, G.R. Lu, and Y.D. Yang, Phys. Rev. **D 68**, 114015 (2003) [Erratum-ibid. **D 71**, 019902 (2005)].
18. T. Kuhr, these proceedings.
19. see, T. Blazek, S.F. King, and J.K. Parry, Phys. Lett. **B 589**, 39 (2004).
20. A.J. Buras, Phys. Lett. **B 566**, 115 (2003).
21. V.M. Abazov, *et al.* (D0), Phys. Rev. **D 74**, 031107 (2006).
22. C.Q. Geng and C.C. Liu, Journal of Phys. **G 29**, 1103 (2003).
23. see K. Anikeev, *et al.*, Fermilab-Pub-01/197 [arXiv:hep-ph/0201071].
24. M. Okamoto, Proc. Sci. LAT2005 , 013 (2005) [arXiv:hep-lat/0510113].
25. A. Lenz and U. Nierste, arXiv:hep-ph/0612167.
26. V.M. Abazov, *et al.* (D0), Phys. Rev. Lett. **97**, 021802 (2006).
27. D. Acosta, *et al.* (CDF), Phys. Rev. Lett. **97**, 062003 (2006).
28. D. Acosta, *et al.* (CDF), Phys. Rev. Lett. **97**, 242003 (2006).
29. D. Acosta, *et al.* (CDF), Phys. Rev. Lett. **94**, 101803 (2005).
30. V.M. Abazov, *et al.* (D0), Phys. Rev. Lett. **98**, 121801 (2007).
31. V.M. Abazov, *et al.* (D0), Phys. Rev. **D 74**, 112002 (2006).
32. V.M. Abazov, *et al.* (D0), Phys. Rev. Lett. **98**, 151801 (2007).
33. V.M. Abazov, *et al.* (D0), arXiv:hep-ex/0702049.
34. V.M. Abazov, *et al.* (D0), arXiv:hep-ex/0702030.
35. S. Nishida, these proceedings.
36. H.J. Lipkin, Phys. Lett. **B 621**, 126 (2005).

STUDIES OF B STATES AT THE TEVATRON

Thomas Kuhr on behalf of the CDF and DØ Collaborations
Institut für Experimentelle Kernphysik, Universität Karlsruhe (TH), Wolfgang-Gaede-Str. 1, 76131 Karlsruhe, Germany

Abstract

The Tevatron is an excellent place to study B hadrons. In this article the latest results of the DØ and CDF collaborations on orbitally excited B^0 and B_s mesons, the B_c mass, η_b production, Λ_b lifetime and Σ_b baryons are presented.

1 Introduction

The large $b\bar{b}$ production rate and the possibility to create all types of B hadrons makes the Tevatron a unique place for studies of B states. On the other hand the huge inelastic cross section and the hadronic environment are experimental challenges.

The analysis of B hadron states allows us to study QCD at a non-perturbative scale and to tune our models of bound quark states. The techniques to calculate such states range from potential models to non-relativistic QCD and lattice QCD. In heavy quark effective theory [1)] (HQET) a system of b and light quarks is treated in first order as a light quark in a static color field of an infinitely heavy b quark. This approach is for example used to explain the spectrum of orbitally excited B^0 and B_s mesons [2)].

2 B^{**}

The bound system of a $\bar{b}$ and d quark[1] with orbital angular momentum of $L = 1$ between the two quarks is called B^{**} or B_J. In the approximation of infinite heavy quark mass the spins of the two quarks decouple so that the sum j_q of the light quark spin and the orbital angular momentum becomes a characterizing quantum number of the B^{**}. Together with the heavy quark spin there are four possible spin combinations. The two $j_q = 1/2$ states can decay via S-wave. Therefore they are expected to be broad and very difficult to distinguish from combinatorial background. Because the two $j_q = 3/2$ states can only decay via D-wave, they are expected to be narrow and observable in the experiment.

The B_2^* with $J^P = 2^+$ can decay to $B^+\pi^-$ and $B^{*+}\pi^-$ while the B_1 with $J^P = 1^+$ can only decay to $B^{*+}\pi^-$. Because the photon from the decay $B^{*+} \to B^+\gamma$ is not detected, three peaks in the reconstructed B^{**} mass spectrum are expected.

DØ observes these three peaks in the B^{**}-B^+ candidate mass difference spectrum (Fig. 1 left) in a data sample of 1 fb^{-1} where the B^+ is reconstructed in the decay mode $J/\psi K^+$ [3)]. CDF utilizes the decay $B^+ \to D^0\pi^+$ in addition to the $J/\psi K^+$ mode for the B^+ reconstruction, but has analyzed only 370 pb^{-1} of data so far [4)]. The distribution of the Q value, which is the remaining kinetic energy of the B^{**} candidate decay, is shown in Fig. 1 (right) for the $D^0\pi^+$ mode. The extracted masses and mass differences of $m(B_1) = 5720.8 \pm 2.5 \pm 1.1$ MeV/c^2 (DØ), $m(B_1) = 5734 \pm 3 \pm 2$ MeV/c^2 (CDF) and $m(B_2^*) - m(B_1) = 25.2 \pm 3.0 \pm 1.1$ MeV/c^2 (DØ), $m(B_2^*) - m(B_1) = 4 \pm 6 \pm 2$ MeV/c^2 (CDF) are not in good agreement.

[1]Charge conjugate states are always implied in this article.

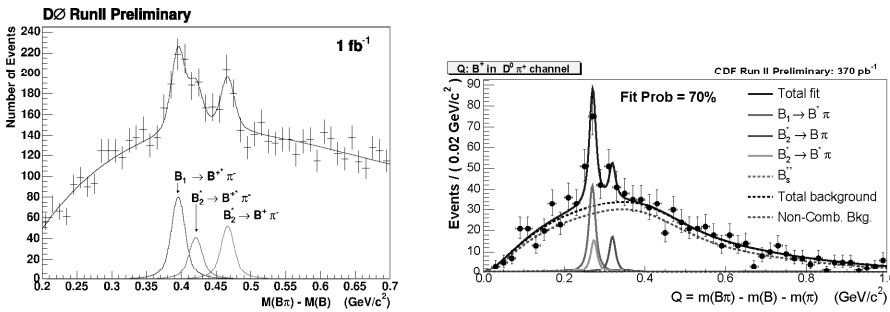

Figure 1: *Mass difference of B^{**} candidates in the B^+ decay mode $J/\psi K^+$ from DØ (left) and Q value of B^{**} candidates in the B^+ decay mode $D^0\pi^+$ from CDF (right)*

3 $\mathbf{B_s^{**}}$

For the B_s^{**} or B_{sJ} states the same structure of two narrow and two broad states as for the B^{**} is expected. The d quark in the B^{**} is just replaced by an s quark. Because the decay $B_s^{**} \to B_s\pi$ violates isospin conservation the B_s^{**} dominantly decays to $B^{(*)+}K^-$. Like in the B^{**} analyses the photon from the B^{*+} decay is not detected which leads to a shift of about 46 MeV/c^2 in the reconstructed mass. DØ uses a sample of 16k $B^+ \to J/\psi K^+$ while CDF uses 31k $B^+ \to J/\psi K^+$ and 27k $B^+ \to D^0\pi^+$. Fig. 2 shows the Q distribution from both experiments for 1 fb^{-1} of data.

The signal measured by DØ is the first direct observation of the B_{s2}^* state [5]. It is confirmed by CDF [6] and the extracted masses of $m(B_{s2}^*) = 5839.1\pm1.4\pm1.5\,\mathrm{MeV/c^2}$ (DØ) and $m(B_{s2}^*) = 5839.64\pm0.30\pm0.14\pm0.5\,\mathrm{MeV/c^2}$ (CDF), where the last error is due to the uncertainty of the B^+ mass [7], are in good agreement. In addition CDF observes for the first time the B_{s1} state and measures its mass as $m(B_{s1}) = 5829.41 \pm 0.21 \pm 0.14 \pm 0.6$ MeV/c^2.

As can be seen in Fig. 2 there is no peak in the background of wrong sign charge combinations. The significance of the B_{s1} signal was evaluated with toy experiments to be well above five standard deviations.

4 $\mathbf{B_c}$

The B_c is an extraordinary particle because it is the only meson with two distinct heavy quarks. However, experimentally it is challenging because its production rate is about three orders of magnitude smaller than the rate of

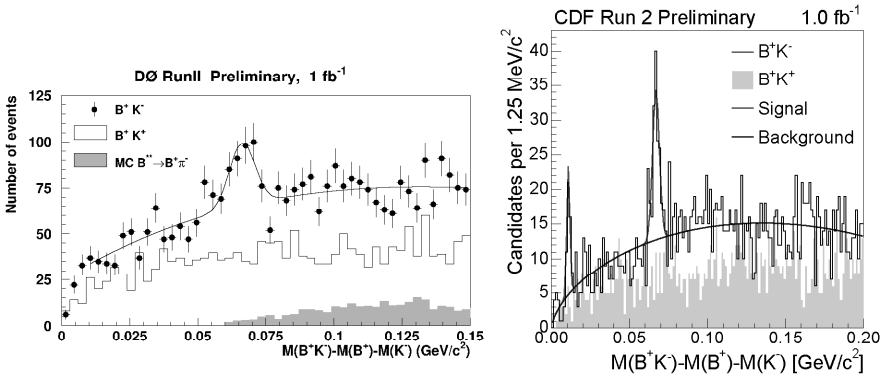

Figure 2: *Q value distribution of B_s^{**} candidates from DØ (left) and from CDF (right).*

B^+ or B^0. It was first observed by DØ and CDF in semileptonic decays. Due to the inclusive reconstruction the precision of the B_c mass measurement was limited.

Therefore CDF looks in 1.1 fb^{-1} of data for fully reconstructed $B_c^+ \to J/\psi\pi^+$ [8]. With selection cuts optimized on the kinematically very similar high statistics $B^+ \to J/\psi K^+$ sample an excess with a significance of more than six standard deviations is observed in the invariant mass spectrum (Fig. 3). An unbinned fit yields a mass of $m(B_c) = 6276.5 \pm 4.0 \pm 2.7$ MeV/c^2. The precision of this measurement challenges theoretical calculations like the recent lattice QCD prediction [9] of $m(B_c) = 6304 \pm 12^{+18}_{-0}$ MeV/c^2.

5 η_b

While the $b\bar{b}$ vector mesons are well known the pseudo-scalar $b\bar{b}$ state, the η_b, is not observed yet. CDF searches for this last missing meson ground state in the decay channel $\eta_b \to J/\psi J/\psi$ [10]. This mode has an experimentally clean signature but on the other hand the predicted branching ratio is low [11]. Only 0.2 to 20 visible events are expected per fb^{-1}.

With cuts optimized for a search no significant signal is observed in the $J/\psi J/\psi$ mass spectrum (Fig. 4 left). Therefore a limit is determined with tighter cuts to ensure well understood efficiencies (Fig. 4 middle and right). The 95% confidence level limit on the visible η_b cross section times branching ratio relative to inclusive J/ψ from b decays is $\sigma(p\bar{p} \to \eta_b X; |y(\eta_b)| <$

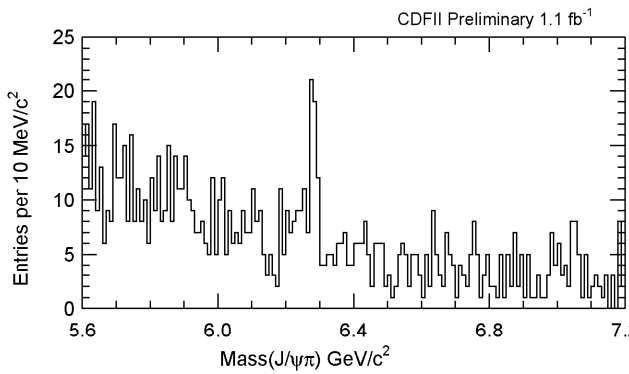

Figure 3: *Invariant mass spectrum of B_c candidates from CDF.*

$0.6, p_T(\eta_b) > 3.0$ GeV/c) $\cdot BR(\eta_b \to J/\psi J/\psi)/\sigma(p\bar{p} \to b \to J/\psi X; |y(J/\psi)| < 0.6, p_T(J/\psi) > 3.0$ GeV/c) $< 5.0 \times 10^{-3}$. Using the $b \to J/\psi X$ cross section measurement [12] this translates into $\sigma(p\bar{p} \to \eta_b X; |y(\eta_b)| < 0.6, p_T(\eta_b) > 3.0$ GeV/c) $\cdot BR(\eta_b \to J/\psi J/\psi) \cdot [BR(J/\psi \to \mu\mu)]^2 < 2.6$ pb.

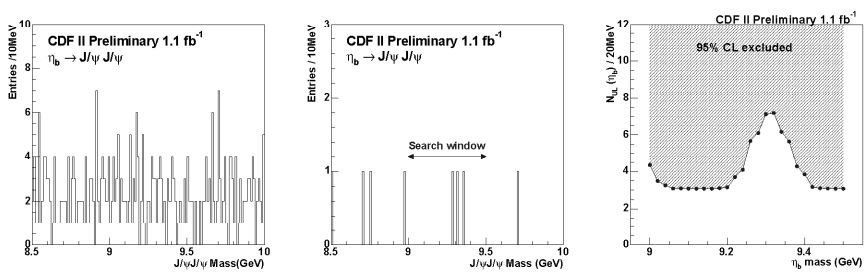

Figure 4: *Invariant mass spectrum of η_b candidates with cuts for a search (left) and for a limit determination (middle) and limit on the number of η_b particles (right).*

6 Λ_b

In the spectator model the lifetime of the Λ_b is expected to be equal to the lifetime of the B^0. When interactions between the weakly decaying b quark and

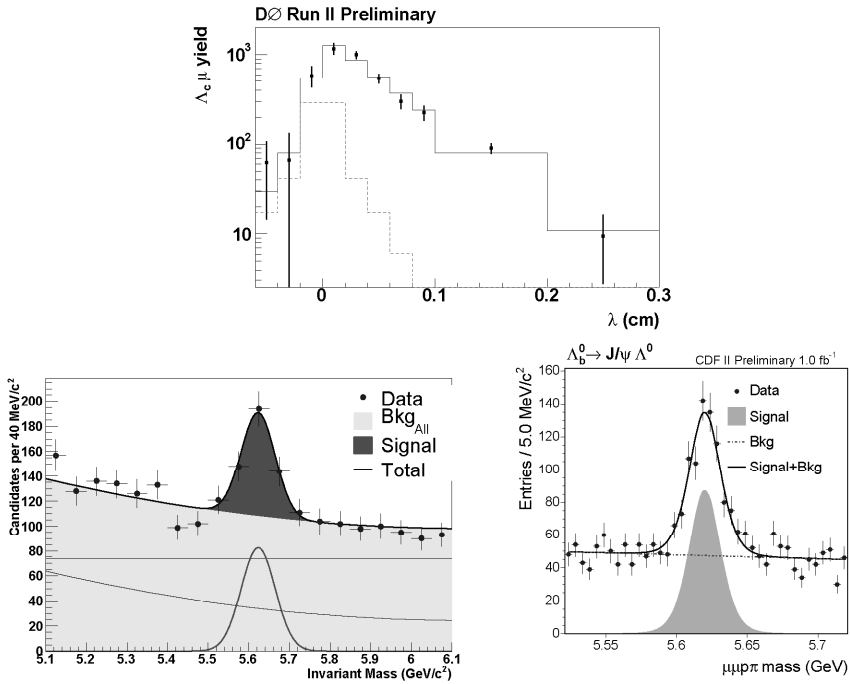

Figure 5: *Visible proper decay length distribution of* $\Lambda_b^0 \to \Lambda_c^+ \mu^- X$ *candidates from DØ (top) and invariant mass spectrum of fully reconstructed* Λ_b *candidates from DØ (bottom left) and CDF (bottom right).*

the spectator quarks are taken into account NLO QCD calculations predict a 10% to 20% lower lifetime for Λ_b [13].

DØ measures in 1.3 fb^{-1} of data the Λ_b lifetime in the semileptonic decay mode $\Lambda_b^0 \to \Lambda_c^+ \mu^- X$ with $\Lambda_c^+ \to K_s^0 p$ [14]. ¿From a fit to the visible proper decay length (Fig. 5 top) which takes into account the missing momentum and a contribution from $c\bar{c}$ events, a lifetime of $\tau(\Lambda_b) = 1.28^{+0.12}_{-0.11} \pm 0.09$ ps is extracted.

Both Tevatron experiments also measure the Λ_b lifetime in fully reconstructed decays $\Lambda_b^0 \to J/\psi\Lambda^0$ [15, 16]. As a cross check the B^0 lifetime was measured in a high statistics sample of kinematically similar $B^0 \to J/\psi K_s^0$ decays and the results are in good agreement with the world average. With a sample of 170 Λ_b baryons (Fig. 5 bottom left) DØ measures in 1.2 fb^{-1} of data a lifetime of $\tau(\Lambda_b) = 1.298 \pm 0.137 \pm 0.050$ ps. Both DØ measurement

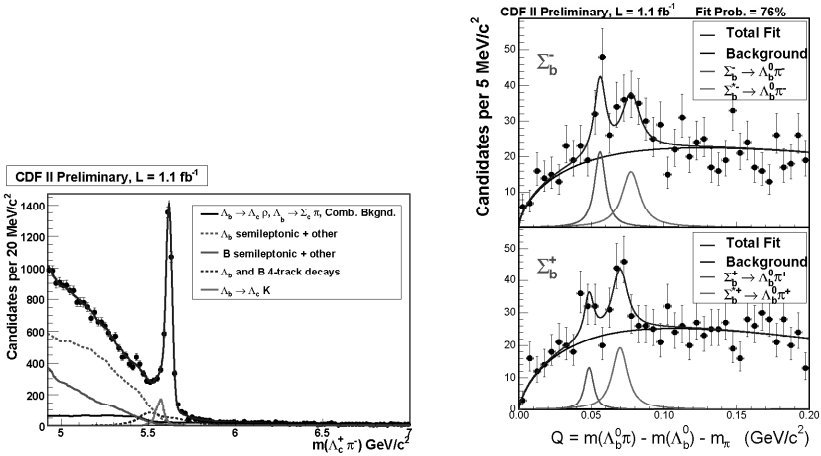

Figure 6: *Invariant mass spectrum of* $\Lambda_b^0 \to \Lambda_c^+\pi^-$ *candidates (left) and Q value distribution of* $\Sigma_b^{(*)}$ *candidates from CDF (right).*

agree well with the 2006 world average of 1.230 ± 0.074 ps and with the NLO QCD calculations. Using 500 Λ_b particles in 1 fb^{-1} (Fig. 5 bottom right) CDF measures a lifetime of $\tau(\Lambda_b) = 1.59 \pm 0.08 \pm 0.03$ ps. This result is 3.2 standard deviations above the world average and consistent with the DØ result in the same decay channel at a level of 1.7 standard deviations.

7 Σ_b

So far the Λ_b was the only directly observed b baryon. At an about 200 MeV/c^2 higher mass the next b baryon is expected, the Σ_b, an isospin 1 particle with a b and two light quarks. The mass splitting between the spin 3/2 Σ_b^* and the spin 1/2 Σ_b ground state is predicted to be 10 to 40 MeV/c^2.

Using 3000 fully reconstructed hadronic decays $\Lambda_b^0 \to \Lambda_c^+\pi^-$ with $\Lambda_c^+ \to pK^-\pi^+$ (Fig 6 left) CDF searches for charged $\Sigma_b^{(*)}$ in the decay mode $\Sigma_b^{(*)\pm} \to \Lambda_b^0\pi^\pm$ [17]. After unblinding the signal region four peaks with a significance of more than five standard deviations are observed (Fig 6 right). The measured masses of $m(\Sigma_b^-) = 5816^{+1.0}_{-1.0} \pm 1.7$ MeV/c^2, $m(\Sigma_b^+) = 5808^{+2.0}_{-2.3} \pm 1.7$ MeV/c^2, $m(\Sigma_b^{*-}) = 5837^{+2.1}_{-1.9} \pm 1.7$ MeV/c^2 and $m(\Sigma_b^{*+}) = 5816^{+1.6}_{-1.8} \pm 1.7$ MeV/c^2 are consistent with the theoretical predictions.

8 Summary

The Tevatron allows a broad spectrum of very competitive or even unique studies of B states. Among the impressive results of the DØ and CDF collaborations are the most precise mass measurements of B^{**}, B_s^{**}, B_c and Σ_b. Moreover, the individual B_s^{**} states and the Σ_b baryon were observed for the first time. With an increasing amount of collected data further improvements of the precision, which may for example resolve the discrepancy in the measured Λ_b lifetime, can be expected. Also new discoveries or limits challenging theoretical predictions, one candidate being the η_b, can be anticipated.

References

1. I. I. Y. Bigi, N. G. Uraltsev and A. I. Vainshtein, Phys. Lett. B **293** (1992) 430 [Erratum-ibid. B **297** (1993) 477] [arXiv:hep-ph/9207214].
2. E. J. Eichten, C. T. Hill and C. Quigg, Phys. Rev. Lett. **71** (1993) 4116 [arXiv:hep-ph/9308337].
   D. Ebert, V. O. Galkin and R. N. Faustov, Phys. Rev. D **57** (1998) 5663 [Erratum-ibid. D **59** (1999) 019902] [arXiv:hep-ph/9712318].
   N. Isgur, Phys. Rev. D **57** (1998) 4041.
   M. Di Pierro and E. Eichten, Phys. Rev. D **64** (2001) 114004 [arXiv:hep-ph/0104208].
3. DØ Collaboration, DØ public note 5026 (2006).
4. CDF Collaboration, CDF public note 7938 (2005).
5. DØ Collaboration, DØ public note 5027 (2006).
6. CDF Collaboration, CDF public note 8468 (2006).
7. W. M. Yao *et al.* [Particle Data Group], J. Phys. G **33** (2006) 1.
8. CDF Collaboration, CDF public note 8004 (2006).
9. I. F. Allison, C. T. H. Davies, A. Gray, A. S. Kronfeld, P. B. Mackenzie and J. N. Simone [HPQCD Collaboration], Phys. Rev. Lett. **94** (2005) 172001 [arXiv:hep-lat/0411027].
10. CDF Collaboration, CDF public note 8448 (2006).
11. E. Braaten, S. Fleming and A. K. Leibovich, Phys. Rev. D **63** (2001) 094006 [arXiv:hep-ph/0008091].
12. D. Acosta *et al.*, Phys. Rev. D **71**, 032002 (2005).

13. C. Tarantino, Nucl. Phys. (Proc. Suppl.) B **156**, 33 (2006).
14. DØ Collaboration, DØ public note 5263 (2006).
15. DØ Collaboration, DØ public note 5179 (2006).
16. CDF Collaboration, CDF public note 8268 (2006).
17. CDF Collaboration, CDF public note 8523 (2006).

RECENT CHARM RESULTS FROM CLEO-C

István Dankó
(for the CLEO Collaboration)
Rensselaer Polytechnic Institute
Troy, NY 12180, USA

Abstract

The CLEO-c experiment has been collecting data at the charm-threshold region. A selection of recent results on charmed meson and charmonia decays are presented.

1 Introduction

The CLEO-c experiment has been taking data at the CESR symmetric e^+e^- collider at the charm threshold region since 2003. The main goal of the experiment is to perform high precision measurements of hadronic branching fractions, leptonic decay constants, and semileptonic form factors of charmed mesons, together with an extensive study of QCD spectroscopy in the charmonium sector in order to provide rigorous constraints on the strong interaction theory, especially Lattice QCD calculations. If the theoretical calculations survive these tests they can be used to provide much needed theoretical input to extract quark mixing (CKM) matrix elements (e.g. V_{ub}, V_{td} and V_{ts}), which remain limited by complications caused by strong interaction dynamics.

The selected topics discussed here are the measurement of the absolute branching fraction of Cabibbo-favored hadronic D^0, D^+, and D_s decays; measurement of the leptonic decays, $D^+_{(s)} \to \ell^+\nu$, and decay constants $f_{D_{(s)}}$; measurement of the D_0 mass; and a study of three-body hadronic decays of χ_{cJ}.

Charged and neutral D mesons are produced at the $\psi(3770)$ which predominantly decays to D^+D^- and $D^0\bar{D}^0$ with a total cross section of about 7 nb. D_s mesons are created at around $E_{\rm cm} = 4170$ MeV, where their production is dominated by $e^+e^- \to D_s^{\star\pm}D_s^{\mp}$ with a cross section about 0.9 nb [1]. The 1^3P_J $(J = 0, 1, 2)$ charmonium states are produced in radiative $\psi(2S)$ decays with a branching fraction of 9% to each. The main advantage of the CLEO experiment compared to B factories and fixed target experiments is the very clean experimental environment with low multiplicity final states, which arises from running at or slightly above production thresholds. Background is further reduced in $e^+e^- \to \psi(3770) \to D\bar{D}$ and $e^+e^- \to D_s^\star\bar{D}_s$ data by fully reconstructing (tagging) one of the $D_{(s)}$ decaying into a hadronic final state.

2 Absolute D^0, D^+, D_s hadronic branching fractions

Precise knowledge of the absolute hadronic branching fractions of the D^0, D^+, D_s mesons is important because they are used to normalize the decays of other charmed mesons and $B_{(s)}$ mesons.

CLEO measures the absolute branching fraction of three D^0, six D^+, and six D_s^+ Cabibbo-favored hadronic decays using single tag and double tag events following a technique pioneered by the MARK-III Collaboration [2]. In single tag events only one of the $D_{(s)}$ or $\bar{D}_{(s)}$ is reconstructed in a specific final state, while in double tag events both $D_{(s)}$ and $\bar{D}_{(s)}$ mesons are reconstructed in one of the hadronic final states. The single and double tag yield can be expressed as $n_i = N_{DD}\mathcal{B}_i\epsilon_i$ and $n_{ij} = N_{DD}\mathcal{B}_i\mathcal{B}_j\epsilon_{ij}$, where N_{DD} is the number of $D^0\bar{D}^0$, D^+D^-, or $D_s^+D_s^-$ events produced; $\mathcal{B}_i$ is the branching fraction of decay mode i; ϵ_i and ϵ_{ij} are the single and double tag efficiencies. Then the

absolute branching fractions can be obtained from the double and single tag ratios and efficiencies as

$$\mathcal{B}_i = \frac{n_{ij}}{n_j}\frac{\epsilon_j}{\epsilon_{ij}}. \quad (1)$$

Since $\epsilon_{ij} \approx \epsilon_i\epsilon_j$, the branching fraction is nearly independent of the efficiency of the tagging mode, and many systematic uncertainties cancel in the ratio.

There is a difference in the kinematics of D and D_s mesons. The D and $\bar{D}$ mesons produced in $e^+e^- \to \psi(3770) \to D\bar{D}$ process have the same well defined energy (and momentum) in the center of mass frame of the colliding e^+e^- beams ($E_D = E_{\rm beam}$). In contrast, a pair of D_s mesons is produced in $e^+e^- \to D_s^{\star\pm}D_s^{\mp}$ followed by the decay $D_s^{\star\pm} \to \gamma D_s^{\pm}$ (96%) or $\pi^0 D_s^{\pm}$ (4%). Therefore, the D_s produced directly has a well defined energy and momentum in the e^+e^- center of mass frame, while the secondary D_s from the $D_s^{\star}$ decay has a much broader momentum distribution around the same value. This difference in kinematics leads to a slightly different selection strategy of $D\bar{D}$ and $D_s^{\pm}D_s^{\mp}$ events.

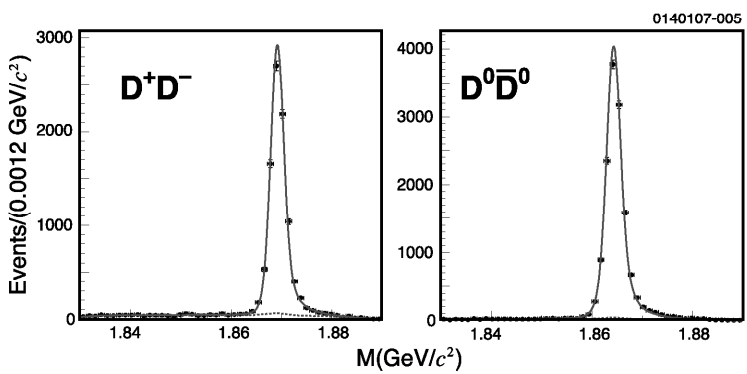

Figure 1: *Beam-constrained mass distribution of D ($\bar{D}$) candidates in double tag events summed over all decay modes.*

In order to identify (tag) the D mesons, we use $\Delta E = E_D - E_{\rm beam}$ and the beam-constrained mass, $M_{\rm bc} = \sqrt{E^2_{\rm beam} - (\vec{p}_D)^2}$, where E_D and $\vec{p}_D$ are the energy and three-momentum of the reconstructed D meson candidate. Substituting the beam energy for E_D improves the mass resolution of D candidates by an order of magnitude, to about 2 MeV/c^2. ΔE peaks around zero and $M_{\rm bc}$ peaks at the nominal D mass. We require ΔE to be consistent with zero within 3 standard deviations, and extract the number of single and double tags from a fit to the one-dimensional and two-dimensional $M_{\rm bc}$ distributions, respectively. Fig. 1 illustrates the beam-constrained mass distribution for double tag events

summed over all decay modes. In 281 pb^{-1} data, we reconstruct 230,000 single tag and $13,575 \pm 120$ double tag $D^0\bar{D}^0$ events, and 167,000 single tag and $8,867 \pm 97$ double tag D^+D^- events.

The D^0 and D^+ branching fractions are determined from a simultaneous least squares (χ^2) fit to all D^0 and D^+ single and double tag yields. The fit properly takes into account correlations among all statistical and systematic uncertainties. The preliminary branching fractions based on 281 pb^{-1} data are listed in Table 1 and compared to the 2004 PDG averages [3], which does not include our earlier results based on 56 pb^{-1} data [4], in Fig. 2.

Table 1: *Preliminary D^0 and D^+ branching fractions with statistical and systematic uncertainties.*

Decay	$\mathcal{B}(\%)$
$D^0 \to K^-\pi^+$	$3.88 \pm 0.04 \pm 0.09$
$D^0 \to K^-\pi^+\pi^0$	$14.6 \pm 0.1 \pm 0.4$
$D^0 \to K^-\pi^+\pi^-\pi^+$	$8.3 \pm 0.1 \pm 0.3$
$D^+ \to K^-\pi^+\pi^+$	$9.2 \pm 0.1 \pm 0.3$
$D^+ \to K^-\pi^+\pi^+\pi^0$	$6.0 \pm 0.1 \pm 0.2$
$D^+ \to K^0_S\pi^+$	$1.55 \pm 0.02 \pm 0.05$
$D^+ \to K^0_S\pi^+\pi^0$	$7.2 \pm 0.1 \pm 0.3$
$D^+ \to K^0_S\pi^+\pi^-\pi^+$	$3.13 \pm 0.05 \pm 0.14$
$D^+ \to K^-K^+\pi^+$	$0.93 \pm 0.02 \pm 0.03$

In order to select $D_s^{\star\pm}D_s^{\mp}$ events, we use the beam-constrained mass ($M_{\rm bc} = \sqrt{E^2_{\rm beam} - (\vec{p}_{D_s})^2}$) and the invariant mass ($M(D_s) = \sqrt{E^2_{D_s} - (\vec{p}_{D_s})^2}$) of the D_s (or $\bar{D}_s$) candidate and ignore the γ or π^0 resulting from the $D_s^\star$ decay. The beam-constrained mass is used as a proxy for the momentum of the D_s candidates (see Fig. 3). We apply a cut on $M_{\rm bc}$ that selects all of the directly-produced D_s and, depending on the decay mode, all or half of the secondary D_s. Then the invariant mass of the D_s candidate is used as a primary analysis variable to extract the number of tags. Single tag yields are obtained from fitting the one dimensional $M(D_s)$ distributions, while double tag yields are determined by counting events in the signal regions in the $M(D_s^+)$ vs. $M(D_s^-)$ plane and subtracting backgrounds estimated from sideband regions.

For this analysis, we use a binned likelihood hybrid fitter which utilizes Gaussian statistics for single tag modes and Poisson statistics for double tag modes, since the least squares χ^2 fitter used for the D branching fraction measurement is not appropriate for the small signals and backgrounds in the D_s double tag samples. The preliminary branching fractions based on 195 pb^{-1} data are summarized in Table 2 and compared to the 2006 PDG averages [5]

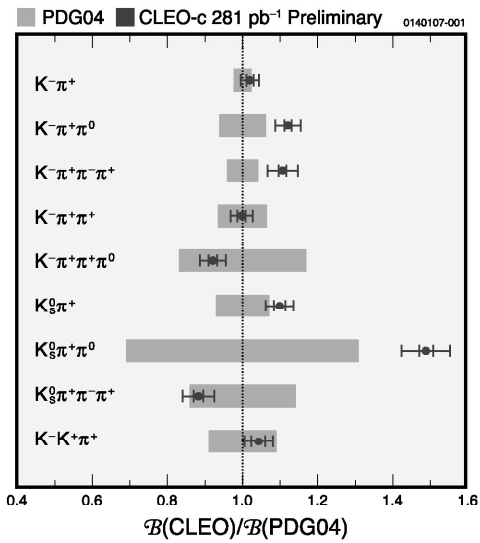

Figure 2: *Ratio of preliminary D hadronic branching fractions to the 2004 PDG averages (dots). The shaded bars represent the errors in the PDG averages.*

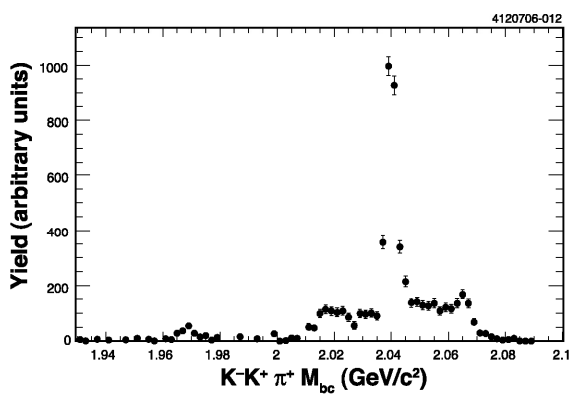

Figure 3: $M_{\rm bc}$ *distribution for* $D_s^+ \to K^+K^-\pi^+$ *events. The narrow peak at* 2.04 GeV/c^2 *is due to* D_s *produced directly, while the broad peak between* $2.01 - 2.07$ GeV/c^2 *is due to* D_s *from* $D_s^\star$ *decay.*

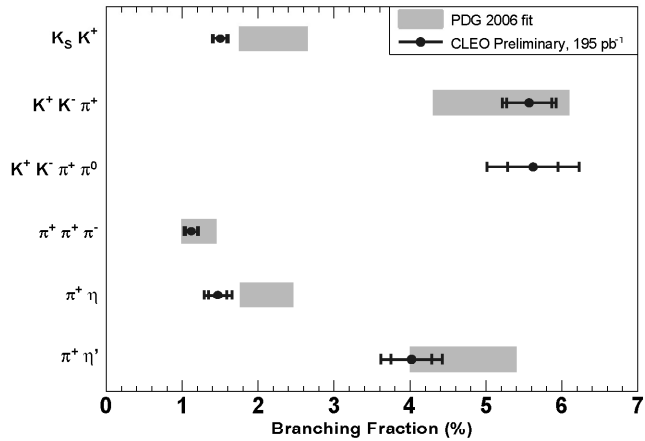

Figure 4: *Preliminary D_s branching fractions (dots with error bars) compared to the 2006 PDG averages (shaded bars).*

in Fig. 4.

Table 2: *Preliminary D_s branching fractions with statistical and systematic uncertainties.*

Decay	$\mathcal{B}(\%)$
$D^+ \to K^0_S K^+$	$1.50 \pm 0.09 \pm 0.05$
$D^+ \to K^+K^-\pi^+$	$5.57 \pm 0.30 \pm 0.19$
$D^+ \to K^+K^-\pi^+\pi^0$	$5.62 \pm 0.33 \pm 0.51$
$D^+ \to \pi^+\pi^+\pi^-$	$1.12 \pm 0.08 \pm 0.05$
$D^+ \to \pi^+\eta$	$1.47 \pm 0.12 \pm 0.14$
$D^+ \to \pi^+\eta'$	$4.02 \pm 0.27 \pm 0.30$

The decay $D_s^+ \to \phi\pi^+ \to K^+K^-\pi^+$, which is one of the largest and easiest to reconstruct, is frequently used as a reference mode to normalize other D_s decays. However, Dalitz plot analysis of this final state by the E687 and FOCUS collaborations has revealed significant signal contribution (from $f^0(980)$ or $a^0(980)$) in the relevant K^+K^- mass region. Because of this extra signal the $\phi\pi^+$ branching fraction might be ill-measured depending on the specific choice of (mass and helicity angle) cuts. Therefore, we report the partial $D_s^+ \to K^+K^-\pi^+$ branching fraction ($\mathcal{B}_{\Delta M}$) where the mass of the K^+K^- system lies within a $\pm\Delta M$ (in MeV/c^2) mass range around the ϕ mass

(1019.5 MeV/c^2), which is more useful from experimental point of view than the $\phi\pi^+$ branching fraction. The partial branching fraction with two choices of ΔM are $\mathcal{B}_{10} = (1.98 \pm 0.12 \pm 0.09)\%$ and $\mathcal{B}_{20} = (2.25 \pm 0.13 \pm 0.12)\%$.

3 D^+ and D_s^+ leptonic decays and decay constants $f_{D_{(s)}}$

In the Standard Model (SM), purely leptonic decays $D^+_{(s)} \to \ell^+\nu_\ell$ proceed via the annihilation of the constituent quarks into a virtual W^+ boson. The decay width is proportional to the decay constant, $f_{D_{(s)}}$, which encapsulates the strong interaction dynamics in the decay:

$$\Gamma(D^+_{(s)} \to \ell^+\nu) = \frac{G_F^2}{8\pi} m^2 M \left(1 - \frac{m^2}{M^2}\right)^2 |V_{cd(s)}|^2 f^2_{D_{(s)}}, \qquad (2)$$

m and M are the mass of the charged lepton and the $D_{(s)}$ meson, respectively, G_F is the Fermi coupling constant, V_{cd} (V_{cs}) is the relevant quark mixing (CKM) matrix element.

Knowledge of the decay constants is critical for the extraction of CKM matrix elements: e.g. the determination of V_{td} and V_{ts} from measurement of $B\bar{B}$ and $B_s\bar{B}_s$ mixing is limited by the uncertainty in the calculation of f_B and f_{B_s}, which currently cannot be measured directly. Experimental measurement of the D meson decay constants ($f_{D_{(s)}}$) provide an important test of strong interaction theories and validate the most promising calculations involving lattice QCD [6].

Since the decay width is a function of m^2 (helicity suppression), the decay rate to $\tau\nu$ is the largest among the three lepton flavors. Although the D^+ (D_s^+) decay rate to $\mu\nu$ is a factor of 2.65 (9.72) smaller in the SM, it is easier to measure than the decay to $\tau\nu$ because of the presence of extra neutrino(s) produced by the subsequent decay of the τ. The decay rate to $e\nu$ is suppressed by about five orders of magnitude which is well below the current experimental sensitivity. Any deviation from the SM ratios would be an indication of new physics [7].

CLEO has measured the $D^+ \to \mu^+\nu$ branching fraction in 281 pb^{-1} data collected at the $\psi(3770)$ [8]. We have fully reconstructed the D^- decaying to six hadronic final states ($K^+\pi^-\pi^-$, $K^+\pi^-\pi^-\pi^0$, $K^0_S\pi^-$, $K^0_S\pi^-\pi^-\pi^+$, $K^0_S\pi^-\pi^0$, $K^+K^-\pi^-$), which represent more then 35% of all D decays. Candidates are selected by requiring ΔE to be consistent with zero within $2.5\sigma_{\Delta E}$, and the number of tags in each mode is extracted from a fit to the $M_{\rm bc}$ distribution. The sum of all tags in the range $-2.5\sigma_{M_{\rm bc}} < M_{\rm bc} - M_D < 2.0\sigma_{M_{\rm bc}}$ is $158,354 \pm 496$ with a background of 30,677. In the selected events, we search for a single additional track consistent with a μ^+ and calculate the missing mass squared

$$MM^2 = (E_{\rm beam} - E_{\mu^+})^2 - (-\vec{p}_{D^-} - \vec{p}_{\mu^+})^2, \qquad (3)$$

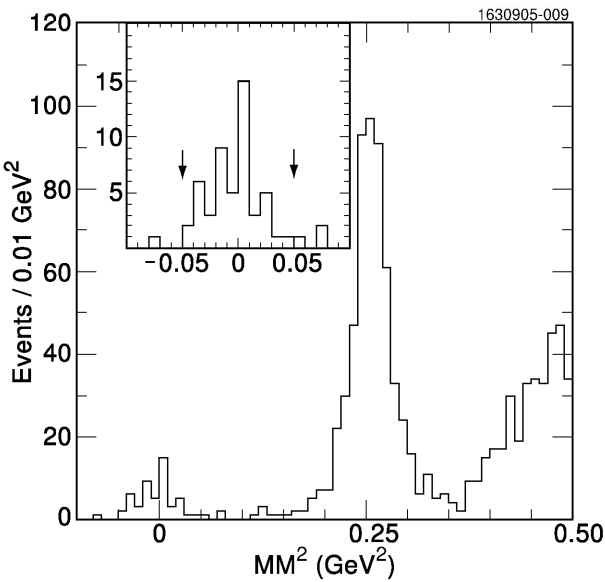

Figure 5: *The MM^2 distribution for $D^+ \to \mu^+\nu$ candidate events in data. The insert shows the region around zero where the arrows indicate the $+2\sigma$ signal region.*

where $\vec{p}_{D^-}$ is the three-momentum of the fully reconstructed D^-. The MM^2 distribution for the data is shown in Fig. 5. The peak near zero is mostly due to $D^+ \to \mu^+\nu$ signal, while the peak at 0.25 GeV^2 is from $D^+ \to \bar{K}^0\pi^+$ decays when a K_L escapes detection.

The signal region within 2σ around zero contains 50 events and the total background is estimated to be $2.8 \pm 0.3^{+0.8}_{-0.3}$ events. After background subtraction and efficiency correction, the measured branching fraction is $\mathcal{B}(D^+ \to \mu^+\nu) = (4.40 \pm 0.66^{+0.09}_{-0.12}) \times 10^{-4}$. The decay constant obtained from Eq. 2 using $|V_{cd}| = 0.2238 \pm 0.0029$ and the D^+ lifetime $(1.040 \pm 0.007$ ps) is $f_D - (222.6 \pm 16.7^{+2.8}_{-3.4})$ MeV.

We also search for $D^+ \to e^+\nu$ decay by requiring that the extra track is consistent with an electron and set a 90% C.L. upper limit of $\mathcal{B}(D^+ \to e^+\nu) < 2.4 \times 10^{-5}$ in the absence of any signal.

The branching fraction of $D_s^+ \to \mu^+\nu$ and $D_s^+ \to \tau^+\nu$ ($\tau^+ \to \pi^+\bar{\nu}$) is measured in 314 pb^{-1} data collected at e^+e^- collision energy near 4170 MeV. We fully reconstruct one D_s^- in eight hadronic decay modes ($K^+K^-\pi^-$, $K_S^0K^-$, $\eta\pi^-$, $\eta'\pi^-$, $\phi\rho^-$, $\pi^+\pi^-\pi^-$, $K^{\star-}K^{\star 0}$, $\eta\rho^-$). Tags are selected by requiring the beam constrained mass to be $2.015 < M_{\rm bc} < 2.067$ GeV/c^2 which is wide

enough to accepts both direct as well as secondary D_s from $D_s^\star$ decay. The number of tags in each mode is extracted from a fit to the invariant mass distribution of the D_s^- candidates. There is a total of $31,302 \pm 472$ reconstructed tags within 2.5σ (2σ for the $\eta\rho^-$ mode) of the D_s mass. In contrast to the hadronic branching fraction measurement, we select a γ candidate assumed to be the photon from the $D_s^\star \to \gamma D_s$ decay, and then calculate the recoil mass against the D_s^- tag and the γ:

$$MM^{\star 2} = (E_{\rm cm} - E_{D_s} - E_\gamma)^2 - (\vec{p}_{\rm cm} - \vec{p}_{D_s} - \vec{p}_\gamma)^2, \qquad (4)$$

where $E_{\rm cm}$ ($\vec{p}_{\rm cm}$) the center of mass energy and momentum of the colliding e^+e^- beam. Regardless whether the D_s^- candidate is from the $D_s^\star$ decay or not the recoil mass should peak at the D_s mass. We use kinematic constrains to improve the mass resolutions and remove multiple combinations. The recoil mass spectrum of each decay mode is fitted individually to extract the number of $D_s^\star D_s$ candidates, which result in a total of $18,645 \pm 426$ events within 2.5σ interval around the D_s mass. The invariant mass and recoil mass distributions for $D_s^- \to K^+K^-\pi^-$ candidates are shown in Fig. 6.

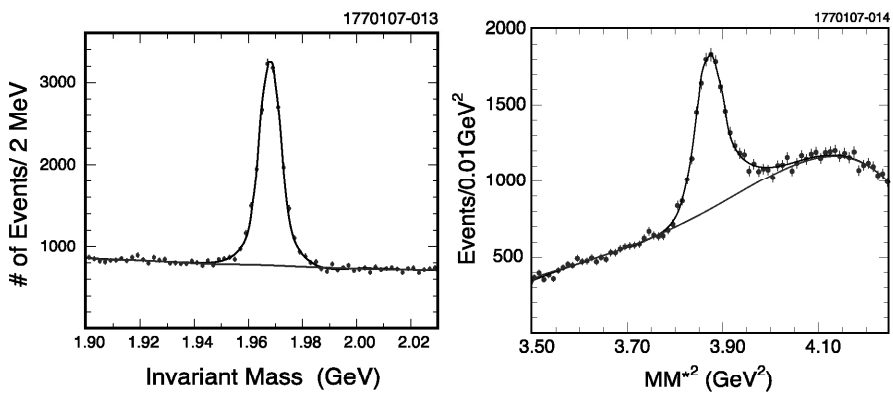

Figure 6: *Invariant mass of $D_s \to K^+K^-\pi^-$ tags (left) and the recoil mass against the same tag and an additional γ (right).*

Then we require a single additional track in the event with opposite charge to the D_s tag and no additional neutral energy cluster with more then 300 MeV. The missing mass is calculated using the energy and momentum of the candidate track (E_μ, $\vec{p}_\mu$):

$$MM^2 = (E_{\rm cm} - E_{D_s} - E_\gamma - E_\mu)^2 - (\vec{p}_{\rm cm} - \vec{p}_{D_s} - \vec{p}_\gamma - \vec{p}_\mu)^2. \qquad (5)$$

We consider three cases depending on whether the additional track is consistent with (i) muon (from $D_s \to \mu\nu$), or (ii) pion (from $D_s \to \tau\nu \to \pi\nu\bar{\nu}$), or (iii)

electron (from $D_s \to e\nu$). The separation between our muon and pion selection is not complete: the muon selection is 99% efficient for muons (with a 60% fake rate for pions), while the pion selection accepts 40% of pions (with a 1% fake rate for muons). The MM^2 distribution for the three cases is shown on Fig. 7. The peak around zero in (i) is mostly due to $D_s \to \mu\nu$ events. In contrast, $D_s \to \tau\nu \to \pi\nu\bar{\nu}$ events has a longer tail on the positive side due to the extra neutrino. Therefore, we define three signal regions: (A) $-0.05 < MM^2 < 0.05$ GeV^2 in (i) for $\mu\nu$ (92 events); (B) $0.05 < MM^2 < 0.20$ GeV^2 in (i) and (C) $-0.05 < MM^2 < 0.20$ GeV^2 in (ii) for $\pi\nu\bar{\nu}$ (31 and 25 events, respectively). The estimated background from sources other than $D_s \to \mu\nu$ or $\pi\nu\bar{\nu}$ decays is 3.5, 3.5, and 3.7 events, respectively, in the three signal regions.

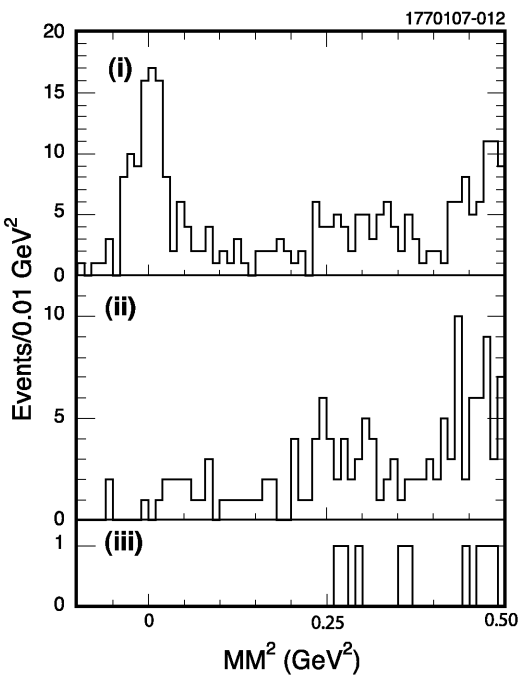

Figure 7: *The MM^2 distribution in data when the additional track is consistent with muon (i), pion (ii), or electron (iii).*

We calculate three branching fractions: $\mathcal{B}(D_s^+ \to \mu^+\nu) = (0.594 \pm 0.066 \pm 0.031)\%$ using signal region (A) only; $\mathcal{B}^{\rm eff}(D_s^+ \to \mu^+\nu) = (0.621 \pm 0.058 \pm 0.032)\%$ from combining all three signal regions (A)+(B)+(C); and $\mathcal{B}(D_s^+ \to \tau^+\nu) = (8.0 \pm 1.3 \pm 0.4)\%$ from the combined $\tau\nu$ regions (B)+(C). In the first two cases, the $D_s \to \tau\nu$ contribution is subtracted assuming the relative

decay rate between $\mu\nu$ and $\tau\nu$ final states is equal to the SM expectation and using $\mathcal{B}(\tau \to \pi\nu) = (10.90 \pm 0.07)\%$. We also set a 90% C.L. upper limit on $\mathcal{B}(D_s^+ \to e^+\nu) < 1.3 \times 10^{-4}$.

The decay constant is calculated from the most precise branching fraction ($\mathcal{B}^{\rm eff}$) using Eq. 2 with $|V_{cs}| = 0.9730$ and the D_s life time of $(500 \pm 7) \times 10^{-15}$ s: $f_{D_s} = (270 \pm 13 \pm 7)$ MeV.

We also measure $D_s^+ \to \tau^+\nu$ with a different technique utilizing the $\tau^+ \to e^+\nu\bar{\nu}$ decay with a total product branching fraction of about 1.3%. In this case, we fully reconstruct the D_s^- candidate in the event and require an additional track consistent with an e^+ but do not attempt to find the γ from the $D_s^\star$ decay. Events with additional tracks and more than 400 MeV total neutral energy in the calorimeter are vetoed (the typical energy of the γ or π^0 from $D^\star$ decay is around 150 MeV). After analyzing 195 pb^{-1} subsample of our data we obtain a preliminary branching fraction $\mathcal{B}(D_s^+ \to \tau^+\nu) = (6.29 \pm 0.78 \pm 0.52)\%$ and decay constant $f_{D_s} = (278 \pm 17 \pm 12)$ MeV.

The weighted average of these two results is $f_{D_s} = (273 \pm 10 \pm 5)$ MeV. Combined with our published f_D value we find a ratio $f_{D_s}/f_D = 1.22 \pm 0.09 \pm 0.03$. The measured decay constants are consistent with most theoretical models. In particular, recent unquenched Lattice QCD calculations [9] yield $f_D = (201 \pm 3 \pm 17)$ MeV, $f_{D_s} = (249 \pm 3 \pm 16)$ MeV, and $f_{D_s}/f_D = 1.24 \pm 0.01 \pm 0.07$.

4 Measurement of D^0 mass

Precise knowledge of the D^0 mass is not only important for its own sake but it can also help with the interpretation of the $X(3872)$ state. Because of the proximity of the X mass (3871.2 ± 0.5 MeV/c^2) to $M(D^0) + M(D^{\star 0})$, one theoretical suggestion is that the $X(3872)$ is a bound state of D^0 and $\bar{D}^{\star 0}$ mesons [10]. However, it is necessary to measure the D^0 mass with better precision than the current PDG average of 1864.1 ± 1.0 MeV/c^2 [5] in order to reach a firm conclusion.

CLEO has measured the D^0 mass [11] in $e^+e^- \to \psi(3770) \to D^0\bar{D}^0$ events using the decay $D^0 \to K_S^0\phi$ followed by $K_S^0 \to \pi^+\pi^-$ and $\phi \to K^+K^-$. In order to obtain a clean sample of signal events, the $\bar{D}^0$ has been reconstructed using the same tagging technique described in section 2, imposing loose requirements on ΔE and $M_{\rm bc}$ of the candidates. The $D^0 \to K_S^0\phi$ decay was selected because the final state pions and kaons have small momenta, and therefore the uncertainty in their measurements makes small contribution to the final result. In addition, the mass of the K_S^0 candidates can be kinematically constrained to its well known value.

Pions from the K_S^0 are required to originate from a displaced vertex and have a $M(\pi^+\pi^-)$ invariant mass in the range 497.7 ± 12.0 MeV/c^2 before the mass-constrained kinematic fit. The ϕ candidates are accepted with a

$M(K^+K^-)$ invariant mass of 1019.46 ± 15 MeV/c^2. The mass distribution of the D^0 candidates in 281 pb^{-1} data is shown in Fig. 8. A likelihood fit using a Gaussian peak and a constant background yields 319 ± 18 D^0 events and a D^0 mass of 1864.847 ± 0.150 MeV/c^2 with a mass resolution of 2.52 ± 0.12 MeV/c^2 (the errors are statistical only). The total systematic error on the mass measurement (0.095 MeV/c^2) is dominated by uncertainty in detector calibration, which is studied using the K_S mass in inclusive $D \to K^0_S X$ decays and the $\psi(2S)$ mass in exclusive $\psi(2S) \to \pi^+\pi^- J/\psi(J/\psi \to \mu^+\mu^-)$ events.

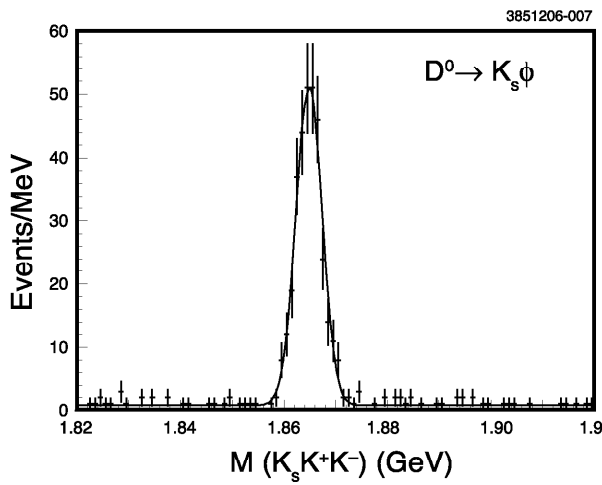

Figure 8: *The invariant mass of* $D^0 \to K^0_s\phi$ *candidates in data.*

Our final D^0 mass with statistical and systematic uncertainties is

$$M(D^0) = 1864.847 \pm 0.150 \pm 0.095 \ \ \text{MeV}/c^2. \tag{6}$$

This gives $M(D^0\bar{D}^{\star 0}) = 2M(D^0) + \Delta M_{D^{\star 0}-D^0} = 3871.81 \pm 0.36$ MeV/c^2, and leads to a binding energy of the X(3872) as a $D^0\bar{D}^{\star 0}$ molecule: $\Delta E_b = M(D^0\bar{D}^{\star 0}) - M(X) = +0.6 \pm 0.6$ MeV/c^2. The error in the binding energy is now dominated by the uncertainty in the mass of the $X(3872)$.

5 Study of $\chi_{cJ} \to h^+h^-h^0$ decays

In contrast to the 1^{--} members of the charmonium states (J/ψ, $\psi(2S)$), the decays of the χ_{cJ} $(J = 0, 1, 2)$ states are not well studied. The different decay mechanism of these states (dominated by annihilation into two (virtual) gluons and contribution from the color-octet mechanism) might provide complimen-

tary information on light hadron spectroscopy and possible glueball dynamics [12].

At CLEO, the χ_{cJ} states are produced in radiative decays of the $\psi(2S)$ and we study their decays to eight selected three-body hadronic modes: $\pi^+\pi^-\eta$, $K^+K^-\eta$, $p\bar{p}\eta$, $\pi^+\pi^-\eta'$, $K^+K^-\pi^0$, $p\bar{p}\pi^0$, $\pi^+K^-K_S$, and $K^+\bar{p}\Lambda$. We have measured branching fractions or set upper limits for the first time in most cases using about 3 million $\psi(2S)$ decays [13]. As an example, Fig. 9 illustrates the invariant mass distribution for two of the hadronic final states.

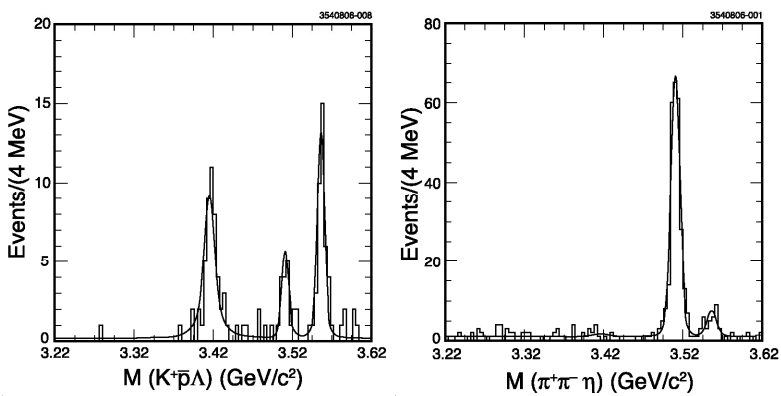

Figure 9: *The invariant mass distribution for* $\chi_{cJ} \to K^+\bar{p}\Lambda$ *(left) and* $\chi_{cJ} \to \pi^+\pi^-\eta$ *(right) candidate events in data.*

We perform a Dalitz-plot analysis of the decays with the highest statistics, $\chi_{c1} \to \pi^+\pi^-\eta$ (228 events), $K^+K^-\pi^0$ (137 events), and $\pi^+K^-K_S^0$ (234 events) in order to study the two-body resonant substructure. We use a simplified model with non-interfering resonances, which is adequate to show the largest contributions in our small sample. Fig. 10 shows the Dalitz plot and three projections for $\chi_{c1} \to \pi^+\pi^-\eta$ and the result of the fit. There are clear contributions from $a_0(980)^{\pm}\pi^{\mp}$ and $f_2(1270)\eta$ intermediate states, and a significant accumulation of events at low $\pi^+\pi^-$ mass which can be described by an S-wave (σ) resonance. This mode might offer the best measurement of the $a_0(980)$ parameters with higher statistics. The decays $\chi_{c1} \to K^+K^-\pi^0$ and $\pi^+K^-K_S^0$ are analyzed simultaneously taking advantage of isospin symmetry. We observe contributions from $K^\star(892)K$, $K^\star(1430)K$, $a_0(980)\pi$ intermediate states. It is not clear whether the $K^\star(1430)$ is $K_0^\star$ or $K_2^\star$, and other $K\pi$ and KK resonances can contribute. Addition of κK or non-resonant component does not improve the fit and the significance of their contribution remains under 3 standard deviation.

More data is required to do a complete partial-wave analysis taking into

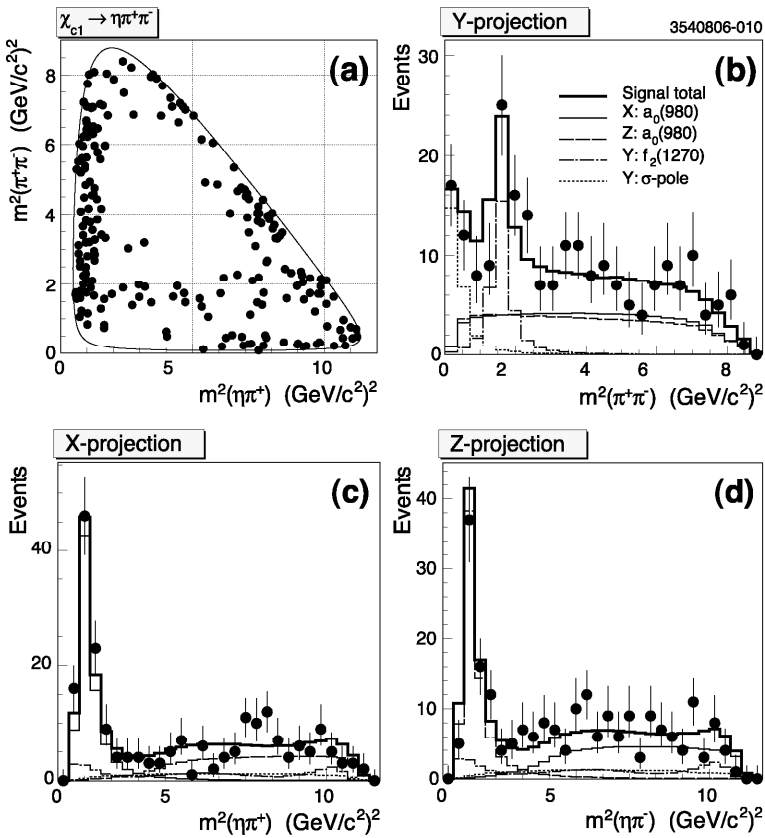

Figure 10: *Dalitz plot and projections of* $\chi_{c1} \to \pi^+\pi^-\eta$ *decay.*

account the χ_{c1} polarization properly and including interference among the resonances.

6 Summary

I have reported mostly preliminary results for hadronic and purely leptonic decays of D and D_s mesons from the CLEO-c experiment. These results represent substantial improvement over previous measurements. The D^+ and D^0 hadronic branching fractions are limited by systematic uncertainties of up to 3%. The D_s hadronic branching fractions are measured with relative uncertainties between $6-12\%$, which are dominated by statistics. The measurement

of the decay constants f_D ($f_{D_{(s)}}$) from purely leptonic decays are also statistics limited with a total relative uncertainty of 8% (4%).

I have also presented the most precise measurement of the D^0 mass, and a study of three-body hadronic decays of the χ_{cJ} states.

Precision of these and other measurements will improve in the near future with more data on the way. CLEO-c has already collected an additional 8 times more data on the $\psi(2S)$, and we plan to increase the $D\bar{D}$ and $D_s^{\star\pm}D_s^{\mp}$ data samples by a factor of 2-3 before data taking ends in April 2008.

7 Acknowledgements

I would like to thank the conference organizers for the invitation and warm hospitality, and acknowledge my colleagues at CLEO and CESR for their hard work in achieving the results presented in this report. This research was supported by the US National Science Foundation.

References

1. R. Polling, in Electronic Proceedings of the Flavor Physics and CP Violation Conference, Vancouver, 2006, (unpublished) [hep-ex/060601].
2. J. Adler *et al* (MARK-III Collab.), Phys. Rev. Lett. **60**, 89 (1988).
3. S. Eidelman *et al.* (Particle Data Group), Phys. Lett. B **592**, 1 (2004).
4. Q. He *et al.* (CLEO Collab.), Phys. Rev. Lett. **95**, 121801 (2005).
5. W.M. Yao *et al.* (Particle Data Group), J. Phys. G **33**, 1 (2006).
6. C. Davis *et al.*, Phys. Rev.Lett. **92**, 022001 (2004).
7. J. Hewett, hep-ph/9505246; A.G. Akeroyd, Prog. Theor. Phys. **111**, 295 (2204).
8. M. Artuso *et al.* (CLEO Collab.), Phys. Rev. Lett. **95**, 251801 (2005).
9. C. Aubin *et al.*, Phys. Rev. Lett. **95**, 122002 (2005).
10. M.B. Voloshin, Phys. Lett. B **579**, 316 (2004); E.S. Swanson, Phys. Lett. B **588**, 189 (2004); N.A. Törnqvist, Phys. Lett. B **590**, 209 (2004).
11. C. Cawlfield *et al.* (CLEO Collab.), Phys. Rev. Lett. **98**, 092002 (2007).
12. N. Brambilla *et al.*, CERN Report No. CERN-2005-005 [hep-ph/0412158]; Q. Zhao, Phys. Rev. D **72**, 074001 (2005).
13. S.B. Athar *et al.* (CLEO Collab.), Phys. Rev. D **75**, 032002 (2007).

RECENT RESULTS FROM BABAR

Giancarlo Piredda
INFN Sezione di Roma La Sapienza

On behalf of the BaBar Collaboration

Abstract

Two recent results are reported. The first is a measurement of the time-dependent CP asymmetry parameters in $B \to D^{(*)}_{CP} h^0$ decays, where h^0 is a light neutral meson π^0, η, or ω and D^0 decays to a CP eigenstate $K^+K^-, K^0_s\pi^0$, or $K^0_s\omega$. The second topic refers to the observation of CP violation in charmless B^0 two-body decay made possible thanks to an improved analysis technique.

1 Introduction

Two Babar recent and important achievements have been reported to this Conference. Both topics show the high level of evolution of the Babar experiment which is now approaching ten years of data taking. Both results are based on about 380 million $\Upsilon(4S) \to B\bar{B}$ events collected at the PEP-II asymmetric-energy e^+e^- collider at SLAC.

The precise measurement of $sin2\beta$ in $b \to c\bar{c}s$ deacy modes constitutes a stringent test of the Standard Model (SM). Many other decay modes that have significant contribution from loop diagrams have also been studied in an attempt to discover or constrain new physics due to unobserved heavy particles in the loops. Here we report (Sect 3) on a measurement of the time-dependent CP asymmetry parameters in $B \to D^{(*)}_{CP} h^0$ decays, where h^0 is a light neutral meson π^0, η, or ω and D^0 decays to a CP eigenstate $K^+K^-, K^0_s\pi^0$, or $K^0_s\omega$. This decay proceeds through a color suppressed tree amplitude and therefore any significant deviation from the SM prediction would be an indication of 'loop-less' new physics.

The second topic (Sect 4) refers to the observation of CP violation in charmless B^0 two-body decay made possible thanks to an improved analysis technique. Previous evidence of direct CP violation in $B^0 \to K^+\pi^-$ has been reported by Babar [2] and Belle [4] while additional measurements of $A_{K\pi}$ have also been published by the CDF [6] and CLEO [7] Collaborations. For what concerns the $B^0 \to \pi^+\pi^-$ channel, Belle recently reported [12] an observation of both time-dependent and direct CP violation using a sample of 535 million $B\bar{B}$ pairs, while our previous measurement [5] on a sample of 227 million $B\bar{B}$ pairs was statistically consistent with no CP violation. Here we present new results on both channels with improved analysis yielding sensitivities in excess of five standard deviations.

Both analyses (Sect 2) proceed through common technique which exploit the coherent production of the $B\bar{B}$ pairs coming from the $\Upsilon(4S)$ decay the high performance of the detector, and the precise knowledge of the beam energies.

2 The Analysis Technique

The Δt distribution for the signal is given by

$$F_{\pm}(\Delta t) = e^{-\Delta t/\tau}/4\tau[1 \mp \Delta\omega \pm (1-2\omega)(\eta_f S sin(\Delta m \Delta t) - C cos(\Delta m \Delta t))] \quad (1)$$

where the upper (lower) sign is for events with the tagside being identified as a $B^0(\bar{B}^0)$, η_f is the CP eigenvalue of the final state, Δm is the $B^0 - \bar{B}^0$ mixing

frequency, τ is the mean lifetime of the neutral B meson, and ω ($\Delta\omega$) is the average (difference) of the probability that a true B^0 is incorrectly identified as a $\bar{B}^0$ or viceversa. If only one diagram contributes to the B^0 decay, we expect $S = -sin2\beta$ and C=0 in the Standard Model (SM). A non-zero value of the C parameter would indicate direct CP violation.

At the B-factory it is possible to exploit the precise knowledge of the beam energy by defining the kinematical variables $m_{ES} = \sqrt{(E^{*2}_{beam} - p^{*2}_B)}$ and $\Delta E = E^*_B - E^*_{beam}$, where $E^*_{beam}(E^*_B)$ is the beam (B candidate) energy and p^*_B is the B candidate momentum, all in the c.m.system. For signal events m_{ES} peaks at the B mass value with a resolution of about 3 $MeV/c <^2$ whereas ΔE peaks around zero with a channel- dependent resolution. Therefore it is quite straightforward to reject backgrounds by appropriate selection in the m_{ES} ΔE plane.

In the Babar detector [1)], charged particles are detected and their momenta measured by a combination of a five-layer silicon vertex tracker and a 40-layer drift chamber (DCH) that covers 92% of the solid angle in the $\Upsilon(4S)$ center-of-mass (CM) frame, both operating in a 1.5-T solenoidal magnetic field. Discrimination between charged pions, kaons, and protons is provided by a combination of an internally reflecting ring-imaging Cherenkov detector (DIRC), which covers 84% of the CM solid angle in the central region of the Babar detector and has a 91% reconstruction efficiency for pions and kaons with momenta above 1.5 GeV/c, and the ionization (dE/dx) measurements in the DCH. Electrons are removed by comparing the track momentum and the associated energy deposition in a CsI(Tl) electromagnetic calorimeter, and with additional informations from dE/dx and DIRC Cherenkov angle (θ_C) measurements.

3 Time-Dependent CP Asymmetry in $B \to D^{(*)}_{CP} h^0$ Decays

We present a measurement of the time-dependent CP asymmetry in B^o meson decays to a neutral D meson and a light neutral meson through a $b \to c\bar{u}d$ color-suppressed tree amplitude. Interference between decay amplitudes with and without $B^0 - \bar{B}^0$ mixing occurs if the neutral D meson decays to a CP eigenstate. The measured time-dependent asymmetry is expected to be different from $sin2\beta$ measured in the charmonium modes due to the sub-leading amplitude $b \to u\bar{cd}$, which has a different weak phase. This amplitude is suppressed by $V_{ub}V^*_{cd}/V_{cb}V^*_{ud} \simeq 0.02$ relative to the leading order diagram. Therefore the deviation is expected to be small in the SM [10)]. No penguin diagram contribute to the decays under study and therefore they are not sensitive to the new physics that only enters loop diagrams in the B decay. However, other new physics such as Supersymmetry without R-parity conservation [9)] could

affect the tree diagram and consequently the CP asymmetry under study.

3.1 The data sample and the decay channels

The analysis uses a data sample of $349 fb^{-1}$ corresponding to $384 \times 10^6 \Upsilon(4S)$ decays into $B\bar{B}$ pairs collected during the years 1999-2006 with the Babar detector at the asymmetric-energy B-factory PEP-II. We fully reconstruct B^0 mesons decaying into a CP eigenstate. From the remaining particles in the event, the vertex of the other B is reconstructed and its flavour identified (tagging). The proper decay time difference $\Delta t = t_{CP} - t_{tag}$, between the signal $B(t_{CP})$ and B_{tag} is determined from the measured distance between the two B decay vertices projected onto the boost axis and the boost ($\beta\gamma = 0.56$) of the center of mass system. For the reconstruction of B^0 candidates we use their decays into $D^{(*)0}\pi^0$ ($D^0 \to K^+K^-, K^0_s\omega$) and $D^{(*)0}\eta(D^0 \to K^+K^-)$ with $D^{*0} \to D^0\pi^0$, and $D^0\omega(D^0 \to K^+K^-, K^0_s\omega, K^0_s\pi^0$.

3.2 The Event Selection

The selection criteria are determined by an analysis based on Monte Carlo simulation of both signal and generic decays of $B\bar{B}$ and $e^+e^- \to q\bar{q}(q = u, d, s, c)$ continuum events. We optimize the ratio $S/\sqrt{(}S + B)$ where S and B are the expected number of signal and background events respectively. The selection requirements vary by mode due to different signal yields and background levels. It is beyond the aim of this concise report to give details that could be found elsewhere [3]. It is worth mentioning, however, selection criteria adopted in modes where an ω is present among the final state particles. The vector meson ω is fully polarized in $D^0 \to K^0_s\omega$ decays. Two angular distributions of the ω decay are used to discriminate against background: $cos\theta^D_N$, the cosine of the angle between the D^0 direction in the D^0 rest frame and the normal to the decay plane of $\omega \to \pi^+\pi^-\pi^0$ in the ω rest frame, and $cos\theta^D_D$, the cosine of the angle between the direction of one pion in the rest frame of the remaining pion pair and the direction of the pion pair. The angular distributions of the signal events follow $cos^2\theta^D_N$ and $1 - cos^2\theta^D_D$ whereas they are almost flat for the backgrounds. We require $cos\theta^D_N > 0.4$ and $cos\theta^D_D < 0.9$.

3.3 Fit Yields

The signal and background yields are determined by a fit to the m_{ES} distribution using a Gaussian function for the signal peak and the Argus [11] function for the combinatorial background. The signal yields are reported in Table I, and the m_{ES} distribution are shown in Fig. 1. ....

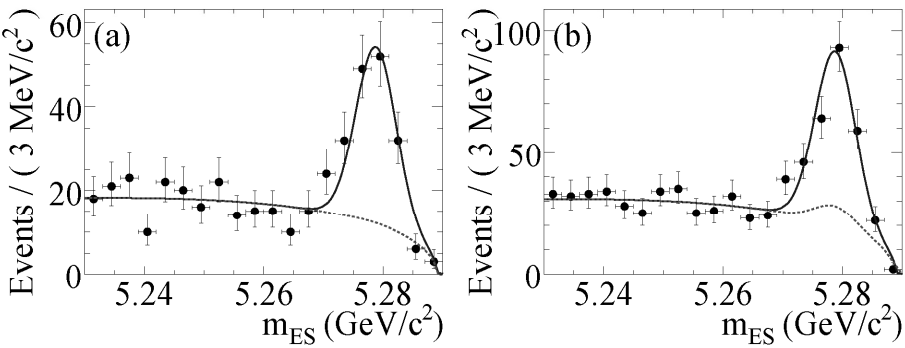

Figure 1: The m_{ES} distribution with a fit to (a) the CP-even and (b) the CP-odd modes combined in the data.The solide curve represents the overall PDF projection and the dashed curve represents the background

In order to extract CP violating parameters S and C, we fit the m_{ES} and Δt distributions of the selected flavor-tagged events using a two-dimensional probability density function (PDF). We fit all decay modes simultaneously using a total of 755 events with a well-defined tag. There are 25 free parameters including the m_{ES} shape, the background resolution function , the CP parameters of signal and background, and the fraction of the combinatorial background. We obtain $S = -0.56 \pm 0.23 \pm 0.05$ and $C = -0.23 \pm 0.16 \pm 0.04$ where the first errors are statistical and the second are systematic. The Δt distribution projections and the asymmetry $A = [N_{B^0_{tag}}(\Delta t) - N_{\bar{B}^0_{tag}}(\Delta t)]/[N_{B^0_{tag}}(\Delta t) + N_{\bar{B}^0_{tag}}(\Delta t)]$ for the events in the signal region are shown in Fig. 2.

We check the consistency between CP-even and CP-odd modes by fitting them separately and find $S_{even} = -0.17 \pm 0.37$ $S_{odd} = -0.82 \pm 0.28$ and $C_{even} = -0.21 \pm 0.25$ $C_{odd} = -0.21 \pm 0.21$.

3.4 Conclusions

This result excludes the CP conserving hypothesis at 2.3 σ level and it is in good agreement with the world average $S = -2sin\beta = -0.675 \pm 0.026$. Being statistically limited, room is left for further improvement.

4 Observation of CP Violation in $B^0 \to K^+\pi^-$ and $B^0 \to \pi^+\pi^-$

The time evolution of the asymmetry between B^0 and $\bar{B}^0$ decays to $\pi^+\pi^-$ is characterized by sine and cosine terms, as shown in eq 1. The amplitudes, referred as $S_{\pi\pi}$ and $C_{\pi\pi}$ in this channel, arise from interference of the decay

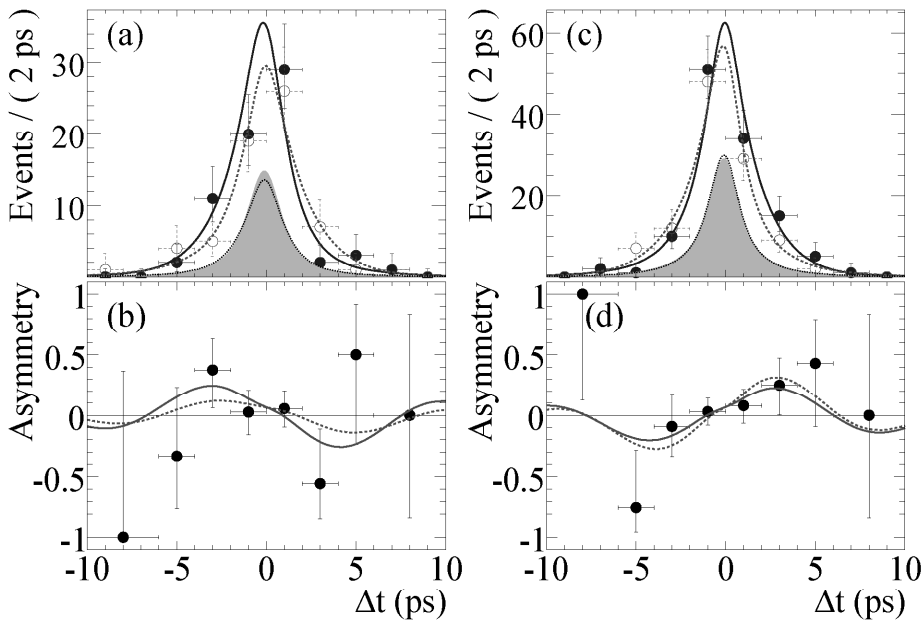

Figure 2: The Δt distributions and asymmetries for (a,b) CP-even and (c,d) CP-odd events in the signal region ($m_{ES} > 5.27 GeV/c^2$. In (a) and (c), the solid points with error bars and solid curve (open circles with error bars and dashed curve) are $B^0 - tagged$ ($\bar{B}^0 - tagged$) data points and Δt projection curves. Shaded areas ($B^0 - tagged$) and the dotted lines ($B^0 - tagged$) are backgroudn distributions. In (b) and (d), the solid curve represents the combined fit result, and the dashed curve represents the result of the fits to CP-even and CP-odd modes separately.

with B^0 $\bar{B}^0$ mixing and interference between the $b \to u$ "tree" and the higher order $b \to d$ penguin decay amplitudes, respectively.

Similarly, the direct CP-violating asymmetry $A_{K\pi}$ between the $\bar{B}^0 \to K^-\pi^+$ and $B^0 \to K^+\pi^-$ decay rates arises from interfrence between $b \to u$ "tree" and $b \to s$ "penguin" amplitudes. Furthermore the $\pi\pi$ channel plays a crucial role in the angle alpha determination. In fact it has been shown [8] that the quantity $sin2\alpha_{eff} = S_{\pi\pi}/\sqrt{(1 - C^2_{\pi\pi})}$ can be related to the angle $\alpha = arg[-V_{td}V^*_{tb}/V_{ud}V^*_{ub}]$ through a model-independent analysis using the isospin related decays $B^\pm \to \pi^\pm\pi^0$ and $B^0 \to \pi^0\pi^0$. Contributions from new particles could affect the asymmetries in these modes primarily through additional penguin B-decay amplitudes.

Table 1: *Belle and Babar $\pi\pi$ asymmetries as shown at ICHEP06*

	Babar	Belle
$B\bar{B}$ yield	347M	$535M$
$\pi^+\pi^-$	675 ± 42	1464
$S_{\pi\pi}$	$-0.53 \pm 0.14 \pm 0.02$	$-0.61 \pm 0.10 \pm 0.04$
$C_{\pi\pi}$	$-0.16 \pm 0.11 \pm 0.03$	$-0.55 \pm 0.08 \pm 0.05$

Table 2: *$K\pi$ asymmetries reported at ICHEP06*

Babar	Belle	CDF
$-0.108 \pm 0.024 \pm 0.008$	$-0.093 \pm 0.018 \pm 0.008$	$-0.086 \pm 0.023 \pm 0.009$

4.1 The Starting Point (ICHEP06)

The $\pi\pi$ results available at ICHEP 2006 edition (based on a sample of $347fb^{-}1$ are reported in the Table 1.

Babar has observed a 3.6 σ evidence for CP violation, whereas Belle claims a large direct CP violation. One additional remark is that Belle has 1.4 more $\pi\pi$ events per fb^{-1}. Moving to the $K\pi$ sector the measurements reported at ICHEP06 are shown in Table 2.

4.2 The Improved Analysis

The analysis method retains many features of our previous analyses [2) 5)]. The most significant improvement in sensitivity compared to our previous results is a 35% increase in the B_{rec} reconstruction efficiency that results from using dE/dx as a discriminating variable for the first time.

The dE/dx measurements are used to both complement the discriminating power of θ_C for charged particles within the DIRC acceptance and as standalone means of particles identification for tracks that have no θ_C information and were not included in our previous measurements. In fact, the DIRC has limited acceptance in the forward region (polar angle) and in the barrel (cracks in azimuth), and therefpre we are able to increase by 16% the $B \to Xh$ sample and by 35% the $B \to \pi\pi$ one by using the drift chamber dE/dx. In a sense we were able to increase the 'effective' luminosity of our sample by adding tracks even during the Pep-II shut-down!

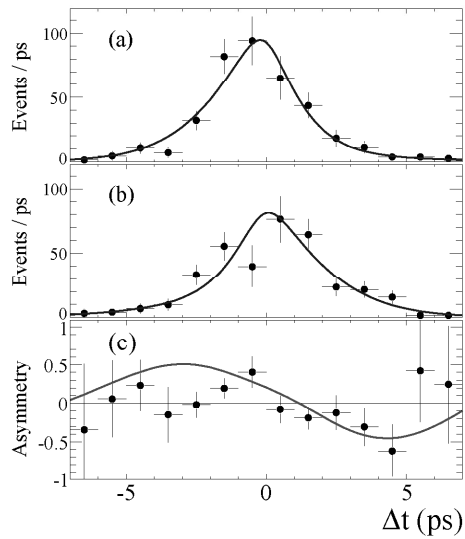

Figure 3: The background-subtracted distributions of the decay-time difference Δt in signal $B^0 \to \pi^+\pi^-$ events. The points with errors show the events where B_{tag} is identified as (a) B^0 or (b) $\bar{B}^0$. The asymmetry, defined as $(n_{B^0} - n_{\bar{B}^0})/(n_{B^0} + n_{\bar{B}^0})$, for signal events in each Δt bin, is shown in (c). The solid curves are the projection of the fit.

The dE/dx calibration takes into account variations in the mean value and resolution of dE/dx with respect to changes in the DCH running conditions over time and each track's charge, polar and azimuthal angles and the number of ionization samples.

The calibration is performed with large ($> 10^6$) high purity samples of protons from $\Lambda \to p\pi^-$, pions and kaons from $D^{*+} \to D^0\pi^+(D^0 \to K^-\pi^+)$ and additional samples of pions from 3-prong $\tau^\pm$ decays and from $K^0_s \to \pi^+\pi^-$ decays that occur in the vicinity of the interaction region.

The $K - \pi$ separation provided by the θ_C and dE/dx is complementary in the $B^0 \to h^+h^-$ kinematical domain. As it is shown in fig 4, the sensitivity varies from θ_C from 2.2σ at 4.4 GeV/c to 11σ at 1.6 GeV/c, while for dE/dx varies from less than 1.0σ at 1.5 GeV/c to 1.9σ at 4.4 GeV/c.

4.3 The Results

Fitting the final sample of about 3×10^5 events, we find $N_{\pi\pi} = 1139 \pm 49$ and $N_{K\pi} = 4372 \pm 82$ and measured the following asymmetries:

$$S_{\pi\pi} = -0.60 \pm 0.11 \pm 0.03(5.2\sigma) \ ,$$

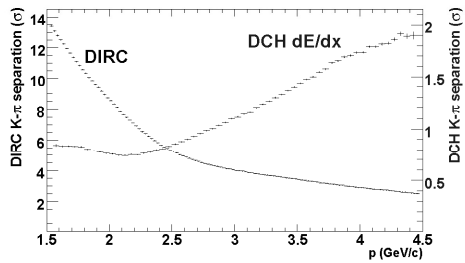

Figure 4: $K - \pi$ separation sensitivity as a function of the momentum in $B^0 \to h^+h^-$ decays

$C_{\pi\pi} = -0.21 \pm 0.09 \pm 0.02(2.2\sigma)$,
$A_{K\pi} = -0.107 \pm 0.018^{+0.007}_{-0.004}(5.5\sigma)$
where the first error is statistical and the second systematic.

As shown in fig 5, the ($S_{\pi\pi} = 0$,$C_{\pi\pi} = 0$) solution is excluded at the 8×10^{-8} level. We care to notice here that these results are obtained on an integrated luminosity of $383 fb^{-1}$ and therefore it is evident that the improvement since ICHEP06 is much better that the mere statistics, due to the improved technique!

5 Concluding Remarks

The Babar program is to take data up to the end of 2008. The increment in luminosity will allow further improvements on the sensitivity of both measurements submitted to these Rencontres.

6 Acknowledgements

I wish to thank the organizers for the invitation to this very interesting Conference held in a spectacular site.

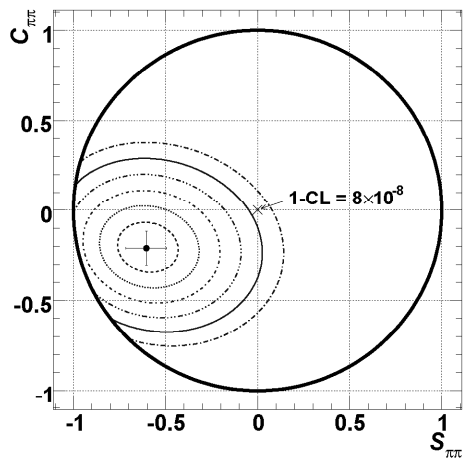

Figure 5: $S_{\pi\pi}$ and $C_{\pi\pi}$: the central values, errors and confidence level corresponding to 1 through 6 σ going from the inner toward the outer region. The (0,0) solution is excluded at the 8×10^{-8} level.

References

1. BABAR Collaboration, B. Aubert *et al*, Nucl. Instrum. Methods Phys. Res., Sect A **479**, 1 (2002).
2. BABAR Collaboration, B. Aubert *et al*, Phys. Rev. Lett. **93**, 131801 (2004).
3. BABAR Collaboration, B. Aubert *et al*, arXiv:hep-ex/0703019 .
4. Belle Collaboration, S. Chao *et al*, Phys. Rev. Lett. **93**, 191802 (2004).
5. BABAR Collaboration, B. Aubert *et al*, Phys. Rev. Lett. **95**, 151803 (2005).
6. A. Abulencia *et al*, (CDF Collaboration), Phys. Rev. Lett. **97**, 211802(2006).
7. S.Chen *et al*, (CLEO Collaboration), Phys. Rev. Lett. **85**, 525(2000).
8. M.Gronau and D.London, Phys. Rev. Lett. **65**, 3381 (1990)
9. Y.Grossman and M.P.Worah Phys. Rev. Lett. B**395**, 241(1997)
10. R.Fleischer, Phys. Rev. Lett. B**562**, 234(2003)
11. H.Albrecht *et al*, (ARGUS Collaboration), Phys. Rev. Lett. B**241**, 278 (1990).
12. Belle Collaboration, K.Ishino *et al*, arXiv:hep-ex/0608035, submitted to Phys. Rev. Lett.

SESSION VI – SEARCHES FOR NEW PHYSICS

• *Thomas Nunnemeann*	Searches for the Higgs Boson and SuperSymmetry at the Tevatron
• *Ben Brau*	Non-SUSY Exotics Searches at the Tevatron
• *Aleksander Filip Żarnecki*	Electroweak Studies and Search for New Phenomena
• *George Redlinger*	Physics Beyond the Standard Model in ATLAS at the Startup of the LHC
• *Mikhail Vysotsky*	New (Virtual) Physics in the Era of the LHC
• *Dmitri Kazakov*	SUSY Phenomenology & SUSY Dark Matter
• *Yoram Rozen*	Hiding the Higgs at the LHC?

SEARCHES FOR THE HIGGS BOSON AND SUPERSYMMETRY AT THE TEVATRON

Thomas Nunnemann
Department für Physik, Ludwig-Maximillians Universität München
Am Coulombwall 1, D-85748 Garching, Germany
On behalf of the D0 and CDF collaborations

Abstract

The D0 and CDF experiments at the proton-antiproton collider Tevatron have extensively searched for the Higgs boson and signals of supersymmetry using a wide range of signatures. The status of these searches is reviewed with a focus on recent measurements.

1 Introduction

At the Tevatron collider, one of the main challenges is the search for the Higgs boson and for supersymmetric particles. The high integrated luminosities being collected by both the CDF and D0 experiments enable searches with unprecedented sensitivity. At the beginning of 2007, both experiments have recorded data sets of more than $2\,\text{fb}^{-1}$. Recent results obtained with up to $1.1\,\text{fb}^{-1}$ are presented in this note. All limits quoted are at 95% confidence level.

2 Searches for the standard model Higgs boson

In the standard model (SM) the Higgs mechanism is responsible for the electroweak symmetry breaking, thereby generating the masses of the Z and W bosons. As a consequence of this mechanism a single neutral scalar particle, namely the Higgs boson, remains after the symmetry breaking. Assuming the validity of the standard model, global fits to the electroweak data prefer a relatively low mass for the Higgs boson, $m_H = 85^{+39}_{-28}\,\text{GeV}$ [1], while direct searches at the LEP collider set a lower bound on the mass of $114.4\,\text{GeV}$ [2].

At low masses, $m_H \lesssim 135\,\text{GeV}$, the SM Higgs boson dominantly decays via $H \to b\bar{b}$. For the main production channel, which is the gluon-gluon fusion process $gg \to H$ this leads to signatures which are irreducible from QCD production of $b\bar{b}$ pairs. Therefore, at the Tevatron the highest sensitivity for low mass Higgs bosons is obtained from the associated production of the Higgs boson with the weak bosons, i.e. WH and ZH. At high masses the SM Higgs boson predominantly decays into WW boson pairs, which has a manageable background for the $gg \to H$ production mode.

2.1 Low-mass Higgs boson, $m_H \lesssim 135\,\text{GeV}$

Both the CDF and D0 collaborations searched for low mass Higgs bosons using the $WH \to \ell\nu b\bar{b}$, $ZH \to \nu\bar{\nu}b\bar{b}$, and $ZH \to \ell\ell b\bar{b}$ production and decay modes. Dominating backgrounds in these searches are the associated production of the weak bosons with $b\bar{b}$ pairs, $Wb\bar{b}$ and $Zb\bar{b}$, as well as the associated production Wjj and Zjj with jets originating from light-flavor quarks, which are falsely identified as b-jets.

The CDF collaboration recently presented a search for the Higgs boson in $WH \to \ell\nu b\bar{b}$ production based on an integrated luminosity of $1\,\text{fb}^{-1}$ [3]. The event selection required a reconstructed electron or muon with a transverse momentum $p_T > 20\,\text{GeV}$, two jets with transverse energy $E_T > 15\,\text{GeV}$ and large missing transverse momentum $\not\!\!E_T > 20\,\text{GeV}$. The jets were identified to originate from b quarks using secondary vertex (SV) and neural network (NN) tagging algorithms. A resonant peak in the dijet mass distribution, M_{jj},

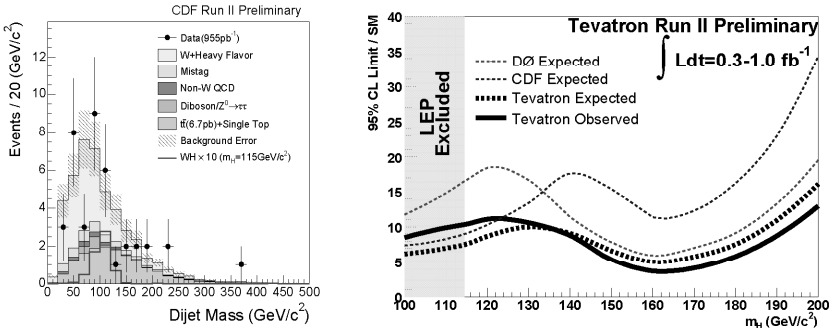

Figure 1: *Left: dijet mass distribution in $W+ \geq 2$ jets events with two secondary vertex tags. Right: combined CDF and DO limits on SM Higgs production, normalized to the predicted SM cross section.*

indicative of $H \to b\bar{b}$ was searched for. The M_{jj} distribution for events with two heavy-flavor jets identified using the SV tagger is shown in Fig. 1 together with the background prediction and the expected Higgs signal. Upper limits on the production cross sections, σ_{95}, were derived as function of Higgs boson mass m_H. For $m_H \sim 115\,\text{GeV}$ the cross section limit from this measurement alone compared to the SM prediction, σ_{SM}, corresponds to a sensitivity of $\sigma_{95}/\sigma_{SM} \sim 20$.

The search for $ZH \to \nu\bar{\nu}b\bar{b}$ production has also a notable sensitivity to $WH \to \ell\nu b\bar{b}$ as the lepton might be undetected. Based on a data sample of $1\,\text{fb}^{-1}$, the CDF collaboration searched for the Higgs boson in events with large $\not\!\!E_{\text{T}}$ and two jets, of which one was required to be tagged [4]. In addition to Zjj, a large background contribution was found to be due to QCD multijet production. For $m_H \sim 115\,\text{GeV}$ a sensitivity of $\sigma_{95}/\sigma_{SM} \sim 30$ was separately obtained for ZH and WH production. Combining both production modes the sensitivity was $\sigma_{95}/\sigma_{SM} \sim 16$.

The $ZH \to \ell\ell b\bar{b}$ channel is disfavored due to the low $Z \to \ell\ell$ branching fraction. Nevertheless, the clear event topology provides good background separation. The D0 collaboration recently presented a search in this channel based on an integrated luminosity of $0.9\,\text{fb}^{-1}$ [5]. The analysis required a reconstructed ee or $\mu\mu$ pair with a dilepton mass consistent with the Z boson mass and at least two jets which were required to be identified as b jets using the NN tagger. For central pseudorapidities, $|\eta| < 1.5$, a b-tagging efficiency of 72% at a light-jet fake rate of 4% was obtained. This search and a similar CDF measurement [6] were found to have sensitivities $\sigma_{95}/\sigma_{SM} \sim 25 - 30$ at

$m_H \sim 115\,\text{GeV}$.

2.2 High-mass Higgs boson, $m_H \gtrsim 135\,\text{GeV}$

The dominant decay mode for $m_H \gtrsim 135\,\text{GeV}$ is $H \to WW^{(*)}$. The W decays into an electron or muon are used to suppress the QCD multijet background. As the Higgs boson has spin-0, the final-state leptons are predominately produced with small azimuthal separation due to spin-correlations between them. Therefore, the Higgs signal can be discriminated from the electroweak production of WW boson pairs.

The D0 collaboration performed a preliminary search based on $0.95\,\text{fb}^{-1}$ using the ee, $e\mu$, and $\mu\mu$ final states [7]. At $m_H \sim 160\,\text{GeV}$, where this channel has optimal sensitivity, a cross-section ratio $\sigma_{95}/\sigma_{SM} \sim 4$ was obtained, which excludes models with four fermion families [8] for $m_H \sim 150 - 185\,\text{GeV}$.

2.3 Combined limits on Higgs boson production

The CDF and D0 limits on SM Higgs production were combined for the first time in summer 2006 [9]. Fig. 1 shows the cross-section ratio σ_{95}/σ_{SM} as function of assumed Higgs boson mass m_H. The combination does not yet include all searches presented above. After the conference a new combination with significantly improved cross-section limits was obtained, which also includes additional results obtained since then.

3 Searches for neutral supersymmetric Higgs bosons

Models with two Higgs-doublets, such as the minimal supersymmetric extension of the standard model (MSSM), predict five physical Higgs bosons, of which three (h, H, A) have neutral electric charge. The phenomenology at large $\tan\beta$ (the ratio of the Higgs vacuum expectation values) is remarkable: The cross section for the gluon-gluon fusion process $gg \to H$ and the associated production $b\bar{b}H$ is largely enhanced and the CP-odd A boson is nearly mass-degenerate with either the light or heavy CP even state, h or H, respectively. The leading decay modes of the two mass-degenerate states, both denoted as ϕ, are $\phi \to b\bar{b}$ ($\sim 90\%$) and $\phi \to \tau\tau$ ($\sim 10\%$). Despite the smaller branching fraction, Higgs searches in the di-τ channel have the advantage of a much smaller background level from multi-jet production.

3.1 Supersymmetric Higgs in multi-jet events: $b\bar{b}\phi \to b\bar{b}b\bar{b}$

The D0 collaboration searched for the supersymmetric Higgs boson in the channel $b\bar{b}\phi \to b\bar{b}b\bar{b}$ using the dijet mass distribution in events with three identified

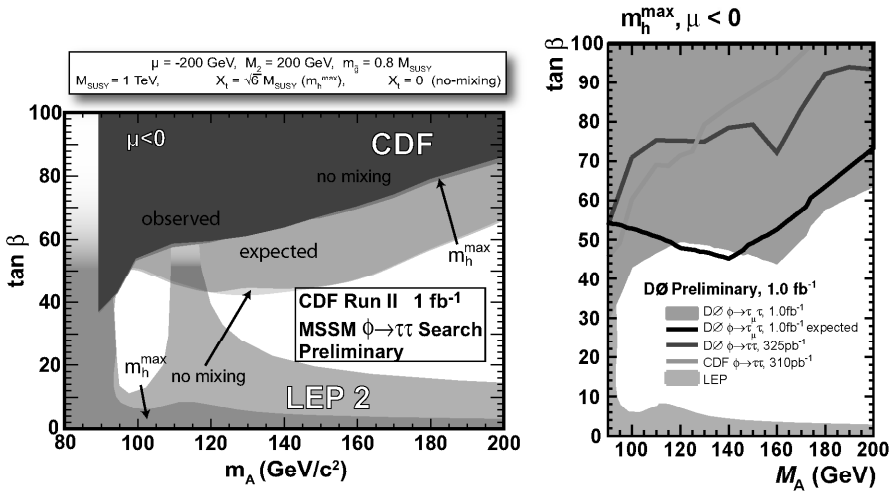

Figure 2: *Excluded regions in the tan$\beta - m_A$ plane obtained by the CDF and D0 collaborations.*

heavy-flavor jets. The published analysis [10] based on an integrated luminosity of 260 pb^{-1}excludes a region at high $\tan\beta$, e.g. for $m_A \sim 120$ GeV the constraint on $\tan\beta$ is $\tan\beta \lesssim 50 - 60$ (depending on the assumed mixing in the scalar top quark sector). The preliminary update based on 0.9 fb^{-1} found exclusion limits improved by about a third [11].

3.2 Supersymmetric Higgs decaying to tau pairs: $\phi \to \tau\tau$

Both, the CDF and D0 collaborations searched for the MSSM Higgs boson decaying via $\phi \to \tau\tau$ using data samples of 1 fb^{-1} each. Whereas the CDF collaboration analyzed τ-decays leading to $e\mu$, $e\tau_h$, and $\mu\tau_h$ final states [12] (with τ_h denoting hadronically decaying τ's), the D0 selection [13] required one τ decaying into a muon. The CDF collaboration observed a small excess of events ($< 2\sigma$, only $e\tau_h$ and $\mu\tau_h$ channels) in the visible mass distribution, which approximates the mass of the hypothetical di-τ resonance. This non-significant excess was not confirmed by the D0 search. The exclusion regions in the plane given by m_A and $\tan\beta$ are shown in Fig. 2. The exclusion regions depend only very mildly on assumptions on the sign of the Higgs mass term μ and the mixing in the scalar top quark sector.

4 Searches for supersymmetry

Supersymmetry (SUSY) is one of the most appealing extensions of the SM, as it solves the hierarchy problem and could provide a candidate for cold dark matter. Supersymmetric models predict the existence of scalar leptons and quarks and spin-1/2 gauginos as super-partners of the standard model leptons, quarks and gauge bosons. R-parity is introduced as a new multiplicative quantum number to differentiate between standard model ($R = 1$) and supersymmetric ($R = -1$) particles. As a consequence of the assumption of R-parity conservation, supersymmetric particles are produced in pairs and the lightest supersymmetric particle (LSP) needs to be stable. In supersymmetric models inspired by supergravity, the lightest neutralino $\tilde{\chi}_1^0$, which is a mixture of the super-partners of the neutral electroweak gauge and Higgs bosons, is usually assumed to be the LSP and is a candidate for cold dark matter. In the following only searches for supersymmetry inspired by minimal supergravity (mSUGRA) and with the assumption of R-parity conservation are presented. Both, the CDF and DO collaborations performed many searches within other supersymmetric models.

4.1 Gaugino pair production

The associated production of a chargino-neutralino pair, $\tilde{\chi}_1^{\pm}\tilde{\chi}_2^0$, can lead to event topologies with three leptons, which has a low SM background. The third lepton might be relatively soft, depending on the mSUGRA parameter space.

Both, the CDF and D0 experiments have searched for the tri-lepton signature taking into account all three lepton flavors and using integrated luminosities up to $1.1\,\mathrm{fb}^{-1}$ [14, 15]. The sensitivity could be increased by not requiring explicit lepton identification for the third lepton and by including final states consisting of a same-sign di-lepton pair. Both experiments derived limits on the cross-section times branching fraction, shown in Fig. 3, which are compared to different mSUGRA inspired scenarios to obtain lower bounds on the chargino mass.

4.2 Scalar quark and gluino production

If sufficiently light, squarks and gluinos could be produced in pairs at the Tevatron. If $M(\tilde{q}) < M(\tilde{g})$, mostly pairs of squarks would be produced, which decay via $\tilde{q} \to q\tilde{\chi}_1^0$, resulting in an event signature of two acoplanar jets and $\not\!\!E_{\mathrm{T}}$. If $M(\tilde{g}) > M(\tilde{q})$, gluinos would decay according to $\tilde{g} \to q\bar{q}\tilde{\chi}_1^0$ and their pair-production would give topologies with many jets and $\not\!\!E_{\mathrm{T}}$. In the case of $M(\tilde{g}) \approx M(\tilde{q})$ and $\tilde{q}\tilde{g}$-production the final state is expected to often consist of three jets and $\not\!\!E_{\mathrm{T}}$.

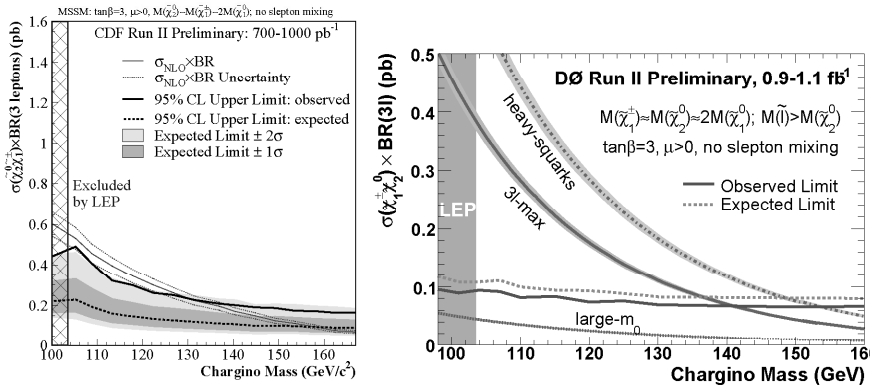

Figure 3: *Limit on associated $\tilde{\chi}_1^{\pm}\tilde{\chi}_2^0$ production in comparison with the expectation of several SUSY scenarios obtained by the CDF and D0 collaborations.*

The D0 collaboration searched for the production of squarks and gluinos using three different event selections which were targeted at the scenarios described above [16]. The exclusion region in the plane given by the squark and gluino masses is shown in Fig. 4. For the most conservative assumptions (and for $\tan\beta = 3$, $A_0 = 0$, $\mu < 0$) squark and gluino mass limits of $m_{\tilde{q}} > 375\,\text{GeV}$ and $m_{\tilde{g}} > 289\,\text{GeV}$, respectively, were derived. When interpreting the cross-section limits within mSUGRA the constraints on the common scalar and gaugino masses at the unification scale, m_0 and $m_{1/2}$, could be improved with respect to limits from LEP.

4.3 Scalar top and bottom quark production

Due to a possible large mixing between the super-partners of the left and right handed top (bottom) quarks, the lighter eigenstate of the scalar top (bottom) quark might be significantly lighter than the super-partners of the other quarks. Both experiments searched for the pair production of scalar bottom and scalar top quarks [17, 18, 19]. The scalar bottom quarks were assumed to decay via $\tilde{b} \to b\tilde{\chi}_1^0$ and the scalar top quarks via the loop induced decay $\tilde{t} \to c\tilde{\chi}_1^0$. Exclusion regions in the plane given by the sbottom (stop) and neutralino masses were derived reaching $m_{\tilde{b}} \approx 220\,\text{GeV}$ and $m_{\tilde{t}} \approx 130\,\text{GeV}$, respectively.

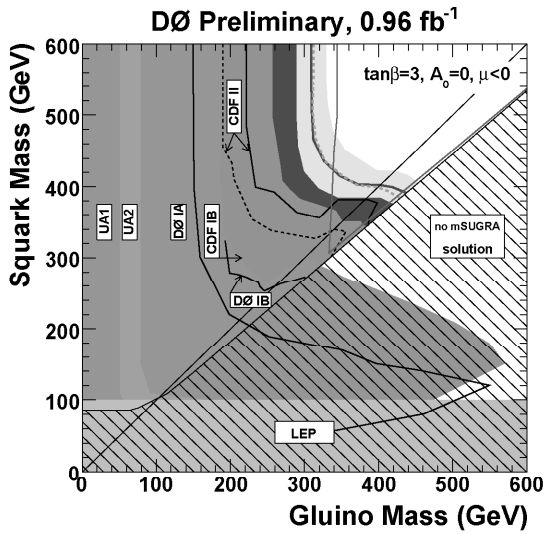

Figure 4: *Exclusion region in the squark and gluino mass plane.*

5 Conclusions and Perspectives

The CDF and D0 experiments at the Tevatron collider have performed a multitude of searches for the standard model and supersymmetric Higgs boson as well as for signals of supersymmetry. At the time of the conference, the searches for the SM Higgs boson which include luminosities up to $1\,\mathrm{fb}^{-1}$ reached a sensitivity of a factor 10 (3) times the SM expectation at $m_H \approx 115\,\mathrm{GeV}$ ($m_H \approx 160\,\mathrm{GeV}$). Imminent improvements of the limits are expected from the increased luminosity and refinements in the b-tagging and the event selection. The "hint" of an MSSM Higgs boson at $m_A \approx 160\,\mathrm{GeV}$ obtained by CDF was not confirmed by D0. No signal for supersymmetry has yet been found at the Tevatron and stringent limits, which are significantly improved compared to Run I, were set. At the beginning of 2007 both experiments have recorded integrated luminosities exceeding $2\,\mathrm{fb}^{-1}$ and are expected to collect much larger data sets during the full period of Run II. Thus, the sensitivity to the production of the Higgs boson and supersymmetric particles will substantially improve in the following years.

Acknowledgments

I would like to thank my colleagues from the CDF and D0 collaborations for providing their excellent results and the organizers for the stimulating conference.

References

1. LEP Collaborations ALEPH, DELPHI, L3, OPAL, J. Alcaraz *et al.*, hep-ex/0612034.
2. LEP Working Group for Higgs boson searches, R. Barate *et al.*, Phys. Lett. **B565**, 61 (2003).
3. CDF Collaboration, CDF note 8390.
4. CDF Collaboration, CDF note 8442.
5. D0 Collaboration, D0 note 5275-CONF.
6. CDF Collaboration, CDF note 8422.
7. D0 Collaboration, D0 notes 5063-CONF and 5194-CONF.
8. E. Arik *et al.*, Eur. Phys. J. C **26**, 9 (2002).
9. CDF and D0 Collaborations, CDF note 8384 and D0 note 5227-CONF.
10. V. M. Abazov *et al.* [D0 Collaboration], Phys. Rev. Lett. **95**, 151801 (2005).
11. D0 Collaboration, D0 note 5503-CONF.
12. CDF Collaboration, CDF note 8676.
13. D0 Collaboration, D0 note 5331-CONF.
14. CDF Collaboration, CDF note 8653.
15. D0 Collaboration, D0 note 5348-CONF.
16. D0 Collaboration, D0 note 5312-CONF.
17. CDF Collaboration, CDF note 8411.
18. V. M. Abazov *et al.* [D0 Collaboration], Phys. Rev. Lett. **97**, 171806 (2006).
19. V. M. Abazov *et al.* [D0 Collaboration], Phys. Lett. B **645**, 119 (2007).

NON-SUSY EXOTICS SEARCHES AT THE TEVATRON

Benjamin P. Brau
(For the CDF and DØ Collaborations)
University of California, Santa Barbara

Abstract

The DØ and CDF experiments have collected more than 2 fb^{-1} in Run II of Fermilab's Tevatron, and have many recent search results which use 1 fb^{-1} or more. Here I summarize the results of a variety of searches for physics beyond the Standard Model with an emphasis on searches for very exotic phenomena. I will present the status of model-inspired searches for large extra dimensions, gravitons, extra quarks, new gauge bosons, leptoquarks, as well as a variety of signature-based searches.

1 Introduction

The CDF and DØ experiments have many recent results [1] from direct searches for evidence of physics beyond the standard model (SM), many of which use 1 fb^{-1} or more. These searches generally fall into two categories, those optimized for sensitivity to a particular new-physics model (model-inspired), and those designed to be generally sensitive to new physics in a particular final state or states (signature-based). Here I summarize the results of many of these recent searches. Slides from my presentation [2] include relevant plots from these searches.

2 Model-Inspired Searches

2.1 Searches for New Gauge Bosons

Many extensions of the standard model which attempt to unify the fundamental forces and solve the hierarchy problem include new massive gauge bosons which would appear as narrow resonances which couple to leptons. CDF has searched for a new neutral gauge boson in its decay to electrons with 1.3 fb^{-1}. The main background to this search is from SM Drell-Yan production, which is irreducible. Other sources of background include di-jet production and other electroweak processes. The dielectron invariant mass spectrum is scanned for narrow resonances in the range 150-900 GeV. The data are consistent with a background-only hypothesis, and limits are obtained on the production cross-section times branching fraction, $\sigma \times \text{BF}(Z' \to ee)$ as a function of m_{ee}, which is approximately 10 fb for much of the mass region searched. Assuming standard model couplings, this corresponds to $m_{Z'} > 923\,\text{GeV}/c^2$ at 95% CL.

DØ has searched for a charged gauge boson W' decaying to $e\nu$ in the $e+\not\!\!E_T$ channel with 0.9 fb^{-1} of data. The dominant background for this search is SM W production. Other background sources are small and include electroweak processes and QCD. No significant excesses are seen in the transverse mass m_T of the $e-\nu$ system, so limits are set on the production cross-section times branching fraction, $\sigma \times \text{BF}(W' \to e\nu)$ as a function of m_T. Assuming standard model couplings, this corresponds to $m_{W'} > 965\,\text{GeV}/c^2$ at 95% CL.

Table 1: *Limits on M_D for 2-6 extra dimensions.*

n	2	3	4	5	6
M_D (TeV/c^2)	> 1.33	> 1.09	> 0.99	> 0.92	> 0.88

2.2 Extra Dimensions

Extra dimensions have been proposed as one possible way to explain the hierarchy of Planck and weak scales. In the ADD [3] model, gravity alone propagates in one or more large extra dimensions, each with some finite volume characterized by R. Because only gravity propagates in the extra dimensions, its strength is diluted relative to other forces. We therefore observe an effective lower-dimensional theory whose scale M_D is related to the the Planck scale and the number and size of the extra dimensions

$$M_{\text{Planck}} = R^n M_D^{2n+1}. \quad (1)$$

The ADD model predicts a Kaluza-Klein tower of graviton states which might be produced at the Tevatron. If produced, the graviton could propagate into the extra dimension(s), resulting in missing transverse energy ($\not\!\!E_T$) from the graviton recoiling against the parton involved in its production. CDF has searched for such a signature in 1.1 fb^{-1} of data by looking for events containing a single energetic jet and $\not\!\!E_T$. The main (irreducible) background for this search is SM Z^0 + jets production, where the Z^0 decays to neutrinos. Other backgrounds include W + jets, where the lepton from the W decay goes undetected, and QCD where $\not\!\!E_T$ is mis-measured. Since the rates for leptonic Z^0 decays are known, data $Z^0 \to ee$ control samples are used to predict the $Z^0 \to \nu\nu$ backgrounds. The background predictions agree well with the observed number and shape of the $\not\!\!E_T$ spectrum in data, so limits are set on the effective Planck mass depending on the number of extra dimensions of approximately 1 TeV, shown in Table 1.

In the simplest Randall-Sundrum warped extra dimension model [4], the Standard model is confined to a lower-dimensional brane. Gravity propagates in the extra dimension and is localized near a second lower-dimensional brane, and is diluted in the warped extra dimension by a factor e^{-kr_c}. On one of the branes, this factor scales down the mass parameters in the higher dimensional Lagrangian, thereby generating a mass scale hierarchy. The product kr_c, where k is on the scale of the higher-dimensional Planck mass and r_c is the size

of the extra dimension, can be chosen to obtain the observed electroweak-Planck hierarchy. Evidence of the extra dimension at particle Colliders would be observable in the form of a Kaluza-Klein tower of discrete, massive graviton resonances.

CDF has searched for such resonances with 1.1 fb^{-1} of data in the exclusive $G \to \gamma\gamma$ channel, which they combine with $G \to ee$ limits obtained from the dielectron search. DØ searches both ee and $\gamma\gamma$ final states simultaneously with 1.1 fb^{-1} of data by requiring energy deposits in their calorimeter be consistent with electromagnetic origin, but with no track requirement or veto. Neither DØ nor CDF sees any significant excess, and both set limits for an assumed coupling $k/M_{\text{pl}} = 0.1$ of $m_G > 865$ and 889 GeV/c^2 respectively.

Gravitons also couple to pairs Z^0 bosons with a larger branching fraction than ee or $\gamma\gamma$, and CDF has searched for this in 1.1 fb^{-1} of data in the four electron final state. The background for this mode is very small, and SM Z^0Z^0 production at high mass is negligible. Because of the branching fraction penalty for Z^0 to electrons, the expected signal is also only a fraction of an event. To maximize sensitivity, electron selection is very loose, and the kinematics of the two Z^0 resonances in the final state are utilized to reject backgrounds with a χ^2 variable encoding consistency of the two Z^0 masses. No high mass events are seen, but one lower mass event observed is consistent with SM Z^0Z^0 production.

2.3 Compositeness

If electrons are composite objects, their constituents could in principle be excited to higher-energy states. DØ has searched for evidence of compositeness by looking for evidence of an excited electron (e^*) produced in the contact interaction $p\bar{p} \to ee^*$, with e^* decaying to $e\gamma$. The main background for this search is Drell-Yan produced in association with a photon. No significant excess is observed, and limits are set as a function of the compositeness scale Λ. For $\Lambda = 1$ TeV, $m_{e^*} > 756$ GeV/c^2 at 95% CL.

2.4 Leptoquarks

Leptoquarks, particles containing both lepton number and color may provide a connection between quark and leptons at higher energy scales. DØ has searched in 1 fb^{-1} of data for pair production of second-generation scalar leptoquarks, where one leptoquark decays to a muon and a c quark, and the other decays

to a muon neutrino and an $\bar{s}$ quark. The signature is a muon, $\not\!\!E_T$, and two jets. The main background is from SM W+jets, which is estimated from Monte Carlo and normalized to data before final selection. No excess is observed, and they set a limit on the mass of the leptoquark at 214 GeV/c^2 at 95% CL.

2.5 New Heavy Quarks

CDF has performed a search for a fourth generation quark b' which couples to Z^0 in conjunction with jets in 1.1fb^{-1} of data. The coupling of a fourth generation quark is constrained to be small, so the direct decay to $W + c$ is suppressed, and the dominant decay would be through a loop to $Z + b$. Since the b' is expected to be pair produced, the signature is one Z, reconstructed in its decay to leptons, two b-jets, and two generic jets. To allow sensitivity to other possible physics beyond the standard model, no b-tagging is used. In this search, the dominant background, standard model production of Z + jets, is estimated with a technique using data. The method is cross-checked in a variety of control samples including W + jets data, where an excess consistent with $t\bar{t}$ production is found. They observe no significant excess in the Z^0 + jets signal region, and set limits on a fourth-generation b' quark model.

3 Signature-Based Searches

3.1 Search for New Physics in High-p_T Z^0

Massive new particles coupling to Z^0 bosons could impart significant transverse momentum to the Z^0. CDF has searched for new physics in 0.95 fb^{-1} of data in the transverse momentum spectrum of Z^0 bosons. The dominant background in this search is SM Drell-Yan production which is estimated with PYTHIA Monte Carlo. The Z p_T spectrum agrees well with background predictions, and limits on anomalous production of inclusive Z^0 bosons as a function of the boson p_T are set. In order to increase sensitivity, the sample is searched for additional leptons, photons, $\not\!\!E_T$, or large total sum transverse energy. These signatures have much smaller standard model rates and are sensitive to different backgrounds. Still, no significant excess is seen.

3.2 Anomalous Production of Leptons, Photons, and $\not\!\!E_T$

In Run 1, CDF observed a single event with two photons, two electron candidates, and $\not\!\!E_T$ was observed. In Run II, with many times the data available

Table 2: *Expected and observed events in CDF searches for leptons, photons, and* $\not\!\!E_T$.

Signature	$\gamma\gamma\gamma$	$\gamma\gamma e$	$\gamma\gamma\mu$	$\gamma\gamma\not\!\!E_T$
Expected	2.2 ± 0.7	6.8 ± 0.8	0.8 ± 0.1	0.24 ± 0.22
Data	4	3	0	0
Signature	$e\gamma\not\!\!E_T$	$\mu\gamma\not\!\!E_T$	$ee\gamma$	$\mu\mu\gamma$
Expected	95 ± 8	56 ± 7	39 ± 5	26 ± 3
Data	96	67	53	21

when that event was seen, CDF has several signature-based searches targeting anomalous production of similar events. Using 0.9-1.2 fb^{-1} of data, CDF has searched for anamalous production of $\gamma\gamma\gamma$, $\gamma\gamma e$, $\gamma\gamma\mu$, $\gamma\gamma\not\!\!E_T$, $l\gamma\not\!\!E_T$, and $ll\gamma$. Background expectations in these signatures range from a fraction of an event to a few tens of events. Expected and observed events in these searches are summarized in Table 2. No significant excesses are observed, nor are any events with two photons and two electrons like the one seen in Run 1.

3.3 Long-Lived Particles

Most searches for new particles assume prompt decays. It is possible that new physics might be longer-lived. CDF has searched for the decays of heavy, neutral, long-lived particles to photons with a new timing system for the electromagnetic calorimeter. Photon candidates from the decays of such a long-lived particle would arrive late compared to the products of the primary interaction. The final state $\gamma\not\!\!E_T$+jet is searched using all data available with timing information, 0.57 fb^{-1}, for late photons arriving 2 to 10 ns later than the primary interaction. The expected background is 1.7 events, and two are observed.

New massive charged massive particles (CHAMPs) with lifetimes long compared to their transit time through the detector would also escape detection by direct searches for their decay products. Such a charged massive particle would appear in the detector as a slow, highly-ionizing penetrating particle with large transverse momentum, and would be detected in the muon detectors (and reconstructed as a muon). CDF has searched in 1 fb^{-1} for such a particle in 1 fb^{-1} of data by measuring the time-of-flight of large transverse momentum tracks in events collected with a high p_T muon trigger. The particle's velocity, β, obtained from the timing measurement, and its momentum are used to

compute the particle's mass. Backgrounds are estimated from muon samples in data. The results are consistent with background expectations, and model-independent cross section limits are set at 48 (10) fb at 95% C.L. for a single fiducial strongly (weakly) interacting CHAMP.

3.4 Model-Independent Algorithmic

In an attempt to divorce expectations about where new physics might appear from methodologies used to search, CDF has employed a broad algorithmic search targeting electroweak-scale new physics. The algorithm employed is as follows. First, events collected on a variety of high p_T triggers are classified by their object content. Backgrounds from SM processes are estimated with Monte Carlo samples. Next, a fit is performed to extract correction factors to the background estimation. These correction factors account for, among others, luminosity, inadequacy of NLO calculations used in the Monte Carlo, particle misidentification rates, trigger efficiencies, and jet energy scale. The data and background predictions are compared in each exclusive final state for differences in expected and observed events and differences in shape. Results from this broad search are expected soon.

4 Conclusions

The CDF and DØ experiments are searching many models and signatures for evidence of new physics. None is observed yet, but both experiments have now recorded more that 2 fb^{-1}, and should have results with this doubling of the data soon. Most of the Run II data is yet to be collected and analyzed, and additional data continues to increase sensitivity to new physics signals.

5 Acknowledgments

I would like to thank Giorgio Bellettini, Giorgio Chiarelli, and Mario Greco for the opportunity to attend the conference. I also thank Jean-Francois Grivaz and Arnd Meyer from DØ and my colleagues at CDF for help in preparation of this talk.

References

1. The CDF and DØ results discussed here are available at `www-cdf.fnal.gov` and `www-d0.fnal.gov`
2. The slides of this presentation are at `https://indico.pi.infn.it/conferenceDisplay.py?confId=3`
3. N. Arkani-Hamed, S. Dimopoulos and G. R. Dvali, Phys. Lett. B **429**, 263 (1998) [arXiv:hep-ph/9803315].
4. L. Randall and R. Sundrum, Phys. Rev. Lett. **83**, 3370 (1999) [arXiv:hep-ph/9905221].

ELECTROWEAK STUDIES AND SEARCH FOR NEW PHENOMENA AT HERA

Aleksander Filip Żarnecki
(on behalf of the H1 and ZEUS collaborations)
Institute of Experimental Physics, University of Warsaw
Hoża 69, 00-681 Warszawa, Poland

Abstract

The H1 and ZEUS collaborations measure the neutral current and charged current cross sections of deep inelastic electron-proton and positron-proton scattering at HERA at high four-momentum transfer squared, Q^2. Due to high precision and large kinematic coverage of the data, it is possible not only to extract proton parton density functions from the HERA data alone, but also to constrain electroweak parameters, such as the weak quark couplings to the Z boson. As no significant deviation from the Standard Model predictions was observed, limits were derived for different models of new physics: four-fermion contact interactions, models with large extra dimensions, a finite charge radius of the quark and models with leptoquark production or exchange. The only sizable deviation from the Standard Model predictions was reported by the H1 collaboration in the search for events with isolated high-p_T leptons and large missing transverse momentum. In the combined HERA I and HERA II e^+p data 18 events with hadronic transverse momentum $P_T^X > 25$ GeV were observed, whereas 7.8 ± 1.3 were expected. No corresponding excess was observed by the ZEUS collaboration.

1 Introduction

The HERA accelerator, built at DESY, Hamburg, allows us to study electron-proton and positron-proton collisions at the center of mass energies of up to 318 GeV. Scattering events are reconstructed in two omni-purpose detectors, H1 [1)] and ZEUS [2)], both equipped with silicon tracking, drift chambers, hermetic calorimetry and muon detector system. During the so called HERA I running phase (1994-2000) about 100 pb^{-1} of data were collected per experiment, mainly coming from e^+p collisions. After the collider upgrade in 2000-2001, resulting in significant increase of luminosity, over 300 pb^{-1} of data were collected per experiment in the so called HERA II phase (2002-2007). Moreover, spin rotators installed at the H1 and ZEUS interaction regions provided electron and positron beams with longitudinal polarization. With average lepton beam polarization of about 30-40% and significant increase of integrated luminosity (especially for e^-p sample) HERA II has significantly extended the physics reach of experiments.

Presented in this contribution are selected results from H1 and ZEUS based on HERA II data analysis.

2 Electroweak studies

Neutral current deep inelastic scattering (NC DIS) $ep \to eX$ at very high squared momentum transfer, Q^2, is sensitive to electroweak effects mainly due to the interference of photon and Z boson exchange which dominates over pure Z exchange effects in most of the kinematic range covered at HERA.

High Q^2 NC DIS cross section, neglecting contribution from longitudinal structure function F_L, can be written in terms of four structure functions F_2^0, xF_3^0, F_2^P and xF_3^P:

$$\frac{d^2\sigma^{\rm NC}(e^\pm p)}{dxdQ^2} = \frac{2\pi\alpha^2}{xQ^4}\left[Y_+F_2^0 \mp Y_-xF_3^0 + P_e\left(Y_+F_2^P \mp Y_-xF_3^P\right)\right] \qquad (1)$$

where: $Y_\pm = 1 \pm (1-y)^2$ and P_e is the lepton beam polarization. Access to electroweak effects is enabled by measuring charge and polarisation cross section differences by which the pure photon exchange, giving the dominant contribution to the structure function F_2^0 is removed. Comparison of e^-p and e^+p cross sections, i.e. the measurement of charge asymmetry allows to extract xF_3^0 contribution which is dominated by the valence quark distributions at high Q^2 and lower x and is sensitive to the axial-vector weak quark couplings to the Z boson. The data on polarised cross section asymmetries, $A^\pm$, can be used to constrain the contribution from the F_2^P structure function, which is sensitive to the d/u ratio at high-x and to the vector quark couplings.

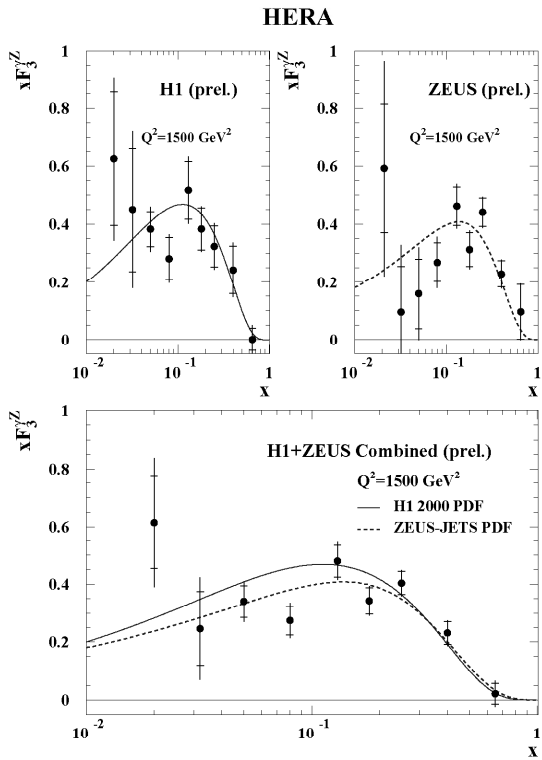

Figure 1: *Measurements of the structure function $xF_3^{\gamma Z}$ by the H1 collaboration (top left), the ZEUS collaboration (top right) and combined (bottom). The curves describe the Standard Model predictions as obtained in NLO QCD fits to the H1 inclusive data and to the inclusive and jet ZEUS data, respectively.*

The H1 and ZEUS experiments have measured NC DIS cross sections in both charge and both helicity states and the results were combined to improve statistical precision and sensitivity to electroweak effects [3]. Shown in fig.1 are the measurements of the structure function $xF_3^{\gamma Z}$ by the H1 and ZEUS collaborations and the combined measurement. Results agree very well with the Standard Model (SM) predictions obtained from the NLO QCD fits to the inclusive data. Corresponding results on polarised cross section asymmetries, $A^{\pm}$, are shown in fig.2. Parity violation due to $\gamma - Z$ interference is clearly visible, in agreement with the Standard Model expectations. This is the first observation of parity violation in neutral current $e^{\pm}p$ scattering at distances down to 10^{-18}m.

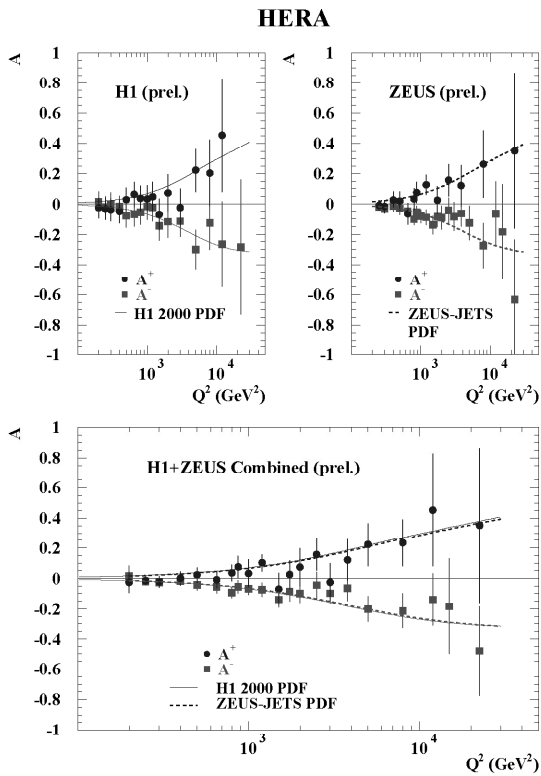

Figure 2: *Measurements of the polarisation asymmetries $A^{\pm}$ by the H1 collaboration (top left), the ZEUS collaboration (top right) and combined (bottom).*

The wide kinematic range covered, as well as the precision of the measurements, allow the determination of the parton distribution functions of the proton from the HERA data alone. Recently, NLO QCD analysis performed by both collaborations were extended to fit electroweak parameters as well. In the ZEUS study [4] inclusive $e^{\pm}p$ cross section data and jet-production data from HERA I were combined with the new data on polarised electron scattering at HERA II to extract constraints on the weak couplings of the quarks. Results on the weak neutral current couplings of u and d quarks to the Z^0 boson are presented in fig.3. Corresponding results from the similar H1 analysis of HERA I data [5], as well as Tevatron and LEP limits are included for comparison. Perfect agreement with the Standard Model predictions is observed.

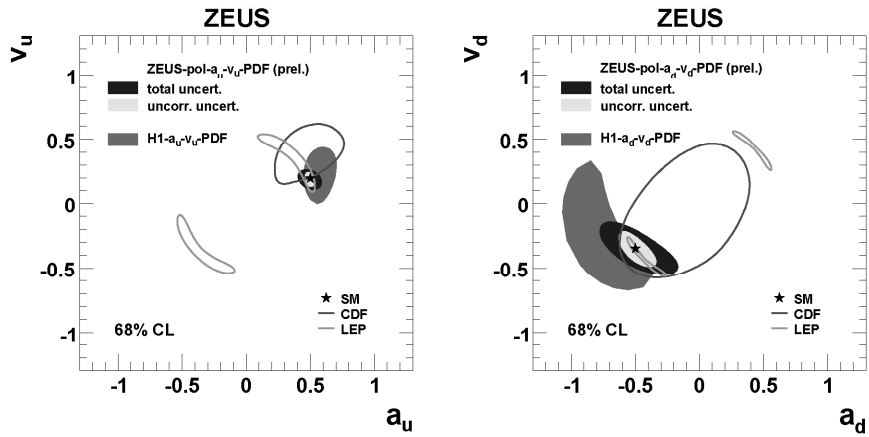

Figure 3: *Results at 68% C.L. on the weak neutral current couplings of u (left plot) and d (right plot) quarks to the Z^0 boson determined from the ZEUS analysis of HERA I and HERA II data. Results from H1 analysis of HERA I data and limits determined by the CDF and LEP experiments (open contours) are included for comparison. The stars show the expected SM values.*

Moreover, determinations of the light-quark couplings at HERA turn out to be competitive in precision with those of the LEP experiments.

3 Search for new phenomena

3.1 Contact Interactions

New interactions between electrons and quarks involving mass scales above the accessible center-of-mass energy can modify the deep inelastic $e^{\pm}p$ scattering cross section at high Q^2 via virtual effects, resulting in observable deviations from the Standard Model predictions. Many such interactions, such as processes mediated by heavy leptoquarks, can be modeled as four-fermion contact interactions. The ZEUS collaboration applied a common method to search for four-fermion interactions, for graviton exchange in models with large extra dimensions, and for a finite charge radius of the quark [6]. Data on scattering of polarized electrons and positrons collected from HERA II were combined with electron and positron data from HERA I. No significant deviation from the Standard Model predictions was observed and 95% limits were derived for the relevant parameters of the investigated models. For the contact-interaction models, limits on the effective mass scale, Λ (i.e. compositeness scale), ranging

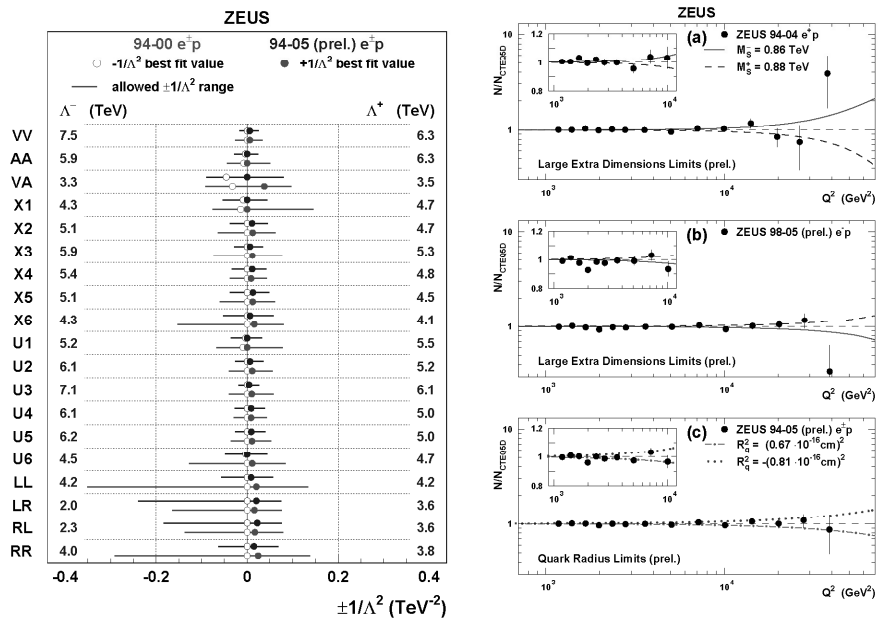

Figure 4: *Left plot: confidence intervals of* $\pm 1/\Lambda^2$ *at 95% C.L. for general CI scenarios studied by ZEUS. The numbers at the margins are the corresponding lower limits on the mass scale* Λ^- *and* Λ^+*. Right plot: ZEUS* e^+p *data (a) and* e^-p *data (b) compared with 95% C.L. exclusion limits for the effective Planck mass scale in models with large extra dimensions, and combined 1994-2000 data (c) compared with 95% C.L. exclusion limits for the effective mean-square radius of the electroweak charge of the quark.*

from 2 to 7.5 TeV were derived, as shown in fig.4(left). For models with large extra dimensions scales below 0.88 TeV (0.86 TeV) were excluded for positive (negative) coupling signs. Comparison of ZEUS data with 95% C.L. exclusion limits for the effective Planck mass scale in models with large extra dimensions is shown in fig.4a and 4b. A quark-charge radius larger than $0.67 \cdot 10^{-16}$cm was excluded, using the classical form-factor approximation, see fig.4c.

3.2 Leptoquarks

The *ep* collider HERA offers also the unique possibility to search for the resonant production of new particles which couple directly to a lepton and a parton. Leptoquarks, colour triplet bosons, which appear naturally in various unifying

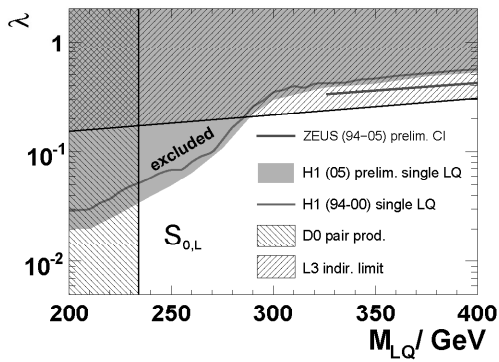

Figure 5: *H1 exclusion limits at 95% C.L. on the coupling as a function of the leptoquark mass for $S_{0,L}$ leptoquark. The indirect limits from ZEUS and L3 and the direct D0 limits are shown for comparison.*

theories beyond the Standard Model are such an example. The H1 collaboration searched for scalar and vector leptoquarks coupling to first generation fermions using the *ep* scattering data collected by the experiment until 2005. With HERA II data sensitivity to leptoquarks with fermion number F=2 is significantly increased w.r.t. HERA I data. No evidence for the direct or indirect production of such particles is found in data samples with a large transverse momentum final state electron or with large missing transverse momentum. The results of the analysis are used to set constraints on leptoquark couplings. Exclusion limits at 95% C.L. on the Yukawa coupling of $S_{0,L}$ leptoquark, as a function of its mass are presented in fig.5. The indirect limits from ZEUS and L3 and the direct D0 limits are included for comparison. For leptoquark couplings of electromagnetic strength, F=2 leptoquarks with masses up to 276-304 GeV are ruled out.

3.3 Isolated leptons

Searches for events containing isolated high-p_T leptons (electrons or muons) and large missing transverse momentum were performed by the H1 and ZEUS collaborations in HERA I and HERA II $e^{\pm}p$ data. For HERA I data an excess of events compared to the SM prediction at large hadronic transverse momentum P_T^X was previously reported by the H1 collaboration but not confirmed by ZEUS. Example of an event with an isolated electron, missing transverse momentum and a prominent hadronic jet found in the HERA II $e^{+}p$ data col-

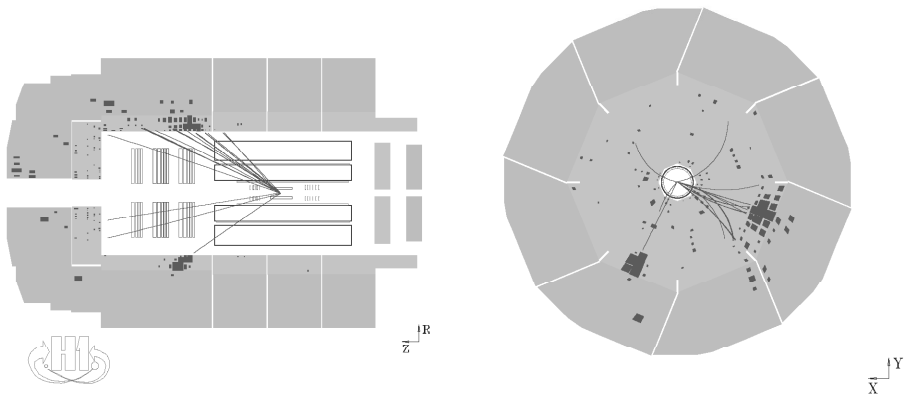

Figure 6: *Display of an event with an isolated electron, missing transverse momentum and a prominent hadronic jet in the HERA II e^+p data collected by the H1 experiment.*

lected by the H1 experiment is presented in fig.6. The main SM process that may produce events with this topology is the production of real W bosons via photoproduction with subsequent leptonic decay: $ep \to eW^{\pm}(\to l\nu)X$. The main SM background to events containing isolated electrons arises from neutral current events, whereas for events with an isolated muon the background arises from lepton pair production and charge current DIS events.

Figure 7 shows the distribution of the hadronic transverse momentum P_T^X for the e^-p and e^+p events selected from the H1 data [8]. Good agreement with Standard Model predictions is observed in low P_T^X region, where elastic $W^{\pm}$ production signal is expected. However, for e^+p data an excess of events over SM predictions is observed for large hadronic transverse momentum $P_T^X > 25$ GeV. In the combined HERA I and HERA II data, 18 such events were observed by the H1 experiment, corresponding to an excess of about 3σ over the Standard Model expectation of 7.8 ± 1.3. No such deviation was observed for e^-p data from H1. All ZEUS data are in good agreement with the Standard Model predictions: [9] for $P_T^X > 25$ GeV, four e^+p events were observed in the combined HERA I and HERA II data compared to the SM expectation of 6.3. A summary of the II1 and ZEUS results on searches for events with isolated electrons or muons and missing transverse momentum at HERA is presented in tab.1.

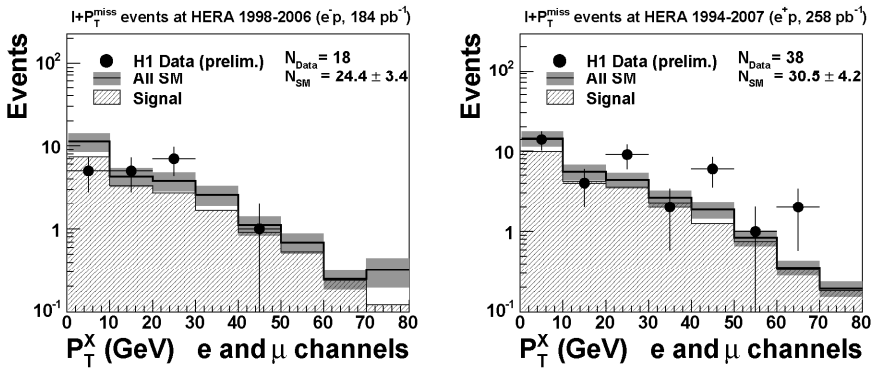

Figure 7: *Results of the search for events with isolated leptons and missing transverse momentum by the H1 collaboration: hadronic transverse momentum distributions in the electron and muon channels, for the combined e^-p (left plot) and e^+p (right plot) data compared to the SM expectation (open histogram).*

4 Conclusions

With high luminosity and lepton beam polarisation at HERA II a new window for precise electroweak studies has been opened. The H1 and ZEUS collaborations presented results on the charge and polarisation asymmetries in deep inelastic scattering. With high precision and large kinematic coverage of the data, NLO QCD analyses performed by both collaborations were extended to extract not only the parton densities in the proton but also to fit electroweak parameters. The obtained constraints on the light-quark couplings to the Z^0 boson are in good agreement with the Standard Model predictions and are competitive in precision with LEP measurements.

Precise measurements of deep inelastic $e^{\pm}p$ scattering at large Q^2 were also exploited to search for possible "new physics" beyond the Standard Model. As no significant deviation from the Standard Model predictions was observed, limits were derived for different models of new physics: four-fermion contact interactions, models with large extra dimensions, a finite charge radius of the quark and models with leptoquark production or exchange. The only sizable deviation from the Standard Model predictions was reported by the H1 collaboration in the search for events with isolated high-p_T leptons and large missing transverse momentum. In the combined HERA I and HERA II e^-p data 18 events with hadronic transverse momentum $P_T^X > 25$ GeV were observed, whereas 7.8 ± 1.3 were expected. However, no corresponding excess was observed by the ZEUS collaboration.

Table 1: *A summary of the H1 (upper table) and ZEUS (lower table) results on searches for events with isolated electrons or muons and missing transverse momentum at HERA. The number of observed events is compared to the SM prediction (observed/expected). The signal component of the SM expectation (W production) is given as a percentage in parentheses.*

H1 (prel.)	e channel	μ channel
e^-p (184 pb^{-1})	$3/3.8 \pm 0.6$ (61%)	$0/3.1 \pm 0.5$ (74%)
e^+p (258 pb^{-1})	$10/4.1 \pm 0.8$ (75%)	$8/3.7 \pm 0.6$ (85%)
$e^\pm p$ (442 pb^{-1})	$13/7.9 \pm 1.4$ (67%)	$8/6.8 \pm 1.1$ (79%)

ZEUS (prel.)	e channel	μ channel
e^-p (204 pb^{-1})	$5/3.8 \pm 0.6$ (55%)	$2/2.2 \pm 0.3$ (86%)
e^+p (228 pb^{-1})	$1/3.2 \pm 0.4$ (75%)	$3/3.1 \pm 0.5$ (80%)
$e^\pm p$ (432 pb^{-1})	$6/7.0 \pm 0.7$ (64%)	$5/5.3 \pm 0.6$ (82%)

HERA running is coming to an end soon. However, large samples of data have been collected by both experiments and are still being analyzed. Many more interesting results are still expected to emerge.

References

1. H1 Collaboration, I. Abt *et al*, Nucl. Instrum. Meth. **A 386** 310 and 348 (1997); R.D. Appuhn *et al*, Nucl. Instrum. Meth. **A 386** 397 (1997).

2. ZEUS Collaboration, U. Holm (ed.), The ZEUS Detector. Status Report (unpublished), DESY (1993), available on `http://www-zeus.desy.de/bluebook/bluebook.html`.

3. H1 and ZEUS Collaborations, Electroweak Neutral Currents at HERA, H1prelim-06-142, ZEUS-prel-06-022, submitted to ICHEP'2006, Moscow, Russia.

4. ZEUS Collaboration, An NLO and EW analysis of inclusive $e^\pm p$ cross section data from the ZEUS experiment, ZEUS-prel-06-003, submitted to ICHEP'2006, Moscow, Russia.

5. H1 Collaboration, A. Aktas *et al*, Phys. Lett. **B632**, 35 (2006).

6. ZEUS Collaboration, Search for contact interactions, leptoquarks, large extra dimensions and finite quark radius in ep collisions at HERA, ZEUS-prel-06-018, submitted to ICHEP'2006, Moscow, Russia.

7. H1 Collaboration, A search for Leptoquarks in $e^- p$ collisions at HERA, H1prelim-06-061, submitted to ICHEP'2006, Moscow, Russia.

8. H1 Collaboration, Search for Events with Isolated Leptons and Missing Transverse Momentum, H1prelim-06-162, submitted to ICHEP'2006, Moscow, Russia, update January 2007.

9. ZEUS Collaboration, Search for High-P_T Isolated Leptons at HERA, ZEUS-prel-06-012, submitted to ICHEP'2006, Moscow, Russia, update February 2007.

PHYSICS BEYOND THE STANDARD MODEL IN ATLAS AT THE STARTUP OF THE LHC

George Redlinger
BNL, USA

Written contribution not received

NEW (VIRTUAL) PHYSICS IN THE ERA OF THE LHC

M.I. Vysotsky
ITEP, Moscow, Russia

Abstract

A simple extension of the Standard Model demonstrates that New Physics non-reachable through direct production at LHC can induce up to 10% corrections to the Standard Model value of parameter ε_K and to the frequencies of $B_d - \bar{B}_d$ and $B_s - \bar{B}_s$ oscillations.

Let us imagine the worst scenario: the only new particle found at the LHC will be the Higgs boson of the Standard Model (SM). A natural question arises: is it possible to find traces of New Physics in low energy observables without observing the production of new particles at LHC? Another facet of this question: What changes of the unitarity triangle can be produced by such particles? This is the problem we will focus on.

In order to influence the quark weak currents the new particles should be strongly interacting. The natural example would be the fourth quark-lepton family: the fourth generation quarks deform unitarity triangle into unitarity quadrangle. However since the sequential fourth generation gets masses through Higgs mechanism, its quarks cannot be heavier than 1 TeV: so, they will be directly produced at LHC. That is why the heavy particles we are looking for should get their masses from a different source. So their contributions to low energy observables decouple, being suppressed as $(\eta/M)^2$, where $\eta = 246$ GeV is the Higgs boson neutral component expectation value and M characterizes new particles masses, $M \geq 5$ TeV in order to avoid their production at LHC. These 1% corrections are too small to be detected taken into account relatively low accuracy of theoretical formulas. Nevertheless we manage to find a model where corrections are enhanced and can be detected.

Let us study the extension of SM by $SU(2)_L$ singlet heavy Dirac quark Q with electric charge $+2/3$ which mixes with the top quark. Recently the constraints from the $B \to X_s\gamma$ branching ratio and electroweak precision observables in this model have been studied [1]. Authors of [1] are interested in manifestations of rather light Q with mass just above Tevatron bound. As a consequence Q mixes strongly with the top quark in their model. So our model with much heavier Q which mixes weakly with top (see below) can be considered as complementary to [1].

The model is described by the following lagrangian:

$$\mathcal{L} = \mathcal{L}_{SM} - M\bar{Q}'Q' + \left[\mu_R \bar{Q}'_L t'_R + \frac{\mu_L}{\eta/\sqrt{2}} H^+ \bar{Q}'_R \begin{pmatrix} t' \\ b' \end{pmatrix}_L + c.c.\right] \quad , \qquad (1)$$

where $\mathcal{L}_{SM}$ is the SM lagrangian, M, μ_R and μ_L are the parameters with the dimension of mass. The term proportional to M contains Dirac mass of the field Q' which is primed since it is not a state with a definite mass due to mixing with t-quark. The term proportional to μ_R describes the mixing of two $SU(2)_L$ singlets: Q'_L and t'_R, the latter being the right component of t-quark field in the Standard Model (in the absence of terms in square brackets). Finally, the term proportional to μ_L describes mixing of a weak isodoublet with Q'. An upper component of this isodoublet is the left component of the field t' which

would be t-quark without the terms in square brackets:

$$t'_L - U^L_{t't''} t''_L + U^L_{t'c'} c'_L + U^L_{t'u'} u'_L \ , \tag{2}$$

where t'', c' and u' are the primary fields of SM lagrangian, while U^L_{ik} are the matrix elements of matrix U^L which transforms the primary fields c'_L and u'_L to the left-handed components of the mass eigenstates c and u and field t''_L to the field t'_L which would be the left-handed component of the top quark in the case $\mu_L = \mu_R = 0$. We do not mix Q quark with u and c quarks in order to avoid FCNC which may induce too large $D^0 - \bar{D}^0$ oscillations.

One can easily see that the lower component of the isodoublet is the combination of the down quark fields with definite masses rotated by CKM matrix V:

$$b'_L = V_{tb} b_L + V_{ts} s_L + V_{td} d_L \ . \tag{3}$$

In order to find the states with definite masses which result from t'–Q' mixing, the following matrix should be diagonalized:

$$(\overline{t'_L t'_R Q'_L Q'_R}) \begin{pmatrix} 0 & m_t & 0 & \mu_L \\ m_t & 0 & \mu_R & 0 \\ 0 & \mu_R & 0 & -M \\ \mu_L & 0 & -M & 0 \end{pmatrix} \begin{pmatrix} t'_L \\ t'_R \\ Q'_L \\ Q'_R \end{pmatrix} \ , \tag{4}$$

where m_t is the mass of t-quark in SM. For the squares of masses of the eigenstates we get:

$$2(\lambda^2)_{t,Q} = M^2 + \mu_R^2 + \mu_L^2 + m_t^2 \mp$$
$$\mp \sqrt{(M^2 + \mu_R^2 + \mu_L^2 + m_t^2)^2 - 4M^2 m_t^2 - 4\mu_L^2 \mu_R^2 + 8 m_t \mu_R \mu_L M} \ , \tag{5}$$

and the eigenstates look like (in what follows we put $m_t = 0$[1]):

$$t = t'_L + (1 - \frac{\lambda_t^2}{\mu_L^2}) \frac{\mu_R \mu_L}{\lambda_t M} t'_R + \frac{\mu_L}{M} (1 - \frac{\lambda_t^2}{\mu_L^2}) Q'_L + \frac{\lambda_t}{\mu_L} Q'_R \ , \tag{6}$$

$$\lambda_t = \frac{\mu_R \mu_L}{M} \left(1 - \frac{\mu_R^2 + \mu_L^2}{2M^2} \right) + O(\frac{1}{M^5}) \ , \tag{7}$$

[1]We did it in order to simplify the formulas a bit; however this can be suggested as an explanation of heaviness of top: t-quark massless in SM gets all its mass due to mixing with heavy Q.

$$Q = Q'_R + (-\frac{\lambda_Q}{M} + \frac{\mu_L^2}{\lambda_Q M})Q'_L + \frac{\mu_L}{\lambda_Q} t'_L + \frac{\mu_R}{M}\left(\frac{\mu_L^2}{\lambda_Q^2} - 1\right) t'_R \ , \tag{8}$$

$$\lambda_Q = -M + O\left(\frac{1}{M}\right) \ , \tag{9}$$

the normalization factors of the quark fields which should be taken into account when calculating Feynman diagrams are omitted.

Now we are ready to discuss the flavor changing quark transitions. $\bar{t}_R(b_L, d_L, s_L)H^+$ transition vertex originates in our model from Q_R admixture in the t-quark wave function:

$$\frac{\mu_L}{\eta/\sqrt{2}} \frac{\lambda_t/\mu_L}{\sqrt{\frac{\mu_L^2\mu_R^2}{\lambda_t^2 M^2}\left(1 - \frac{\lambda_t^2}{\mu_L^2}\right)^2 + \frac{\lambda_t^2}{\mu_L^2}}} \bar{t}_R b'_L H^+ =$$

$$= \frac{\lambda_t}{\eta/\sqrt{2}} \frac{1}{\sqrt{1 + (\frac{\mu_L}{M})^2\left(1 - \frac{\lambda_t^2}{\mu_L^2}\right)^2}} \bar{t}_R b'_L H^+ \ , \tag{10}$$

that is why up to the corrections $\sim (\mu_L/M)^2$ the box diagrams for $B_{d,s} - \bar{B}_{d,s}$, $K^0 - \bar{K}^0$ transitions with the intermediate t-quarks are the same as in SM[2].

How large can the term $(\mu_L/M)^2$ be? According to Eq.(1) μ_L cannot be larger than 500 GeV: in the opposite case we will be out of the perturbation theory domain and no calculations can be trusted. That is why trying to have the largest possible deviations from SM we will take $\mu_L = 500$ GeV in what follows. The smallest value of M which will prevent the production of Q-quarks at LHC is about 5 TeV, and we will use it in order to maximize deviations from SM (consequently $\mu_R = m_t M/\mu_L \approx 1.7$ TeV). At one loop level Q-quark contributes to $Z \to b\bar{b}$ decay. The analysis of the experimental data made in [1] lead to $\mu_L/M \leq 0.4$, and we are on the safe side. The constraint from $B \to X_s\gamma$ decay is even weaker. The box with two intermediate t-quarks is equal to that in SM with $(\mu_L/M)^2 \approx 1\%$ accuracy. Theoretical uncertainties in matrix elements calculations do not allow to detect 1% deviation from SM results.

Our model generates extra contributions to $\Delta F = 2$ four-fermion operators due to the boxes with intermediate Q-quarks. The boxes with H^+ exchanges generate leading contributions in the limit $m_t, M \gg M_W$. The box

[2]Since H^+ is the longitudinal W^+-boson polarization its interaction is the same as that of W^+ and the square root in the denominator from (t_R, Q_R) proper normalization equals that for (t_L, Q_L) component.

with one t-quark substituted by Q gives coefficient $\sim G_F^2 m_t^2 (\mu_L/M)^2 \ln(M/m_t)^2$: once more the correction is damped by the factor $(\mu_L/M)^2 \approx 1\%$ relative to the SM contribution.

The largest correction comes from the box with two intermediate Q-quarks:

$$\left(\frac{|\mu_L|}{\eta/\sqrt{2}}\right)^4 \frac{1}{M^2}(\bar{b}_L\gamma_\mu d_L)(\bar{b}_L\gamma_\mu d_L) \ , \tag{11}$$

where as an example we present the operator responsible for $B_d \quad \bar{B}_d$ oscillations. In this way we get:

$$\frac{\mathrm{box}(QQ)}{\mathrm{box}(tt)} \approx \frac{\mu_L^4}{m_t^2 M^2} \approx 10\% \ . \tag{12}$$

The explicit formula which takes into account (tt) and (QQ) boxes can be easily obtained from that of SM [2]:

$$\begin{aligned}
&\Delta m_{B_d} = \\
&= \frac{G_F^2 B_{B_d} f_{B_d}^2}{6\pi^2} m_B \left[m_t^2 I\left(\frac{m_t^2}{M_W^2}\right) + M^2 \left(\frac{|\mu_L|}{M}\right)^4 I\left(\frac{M^2}{M_W^2}\right)\right] \eta_B |V_{td}|^2 \\
&I(\xi) \quad = \quad \left\{ \frac{\xi^2 - 11\xi + 4}{4(\xi-1)^2} - \frac{3\xi^2 \ln \xi}{2(1-\xi)^3} \right\} \\
&I(0) \quad = \quad 1 \ ; \ I\left(\frac{m_t^2}{M_W^2}\right) \approx 0.55 \ ; \ I(\infty) = 0.25 \ .
\end{aligned} \tag{13}$$

In conclusion we have found a simple extension of SM with one additional heavy quark Q, $M_Q \approx 5$ TeV (non-reachable by direct production at LHC), in which the corrections to CP violating factor ε in $K - \bar{K}$ transitions and the values of Δm_{B_d} and Δm_{B_s} are universal and can reach 10%. We demonstrate that even with no new particles found at LHC one cannot claim that the Unitarity Triangle is universal and unambiguously extractable from different observables with the accuracy better than 10%. In our case the triangle determined by angles found from CP-asymmetries in B-decays and by one side $(V_{cb}^* V_{cd})$ has the value of side $(V_{tb}^* V_{td})$ which, being substituted into the SM expression for Δm_{B_d}, produces the number smaller than the one extracted from the measurement of the $B_d - \bar{B}_d$ oscillation frequency by $\approx$10%. However, to detect this discrepancy one needs to have an accuracy in the value of the product $f_{B_d}^2 B_{B_d}$ better than 10% (the present day accuracy is about 2 times worse [3]).

Heavy quark Q will lead to extra radiative corrections to electroweak observables (M_W, M_Z, Γ_Z ...). In this way the central value of the higgs mass

which is extracted from the fit will be shifted. We plan to make necessary calculations in the nearest future.

In recent paper [4] the contribution to $\Delta m_{B_{d,s}}$ due to singlet heavy fermion with electric charge $+2/3$ has been studied. The analyzed model is motivated by a Little Higgs scenario. In this scenario our factor μ_L is substituted by $x_L\eta$, where $0 \leq x_L \leq 1$ [5]. That is why even for $x_L = 1$ correction to $\Delta m_{B_{d,s}}$ is damped by the factor $2^4 = 16$ compared to our value.

This talk is based on the paper [6] which originates as the answer to A. Golutvin's question. I am grateful to V. Novikov and A. Rozanov for interesting discussions.

I am very grateful to the Conference organizers and in particular to Mario Greco for their hospitality. This work was partly supported by grants RFBR 05-02-17203, 07-02-00021 and HSh-2603.2006.2.

References

1. J. Alwall, R. Frederix, J.-M. Gerard, A. Giammanco, M. Herquet, S. Kalinin, E. Kou, V. Lemaitre, F. Maltoni, hep-ph/0607115 (2006).

2. M.I. Vysotsky, Yad. Fiz. **31**, 1535 (1980); Sov. J. Nucl. Phys. **31**, 797 (1980);

   T. Inami, C.S. Lim, Prog. Theor. Phys. **65**, 297 (1981).

3. Review of Particle Properties, W.-M. Yao et al., J. Phys. G **33**, 1 (2006).

4. M. Blanke, A.J. Buras, hep-ph/0610037 (2006).

5. Tao Han, Heather E. Logan, Bob McElrath, Lian-Tao Wang, Phys. Rev. D **67**, 095004 (2003).

6. M.I. Vysotsky, Phys. Lett. B **644**, 352 (2007).

SUSY PHENOMENOLOGY & SUSY DARK MATTER

Dmitri Kazakov
Bogoliubov Laboratory of Theoretical Physics, Joint Institute for Nuclear Research, Dubna, Russia
Institute for Theoretical and Experimental Physics, Moscow, Russia

Abstract

Recently it was shown that the excess of diffuse Galactic gamma rays above 1 GeV traces the Dark Matter halo, as proven by reconstructing the peculiar shape of the rotation curve of our Galaxy from the gamma ray excess. This can be interpreted as a Dark Matter annihilation signal. In this talk we show that this interpretation is consistent with Supersymmetry. It is found that the EGRET excess combined with all electroweak constraints and WMAP CMB data is fully consistent with the minimal mSUGRA model with the neutralino mass around 60 GeV. It leads to the SUSY mass spectrum in the TeV range for scalars and gauginos below 500 GeV. The corresponding cross-sections for SUSY production are within the reach of the LHC.

1 Introduction

Approaching launch of the LHC requires the hints to look for new physics at the TeV scale. The mainstream is the search for supersymmetry. Much work has been done in this direction, although, we do not have any definite indication on the range of SUSY particle masses so far. Several options are available with various phenomenological consequences. In this situation we argue for the possibility that we have already seen the manifestation of supersymmetry though not at colliders but in the sky. It is the purpose of the present talk to show that there exists an intriguing hint of the Dark Matter annihilation signal which is compatible with Supersymmetry.

Cold Dark Matter (CDM) makes up 23% of the energy of the universe, as deduced from the temperature anisotropies in the Cosmic Microwave Background (CMB) in combination with data on the Hubble expansion and the density fluctuations in the universe [1]. One of the most popular CDM candidates is the neutralino, a stable neutral particle predicted by Supersymmetry [2, 3]. In a recent paper [4] we showed that the observed excess of diffuse Galactic gamma rays obtained by EGRET collaboration has all the properties of the π^0 decays of such mono-energetic quarks originating from the annihilation of neutralinos with a mass around 60 GeV.

We concentrate on the Minimal Supersymmetric Model with supergravity inspired symmetry breaking (mSUGRA model) [5]. Imposing various constraints on the SUSY breaking parameter space one gets the allowed regions with different phenomenological properties. Assuming that the EGRET excess originates from the annihilation of the stable, neutral lightest supersymmetric particles, the neutralinos, we get new constraint. It is compatible with the amount of the Dark Matter and strongly restricts the masses from all other SUSY particles, if mass unification at the GUT scale is assumed. It will be shown that combining the EGRET data with other constraints, like the electroweak precision data, Higgs mass limits, chargino limits, radiative electroweak symmetry breaking and relic density leads to a very constrained SUSY mass spectrum with light gauginos and heavy squarks and sleptons.

Having in mind this spectrum one can discuss a possibility of SUSY observation at colliders, in particular the creation of light sparticles with relatively high cross-sections. The advantage of this benchmark point is that it is adjusted to existing astrophysical data which might be the manifestation of supersymmetry. One has definite predictions which can be tested at colliders thus providing a direct check of this scenario.

2 SUSY Parameter Space

In what follows we consider the mSUGRA model, i.e. the Minimal Supersymmetric Standard Model (MSSM) with supergravity inspired supersymmetry breaking terms. Then, assuming universality hypothesis, one has the SUSY parameter space characterised by 5 parameters: m_0, $m_{1/2}$, $\tan\beta$, sign(μ) and A_0 [5]. Various experimental and theoretical requirements severely constraint the allowed region of this space. We show below in Fig.1 the projection of mSUGRA parameter space onto m_0-$m_{1/2}$ plane for fixed values of $\tan\beta$ and A_0. One can see the role of some particular requirements: the left upper corner of the plane is forbidden due to the requirement of neutrality of the LSP, the left bottom corner is forbidden due to the Higgs mass limit from LEP and the $b \to s\gamma$ branching ratio, the right bottom corner does not allow the radiative electroweak symmetry breaking. Accepting the high experimental accuracy of the measurement of the amount of the DM from WMAP, one also gets a narrow (blue) band allowing the right amount of the DM assuming it is totally made of supersymmetric particles [6].

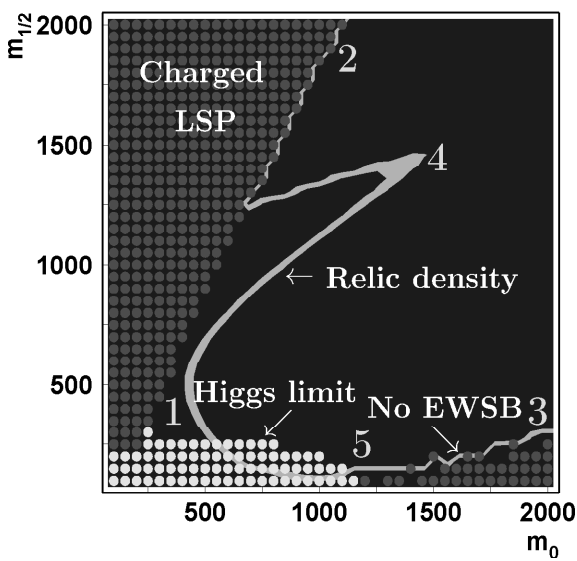

Figure 1: *The allowed regions of mSUGRA parameter space: bulk region (1), co annihilation region (2), focus point region (3), funnel region (4) and EGRET region (5). Forbidden regions are indicated by colour. The narrow blue band corresponds to the DM relic density within the WMAP limits.*

Different regions along this band indicated by numbers correspond to

different phenomenological consequences. They have a certain mass spectrum typical to the each region that defines the main production of SUSY particles and their main decay channels [7].

1) The first, mostly studied region is the *bulk annihilation region*, this is the region of relatively small m_0 and $m_{1/2}$ ($m_0 \approx 50 \div 150$ GeV, $m_{1/2} \approx 50 \div 350$ GeV). It is bounded from below by the non-observation of the Higgs boson and the absence of radiative electroweak symmetry breaking as well as by consistency with the $b \to s\gamma$ decay rate. From the left there is a forbidden region where stau is the LSP.

   One of the main processes in this region is the annihilation of pair of neutralinos into quarks through the exchange of a squark in the t-channel $\tilde{\chi}_1^0\tilde{\chi}_1^0 \to q\bar{q}$. The parameters can be adjusted in a way to give the right amount of the Dark matter. The superpartners here are relatively light below ~ 500 Gev.

   The size of the region depends on $\tan\beta$ and for low values of $\tan\beta$ it practically disappears due to the non-observation of the Higgs boson.

2) The other interesting region is the so-called *stau co-annihilation* region. Here typically one has small values of m_0 and much bigger values of $m_{1/2}$. It is located along the border line between the regions where $\tilde{\tau}_1$-slepton is the LSP and neutralino $\tilde{\chi}_1^0$ is the LSP. Evidently this corresponds to the case when the particles are almost degenerate in masses $m_{\tilde{\chi}_1^0} \approx m_{\tilde{\tau}_1}$ and in the early Universe there were co-annihilation processes $\tilde{\chi}_1^0\tilde{\tau}_1$ ($\tilde{\chi}_1^0\tilde{\tau}_1 \to \tau^* \to \tau\gamma$) as well as co-annihilation $\tilde{\tau}_1\tilde{\tau}_1$. Neutralino in this case is mostly higgsino and its mass may be large up to 500 GeV without violating the WMAP bound.

   Co-annihilation region is interesting from the point of view of existence of long-lived charged sleptons. Their life-time may be large enough to be produced in proton-proton collisions and to fly away from the detector area or to decay inside the detector at a considerable distance from the collision point. Clearly that such an event can not be unnoticed. However, to realize this possibility one need a fine-tuning of the parameters of the model [8].

3) As has been already mentioned for large m_0 small values of $m_{1/2}$ are forbidden due to the absence of radiative electroweak symmetry breaking. However, along the border of forbidden region, the WMAP allowed band may stay long enough leading to the masses of squarks and sleptons up to a few TeV. This region is called the *focus point region* since the values of the Higgs mass parameters here tend to the focus point when running the renormalization group equations. In this region the Higgs mixing

parameter μ happens to be small $|\mu| \sim M_Z$. Then it is possible that two light neutralinos and the light chargino are practically degenerate $m_{\chi_1^0} \sim m_{\chi_2^0} \sim m_{\chi_1^\pm} \sim \mu$. The lightest neutralino in this case is mostly higgsino. The main annihilation channel is the one into the pair of gauge bosons $\tilde{\chi}_1^0\tilde{\chi}_1^0 \to ZZ$ $\tilde{\chi}_1^0\tilde{\chi}_1^0 \to W^+W^-$ but due to degeneracy of masses of neutralino and chargino there are also possible the co-annihilation processes $\chi_1^0\chi_1^\pm$, $\chi_1^0\chi_2^0$, $\chi_1^+\chi_1^-$ $\chi_2^0\chi_1^\pm$.

Despite the large values of $m_{1/2}$ up to 1 TeV, μ remains small and leads to chargino and neutralino massses of the order of a few hundreds of GeV. This tells us that the focus point region is accessible by LHC. Even the cross section of gluino pair production is big enough to observe this process.

4) For large values of $\tan\beta$ it is possible that $m_A \approx 2m_{\tilde{\chi}_1^0}$. There is no need for precise equality because the width of the CP-odd Higgs boson A is about tens of GeV. In this region of $(m_0, m_{1/2})$ plane the allowed WMAP band has a sharp turn in the form of a funnel: *A-funnel region.* The main channel of annihilation in this region is $\tilde{\chi}_1^0\tilde{\chi}_1^0 \to A \to b\bar{b}$ or $\tau\bar{\tau}$. The reason for such a behaviour is that for increasing $\tan\beta$ the mass of a pseudoscalar Higgs boson A decreases while the mass of neutralino practically does not change. Then inevitably the resonance situation when $m_A = 2m_{\tilde{\chi}_1^0}$ occurs. And despite that fact that neutralino in this case is almost photino and does not interact with the Higgs boson A, the tiny admixture of higgsino leads to considerable effect due to relatively big coupling of the A-boson to quarks and leptons $Ab\bar{b}$ $A\tau\bar{\tau}$. For the same reason the exchange of the heavy Higgs boson H might give an essential contribution.

Besides, in this region the cross section of neutralino χ_1^0 scattering on the nucleus is of the order of $10^{-8} \div 10^{-9}$ pb which is close to the values corresponding to the sensitivity of the modern and the nearest future experiments on the direct Dark matter searches.

In addition to the above mentioned regions there are some small exotic ones. For example, for a specific choice of parameters (very big $|A_0|$, moderate or big m_0 and small $m_{1/2}$)) as a result of mixing one of the t-squarks becomes practically degenerate with the lightest neutralino χ_1^0. Then one may have relatively stable stop quark [9]. It is similar to quasi-stable stau and also needs severe fine-tuning. In this case it is possible the process of $\tilde{\chi}_1^0\tilde{t}_1$ co-annihilation. For small values of $m_{1/2}$ (and for appropriate choice of the other parameters) there is a possibility of neutralino annihilation due to light Higgs boson exchange in the s-channel. This situation is analogous to that of annihilation through A or H.

3 DM annihilation in Galactic halo

Indirect detection of the DM is aimed to look for a secondary effect of DM annihilation in the form of extra gamma rays and charged particles (positrons and antiprotons) in cosmic rays. These particles should have an energy spectrum which reflects their origin from annihilation of massive particles and is different from the background of the known sources. Hence, one should have some shoulders in the cosmic ray spectrum. There are several experiments of this type: EGRET (diffuse gamma rays) to be followed by GLAST, HEAT and AMS01 (positrons) to be followed by PAMELA, BESS (antiprotons) to be followed by AMS02. All of these experiments see some deviation from the background in the energy spectrum, though experimental uncertainties are rather big.

The spectral shape of the diffuse Galactic gamma rays has been measured by the EGRET satellite in the range 0.1 - 10 GeV [10]. It allows an independent analysis in many different sky directions. Comparing the background with the EGRET data shows that above 1 GeV there is a large excess of gamma rays which reaches more than a factor of two towards the Galactic centre. However, fitting the background together with the DMA yields a perfect fit in all sky directions for a DM particle mass around 60 GeV as shown in Fig.2 [11].

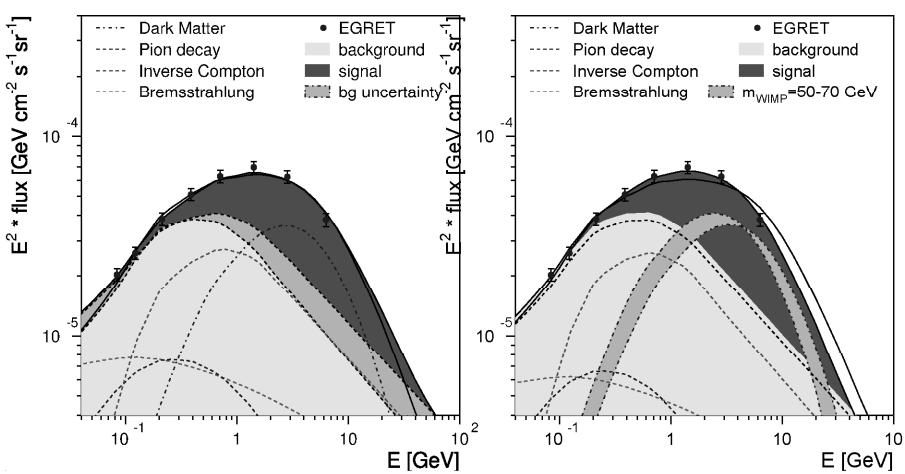

Figure 2: *The EGRET gamma ray spectrum fitted with DM annihilation for* $m_0 = 1400$ *GeV,* $m_{1/2} = 175$ *GeV,* $\tan\beta = 51$. *The possible variation of the background (blue shaded area above) is not enough to accommodate the EGRET signal. The variation of the WIMP mass between 50 and 70 GeV shown by blue shaded area below is allowed by the EGRET data with the conventional background*

In the left plot we show also the possible variations of the background (light blue band) while in the right plot we present the allowed variations of the neutralino mass. The same fits are made for all available 180 directions in the sky with the same result. In a recent paper [11] we showed that the observed excess of diffuse Galactic gamma rays has all the properties of the π^0 decays of mono-energetic quarks originating from the annihilation of the DM.

Considering the excess in all sky directions with a sufficiently large resolution allows to reconstruct the DM halo profile [11], which in turn can be used - in combination with the distribution of visible matter - to reconstruct the shape of the rotation curve (see Fig.3). The absolute normalization of the DM density distribution or halo profile can be obtained by requiring that the local rotation velocity of our solar system at 8.3 kpc is 220 km/s. It provides the first explanation for the peculiar change of slope in the rotation curve at around 11 kpc, indicating that the excess traces DM.

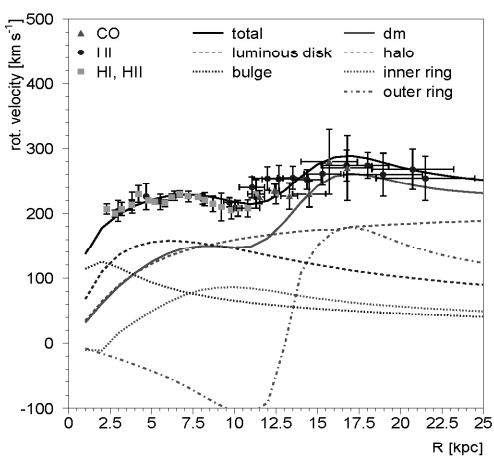

Figure 3: *Rotation curve of the Milky way with account of the DM profile*

Notice that the form of the rotation curve obtained with account of the DM profile is in agreement with the angular distribution of diffuse gamma rays obtained by EGRET telescope. The fit to all sky directions can be well described by the basic isothermal profile plus the substructure in the form of two toroidal rings at approximately 4 and 14 kpc. They clearly dominate for low latitudes, but are small for latitudes above 10 degrees. Fig.4 displays the halo distribution in the disk (xy-plane) and perpendicular to the plane (xz-plane) in a 3D plot. The rings serve the twofold aim. One the one hand side they describe the maxima in the angular distribution the gamma rays at

approximately 30 and 90 degrees and on the other hand they allow to get a minima in rotation curve as clearly seen in Fig.3. It should be stressed that the smooth profile always leads to a monotonic rotation curve without minima.

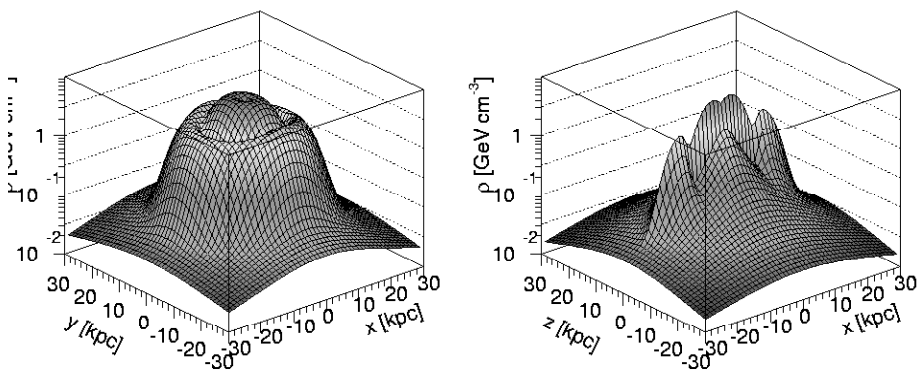

Figure 4: *3D-presentations of the isothermal halo profile in the Galactic plane (xy-projection) (top row) and perpendicular to the disk (xz-plane) (bottom row) without (left) and with (right) toroidal ringlike structures at 4 and 14 kpc.*

4 New constraint on SUSY parameter space

This intriguing hint of DMA is compatible with supersymmetry, assuming that the EGRET excess originates from the annihilation of the stable, neutral lightest supersymmetric particles, the neutralinos. Their mass is then constrained to be between 50 and 100 GeV ($m_{1/2}$ between 125 and 175 GeV) from the EGRET data, which strongly constrains the masses of all other SUSY particles, if mass unification at the GUT scale is assumed. Combining the EGRET data with other selects the only possible solution corresponding to the region 5. We show in Fig.5 the zoomed plot of this region indicating all the individual constraints. Choosing a point in this region gives the SUSY mass spectrum with light gauginos and heavy squarks and sleptons (see the Table 1).

The lightest neutralino is a mixture of all spin 1/2 neutral particles: $|\chi_o\rangle = N_1|B_0\rangle + N_2|W_0^3\rangle + N_3|II_1\rangle + N_4|II_2\rangle$ with (N_1, N_2, N_3, N_4)=(0.95,-0.10,0.27,-0.09) meaning that the lightest neutralino is an almost pure bino in this case meaning that the DM is a superpartner of the CMB.

For light neutralinos, i.e. small $m_{1/2}$, the Higgs mass limit requires m_0 to be in the TeV range, as indicated in Fig.5 by the almost vertical line, labeled

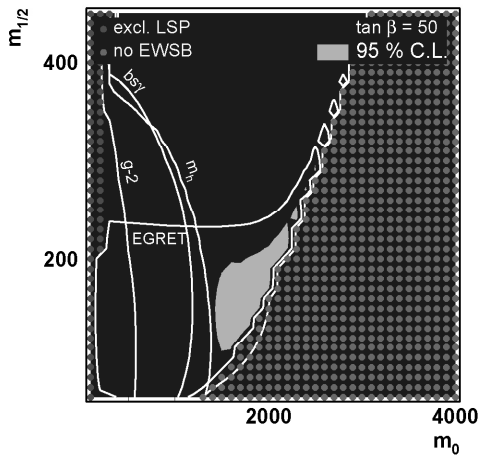

Figure 5: The allowed regions of the mSUGRA parameter space with account of EGRET data. The light shaded area (blue) indicates the 95% C.L. parameter range allowed by EGRET data, the individual constraints have been indicated by the lines and dots.

m_h. The EGRET data requires $m_{1/2}$ to be below the almost horizontal line at $m_{1/2} = 230$ GeV. In addition, the excluded regions from $b \to s\gamma$ and the anomalous magnetic moment of the muon have been indicated (left from the corresponding lines). We used `micrOMEGAs 1.4` [12] for the relic density calculation and we opted for the SUSY mass spectrum from the `Suspect 2.3.4` program [13]. The lower limits on m_0 discussed above are practically independent of A_0. The spectrum and the corresponding values of the relic density Ωh^2, $b \to s\gamma$ and Δa_μ have been tabulated in Table 1 for a typical set of parameters compatible with all constraints.

5 Search for SUSY at LHC

The detection of a SUSY-like signal at LHC corresponding to the EGRET point of mSUGRA would be a strong indication both for supersymmetry and for solution of the dark matter problem. The set of parameters from Table 1 was used as input for the ISAJET code [15] which calculated the superparticle spectrum and the PYTHIA generator [16] was used for event generation. The whole

Parameter	**Value**	**Particle**	**Mass [GeV]**
m_0	1500 GeV	$\tilde{\chi}^0_{1,2,3,4}$	64, 113, 194, 229
$m_{1/2}$	170 GeV	$\tilde{\chi}^{\pm}_{1,2}, \tilde{g}$	110, 230, 516
A_0	$0 \cdot m_0$	$\tilde{u}_{1,2} = \tilde{c}_{1,2}$	1519, 1523
$\tan\beta$	52.2	$\tilde{d}_{1,2} = \tilde{s}_{1,2}$	1522, 1524
sign μ	+	$\tilde{t}_{1,2}$	906, 1046
$\alpha_s(M_Z)$	0.122	$\tilde{b}_{1,2}$	1039, 1152
$\alpha_{em}(M_Z)$	0.0078153697	$\tilde{e}_{1,2} = \tilde{\mu}_{1,2}$	1497, 1499
$1/\alpha_{em}$	127.953	$\tilde{\tau}_{1,2}$	1035, 1288
$\sin^2(\theta_W)_{\overline{MS}}$	0.2314	$\tilde{\nu}_e, \tilde{\nu}_\mu, \tilde{\nu}_\tau$	1495, 1495, 1286
m_t	175 GeV	$h, H, A, H^{\pm}$	115, 372, 372, 383
m_b	4.214 GeV		
		Observable	**Value**
		$Br(b \to X_s\gamma)$	$3.02 \cdot 10^{-4}$
		Δa_μ	$1.07 \cdot 10^{-9}$
		Ωh^2	0.117

Table 1: *Typical mSUGRA parameters from the EGRET analysis and electroweak constraints and the corresponding mass spectrum of the SUSY particles and observables*

generation process was performed within the ATLAS software ATHENA [17]. Common property of SUSY-like processes with conserved R-parity is undetectable LSP in the final state which takes away high transverse momentum. The process with the highest cross section in pp collisions is the gluon fusion with production of two gluinos and their subsequent decay. One has the whole variety of possibilities. The processes with the highest cross-sections are those with b-jets alas they have severe SM background. Cleaner processes are those with leptons in the final state but the cross-sections are lower.

As an example we consider the low background process : $gg \to \tilde{g}\tilde{g} \hookrightarrow \overline{b} + b + \tilde{\chi}^0_2 \hookrightarrow \mu^- + \mu^+ + \tilde{\chi}^0_1$ shown in Fig.6. In the final state one has four b-quarks (b-jets), four muons and a pair of stable neutralinos $\tilde{\chi}^0_1$ giving the high missing transverse momentum. There are B-hadrons in these jets, and, in general, the event could have 4 secondary vertices, which allows one to reduce the background at the trigger level.

The cross-section of the hard $gg \to \tilde{g}\tilde{g}$ process at $\sqrt{s} - 14$ TeV varies between 5.6–14.2 pb (PYTHIA) at the chosen values of SUSY parameters and depends on parton distributions. For the PDF of GRV94D [18] and $Q^2_{min} =$ 0.5 GeV the cross section is ≈ 13 pb. However, the final cross-section of the

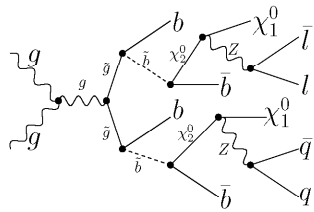

Figure 6: *Creation of gluino pair with subsequent cascade decay*

total cascade process drops to few fb due to small branching ratios.

It is the transverse momentum of pair of neutralinos shown in Fig.7 [19] that allows to distinguish this process from the background. The b-tagging of all b-jets and the careful reconstruction of their energy are also important for the study of the considered processes. B-hadrons with b-quarks inside live long enough to go far away off the creation point. As a result one can observe a secondary vertex of B-hadron decay at a certain distance from the primary beams collision initial vertex. This secondary vertex allows to tag hadronic jets from b-quarks. All together one expects around 150 of such events for ATLAS

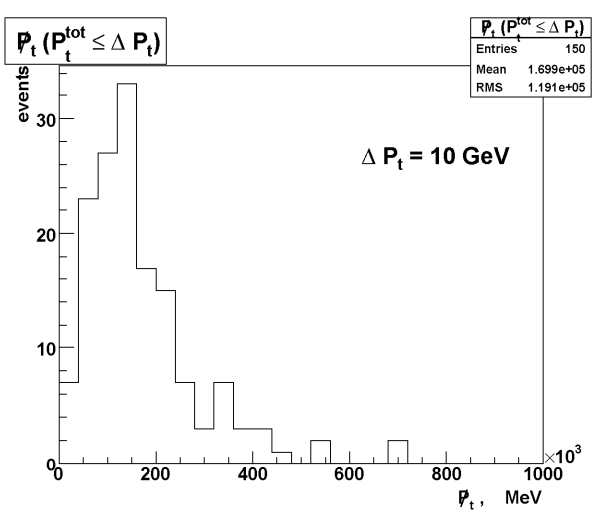

Figure 7: *Total missing transverse momentum P_t of two neutralinos. Event selection is made assuming that the total P_t of gluino pair is less than 10 GeV.*

detector after a year of running with the total LHC luminosity of 10^{34} cm^{-2}s^{-1}.

6 Conclusion

If one accepts:

- The interpretation of excess in diffuse galactic gamma rays as a signal of the DM annihilation,
- The interpretation of the Cold DM as SUSY neutralino particles;

Then:

- SUSY provides simultaneous consistent description of all observable data including astrophysics,
- Parameter space of SUSY is highly restricted,
- In the narrow allowed region of parameter space the SUSY mass spectrum is predicted,
- Light superpartners might be observable at the LHC.

Acknowledgements

Financial support from INFN and RFBR grant # 05-02-17603 are kindly acknowledged. The author is grateful to the organizers of the La Thuile meeting for hospitality and creating of pleasant atmosphere.

References

1. C. L. Bennett *et al.*, Preliminary Maps and Basic Results," Astrophys. J. Suppl. **148** (2003) 1, [arXiv:astro-ph/0302207].

2. J. R. Ellis, J. S. Hagelin, D. V. Nanopoulos, K. A. Olive and M. Srednicki, Nucl. Phys. B **238** (1984) 453.

3. G. Jungman, M. Kamionkowski and K. Griest, Phys. Rept. **267** (1996) 195, [arXiv:hep-ph/9506380].

4. W. de Boer, C. Sander, V. Zhukov, A. V. Gladyshev and D. I. Kazakov, Phys. Lett. **B636** (2006) 13, [arXiv:hep-ph/0511154].

5. Reviews and original references can be found in:
   W. de Boer, Prog. Part. Nucl. Phys. **33** (1994) 201 [arXiv:hep-ph/9402266];
   D. I. Kazakov, CERN 2001-003, [arXiv:hep-ph/0012288]; CERN-2006-003, [arXiv:hep-ph/0411064];
   P. Fayet and S. Ferrara, Phys. Rept. **32** (1977) 249;
   H. P. Nilles, Phys. Rept. **110** (1984) 1;
   H. E. Haber and G. L. Kane, Phys. Rept. **117** (1985) 75;
   M. F. Sohnius, Phys. Rept. **128** (1985) 39;
   A. B. Lahanas and D. V. Nanopoulos, Phys. Rept. **145** (1987) 1.

6. A.V. Gladyshev and D.I. Kazakov, *Supersymmetry and LHC*, Lectures given at the 9th Moscow International School of Physics (XXXIV ITEP Winter School of Physics), [arXiv:hep-ph/0606288].

7. J. Ellis, K. Olive, Y. Santoso, V. Spanos, Phys. Lett. **B565** (2003) 176; H. Baer, C. Balazs and A. Belyaev, JHEP **0203** (2002) 042; H. Baer, C. Balazs, JCAP **05** (2003) 006; A. Lahanas, D. V. Nanopoulos, Phys. Lett. **B568** (2003) 55; A. B.Lahanas, N. E. Mavromatos, D. V. Nanopoulos, Int. J. Mod. Phys. **D12** (2003) 1529.

8. A.V. Gladyshev, D.I. Kazakov and M.G. Paucar, Mod.Phys.Lett. **A20** (2005) 3085.

9. A.V. Gladyshev, D.I. Kazakov and M.G. Paucar, [arXiv:0704.1429].

10. R.C. Hartman, *et al.*, ApJ **S123** (1999) 79; S.D. Hunter, *et al.*, ApJ **481** (1997) 205.

11. W. de Boer, C. Sander, V. Zhukov, A. V. Gladyshev and D. I. Kazakov, Astron.& Astrophys. **444** (2005) L51, [arXiv:astro-ph/0508617];

12. G. Belanger, F. Boudjema, A. Pukhov, and A. Semenov, [arXiv:hep-ph/0405253]; G. Belanger, F. Boudjema, A. Pukhov, and A. Semenov, Comput. Phys. Commun. **149** (2002) 103, [arXiv:hep-ph/0112278].

13. A. Djouadi, J. L. Kneur and G. Moultaka, [arXiv:hep-ph/0211331].

14. W. de Boer, M. Huber, A.V. Gladyshev, and D.I. Kazakov, Eur. Phys. J. **C20** (2001) 689, [arXiv:hep-ph/0102163].

15. F.E. Paige, S.D. Protopopescu, H. Baer, and X. Tata, ISAJET 7.69: A Monte Carlo event generator for $pp, \bar{p}p$ and e^+e^- reactions, [arXiv:hep-ph/0312045].

16. T. Sjostrand, L. Lonnblad, S. Mrenna, and P. Skands, Pythia 6.3 physics and manual, FERMILAB-PUB-03-457, LU-TP-03-38, [arXiv:hep-ph/0308153].

17. Athena Core Software, `http://atlas-computing.web.cern.ch/atlas-computing/ packages/athenaCore/athenaCore.php`

18. M. Gluck, E. Reya and I. Schienbein, Phys. Rev. **D60** (1999) 054019, Erratum Phys. Rev. **D62** (2000) 019902.

19. V.A. Bednyakov, J.A. Budagov, A.V. Gladyshev, D.I. Kazakov, G.D. Khoriauli, and D.I. Khubua, JINR–E1–2006–97, [arXiv:hep-ex/0608060].

HIDING THE HIGGS AT THE LHC

Yoram Rozen
Phys. Dep., Technion, Israel Institute of Technology Institution, Haifa 32000, Israel

Abstract

We study a simple extension of the standard model where scalar singlets that mix with the Higgs doublet are added. This modification to the standard model could have a significant impact on Higgs searches at the LHC. The Higgs doublet is not a mass eigenstate and therefore the expected nice peak of the standard model Higgs disappears. We analyze this scenario finding the required properties of the singlets in order to make the Higgs "invisible" at the LHC. In some part of the parameter space even one singlet could make the discovery of the SM Higgs problematic. In other parts, the Higgs can be discovered even in the presence of many singlets.

1 Introduction

The Higgs particle of the Standard Model (SM) is expected to be discovered at the LHC. In extensions of the standard model, however, the situation could be different. Modifications to the scalar sector alter the experimental signatures of the Higgs boson in a model dependent way. Therefore, there is no guarantee that a very general Higgs boson can be found at the LHC.

The available experimental data provide constraints on the Higgs mass, m_H (for a review see [1]). The strongest lower bound comes from direct searches at LEP2, $m_H > 114.4\ GeV$ at 95% CL [2]. An upper bound is derived from electroweak precision measurements and reads $m_H < 219\ GeV$ at 95% CL [3]. Since the sensitivity of electroweak precision measurements to m_H is logarithmic, we cannot exclude at a very high confidence level the case where m_H is just a factor of a few above this limit.

One of the main goals of the LHC is to discover the Higgs boson. Both the ATLAS and CMS collaborations will search for the Higgs boson in the mass range of $10^2 - 10^3\ GeV$. The Higgs is expected to be discovered through different channels depending on its mass. In the low mass regime, the most promising channel would be $H \to \gamma\gamma$ [4]. For $m_H \gtrsim 150\ GeV$, the preferred decay is $H \to VV^{(*)}$ (with $V = Z, W$) with different substantial decays of the vector bosons. These searches are expected to provide at least a 5σ signal for the Higgs after few years of operation of the LHC.

There are also several theoretical constraints on m_H (see, for example, [5]). For example, the unitarity bound reads $m_H \lesssim 700\ GeV$. One can also consider the possibility that the Higgs does not exist. This possibility gives rise to a constraint on new physics scale $\Lambda \lesssim 1$ TeV. Thus, we expect that the LHC will find either the Higgs boson or some kind of new physics.

What if nothing is found at the LHC, that is, neither the Higgs boson nor new physics? Such a scenario seems to imply that (*i*) the Higgs boson does not exist; (*ii*) there is new physics that is responsible for electroweak-symmetry breaking (EWSB); and (*iii*) the experimental signals of this new physics are such that it cannot be discovered at the LHC. There is, however, another possibility: The Higgs exists and it is responsible for EWSB but there is new physics that "hides" the Higgs signals. Furthermore, this new physics does not show up in any other channel and therefore cannot be discovered at the LHC.

Here we talk about such a scenario which hides the Higgs and does not show any signal of new physics. We extend the scalar sector of the SM by introducing additional SM singlets which mix with the Higgs doublet of the SM. The resulting spectrum consists of many scalars. Each of these scalars

is mainly a singlet with a small component of the SM doublet. Thus, the production rate for any of these mass eigenstates is much smaller than that of a SM Higgs with the same mass. In the limit of many singlets each mass eigenstate produces a very small signal that cannot be separated from the background. In that case the Higgs is practically hidden. For a more detailed description with a numerical analysis of the possible number of scalar fields see [6] which also include a comperhansive review of related works.

2 The model

In order to understand the main features of our scenario we start with a simple case where one singlet, $S(1,1)_0$, is added to the SM. For simplicity we further introduce a Z_2 symmetry such that S is odd under it, while all other fields are even under this Z_2. Denoting the SM Higgs doublet by H, the most general renormalizable scalar potential is

$$\mu_H^2|H|^2 + \frac{\mu_S^2}{2}S^2 + \lambda_H|H|^4 + \frac{\lambda_S}{4}S^4 + \frac{\eta}{2}S^2|H|^2. \tag{1}$$

In the following we assume that

$$\mu_H \sim \mu_S, \qquad \lambda_H \sim \lambda_S \sim \eta. \tag{2}$$

While our assumptions, that all dimensionful parameters are at the same scale and all dimensionless couplings are of the same order, are simple and not necessarily fine-tuned, they are not based on a fundamental framework of new physics. We make them because they lead to interesting phenomenology.

We are interested in the vacuum structure of this potential. Since the Higgs vev is responsible for EWSB we demand $\langle H\rangle \neq 0$. As for the vev of S, the solution $\langle S\rangle = 0$ is not interesting as there is no mixing between S and H. Thus, we consider only solutions where $\langle H\rangle \neq 0$ and $\langle S\rangle \neq 0$. It is worth mentioning that in general there is a large part of the parameter space where both fields acquire a vev.

Next, we analyze the mass spectrum. We substitute

$$\mathcal{R}e(H) \to \frac{h + v_H}{\sqrt{2}}, \qquad S \to s + v_S, \tag{3}$$

where h and s are real scalar fields and v_H and v_S are the vacuum expectation values of H and S respectively. The mass-squared matrix in the (h,s) basis is

$$M^2 = \begin{pmatrix} \mu_H^2 + 3\lambda_H v_H^2 + \frac{1}{2}\eta\, v_S^2 & \eta v_H v_S \\ \eta v_H v_S & \mu_S^2 + 3\lambda_S v_S^2 + \frac{1}{2}\eta\, v_H^2 \end{pmatrix}. \tag{4}$$

Diagonalizing M^2, we get two mass eigenstates, ϕ_0 and ϕ_1 with masses m_0 and m_1. We define $m_0 \leq m_1$ and due to our assumptions we expect $m_0 \sim m_1$. We further consider only cases where the two mass eigenstates are not close to be degenerate, that is, $m_1 - m_0 \gg \Gamma_0, \Gamma_1$. The two mass eigenstates are related to the weak eigenstates h and s by a 2×2 orthogonal rotation matrix V

$$\begin{pmatrix} h \\ s \end{pmatrix} = V \begin{pmatrix} \phi_0 \\ \phi_1 \end{pmatrix}, \qquad V = \begin{pmatrix} \cos\theta & \sin\theta \\ -\sin\theta & \cos\theta \end{pmatrix}. \tag{5}$$

Note that θ can assume any value between 0 and $\pi/2$. In general θ can be very small, but due to our assumption, Eq. (2), we expect $\theta \sim O(1)$. The model discussed here contains five parameters. They can be chosen to be the five parameters in (1). Instead, we can chose them to be the two masses, m_0 and m_1, the two vevs, v_S and v_H and the mixing angle θ.

We are now in position to study the phenomenology of the model. The couplings of the scalars to the SM fields can be obtained from that of the SM Higgs by projecting onto the doublet component. In particular, we are interested in the coupling of a scalar to a pair of SM fields, either fermions or vector bosons

$$\frac{V_{hi}}{v_H}\left(m_f\,\phi_i \bar{f} f + m_Z^2\,\phi_i\,Z_\mu Z^\mu + 2m_W^2\,\phi_i\,W_\mu^+ W^{\mu-}\right). \tag{6}$$

We see that the couplings are just the SM couplings projected by V_{hi}. The couplings between two scalars and two gauge bosons are given by the SM ones multiplied by $V_{hi}V_{hj}$

$$\frac{V_{hi}V_{hj}}{2v_H^2}\left(m_Z^2\,\phi_i\phi_j\,Z_\mu Z^\mu + 2m_W^2\,\phi_i\phi_j\,W_\mu^+ W^{\mu-}\right). \tag{7}$$

Last we need the self interactions term, i.e., interaction that involve only scalars. The interesting part for our study is the couplings that can be responsible for decays of a heavy scalar into light scalars, $\phi_1 \to 2\phi_0$ and $\phi_1 \to 3\phi_0$. These couplings are given by

$$\begin{aligned} &\frac{1}{4}\Big[\left(\lambda_S - \lambda_H - (\lambda_S + \lambda_H - \eta)\cos 2\theta\right)\sin 2\theta\Big]\phi_1\phi_0^3 + \\ &[v_\phi \cos\theta\left((3\lambda_S - \eta)\sin^2\theta + \frac{\eta}{2}\cos^2\theta\right) \\ &-v_H \sin\theta\left((3\lambda_H - \eta)\cos^2\theta + \frac{\eta}{2}\sin^2\theta\right)]\phi_1\phi_0^2. \end{aligned} \tag{8}$$

In general there are no specific relations between the strength of the scalar couplings, Eq. (8), and the couplings between scalars and gauge bosons, Eqs. (6)

and (7). For example, the coupling of $\phi_1\phi_0^2$ can be similar, smaller or larger to that of $\phi_1 W^+W^-$.

We can generalize the above model by introducing N new singlets, S_α, with $\alpha = 1..N$. Again, we analyze the most interesting case where all the scalar fields acquire vevs. The algebra is more cumbersome, but we end up with a result similar to the case of one extra singlet. There are $N+1$ mass eigenstates ϕ_i $(i = 0..N)$. We expand around the vacuum in a similar way as Eq. (3). In terms of the weak eigenstates, $\phi^W \equiv (h, s_\alpha)$, the mass eigenstates ϕ are given by $\phi = V\phi^W$, such that V is an $(N+1) \times (N+1)$ orthogonal matrix. The couplings to the SM fields are then given as in the one singlet case by Eqs. (6) and (7). The analog of Eq. (8) is more complicated. It can be obtained in a straightforward way and we do not write it explicitly here. We only mention that also in the more general case considered here the couplings between the scalars can be smaller, similar, or larger with respect to other couplings which involves gauge bosons.

3 Phenomenology of the model

Next we study the phenomenology of the N singlets model. We first look at the effect of this model on electroweak precision measurements (see also [7]) and then move to discuss the collider signatures.

The SM Higgs contribution to electroweak precision measurements comes through the S and T parameters. [8] That is, the gauge boson self energies are the only numerically relevant diagrams with the Higgs. Of course varying m_H affects all observables, but in a way consistent with changing just S and T. Thus, in order to see the effects of our model, all we need to do is to replace the SM Higgs contributions to S and T with the sum of all contributions weighted by the mixing angles. Consider a one-loop diagram with the ith mass eigenstate. Its contribution to S and T is equal to that of the corresponding SM diagram multiplied by $|V_{hi}|^2$. In the leading log approximation, we therefore substitute

$$\log(m_h^2) \to \sum_i |V_{hi}|^2 \log(m_i^2). \tag{9}$$

Thus, the bound on the Higgs mass in the SM is replaced by a bound on a function of the masses and mixing angles. In particular, we can have heavy mass eigenstates up to 1 TeV without violating the electroweak data.

In order to discuss the implications of our model on collider searches of the Higgs, we recall some issues regarding the search for the SM Higgs. Depending on the Higgs mass, there are several decay channels that are used to search for the Higgs. They are discussed at length in Ref. [1] and are summarized in figs. 22 and 23 there. Roughly speaking, we can say that

1. At the low mass range, the Higgs is mainly searched for by looking into a resonance in different channels (like $H \to \gamma\gamma$ or $H \to ZZ^{(*)} \to 4l$).

2. For $m_h \gtrsim 400$ GeV the search channels are mainly $H \to ZZ \to ll\nu\nu$ and $H \to WW \to l\nu jj$ where the search is for missing mass/momentum.

A relevant point to the Higgs search is the width of the Higgs, Γ_h. The experimental resolution is expected to be $\sigma \sim 2$ GeV [9] which is roughly the width of a Higgs with $m_h \sim 200$ GeV. For $\Gamma_h < \sigma$ a reduction of the Higgs width due to added singlets is practically impossible to detected, while for $\Gamma_h > \sigma$ this effect is more noticeble.

Now we move back to our model. The main effect of our model on collider searches for the Higgs is that the cross section of each mass eigenstate is suppressed compared to a SM Higgs of the same mass. The leading production process at the LHC is gluon fusion through one-loop triangle diagram. Thus, the production cross section for each mass eigenstate is suppressed by a factor of $|V_{hi}|^2$. In the limit of many new singlets, $|V_{hi}|$ is small, and thus the cross section become very small.

The other effects depend on the parameters of the model. First consider the scenario where decays of the form $\phi_i \to 2\phi_j$ are forbidden or negligible. Then, all the decay rates of the ith mass eigenstate are suppressed by the same factor of $|V_{hi}|^2$. Thus, the branching ratios are the same as those of a SM Higgs with the same mass. The total width of each mass eigenstate is smaller by a factor of $|V_{hi}|^2$ compared to the width of a SM Higgs with the same mass.

We can think about three different cases for the above scenario. First we discuss the low mass range where the Higgs is searched for by a resonance and the width of the Higgs is small compared to the experimental resolution. Then the signal of each mass eigenstates is reduced by $|V_{hi}|^2$. (The width is also reduced by the same amount but this reduction cannot be noticed.) With many singlets, when $|V_{hi}|^2$ is very small for all i, the signal significance will drop below detection level. With about ten singlets no signal of the Higgs can be found if all mass eigenstates are below about 300 GeV. In some cases even one singlet is enough to "hide" the Higgs, while in other cases more than ten singlets are needed.

When the width of each mass eigenstate, Γ_i, is large, $\Gamma_i > \sigma$ the division of the signal between the singlets reduces the significance of each resonance $|V_{hi}|$. The reason is that while the total signal is reduced by $|V_{hi}|^2$, this reduction simultaneously affects the width of the resonance. Indeed in our study we found that when we have masses above about 300 GeV, more singlets are needed in order to hide the Higgs signals then in the lower mass case.

The third case is where some of the mass eigenstates are heavy with $m_i \gtrsim 400$ GeV. All these mass eigenstates contribute to the missing energy

signal. Hence, the combined excess of these eigenstates over the background will be similar to that of a SM Higgs with $m_h \gtrsim 400$ GeV. In this case it is possible to hide the Higgs signal by adding light mass eigenstates whose signals are reduced by the $|V_{hi}|^2$ factors.

Last we discuss the scenario where decays like $\phi_i \to 2\phi_j$ are important. In particular, the interesting case is when all the heavy scalars decay almost entirely to the lightest one. In that case the situation is similar to the SM Higgs. Only one mass eigenstate is produced and its branching ratios are the same as a SM Higgs with the same mass. Yet, the production cross section and width are smaller than for a SM Higgs. This is because the production cross section for a heavy mass eigenstate is always less than half that of the light one. Thus, the fact that a heavy mass eigenstate decays into two light scalars cannot compensate for the reduction in the production rate and the parameter spcae allow for the possibility of the Higgs being hidden.

4 Discussion and conclusions

The Higgs boson is expected to be discovered at the LHC. Depending on its mass, different channels will be used to discover it. The standard model will be in a very bad position if the Higgs is not found. In this work we have shown that additional singlets might explain an absence of a Higgs signal without any signal of new physics. We analyzed scenarios corresponding to different masses in the range of $10^2 \lesssim m_i \lesssim 10^3$ GeV. We assumed that all dimension-full parameters are of the order of the weak scale and all dimensionless parameters are of order one. In particular we asked how many singlets are needed in order to "hide" the Higgs. The answer depends crucially on the model parameters. In some cases, in particular when the mass eigenstates are close to 100 GeV, we found that a single additional singlet could reduce the significance below discovery level. In other cases, mainly when many of the masses are roughly above 300 GeV we found that tens of singlets are needed to hide the Higgs.

We have concentrated on the Higgs search at the LHC. In fact, it could affect the searches for the Higgs also at LEP and the Tevatron and it is possible that the Higgs signal is hidden by a many-singlet solution. Yet, we did not investigate this issue in details. For the case of one extra singlet such a study was done in. [10)]

To conclude, we present a model in which the standard model Higgs field generates electroweak symmetry breaking but still the Higgs particle cannot be discovered at the LHC. Our model is very simple, and while it is not based on a well motivated theoretical framework, it serves as an example that the SM Higgs mechanism can escape detection at the LHC.

Acknowledgments

We are grateful to Ehud Duchovni, Andrey Katz, Amos Ori, and Witold Skiba for useful discussions and Yossi Nir, Yael Shadmi and Ze'ev Surujon for comments on the manuscript. The work of Y.G. is supported in part by the Israel Science Foundation under Grant No. 378/05. The work of Y.R. is supported in part by the Israel Science Foundation under Grant No. 1446/05.

References

1. L. Reina, "TASI 2004 lecture notes: Higgs boson physics," arXiv:hep-ph/0512377.
2. R. Barate *et al.* [LEP Working Group for Higgs boson searches], Phys. Lett. B **565**, 61 (2003) [arXiv:hep-ex/0306033].
3. LEP Collaborations et. al., Phys. Rept. **427**, 257 (2006) [arXiv:hep-ex/0509008].
4. S. Asai *et al.* (ATLAS collaboration), Eur. Phys. J. C **32S2**, 19 (2004) [arXiv:hep-ph/0402254].
5. J. Gunion, H. Haber, G. Kane, and S. Dawson, *The Higgs Hunter's Guide*, Addison–Wesley, Reading (USA), 1990.
6. O. Bahat-Treidel, Y. Grossman and Y. Rozen, *Hiding the Higgs at the LHC*, J. High Energy Phys. JHEP05(2007)022. [arXiv:hep-ph/0611162].
7. D. G. Cerdeno, A. Dedes and T. E. J. Underwood, JHEP **0609**, 067 (2006) [arXiv:hep-ph/0607157].
8. M. E. Peskin and T. Takeuchi, Phys. Rev. D **46**, 381 (1992).
9. ATLAS collaboration, ATLAS Detector and Physics performance Technical Design Report, LHCC/99-14/15.
10. D. O'Connell, M. J. Ramsey-Musolf and M. B. Wise, arXiv:hep-ph/0611014.

SESSION VII – PERSPECTIVES

ON THE BRINK OF REVELATION AND REVOLUTION: ELECTROWEAK SYMMETRY BREAKING IN 2008/2009

Richard St. Denis
University of Glasgow – Department of Physics and Astronomy
Glasgow G12 8QQ – United Kingdom

Abstract

In this paper a discussion of the rapid progress in measurements of the top quark, W mass and in direct searches for the Higgs at the Tevatron is examined a physics strategy for studying electroweak symmetry breaking at the LHC and Tevatron in the next years is considered.

1 Overview

Over the last three years the Tevatron experiments have enjoyed an annual doubling of the integrated luminosity delivered and recorded. This has led to a watershed of new results in the area of electroweak symmetry breaking and in particular in direct searches for the Higgs. At the same time, completion of the Large Hadron collider and the associated experiments nears. In this paper an examination of the results at hand is made with a view to how the picture of electroweak symmetry breaking may evolve in the next two years. The discussion is organized as follows. First an examination of the Tevatron physics reach is reviewed. This is followed by a discussion of virtual and direct Higgs detection. After this recent results on a SUSY Higgs search and its implications are considered. Finally based on the projected schedule for the LHC and expectations for the performace of the Tevatron experiments, a scenario for the development of the research enviroment for electroweak symmetry breaking is discussed.

2 The Tevatron Physics Reach

The physics reach of the Tevatron is built on a mountain of measurements that ensure the ability of the collaborations to use their detectors to do physics. Each measurement is for itself a significant result. Measurements begin with the largest cross section processes, those of B physics, but focussing on measurements having small branching ratios and difficult backgrounds. The most recent such measurement is that of B_s oscillations where Δm_s has been determined by CDF [1] to be $\Delta m_s = 17.77 \pm 0.10 \pm 0.07$ ps^{-1}. Proceeding from there to the high transverse momentum leptons but requiring exquisite understanding of the details of the detector performance is the world's most precise single measurement of the W-mass by CDF [2] of 80413± 34(stat) ± 34 (sys) MeV/c^2. Continuing onwards to rarer processes one finds the measurment of the top quark mass from the Tevatron, a value which currently stands at 170.9±1.8 GeV/c^2 [3]. The measurements of the W^+W^- pair production [4] cross section and the first observation of $W^{\pm}Z^0$ events [5] exhaust the loftiest current observations of electroweak processes. The summit to be reached, first by passing observation and measurement of Z^0Z^0 pair production, is the discovery of the Standard Model Higgs. This journey through lower and lower cross section processes represents one approach to provide convincing evidence of these processes, first as discovery then as measurments constraining the Standard Model. The precision measurements themselves provide confidence in the experimental method and at the same time give insight into rare proceses through their contribution to virtual mass corrections. Discussion of this approach is the subject of Section 3. A clear assault on the summit with direct

searches for the Higgs is another approach and is discussed in Section 4. Along the way, some new physics may well appear, with Supersymmetry being the most popular candidate and a discussion of this in light of a recent search for SUSY Higgs is mentioned in Section 5. Finally there is an entirely different approach. This is s search for Higgs production in diffractive scattering discussed elsewhere in these proceedings [6].

3 Indirect Searches for Higgs

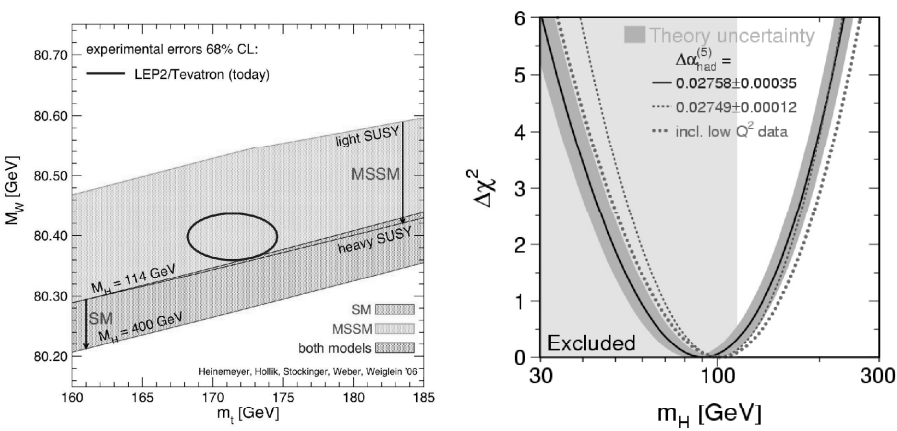

Figure 1: *Mass of the top quark vs Mass of the W boson compared to MSSM SUSY and Standard Model expectations (left) and best fit Higgs mass to the electroweak data.*

Indirect searches for the Higgs amount to measurements of the W and top mass which are sensitive to loop corrections containing a Standard Model Higgs, SUSY particles or other new physics. In February of 2006, the situation was as follows [7]. The best fit mass of the Standard Model Higgs was $M_h = 91\ ^{+45}_{-32}$ GeV/c^2 with $M_h < 186$ GeV/c^2 with 95% confidence and $M_h < 210$ GeV/c^2 with 95% if the LEP limits on a direct search for the Higgs [8] are included. In one short year, as shown in fig. 1 [9] [10], the situation has changed significantly due to new measurements of the top and W masses. The most probable value of of the Higgs mass is now $M_h = 80$ GeV/c^2. The probability that the Higgs has a mass larger than 114.GeV/c^2 is 19% and $M_h < 156$ GeV/c^2 with 95% confidence. These observations give strong indications for the search strategies that one should undertake when looking for the Standard Model Higgs. While it is striking that the 1 σ contour has crept into the SUSY-favored region, it is

important to realize that the 3σ contours overlap the Standard Model portion of the m_{top}–m_W plane.

4 Direct Searches for the Standard Model Higgs

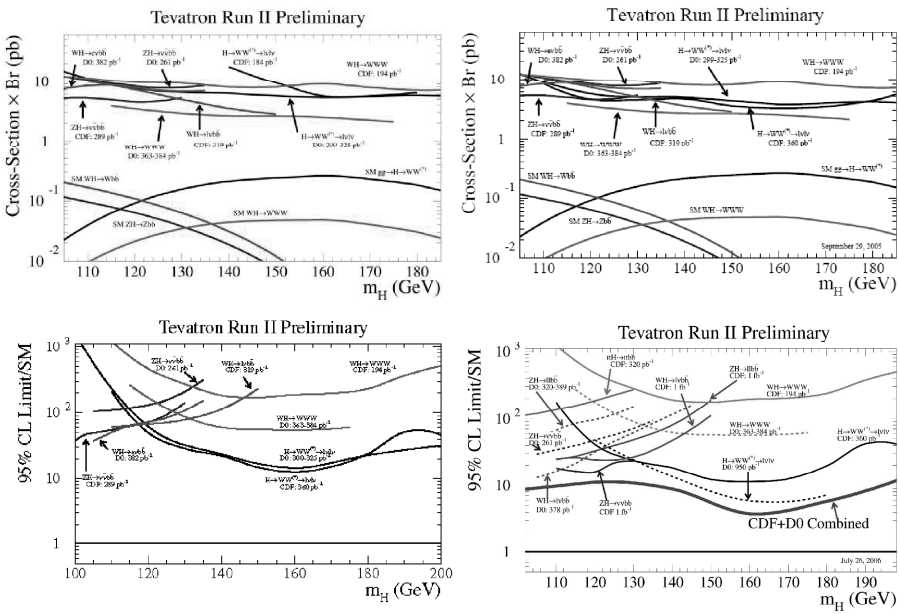

Figure 2: *Limits on Standard Model Higgs production cross sections from a. Summer 2005 (upper left), b. September 2005 (upper right), c. February 2006 (lower left) and d. Summer 2006 (lower right). The y-axis in the upper figures is cross section. In the lower figures the y-axis is relative to the expected Standard Model Higgs cross section.*

There are four main production mechanisms for the Standard Model Higgs when searching at hadron colliders: Gluon fusion, which dominates at the Tevatron and LHC, associated production or "Higgsstrahhlung", the mechanism holding the best hope for Higgs in the range up to about 130 GeV/c^2 and is most actively pursued at the Tevatron, and vector boson fusion and $t\bar{t}H^0$ production which are of interest particularly at LHC.

The strategy for direct searches at the Tevatron is influenced by the tantalizing results from LEP where ALEPH claimed 3σ evidence for a Standard Model Higgs at $M_h = 115$ GeV/c^2 [11]. In light of a lack of confir-

mation of the other LEP experiments, the boundary for direct searches for the Higgs is set at $M_h > 114.4$ GeV/c^2 at 95% confidence [8]. The current experimental searches at the Tevatron focus on the gluon fusion process $gg \to H^0 \to W^+W^- \to \ell^+\ell^-\bar{\nu}_{\ell+}\nu_{\ell-}$ and the associated production processes $q\bar{q} \to (W^\pm/Z^0)H^0$ where $W^\pm \to \ell^\pm\nu_\ell$, $Z^0 \to \nu_\ell\bar{\nu}_\ell$ or $Z^0 \to \ell^+\ell^-$ and $H^0 \to b\bar{b}$. The leptons ℓ may be electrons, muons or taus. In the case of taus current searches are limited to the τ decay channels $\tau^- \to e^-\bar{\nu}_e$ or $\tau^- \to \mu^-\bar{\nu}_\mu$ and charge conjugate channels. These search modes divide experimentally into two major camps of effort: those that need precise measurement of particle decay vertices employing silicon tracking and those that do not. The associated production channels fall into the first camp and the W boson pair production modes fall into the second camp.

The sensitivity of these searches to the Standard Model Higgs cross section is increasing rapidly with time. Results that were presented in all the various search modes for the Summer 2005 conferences are shown in fig. 2a and by September of 2005 had changed to those shown in fig. 2b, with sensitivity in the region around $M_h \simeq 160$ GeV/c^2 improved by over an order of magnitude with about twice the integrated luminosity analyzed. This illustrates that the rapid progress is made not only based on an increase in the amount of data analyzed but also by the techniques employed and the understanding of the detectors. For the decay of Higgs into W pairs, the handling of leptons having transverse momenta between 10 and 20 GeV/c^2 led to significant improvements in acceptance and hence sensitivity to smaller cross sections. By February of 2006, further improvements were made and this is illustrated in fig. 2c where the sensitivity at $M_h = 160$ GeV/c^2 has come to within a factor of 12 of the Standard Model expectation. Since that time there are improvements in mass resolution in the reconstruction of the Higgs mass in decays to b quarks, sophisticated neural network analyses, better control of the systematic uncertainties in tagging jets containing b quarks, and a factor of three in integrated luminosity. As shown in fig. 2d the low mass Higgs measurements have come from having a sensitivity of a factor of 30 to 60 above the Standard Model prediction to being within a factor of 10 by the time of this conference in February 2007 [12]. At higher mass, sensitivity to the Higgs at $M_h = 160$ GeV/c^2 is about a factor of 4 larger than that of the Standard Model. All of these results are for an integrated luminosity of 1 fb^{-1} or less. This rapid progress is expected to continue as the Tevatron performance has been exceptional, with both CDF and D0 having recorded more than 2 fb^{-1} of integrated luminosity.

To illustrate the experimental issues and hence gain insight into the prospects for improvements, some of the challenges are considered in each of the various channels. First in associated production for the ZH mode where the Z decays to neutrinos, the trigger is 35 GeV of missing energy and two jets

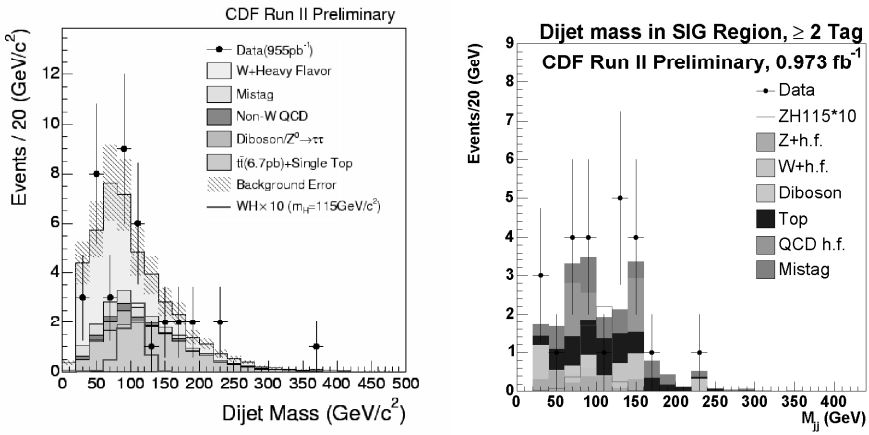

Figure 3: *CDF results for Higgs searches: invariant mass distribution of jets in Higgs search in WH mode and ZH mode with Z decaying to neutrinos.*

above 20 GeV with one jet having $|\eta| < 0.7$. The dominant background is QCD production of b jets with mismeasurement leading to apparent missing energy. For the WZ production, the trigger is an electron or muon with transverse momentum, $p_t > 20$ GeV/c^2. The topology is distinguished by the lepton, missing energy and and one or two identified b jets. The dominant background is top production. Finally, for WZ production where the Z decays to leptons, the trigger is again an electron or muon with $p_t > 20$ GeV/c^2. The topology is distinguished by the two leptons and one or two identified b jets. In this case there is also a kinematic distinction of the leptons forming a Z mass. In all these associated production channels there are additional kinematic constraints on the b jets forming a HIggs mass. Acceptance for the leptons, improving the trigger and missing energy resolution in the trigger, recognizing the topological and kinematic properties are all areas for experimental improvement. Of particularly acute importance is the efficient and correct recognition of b jets, a topological constraint, plus the measurement of the invariant mass with the b jets, a kinematic constraint. Efficient exploitation of the kinematic and topological features of Higgs events can be obtained from use of more sophisticated matrix element or Artificial Neural Network techinques. The latter is employed in the case of ZH where Z decays to leptons. Such methods can also be applied to other modes and promise to bring significant improvement in the sensitivity to detection of Standard Model Higgs. Control over systematic uncertainties and gain in sensitivity is obtained through the combination of these various channels. There are common uncertainties associated with b jet identification

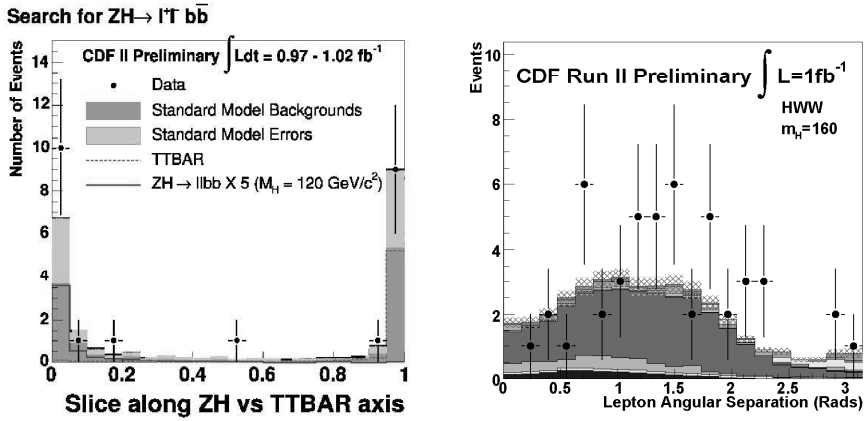

Figure 4: *CDF results for Higgs searches: NN scores for ZH production with Z decaying to visible leptons (lower left) and azimuthal separation of leptons in Higgs decays to W pairs (Magenta: WW, Light Blue: Wγ, Dark Blue: Higgs) (lower right).*

and Higgs mass determination from b jets.

Results for the various associated production modes are summarized in fig. 3 for WH, ZH production where the Z decays to neutrinos and in fig. 4 where the Z decays to visible leptons. The dijet mass is the distinguishing plot for WH production and the neutrino decay mode of the Z in ZH production. Both figures exemplify the importance of the invariant mass resolution of the Higgs decay to b jets in light of the significant background from W plus heavy flavor and top for WH and QCD or Z plus jets in the ZH mode. In ZH associated production with visible leptonic decays of the Z shows the neural net output, where a score of 0.0 is the signal region. The uncertainty in the production of Z plus jets dominates and the shaded area shows how important it is to constrain this.

The search for the decay of Higgs to W boson pairs which decay to leptons has sensitivity that is comparable to the associated production modes down to a Higgs mass of about $M_h = 120$ to 130 GeV/c^2 and a reach above 170 GeV/c^2 with the best sensitivity around $M_h = 2M_w$, where M_w is the W boson mass. This mode is characterized by two high transverse momentum leptons which have a spin correlation that distinguishes the angle between them from other Standard Model modes of dilepton production. A simple cut on a dilepton mass at $M_{\ell\ell} > 16$ GeV/c^2 removes the large number of dileptons from B decays as evidenced by the fact that the kinematics of the remaining dilepton events are well described by the Drell-Yan predictions. Thus Drell-Yan

Table 1: *Numbers of events per experiment of W pairs from Higgs decays potentially produced in the 2fb*$^{-}$1 *recorded at the Tevatron. This is broken down into gluon fusion (gg) production and vector boson fusion (VBF) production. The number accepted is also given.*

M_h GeV/c^2	120	140	160	180	200
Initial State					
2-6 gg	28	66	82	58	32
VBF	2	6	8	6	4
Total	30	72	90	64	36
Accepted	2	7	11	8	5

production becomes the dominant source of lepton pairs at the Tevatron. These leptons tend to have an azimuthal separation of 180 degrees and these events are easily distinguished from Higgs events. The sample of events with azimuthal separation smaller than 180 degrees is dominated by W pair production without an intermediate Higgs. These leptons tend not to have the strong azimuthal correlation offered by the Higgs decay. The potential number of events recorded and detectable in 2fb^1 are indicated in tab. 1 for various Higgs masses for these modes. WZ, ZZ and Wγ events also contribute.

As detecting the Higgs amounts to measurement of the cross section, attention must be paid to the measurement of the lepton acceptance. For this the Drell-Yan events offer the important measurement and obtaining consistent Z cross sections for all parts of the detector are required. Communicating these acceptances is also difficult and it is necessary to first provide a proof of principle that the detector is well-enough understood that the Drell-Yan cross section may be measured. Then searches for the Higgs require that the same cross sections can be obtained at the same time that the Higgs search is conducted. The measurements of $\sigma(p\bar{p} \to Z^0) \times Br(Z^0 \to e^+e^-)$ and $\sigma(p\bar{p} \to Z^0) \times Br(Z^0 \to \mu^+\mu^-)$ for various combinations of leptons measured in various parts are kept consistent to 1%. Since the measurement of this cross section amounts to a measurement of the quark-antiquark collision luminosity and since the WW production is dominated by this same initial state, the measurement offers a crucial control on the dominant backgrounds. The resulting distribution of the angular separation of the leptons is shown in fig. 4 for a $M_h = 160$ GeV/c^2.

5 SUSY

A recent search for neutral SUSY Higgs [12)] was made in the mode where the SUSY Higgs decays to tau pairs. The MSSM SUSY model has five Higgs

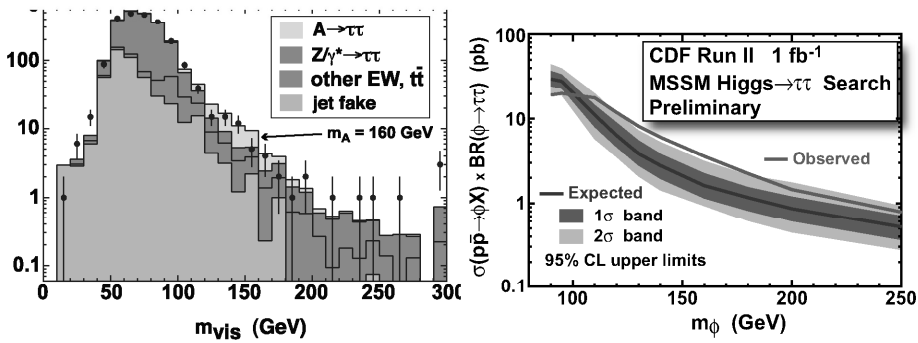

Figure 5: *Distribution of the invariant mass of the visible products of tau decays in the CDF search for SUSY Higgs and resulting exclusion limits for SUSY Higgs. The results for the higher statistics sample where one tau decays e or μ and the other hadronically is shown. The results are preliminary.*

particles, H^0, h^0 A^0 and $H^{\pm}$. The phenomenology is characterized by the ratio of the down and up type quark vacuum expectation values expressed as the parameter $\tan\beta$. The b quark enhances both production and decay of these neutral Higgs particles and when $\tan\beta$ is large, of order 50, the rate becomes sufficient to detect the neutral SUSY Higgs at the Tevatron. In this model, either the H^0 is light and Standard-Model-like with the h^0 and A^0 degenerate and enhanced by $\tan\beta$ or the h^0 is light and Standard-Model-like with the H^0 and A^0 degenerate and enhanced by $\tan\beta$. The lighter Higgs must have a mass less than about 130 GeV/c^2. The degenerate state is denoted by the symbol ϕ. The search is conducted on decays of $\phi \to \tau^+\tau^-$ where one tau decays to a muon or electron plus neutrinos and the other either again to muon or electron plus neutrinos, or to hadrons and a neutrino. The invariant mass of the taus is examined but due to the unmeasured neutrinos, only a visible portion of the mass is measured. Results for CDF [12] are shown in fig. 5 and small deviation around $M_\phi = 160$ GeV/c^2 is observed, leading to exclusion limits being somewhat less constrained than expected. A study by D0 [12] has shown no such deviation and additional statistics are anxiously awaited.

Global fits to the SUSY results [13] have been performed and the results are shown in fig. 6. The intriguing outcome is that for low $\tan\beta$ the sparticle spectrum exhibits a preference to low mass. The characteristic scale, $m_{1/2}$, has a value around 250 to 300 GeV/c^2, implying that the sparticle spectrum may possibly be within the reach of the Tevatron. For this case the SUSY Higgs would possibly be difficult to observe. For high values of $\tan\beta$ the likelihood favors $m_{1/2}$ of order 600 GeV/c^2 where discovery of sparticles would

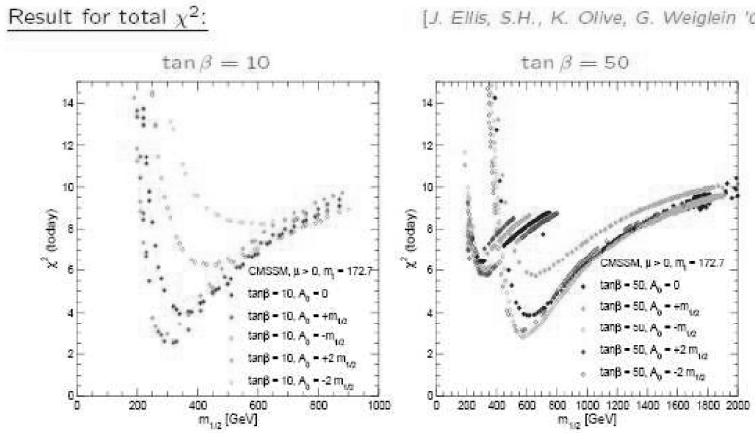

Figure 6: *Likelihood fits to the SUSY Model.*

be exclusively in the realm of the LHC, but the neutral SUSY Higgs could be seen at the Tevatron. This is of course dependent on the mass of the Higgs and that can be large so that it may not be seen at the Tevatron even with large $\tan\beta$ and would place SUSY entirely within the realm of the LHC.

6 LHC and a Scenario

The progress outlined in the last sections has been based mainly on results from the Tevatron. As the LHC comes into play the question arises as to how the understanding of electroweak symmetry breaking will continue to evolve. A broad comparison of the physics output of the LHC with 1 fb^{-1} of data to the total statistics from previous colliders [1] has been given [14] and is reproduced in Table 2. The potential for Higgs discovery at LHC is shown in fig. 7 for an integrated luminosity of 30 fb^{-1}. From this figure, one observes that the higher mass regions may well be excluded by the Tevatron both by direct search in the W pair decay channel and by virtual measurements coming form precision top and W masses. At the Tevatron there is great potential to exclude or see deviations in the intermediate mass range, $130 < M_h < 170$ GeV/c^2. This leaves the low mass range where both the Tevatron and the LHC will require more time to exclude or discover the Higgs.

In February 2006, this lead to the following scenario:

[1] A total integrated luminosity of 8 fb^{-1} has been assumed for the Tevatron.

Table 2: *Examples of production rates of some benchmark physics processes for the LHC and past colliders.*

Channel(s)	Ev/Exp/fb^{-1} (LHC)	Total Statistics from Previous Colliders
$W \to \mu\nu$	7×10^6	10^4 (LEP) 10^6 (TeV)
$Z \to \mu\mu$	10^6	10^6 (LEP) 10^5 (TeV)
$t\bar{t} \to \mu\nu + X$	10^5	10^4 (TeV)
gluino-gluino ($m = 1$ TeV)	10^2 - 10^3	–

- **LHC 2007:** The LHC has its first pilot run. Calibrations with Z,W are completed and an integrated luminosity of 200 pb^{-1} is accumulated.
- **LHC 2008:** The first full LHC physics run is completed with an integrated luminosity of 1 fb^{-1}.
- **TEV 2007:** The Tevatron has accumulated 4 fb^{-1} total. The WW decay mode is sensitive in the region $140 < M_h < 170$ GeV/c^2. The W and top mass accuracy narrows in on Higgs mass so that:
  - Deviations are building in the higher mass range. LHC focusses on this in 2009.

    Standard Model fits exclude the upper range ($M_h > 170$ GeV/c^2) and $M_h < 150$ GeV/c^2.
- If the exclusion of higher masses is in fact the case then:
  - **TEV 2009:** Evidence for a Higgs for $M_h = 115$ GeV/c^2 is seen at 3σ level.
  - **LHC/TEV 2011:** With 30 fb^{-1} of integrated luminosity, the LHC experiments confirm the discovery of Higgs at $M_h = 115$ GeV/c^2 in the $\gamma\gamma$ decay mode.
- If deviations are seen at higher masses:
  - **LHC 2010:** With 10 fb^{-1} of integrated luminosity, the LHC experiments claim discovery of a higher mass Higgs.

In this scenario then it seems that the Tevatron should continue to run well into 2009/2010. This is especially true if the low mass higgs emerges as the favoured value.

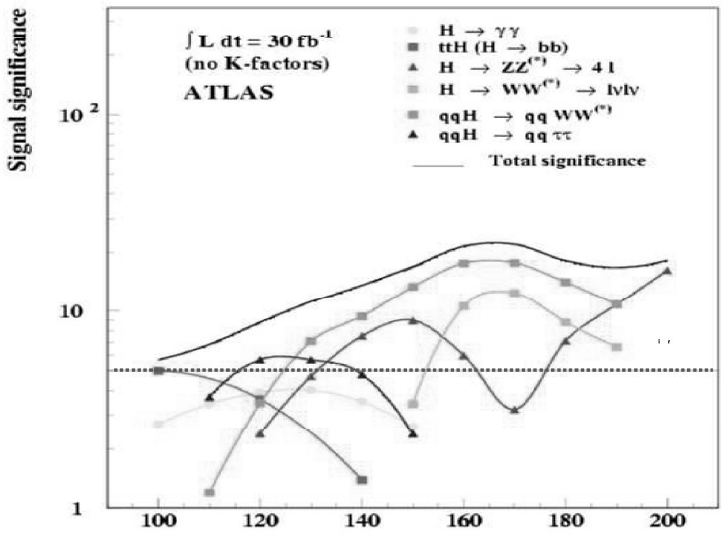

Figure 7: *Discovery potential of LHC for Higgs.*

Turning to February 2007, the situation has developed rapidly and changed, as was stated in the previous sections. The end result is to simply add approximately six months to one year to the estimates above. The evidence from precision fits favors somewhat more strongly the lower mass region.

7 Conclusions

This conference is held at a remarkable moment in the understanding of electroweak symmetry breaking. Rapid changes in data collection and more sophisticated experimental technique are leading to a constantly changing picture. The evidence presented here included the following highlights:

- The ALEPH 3σ evidence for Higgs at a mass of 115 GeV/c^2;
- Active searches for SUSY Higgs with promise of rapid resolution of 2σ effects at the Tevatron very soon.
- Outstanding increase in the precision of the top and W mass measurements leading to new constraints on the Standard Model and other models of new physics, especially of SUSY.

- Promise of a huge new increase in data collected in the next couple of years at both the Tevatron and LHC.

The changes in the understanding of the electroweak symmetry breaking at the Tevatron results are happening on the time scale of months and there is promise of a significant narrowing of the range of masses in which the Higgs boson may lie. If the scenarios play out to favor the low mass Higgs, this period of rapid development will be followed by a longer period of improving analyses as the Tevatron and LHC attempt to deal with the challenges of these low mass searches. In this case it is partcularly interesting to note that the main search modes for the Tevatron are not pursued at the LHC and that only the $H^0 \to \gamma\gamma$ mode is being investigated there. It is unlikely that this will remain the case for long as opportunities for innovation and exploitation of the data will clearly be pursued with vigor as the summit of the Higgs is finally claimed.

8 Acknowledgements

The author would like to thank the organizers for this invitation to speak.

References

1. A. Abulencia *et al*, Phys. Rev. Lett. **97**, 242003 (2006).
2. Ch. Hays, these proceedings.
3. P. Fernández, these proceedings.
4. D. Acosta *et al*, Phys. Rev. Lett. **94**, 211801 (2005), V.M. Abazov *et al*, Phys. Rev. Lett. **94**, 151801 (2005).
5. A. Abulencia *et al*, Phys. Rev. Lett. **98**, 161801 (2007).
6. D. Guilianos, these proceedings.
7. The ALEPH, DELPHI, L3, OPAL, SLD Collaborations, the LEP Electroweak Working Group, the SLD Electroweak and Heavy Flavour Groups, Phys. Rept.**427** (2006) 257.
8. ALEPH, DELPHI, L3 and OPAL Collaborations
   The LEP Working Group for Higgs Boson Searches, Search for the Standard Model Higgs Boson at LEP, CERN-EP-2003-011.
9. S. Heinemeyer, W. Hollik, D. Stockinger, A.M. Weber and G. Weiglein, hep-ph/0604147, updated for Winter 2007.

10. Lep Electroweak Working Group, Winter 2007 update, http://lepewwg.web.cern.ch/LEPEWWG/plots/winter2007/.

11. A. Heister *et al*, Physics Letters B **526**, Issues 3-4, (2002) 191.

12. T. Nunnemeann, these proceedings.

13. John Ellis *et al*, J. High Energy Phys. JHEP **05** (2006)005.

14. F. Gionatti, Probing The Hierarchy Problem with the LHC, in: Proc. XXII International Symposium on Lepton and Photon Interactions at High Energies (ed. R. Brenner, C. P. de los Heros, and J. Rathsman, Uppsala, June 2005), International Journal of Modern Physics A, **21**, Nos. 8-9 (2006)

A NEW APPROACH TO NONRENORMALIZABLE THEORIES

Ruggero Ferrari
Daniele Bettinelli and Andrea Quadri
Dip. di Fisica, Università degli Studi di Milano and INFN, Sez. di Milano

Abstract

The problem of constructing a sensible physical theory out of a nonrenormalizable classical action is discussed and instanced in the paradigmatic case of the nonlinear sigma model.

At variance with the approach of algebraic renormalization, the perturbative expansion in $\hbar$ is not constructed on the most general classical action, where each new independent divergent amplitude induces a novel parameter. Instead a solution is searched where the number of free parameters is fixed and all the requirements associated to symmetry properties, defining equations, locality, physical unitarity are met. Once these conditions are obeyed, the theory can be tested experimentally.

This program can be realized in the case of the nonlinear sigma model. This is achieved if one looks at the fields as parameters of a gauge field of zero strength (flat connection).

In this important example, some technical items are developed which will be useful in other more complex models (e.g. massive Yang-Mills theory) as local functional equations, hierarchy, weak power-counting.

The final result is a model depending on two parameters: the v.e.v. of the spontaneous breakdown of symmetry and the scale of the radiative corrections.

The subtraction of the divergences is performed in dimensional regularization by minimal subtraction on the properly normalized 1-PI amplitudes.

1 Introduction

The Standard Model, as a quantum field theory, relies on two solid pillars: the absence of anomalies and the power-counting renormalizability (PCR). The first guarantees the validity of Slavnov- Taylor identity and consequently the physical unitarity of the model. PCR seems more a manifestation of the technical difficulty to deal with models containing interaction terms of dimension higher than four, but it implies the necessity of extra physical modes as the Higgs boson.

In a series of papers we investigated the possibility of constructing a consistent theory out of a non polynomial classical action [1) - 5)]. By "consistency" we mean a perturbation theory in $\hbar$ where divergences are removed by local counterterms order by order in a symmetric fashion, i.e. by preserving the defining equations and the invariance properties under the relevant local and global transformations on the fields. By "theory" we mean a calculation procedure which starts from a classical effective action depending on a finite number of parameters and where the radiative corrections are controlled by an extra mass scale and the physical unitarity is guaranteed. We stress that in our approach: i) no extra free parameters are introduced in connection with new divergent amplitudes and ii) predictivity is implied by the presence of a finite number of free parameters.

By our approach we abandon the view of renormalization as a replacement of the bare parameters of the Lagrangian in favor of the physical ones. We look at the removal of the divergences as a pure mathematical problem: if a procedure exists that respects all the requirements listed above, than we have a consistent theory. The question of uniqueness of the procedure might be posed, but we shall not discuss this item here.

We apply this approach to the nonlinear sigma model. A quantum field theory based on the Feynman rules of the nonlinear sigma model is plagued not only by the presence of an infinite number of superficially divergent amplitudes but also by the fact that the divergences are not chiral invariant. These difficulties are present already at the one loop level, as has been widely discussed in the existing literature [6)- 13)].

We can go through successfully with our program in the case of the nonlinear sigma model, because the pion fields can be seen as parameters of a gauge field of zero strength (flat connection). Within this formulation one can

use the powerful methods of the gauge theories. In particular a local functional equation for the generating functional of the 1 PI amplitudes [1] can be introduced in order to define the model itself. The equation stems from the invariance under local chiral (left) transformations of the Haar measure in the path integral. This formulation overcomes the difficulty due to the lack of chiral symmetry of the divergences. The subtraction of the divergences is performed in dimensional regularization by using minimal subtraction on the properly normalized 1-PI amplitudes. In the present work we discuss this subtraction procedure and compare it with algebraic renormalization [14]-[17] and with effective field theory approach [18].

The construction of the perturbative series starts from the Feynman rules of the nonlinear sigma model. The radiative corrections are regularized by continuation in the dimensions. The strategy by which the divergences are removed in the limit $D = 4$ makes use of two important properties of the functional equation, that are duly discussed in Ref. [1], [2] and [3]: i) hierarchy and ii) Weak Power Counting (WPC). As summarized in Section 2 the functional equation has a rigid hierarchy structure in the loop expansion: all amplitudes involving the pion fields (descendant amplitudes) are derived from those involving only insertions of the flat connection ($F_{a\mu}$) and the order parameter (the constraint ϕ_0), the ancestor amplitudes. The important consequence of this fact comes from the second property: the WPC. At each order of the loop expansion the number of divergent ancestor amplitudes is finite, since the superficial divergence of a graph is (N_J and N_K are the number of flat connection and order parameter insertions)

$$(D-2)n + 2 - N_J - 2N_{K_0}. \tag{1}$$

Thus at each loop order all amplitudes are made finite by a finite number of subtractions. Moreover WPC remains valid only if one does not introduce terms of higher dimensions in the tree-level Feynman rules. These facts suggest our subtraction strategy: if one finds a way to perform subtractions without introducing free parameters for higher dimensions counterterms in the tree level Feynman rules, then one gets a consistent theory with a finite number of physical parameters. The subtraction strategy is suggested by the functional equation itself. The violation of the equation at $n-$th order, when the counterterms are introduced up to order $n-1$, has simple pole structure in $D-4$. Then minimal subtraction automatically restores the functional equation.

These subtraction rules are at variance not only with the fundamentals of algebraic renormalization, but also with the effective theory approach and with the strategy proposed by the renormalization in the 'modern' sense of [19]. In fact in the present approach the subtraction procedure is a fundamental part of the construction of the theory and in practical way it means that one cannot introduce new vertex Feynman rules in connection with counterterms. Thus the subtraction procedure we are proposing has some aspects that make it look as an *ad hoc* strategy in the choice both of the regularization method and of the counterterms. In this work we try to show that if one wants a (predictive) theory by starting from the tree level nonlinear sigma model, then our proposal is a consistent and sensible strategy.

The question whether this subtraction can be performed by means of other regularization schemes has been considered. Limited results have been achieved. By using the renormalized linear sigma model in the limit of large coupling constant one can get, after subtraction of divergent terms, the nonlinear sigma model we are proposing (one loop has been checked in ref. [20]). This requires a fine tuning in the finite subtractions and consequently there is no evidence for a particular advantageous choice in the finite subtraction as in dimensional regularization. In order to study this issue it is very useful to consider the most general solution allowed by the linearized homogeneous functional equation. At one loop this means seven arbitrary coefficients associated to the invariants reported in Sect. 5. The same pattern is present in other regularization procedures as Pauli-Villars.

The issue of the number of physical parameters in a theory which is not renormalizable by power-counting has been discussed several times in the recent literature. In [21] it has been proposed to introduce a framework for reducing [22] the infinite number of free parameters to a smaller, eventually finite, one. A similar strategy has been advocated in [23] in the context of Wilson's approach to renormalization [24].

In this paper we argue that the lore, by which an infinite number of experiments is required in order to fix the counterterms for a nonrenormalizable theory, stems from an inappropriate use of the point of view of the algebraic renormalization to theories that cannot be treated according to such a procedure.

In the case of the nonlinear sigma model the theory is defined through

the effective action Γ which has to obey a nonlinear local functional equation. At the one loop level the counterterms $\widehat{\Gamma}^{(1)}$ obey a linearized form of the same equation. These counterterms have a particular feature: they are not present in the vertex functional $\Gamma^{(0)}$ at the tree level. Some of them do not obey the *nonlinear* defining functional equation. Others modify in a substantial way the unperturbed space of states (by introducing ghost states associated to kinetic terms in $\Box^2$). Finally there are some that could be introduced in the vertex functional $\Gamma^{(0)}$ at the tree level, since they obey the defining local functional equation, but they would spoil the WPC. Thus the procedure of assigning free parameters to the counterterms is not viable.

We discuss also the possibility of assigning free parameters to the counterterms at the one loop level. We argue that this strategy is not sustainable from the physical point of view, since parameters should enter in the zero loop vertex functional $\Gamma^{(0)}$. We stress this fundamental point: the parameters of the classical action might differ from the physical parameters of the zero loop vertex functional. The presence of a vacuum state that induces a reshuffling of the perturbative expansion (spontaneous symmetry breaking) is one example where such a distinction is essential.

After we have excluded free parameters in association to the counterterms, the question remains of the number of independent parameters. One parameter is present in $\Gamma^{(0)}$; for instance, the vacuum expectation value of ϕ_0. However an extra mass parameter can be introduced in order to perform dimensional subtraction. We argue that this parameter has the very important role of fixing the scale of the radiative corrections. One can formulate the model in such a way that the dimensional subtraction scale appears as a front factor of the whole set of Feynman rules. The final consequence of this requirement is that our subtraction procedure yields a nonlinear sigma model depending on only two parameters, e.g. the v.e.v. of the spontaneous breakdown and the dimensional subtraction scale.

The present paper is devoted to a detailed illustration of the above mentioned facts and it is written in the spirit of a novel view on those nonrenormalizable theories that can be consistently subtracted (i.e. symmetrically and locally). The discussion is done at the one loop level, but the necessary tools for the extension at higher order are also provided. In particular we discuss the equation obeyed by the counterterms at any order in the loop expansion.

2 The Nonlinear Sigma Model

The D-dimensional classical action of the nonlinear sigma model in the flat connection formalism [1] is

$$\Gamma^{(0)} = \Lambda^{D-4} \int d^D x \, \frac{v^2}{8} \Big(F_a^\mu - J_a^\mu \Big)^2 + \int d^D x \, K_0 \phi_0 . \tag{2}$$

The flat connection is

$$\begin{aligned} F^\mu &= F_a^\mu \frac{1}{2} \tau_a = i \Omega \partial_\mu \Omega^\dagger \\ \Omega &= \frac{1}{v} (\phi_0 + i \tau_a \phi_a) \end{aligned} \tag{3}$$

where v is the v.e.v. of the order parameter field ϕ_0, $\vec{J}_\mu$ is the background connection and K_0 is the source of the constraint ϕ_0 of the nonlinear sigma model

$$\phi_0 = \sqrt{v^2 - \vec{\phi}^2} \, . \tag{4}$$

2.1 Divergences in the nonlinear Sigma Model

When one considers the perturbative solution in $\hbar$ of (2)

$$\begin{aligned} &\Lambda^{D-4} \int d^D x \, \frac{v^2}{8} \Big(F_a^\mu - J_a^\mu \Big)^2 + \int d^D x \, K_0 \phi_0 \\ &= \Lambda^{D-4} \int d^D x \left(\frac{1}{2} \partial_\mu \phi_a \partial^\mu \phi_a + \frac{1}{2} \frac{(\phi_b \partial^\mu \phi_b)(\phi_c \partial_\mu \phi_c)}{v^2 - \phi^2} \right), \end{aligned} \tag{5}$$

it is soon evident that the non polynomial interaction term gives rise to infinitely many divergent amplitudes already at one loop as in Fig. 1. Explicit calculations then show that the global chiral symmetry is broken by the divergent parts.

The usual approach to remove the divergences, by means of free parameters, fails to provide a theory for many reasons: i) one needs an infinite number of free parameters; ii) the new terms associated to the divergent amplitudes worsen the ultraviolet behavior of the tree level action; iii) the global chiral symmetry is broken. In one word: it is not a theory.

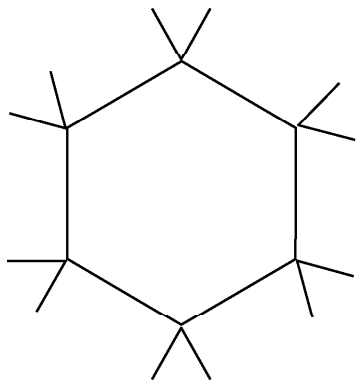

Figure 1: *Example of divergent 1-loop graph.*

2.2 Flat Connection Approach

The formulation of the nonlinear sigma model formulated in terms of a flat connection $F_\mu = i\Omega\partial_\mu\Omega^\dagger$ allows us to use the methods of local gauge theories. The path integral measure $\mathcal{D}[\phi]\delta(\phi_0^2 + \vec{\phi}^2 - v^2)$ is invariant under local chiral transformations induced by left multiplication on Ω by SU(2) matrices

$$U(\omega) \simeq 1 + \frac{i}{2}\tau_a\omega_a. \tag{6}$$

Then $\Gamma^{(0)}$ obeys a D-dimensional local functional equation associated to the local chiral transformations. This equation is required to be valid for the effective action on the basis of a path integral formulation of the model

$$-\partial^\mu\frac{\delta\Gamma}{\delta J_a^\mu} - \epsilon_{abc}J_b^\mu\frac{\delta\Gamma}{\delta J_c^\mu} + \frac{1}{2}\epsilon_{abc}\phi_c\frac{\delta\Gamma}{\delta\phi_b} + \frac{1}{2}\phi_a K_0 + \frac{1}{2}\frac{\delta\Gamma}{\delta K_0}\frac{\delta\Gamma}{\delta\phi_a} = 0\,. \tag{7}$$

The equation is local (no x-integration). The generating functional of the Green functions obeys the corresponding equation

$$\Big(\partial^\mu\frac{\delta}{\delta J_a^\mu} + \epsilon_{abc}J_b^\mu\frac{\delta}{\delta J_c^\mu} + \frac{1}{2}\epsilon_{abc}K_b\frac{\delta}{\delta K_c} - \frac{1}{2}K_0\frac{\delta}{\delta K_a} + \frac{1}{2}K_a\frac{\delta}{\delta K_0}\Big)Z = 0. \tag{8}$$

The spontaneous breakdown of the global chiral symmetry is fixed by the boundary condition

$$\frac{\delta\Gamma}{\delta K_0}\bigg|_{\vec{\phi}=\vec{J}_\mu=K_0=0} = v. \tag{9}$$

It will be required that these equations ((7), (8)and (9)) remain valid also for the subtracted amplitudes (symmetric subtraction).

The tree level amplitudes are fixed by the conditions

$$\begin{aligned}
&\frac{\delta^2\Gamma^{(0)}}{\delta J_a^\mu(x)\delta J_b^\nu(y)} = \frac{v^2\Lambda^{D-4}}{4} g_{\mu\nu}\delta_{ab}\delta_D(x-y) \\
&\frac{\delta^2\Gamma^{(0)}}{\delta K_0(x)\delta K_0(y)} = 0 \\
&\frac{\delta^2\Gamma^{(0)}}{\delta K_0(x)\delta J_b^\nu(y)} = 0.
\end{aligned} \tag{10}$$

The naïve Feynman rules in D dimensions given implicitly in eq. (5) yield amplitudes that solve eqs. (7) and (8) at any order of the perturbative expansion. This property has been conjectured in ref. [1] and proved in ref. [4].

3 Hierarchy

The non linearity of the equation (7) is responsible for many peculiar facts. In particular by eq.(9) $\frac{\delta\Gamma}{\delta K_0}$ is invertible as a formal power series. Therefore by using eq.(7) all amplitudes involving the $\vec{\phi}$ fields (descendants) can be derived from those of $\vec{F}_\mu$ and ϕ_0 (ancestors), i.e. the functional derivatives with respect to $\vec{J}_\mu$ and K_0 (hierarchy).

Hierarchy is very important for the procedure of divergences subtraction. First of all one needs to make finite only the ancestor amplitudes. The subtraction of the divergences for the descendant amplitudes will follows automatically, since the lasts are functions of the previouses. Second, one can try to exploit the properties of the eq. (7), e.g. symmetries, in order to devise the counterterms as functionals of the ancestor variables $\vec{J}_\mu, K_0$, where the $\vec{\phi}$ can be introduced in agreement with the results of hierarchy. This amounts to integrate functionally eq. (7) as done in Ref. [5].

4 Weak Power-Counting

Hierarchy reduces drastically the number of independent divergent amplitudes. According to the Feynman rules provided by eq. (5) the superficial degree of divergence of a n_L-th loop amplitude involving N_J insertions of the flat

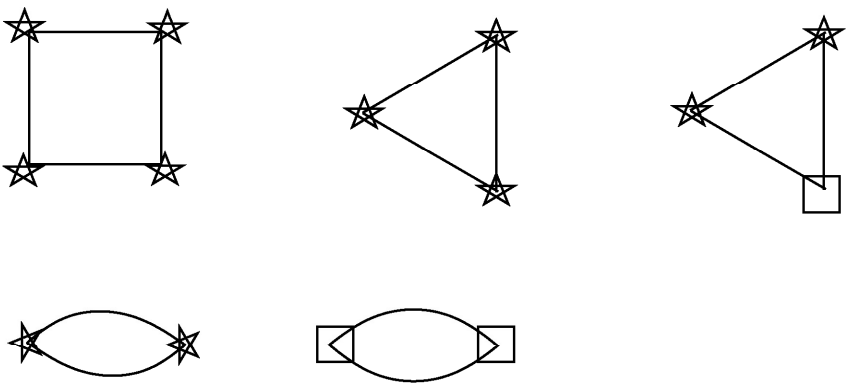

Figure 2: *Ancestor divergent 1-loop graphs. Stars are* $\vec{J}_\mu$ *and boxes are* K_0.

connection and N_{K_0} insertions of the nonlinear sigma model constraint is

$$\delta = (D-2)n_L + 2 - N_J - 2N_{K_0}\,. \tag{11}$$

For instance at one loop the ancestor divergent graphs are those depicted in Fig. 2.

The proof of eq. (11) is straightforward in D dimensions and without counterterms. The crucial question is whether this relation is still valid after the introduction of the counterterms necessary in order to take the limit $D = 4$. Details will not be given here. However we can argue that the relation in eq. (11) is not modified by our subtraction procedure, since the divergences are not removed by renormalization of novel free parameters in the tree level effective action. Instead the counterterms are subtraction rules at the appropriate $\hbar$ order. It can be verified that this fact does not alter eq.(11) since the worsened ultraviolet behavior of the counterterms is exactly compensated by the corresponding reduced number of loops in order to get the given power of $\hbar$. By this argument the finger-counting of the superficial degree of divergence as in eq. (11) becomes a theorem: the power-counting is stable under the subtraction procedure.

5 Subtraction of Divergences at $D = 4$

Subtractions at $D = 4$ are performed in dimensional regularization. The procedure can be better described if the external source K_0 has a canonical dimension

independent of D. The effective action (2) at the tree level takes the form

$$\Gamma^{(0)} = \Lambda^{D-4} \int d^D x \left(\frac{v^2}{8} \left(F_a^\mu - J_a^\mu \right)^2 + K_0 \phi_0 \right). \tag{12}$$

Eqs. (7), (8) and (9) are accordingly modified. For instance

$$-\partial^\mu \frac{\delta \Gamma}{\delta J_a^\mu} - \epsilon_{abc} J_b^\mu \frac{\delta \Gamma}{\delta J_c^\mu} + \frac{1}{2} \epsilon_{abc} \phi_c \frac{\delta \Gamma}{\delta \phi_b} + \frac{1}{2} \Lambda^{D-4} \phi_a K_0 + \frac{1}{2\Lambda^{D-4}} \frac{\delta \Gamma}{\delta K_0} \frac{\delta \Gamma}{\delta \phi_a} = 0 \tag{13}$$

and

$$\left. \frac{\delta \Gamma}{\delta K_0} \right|_{\vec{\phi} = \vec{J}_\mu = K_0 = 0} = v \Lambda^{D-4}. \tag{14}$$

The counterterms $\mathcal{M}^{(j)}$ will be introduced as local functionals of $\vec{J}_\mu$, K_0 and $\vec{\phi}$ which now have canonical dimensions independent of D. The whole set of Feynman rules $\widehat{\Gamma}$ is then written in the form

$$\widehat{\Gamma} = \Lambda^{D-4} \int d^D x \left(\frac{v^2}{8} \left(F_a^\mu - J_a^\mu \right)^2 + K_0 \phi_0 + \sum_{j>0} \mathcal{M}^{(j)} \right) \tag{15}$$

where j denotes the order $\hbar^j$. The dependence on D is confined in the prefactor Λ^{D-4}. Our *Ansatz* on the subtraction procedure is on the form of $\mathcal{M}^{(j)}$: they contain only pole parts in $D-4$. No finite parts are introduced, since these cannot be fixed *a priori*. As a consequence of the *Ansatz* the pole parts $\mathcal{M}^{(j)}$ at order j are given by the Laurent expansion of

$$-\frac{1}{\Lambda^{D-4}} \Gamma^{(j)} \tag{16}$$

where $\Gamma^{(j)}$ is collection of the 1-PI amplitudes at order j after all the counterterms have been introduced up to order $j-1$.

Whether this subtraction procedure is consistent with the defining equations (13) and (14) is a highly non trivial question.

5.1 Subtraction at one Loop

At one loop level the counterterms (obtainable from the pole parts of the vertex functional $\Gamma^{(1)}$) obey a linearized form of the local equation eq.(13)

$$\mathcal{S}_a(\widehat{\Gamma}^{(1)}) = \Big[\frac{1}{2\Lambda^{D-4}} \frac{\delta \Gamma^{(0)}}{\delta \phi_a} \frac{\delta}{\delta K_0} + \frac{1}{2} \phi_0 \frac{\delta}{\delta \phi_a} + \frac{1}{2} \epsilon_{abc} \phi_c \frac{\delta}{\delta \phi_b}$$
$$-\partial^\mu \frac{\delta}{\delta J_a^\mu} - \epsilon_{abc} J_b^\mu \frac{\delta}{\delta J_c^\mu} \Big] \widehat{\Gamma}^{(1)} = 0 \,. \tag{17}$$

It is easy to trace in eq. (17) the transformations induced through the dependence on $\vec{J}_\mu$ and $\vec{\phi}$.

5.2 Subtraction at n-Loops

The proof for any order in $\hbar$ has been given in Reference [4]. We outline some of the steps of the proof since they are illuminating for our subtracting strategy.

One can give a diagrammatic proof of the following relation between the local functional equation (8) for the generating functional Z and the equation for the counterterms (quantum action principle).

$$\Big(-\partial^\mu \frac{\delta}{\delta J_a^\mu} - \epsilon_{abc} J_b^\mu \frac{\delta}{\delta J_c^\mu} + \frac{\Lambda^{D-4}}{2} K_0 \frac{\delta}{\delta K_a} - \frac{1}{2\Lambda^{D-4}} K_a \frac{\delta}{\delta K_0} - \frac{1}{2} \epsilon_{abc} K_b \frac{\delta}{\delta K_c} \Big) Z$$
$$= i \Big(-\partial^\mu \frac{\delta \widehat{\Gamma}}{\delta J_a^\mu} - \epsilon_{abc} J_b^\mu \frac{\delta \widehat{\Gamma}}{\delta J_c^\mu} - \frac{\Lambda^{D-4}}{2} K_0 \phi_a + \frac{1}{2\Lambda^{D-4}} \frac{\delta \widehat{\Gamma}}{\delta K_0} \frac{\delta \widehat{\Gamma}}{\delta \phi_a} + \frac{1}{2} \epsilon_{abc} \phi_c \frac{\delta \widehat{\Gamma}}{\delta \phi_b} \Big)$$

where the dot indicates the insertion of the local operators, i.e. operators to be put inside the path-integral. Since the L.H.S. is zero by eq. (8) we can generalize the condition (17) for the counterterms to

$$\mathcal{S}_a(\widehat{\Gamma}^{(n)}) = \Big[\frac{1}{2\Lambda^{D-4}} \frac{\delta \Gamma^{(0)}}{\delta \phi_a} \frac{\delta}{\delta K_0} + \frac{1}{2} \phi_0 \frac{\delta}{\delta \phi_a} + \frac{1}{2} \epsilon_{abc} \phi_c \frac{\delta}{\delta \phi_b}$$
$$- \partial^\mu \frac{\delta}{\delta J_a^\mu} - \epsilon_{abc} J_b^\mu \frac{\delta}{\delta J_c^\mu} \Big] \widehat{\Gamma}^{(n)} = - \frac{1}{2\Lambda^{D-4}} \sum_{j=1}^{n-1} \frac{\delta \widehat{\Gamma}^{(j)}}{\delta K_0} \frac{\delta \widehat{\Gamma}^{(n-j)}}{\delta \phi_a} \,. \qquad (19)$$

The above equation is the key point of the subtraction procedure. Assume that counterterms have been introduced up to order $n-1$. At order n eq. (13) is broken by the fact that the n-th order counterterm $\widehat{\Gamma}^{(n)}$ is absent. Thus we have

$$\Big(-\partial^\mu \frac{\delta}{\delta J_a^\mu} - \epsilon_{abc} J_b^\mu \frac{\delta}{\delta J_c^\mu} + \frac{1}{2} \epsilon_{abc} \phi_c \frac{\delta}{\delta \phi_b} + \frac{1}{2} \phi_0 \frac{\delta}{\delta \phi_a}$$
$$+ \frac{1}{2\Lambda^{(D-4)}} \frac{\delta \Gamma^{(0)}}{\delta \phi_a} \frac{\delta}{\delta K_0} \Big) \Gamma^{(n)} + \frac{1}{2\Lambda^{(D-4)}} \sum_{j=1}^{n-1} \frac{\delta}{\delta K_0} \Gamma^{(n-j)} \frac{\delta}{\delta \phi_a} \Gamma^{(j)}$$
$$= \frac{1}{2\Lambda^{(D-4)}} \sum_{j=1}^{n-1} \frac{\delta}{\delta K_0} \widehat{\Gamma}^{(n-j)} \frac{\delta}{\delta \phi_a} \widehat{\Gamma}^{(j)} . \qquad (20)$$

The above equation is the origin of our subtraction procedure. If one divides both members by $\Lambda^{(D-4)}$ the R.H.S. contains only pole parts according to the *Ansatz* in eq. (15) (no finite parts are left over). Thus removing only the pole parts in both members divided by $\Lambda^{(D-4)}$ reestablishes the local functional equation (13).

It should be stressed that the prescription of removing the poles from $\Lambda^{(4-D)}\Gamma^{(n)}$ is a well defined choice on the finite parts. This choice depends on the value of Λ, which becomes a free parameter of the theory. For $n > 0$ the subtracted effective action is

$$\begin{aligned}\Gamma^{(n)} + \widehat{\Gamma}^{(n)} &\equiv \left(\Gamma^{(n)} + \Lambda^{(D-4)} \int d^D x \mathcal{M}^{(n)}(x)\right)\Big|_{D=4} \\ &= \Lambda^{(D-4)}\left(\frac{1}{\Lambda^{(D-4)}}\Gamma^{(n)} + \int d^D x \mathcal{M}^{(n)}(x)\right)\Big|_{D=4} \\ &= \left(\frac{1}{\Lambda^{(D-4)}}\Gamma^{(n)} + \int d^D x \mathcal{M}^{(n)}(x)\right)\Big|_{D=4} \end{aligned} \tag{21}$$

6 One Loop invariants

It is very interesting how the hierarchy is implemented in the counterterms. Since the counterterms obey the eq. (19), in the one loop case one has to find all local independent solutions of the linearized eq. (17). The invariants must have dimension 4 in order to meet the condition $\delta \geq 0$ in eq. (11).

For sake of simplicity, instead of $\mathcal{S}_a$ of eq.(17) we use the operator [2)]

$$\begin{aligned} s \equiv \int d^D x\, \omega_a \mathcal{S}_a = \int d^D x \Big[\frac{1}{2}\Big(\omega_a \phi_0 + \epsilon_{ajk}\phi_j \omega_k\Big)\frac{\delta}{\delta \phi_a} \\ + \frac{1}{2\Lambda^{D-4}}\omega_a \frac{\delta \Gamma^{(0)}}{\delta \phi_a}\frac{\delta}{\delta K_0} + \Big(\partial^\mu \omega_a + \epsilon_{aij} J_i^\mu \omega_j\Big)\frac{\delta}{\delta J_a^\mu}\Big] \end{aligned} \tag{22}$$

and consider the Legendre transform

$$K_a \equiv -\frac{\delta}{\delta \phi_a}\Gamma^{(0)}. \tag{23}$$

Then we use following identities

$$\begin{aligned} s\ \Gamma^{(0)} &= -\int d^D y\, \omega_a \frac{1}{2}\Big(\phi_0 K_a - \Lambda^{D-4}\phi_a K_0\Big) \\ [\frac{\delta}{\delta \phi_a(x)}, s] &= \omega_k(x)\frac{1}{2}\Big(-\delta_{kb}\frac{\phi_a(x)}{\phi_0(x)} + \epsilon_{bak}\Big)\frac{\delta}{\delta \phi_b(x)} \end{aligned}$$

$$-\frac{1}{2\Lambda^{D-4}}\int d^D y \omega_b(y)\frac{\delta K_b(y)}{\delta\phi_a(x)}\frac{\delta}{\delta K_0(y)} \tag{24}$$

and one gets

$$\begin{aligned}
& s\ K_a(x) = -s\ \frac{\delta}{\delta\phi_a}\Gamma^{(0)} = [\frac{\delta}{\delta\phi_a(x)}, s]\Gamma^{(0)} - \frac{\delta}{\delta\phi_a(x)}\ s\ \Gamma^{(0)} \\
& = -\omega_k(x)\frac{1}{2}\left(-\delta_{kb}\frac{\phi_a(x)}{\phi_0(x)} + \epsilon_{bak}\right)K_b(x) \\
& -\frac{1}{2}\omega_b(x)\frac{\delta K_b(y)}{\delta\phi_a(x)}\phi_0(x) \\
& +\omega_b(x)\frac{1}{2}\left(-\frac{\phi_a(x)}{\phi_0(x)}K_b + \phi_0\frac{\delta K_b(y)}{\delta\phi_a(x)} + \Lambda^{D-4}\delta_{ab}K_0\right) \\
& = \frac{1}{2}\epsilon_{abk}\omega_k K_b + \frac{1}{2}\Lambda^{D-4}\omega_a K_0
\end{aligned} \tag{25}$$

and

$$s\ K_0 = -\frac{1}{2\Lambda^{D-4}}\omega_a K_a. \tag{26}$$

Then

$$\begin{aligned}
& \overline{K}_0 \equiv K_0\phi_0 + \frac{1}{\Lambda^{D-4}}K_a\phi_a \\
& = K_0\phi_0 - v^2\phi_a\frac{\partial}{\partial\phi_a}(\vec{F}_\mu - \vec{J}_\mu)^2 + \frac{K_0}{\phi_0}\phi_a\phi_a \\
& = \frac{v^2 K_0}{\phi_0} - v^2\phi_a\frac{\partial}{\partial\phi_a}(\vec{F}_\mu - \vec{J}_\mu)^2
\end{aligned} \tag{27}$$

is invariant under s:

$$s\ \overline{K}_0 = 0. \tag{28}$$

6.1 The Role of Global $SU(2)_R$ Symmetry

Other invariants can be obtained by using *bleached* variables [5]. One constructs the bleached variables by means of the transformation properties of $\vec{J}_\mu$ and Ω under the operator s of eq. (22). Accordingly the following variables

$$\left[\Omega^\dagger\left(J_\mu - i\Omega\partial_\mu\Omega^\dagger\right)\Omega\right]_{ab} \tag{29}$$

are invariant under s-transformations for any a and b, where a, b are right-indices. The same is true for any point derivative of the above operators. Notice that

$$\begin{aligned}
&\partial_\nu \left[\Omega^\dagger \left(J_\mu - i\Omega\partial_\mu\Omega^\dagger\right)\Omega\right]_{ab} \\
&= \left\{\Omega^\dagger\left[-iF_\nu\left(J_\mu - F_\mu\right) + \partial_\nu\left(J_\mu - F_\mu\right) + i\left(J_\mu - F_\mu\right)F_\nu\right]\Omega\right\}_{ab} \\
&= \left\{\Omega^\dagger D_\nu[F]\left(J_\mu - F_\mu\right)\Omega\right\}_{ab} \qquad (30)
\end{aligned}$$

The invariant solutions can be obtained from monomial constructed in terms of the invariant variables in eqs. (27), (29) and (30). The $SU(2)_R$ indices have to be saturated. The invariant solutions of the linearized functional equation which enter at the one loop level are of dimension four. We list here the basis obtained in Reference [2] by using the component notation.

$$\begin{aligned}
\mathcal{I}_1 &= \int d^D x \left[D_\mu(F-J)_\nu\right]_a \left[D^\mu(F-J)^\nu\right]_a, \\
\mathcal{I}_2 &= \int d^D x \left[D_\mu(F-J)^\mu\right]_a \left[D_\nu(F-J)^\nu\right]_a, \\
\mathcal{I}_3 &= \int d^D x\, \epsilon_{abc}\left[D_\mu(F-J)_\nu\right]_a \left(F_b^\mu - J_b^\mu\right)\left(F_c^\nu - J_c^\nu\right), \\
\mathcal{I}_4 &= \int d^D x \left(\overline{K}_0\right)^2, \\
\mathcal{I}_5 &= \int d^D x \left(\overline{K}_0\right)\left(F_b^\mu - J_b^\mu\right)^2, \\
\mathcal{I}_6 &= \int d^D x \left(F_a^\mu - J_a^\mu\right)^2\left(F_b^\nu - J_b^\nu\right)^2, \\
\mathcal{I}_7 &= \int d^D x \left(F_a^\mu - J_a^\mu\right)\left(F_a^\nu - J_a^\nu\right)\left(F_{b\mu} - J_{b\mu}\right)\left(F_{b\nu} - J_{b\nu}\right), \qquad (31)
\end{aligned}$$

where D_μ denotes the covariant derivative w.r.t $F_{a\mu}$:

$$D_{ab\mu} = \delta_{ab}\partial_\mu + \epsilon_{acb}F_{c\mu}\,. \qquad (32)$$

In terms of ϕ fields the flat connection is

$$F_a^\mu = \frac{2}{v^2}\left(\phi_0\partial^\mu\phi_a - \partial^\mu\phi_0\phi_a + \epsilon_{abc}\partial^\mu\phi_b\phi_c\right). \qquad (33)$$

By dimensional arguments one expects that at one loop the counterterms (the $1/(D-4)$ pole parts) are linear combinations of $\mathcal{I}_1 \ldots \mathcal{I}_7$. In Ref. [2] the linear combination is explicitly evaluated, by using the ancestor graphs in Fig. 2. One gets

$$\hat{\Gamma}^{(1)} = \frac{\Lambda^{D-4}}{D-4}\Big[-\frac{1}{(4\pi)^2}\frac{1}{12}\Big(\mathcal{I}_1-\mathcal{I}_2-\mathcal{I}_3\Big)+\frac{1}{(4\pi)^2}\frac{1}{48}\Big(\mathcal{I}_6+2\mathcal{I}_7\Big) + \frac{1}{(4\pi)^2}\frac{3}{2}\mathcal{I}_4+\frac{1}{(4\pi)^2}\frac{1}{2}\mathcal{I}_5\Big]\,. \tag{34}$$

On dimensional grounds other solutions of eq.(17) are excluded, e.g.

$$\int d^D x \overline{K}_0. \tag{35}$$

The invariants $\mathcal{I}_1 \ldots \mathcal{I}_7$ implement the hierarchy for the counterterms. Their ϕ dependence through F_μ and ϕ_0 fixes completely all the counterterms for the descendant amplitudes at one loop level. There exists an identity which turns out to be interesting when one derives the descendant counterterms from $\hat{\Gamma}^{(1)}$. One verifies that

$$2(\mathcal{I}_1-\mathcal{I}_2)-4\mathcal{I}_3+\mathcal{I}_6-\mathcal{I}_7=\int d^D x\, G_{a\mu\nu}[J]G_a^{\mu\nu}[J]\,, \tag{36}$$

Since the field strength $G_a^{\mu\nu}[J]$ depends only on the field strength of the external source $J_{a\mu}$, this particular combination has no descendants.

7 Parameters Fixing

In this section we show that we cannot introduce at the tree level new Feynman vertices associated to the one-loop counterterms if we want to produce a sensible and consistent theory.

Minimal subtraction is of course a very interesting option in order to make finite the perturbative series. The proof, that this subtraction algorithm is symmetric (i.e. eq. (7) is stable), makes the procedure consistent. Thus this theory can be tested by experiments.

A frequent objection to the present proposal of making finite a nonrenormalizable theory is that one needs seven parameter-fixing appropriate measures in order to evaluate the coefficients of $\mathcal{I}_1 \ldots \mathcal{I}_7$. This objection is legitimate if the above mentioned invariants are action-like. As one should do in power

counting renormalizable theories, according to algebraic renormalization. Here the situation is more involved. This is evident if we paraphrase the problem in the following way. Can we introduce at the tree level the seven invariants with arbitrary coefficients and treat them as *bona fide* interaction terms intervening in the loop expansion as the original one provided in $\Gamma^{(0)}$ of eq. (2)? The answer to this question is in general negative. If one allows this modification of the unperturbed effective action, the one loop corrections will be modified by extra terms generated by the newly introduced Feynman rules, thus bringing to a never ending story.

In particular the introduction at tree level of the vertices described by the invariants in eq.(31) implies new Feynman rules which invalidate the weak power-counting [2]. The superficial degree of divergence of the ancestor amplitudes is not any more given by eq. (11). As a direct consequence of the violation of the weak power-counting, already at one loop the number of divergent ancestor amplitudes is infinite.

A closer look to $\mathcal{I}_1 \ldots \mathcal{I}_7$ shows that there are also other reasons that forbid the use of some of these invariants as unperturbed effective action terms. $\mathcal{I}_1, \mathcal{I}_2$ can be introduced into $\Gamma^{(0)}$ without breaking eq. (7). However they modify the spectrum of the unperturbed states (by introducing negative norm states) through kinetic terms with four derivatives, unless they appear in the combination $\mathcal{I}_1 - \mathcal{I}_2$. $\mathcal{I}_4, \mathcal{I}_5$ cannot be introduced into $\Gamma^{(0)}$ because they violate eq. (7).

8 Finite Subtractions

After we excluded the possibility of introducing in the tree level effective action the invariants $\mathcal{I}_1 \ldots \mathcal{I}_7$, there is still the possibility to use them for a finite, in principle arbitrary, renormalization. I.e. in the book keeping of the Feynman rules one could enter new terms

$$\hbar \sum_j \lambda_j \int d^D x \, \mathcal{I}_j(x) \,, \tag{37}$$

where we have explicitly exhibited the $\hbar$ factor in order to remind that these vertices are of first order in $\hbar$ expansion. λ_j are arbitrary real parameters.

More explicitly we can tell the story in the following way. The subtraction of the poles in $D-4$ requires a series of counterterms of the form (37) where

the coefficients carry the pole factor $1/(D-4)$. Then it seems reasonable to use these extra degrees of freedom as free parameters.

In the PCR case the fixing of the finite parts of the symmetric counterterms can be seen as a way to introduce the renormalization by a reset of the parameters entering into the classical action. The situation is clearly different in the present case, since the invariants $\mathcal{I}_1, \ldots, \mathcal{I}_7$ are not action-like and therefore the additional parameters λ_j can be introduced only as quantum corrections.

The meaning of this latter procedure, outside an effective field theory approach [18], seems to us rather unclear from the physical point of view, since independent parameters are used in the radiative corrections.

The alternative approach (which we favor) is to assume that symmetrically subtracted theories (and not only PCR theories) should obey the principle ruling PCR models, namely that parameters have to be introduced *ab initio* in the vertex functional $\Gamma^{(0)}$ at the tree level.

9 Minimal Subtraction vs. Effective Field Theory Approach

The above discussion illustrates the fact that we face an antinomy. From a mathematical point of view, finite subtractions as in eq. (37) are allowed and yield the most general solution to the subtraction procedure. From a physical point of view, free parameters as λ_j cannot be introduced in the radiative corrections.

In order to shed some light on this issue it is helpful to compare in some detail minimal subtraction with the effective field theory approach.

9.1 Minimal Subtraction

In minimal subtraction we use pure pole subtraction in order to make the theory finite in $D = 4$. Even with this clear cut strategy, still there is some freedom left connected to the presence of a second scale parameter in the Feynman rules in dimensional renormalization. The tree level effective action in eq. (12) has been written in order to evidence the dependence from the radiative scale parameter Λ.

The (non trivial) finite parts of the subtractions are governed by the sole front factor $\Lambda^{-(D-4)}$ in eq. (12). The resulting amplitudes depend on the

parameters v and Λ. The last one is not present in the classical action at $D = 4$: it sneaks in as a scale of the radiative corrections.

A similar mechanism has a renowned antecedent in the theory of Lamb shift [25], where the radiative corrections due to the excited state transitions need a ultraviolet cut-off which is not present at the lowest level of the theory of the Hydrogen atom.

A comment is in order here. In PCR theories the free parameters in the classical action can be fixed by a set of normalization conditions at a given mass scale Λ. Moreover, a shift in Λ is reabsorbed by a shift in the same free parameters entering into the classical action (renormalization group).

On the contrary in the NLSM a shift in Λ cannot be compensated by a shift in v. Therefore Λ has to be treated as a second independent free parameter (in addition to v) to be determined through the fit with the experimental data.

9.2 Effective field theory approach

The subtraction scheme based on minimal subtraction is symmetric and fulfills the WPC. Moreover from the above discussion it turns out that it admits only two physical parameters, both of them entering in the tree level D-dimensional vertex functional fixing the tree-level Feynman rules.

In addition this scheme fulfills weak independence on the regularization, namely the Green functions of minimal subtraction can be reproduced in any symmetric regularization by a fine-tuning of the coefficients of the relevant invariants $\mathcal{I}_j$. This follows since the WPC is regularization-independent.

As such, minimal subtraction looks like a viable proposal for making the theory finite in $D = 4$.

Let us compare it with the effective field theory approach. In this latter case the coefficients of the invariants $\mathcal{I}_j$ are considered as independent free parameters to be fixed by a suitable set of normalization conditions. Since the number of invariants $\mathcal{I}_j$ allowed by the WPC increases with the number of loops, there are infinitely many normalization conditions to be given (effective field theory).

In the effective field theory approach strong independence on the regularization holds: in fact the results of any symmetric regularization, in the presence of whatever choice of normalization conditions, can be reproduced in a different symmetric regularization scheme by a fine-tuning of the coefficients of

the relevant invariants $\mathcal{I}_j$. The equivalence of arbitrary regularizations requires to make full use of the infinite number of free parameters (with the prescribed grading in $\hbar$) mathematically allowed by the subtraction procedure and the functional equation.

It is clear that the effective field theory approach is incompatible with minimal subtraction. In fact in the latter only two free parameters are at disposal, and hence the infinite set of normalization conditions which have to be fixed according to the effective approach cannot be reproduced.

10 Conclusions

In this work we have outlined a new approach to nonrenormalizable field theories. One abandons the point of view of algebraic renormalization where each independent divergent amplitude necessitates of a free parameter in the effective action at the tree level. Instead one looks for a subtraction procedure, where the number of free parameters is finite and which is respectful of the relevant properties of model, as defining equations, locality of the counterterms, symmetry properties and physical unitarity (symmetric subtraction). We have examined the $SU(2)$ nonlinear sigma model, where the fields are parameters of a gauge field with zero strength (flat connection). The invariance of the path integral measure under local left $SU(2)$ transformations gives a local functional equation that contains all the properties for a symmetric subtraction of the divergences. One is hierarchy among the 1-PI amplitudes where the ancestors determine completely the descendants, i.e. those containing at least one chiral field. The ancestor variables are the flat connection and the constrained field. The second important property is the weak power-counting theorem for the ancestor amplitudes: at each order in $\hbar$ the number of independent superficially divergent amplitudes is finite. This properties suggests the strategy of removal of the divergences, which consists in the minimal subtraction of the poles in $D-4$ of the properly normalized amplitudes. The procedure is consistent: the local functional equation, locality of counterterms, symmetry properties are not modified by the counterterms. The strategy has been recently applied to the massive Yang-Mills theory [26].

The final output of this method of removing the divergences is a computation strategy where only a finite number of free parameters appear. In the case of the nonlinear sigma model they are the v.e.v. of the order parameter

field in the tree level effective action and the scale of the radiative corrections which enters through the dimensional regularization.

We have briefly argued that algebraic renormalization cannot be used both because the number of free parameters is infinite and because the counterterms of order n modify the superficial degree of divergence of the terms of order less or equal n.

Moreover we have avoided the possibility to introduce free parameters at any given order in $\hbar$, as it is done in effective field theory. This is possible from a mathematical point of view, since any local independent solution of the homogeneous equation can carry its own free parameter. However we have the prejudice that all parameters should be present in the tree level effective action. Radiative corrections are expected to modify the tree level amplitudes but not to introduce new degrees of freedom, with the exeption of the scale which naturally enters in the subtraction procedure.

11 Acknowledgments

One of us (R.F.) is very much indebted to A.A. Slavnov for stimulating discussions.

References

1. R. Ferrari, JHEP **0508** (2005) 048 [arXiv:hep-th/0504023].
2. R. Ferrari and A. Quadri, Int. J. Theor. Phys. **45** (2006) 2497 [arXiv:hep-th/0506220].
3. R. Ferrari and A. Quadri, JHEP **0601** (2006) 003 [arXiv:hep-th/0511032].
4. D. Bettinelli, R. Ferrari and A. Quadri, "A comment on the renormalization of the nonlinear sigma model," arXiv:hep-th/0701197.
5. D. Bettinelli, R. Ferrari and A. Quadri, JHEP **0703** (2007) 065 [arXiv:hep-th/0701212].
6. J. M. Charap, Phys. Rev. D **2** (1970) 1554.
7. J. M. Charap, Phys. Rev. D **3**, 1998 (1971).
8. J. Honerkamp and K. Meetz, Phys. Rev. D **3** (1971) 1996.

9. I. S. Gerstein, R. Jackiw, S. Weinberg and B. W. Lee, Phys. Rev. D **3** (1971) 2486.

10. G. Ecker and J. Honerkamp, Nucl. Phys. B **35** (1971) 481.

11. L. D. Faddeev and A. A. Slavnov, Lett. Nuovo Cimento **8** (1973) 117.

12. L. Tataru, Phys. Rev. D **12** (1975) 3351.

13. T. Appelquist and C. W. Bernard, Phys. Rev. D **23** (1981) 425.

14. K. Symanzik, Commun. Math. Phys. **16** (1970) 48.

15. O. Piguet and S. P. Sorella, Lect. Notes Phys. **M28**, 1 (1995).

16. R. Ferrari and P.A. Grassi, Phys. Rev. **D60**: 65010 (1999).

17. R. Ferrari, P.A. Grassi and A. Quadri, Phys. Lett. **B472**, 346-356 (2000).

18. J. Gasser and H. Leutwyler, Annals Phys. **158** (1984) 142; J. Gasser and H. Leutwyler, Nucl. Phys. B **250** (1985) 465.

19. J. Gomis and S. Weinberg, Nucl. Phys. B **469** (1996) 473 [arXiv:hep-th/9510087].

20. D. Bettinelli, R. Ferrari and A. Quadri, "The hierarchy principle and the large mass limit of the linear sigma model," [arXiv:hep-th/0611063], to appear in Int. J. Theor. Phys.

21. D. Anselmi, Class. Quant. Grav. **12** (1995) 319 [arXiv:hep-th/9407023]; Class. Quant. Grav. **20** (2003) 2355 [arXiv:hep-th/0212013]; JHEP **0507** (2005) 077 [arXiv:hep-th/0502237]; JHEP **0508** (2005) 029 [arXiv:hep-th/0503131]; D. Anselmi and M. Halat, JHEP **0601** (2006) 077 [arXiv:hep-th/0509196].

22. W. Zimmermann, Commun. Math. Phys. **97** (1985) 211.

23. J. Kubo and M. Nunami, Eur. Phys. J. C **26** (2003) 461 [arXiv:hep-th/0112032].

24. K. G. Wilson, Phys. Rev. B **4** (1971) 3174; Rev. Mod. Phys. **47** (1975) 773; K. G. Wilson and J. B. Kogut, Phys. Rept. **12** (1974) 75.

    P. Breitenlohner and D. Maison, Commun. Math. Phys. **52** (1977) 39; Commun. Math. Phys. **52** (1977) 55; Commun. Math. Phys. **52** (1977) 11.

25. H. A. Bethe, Phys. Rev. **72**, 339 (1947).

26. D. Bettinelli, R. Ferrari and A. Quadri, arXiv:0705.2339 [hep-th].

TOWARDS A SUPER-B FACTORY

Marcello Giorgi
Pisa, Italy

Written contribution not received

PROSPECTS OF HEP IN THE UNITED STATES

Clemens Heusch
Santa Cruz, USA

Written contribution not received

PHYSICS AND DETECTORS AT ILC

Michael Danilov
Moscow, Russia

Written contribution not received

SESSION VIII – PHYSICS AND SOCIETY [1]

- *Ari Aviram* — Nanotechnology - Control of Properties at the Molecular Level
- *Ennio Macchi* — Technologies and Plans to Produce "Clean Energy"
- *Emile Okal* — Tsunamis: A Physical link from Disaster to Prevention

[1] The original contributions can be found on the LaThuile website http://www.pi.infn.it/lathuile/

TSUNAMIS: A PHYSICAL LINK FROM DISASTER TO PREVENTION

Emile Okal
Evaston, USA

Written contribution not received

NANOTECHNOLOGY – CONTROL OF PROPERTIES AT THE MOLECULAR LEVEL

Ari Aviram
Qtronix, USA

Written contribution not received

TECHNOLOGIES AND PLANS TO PRODUCE "CLEAN ENERGY"

Ennio Macchi
Milano, Italy

Written contribution not received

PARTICIPANTS

Ahriche Amine	Bielefeld	Germany
Anisimov Alexey	Lausanne	Switzerland
Autiero Dario	Lyon	France
Aviram Ari	Qtronix	USA
Azzi Patrizia	Padova	Italy
Balev Spasimir	JINR	Russia
Behar Silvia	Haifa	Israel
Bellettini Giorgio	Pisa	Italy
Beringer Juerg	LBNL	USA
Bertolini Enzo	CORECOM	Italy
Bilokon Halina	LNF	Italy
Bondar Alexander	Novosibirsk	Russia
Boscherini Davide	Bologna	Italy
Brau Benjamin	Santa Barbara	USA
Castaldi Rino	Pisa	Italy
Castro Andrea	Bologna	Italy
Chiarelli Giorgio	Pisa	Italy
Ciuchini Marco	Roma	Italy
Coccia Eugenio	LNGS	Italy
Conrad Jan	Stockholm	Sweden
D'agostini Giulio	Roma	Italy
Danilov Michael	Moscow	Russia
Danko Istvan	New York	USA
Dar Arnon	Haifa	Israel
De Rujula Alvaro	CERN	Switzerland
De Simone Patrizia	LNF	Italy
De Wolf Els	Amsterdam	Netherlands
Diambrini-Palazzi Giordano	Roma	Italy
Dittmar Michael	Zurich	Switzerland
Dokuchaev Vyacheslav	Moscow	Russia

Dolgov Alexander	Ferrara	Italy
Eleftheriadis Christos	Thessaloniki	Greece
Ermolaev Boris	St. Petersburg	Russia
Evans Harold	Bloomington	USA
Ferrari Ruggero	Milano	Italy
Ferroni Fernando	Roma	Italy
Finley David	Fermilab	USA
Flugge Gunter	Aachen	Germany
Fratina Sasa	Ljubljana	Slovenia
Galtieri Angela	LBL	USA
Gervino Gianpiero	Torino	Italy
Giorgi Marcello	Pisa	Italy
Goulianos Konstantin	New York	USA
Greco Mario	Roma	Italy
Gross Eilam	Rehovot	Israel
Harder Kristian	RAL	UK
Hays Chris	Oxford	UK
Heusch Clemens	Santa Cruz	USA
Hung Pham Q.	Virginia	USA
Iacobucci Giuseppe	Bologna	Italy
Imperial Albino	Aosta	Italy
JÖnsson Leif	Lund	Sweden
Juste Aurelio	Fermilab	USA
Kazakov Dmitri	Moscow	Russia
Khoze Valeri	Durham	UK
Khuri Nicola	New York	USA
Kuhr Thomas	Karlsruhe	Germany
Lavagno Andrea	Torino	Italy
Leone Sandra	Pisa	Italy
Ligabue Franco	Pisa	Italy

Liuti Simonetta	Virginia	USA
Macchi Ennio	Milano	Italy
Mannocchi Giampaolo	Frascati	Italy
Marcellini Stefano	Bologna	Italy
Mariotti Mos	Padova	Italy
Mateev Matey	Sofia	Bulgaria
Mauger Christopher	Pasadena	USA
Meggiolaro Enrico	Pisa	Italy
Miele Gennaro	Napoli	Italy
Miglioranzi Silvia	DESY	Germany
Migneco Emilio	LNS	Italy
Fernandez Pedro	LBL	USA
Nishida Shohei	KEK	Japan
Novikov Victor	Moscow	Russia
Nunnemann Thomas	Garching	Germany
Okal Emile	Evaston	USA
Petronzio Roberto	Roma	Italy
Piacentini Francesco	Madrid	Spain
Piccinini Fulvio	Pavia	Italy
Picozza Piergiorgio	Roma	Italy
Piredda Giancarlo	Roma	Italy
Rama Matteo	LNF	Italy
Redlinger George	BNL	USA
Rescigno Marco	Roma	Italy
Rodriguez Frias Maria Dolores	Madrid	Spain
Rozen Yoram	Haifa	Israel
Ruspa Marta	Novara	Italy
Salto Oriol	Barcelona	USA
Santos Helena	Lisbon	Portugal
Saolidou Niki	Fermilab	USA
Schwanda Christoph	Vienna	Austria

Seo Seon-Hee	Philadelphia	USA
Spagnolo Paolo	Pisa	Italy
Stdenis Richard	Glasgow	UK
Studenikin Alexander	Moscow	Russia
Szwed Jerzy	Krakov	Poland
Tenchini Roberto	Pisa	Italy
Trinchero Gian Carlo	Torino	Italy
Truc Fabio	CORECOM	Italy
Venturiandrea	Pisa	Italy
Verde Licia	Philadelphia	USA
Vysotsky Mikhail	Moscow	Russia
Weber Michele	Fermilab	USA
Womersley John	RAL	UK
Yi Jong	Manchester	UK
Zarnecki Aleksander Filip	Warsaw	Poland

FRASCATI PHYSICS SERIES VOLUMES

Volume I
Heavy Quarks at Fixed Target
Eds.: S. Bianco and F.L. Fabbri
Frascati, May 31–June 2, 1993
ISBN—88–86409–00–1

Volume II – Special Issue
Les Rencontres de Physique de la Vallée d'Aoste – Results and Perspectives in Particle Physics
Ed.: M. Greco
La Thuile, Aosta Valley, March 5 –11, 1995
ISBN—88–86409–03–6

Volume III
Heavy Quarks at Fixed Target
Ed.: B. Cox
University of Virginia, Charlottesville
October 7–10, 1994, 11
ISBN—88–86409–04–4

Volume IV
Workshop on Physics and Detectors for DAΦNE
Eds.: R. Baldini, F. Bossi, G. Capon, G. Pancheri
Frascati, April 4–7, 1995
ISBN—88–86409–05–2

Volume V – Special Issue
Les Rencontres de Physique de la Vallée d'Aoste – Results and Perspectives in Particle Physics
Ed.: M. Greco
La Thuile, Aosta Valley, March 3–9, 1996
ISBN—88–86409–07–9

Volume VI
Calorimetry in High Energy Physics
Eds.: A. Antonelli, S. Bianco, A. Calcaterra, F.L. Fabbri
Frascati, June 8–14, 1996
ISBN—88–86409–10–9

Volume VII
Heavy Quarks at Fixed Target
Ed.: L. Kőpke
Rhinefels Castle, St. Goar, October 3–6, 1996
ISBN—88–86409–11–7

Volume VIII
ADONE a milestone on the particle way
Ed.: V. Valente 1997
ISBN—88–86409–12–5

Volume IX – Special Issue
Les Rencontres de Physique de la Vallée d'Aoste – Results and Perspectives in Particle Physics
Ed.: M. Greco
La Thuile, Aosta Valley, March 2–8, 1997
ISBN–88–86409–13–3

Volume X
Advanced ICFA Beam Dynamics
Workshop on Beam Dynamics Issue for e^+e^- Factories
Eds.: L. Palumbo, G. Vignola
Frascati, October 20–25, 1997
ISBN—88–86409–14–1

Volume XI
Proceedings of the XVIII International Conference on Physics in Collision
Eds.: S. Bianco, A. Calcaterra, P. De Simone, F. L. Fabbri
Frascati, June 17–19, 1998
ISBN—88–86409–15–X

Volume XII – Special Issue
Les Rencontres de Physique de la Vallée d'Aoste – Results and Perspectives in Particle Physics
Ed.: M. Greco
La Thuile, Aosta Valley, March 1–7, 1998
ISBN—88–86409–16–8

Volume XIII
Bruno Touschek and the Birth of thee$^+$ e$^-$
Ed.: G. Isidori
Frascati, 16 November, 1998
ISBN—88–86409–17–6

Volume XIV – Special Issue
Les Rencontres de Physique de la Vallée d'Aoste – Results and Perspectives in Particle Physics
Ed.: M. Greco
La Thuile, Aosta Valley, February 28–March 6, 1999
ISBN—88–86409–18–4

Volume XV
Workshop on Hadron Spectroscopy
Eds.: T. Bressani, A. Feliciello, A. Filippi
Frascati, March 8 2 1999
ISBN—88–86409–19–2

Volume XVI
Physics and Detectors for DAΦNE
Eds.: S. Bianco, F. Bossi, G. Capon, F.L. Fabbri, P. Gianotti, G. Isidori, F. Murtas
Frascati, November 16 –19, 1999
ISBN—88–86409–21–4

Volume XVII – Special Issue
Les Rencontres de Physique de la Vallée d'Aoste – Results and Perspectives in Particle Physics
Ed.: M. Greco
La Thuile, Aosta Valley, February 27 March 4, 2000
ISBN—88–86409–23–0

Volume XVIII
LNF Spring School
Ed.: G. Pancheri
Frascati 15–20 May, 2000
ISBN—88–86409–24–9

Volume XIX
XX Physics in Collision
Ed.: G. Barreira
Lisbon June 29–July1st. 2000
ISBN—88–86409–25–7

Volume XX
Heavy Quarks at Fixed Target
Eds.: I. Bediaga, J. Miranda, A. Reis
Rio de Janeiro, Brasil, October 9–12, 2000
ISBN—88–86409–26–5

Volume XXI
IX International Conference on Calorimetry in High Energy Physics
Eds.: B. Aubert, J. Colas, P. Nédélec, L. Poggioli
Annecy Le Vieux Cedex, France, October 9–14, 2000
ISBN—88–86409–27–3

Volume XXII – Special Issue
Les Rencontres de Physique de la Vallée d'Aoste – Results and Perspectives in Particle Physics
Ed.: M. Greco
La Thuile, Aosta Valley, March 4–10, 2001
ISBN—88–86409–28–1

Volume XXIII
XXI Physics in Collision
Ed.: Soo–Bong Kim
Seoul, Korea, June 28 30, 2001
ISBN—88–86409–30–3

Volume XXIV
International School of Space Science – 2001 Course on: Astroparticle and Gamma–ray Physics in Space
Eds.: A. Morselli, P. Picozza
L'Aquila, Italy, August 30 September 7, 2000
ISBN—88–86409–31–1

Volume XXV
TRDs for the 3rd Millennium Workshop on Advanced Transition Radiation Detectors for Accelerator and Space Applications
Eds. N. Giglietto, P. Spinelli
Bari, Italy, September 20–23, 2001
ISBN—88–86409–32–X

Volume XXVI
KAON 2001 International Conference on CP Violation
Eds.: F. Costantini, G. Isidori, M. Sozzi
Pisa Italy, June 12th 17th, 2001
ISBN—88–86409–33–8

Volume XXVII – Special Issue
Les Rencontres de Physique de la Vallée d'Aoste – Results and Perspectives in Particle Physics
Ed.: M. Greco
La Thuile, Aosta Valley, March 3–9, 2002
ISBN—88–86409–34–6

Volume XXVIII
Heavy Quarks at Leptons 2002
Eds.: G. Cataldi, F. Grancagnolo, R. Perrino, S. Spagnolo
Vietri sul mare (Italy), May 27th June 1st, 2002
ISBN—88–86409–35–4

Volume XXIX
Workshop on Radiation Dosimetry: Basic Technologies, Medical Applications, Environmental Applications
Ed.: A. Zanini
Rome (Italy), February 56, 2002
ISBN—88–86409–36–2

Volume XXIX – Suppl.
Workshop on Radiation Dosimetry: Basic Technologies, Medical Applications, Environmental Applications
Ed.: A. Zanini
Rome (Italy), February 56, 2002
ISBN—88–86409–36–2

Volume XXX – Special Issue
Les Rencontres de Physique de la Vallée d'Aoste – Results and Perspectives in Particle Physics
Ed.: M. Greco
La Thuile, Aosta Valley, March 9–15, 2003
ISBN—88–86409–39–9

Volume XXXI
Frontier Science 2002 – Charm, Beauty and CP, First International Workshop on Frontier Science
Eds.: L. Benussi, R. de Sangro, F.L. Fabbri, P. Valente
Frascati, October 6–11, 2002
ISBN—88–86409–37–0

Volume XXXII
19th International Conference on x–ray and Inner–Shell Processes
Eds.: A. Bianconi, A. Marcelli, N.L. Saini
Universitá di Roma La Sapienza June 24–28, 2002
ISBN—88–86409–39–07

Volume XXXIII
Bruno Touschek Memorial Lectures
Ed.: M. Greco, G. Pancheri
Frascati, May 11, 1987
ISBN—88–86409–40–0

Volume XXXIV – Special Issue
Les Rencontres de Physique de la Vallée d'Aoste – Results and Perspectives in Particle Physics
Ed.: M. Greco
La Thuile, Aosta Valley, February 29 – March 6, 2004
ISBN—88–86409–42–7

Volume XXXV
Heavy Quarks And Leptons 2004
Ed.: A. López
San Juan, Puerto Rico, 1–5 June 2004
ISBN—88–86409–43–5

Volume XXXVI
DAΦNE 2004: Physics At Meson Factories
Eds.: F. Anulli, M. Bertani, G. Capon, C. Curceanu–Petrascu,
F.L. Fabbri, S. Miscetti
Frascati, June 7–11, 2004
ISBN—88–86409–53–2

Volume XXXVII
Frontier Science 2004. Physics and Astrophysics in Space
Eds.: A. Morselli, P. Picozza, M. Ricci
Frascati, 14–19 June, 2004
ISBN—88–86409–52–4

Volume XXXVIII
II Workshop Italiano sulla Fisica di ATLAS e CMS
Eds.: Gianpaolo Carlino and Pierluigi Paolucci
Napoli, October 13 – 15, 2004
ISBN—88–86409–44–3

Volume XXXIX – Special Issue
Les Rencontres de Physique de la Vallée d'Aoste –
Results and Perspectives in Particle Physics
Ed.: M. Greco
La Thuile, Aosta Valley, February 27 – March 5, 2005
ISBN—88–86409–45–1

Volume XL
Frontier Science 2005 – New Frontiers in Subnuclear Physics
Eds.: A. Pullia, M. Paganoni
Milano, September 12 - 17, 2005
ISBN—88–86409–46–X

Volume XLI
Discoveries in Flavour Physics at e^+e^- Colliders
Eds.: L. Benussi, S. Bianco, C. Bloise, R. de Sangro, C. Gatti,
G. Isidori, M. Martini, F. Mescia, S. Miscetti
Frascati, February 28th - March 3rd, 2006
ISBN—88–86409–51–6

Volume XLII – Special Issue
Les Rencontres de Physique de la Vallée d'Aoste – Results and Perspectives in Particle Physics
Ed.: M. Greco
La Thuile, Aosta Valley, March 5 March 11, 2006
ISBN—88–86409–47–8

Volume XLIII
Neutral Kaon Interferometry at A Phi-Factory: from Quantum Mechanics to Quantum Gravity
Ed.: A. Di Domenico
Frascati, March 24th 2006
In Press